Copy No. 4

DEFENCE DÉFENSE

ABSTRACTS and SUMMARIES

of

8th CF/CRAD MEETING on NAVAL APPLICATIONS of MATERIALS TECHNOLOGY

11-13 May 1999

Compiled by
J.R. Matthews

DEFENCE RESEARCH ESTABLISHMENT ATLANTIC

Special Report
DREA SR1999-162
October 1999

National Defence Défense nationale

Canada

8th CF/CRAD Meeting on Naval Applications of Materials Technology

ABSTRACT

This was the eighth naval materials CF/CRAD (Canadian Forces/Chief Research and Development) meeting. These meetings have been held every two years since 1985. The first four meetings were devoted to fabrication and inspection of submarine pressure hulls with sessions on welding, inspection and fracture. The last four have expanded to include all aspects of naval materials.

The purpose of these meetings has been to bring together industrial research contractors, university contractors, defence scientists, and NDHQ (National Defence Headquarters) design authorities from the naval materials technology area and invited scientists and engineers from other countries to share advances in naval materials technology in a conference like setting.

The program includes Welding and Laser Surface Modification, Environmental Research, Corrosion and Coatings, Vibroacoustic Materials, Ship Fracture, Fatigue, Firesafe Materials, Non-Destructive Evaluation, Metallurgy and Failure Analysis, Organic Materials (Polymers), Fuels and Lubricants and Naval Consulting.

8^e réunion du CR Dev/Dés FC sur les applications de la technologie des matériaux au domaine naval

RÉSUMÉ

Le CR Dév/FC (Chef recherche et développement/Forces armées canadienne) a tenu sa huitième réunion sur les applications de la technologie des matériaux au domaine naval. Ces réunions ont lieu tous les deux ans depuis 1985. Les quatre premières rencontres ont porté sur la fabrication et l'inspection des coques épaisses de sous-marins. Elles comprenaient des ateliers sur la soudure, l'inspection et la rupture. Les thèmes des quatre plus récentes réunions couvraient tous les aspects des matériaux appliqués au domaine naval.

Ces réunions ont pour objet de rassembler des entrepreneurs spécialisés en recherche industrielle ou provenant du secteur universitaire, des scientifiques de la défense représentants du QGDN responsable de projets de conception dans le domaine de la technologie des matériaux appliqués au secteur naval ainsi que des scientifiques et des ingénieurs invités venus de l'étranger afin de leur permettre de partager leur savoir sur les progrès de la technologie des matériaux dans le cadre de rencontres de type conférence.

Les thèmes abordés au cours de la réunion portaient entre autres sur la soudure et la modification d'une surface au laser, la recherche en environnement, la corrosion et les revêtements, les matériaux vibro-acoustiques, la rupture de navires, la fatigue, les matériaux ignifuge, l'évaluation non-destructifs, la métallurgie et analyse des défaillances, les matériaux organiques (polymères), les carburants et lubrifiants et la consultation navale.

INDEX

8th CF/CRAD MEETING
on
NAVAL APPLICATIONS OF MATERIALS TECHNOLOGY

Park Center
Ramada Renaissance Hotel
Dartmouth N.S.
11th, 12th and 13th May 1999

Tuesday May 11th

Registration: 8:00 am

Welcome/Opening Remarks: 9:00

Capt(N) G.D. Humby
Commander, Fleet Maintenance Facility Cape Scott

SESSION I: Park Centre
Chairman: Dr. R. Morchat

page

1. The Materials and Welding Associated with the Construction of SSK Submarine Hulls, by A. Aitchison, Marconi Naval Systems, Barrow in Furness, England, and J. Bird, Directorate of Naval Architecture, MoD(PE), Bristol, England 1

2. UNIT Overview – An R&D Project to Improve the Way We Do NDT, Michel Brassard, Tektrend 15

3. Materials Selection for U.S. Navy Ships, by P.W. Holsberg and E.J. Czyryca, Naval Surface Warfare Center 27

SESSION II: Park Room
Chairman: Dr John Hiltz

4. Novel Materials for Improved Fire Safety of Naval Platforms, by D.E. Veinot, DREA 54

5. A Computational Study on Material Model Selection for Shape Memory Alloys, by Dr. V.G. DeGiorgi, Naval Research Laboratory, and H. Saleem, George Washington University 70

6. Welding Procedures for Welding HY80 Steel, C.J. Nicholson, L. Malik and D. Begg, Fleet, J.R. Matthews and V. Roy, DREA, and S.J. Dickout, NDHQ 83

7. **Investigation of Plastic Zone Development in Dynamic Tear Test Specimens, by T.S. Koko, Martec, and J.R. Matthews, V. Roy, and C.V. Hyatt, DREA** 100

8. **Brittle Bead Weld Selection for Crack Arrest Tests, by L.N. Pussegoda and L.Malik, Fleet, and J. Morrison, EDRD** 129

9. **Advanced Lithium Ion Super Polymer Rechargeable Batteries, by S. Das Gupta, J.K. Jacobs and D. Murdoch, Electrofuel Inc.** 139

Tuesday Evening, 11th May
RECEPTION and BANQUET
Roccos Italian Restaurant

Wednesday 12th May

SESSION III: Park Room A
Chairman: Dwight Veinot

10. **Is There an Effective and Environmentally Friendly Way to Control Microbiological Contamination in Distillate, by R.D. Haggett, DREA** 148

11. **Application of Ultraviolet Spectroscopy for Monitoring Oil in Water, by Clive MacGregor, Seatech Ltd., and Dwight Veinot, DREA** 164

12. **Effect of Particulate Size on Membrane Performance in Bilge Water Treatment Systems, by M. Nottegar and A.Y. Tremblay, University of Ottawa** 173

13. **Mineralogical Characterization of Airborne Industrial Pollutants, by Gary Fisher, DREA** 182

14. **Application of High-Frequency Pulsed Water Jets for the Removal of Marine Coatings, by M.M. Vijay, W. Yan and A. Tieu, VLN Advanced Technologies, and S. Pecman, NDHQ** 196

SESSION IV: Park Room B
Chairman: Dr. Calvin Hyatt

15. **Copper Nickel Chromium For Marine Applications, by J.C. Galsworthy, DERA Farnborough, and J. Bird, DNA, MoD, UK** 197

16. **Corrosion Problems with Copper-Nickel Components in Sea Water Systems, by D.R. Lenard and R.R. Welland, EDRD** 204

17. **Effect of Impurity Elements on the Mechanical Properties of Aluminum Bronze Alloy C95800, by M. Sadayappan, R. Zavadil and M. Sahoo, Materials Technology Lab, Ottawa** 221

18. **Chemical Analysis of Nickel Aluminum Bronze Alloys, by Gary Fisher, DREA** 235

19. **Characterization of a Nickel Aluminum Bronze Laser-Clad Weldment, by J.A. Gianetto and R.H. Packwood, MTL-CANMET** 243

SESSION V: Park Room A
Chairman: Dr. Calvin Hyatt

20. **The Development of Microstructure in the Laser Cladding of Nickel Aluminum Bronze, by C.V. Hyatt, DREA, J. Craig Bennett, Acadia Univ, and J. Gianetto, CANMET** 256

21. **Passivation of Laser-Treated Nickel Aluminum Bronze as Measured by Electrochemical Impedance Spectroscopy, by R.D. Klassen, RMC, C.V. Hyatt, DREA, and P.R. Roberge, RMC** 266

22. **Transmission Electron Microscopy of Laser Surface Melted Nickel Aluminum Bronze, by J.C Bennett, Acadia University, and C.V. Hyatt, DREA** 276

23. **Laser Cladding of Ni-Al Bronze for Repairing Marine Components, by L. Xue, and J.-Y. Chen, NRC, C.V. Hyatt, DREA, and M. Islam, NRC** 288

24. **Investigation of Cracked Propeller Blades on an Icebreaker, by L.N. Pussegoda and L. Malik, Fleet Technology Ltd.** 303

SESSION VI: Park Room B
Chairman: Ken KarisAllen

25. **Linear Elastic Fracture Toughness (KIc) and Dynamic Tear Transition, by V. Roy, DREA, Ken KarisAllen, FACTS, and J. R. Matthews, DREA** 312

26. **Dynamic and Static Fracture Toughness Measurement of Thin Marine Steels and Weldments, by Ken KarisAllen, FACTS, and J. R. Matthews, DREA** 335

27. **Fracture Properties of 350WT Steel at Very High Loading Rates, by M.N. Bassim, University of Manitoba, and J.R. Matthews, DREA** 344

28. **Critical Strain Energy Density from Tensile Specimens, G.R. Pelletier and J.R. Matthews, DREA** 355

29. **Fracture Toughness Transition Curves for a 350WT Plate, by Jack Morrison and J. Xiaozhu Wu, EDRD, and Al Hull, Engineering Materials Research, Downsview, ON** 373

Wednesday Evening 12th May
Bus Trip to Lunenburg
Guide: Dwight Veinot

Thursday 13th May

SESSION VII: Park Centre A
Chairman: Dr. Jeff Szabo

30. **Dynamic Mechanical Property Prediction by Group Contribution Analysis, by J.P. Szabo and J.C. Roberts, DREA** 385

31. **Failure Analysis of Polymeric Materials, by John A. Hiltz and Gary C. Fisher, DREA** 398

32. **Evaluation and Application of GRP Composite Fasteners for Sonar Dome Components, by T.S. Koko and K.D. MacKay, Martec, and G.V. Corbett, NDHQ** 422

33. **Inorganic Intumescent Filler for Polymer Composites, by J.O. Bernt, Bernt and Associates Ltd.** 432

34. **Reliability of Smart Composite Materials, by D.O. MacDonald, InNova, and A. Kalamkarov, A. Georgiades and S.B. Fitzgerald, DalTech** 436

SESSION XIII: Park Centre A
Chairman: Dr. Richard Morchat

35. **Designing for Performance in Human-Machine Systems, by Norman G. Vinson, Janice A. Singer and Marceli Wein, Institute for Information Technology, NRC, Ottawa** 451

36. **The Characterization of Piezoelectric and Electrorestrictive Materials for Underwater Acoustic Transducers, by Professor Binu Mukherjee, S. Sherrit and G. Yang, RMC** 458

37. **EMAT Generation of Horizontally Polarized Guided Shear Waves for Ultrasonic Inspection, by Julie Gauthier, Ahmad Chahbaz and Raymond Bergeron, Tektrend** 478

38. **Plasticity and Time Dependant Response of Spectra Fabric Composite Laminates, Alan Russell and Dan Liesch, Dockyard Laboratory Pacific** 488

SESSION IX: Park Centre B
Chairman: John Porter

39. **An Assessment of an Alternative Submarine Steel, by Dr J.J. Butler, J-J. Dufrane, K. George and J. Bird, Defence Evaluationn and Research Agency, and Fabrique De Fer** 509

40. **Assessment of the Fracture Toughness of Pipeline Girth Welds, by J.A. Gianetto, G. Shen, and W.R. Tyson, MTL-CANMET, and A.G. Glover, Nova Gas Transmission Ltd.** 522

41. **Probabilistic Modeling of Corroded Ship Structural Panels, by I.R. Orisamolu, D.P. Brennan and U.O. Akpan, Martec Ltd., to be presented by Mr. D.P. Brennan** 535

42. **Application of Probabilistic Corrosion Models for Reliability Assessment of Ship Structural Panels, by I.R. Orisamolu, U.O. Akpan and D.P.Brennan** 536

43. **Residual and applied Stress Characterization of NiAl Bronze Using X-Ray Diffraction, by Michael E. Brauss and James A. Pineault, Proto, and John Porter, DREA** 537

SESSION X: Park Centre B
Chairman: John Porter

44. **Current Developments in Residual Stress Measurement by Invasive But Non-Destructive Methods. Is the Complementarity There?", by G. Roy, MTL-CANMET, J.Porter, DREA, T. Holden, NRC, and J. Pineault, Proto** 538

45. **Materials Solutions to the Aging Aircraft Problem, by K.I. McRae, Air Vehicles Research Detachment** 539

46. **Progress and Plans of the Improved Ship Structures Maintenance Management (ISSMM) Project, by Neil Pegg and John Porter, DREA, and LCdr A.R. Graham, NDHQ** 557

47. **Fatigue Crack Initiation and Growth in A517 SAW Weldments Under Variable Amplitude Loading, by Christopher Bayley, Fleet, and John Porter, DREA** 567

48. **Developmental Activities Towards a Real-Time Defect Severity Assessment System for Naval Platforms, by John Porter, DREA, Chris Bayley, Fleet, LCdr. Chris Hargreaves, NDHQ, Colin Smith, NETE, and Luksa Luznik, Fleet** 581

#511875 ①

The Materials and Welding Associated with the Construction of SSK Submarine Hulls

A. Aitchison
Marconi Naval Systems, Barrow in Furness, England. LA14 1AF

J. Bird
Directorate of Naval Architecture, MoD(PE), Bristol, England.

ABSTRACT

The construction of SSK Upholder class submarines is an important issue for the Canadian Navy now that the four vessels are to be transferred, beginning in the year 2000, from the United Kingdom to Canada. This is because an understanding of the fabrication methods will generate confidence in the integrity of the hull envelope and will directly assist the Canadian Navy when it becomes necessary to carry out future repair and refits. This paper describes the materials and methods of construction used in the fabrication of the hull envelope by people who were involved in the qualification of the weld procedures and one who was directly involved in the construction of this class of submarine. The paper records a number of new developments in welding, related to construction issues, which may have a role to play in future submarine maintenance.

Introduction

The transfer of the four Upholder Class Submarine from the UK to Canada from early 2000 onwards will undoubtedly lead to questions being raised as to the materials and methods of construction. This is particularly relevant with regard to service performance, refit and repair requirements. Initially what will actually be transferred should be known in some detail to the Canadian Navy and also the condition of these structures. The latter requirement may still necessitate hull structural survey in order to identify the initial condition on which future action can be based. This is because the submarine may have been worked up to operational condition for transfer but a complete condition report may not be available which details the overall condition resulting from the vessels being laid up over the past 10 years. Consequently some work, by the Canadians, maybe required before the first major refit to address any short comings resulting from the period of, extended, lay up.

This paper details the materials, consumables and welding procedures used in the construction of the Upholder Class submarines. The objective is to inform the Canadian authorities of these details so that they will be in possession of the appropriate knowledge should early maintenance of the hull envelope be required. The paper only deals with the materials and construction of the hull envelope and not the materials for systems, propulsor etc.

It should be noted that the Upholder class of submarines were built by the VSEL consortium at Barrow in Furness and Cammell Lairds, Birkenhead. SSK 01, Upholder was built at Barrow in Furness and SSK 02, Unseen, 03 Ursula and 04 Unicorn, being built at Birkenhead.

Steel

The early classes of submarine fabricated by the Royal Navy were constructed using riveted mild steel. The first use of welding in construction was employed in welding the ballast tanks of the A class around 1938. The first fully welded vessels were the T Class, beginning in 1942, starting with HMS Tiptoe, using 'S' grade steel. The O & P Class, of which four were supplied to Canada, employed QT28 in the construction of the hull envelope and UXW steel to fabricate the Tee frames. It was during the construction of these vessels that lamellar tearing was first encountered but its true significance was not fully recognised at the time. This had to wait until the construction of the UK nuclear submarine, HMS Dreadnought, which was fabricated from QT 35, a somewhat higher strength hull steel. (1).

More recent submarine construction in the UK first used HY80 steel followed by Q1N, the British version of HY80 steel. Table 1. It is the latter steel that was used to fabricate the Upholder class submarines and indeed, for the Trident Submarine build programme recently completed by the Barrow shipyard. This steel has been manufactured either using the basic electric arc melting or the basic oxygen steel making process followed, in both cases, by vacuum arc degassing. The composition of Q1N is similar to HY80 but at the time of initial manufacture was lower in the impurities Sulphur and Phosphorous. The steel used aluminium deoxidation practice and aluminium grain refining before the liquid Q1N steel was bottom poured in to 20 ton ingots. The as cast ingots were subsequently rolled, with a degree of cross rolling into the requisite plate thickness followed by quenching and tempering to attain the necessary 0.2% proof strength level. All plates were solution treated at 920°C, one hour per inch of thickness followed by water quenching in platen or roller quenching facilities. Tempering was carried out at between 625°C to 650°C for the requisite time depending on plate thickness, in order to achieve the specified 0.2% proof strength level. Table 2. The latest production of Q1N plate involves the direct rolling of Q1N ingot to the requisite plate thickness.

The use of low sulphur steel, basic electric furnace refining, aluminium deoxidisation, Aluminium grain refining and vacuum degassing ensured that the Manganese Sulphide, Manganese Silicate and alumino-silicate laminations, the cause of lamellar tearing in the QT35 were eliminated. The current supply of Q1N is free of these defects and so the steel has excellent through thickness properties. In order to maintain this quality all plates are subject to a through thickness NDE examination using an ultra sonic pulsed echo technique on a six inch square grid pattern. All plate not meeting the necessary requirements is rejected.

Mechanical Testing

The Q1N material specifications NES 736 Part 1- Plate; Part 2 - Forgings; Part 3 - Castings and NES 769 –Welding Consumables for Structural Steel. Approval System, and NES 770 Welding and Fabrication of Q1N steel, require that all materials used in submarine construction meet certain minimum standards. Tensile tests are used to determine 0.2% proof strength, charpy, and dynamic CTOD for toughness with bulge explosion tests for crack initiation and arrest properties. The latter is covered using plain or crack starter bulge explosion, flawed bulge explosion or hull toughness element tests. For the Upholder class, only two test methods were employed, namely the plain and crack starter bulge or the flawed bulge explosion tests..

The Q1N plate would have been qualified prior to its use in Upholder but the weld metal Table 3. would have been qualified depending on the weld procedures used either as a result of previous similar construction and/or specifically for the fabrication of the Upholder class. The test panels used to qualify weld metals and procedures are shown in Figure 1, incorporating the specific joint preparation, welding consumable(s), welding process and relevant welding parameters. Following radiography and ultrasonic examinations to confirm weld integrity the various weld property material tests would have been carried out to validate the welding consumable etc., before it was allowed to be used in construction. Table 4. There would have been close control of the welder, welding the weld procedure tests panels, who would have been monitored by a team of experienced welding inspectors to ensure the weld joint was completed as per the procedure.

It was not usual practice to employ weld run off plates in order to monitor weld properties during construction but in many instances weld property checks were made on cut outs removed from the hull. These samples were taken where access was required for penetrations and welds contained in that particular cut out piece would have been tested. Tests on material from these sources provided confirmation that the weld metal properties developed in the procedures were being achieved in the submarine hull welds.

Welding Consumables used in SSK Construction.

Whilst the Fortrex 11018 SMA electrodes were used on at least SSK001 and 002 Units there was a gradual change to the improved Fortrex NQ1 SMA electrode. Table 3. In each case it was imperative that the start area of each electrode run was gouged/ground free of possible porosity defects, this applied to the use of all SMA electrodes on structural steel throughout the build. Close control of run out lengths was maintained with QC Inspectors checking individual welders to ensure they were compliant with the laid down welding procedures thus maintaining the specified heat input requirements in order to develop the required mechanical properties. Table 4.

So as to minimise the possibility of hydrogen pick up in the weldment and thus the run the risk of encountering Hydrogen induced cold cracking in the HAZ, all SMA electrodes were baked at 400°C for 4 hours and then stored at 150°C until required for welding. VSEL practice was to issue the electrodes in plain quivers with silica gel granules placed in the cap, which must remain closed at all times, after taking out an electrode for the purpose of welding. Some companies use heated quivers set at a validated temperature to minimise the risk of moisture pickup from the atmosphere. Without proper control of electrodes moisture pick up can be significant depending on the atmospheric conditions of temperature and relative humidity. (2).

During earlier construction arc blow problems had been experienced with DC rectifiers in the shipyard, thus all SMA structural welds were carried out using AC power sources . Multi-operator main transformers were located in the shop and berth area from which numerous single reactance units were taken and placed in banks to allow welders easy access for connections via welding cables extending up to 50 metres from these units. Earthing needed to be strictly checked to ensure very good connections to sub units and the submarine on the berth if variations in current during were to be avoided.

Development work for the Trident project had involved the development of a 1.2mm diameter hybrid flux cored wire (FCAW), Dualshield 101TM, which met all the welding criteria, for welding Q1N steel, for use in nuclear submarine construction. Coupled with the technical merits of the consumable it soon became evident that substantial increases in productivity could be, and were achieved over existing SMA welding practices. The wire was all positional and gained immediate acceptance for almost 80% of welding carried out during the construction of Trident. Concern was raised about the levels of weld metal hydrogen that could possibly be achieved using this wire in restrained butt welds. Shop floor tests (3) using a 'Yanaco' weld metal hydrogen analyser revealed minimal pick-up, even when taken over several days. In any case, the wire reels not used completely during the working day were stored in temperature controlled ovens set at 60°C. All reels were dated on release from the stores and controlled throughout their use.

For submerged arc welding the wire type used was a bare solid wire, Table 3. selected to ensure there was no hydrogen pick-up from wire drawing compounds that were sometimes found under coppered wire products. Care was taken to keep the wire free of rust and grease that could be picked up in the working environment. It was essential that the flux was kept dry and to this end it was mandatory that it should be baked at 400°C for 4 hours and kept at 150°C until ready to be used in the construction of decking or hull butt welds.

In order to maximise efficiency in the use of submerged arc welding flux, used and new flux was mixed but regulated to ensure there was not an excess of fine granules in the flux. It had been found that an excess of fine granules tended to mask the molten pool and hinder the release of gases, in extreme cases this it has been known to create large gas pores in the weld metal. All welding products were purchased from approved welding suppliers and batch test certificates were obtained for every individual batch of electrodes, wires and flux used to ensure the products were up to the standards and the mechanical properties stated in MOD specifications.

During fabrication QC Inspectors were tasked to obtain samples of both electrodes and flux from the shop floor and deliver them to the Chemist's department for moisture assessment. Moisture levels were assessed using the Gayley Woodings system, results being reported within hours of receiving the sample. Electrodes were sent in sealed copper tubes and the flux in sealed small chemistry bottles. Both were labelled and sent with a card recording where and when the sample was collected.

Construction

During the construction of the various vessels of this class of submarine there were several welding consumables and processes used on the same welded joints do to the vessels being built at the two shipyards belonging to the then VSEL Consortium. The aim of this paper is to relate the build of SSK with the MOD approved processes and consumables without detailing to specific hull seams and butt welds.

The Tee frames used in Upholder class construction were either rolled Q1N or where applicable extruded HY80. These tees would have been examined, shot blasted and primer painted before being bent to a set diameter using pinch rolls, a Hugh Smith Frame/Bulb Bar Radial

Bending Machine. Each T bar end would have been prepared for welding by gouging and grinding to the specified joint preparation. Using a simple jig and mandrel, the Tee sections were assembled with a set joint gap to form a full diameter ring, Figure 2: a glass or ceramic rod backing medium would then have been fixed on the one side and held down, before preheat was applied using strip electrical heating elements on either side of each joint. On attaining 70°C, the modified preheat temperature, the rings were first welded to the mandrel arms, in order to maintain the correct shape, using low hydrogen shielded metal arc electrodes, the first boats used the Murex Fortrex 11018 type or Murex NQ1type (E9016). Following the welding of the outer root gap, with 4.0mm diameter electrodes over the glass or ceramic rod, the welder was then able to complete the outer joint area using the 4.0mm diameter electrodes.

Once the first side web and table welds on all three connections had been completed, the preheat was stripped away to allow the rings to be turned over and the second side welded with preheat in operation after grinding back the root area of the weld to remove any defects which may have occurred. Full NDE inspection UT and RT was applied after a minimum of 24 hours waiting time, designed to allow for any entrapped weld metal hydrogen to escape. Any welding repairs would have been immediately undertaken and checked again to attain the required standard.

On completion of the Tee frame butt welds the rings were lifted onto a jig and set in position for a circumferential oxy-propane cutting machine, rotating from a fixed centre point, to cut the circumferential T frame web weld preparation. The machine cut the top and bottom edges of the weld preparation at the same time and a preheating torch was placed in front of the burning torches to preheat the plate, thus ensuring a good clean crack free cut. The cut surfaces thereafter only required a light grind to remove the surface oxide layer on the joint preparation and to correct the internal ring diameter dimension. This practice would essentially be the same for both rolled NQ1 and extruded HY80 tees. Following this operation the stiffener rings, axis vertical were placed on brackets set at the correct pitches on vertical steel channels to form the sub unit 'ribs' and fixed at the required pitch as per the submarine hull design. Figure 2.

The VSEL practice at this time was to use the stiffener rings to form a jig in order to construct the individual three frame hoops. This allowed the rolled plates to be positioned around the stiffening rings, which acted as a mandrel, being secured by means of numerous temporary attachments in the form of bolts and plates, the latter being welded to the hull plating, preheat being maintained at a genuine 70°C by hand held preheating gas (oxy propane) torches. Severe cracking problems can occur if insufficient preheat is undertaken on these highly stressed welds so the maintenance of accurate temperature control was essential.

The plate material, Q1N steel, used to form the hull envelope was procured to exacting specifications regarding quality and thickness. On arrival at Barrow all the plates were inspected by UT on a grid matrix to ensure that there were no laminations in the plates. Subsequently the plates were shot blasted and primed with Kharki Interplate NAA750/WAA001 weldable primer paint to a maximum DFT of 30 microns and given a unique plate number. All through the build sequence this unique number, for the specific plate, was marked on every subsection in order to identify from what and where each part of the plate was in the boat. Where necessary the hull plates would be either oxy-propane or plasma cut to size, before being transferred to a Hugh

Smith Edge Milling machine, for milling the double vee butt joint preparation on both ends of the plate. These preparations form the longitudinal seam joints which make up the individual sub units. With only one exception all the three plates that comprised one sub unit were prepared in this manner. The exception to this procedure was the closure weld where the final preparation was cut and gouged to fit. These plates were rolled to the required hull diameter on the Heausler German rolls. Formerly the ends of the plates had to be 'cracked' on one side and then turned over to complete the rolling operation. This cracking operation was to ensure that the sections were curved right up to the end and did not have a flat section. New equipment has now been installed which allows the steel plates to be rolled throughout the whole of their length without recourse to this action. After being checked by QC Inspectors the sections were then shipped to the main assembly hall for erection of sub units.

Before work was allowed to continue QC Inspectors checked the sub unit for the correct dimensional tolerances. Thereafter, electric strip heating was applied to the vertical seams and webs of each stiffener ring, all weld preparations were covered with a VSEL designed insulation tape to lessen heat loss and also reduce any burning risks to welders and platers working on the sub unit. Where possible and convenient, two vertical seams were welded at the same time, welding starting on the inside onto a glass rod backing pressed and held in the root of the outer joint which nominally was set to a 6 mm gap. Welding started in the central area of the seam, and completed to approximately a third of the seam length to lock the joint together. The top and bottom sections were filled alternately to form the skin of the hoop, Figure 2. and capped.

Whilst the joint design was made to eradicate air arc gouging, the production department used the latter process sparingly, in order to remove root defects before grinding the joint ready for the outer welding runs. Preheat was lowered or cut off during any grinding action. The method used on the inner weld was repeated on the outer preparation until the joint had been completed. The closing joint was cut and ground to make the required joint preparation and welded as per the previous seam welds.

The stiffener rings were welded to the hull using a Lincoln submerged arc Squirt welder. The equipment, connected to an arm, attached to a bearing disc, mounted in the centre of the mandrel, used 2.4mm diameter Oerlikon OES 3NiMo1 wire and basic OP41TT flux when depositing the weld metal.. The rings were welded in sequence and on finishing all the first sides, the sub-unit was turned over to enable the second sides to be welded, after applying a light grind to remove any defects in the root area. The preheat cables, disconnected for the turning of the units were reconnected and welding started once the specified minimum 70°C preheat had been reached in the area around the joints. Some of the joints at Cammell Lairds, the other sister company shipbuilder, were in fact welded using the newly developed Dualshield 101TM flux cored wire, since the relatively thin stiffeners were difficult to keep in tolerance with the submerged arc welding method. The rings on nuclear submarines were thicker and did not cause the same problems as the thinner webs on SSK. The use of FCAW significantly reduced distortion problems. Subsequently the use of temper beads was discontinued in this particular case, as it had been found that when attempting to attain the required weld reinforcement, the use of temper beads resulted in low uneven weld runs and poor shape. A blended shape was required to minimise stress raiser points in the toe areas, previously there had been considerable dressing by grinding required in order to attain the required standard.

The seams were fully inspected using Visual; MPI; RT and UT, but the full penetrating tee butt welds were examined by UT from the outside and Visual/MPI on the inner weld surfaces. All welds were examined after a minimum of 24 hours of the completion of the welding. QC inspections were once again undertaken to check the welded sub unit was within the design tolerances, any faults would need rectification work and subsequent re- NDE inspection.

In total twelve parallel-sided sub-units were produced, two of them (2.3 and 2.X) having HY80 extruded sections in place of one of the rolled Q1N tee stiffener rings. These two Tee frames were for the watertight bulkheads at frame 56 and 35 respectively, whilst sub –units 1.1, 1.2 and 1.3 were tapered units, requiring special skills to weld together correctly and in tolerance. The watertight bulkheads were made with Q1N steel, the long seams submerged arc welded and the connection to the extruded Tee frames made using the SMA process. The stiffener frames on the bulkhead itself were full penetration T-butt joints and were also welded using SMA electrodes. In principle all Tee frame welds in the construction of the submarine were full penetration welds.

The two dome end bulkheads were made and formed at Motherwell Bridge using the Fortrex 11018 electrodes to weld the preformed petals together. This is contrary to the way the O&P class domes were manufactured which was by spinning.

In the next stage the welding together of the sub-units to form shop or partial outfit units was carried out, including the incorporation of the dome end bulkheads. At this time the stiffener rings still had the spider channels in place spreading out from a central ring and connected and welded around the ring tables. To make one shop or partial outfit units the smaller sub units were set up on supports, with their axis horizontal, immediately in front of the large submerged arc welding rotator. The final units usually comprised of three sub-units except for the central unit which had four. Once they had been positioned correctly a large steel mandrel was fed through and connected to the rotator and the individual spider rings, making all items secure. A cantilever holding the submerged arc machines was swung over and positioned to allow two butt welds to be made at the same time. Prior to this, electrical strip preheating elements had been wrapped around each butt joint on the outside, they were held down by cross clips, which in turned were bolted down to the hull capacitance discharge CD studs which had been studded all around the hull. These studs were 'surface attachments' and not circumferentially welded as per SMA arc welded studs. Insulation strip was also used in the same way as for the vertical seam welds. Due to lack of space inside the units manual shielded arc welding was carried out on the inner side first once preheat had attained the correct temperature.

It should be noted here that through experience VSEL had slowly over the years reduced the temperature from 120°C to 70°C without cracking problems. Other non- experienced fabricators would be advised to keep to the original higher temperatures, even though this causes potential distortion problems and increased worker discomfort. The welding of the inside preparation was split into four sections using four welders to attain a balanced back-step welding sequence, see sketch.

Preheat was adjusted to keep the temperature as low as specified, as conditions could get very hot in the roof area of the units. With the completion of the inside welds the outside preparation was arc air gouged and ground back to sound metal ready for MP inspection before submerged arc welding started. The outside joint was submerged arc welded using a single solid wire called OES3NiMo1 with a basic flux OP41TT. The welding parameters employed were 500 A, 29-30 V and 500 mm /min travel speed. Both inside and outside weld reinforcements were gouged and ground smooth and flushed to facilitate for full NDE.

The next stage was to weld the two dome end bulkheads to their respective hull units, the fore end to unit 3A and the aft end to sub unit 1.1 and then both to unit 1B The welding processes used were mainly SMA and eventually as building progressed to the later boats, with the new semi-automatic welding wire and shielding gas.

On completion of the main circumferential hull butt welds it was now possible to weld in No 1 and 2 decks and the major castings and tank structures. The torpedo tube castings presented the most difficult problem since close control over welding sequence was necessary there being a combination of four tubes and the weapons embarkation casting in close proximity in the upper fore end dome area. Welding of these items was carried out using manual metal arc electrodes with an asymmetrical joint preparation, welding commenced on the inside and the outer joint preparation was completed using air arc gouging and grinding. After MPI, the welder would complete the joint using SMA electrodes and once again both sides of the weld would be flushed to enable NDE to be carried out to the specifications laid down.

Unlike the nuclear submarine this class of boat was designed to have a ballast keel which was fabricated in parts and welded to the hull unit sections in the assembly shop using both the SMA and FCAW welding processes

Whilst the hull and associated components were being completed a further set of tradesmen were constructing the external fore-end structure complete with ballast tanks, chain and anchor lockers and the seats for the sonar. The weapons embarking flat was a 'winged ' like fabrication which enabled, when fitted, the torpedoes to be slid down into the submarine via the hatch opening. Likewise, the bridge fin was built up with the main component being the Q1N steel conning tower casting assembly welded as a separate item before becoming part of the bridge section.

The aft end external structure was linked around the shaft tube, rudder housings, port and starboard hydroplane stabilisers together with No 3 and 4 main ballast tanks. Endless QC checks were made throughout the build time until the units were shipped at planned intervals down to the berth.

At this time the berth was a sloped area extending down to the Walney Channel. Future submarines would be launched via the 25,000 tonne ship lift immediately outside the main Devonshire Dock Hall (DDH) building hall. In fact all the SSK submarines have used this facility over several years for inspections and repairs as considered necessary, and now the pre-delivery refurbishment before the Upholder class submarines are moved to Canada..

For the completion of the hull on the berth traditional methods of setting the units onto the berth blocks were employed and great care and skill was taken in aligning and positioning the second unit next to Unit 3 (external structure and pressure hull fore end). Once positioned the two units were held together by steel temporary attachments welded, using the SMA process, onto the outer hull walls. Preheat strip elements were wrapped round the circumferential butt joint area and connected to the power sources. On attaining the required preheat temperature levels welding was commenced on the inside using similar block welding sequences, with SMA electrodes as used in the assembly shop. A covered tower, with welding stations and ladders inside, was lowered by crane to cover the joint so as to protect both the materials and personnel from the elements of wind and rain. The outer joint preparation was arc air gouged to remove root defects in the joint and another team of welders welded in block sequences similar to the inner weld, after NDE had cleared the weld of unacceptable defects.. There were two major static hull butt welds at the berth connecting the three large prefabricated submarine modules together.

The last major welding tasks concerned the closure plate welds for the shipping opening and access opening, on the top side of the hull to the stern of the boat, behind the bridge. The curved section of plate with rolled tee frames welded into the relevant position was positioned accurately and held in place by temporary attachments. Preheat was applied via the electrical strip elements. The inner weld was completed using a strict weld procedure sequence devised to minimise distortion and out of tolerance in the connection to the pressure hull. Air arc gouging and grinding of the outer butt joint preparation was carried out and checked before welding was completed as per the weld procedure sequence instructions. An intricate next stage required the welder to weld in frame sections between the existing frames and those welded onto the closure plate. This work was more complicated for welded frame sections between castings and the frame stiffener rings. Space and ease of welding were very restricted (non-existent), but even so the welds were fully inspected to the high standards of hull weldments. All these welds were completed using SMA electrodes.

Future Welding Developments of Interest to SSK Maintenance.

The use of the flux cored wire has been a great success in the Trident build programme, once welders had been correctly trained and gained acceptance of its potential in shipbuilding. Its use would be of interest to major re-fits and closure plate welds, but smaller work would still require the use of SMA welding if the welder skills for FCAW were not generally available.

Many brackets and support hangars were welded into position by SMA welding, but now the use of drawn arc studs and hangar brackets are preferred for the submarine build programmes. Care is necessary in applying the studs correctly, especially to the hull, but modern equipment with electronic controls and pre-set welding programmes have eliminated most of the early problems. The speed of application, no need to preheat the weld area, hold considerable benefits during refit. In addition the risk of fires caused by stray arcing and welding sparks are reduced considerably, especially in confined spaces where machinery etc may still be in place.

VSEL and MOD have recently completed trials using pulsed MIG and FCAW welding processes to assess the use of duplex stainless steel welding consumables for use on submarine refit work. The results have been very encouraging, especially in the Hull Toughness Element test, which applies an uni-axial stress to a welded test panel by means of a controlled explosion. The results have been superior to any ferritic structural steel weld as no crack emanated from the explosive test. Concerns about corrosion between the steel and weld material and sea water need not be a problem since all the hull is coated with protective primer and hull paints. The main problem may be the slight increase in welder skills required to manipulate the austenitic wires and the cost, perhaps three times a low alloy steel wire. However austenitic consumable costs continue to fall as a result of a significant increase in the tonnage use and a continuing search by the manufactures for new markets for the product. Originally the tests were carried out to identify a product which did not require preheat (except perhaps below 0°C in Arctic conditions) and to this end the trial was very successful. The use of a manual metal arc electrode may be more useful in confined areas, but the attainment of the currently specified minimum charpy values of 50 Joules at –50°C for weld metal may be just too high for such a consumable. However because the material does not have ductile/brittle transition behaviour, being austenitic, it may be possible to relax the charpy impact requirement without increasing the risk of early crack initiation or rapid crack propagation in the material. On a practical measure the SMA consumable would undoubtedly be superior to low alloy steel welds under shock loading conditions. Further work is necessary on SMA electrodes to gain approval for use on Naval Submarines.

Another area of recent development has concerned the use of electron beam welding of marine components from wrought Q1N steel in place of Q1N castings. Very few companies are capable of producing castings to the required Q1N steel quality requirements and they have to be made to lower standards than the hull envelope structure. This has caused problems when cladding the internal bores with Monel or Inconel and when joining a casting to the hull. For example, pores, in castings, acceptable to the casting code, have been located by RT when inspecting the valve to hull joint and found to be outside the plate weld acceptance level. Valves made from wrought Q1N plate and EB welded together can be assembled quickly to higher standards and present no problems regarding cladding or welding into the hull of a submarine, because being wrought products they do not contain porosity defects.

References

1. Thomson ADE, Christopher P, Bird J. Short Transverse Properties of Certain High Strength Steels. Transactions of ASME. November 1968.

2. Von Dickahut, G. and Hotz, U., Einfluss der Luftfeuche wahrend des Electrodenhandschweissens auf der Gehalt an Diffusiblem Wasserstoff im Schweissgut. Schweissmitteeilungen No. 123, June 1990.

3. Wood G. Effect of Welding Parameters on Hydrogen Levels in Weld Metal Using Dualshield 101TM Flux Cored Wire. VSEL Weld Development Report 1988

4. Aitchison A. Assessment of FCAW and PMIG Duplex Stainless Steel Welding Consumables.VSEL Weld Report NC2170/10/456/154.
5. Punshon C, Aitchison A, Bird J. Electron Beam Welding High Strength Marine Valves from Wrought Steel. JOM 7 Seminar, Helsingor June 1995.

© British Crown Copyright 1999/MOD
Published with the permission of the Controller of Her Britannic Majesty's Stationary Office.

Table.1 Typical Submarine Steel Plate Compositions

Submarine Class	Steel Type	C	Mn	Si	S	P	Ni	Cr	Mo	V
A Class Amphion	S	0.21	0.80	0.35	0.06	0.06	-	-	-	-
P Class Porpoise	UXW	0.14	1.40	0.25	0.04	0.05	0.35	0.23	0.25	
O Class Oberon	QT28	0.15	1.15	0.08	0.03	0.022	0.40	0.25	0.26	
SSN01 Dreadnought	QT35	0.15	1.20	0.30	0.040	0.035	1.20	1.00	0.50	0.12
SSBN Resolution	HY80	0.14	0.32	0.25	0.004	0.011	3.20	1.60	0.45	0.01
SSK, SSN SSBN Upholder Trafalgar Trident	Q1N	0.13	0.26	0.29	0.005	0.012	2.85	1.40	0.45	0.01

Table. 2 Mechanical Property Requirements for Submarine Steels and Weld Metal

Submarine Class	Steel Type	PS MPa	UTS MPa	EL %	Cv	CE
A Class Amphion	S	285	460	20	-	0.49
P Class Porpoise	UXW	387	575-665	15	27J at -20°C	0.59
O Class Oberon	QT28	430	540-695	20	61J at -20°C	0.52
SSN01 Dreadnought	QT35	550/650	1.1x 0.2%PS	20	81J at -40°C	0.70
SSBN Resolution	HY80	550/690		20	75ft lbs at -84•C	0.85
SSK, SSN SSBN Upholder Trafalgar Trident	Q1N	550/650	< 0.88 PS/UTS	20	101J at -84°C	0.85
Q1N Weld Metal	SMA FCAW Sub Arc GMA	> 550		20	55J at -55•C	

Table. 3 Typical Deposited Weld Metal Compositions

Process Type	Company and Consumable Name	C	Mn	Si	S	P	Ni	Cr	Mo	V
SMA	Murex Fortrex 11018	0.04	1.27	0.20	0.009	0.012	2.05	0.12	0.32	0.016
SMA	Murex Fortrex NQ1	0.05	1.50	0.35	0.010	0.014	0.82	0.01	0.21	0.006
SAW	Oerlikon OES3NiMo1 wire & OP12TT flux	0.072	1.09	0.30	0.006	0.012	1.33	-	0.53	-
FCAW	Alloy Rods Dualshield 101 TM wire with Argon 5% CO_2 shielding gas	0.08	1.09	0.34	0.009	0.006	1.80	0.08	0.03	0.03

Table. 4 Typical Deposited Weld Metal Properties

Process Type	Company and Consumable Name	0.2%PS MPa	UTS MPa	Elong. %	Charpy. Joules at Test Temp.
SMA	Murex Fortrex 11018	644	718	20	75, 67, 65. at -20°C
SMA	Murex Fortrex NQ1	594	675	22	121, 116, 136. at -50°C
SAW	Oerlikon OES3NiMo1 wire & OP121TT flux	660	780	20	120-136, at -20°C 70-90, at -50°C
FCAW	Alloy Rods Dualshield 101TM wire with Argon 5% CO_2 shielding gas	599	660	21	106-122, At -20°C 70-85, at -50°C

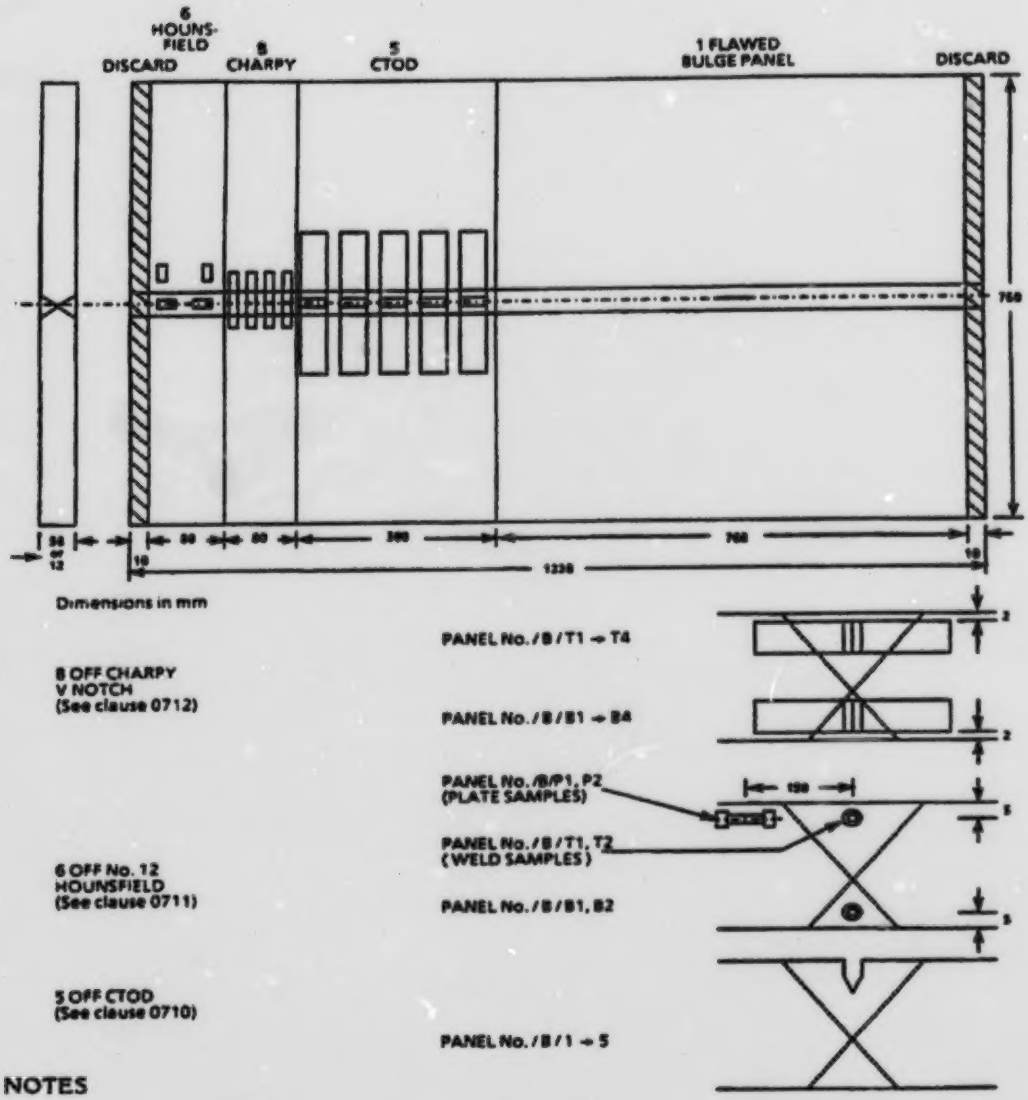
6 HOUNS- FIELD
DISCARD
8 CHARPY
5 CTOD
1 FLAWED BULGE PANEL
DISCARD
760
38 or 12
50
60
380
760
10
10
1238
Dimensions in mm
8 OFF CHARPY V NOTCH (See clause 0712)
PANEL No. /B/T1 → T4
PANEL No. /B/B1 → B4
2
2
PANEL No. /B/P1, P2 (PLATE SAMPLES)
PANEL No. /B/T1, T2 (WELD SAMPLES)
150
5
6 OFF No. 12 HOUNSFIELD (See clause 0711)
PANEL No. /B/B1, B2
5
5 OFF CTOD (See clause 0710)
PANEL No. /B/1 → 5

NOTES

1. Preparation to be identical to weld procedure.
2. Test panel length can be reduced when either FBE or CTOD are not required.
3. For procedures to weld plate of 20mm to 100mm thickness the test plate thickness is to be 50mm, below 20mm the test plate thickness is to be 20mm.

Figure 1 Weld Procedure Approval Plate

A. SHELL WELDING FIXTURE

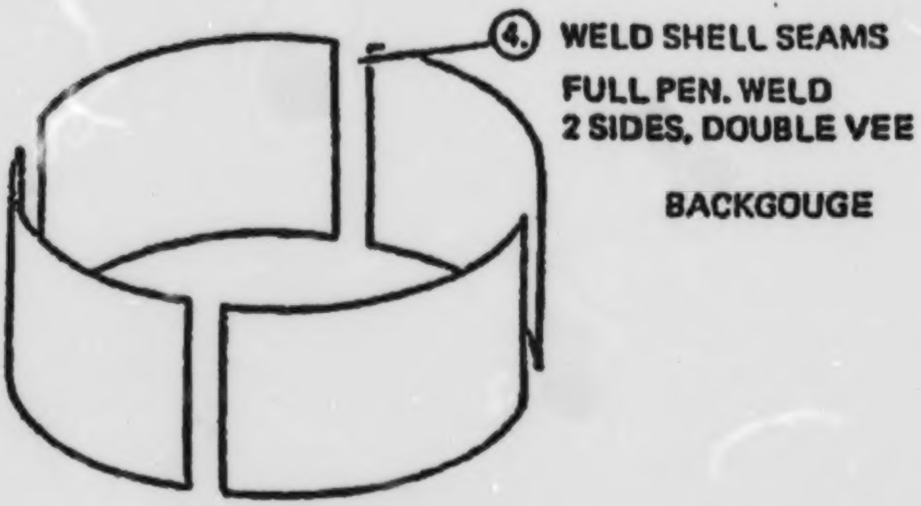
④ WELD SHELL SEAMS
FULL PEN. WELD
2 SIDES, DOUBLE VEE
BACKGOUGE

B. FRAME INSTALLATION FIXTURE

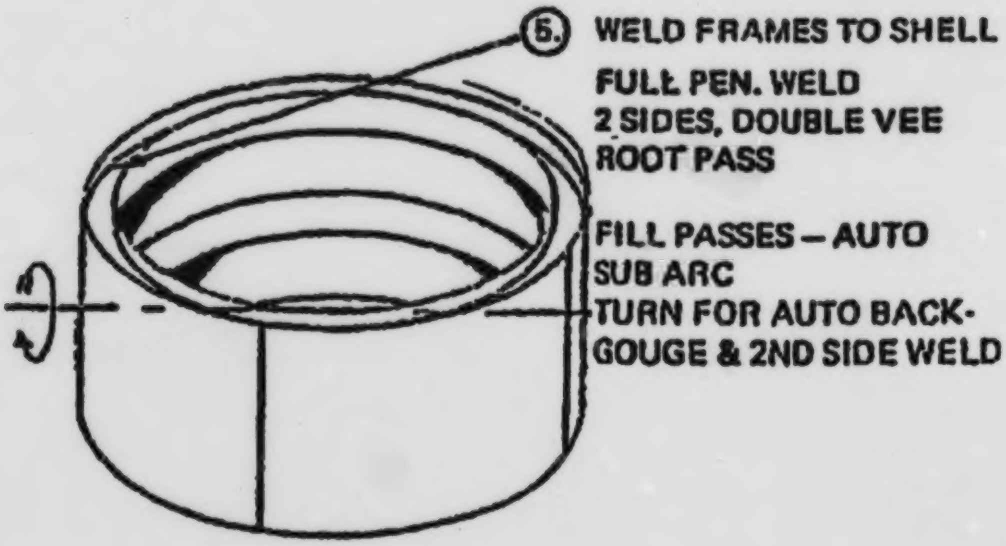
⑤ WELD FRAMES TO SHELL
FULL PEN. WELD
2 SIDES, DOUBLE VEE
ROOT PASS
FILL PASSES – AUTO
SUB ARC
TURN FOR AUTO BACK-
GOUGE & 2ND SIDE WELD

Figure 2 Build Sequence

#511876 ②

UNIT Overview - A R&D project to improve the way we do NDT

by Michel Brassard

Tektrend International Inc

ABSTRACT

We will present the results of an on-going research program to create an augmented reality for nondestructive evaluations where a CAD representation of the part or structure under inspection is augmented with a real-time display of the robot and display of the inspection results from a viewpoint and at a scale selected by the inspector. This graphic display aims at providing a unique workplace metaphor for the inspector more suited to the inspection environment than the desktop metaphor prevalent in most interfaces.

The project applies the tools of data representation and robot control in conjunction with application specific tools for ultrasonic and eddy-current inspection and data processing. Intelligent systems technologies is applied in the areas of automation of probe manipulation for data acquisition and the data processing, interpretation and display.

The robot vehicle will attach to surfaces in any orientation on both magnetic and non-magnetic materials with self-locomotion independent of attachment tooling and articulation assemblies. It is designed to be applicable to a wide range of well-defined requirements within the scope of motion confined to a surface with 3D topology.

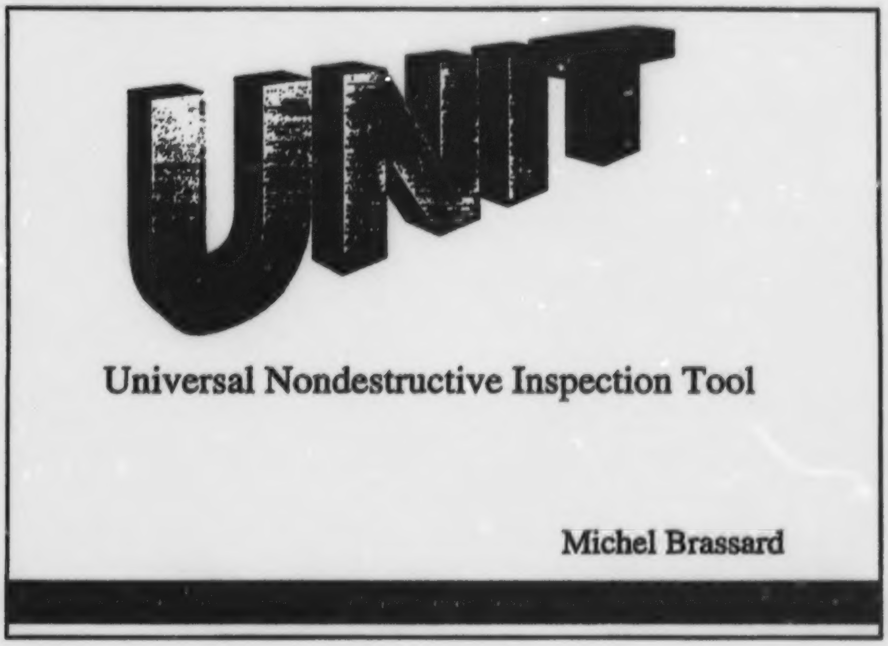

UNIT

Universal Nondestructive Inspection Tool

Michel Brassard

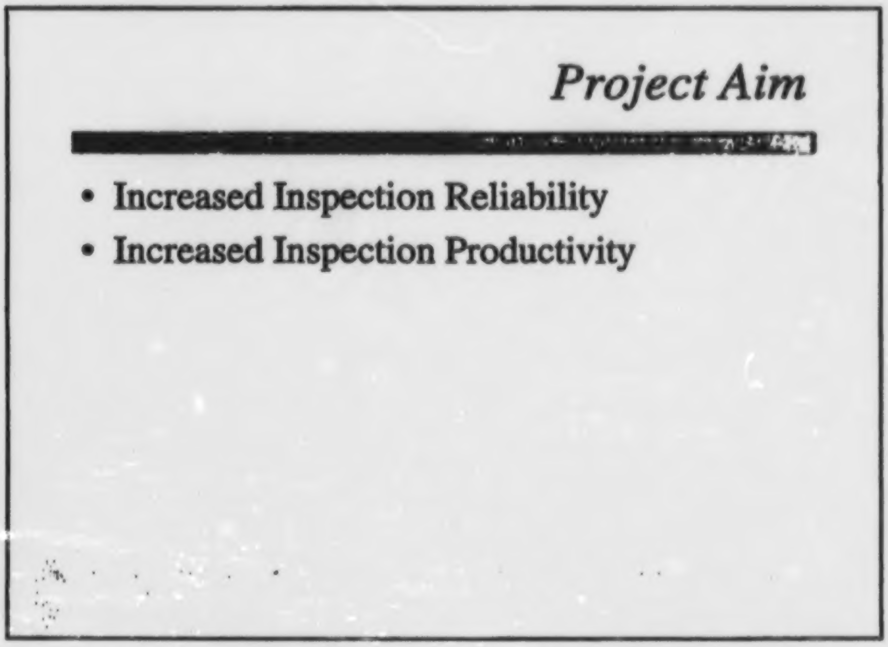

Project Aim

- Increased Inspection Reliability
- Increased Inspection Productivity

How can we do this?

- Increased Inspection Reliability

Reduce the dependence on the operator for subjective decicions

Providing the data in a form that makes the interpretation easier

How can we do this?

- Increased Inspection Productivity

Increase speed of inspection

Speed of set-up, avoid need for re-inspection, easier reporting

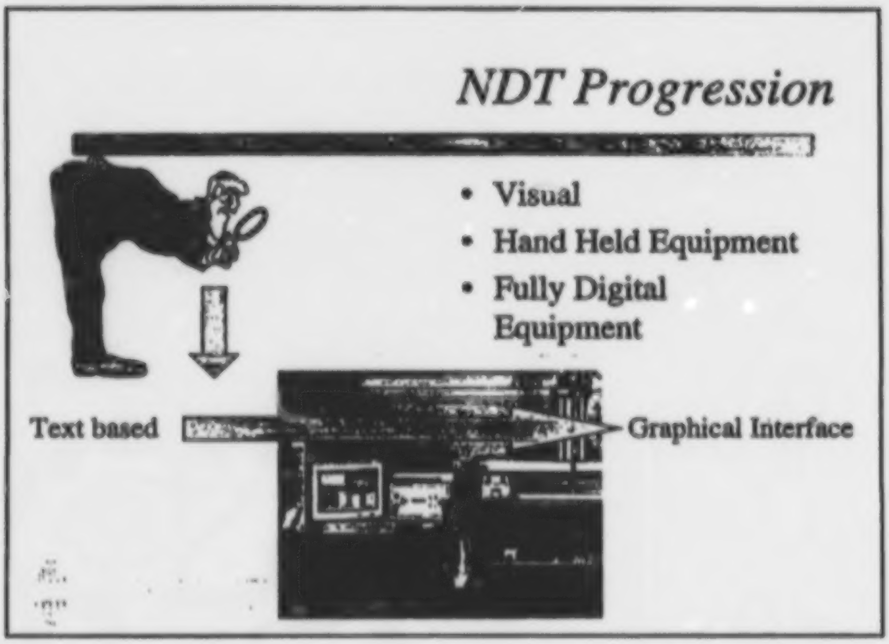

NDT Progression

- Visual
- Hand Held Equipment
- Fully Digital Equipment

Text based

Graphical Interface

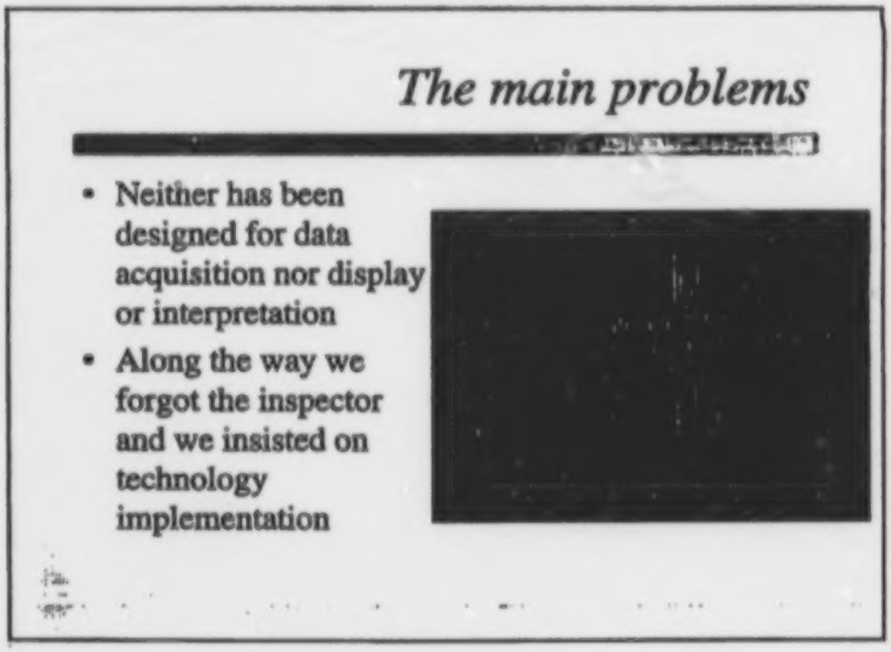

The main problems

- Neither has been designed for data acquisition nor display or interpretation
- Along the way we forgot the inspector and we insisted on technology implementation

Performance Targets

- **Develop an immersive virtual/augmented reality man-machine visualization interface for the inspection workplace**
- **Develop the support technologies required to implement this IVIE (Integrated Virtual Inspection Environment) interface**
- **Integrate this workplace interface with automated data acquisition tools into a Universal Nondestructive Inspection Tool (UNIT)**

Work Modules

- **User Centered Specification**
- **Interface**
- **Workplace CAD Models**
- **Data Management**
- **Flaw Modeling**
- **Manipulators**
- **Embedded Electronics**
- **End Application Integration**
- **Positioning**

User Center Specifications

- User Interview
  - Issues of concern
  - Issues relate to the task analysis, the user as well as organizational and environmental profiles.
- Application centered specifications

Some of the items discussed

Who does what ?

Procedures, norms and guidelines.

What are the performance requirements?

Expert/novice differences.

What functions must be supported by the interface?

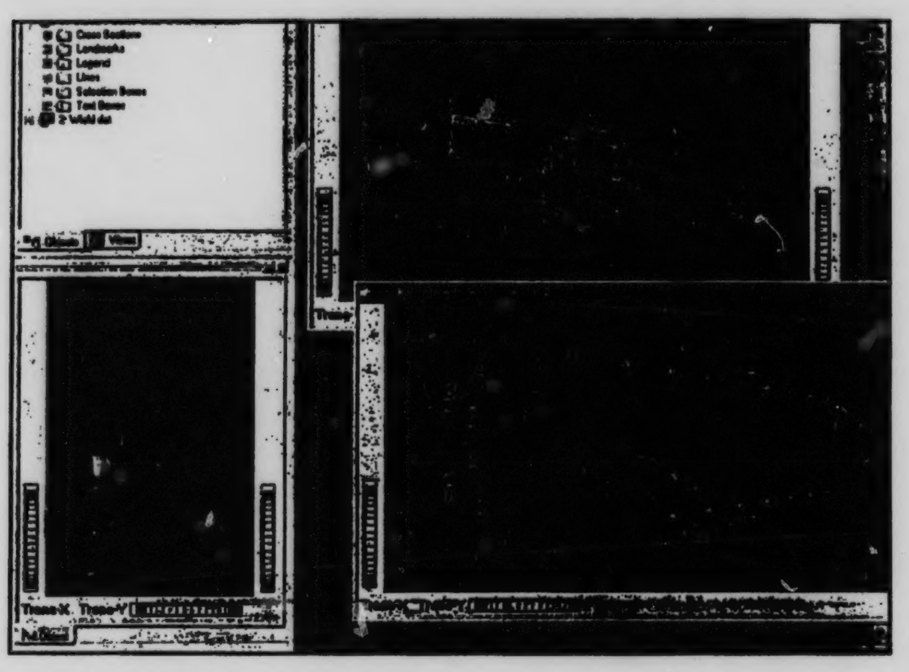
Cross Sections
Landmarks
Legend
Lines
Selection Boxes
Text Boxes
World dat
Objects
Views
Trans-X
Trans-Y

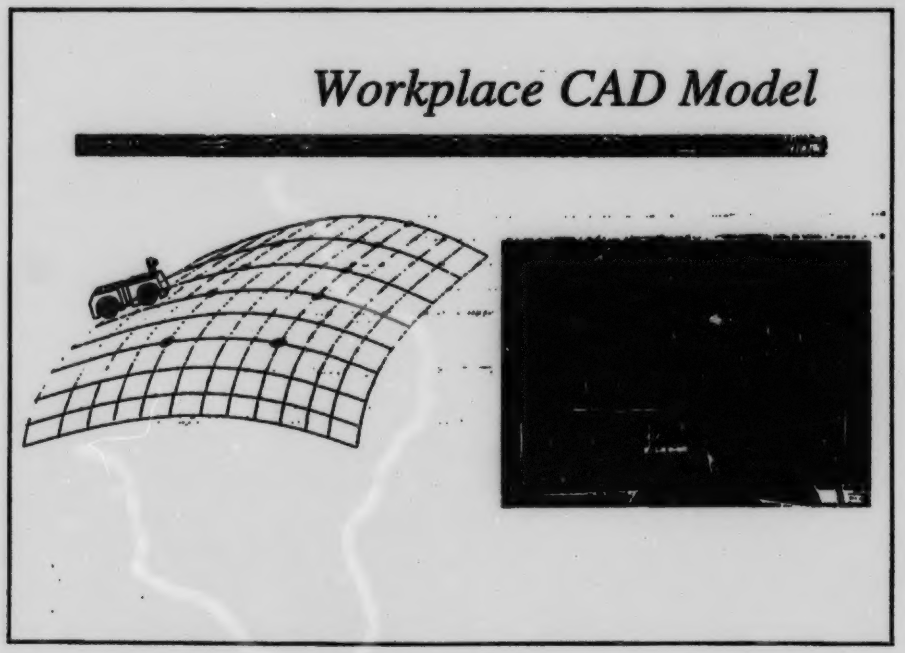

Workplace CAD Model

3D Localization

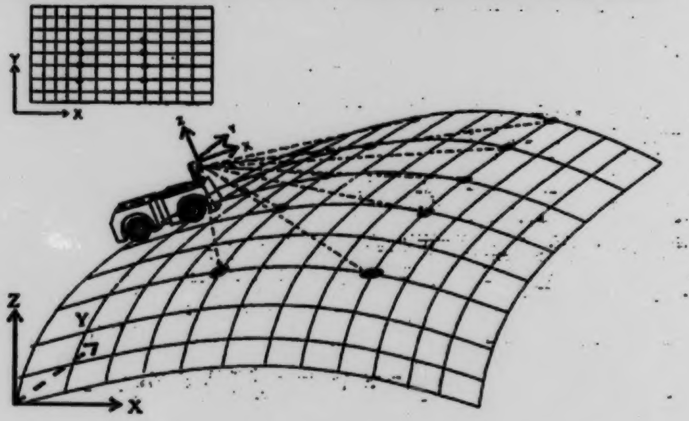

CAD Image Input

Data Management

- Data acquisition module
  - Based on a client-server architecture
- Formatting and storage module
  - Data compression and optimization
  - Formats definition and compatibility
  - Database management
- Data access module
  - Data retrieving protocols

Flaw Modeling

- Post-processing survey and tests
  - Signal filtering
  - Flaw detection & sizing
  - Flaw reconstruction
  - Feature extraction, flaw characterization
  - Volumetric flaw modeling
- Detailed specifications
- Implementation of final algorithms

Signal distorsion causes

- Attenuation
- Phase velocity dispersion
- Coherent noise (« Speckle »)
- Diffraction
- Non-linear propagation
- Pulse duration
- Barkhausen effect
- Static Energy Noise

1D Filtering

- Deconvolution techniques
- Wiener Filtering and Spectral Extrapolation
- L1-Deconvolution
- Envelope Estimation
- Parameter Estimation Technique

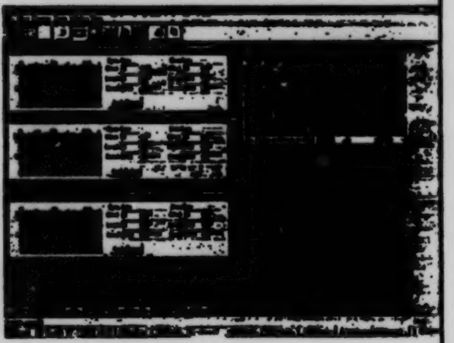

2D Filtering and Signal Enhancement

- **Wavelet Analysis**
- **Split Spectrum Process**
- **Median, low-pass filte**
- **Inverse and noise reduction filtering (Wiener)**
- **Histogram transformations**
- **Adaptative filtering, pattern matching**

Conclusion

- Developing an inspection methaphor
- Adaptive tools
- All of this is useless unless it makes your job easier. Usability is the key.
- We must therefore improve the relationship between the inspector and the machine.

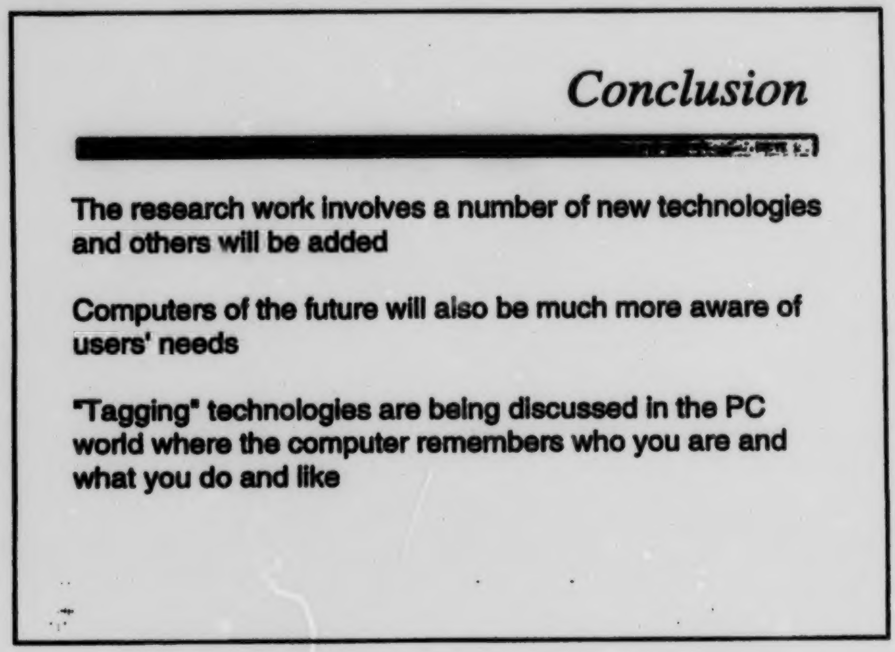

Conclusion

The research work involves a number of new technologies and others will be added

Computers of the future will also be much more aware of users' needs

"Tagging" technologies are being discussed in the PC world where the computer remembers who you are and what you do and like

#511877

Materials Selection for U.S. Navy Ships

by P.W. Holsberg and E.J. Czyryca

Carderock Division, Naval Surface Warfare Center
9500 West Bethesda, MD 20817

ABSTRACT

Over the past several years the U.S. Navy has formally implemented its metallic materials selection process (MSP). The MSP provides guidance for the design agent for selection of materials for critical, non-nuclear applications. It further requires the design agent to document all information used in the selection process. In critical applications, a fracture toughness review process (FTRP) is invoked, where all material properties required for fitness for service over the life of the ship are defined, determined and/or documented. A metallic materials properties database (MMPD) is now being established to be available to aid in the processes. Details of each process and their relationship with each other and the database are discussed.

MATERIALS SELECTION FOR U.S. NAVY SHIPS

by
Paul W. Holsberg, NSWCCD Code 61
Ernest J. Czyryca, NSWCCD Code 614

Presented at
8th CF/CRAD on NAVAL APPLICATIONS OF
MATERIALS TECHNOLOGY
11 May 1999

MATERIAL SELECTION REQUIREMENTS

- **METALLIC MATERIAL SELECTION REQUIREMENTS**

- **Provides guidance and direction for the design agent to select materials for use in critical, non-nuclear applications**
- **Requires design agent to document Material Selection Information (MSI) for critical applications**

MATERIAL SELECTION REQUIREMENTS

- **ESTABLISH CRITICALITY OF APPLICATION**
- **Category I - Loss of Life, Ship, or Primary Mission**
- **Category II - Severe Personal Injury, Loss of Secondary Mission, Weight Handling Equipment Failure, or Replacement Cost Exceeds $1M per Ship**

MATERIAL SELECTION REQUIREMENTS

- **IF CRITICAL, DESIGN AGENT DOCUMENTS MATERIAL SELECTION INFORMATION (MSI) FOR CANDIDATE MATERIAL**
- **Category I - Needs NAVSEA approval for MSI**
- **Category II - Design Agent's Senior Design Manager approves MSI**

MATERIAL SELECTION PROCESS

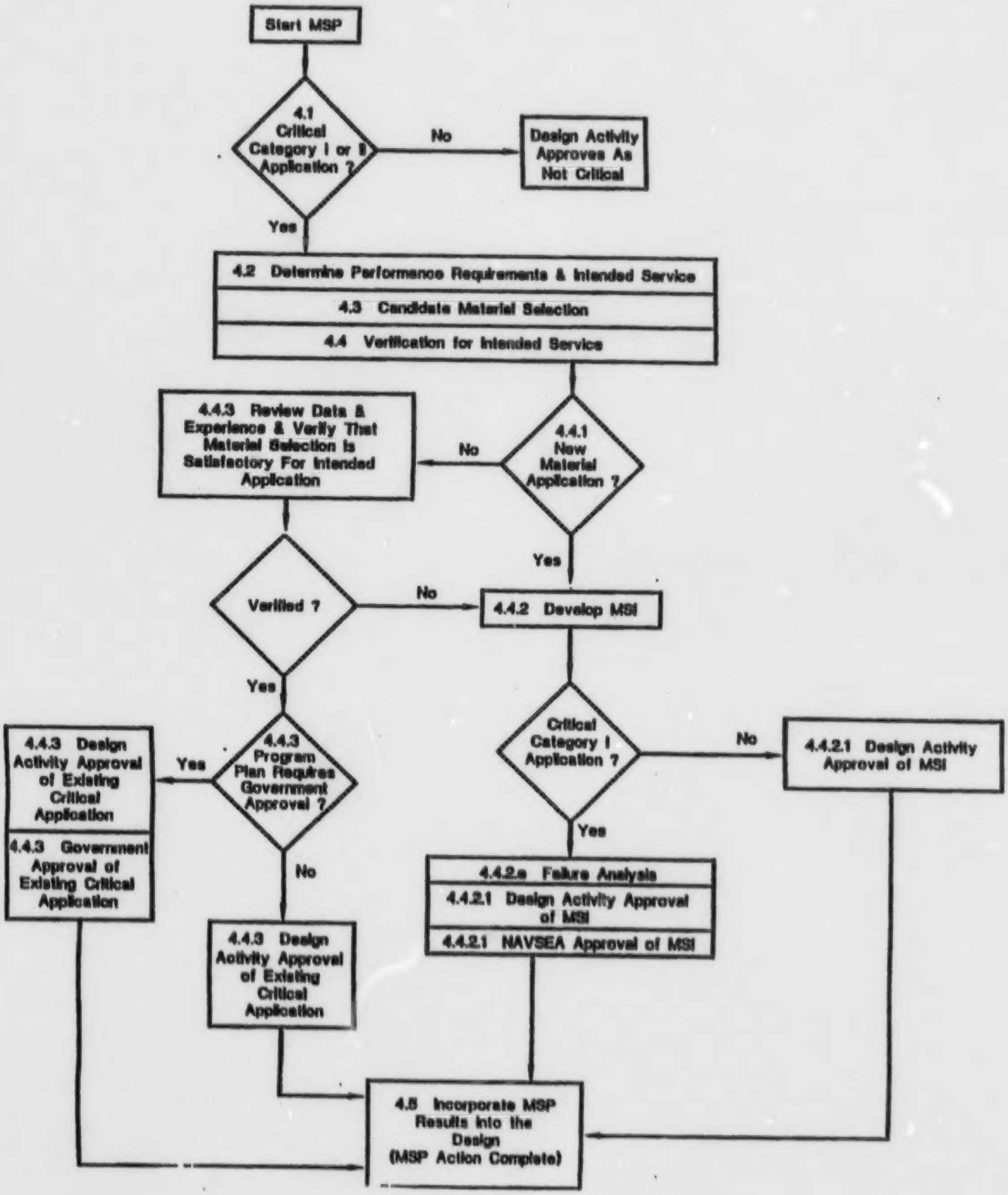
Start MSP
4.1 Critical Category I or II Application ?
No
Design Activity Approves As Not Critical
Yes
4.2 Determine Performance Requirements & Intended Service
4.3 Candidate Material Selection
4.4 Verification for Intended Service
4.4.3 Review Data & Experience & Verify That Material Selection Is Satisfactory For Intended Application
No
4.4.1 New Material Application ?
Yes
Verified ?
No
4.4.2 Develop MSI
Yes
4.4.3 Design Activity Approval of Existing Critical Application
4.4.3 Government Approval of Existing Critical Application
Yes
4.4.3 Program Plan Requires Government Approval ?
No
4.4.3 Design Activity Approval of Existing Critical Application
Critical Category I Application ?
No
4.4.2.1 Design Activity Approval of MSI
Yes
4.4.2.e Failure Analysis
4.4.2.1 Design Activity Approval of MSI
4.4.2.1 NAVSEA Approval of MSI
4.5 Incorporate MSP Results into the Design (MSP Action Complete)

MATERIAL CHARACTERISTICS

- **MATERIAL PROPERTIES - Strength, toughness, damping, physical properties, frictional properties, fatigue strength, creep and stress relaxation, cavitation resistance, toxic effects**
- **DESIGN CRITERIA - Some existing designs are alloy system specific. The validity for new alloy systems must be justified.**

MATERIAL CHARACTERISTICS

- **IN-SERVICE VARIABLES - Expected operational environmental factors, life expectancy, ballistic and shock properties, fire effects, material degradation (corrosion and temperature)**
- **MANUFACTURING PROCESSES - Welding, brazing, hot and cold forming, peening, coating, cladding, inspectability, availability, fabrication requirements and effects**
- **LIFE CYCLE COSTS**

MATERIAL SELECTION REQUIREMENTS

- **ADJUNCTS**

- **FRACTURE TOUGHNESS REVIEW PROCESS (FTRP)**
- **METALLIC MATERIALS PROPERTIES DATABASE (MMPDb)**

NEW MATERIAL SELECTION REQUIREMENTS (MSR)

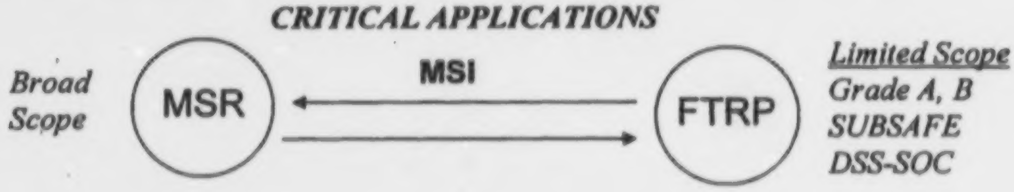

CRITICAL APPLICATIONS

Broad Scope

MSR

MSI

FTRP

Limited Scope
Grade A, B
SUBSAFE
DSS-SOC

- Requirements driven by consequences of failure
- FTRP establishes procedures to verify that fracture performance is adequate for intended application
- Fracture-Informed design

BACKGROUND

- **MOTIVATION: To prevent catastrophic failures by avoiding materials with a propensity for brittle fracture during design phase, thus focusing the material selection for critical applications on fracture-resistant materials (materials that exhibit significant plasticity in the presence of flaws)**

MATERIAL SELECTION

TRADITIONAL NAVY APPROACH

Non-nuclear, submarine applications

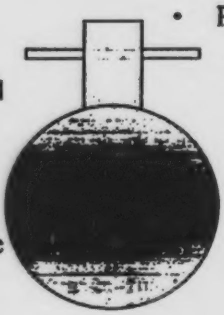

- NON-PRESSURE HULL BOUNDARY
  - Emphasis on mechanical and physical properties
    - Strength
    - Ductility
    - Corrosion resistance
    - Density
  - Fracture behavior not explicitly considered

- PRESSURE HULL BOUNDARY

  Strength an Important Factor

  BUT

  Emphasis on fracture behavior of welds

  AND

  Weld system development to prevent cracking

TRADITIONAL APPROACH TO MATERIAL SCREENING

- Traditional Navy approach differentiated between pressure and non-pressure hull boundary parts
- Non-pressure hull boundary parts have been selected based on strength, ductility and corrosion resistance only
- Pressure hull boundary parts must be made of materials exhibiting significant plasticity in the presence of flaws under high strain rates
- Selections are based on explosion bulge & crack starter tests, used to qualify pressure hull materials. Successful completion of these tests qualifies material and fracture is not a concern. No additional NDE is required for workmanship level flaws. Fracture mechanics based procedures are not incorporated in design process

FRACTURE MECHANICS APPROACH TO MATERIAL SCREENING

- FTRP departs from traditional methods. Parts are differentiated as far what the impact on the consequences of failure. Can Navy live with them?
- Parts can be either critical or non-critical.
- For non-critical parts no additional review requirements are imposed beyond design specifications
- FTRP is broken down into four (4) Parts, I,II,III, & IV. Part I is invoked. It may or may not trigger the other parts.

  Part II provides screening criteria and quantifies whether material provides significant plasticity. At this point either the traditional Navy approach or the fracture mechanics based approach can be used.

FRACTURE MECHANICS BASIS FOR MATERIAL SCREENING

- **Fundamental basis of fracture mechanics:**
  - **All Engineering Materials contain defects**

Defects vary in size from nano-scale to macro-scale. Macro-defects are within the capability of NDE methods.

Flaws or cracks act like stress raisers, thus giving rise to plastic deformation locally

Severity of stresses & strains at the crack tip is characterized by Stress Intensity Factor (SIF) K in linear fracture mechanics (LEFM) and by J in Elastic-plastic (EPFM) fracture mechanics

FRACTURE MECHANICS BASIS FOR MATERIAL SCREENING

(Cont'd)

- **Material's Resistance to Growth of pre-existing crack is referred to as FRACTURE TOUGHNESS. It is a material property under plain strain conditions (K_{Ic}) for LEFM and for EPFM (J_{Ic})**
- **Material's increasing Resistance to additional Growth is referred to as TEARING MODULUS (T). Not a material property**

What Combination of Strength and Fracture Toughness is adequate for a material to develop significant plasticity under high strain rates in the presence of flaws?

- **NRL (Pellini) developed RAD shown next. This method correlated Dynamic Tear Test (DT) with Yield Strength**
- **Traditional Strength of Materials emphasize plastic deformation, buckling failure modes, excessive deflections but do not address flaws**
- **FTRP addresses question by employing Failure Assessment Diagram (FAD), the locus of fracture & overload competing failure modes**

EXPLOSION BULGE TEST

- **Bi-axial tension opens existing flaws**
- **Explosive loading - high strain rate**
- **Large plastic deformation**
- **Thick section - high constraint**

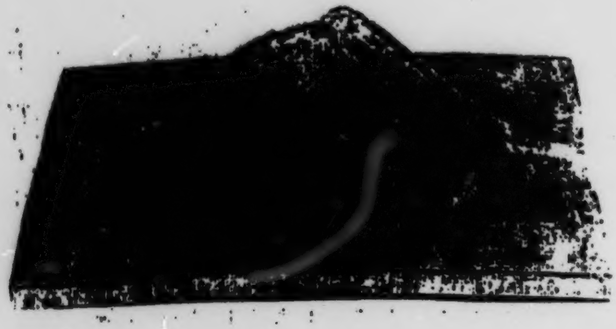

NEW PERFORMANCE REQUIREMENTS DRIVE MATERIAL SELECTION

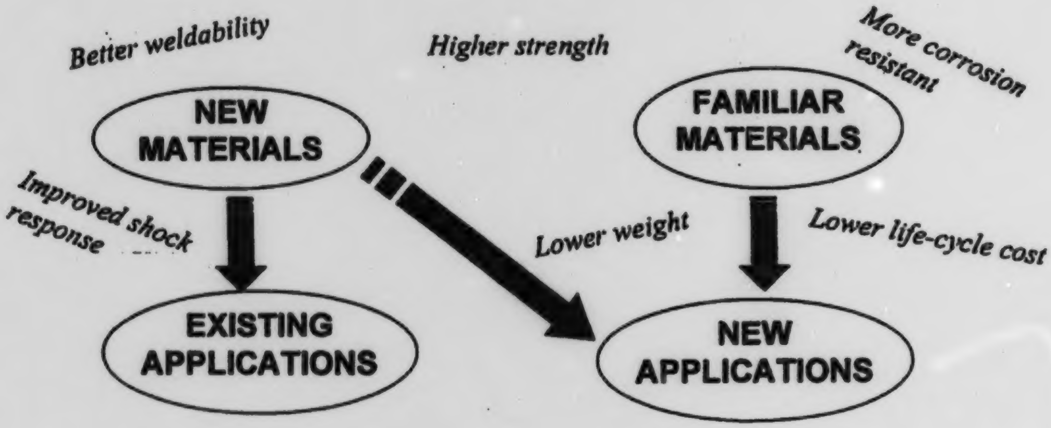

Better weldability

Higher strength

More corrosion resistant

NEW MATERIALS

FAMILIAR MATERIALS

Improved shock response

Lower weight

Lower life-cycle cost

EXISTING APPLICATIONS

NEW APPLICATIONS

NO MATERIAL IS FRACTURE-PROOF

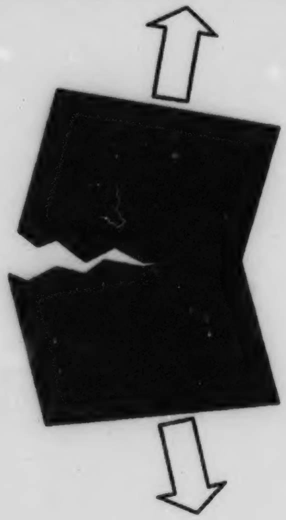

- Possibility of fracture determined by:
  - Applied Load
  - Flaw Size
  - Material Properties

"GOOD" MATERIAL CHARACTERISTICS

- What do we mean by a "GOOD" material, from a fracture point of view?
  - High Fracture Toughness, K_{mat}
  - High Tearing Resistance, T
  - High Toughness to Yield Ratio, K_{mat}/σ_{ys}
  - Good resistance to EAC

Even "GOOD" materials can fail by fracture if flaws are large enough, stresses high enough and design promotes it.

FTRP MATERIAL SCREENING CRITERIA

- TRADITIONAL
  - Pass structural element test such as Explosion Bulge, HTE or ETT.
  - Resistant to EAC
- *Focus is on overall structural behavior*
- *Extreme test - not applicable to some applications*
- *Does not measure a material property*

- FRACTURE MECHANICS
  - Meet minimum Flaw Tolerance
  - Meet minimum Tearing Modulus
  - Resistant to EAC
  - Confirmation with structural element test
- *Focus is on material properties that govern structural behavior*
- *Small specimen testing*
- *Evaluate influence of chemistry, product form, processing, fabrication and repair on fracture behavior*

WHAT IF MATERIAL DOES NOT PASS SCREENING?

Select Alternate Material

OR

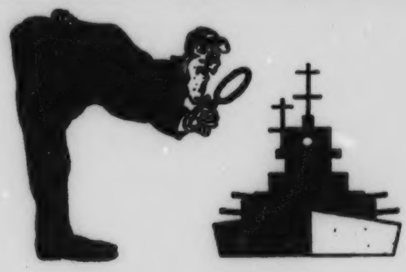

Evaluate specific part for intended application (Parts III & IV)

PART III : FLAW ASSESSMENT

- Determine if largest crack that could be missed would be critical under the most severe loading conditions at start of life. This requires knowledge of:
  - Materials, design and fabrication
  - NDE detection limits
  - Stresses in part
  - Material properties
  - Factors of Safety

PART IV : SUB-CRITICAL CRACK GROWTH

- Sub-critical crack growth mechanisms
  - *Fatigue*
  - *Stress Corrosion Cracking*
  - *Sustained Load Cracking*
- Determine if initial flaws could grow to critical size before end-of-life.

●
○
○

YES

Initial NDE + Periodic inspection and/or part replacement

○
○
○

NO

Initial NDE

MATERIAL SELECTION REQUIREMENTS

- **NAVY METALLIC MATERIALS PROPERTIES DATABASE**
- **Proposed electronic database tool to assist designers in selection of materials for critical applications**
- **Provides material properties and characteristics to enable activity use of the MSR and FTRP**
- **MARINE GRADE HIGH STRENGTH FASTENERS HANDBOOK**
- **Provides fastener alloy data, input to database**

NAVY MATERIALS PROPERTY DATABASE

E. J. Czyryca
Naval Surface Warfare Center
Carderock Division / Metals Department

301 227 5073
czyrycaEJ@nswccd.navy.mil

NAVY MATERIALS PROPERTY DATABASE

Objective: Provide all material system information in an accessible source to support design agent material selection and design of ship and submarine structures and machinery components. For critical applications, facilitate

NAVSEA Material Selection Requirements (MSR)

NAVSEA Fracture Toughness Review Process (FTRP)

[electronic database + expert system]

Navy Design Agent Metallic Material Selection

- ***Material Selection Requirements (MSR)***
  - **⇒Provides guidance and direction for the design agent to select materials for use in critical, non-nuclear applications**
  - **⇒Requires design agent to document Material Selection Information for critical applications**

Navy Design Agent Metallic Material Selection

- *Fracture Toughness Review Process (FTRP)*

⇒**Provides detailed *method* for assessing fracture safety for critical, non-nuclear components**

⇒**Defines material properties needed to demonstrate adequate fracture resistance; e.g. K_{Ic}, J_{Ic}, K_{ID}, J_{ID}, K_{Iscc}, σ / ε curves, fatigue data (S/N, da/dN - ΔK)**

Navy Design Agent Metallic Material Selection

Navy Materials Properties Database

⇒**Proposed electronic database tool to assist designers in selection of materials for critical applications**

⇒**Provides material properties and characteristics to enable design activity use of the MSR and FTRP**

NAVY MATERIALS PROPERTY DATABASE

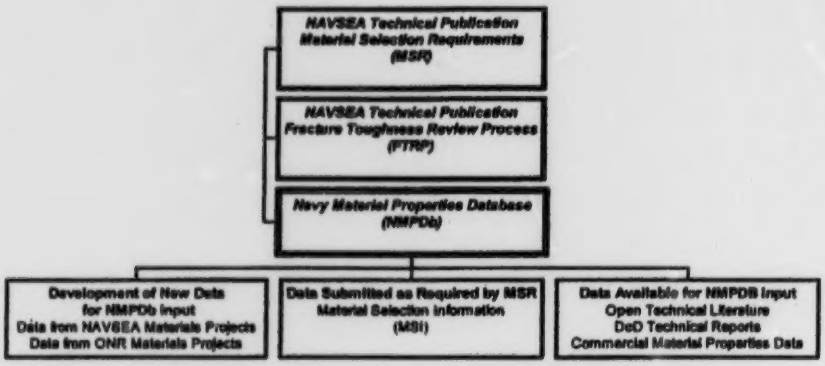

NAVSEA Technical Publication
Material Selection Requirements
(MSR)

NAVSEA Technical Publication
Fracture Toughness Review Process
(FTRP)

Navy Material Properties Database
(NMPDb)

Development of New Data
for NMPDb Input
Data from NAVSEA Materials Projects
Data from ONR Materials Projects

Data Submitted as Required by MSR
Material Selection Information
(MSI)

Data Available for NMPDB Input
Open Technical Literature
DoD Technical Reports
Commercial Material Properties Data

NAVY MATERIALS PROPERTY DATABASE

USAF, FAA, and NASA design activity resources for material properties for design and analysis:

- **Metallic Materials and Elements for Aerospace Vehicle Structures, MIL-HBK-5G / 2 vols.**
- **Aerospace Structural Metals Handbook / 5 vols**
- **Derivation of Crack Growth Properties of Materials for NASA/FLAGRO 2.0 / 3 vols**
- **Damage Tolerant Design Handbook / 4 vols**
- **Structural Alloys Handbook / 3 vols**

These resources are being converted to electronic format

MATERIAL CHARACTERISTICS TO BE ADDRESSED

Navy metallic systems vs Aerospace alloys

- ✓ EFFECT OF MARINE ENVIRONMENTS / EFFECT OF APPLIED CATHODIC POTENTIAL
- ✓ MAGNETIC PROPERTIES
- ✓ LOW-CYCLE FATIGUE / CORROSION FATIGUE
- ✓ WELDABILITY AND THE PROPERTIES OF WELDMENTS (HAZ & WELD METAL)
- ✓ BALLISTIC LIMITS FOR PROTECTION APPLICATIONS
- ✓ FRACTURE TOUGHNESS OF THICK SECTIONS AND WELDS AT LOW TEMPERATURE
- ✓ UNDEX OR AIR BLAST LOADING RATES

NAVY MATERIALS PROPERTY DATABASE

- **Phase I - Database Project Definition**
  - Establish NMPDb Working Group / Database scope & requirements
  - Establish data format & data presentation / data evaluation criteria
- **Phase II - Database Interim Format**
  - Software development / data retrieval / prioritize material sets & properties for interim format
  - Interim format / review & comment
- **Phase III - Database Expansion**
  - Software refined / expert system functions implemented
  - Expand database material sets & properties
  - Customer trials / review & tailor
- **Phase IV - Database Implementation & Maintenance**
  - Stand-up database / formalize database & software maintenance

NAVY MATERIALS PROPERTIES DATABASE WORKING GROUP ISSUES

- **DATABASE REQUIREMENTS**
- **DATA REQUIREMENTS**
- **DATA RETREIVAL / COLLECTION**
- **DATA QUALITY EVALUATION PROCESS**
- **DATA ENTRY / VALIDATION & APPROVAL PROCESS**
- **DATABASE VIRTUAL LIBRARY**
- **HARDWARE / SOFTWARE REQUIREMENTS**

NAVY MATERIALS PROPERTY DATABASE

AMPTIAC

Advanced Materials and Processes Technology
Information Analysis Center, Rome NY

- Administered by Defense Technical Information Center, operated by IIT Research Institute
- Consolidates previous materials IAC's
- Maintains defense materials library holdings
- Material database development / maintenance core mission
- Metals expertise (data evaluation) / DBMS software expertise

SUGGESTED INITIAL SET OF ALLOYS for NMPDb

Structural Steels	HY-80/100 Steel HSLA-80/100 Steel
Machinery Steels	Ni-Cr-Mo Steels Cr-Mo Steels
Stainless Steels	17-4 PH Steel XM-13 Steel Ferralium A286
Nickel Alloys	Alloy 625 Inconel 718 Monel K-500 Monel 400 H-Monel (cast)

SUGGESTED INITIAL SET OF ALLOYS for NMPDb

Copper Alloys	Ni-Al Bronze Hiduron (Cu-Ni) Copper-Be
Titanium Alloys	CP Titanium Gr. 2 CP Titanium Gr. 3 CP Titanium Gr. 3 Ti-6Al-4V ELI/VLI grades
Aluminum Alloys	5086 Al-Mg 5456 Al-Mg 6061-T6
Superalloys	MP159 / MP35N Haynes Alloy 25

LIST OF MATERIAL CHARACTERISTICS TO BE INCLUDED IN NMPDb

- Material system commentary
- Base Metal Mechanical Properties
- Base Metal Physical properties
- Weldment Mechanical Properties (Weld metal & HAZ)
- Weld metal physical properties
- Material system welding characteristics
- Material system fabrication characteristics

SUGGESTED LIST OF CHARACTERISTICS TO BE INCLUDED IN NAVY METALLIC MATERIALS PROPERTY DATABASE

I. MATERIAL SYSTEM COMMENTARY
  A. Description of alloy system
  B. Product forms [plate / thickness range, castings, forging]
  C. Manufacturing considerations [machining, surfacing, cutting]
  D. Fabrication considerations [welding, forming, fastening]
  E. Heat treatment considerations
  F. Environmental considerations
  G. Cost factors [relative]
  H. Availability [of all product forms]
  I. Specifications
  J. Service applications [prior experience in naval systems]

II. BASE METAL MECHANICAL PROPERTIES [for each product form in all possible options for heat treatment, stress relief, etc. and for full thickness range]
  A. Tensile properties
    1. tensile properties for longitudinal, transverse, and through-thickness
    2. precision stress-strain curves to large plastic strain
    3. true stress-true strain curves
    4. strain hardening characteristics
    5. cold-forming effects (pre-strain, Baushchinger effect)
    6. high strain-rate tensile properties
    7. effects of elevated temperature
    8. effects of cryogenic temperature

  B. Compression properties
    1. compression properties for longitudinal, transverse, and through-thickness
    2. precision stress-strain curves to large plastic strain
    3. true stress-true strain curves
    4. strain hardening characteristics
    5. cold-forming effects (pre-strain, Baushchinger effect)
    6. high strain-rate compression properties
    7. effects of elevated temperature
    8. effects of cryogenic temperature

C. Elastic constants
   1. elastic modulus (tension / compression)
   2. shear modulus
   3. Poisson's ratio

D. Hardness

E. Shear strength
   1. direct shear
   2. torsional shear

F. Fracture toughness properties
   1. K_{Ic} / J_{Ic} versus temperature
   2. K_{Id} / J_{Id} versus temperature
   3. Charpy V-notch impact toughness versus temperature
   4. dynamic tear impact toughness versus temperature
   5. nil-ductility transition temperature [ferrous products]
   6. crack-arrest toughness

G. Fatigue properties
   1. cyclic stress-strain curves
   2. low-cycle fatigue (strain-range vs. cycles to crack initiation)
   3. high-cycle fatigue (S/N curves)
   4. fatigue crack growth rate curves

H. Marine corrosion properties
   1. general corrosion
   2. crevice corrosion
   3. galvanic corrosion
   4. high-velocity corrosion
   5. corrosion Fatigue
      a) low-cycle fatigue (strain-range vs. cycles to crack initiation)
      b) high-cycle fatigue (S/N curves)
      c) fatigue crack growth rate curves
      d) effects of cathodic/anodic potentials
   6. stress corrosion
      a) uncracked, direct exposure
      b) stress corrosion cracking resistance (K_{Iscc})
      c) effects of cathodic/anodic potentials

I. Ballistic limits

J. Frictional properties
    1. coefficient of friction vs. other metals
    2. lubricants
    3. galling & seizing

III. BASE METAL PHYSICAL PROPERTIES
  A. Density

  B. Thermal properties
    1. melting point [range]
    2. specific heat
    3. thermal conductivity
    4. thermal expansion

  C. Magnetic properties
    1. magnetic permeability

  D. Electrical properties
    1. electrical resistivity

  E. Microstructural characteristics
    1. phase diagram
    2. typical microstructures
    3. critical transformation temperatures
    4. TTT & CCT diagrams

IV. WELDMENT MECHANICAL PROPERTIES (Weld metal & HAZ) [for each product form, all welding processes for full thickness range with applicable welding consumables and welding positions]
  A. Tensile properties
    1. tensile properties for all weld metal and transverse (across the weld)
    2. precision stress-strain curves to large plastic strain (all weld metal)
    3. weld metal true stress-true strain curves
    4. weld metal strain hardening characteristics
    5. weld metal high strain-rate tensile properties
    6. effects of elevated temperature
    7. effects of cryogenic temperature

B. Compression properties
  1. compression properties for all weld metal and transverse (across the weld)
  2. true stress-true strain curves
  3. strain hardening characteristics

C. Elastic constants [weld metal]
  1. elastic modulus (tension / compression)
  2. shear modulus
  3. Poisson's ratio

D. Hardness
  1. profile across weld & HAZ
  2. through multi-pass weld

E. Shear strength
  1. weld metal direct shear
  2. weld metal torsional shear
  3. longitudinal shear of fillet welds
  4. transverse shear of fillet welds

F. Charpy V-notch impact toughness versus temperature
  1. all weld metal with V-notch in welding direction
  2. HAZ with V-notch 1 mm from fusion line

G. Fracture toughness properties
  1. K_{Ic} / J_{Ic} of weld metal versus temperature
  2. K_{Id} / J_{Id} of weld metal versus temperature
  3. dynamic tear impact toughness of weld metal versus temperature
  4. K_{Ic} / J_{Ic} of HAZ versus temperature
  5. K_{Id} / J_{Id} of HAZ versus temperature
  6. dynamic tear impact toughness of HAZ versus temperature
  7. nil-ductility transition temperature [ferrous weld metals]
  8. crack-arrest toughness of weld metal

H. Explosion tests
  1. explosion bulge test series
  2. crack-starter explosion bulge test series
  3. explosion tear (hull toughness element) tests

- I. Fatigue properties
    - 1. cyclic stress-strain curves for weld metal
    - 2. low-cycle fatigue of weld metal (strain-range vs. cycles to crack initiation)
    - 3. low-cycle fatigue of weldment (strain-range vs. cycles to crack initiation)
    - 4. high-cycle fatigue of weldments (S/N curves)
    - 5. fatigue crack growth rate curves for weld metal & HAZ

- J. Marine corrosion properties
    - 1. welded panel general corrosion (preferential weld/HAZ attack)
    - 2. crevice corrosion (as above)
    - 3. high-velocity corrosion (as above)
    - 4. corrosion fatigue of weldments
        - a) low-cycle fatigue of weldment (strain-range vs. cycles to crack initiation)
        - b) high-cycle fatigue of weldment (S/N curves)
        - c) fatigue crack growth rate curves
        - d) effects of cathodic/anodic potentials
    - 5. stress corrosion
        - a) uncracked, direct exposure
        - b) stress corrosion cracking resistance (K_{Iscc})
        - c) effects of cathodic/anodic potentials

- K. Ballistic limits

- L. Dissimilar metal weldment properties
    - 1. full strength butt joints
    - 2. attachments / stud welding
    - 3. weld cladding / surfacing

V. WELD METAL PHYSICAL PROPERTIES
- A. Density
- B. Thermal properties
    - 1. melting point [range]
    - 2. specific heat
    - 3. thermal conductivity
    - 4. thermal expansion
- C. Magnetic properties
    - 1. magnetic permeability
- D. Electrical properties
    - 1. electrical resistivity

E. Microstructural characteristics
    1. phase diagram
    2. typical microstructures
    3. critical transformation temperatures
    4. TTT & CCT diagrams

VI. MATERIAL SYSTEM WELDING CHARACTERISTICS

A. Weldability (sensitivity to cracking) properties
    1. root bend, face bend, & side bend tests
    2. restrained-root cracking / keyhole restraint tests
    3. cruciform tests
    4. implant tests
    5. circular patch / circular fillet tests
    6. trough tests
    7. controlled thermal severity tests
    8. varestraint / transvarestraint hot-cracking tests
    9. long-plate restrained weld tests

B. Welding process operational envelope limits
    1. At lowest preheat & interpass temperature limits [highest weld metal C.R.]
    2. At highest preheat & interpass temperature limits [Lowest weld metal C.R.]

VII. MATERIAL SYSTEM FABRICATION CHARACTERISTICS

A. Manufacturing data
    1. machining information
    2. punching, shearing, sawing, cutting information
    3. cold forming procedures / limits
    4. fasteners / fastening procedures

B. Welding procedures
    1. welding process procedures and qualification
    2. repair welding
    3. NDE procedures

#511878 ④

Novel Materials for Improved Fire Safety of Naval Platforms

by D. E. Veinot

Defence Research Establishment Atlantic
Dartmouth, Nova Scotia, Canada

ABSTRACT

Fire at sea has been called "the ultimate nightmare." Ships' damage control teams must respond to fire at sea rapidly and contain or extinguish the fire as soon as possible often under very difficult situations exacerbated by the dense smoke and toxic fumes released as materials burn. Ships carry a considerable mass of combustible materials including interior furnishings, electrical cables and painted bulkheads and deckheads to name a few. Moreover, fire can spread rapidly throughout the ship from one compartment to another along burning electrical cable pathways. The use of construction materials, which are inherently fire resistant, can provide a measure of protection against fire but this is often costly or impossible to do owing to unavailability of fire resistant products. It follows, then, that materials vulnerable to fire will inevitably be present on ships and that any measure that can be used to reduce their vulnerability thus minimizing fire growth would be beneficial to surviving a fire at sea, and, in the case of a warship, possibly critical to mission success. This briefing will describe some of the studies that have led to the development of novel, non-toxic, non-combustible, inorganic intumescent coatings that can be used to retrofit a variety of vulnerable substrates and provide an increased measure of fire resistance. Further, the presentation will describe some products of commercial initiatives that have grown out of this basic technology in Canadian industry.

NOVEL MATERIALS FOR IMPROVED FIRE SAFETY OF NAVAL PLATFORMS

D. E. Veinot
Defence Research Establishment Atlantic

Outline

- Background
- Approach: Intumescent Coatings
- Organic versus Inorganic Systems
- Experimental Work and Evaluations
- Commercialization Opportunities
- Summary

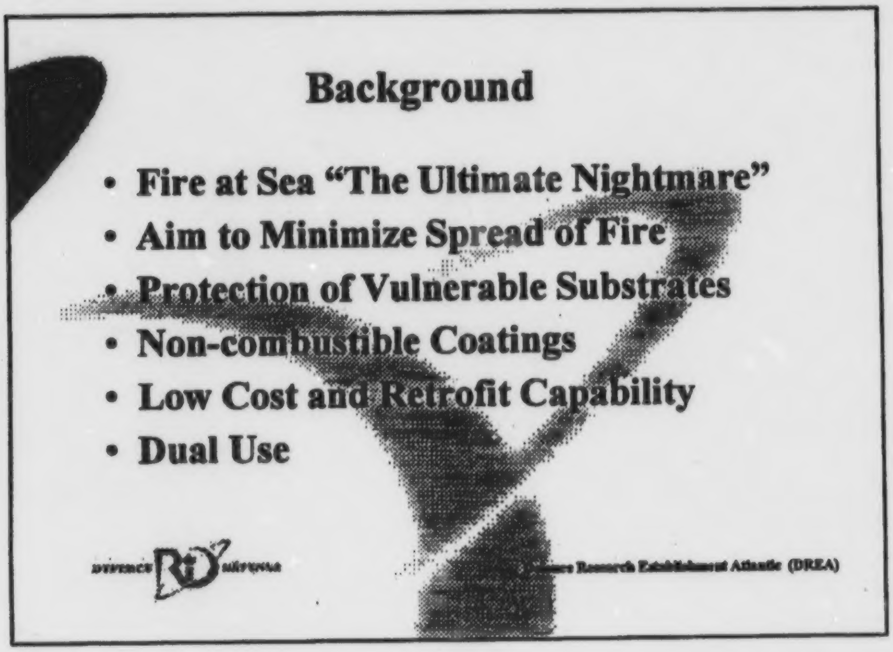

Background

- Fire at Sea "The Ultimate Nightmare"
- Aim to Minimize Spread of Fire
- Protection of Vulnerable Substrates
- Non-combustible Coatings
- Low Cost and Retrofit Capability
- Dual Use

ence Research Establishment Atlantic (DREA)

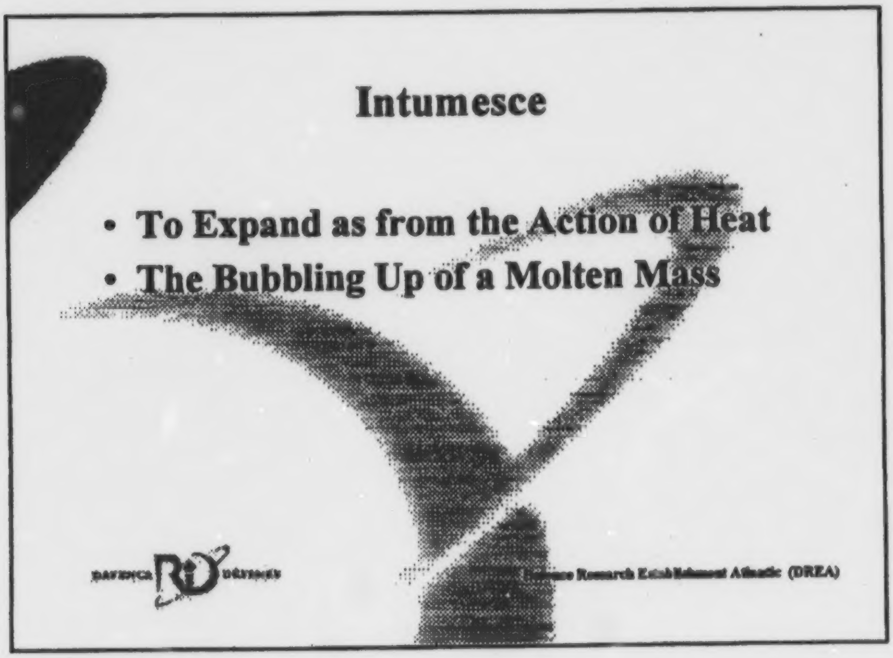

Intumesce

- To Expand as from the Action of Heat
- The Bubbling Up of a Molten Mass

nce Research Establishment Atlantic (DREA)

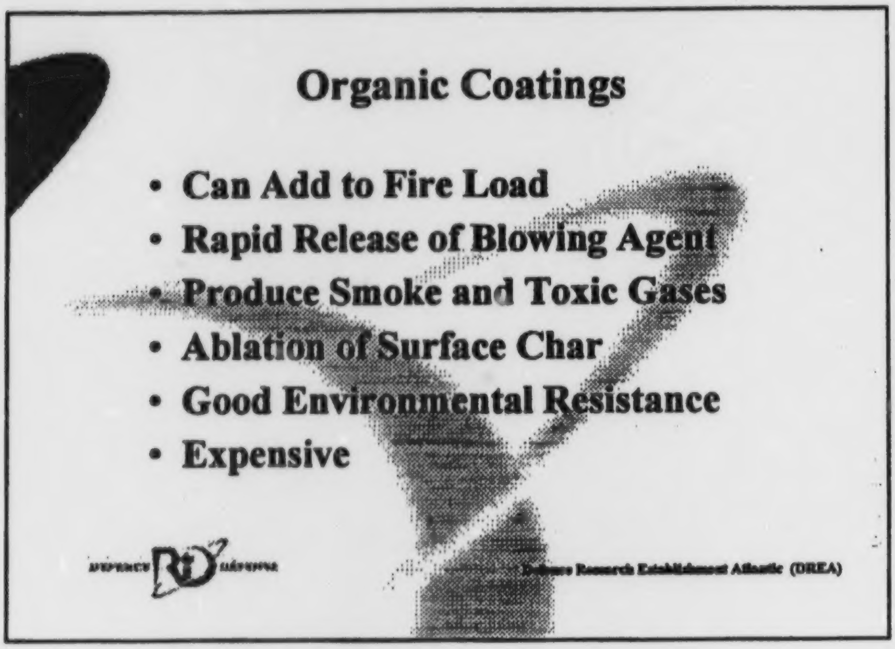

Organic Coatings

- Can Add to Fire Load
- Rapid Release of Blowing Agent
- Produce Smoke and Toxic Gases
- Ablation of Surface Char
- Good Environmental Resistance
- Expensive

DEFENCE DÉFENSE

Defence Research Establishment Atlantic (DREA)

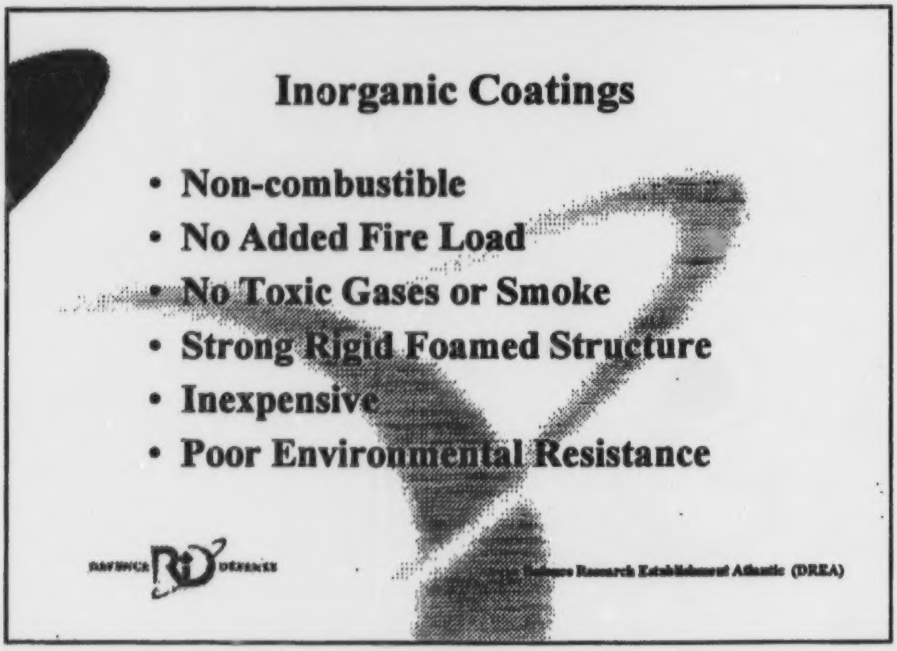

Inorganic Coatings

- Non-combustible
- No Added Fire Load
- No Toxic Gases or Smoke
- Strong Rigid Foamed Structure
- Inexpensive
- Poor Environmental Resistance

DEFENCE DÉFENSE

Defence Research Establishment Atlantic (DREA)

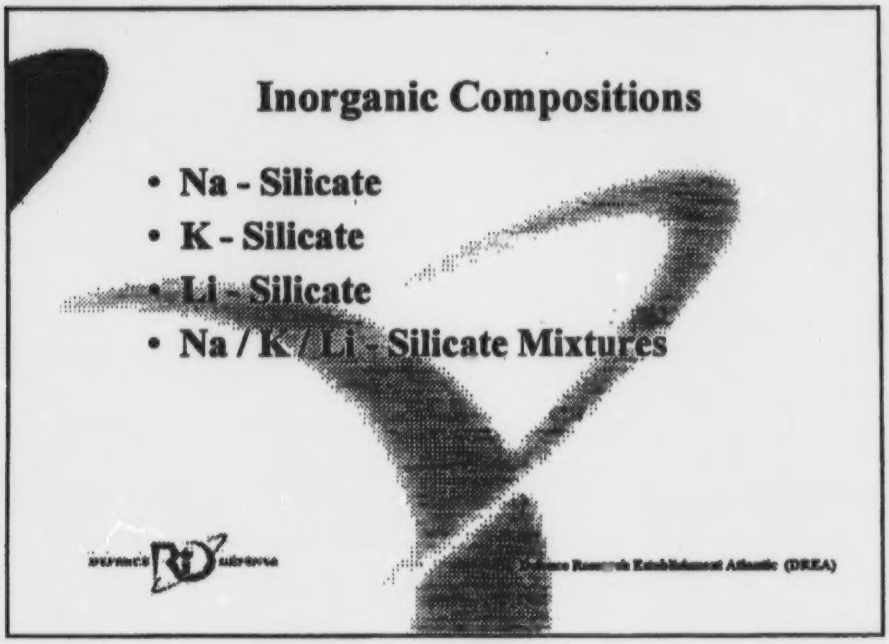

Inorganic Compositions

- Na - Silicate
- K - Silicate
- Li - Silicate
- Na / K / Li - Silicate Mixtures

Defence Research Establishment Atlantic (DREA)

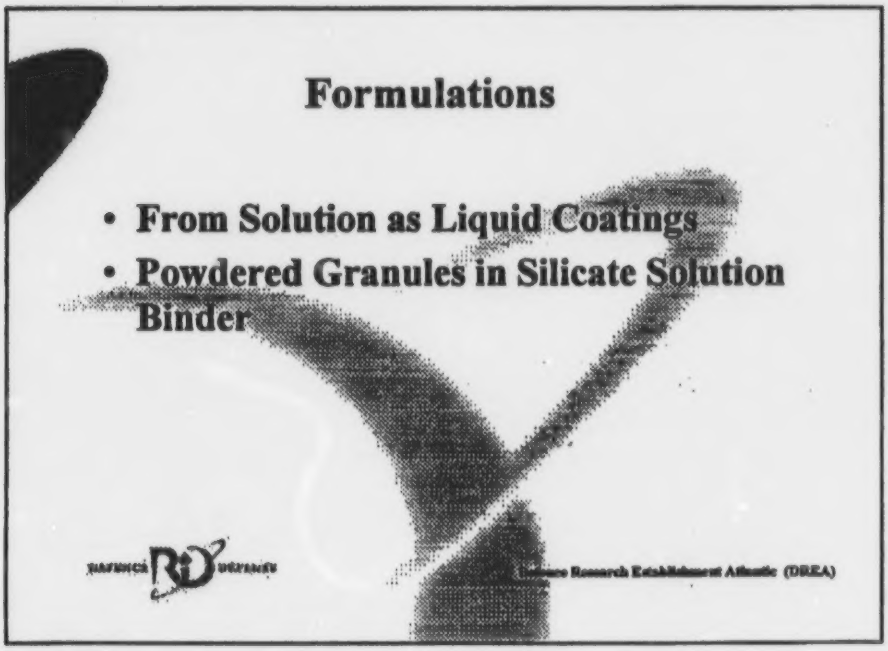

Formulations

- From Solution as Liquid Coatings
- Powdered Granules in Silicate Solution Binder

Defence Research Establishment Atlantic (DREA)

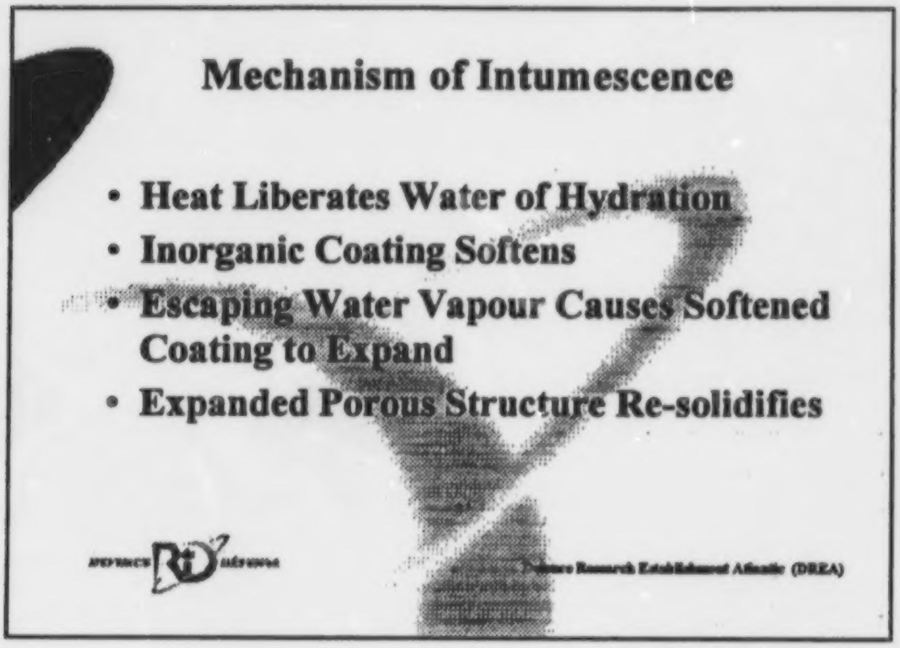

Mechanism of Intumescence

- Heat Liberates Water of Hydration
- Inorganic Coating Softens
- Escaping Water Vapour Causes Softened Coating to Expand
- Expanded Porous Structure Re-solidifies

Defence Research Establishment Atlantic (DREA)

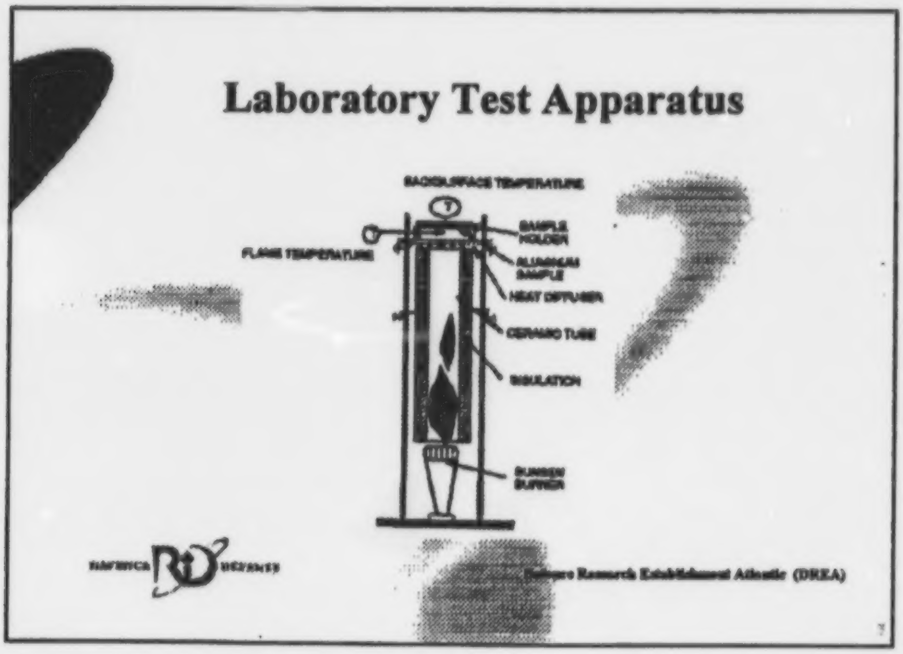

Laboratory Test Apparatus

BACKSURFACE TEMPERATURE
T
SAMPLE HOLDER
FLAME TEMPERATURE
ALUMINUM SAMPLE
HEAT DIFFUSER
CERAMIC TUBE
INSULATION
BUNSEN BURNER

Defence Research Establishment Atlantic (DREA)

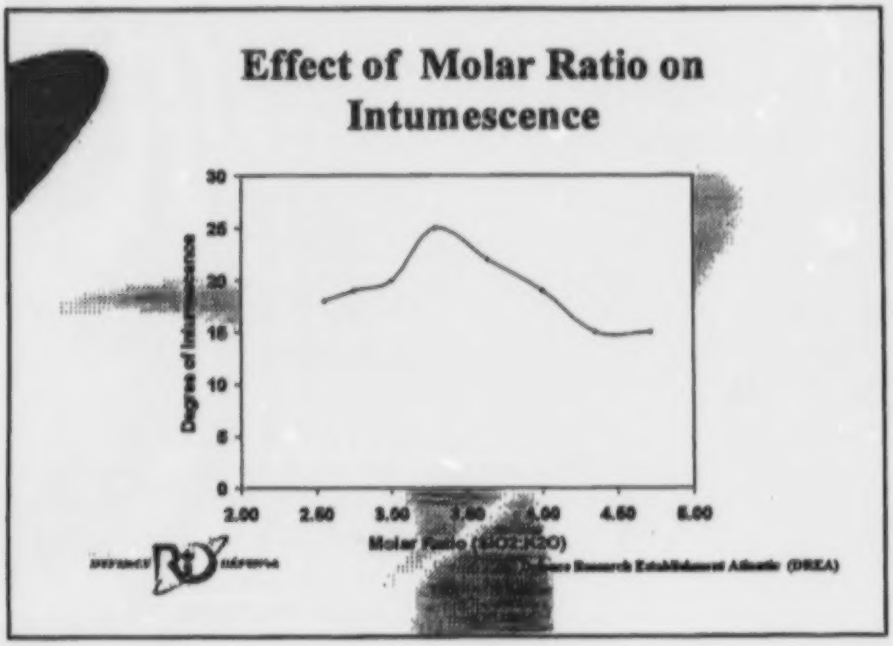

Effect of Molar Ratio on Intumescence

Defence Research Establishment Atlantic (DREA)

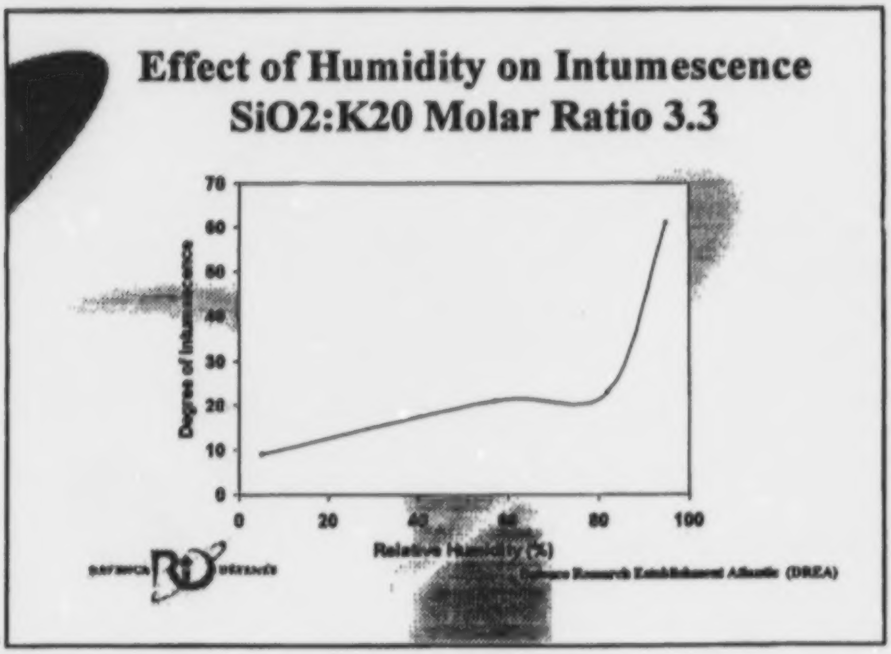

Effect of Humidity on Intumescence SiO2:K20 Molar Ratio 3.3

Defence Research Establishment Atlantic (DREA)

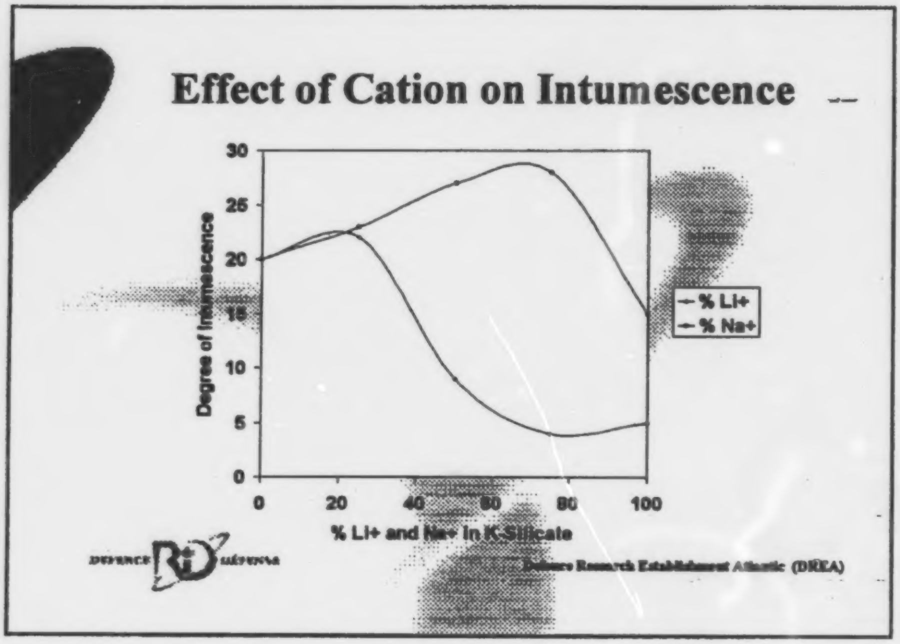

Effect of Cation on Intumescence

Defence Research Establishment Atlantic (DREA)

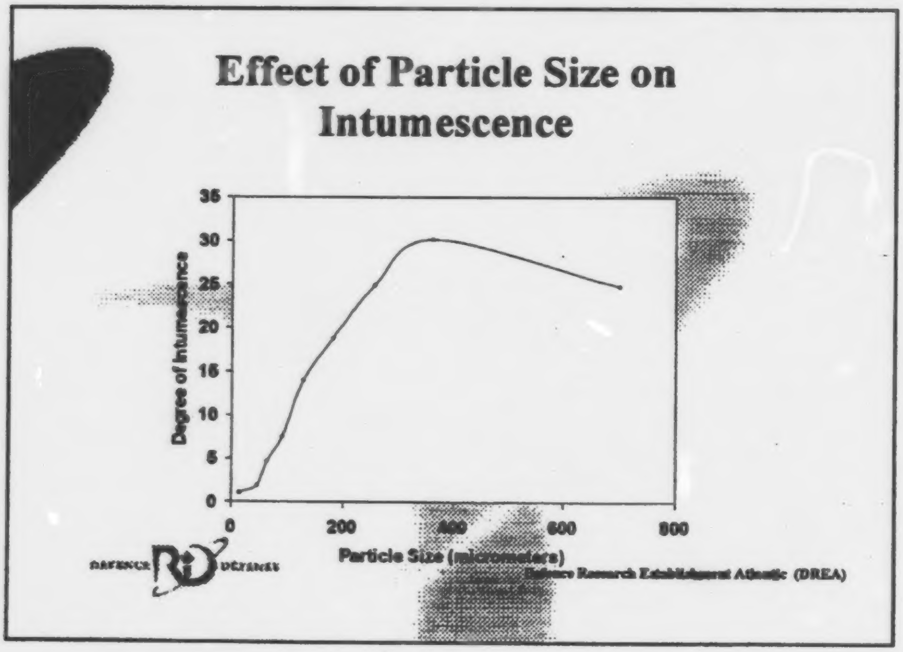

Effect of Particle Size on Intumescence

Defence Research Establishment Atlantic (DREA)

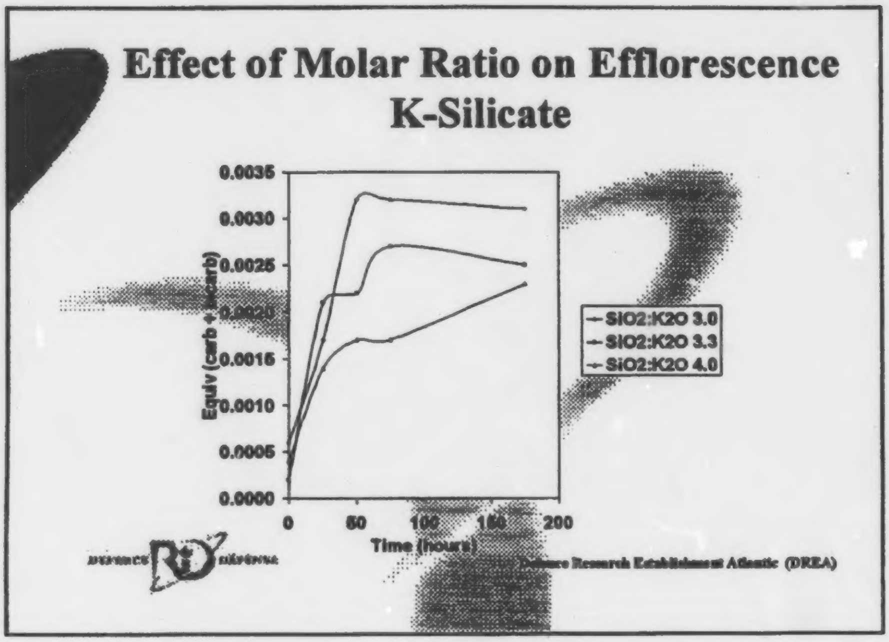

Effect of Molar Ratio on Efflorescence K-Silicate

Defence Research Establishment Atlantic (DREA)

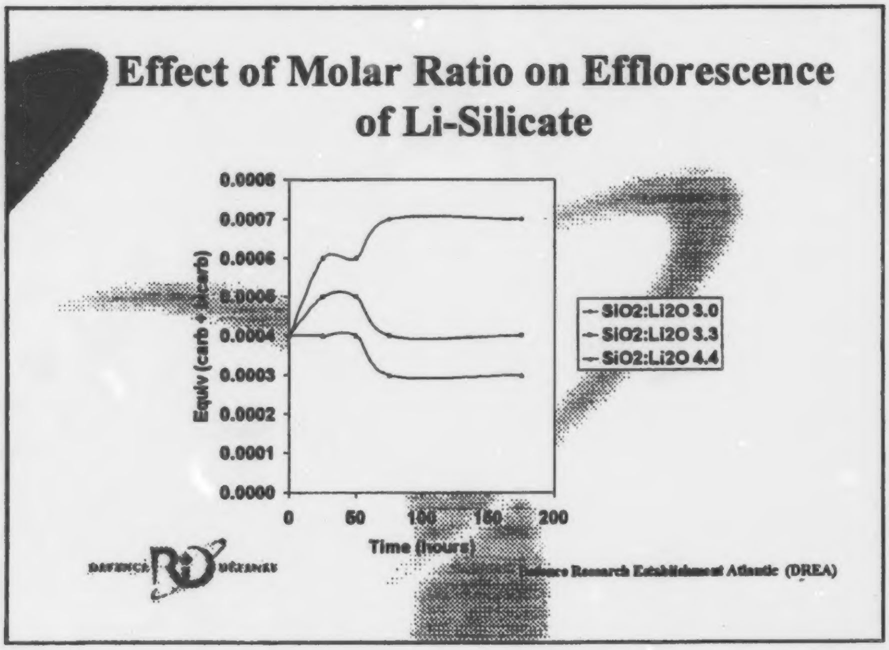

Effect of Molar Ratio on Efflorescence of Li-Silicate

Defence Research Establishment Atlantic (DREA)

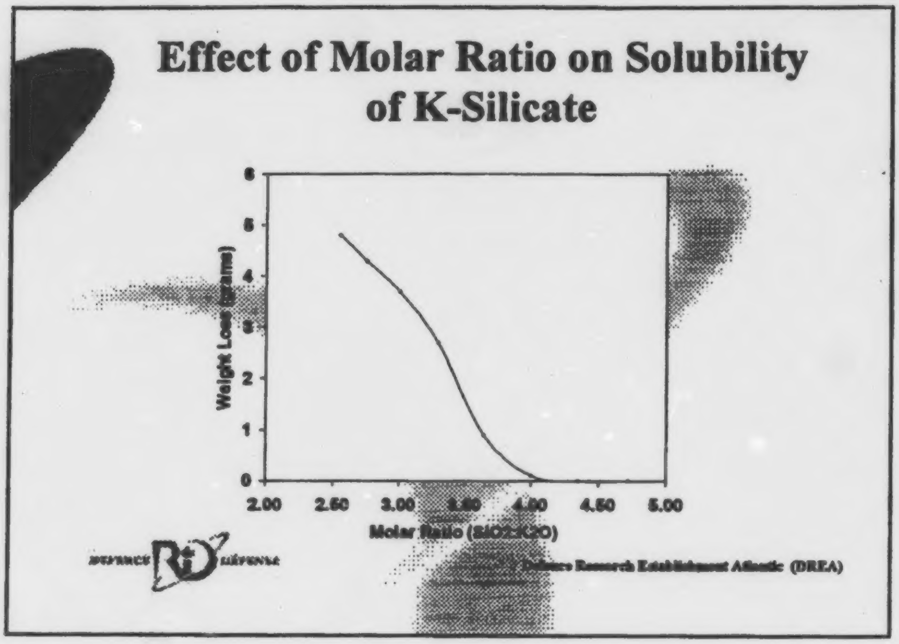

Effect of Molar Ratio on Solubility of K-Silicate

Defence Research Establishment Atlantic (DREA)

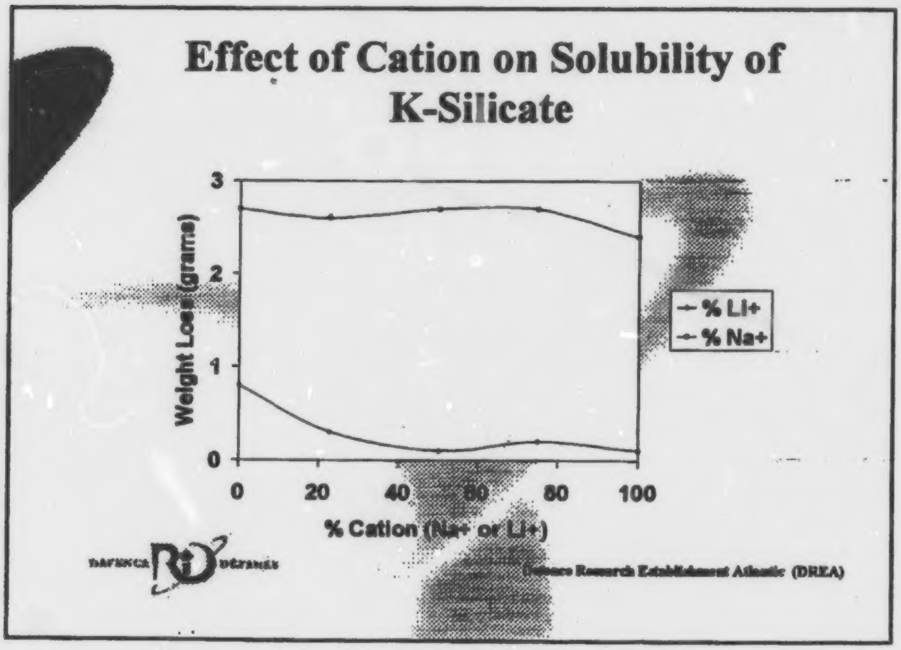

Effect of Cation on Solubility of K-Silicate

Defence Research Establishment Atlantic (DREA)

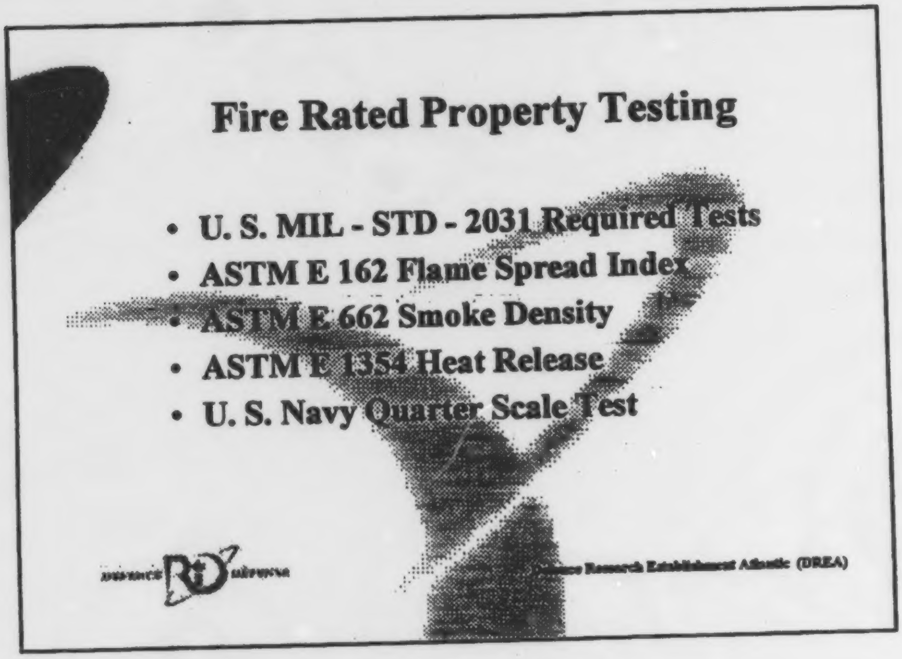

Fire Rated Property Testing

- U. S. MIL - STD - 2031 Required Tests
- ASTM E 162 Flame Spread Index
- ASTM E 662 Smoke Density
- ASTM E 1354 Heat Release
- U. S. Navy Quarter Scale Test

ence Research Establishment Atlantic (DREA)

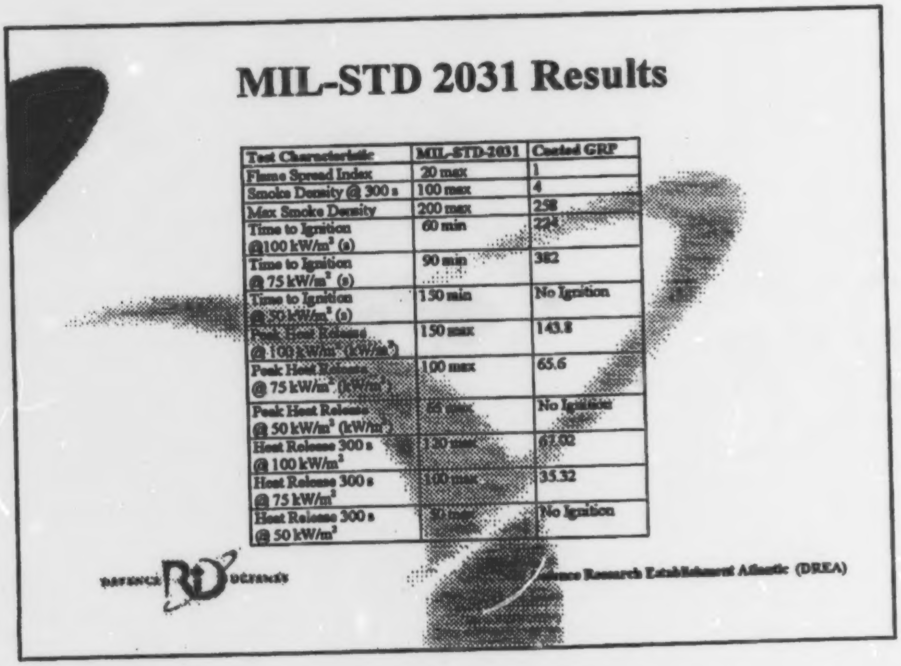

MIL-STD 2031 Results

Test Characteristic	MIL-STD-2031	Coated GRP
Flame Spread Index	20 max	1
Smoke Density @ 300 s	100 max	4
Max Smoke Density	200 max	258
Time to Ignition @100 kW/m^2 (s)	60 min	224
Time to Ignition @ 75 kW/m^2 (s)	90 min	382
Time to Ignition @ 50 kW/m^2 (s)	150 min	No Ignition
Peak Heat Release @ 100 kW/m^2 (kW/m^2)	150 max	143.8
Peak Heat Release @ 75 kW/m^2 (kW/m^2)	100 max	65.6
Peak Heat Release @ 50 kW/m^2 (kW/m^2)	65 max	No Ignition
Heat Release 300 s @ 100 kW/m^2	120 max	67.02
Heat Release 300 s @ 75 kW/m^2	100 max	35.32
Heat Release 300 s @ 50 kW/m^2	50 max	No Ignition

ence Research Establishment Atlantic (DREA)

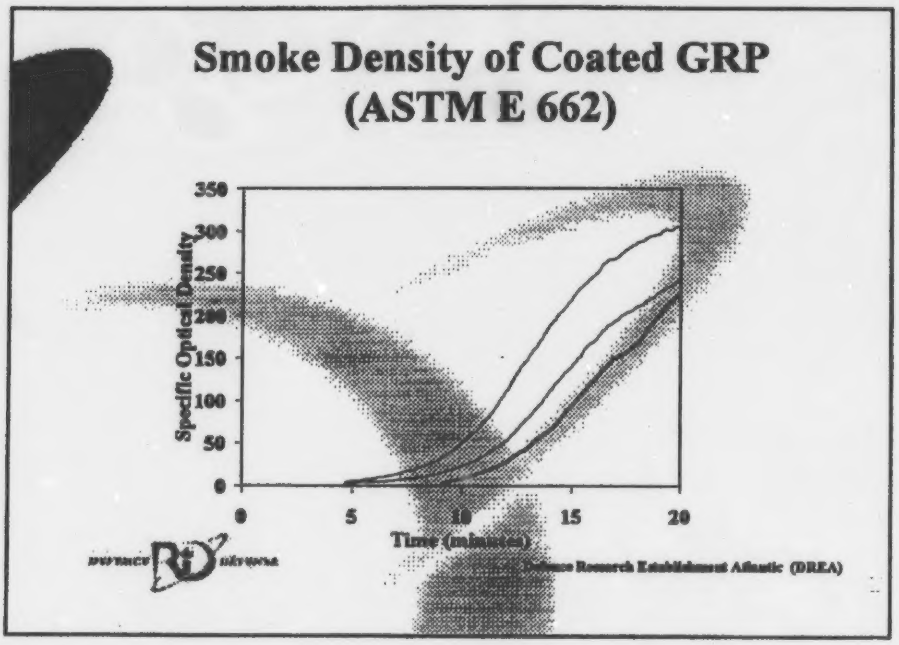

Smoke Density of Coated GRP (ASTM E 662)

Defence Research Establishment Atlantic (DREA)

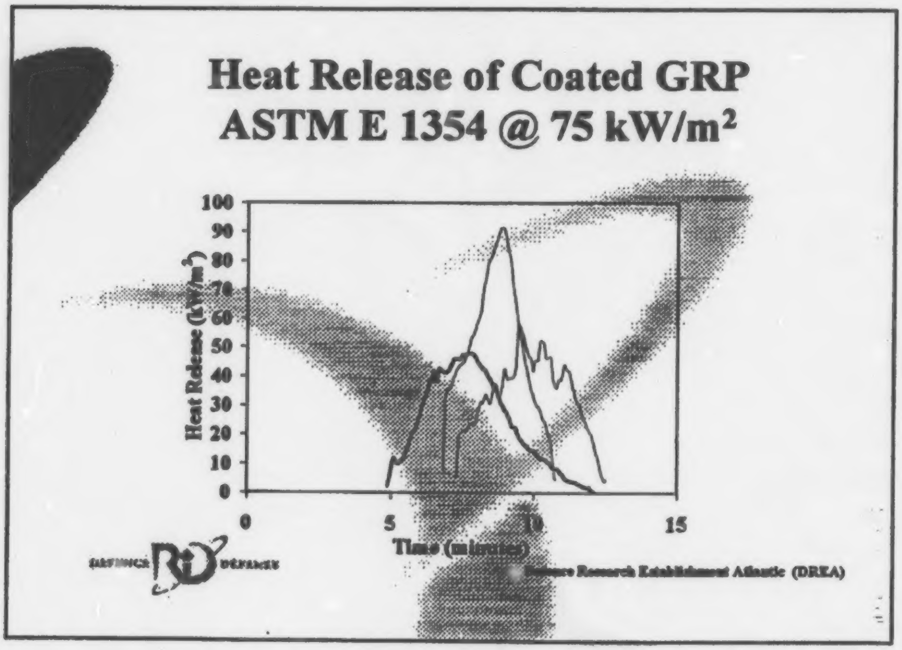

Heat Release of Coated GRP ASTM E 1354 @ 75 kW/m²

Defence Research Establishment Atlantic (DREA)

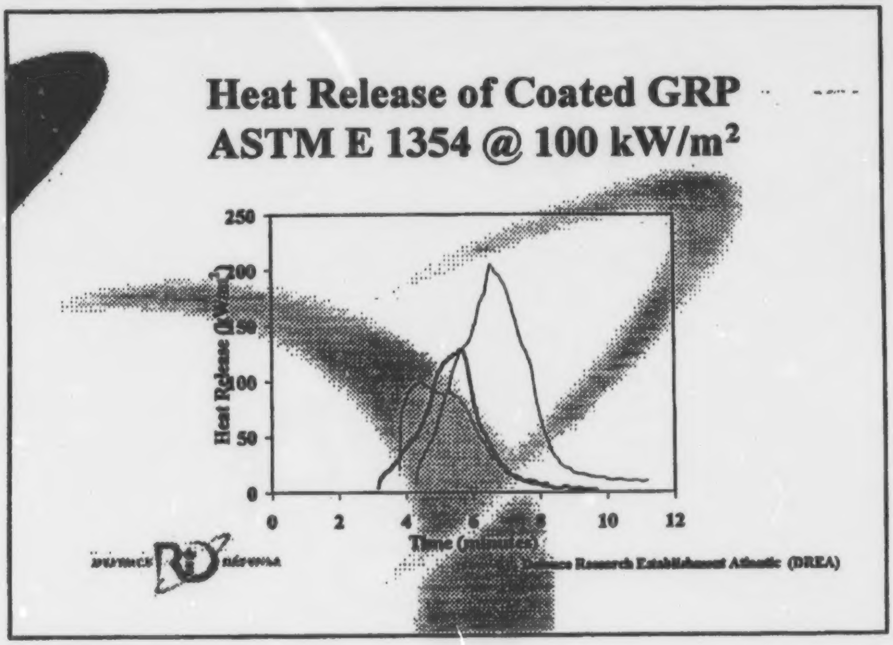

Heat Release of Coated GRP
ASTM E 1354 @ 100 kW/m²

Defence Research Establishment Atlantic (DREA)

United States Navy Quarter Scale Test

- Arranged Through TTCP with NSWC
- Vinyl Ester GRP Substrate
- Inorganic Powder / Binder Coating
- Spray Application to 20-40 mil Thickness
- Adhesion

Defence Research Establishment Atlantic (DREA)

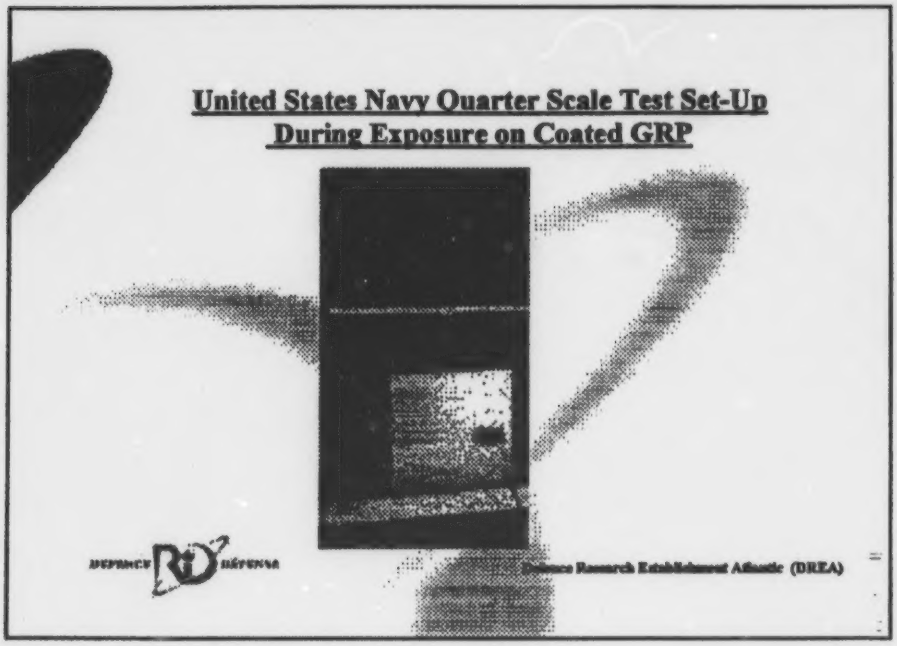

United States Navy Quarter Scale Test Set-Up During Exposure on Coated GRP

DEFENCE R&D DÉFENSE

Defence Research Establishment Atlantic (DREA)

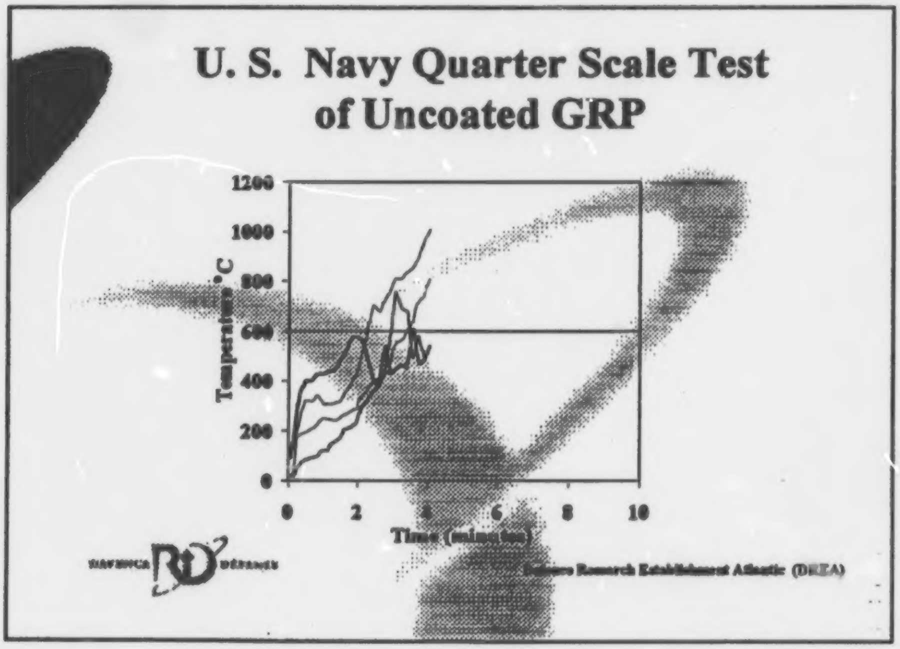

U. S. Navy Quarter Scale Test of Uncoated GRP

DEFENCE R&D DÉFENSE

Defence Research Establishment Atlantic (DREA)

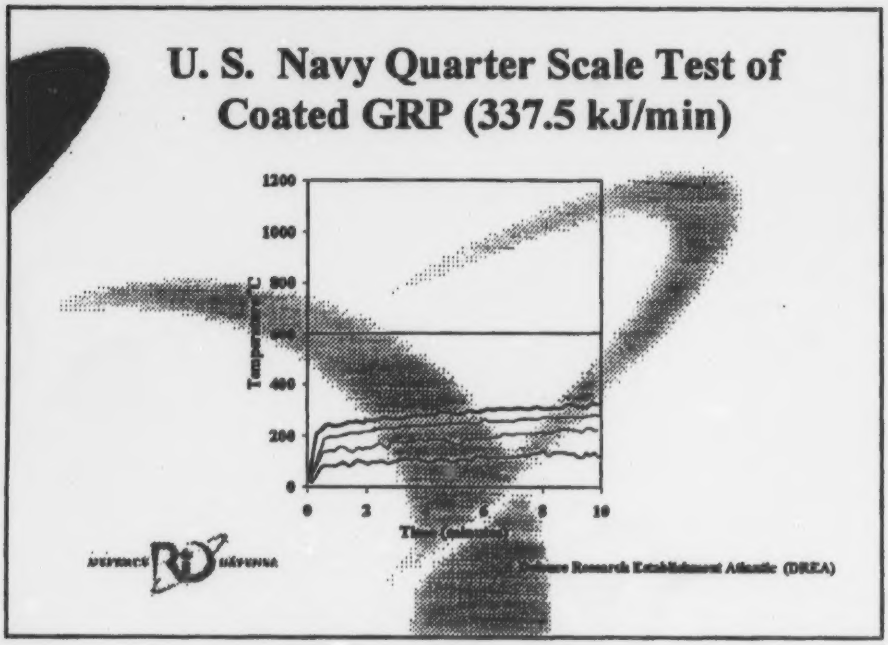

U. S. Navy Quarter Scale Test of Coated GRP (337.5 kJ/min)

DEFENCE R&D DÉFENSE

Defence Research Establishment Atlantic (DREA)

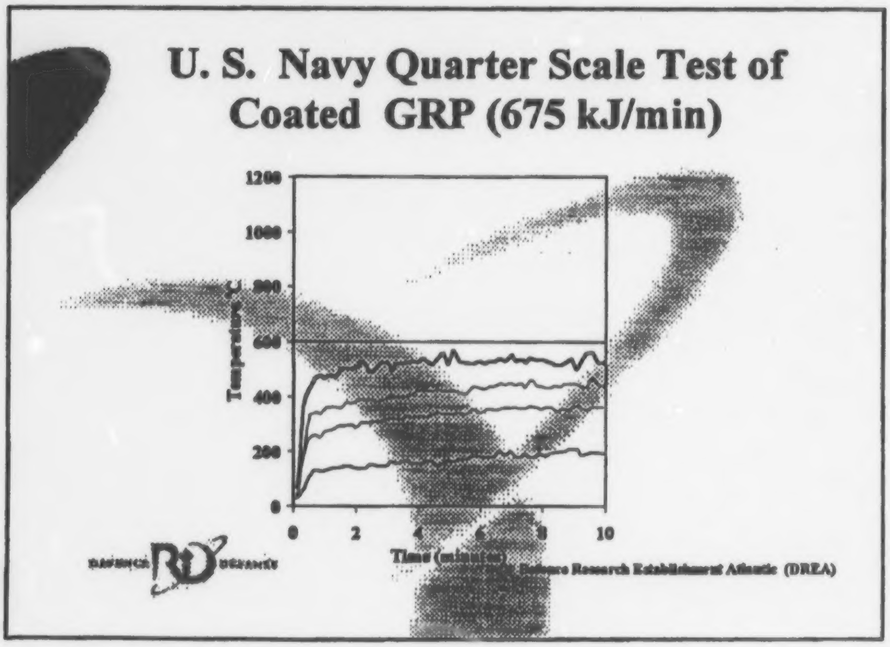

U. S. Navy Quarter Scale Test of Coated GRP (675 kJ/min)

DEFENCE R&D DÉFENSE

Defence Research Establishment Atlantic (DREA)

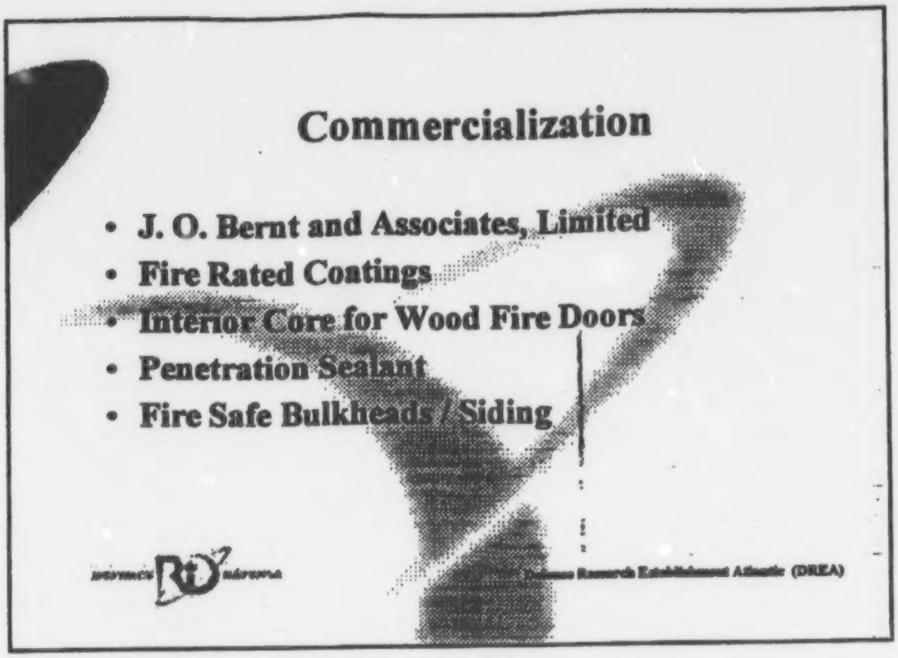

Commercialization

- J. O. Bernt and Associates, Limited
- Fire Rated Coatings
- Interior Core for Wood Fire Doors
- Penetration Sealant
- Fire Safe Bulkheads / Siding

Defence Research Establishment Atlantic (DREA)

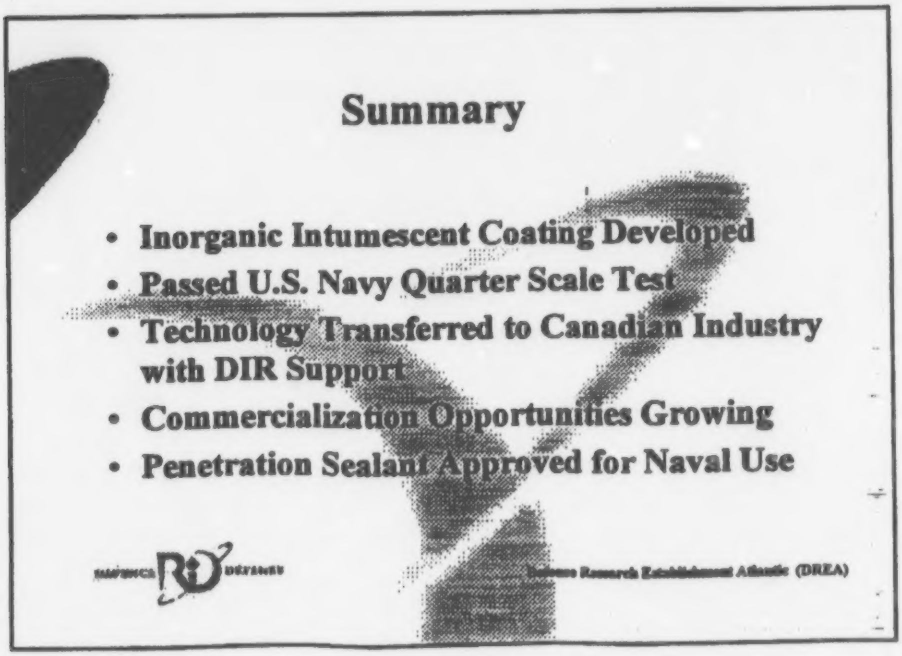

Summary

- Inorganic Intumescent Coating Developed
- Passed U.S. Navy Quarter Scale Test
- Technology Transferred to Canadian Industry with DIR Support
- Commercialization Opportunities Growing
- Penetration Sealant Approved for Naval Use

Defence Research Establishment Atlantic (DREA)

#511879 (5)

A Computational Study on Material Model Selection for Shape Memory Alloys

Dr. V. G. DeGiorgi

Multifunctional Materials Branch, Code 6350
Naval Research Laboratory
Washington, DC 20375, USA
degiorgi@anvil.nrl.navy.mil

H. Saleem
Science and Engineering Apprentice Program
George Washington University
Washington, DC 20052 USA

ABSTRACT

Computational simulations are an essential component in today's design process. The design and fabrication of smart materials in a production environment requires analytical and computational tools that can describe smart material behavior. Of concern in this paper are the material constitutive models to be used in computational analyses. Often there are questions concerning the accuracy of constitutive models for the active components such as shape memory alloys (SMAs). These constitutive models can substantially increase computational costs in terms of both memory and time requirements. Model size limitations and use of complex constitutive models are often competing factors. Therefore whether the use of complex constitutive models for smart components actually benefit the analysis of the device is an issue of concern to those in the smart materials design community.

The current work examines the differences in computational simulations due to the choice of constitutive model for shape memory alloy. The device considered is a thick walled tube fabricated of SMA metal and subjected to torsion loading. The constitutive models examined are Tanaka's exponential model [1], Rogers-Liang cosine model [2] and Boyd-Lagoudas et al. polynomial model [3,4]. One common feature to all models is the complexity in the number of material parameters required. Experimental work used for comparison was performed independently and completed prior to initiation of the computational study [5].

INTRODUCTION

Smart materials and devices are emerging from the laboratory environment and becoming recognized as viable design options. New applications are appearing almost daily. Critical to the success of this transition are the analysis and design tools available. One important question that must be addressed is:

> Are sufficient tools available so that anyone other than a research scientist can create a practical smart material or device with assurance that its performance will be acceptable?

This is a key issue facing smart materials and devices. A build and test philosophy often dominates in the laboratory environment but is unacceptable in the manufacturing environment. What is needed in the manufacturing environment is a design methodology for smart materials and devices that parallels accepted practices for conventional materials. The designer needs tools that allow for prediction of behavior and structural integrity. The designer must have confidence that the product will perform as expected. Building prototypes of all possible design options is not a viable design methodology if smart materials and devices are to be competitive with conventional designs. In brief, analytical and computational tools are required that provide accurate simulations of smart material and device behavior.

An accepted design methodology for conventional material is finite element analysis. The versatility of finite element analysis for all aspects of design is well established. Parameter studies in which minor modifications to the design are evaluated are common practice. The basic information required for finite element analyses are component geometry and material properties. The need for accurate material properties exists for both active and conventional materials. Simple constitutive response models may be computationally efficient but may not accurately represent material performance. In this paper the performance of and the variation in calculated results due to the selection of SMA constitutive model are examined.

Many smart materials and devices have used the active response of shape memory alloys (SMAs). SMAs can provide large displacement and large strain capabilities at relatively low frequencies. Methodologies for accurately predicting performance are necessary for the designer to take advantage of SMA capabilities.

The development of SMA constitutive models is an area of much research. During the past two decades there have been many constitutive models proposed for SMAs. There are continual advancements, modifications as well as combinations of existing constitutive models. In addition new constitutive models are being presented. Many of these constitutive models are very complex and require a large number of measured constants to characterize the material. Many are cumbersome to use in the design environment. Many are one-dimensional or based on single-crystal behavior and not appropriate for use in the design of bulk material components. To date there is no consensus as to the 'best' model. The resulting situation is one where there are many competing models with little guidance on accuracy and appropriateness. This creates a frustrating situation for the designer. As stated previously the move of smart materials and devices from the laboratory to a production environment is dependent on designers having ready access to constitutive models that have a known accuracy in prediction. Accuracy and ease of use are real issues. Schroeder et al. [6] discusses the advantages and disadvantages of a select group of SMA constitutive models. Similarly, the purpose of the current work is the evaluation of two possible design simplifications and three established constitutive models for a specific design.

In this study variations in finite element calculated results that are solely due to the selection of SMA constitutive model are investigated. Five material constitutive response modeling approaches are evaluated: 100% martensite, 100% austenite, Tanaka [1], Liang-Rogers [2] and Lagoudas et al [3,4]. Computational results are compared for the different models to determine if there is a pattern of performance based on model selection.

The component modeled is a tube subjected to a constant torsion loading. The tube is a thick walled hollow cylinder fabricated from a NiTi (K-Alloy) SMA alloy with an outer radius of 0.579 cm and a wall thickness of 0.267 cm. The resulting wall thickness/diameter ratio is 0.23. The gage length of the tube is 5.84 cm. The tube is fabricated from bulk SMA material. The geometry selected is a SMA actuator design that was developed as part of the Northrop-Grumman lead Smart Wing program [7]. The purpose of the tube is to twist a wing frame raising the leading edge while lowering the trailing edge.

The tube geometry and material were chosen from a series of three tube geometries and two materials used in a series of experiments designed to examine the physical behavior of the tube under torsion and tension-torsion loading [5]. All tube geometries were similar in that all could be classified as thick walled. A single geometry and material combination was selected allowing the current work to concentrate on the variation of calculated results due to constitutive model selection. It was felt that little additional information on constitutive modeling performance could be obtained by examining additional geometries or a second material.

The usefulness of advanced constitutive models that capture SMA phenomenon is dependent on the accuracy of the model when used to evaluate performance for realistic structures. In addition to accuracy, computational requirements must also be considered when constitutive model performance is evaluated. A very accurate model that requires significantly more computer time may not be used in a design analysis due to cost or time limitations. In order to be a viable design tool constitutive models must be both accurate and require only an acceptable amount of computer resources. Acceptable run times are often based as much on corporate culture as on computer or cost considerations. Therefore it is important to provide the potential user with baseline information on run times using different constitutive models. This information is provided here for the models evaluated.

MATERIAL CONSTITUTIVE RESPONSE

As noted in the previous section numerous constitutive models have been proposed for SMAs. This paper examines differences in calculated results obtained for the SMA torque tube based on assumptions of 100% martensite, 100% austenite and on the use of three accepted constitutive models. The 100% martensite and 100% austenite cases use conventional finite element constitutive response and are evaluated to determine if these extremes provide bounds for device behavior. This modeling approach is appealing to the designer because it makes no additional demands on computational time and requires only conventional material parameters; i.e. modulus of elasticity, yield stress, Poisson's ratio and description of stress-strain response. In this approach, SMA behavior is represented in the same manner as other non-linear structural materials.

The constitutive models selected for the study are all thermodynamic based models. The three constitutive models can be considered to represent the evolution of a constitutive model. Tanaka's model as used in this work is based on 1D model describing the phase transformation of SMAs using energy balance equations and the Clausius-Duhem inequality. The internal state variable used to define the state of the material is ξ the martensite volume fraction. Details of the model are not presented here but can be found in Reference 3. In this model the transformation kinetics defined by ξ are describing using an exponential function. Tanaka's model has been extended to 3D by Boyd-Lagoudas [8].

Liang-Roger model is formulated in the same manner as Tanaka's constitutive model. A primary difference in the two models is use of a cosine function in the Liang-Rogers model to define ξ, the martensite volume fraction. The cosine function was defined empirically and agrees well with experimental data. A driving force for replacement of the exponential representation of ξ is the elimination of singularity points at 100% martensite and 100% austenite conditions. It was shown by Liang-Rogers that the cosine representation more accurately represented transformation behavior. The Liang-Rogers model evaluated can be considered to be a modification and extension of Tanaka's model.

The model of Lagoudas et al. is a thermodynamic derivation of the constitutive response of SMA materials. The model is an extension of prior work by various researchers. Details of the derivation of the model can be found in References [3] and [4]. The model uses a polynomial representation for ξ. In addition the Lagoudas et al. model accounts for 4 of the 5 phenomena of SMA material response. The five phenomena are pseudoelsaticity by transformation, pseudoelasticity by reorientation or ferroelasticity, the shape memory effect by transformation, the shape memory effect by reorientation and the two way shape memory effect. All characteristics of behavior except the two way shape memory effect are included in the model.

The three models chosen represent the evolution of concepts in the constitutive response of SMAs. Each model successful builds on its predecessors. It is not apparent whether the added complexity resulting from extensions and modifications of the original thermodynamic model is required for all geometries and design conditions. One goal of the current work is to examine the effects of model evolution on calculated results. Whether the later thermodynamic models with more complex representations of ξ provide increased accuracy is of interest. The increase in computational costs, measured in terms of run time, due to increase in representation complexity is also of concern to the designer. Unfortunately, in many cases, computational resources drive the choice of constitutive models. Comparisons such as presented here will assist the designer by providing insight into variations in accuracy based on model selection.

In all cases the constitutive models have been coded in terms of 3D stress states and defined as solution subroutines for use with ABAQUS, a commercial finite element program.

Material parameter data is based on Keefe et al. experimental results [5] and parameters defining a generic SMA alloy [9]. The martensite and austenite shear modulus values are 26.2 GPa and 48.6 GPa, respectively. Poisson's ratio is 0.33. Parameters unique to the three constitutive models are taken as equal to those for typical SMA material as defined in the User's Manual [9]. It is recognized that increased accuracy can be obtained by parameter testing for specific SMA material. In the present work, all models used general material response data. No model has more accurate material parameter than the other constitutive models. While this may not be ideal for engineering analysis of a smart material, it common for handbook values only to be available to the analyst. The issue of material parameter accuracy is important but is not addressed in this work. The approach taken of using standard values for all constitutive model parameters is considered appropriate for this comparison study of calculated results.

NUMERICAL SIMULATION

The commercial finite element code ABAQUS [10] is used for all analyses. The total length of tube modeled is 7.62 cm. The gage length of 5.84 cm is centered along the length of tube modeled. An exploded view of the model is shown in Figure 1. Sufficient extensions are included above and below the gage length to isolate any boundary condition end effects from the gage length. The gage section consists of 10752 elements; 6 elements in the thickness direction, 32 elements around the circumference and 56 layers in the length direction. Extension sections consist of 6 elements in the thickness direction, 32 elements around the circumference and 5 layers in the length direction. The model of end extensions and gage length of tubing consists of 12672 elements and 15010 nodes. All elements are 8 noded quadrilateral bricks. All elements are assigned the same material properties. In the case of user subroutine constitutive response, material characteristics vary from element to element as a result of the stress state in each element under load. Both stress and temperature induced transformations from one material phase to the other are included in the user subroutine.

The actuator design considered provides a moment to the wing box when the tube is installed and subjected to increased temperature. The experimental process establishes the twist response to an applied moment. This behavior is what is duplicated in the finite element simulation. In order to apply a uniform moment to the tube rigid surfaces are attached to the both ends of the cylinder. One end of the cylinder is fixed. A torsional loading is applied to the other end by means of an applied constant radial velocity. Rate effects are not included in the analysis.

100% martensite and 100% austenite cases are defined using standard ABAQUS modeling capabilities. No special elements or constitutive models are used for these runs. Two material formulations were examined; linear elastic-nearly perfectly plastic and linear elastic-plasticity slope of (1/4)E. The first formulation is nearly perfectly plastic because it was found a small slope was necessary to assistance in solution convergence near the yield point. A relationship of 6895 MPa: 1 cm/cm strain was assumed for the slope of the inelastic portion of the nearly perfectly plastic curve. In the higher plastic slope cases where the plasticity slope is defined as (1/4)E. The value of elastic modulus, E, depends on the base material assumption for the run. E_m is used for the martensite case; E_a is used for the austenite case. The resulting slope between stress and strain for the inelastic response curve are 6550 GPa: 1 cm/cm strain for martensite and 12152 GPa: 1 cm/cm strain for austenite. The yield point is estimated based on general yield information on SMAs. Yield was defined as occurring at 0.2% offset strain. This definition resulted in yield values of 52.4 MPa for austenite and 97.2 MPa for martensite. These values correspond well with reported value of 50 MPa for austenite and the reported range of 100-150 MPa for martensite [11].

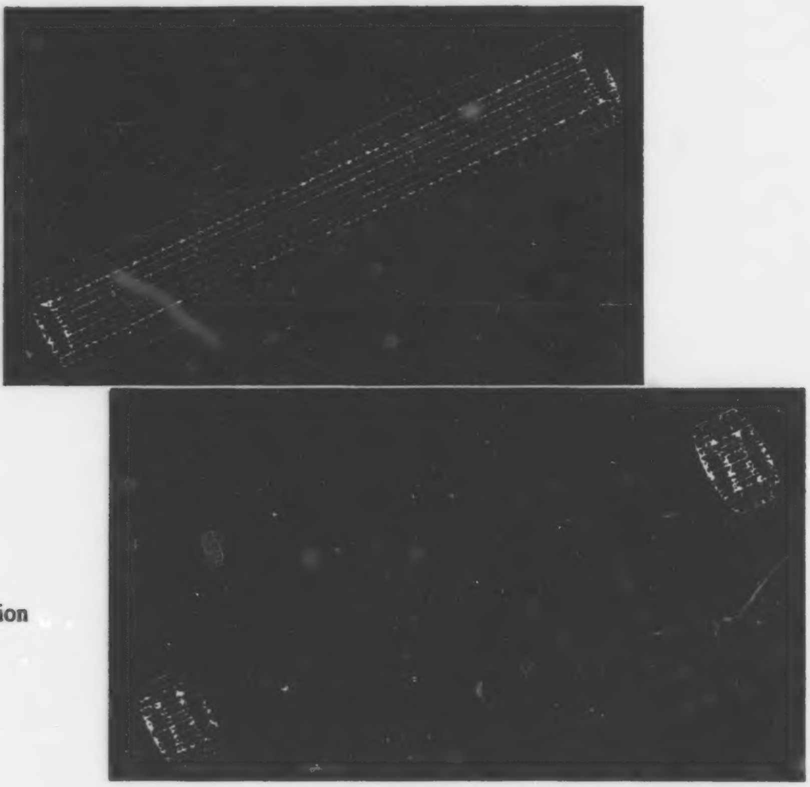
Torque tube

End caps used for application
of boundary conditions

Figure 1. SMA Tube Geometry and Finite Element Model Mesh

A_s temperature is assumed to be 17°C and A_f temperature is assumed to be 34°C. These values compare favorably with reported values [11].

ABAQUS allows for users to define the material constitutive response used in the analysis. The user is responsible for accurately describing the stress-strain relationship for individual elements through use of user defined subroutines. This is the approach used to define constitutive response for Tanaka, Liang-Rogers and Lagoudas et al. models. User subroutines for all constitutive models used were provided by Lagoudas [9]. Coding as provided had been validated for use in ABAQUS. Test runs were completed to determine model stability under loading conditions.

NUMERICAL SIMULATION RESULTS

Single cases are run for each of the pure materials. There is no variation in material properties with temperature incorporated into the pure material. Standard ABAQUS solution procedures are used for these analyses.

Two series of numerical simulations were completed for the three constitutive models; the first at 34°C, the austenite finish temperature, and the second at 24°C, an intermediate temperature. In addition analyses were completed for 60°C, 80°C, 100°C, 120°C and 140°C for the Tanaka and Lagoudas et al. models. These are temperatures well above the austenite finish temperature and were of interest for possible applications. Additional temperature runs were not made for the Liang-Rogers model due to numerical difficulties encountered in the 24° and 34°C runs for the specified geometry and loading conditions. In all computational models the martensite volume fraction is set to zero at the start of the simulations. The temperature is held constant in the numerical simulation. This is equivalent to the constant temperature environment created by the heating tape on the SMA tube in the experimental procedure [5].

Comparison of Numerical Results

The result of primary interest is the applied moment vs. angle of twist loading history. Calculated results are compared for the different modeling methods for the different temperature levels.

The applied moment vs. angle of twist is shown in Figure 2 for the 100% martensite and 100% austenite cases. The increase of slope in the plastic region has a significant effect on results. Also shown in Figure 2 are moment vs. angle of twist for Tanaka, Liang-Rogers and Lagoudas et al. models at 24°C, a temperature between the austenite start and finish temperatures. At this temperature phase transformations are stress and temperature induced. In this case the martensite nearly perfectly plastic case becomes a lower bound only for higher values of angle of twist (greater than 3.5 degrees/cm). Tanaka's model is a lower bound for low to moderate angles of twist (0 to 3 degrees/cm). Liang-Rogers model become numerically unstable at a lower angle of twist than at the higher temperature case. Lagoudas et al. model again predicts a stiffer structure requiring more moment to twist at higher angles of twist. The 100% austenite nearly perfectly plastic with a slope of (1/4)E for the inelastic portion of the stress-strain curve is the upper bound for all cases considered. It is interesting to note that all curves for low to moderate angles of twist (0-2.5 degrees/cm) are bracketed by Tanaka and 100% austenite elastic-nearly perfectly plastic. This is in contrast to the 34°C case where the majority of results are bracketed by the 100% austenite elastic-perfectly plastic and (1/4)E inelastic slope cases.

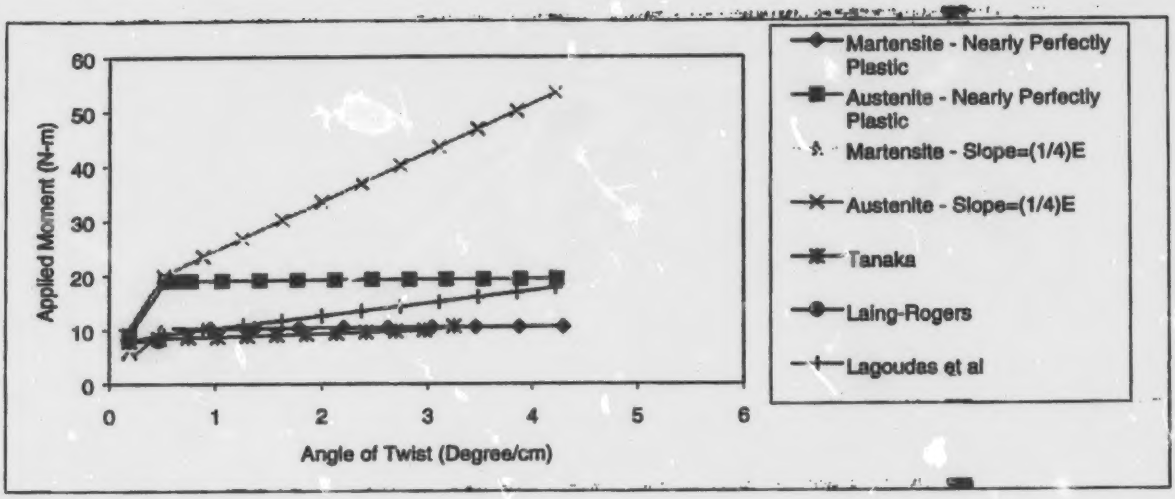

Figure 2. Applied Moment vs. Angle of Twist, Intermediate Temperature (24°C)

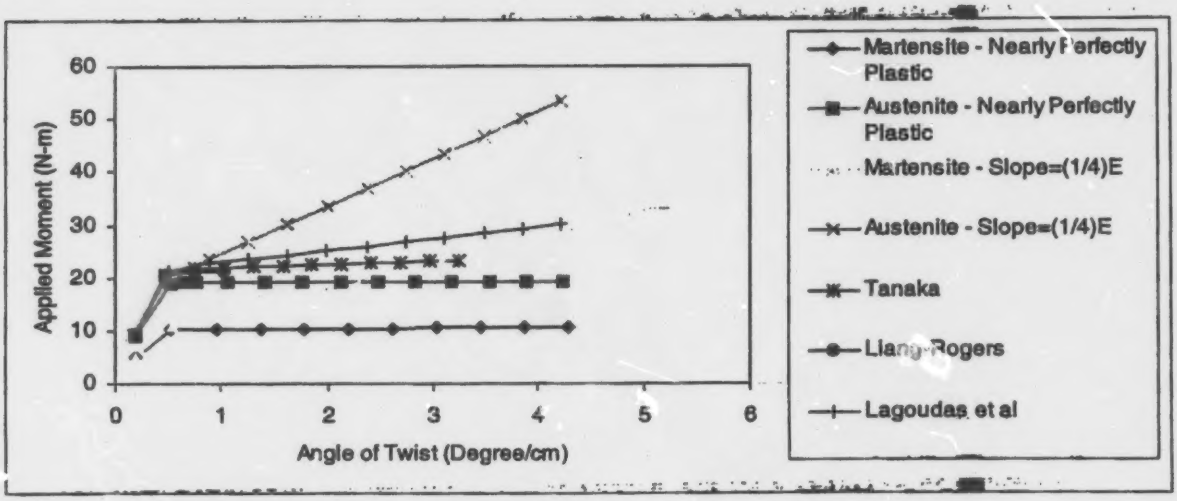

Figure 3. Applied Moment vs. Angle of Twist, Austenite Finish Temperature 34°C

Figure 3 shows the variation in calculated results at the austenite finish temperature (34°C). At this temperature transformations are stress induced. At this temperature 100% martensite elastic-nearly perfectly plastic represent a lower bound for calculated results. Austenite models with a slope of (1/4)E on the inelastic portion of the stress-strain curve serve as an upper bound. Lagoudas et al. model predicts a stiffer structure than Tanaka and Liang-Rogers. Lagoudas et al. requires more moment to twist the tube. Liang-Rogers solution exhibited severe numerical convergence problems within the ABAQUS finite element code at low levels of angle of twist (0.5 to 1.0 degrees/cm).

Figure 4 shows the applied moment vs. angle of twist for all temperatures as calculated using Tanaka's constitutive model When the temperature is at or below the austenite finish temperature, calculated results show significant reductions in response. Calculated results for temperatures at or below the austenite finish temperature start to diverge from higher temperature results at an approximate angle of twist of 0.2 degree/cm. Higher temperature responses show negligible differences until much larger angles of twist; 1 degree/cm for 60°C and larger angles for higher temperatures. As temperature increases, the region of linear moment-angle of twist response increases. Identical results are seen for all temperatures for the linear response regime. At lower temperatures smaller amounts of applied load are required to obtain a set value of angle of twist. This is consistent with the more compliant nature of the martensite phase.

All analyses complete 24 increments of loading. Greater angles of twist (4.2 degrees/cm) are obtained for temperatures at or below the austenite finish temperature. The maximum angle of twist obtained for higher temperature conditions is 3.2 degrees/cm. There is some indication in computational results that convergence is easier to obtain for Tanaka model in the lower temperature regime.

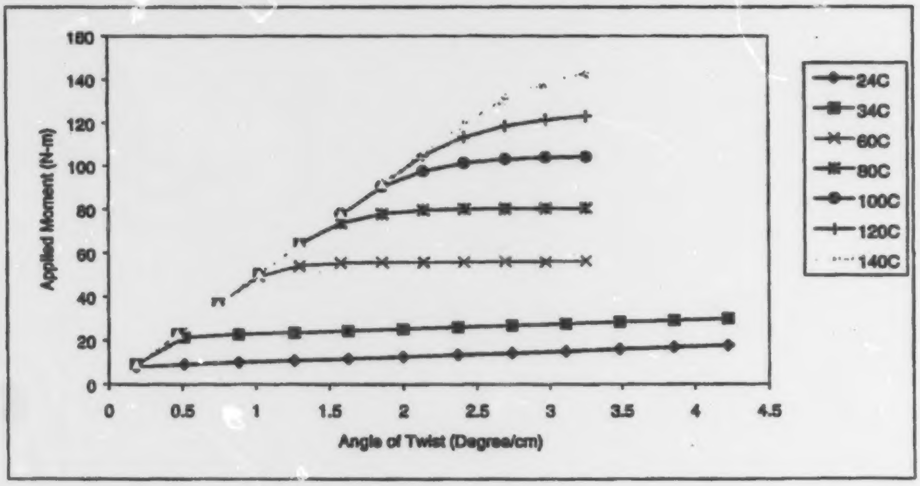

Figure 4. Applied Moment vs. Angle of Twist for Tanaka Constitutive model.

Figure 5 shows the applied moment vs. angle of twist for all temperatures as calculated using Lagoudas et al. constitutive model. As in the previous case, calculated results at and below the austenite finish temperature diverge from higher temperature results at a very low angle of twist; approximately 0.2 degree/cm. Lagoudas et al. constitutive model shows an earlier departure from linear moment-angle of twist response for higher temperatures than is seen in Tanaka's model. When the temperature is below the austenite finish temperature the calculated response shows that an only very small increase in applied moment is required for a large increase in angle of twist. Again, this is consistent with the more compliant nature of the martensite phase.

Figure 5. Applied Moment vs. Angle of Twist for Lagoudas et al. Constitutive model.

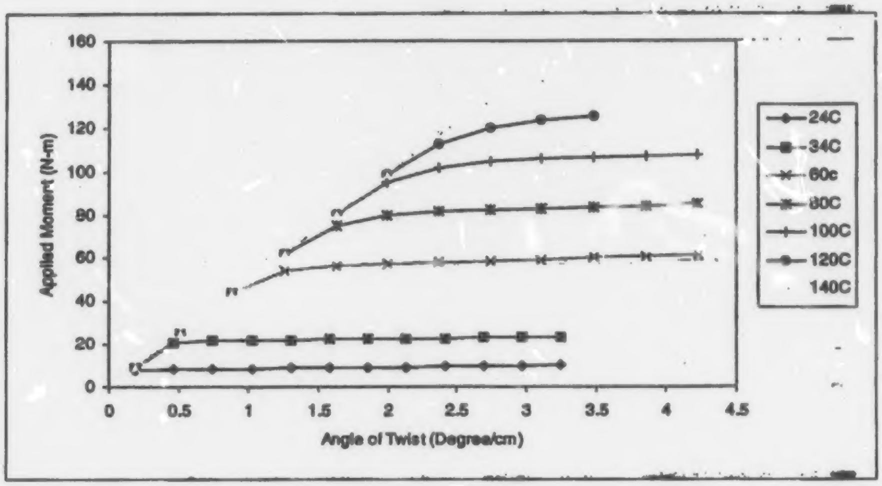

All analyses with the exception of 120°C case consist of 24 increments. The 120°C case consists of only 20 increments due to system failure during the run. Sufficient data was obtained so that it was not necessary to repeat this run. For Lagoudas et al. model greater angle of twists are obtained for temperatures above the austenite finish temperature. This is in contrast to the performance of Tanaka's model. All cases used identical convergence criteria. This is an indication of the differences in solution performance between the two constitutive models.

All analyses were run on a ring of Sun Ultras. The system used is a Department of Defense High Performance Computing Resource maintained by NRL Center for Computational Science. The system currently consists of 20 machines (32 processors) linked together. The connection between individual sun workstations is invisible to the user. Computer run times are shown in Table 1 for all conditions run. Run times reported are for similar numbers of load increments.

For the computer system used run times for Tanaka or Lagoudas et al. constitutive models are similar. Tanaka requires more time for temperatures between the austenite start and finish temperatures. Lagoudas et al. requires more time for temperatures greater than the austenite finish temperature. For the computer system used the times are not unreasonable. The only computational time determined to be unreasonable is for Liang-Rogers constitutive model and is attributable to the numerical solution problems encountered.

Table 1. Average Run Times for SMA Analyses

Condition		Average Run Time (CPU Second) 24 Increments
100% Martensite or 100% Austenite		9300
Tanaka	$T=A_f$	9340
	$A_s<T<A_f$	13450
	$T>A_f$	11302
Liang-Rogers	$T=A_f$	>13000 for 6 inc., had to abort job
	$A_s<T<A_f$	>13000 for 6 inc., had to abort job
	$T>A_f$	did not run
Lagoudas et al	$T=A_f$	9140
	$A_s<T<A_f$	9260
	$T>A_f$	13384

SUMMARY

A series of computational simulations were performed using finite element techniques to examine the differences that result from the selection of constitutive models. The device examined was a hollow tube fabricated of TiNi-Cu (K-Alloy) SMA and subjected to torsion loading. The use of 100% martensite and 100% austenite as possible bounding solutions was investigated along with the use of Tanaka [1], Liang-Rogers[2] and Lagoudas et al. [3,4] constitutive models. In the current work average generic SMA material properties were used. More accurate evaluation of constitutive parameters should increase the accuracy of computational predictions. Use of generic or handbook values is consistent with common design practices and therefore considered appropriate for this comparison study. Computer time required for the different approaches was tabulated for consideration. The work performed indicates that:

- Use of 100% austenite and 100% martensite material and conventional finite element solution techniques may or may not bound more complex constitutive responses.

- Liang-Rogers model had severe numerical difficulties once angle of twist and therefore strain reached relatively moderate values. This may be a result of the representation of ξ or stress field embedded in the model. This is an indication that the model is not as robust as either Tanaka's or Lagoudas et al.

- Tanaka and Lagoudas et al. models remained stable for high values of angle of twist. Solutions remained stable for values much higher than reported here.

- In most cases computer time requirements were similar on the cluster of Sun workstations used for the current work. The run time requirements varied for temperature regime and constitutive model used. The times were not unreasonable for the computer system and the class of problems generally run on the system by the authors.

Based on this study, complex constitutive models for SMAs are a reasonable design tool with some increases in computational resources required. However, there is still wide variation in results indicating that much work needs to be done in the field of computational model development for SMA. Additional work is required on material parameter testing in order to build a sufficient database for the accurate selection of representative material parameters for a particular SMA alloy. It is recognized that SMA material response has a strong dependence on hystersis. This will have to be addressed in future work, both computational and experimental. Creation of an experimental database of material parameters will eliminate one source of errors; i.e. generic material properties will be replaced by actual properties.

In summary there is much work that needs to be done on material constitutive response for SMAs. However, existing SMA models can be used in finite element analyses. An increased level of computer resources is needed for these analyses but the related cost is not prohibitive. The authors' opinion is that it is best to perform computational analyses with one of the complex constitutive models rather than rely on a bounding solution approach. Because there is no significant impact with respect to computer time requirements, it is recommended that the most general model be used. In the set of models evaluated in this work the most general model is that of Lagoudas et al. This model appears robust and numerically stable to high strain levels. Material parameters will be an issue but will be an issue with any model selected.

ACKNOWLEDGMENTS

This work was performed as part of the DARPA Smart Wing Phase II program. The assistance of Dr. D. C. Lagoudas in providing the ABAQUS user subroutine used is gratefully acknowledged. The following are acknowledged for their support of this work: Dr. Robert Crowe, formerly of Defense Research Advanced Projects Agency, Dr. Ephrahim Garcia, Defense Advanced Research Projects Agency, and Dr. Brian Sanders, AFOSR.

REFERENCES

1. K. Tanaka, "A Thermomechanical Sketch of Shape Memory Effect: One-Dimensional Behavior," Res. Mech., Vol. 18, 251, 1986.
2. C. Liang and C. A. Rogers, "Multi-Dimensional Constitutive Model for Shape Memory Alloys," J. Eng. Math., Vol. 26, 429, 1992.
3. J. G. Boyd and D. C. Lagoudas, "A Thermodynamic Constitutive Model for Shape Memory Materials, Part I," Int. J. Plasticity, Vol. 12, 6, 805, 1996.
4. D. C. Lagoudas, Z. Bo, and M. A. Qidwai, "A Unified Thermodynamic Constitutive Model for SMA and Finite Element Analysis of Active Metal Matrix Composites," Mechanics of Composite Matl and Struc, Vol. 4, 153, 1996.

5. A. C. Keefe, G. P. Carmen, A. P. Jardine, "Shape Memory Torsional Actuators," SPIE, Vol. 3324, 58, 1998.
6. B. Schroeder, C. Boller, J. Kramer and B. Kroplin, "Comparative assessment of models for describing the constitutive behaviour of shape memory alloys," Proceedings of 4th European and 2nd MIMR Conference, 305, 1998.
7. J. Kudva, K. Appa, C. Martin, P. Jardine, G. Sendeckyj, T. Harris, A. M. McGowan and R. Lake, "Design, Fabrication and Testing of the DARPA/WL 'Smart Wing' Wind Tunnel Model," AIAA, 1997.
8. J. G. Boyd and D. C. Lagoudas, "Thermomechanical response of shape memory composites," J. Intell. Mater. Syst. Structures, Vol. 5, 333, 1994.
9. D. C. Lagoudas et al, User's Manual for Subroutine UMAT, Draft, Personal communication, 1998.
10. ABAQUS Version 5.4 User's Guide, Hibbitt, Karlsson and Sorensen, Providence, RI, 1994.
11. C. A. Rogers, "Shape Memory Alloy Hybrid Composites for Active Structural Acoustic Control," Center for Intelligent Material Systems and Structures, VPI, Final Report to Office of Naval Research, Dec. 31, 1993.

#511880 ©

Welding Procedures for Welding HY80 Steel

by C.J. Nicholson*, L. Malik, D. Begg*, J.R. Matthews**, V. Roy,
and S.J. Dickout***

*Fleet Technology Limited

**Defence Research Establishment Atlantic, Dockyard Laboratory, PO Box 99000
Station Forces, Halifax, Nova Scotia, B3K 5X5

***NDHQ, DGMEPM, DMSS 2-4

ABSTRACT

In light of the acquisition of the Upholder class submarines by the Canadian Navy, some benchmark procedures have been developed for welding HY80 steel. These procedures for welding in the vertical up position comprised one for the shielded metal arc welding process, and two for semi-automatic processes (GMAW with TIME shielding gas and MCAW with argon 2% oxygen as the shielding gas). The filler metals employed were matching in strength. State of the art, Lincoln Powerwave 450 welding machine was used for all the welds.

The main considerations in finalizing the welding procedures were to minimize the heat input and interpass grinding but without incidence of lack of fusion type of flaws. The weld metal notch toughness for the three welds is reported.

Welding Procedures for Joining HY-80 Steel

by

- **C. J. Nicholson, Dr. L. Malik, D. Begg (Fleet Technology Limited)**
- **Dr. J. R. Matthews, V. Roy (DREA)**
- **S.J. Dickout (DGMEPM - DMSS 2-4)**

presented at

8th CF/CRAD Meeting on Naval Applications of Materials Technology
Dartmouth, N.S., May 11-13, 1999

FTL FLEET TECHNOLOGY LTD.

Background

- **The Acquisition of the Upholder Class Submarines has Increased CF Welding Procedure Requirements:**
  - Oberon Class constructed from QT28
  - Upholder Class constructed from Q1N (HY-80 equivalent)
- **CF Welding Practice Calls for SMAW for Pressure Hull Welding, However, There is a Desire to Move to P-GMAW in the Future to Take Advantage of Superior Mechanical Properties.**

FTL FLEET TECHNOLOGY LTD.

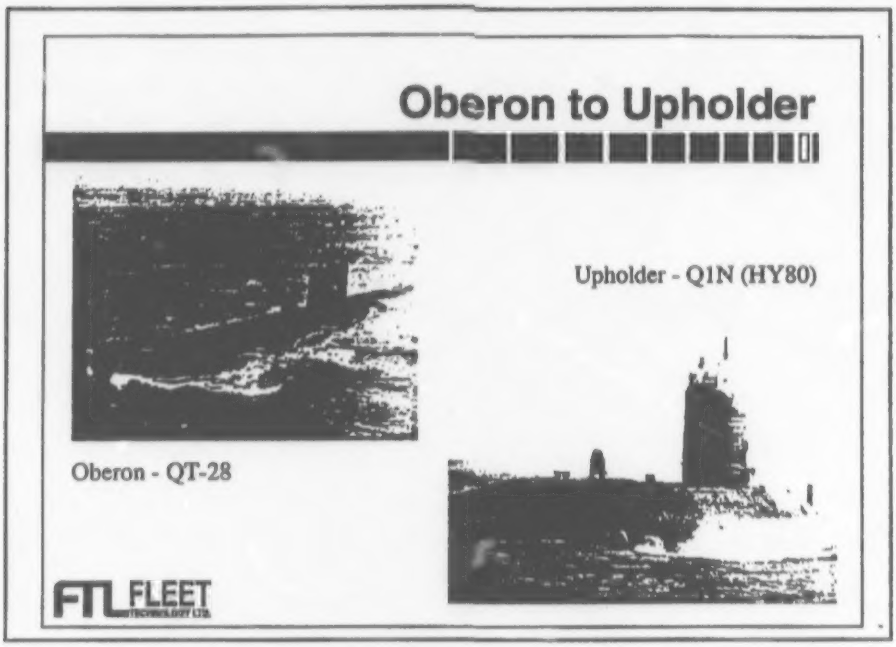

Oberon to Upholder

Upholder - Q1N (HY80)

Oberon - QT-28

Objectives

- Identify a Preferred SMAW Electrode for CF HY-80 Applications (DMSS).
- Develop and Evaluate an SMAW Procedure Suitable for Emergency Repairs and Minor Modifications (DMSS).
- Develop and Evaluate Benchmark P-GMAW Procedures (DREA).

Scope

GMAW

- **Procedures Developed and Evaluated for ER100S-1 and MIL-100S-2C Consumables in 3G Position**

SMAW

- **E10018M1 Electrode Selected for Matching Strength and Improved Ductility Over E11018.**
- **Procedure Developed and Evaluated in 3G Position to Simulate Most Difficult Scenario Likely to be Encountered in Repairs or Modifications.**

FTL FLEET TECHNOLOGY LTD.

Process Descriptions

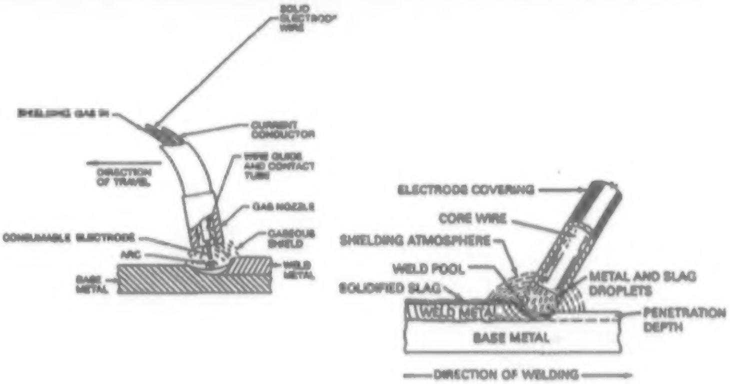
SOLID ELECTRODE WIRE
SHIELDING GAS IN
CURRENT CONDUCTOR
DIRECTION OF TRAVEL
WIRE GUIDE AND CONTACT TUBE
GAS NOZZLE
CONSUMABLE ELECTRODE
GASEOUS SHIELD
ARC
WELD METAL
BASE METAL
ELECTRODE COVERING
CORE WIRE
SHIELDING ATMOSPHERE
WELD POOL
METAL AND SLAG DROPLETS
SOLIDIFIED SLAG
WELD METAL
PENETRATION DEPTH
BASE METAL
DIRECTION OF WELDING

FTL FLEET TECHNOLOGY LTD.

Consumable Selection - GMAW

- **ER100S-1 Solid Wire With TIME Gas Shielding Selected Based on Good Performance in Past Test Programs.**
- **Metal Cored MIL-100-S2 with 2% O_2 Gas Shielding Selected Based on Good Published Properties and a Desire to Investigate Possible Alternatives to Solid Wire.**

FTL FLEET TECHNOLOGY LTD.

Consumable Selection - SMAW

Electrode	Designation	Specification	Yield (ksi)	UTS (ksi)	CVN ft.lbs.@°C	Hydrogen mL/100 g
ESAB	10018-M1	MIL-E-22200/10	89.5	97.4	67 @ -51	2.6
Air Liquide	10018-M	CSA W48.3	97	103	26 @ -50	N/A
Hobart	10018-M	MIL-E-22200/1	95.3	106	56@-51	N/A
Lincoln	10018-M1	MIL-E-22200/10C	90 (1G)* 109 (3G)	102 116	66 @ -51 48 @ -51	1.0
Fortrex O2N	10016		109 (3G)	118	44 - 74 @-50	3.0
Spec.	10018-M1	MIL-E-22200/10C	82 to 110		35 @ -51	3.2 to 3.5

* Heat input 41.1 kJ/in (1.62 kJ/mm) in the 1G position and 35.1 kJ/in (1.38 kJ/mm) in the 3G position.

Lincoln Electrode Selected Based Upon:
- Good Toughness and Strength
- Lowest Diffusible Hydrogen
- Only Supplier With Bonded Stock Tested to MIL-E-22200/10C

FTL FLEET TECHNOLOGY LTD.

Procedure Development - GMAW

- Past GMAW - TIME work at DREA has produced excellent toughness but lots of defects or required extensive grinding.
- The goal with this procedure was to produce good toughness with minimal defects and minimal interpass grinding.
- Procedure developed provided good wetting with a "crisp" arc.

GMAW Procedure Details

Filler Metal Classification	100S-1
Filler Metal Diameter (mm)	1.2
Preheat Temperature – min (°C)	90
Interpass Temperature – max (°C)	120
Heat Input (kJ/mm) - Range - Average	0.64 to 1.0 0.89
Shielding Gas	T.I.M.E: 26.5%He- 8%CO_2-0.5%O_2-bal Ar

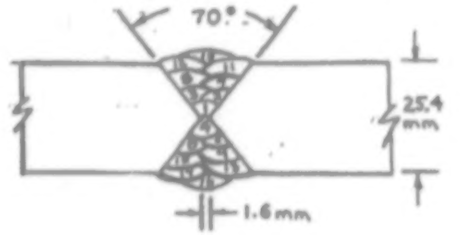

Procedure Development - MCAW

- **Same goals as with solid wire, it was hoped that lower current densities could be used, allowing even lower heat inputs to be and thus better toughness.**
- **It was found that "stringer beads" were very difficult to obtain with an acceptable profile so wide weaves and resulting high heat inputs were required.**
- **Weld puddle found to be very "sluggish" with poor wetting action.**

MCAW Procedure Details

Filler Metal Classification	100S-2C
Filler Metal Diameter (mm)	1.2
Preheat Temperature – min (°C)	90
Interpass Temperature – max (°C)	120
Heat Input (kJ/mm) - Range **- Average**	1.2 to 2.4 1.83
Shielding Gas	M2: Ar-2%O$_2$

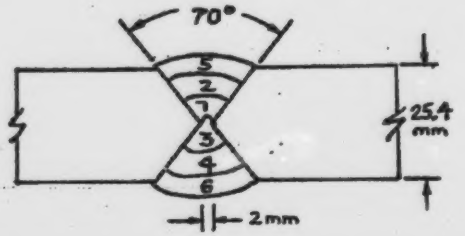

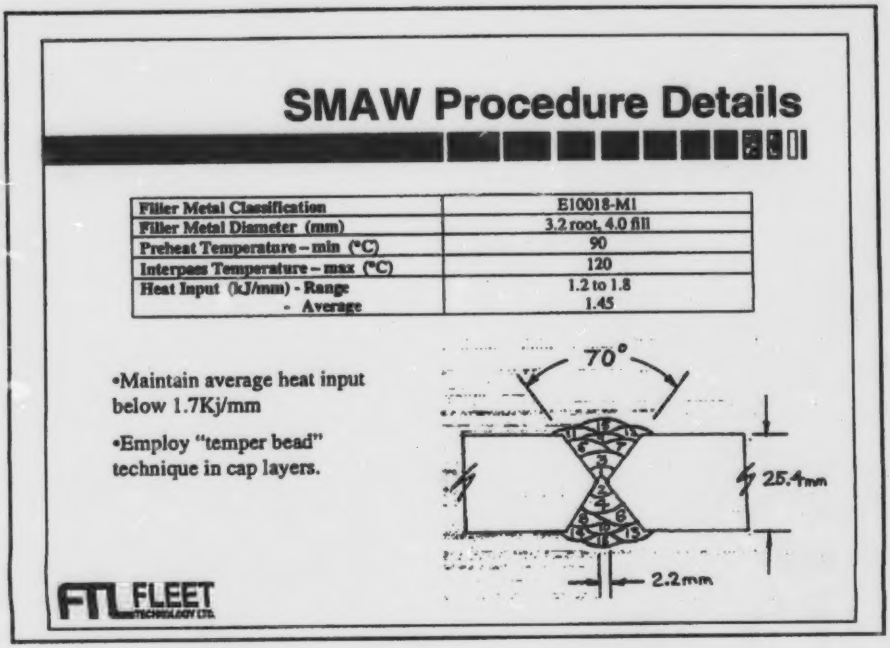

SMAW Procedure Details

Filler Metal Classification	E10018-M1
Filler Metal Diameter (mm)	3.2 root, 4.0 fill
Preheat Temperature – min (°C)	90
Interpass Temperature – max (°C)	120
Heat Input (kJ/mm) - Range	1.2 to 1.8
- Average	1.45

- Maintain average heat input below 1.7Kj/mm
- Employ "temper bead" technique in cap layers.

70°
25.4mm
2.2mm

FTL FLEET TECHNOLOGY LTD.

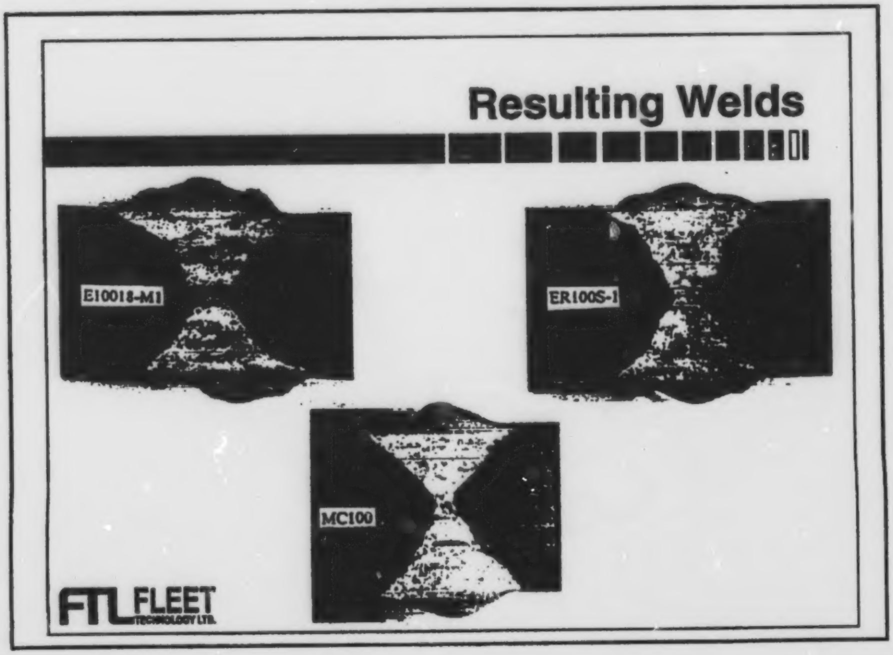

Resulting Welds

FTL FLEET TECHNOLOGY LTD.

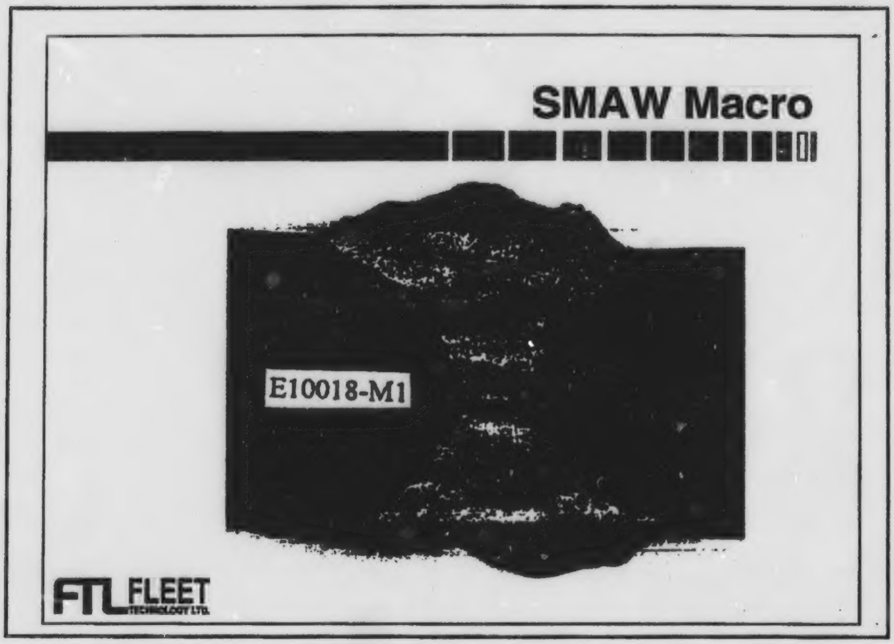

SMAW Macro

E10018-M1
FTL FLEET TECHNOLOGY LTD.

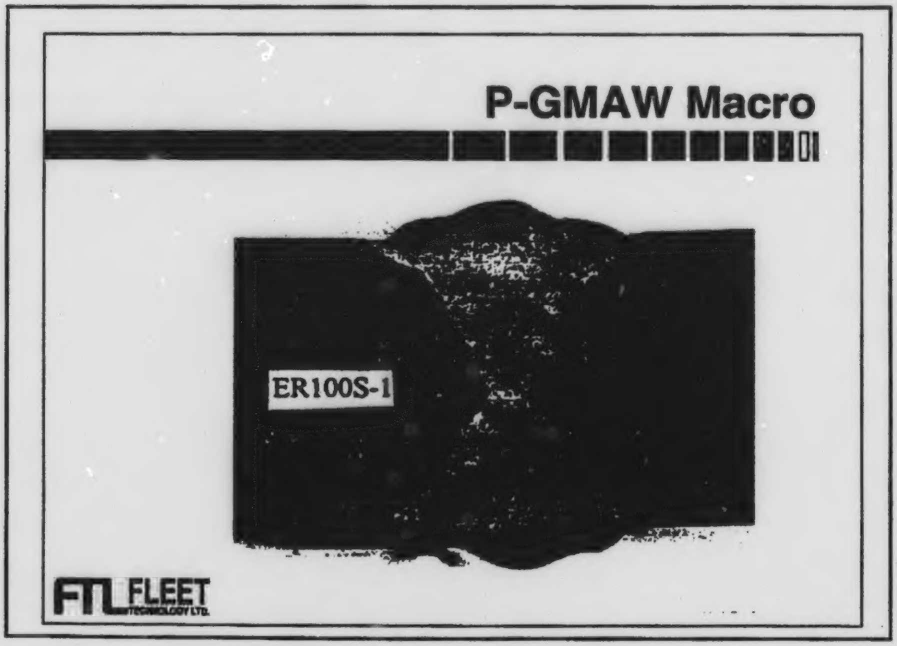

P-GMAW Macro

ER100S-1
FTL FLEET TECHNOLOGY LTD.

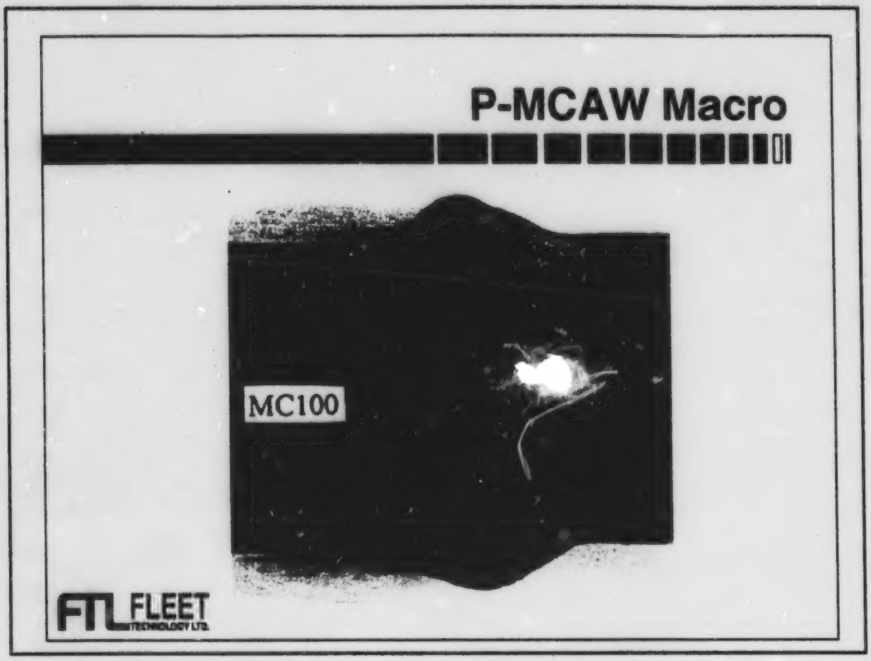

P-MCAW Macro

FTL FLEET TECHNOLOGY LTD.

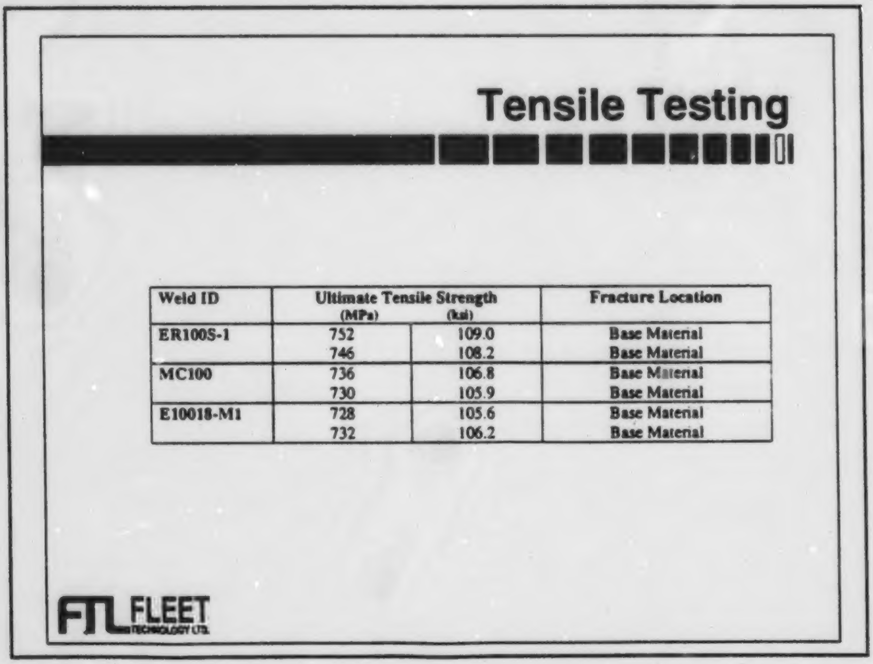

Tensile Testing

Weld ID	Ultimate Tensile Strength (MPa)	(ksi)	Fracture Location
ER100S-1	752	109.0	Base Material
	746	108.2	Base Material
MC100	736	106.8	Base Material
	730	105.9	Base Material
E10018-M1	728	105.6	Base Material
	732	106.2	Base Material

FTL FLEET TECHNOLOGY LTD.

Hardness Results

Hardness Results (HV, 5Kg load)

Weld ID	Location	Hardness (avg.)	Range
ER100S-1 + T.I.M.E	base metal	231	225 – 236
	HAZ	394	386 – 396
	weldmetal @1.5 mm subsurface	276	265 – 299
	weldmetal @ t/2	308	306 – 310
MC100 + Ar-2%0₂	base metal	234	225 – 246
	HAZ	381	376 – 386
	weldmetal @1.5 mm subsurface	277	268 – 303
	weldmetal @ t/2	314	313 – 317
E10018-M1	base metal	228	223 – 234
	HAZ	384	332 – 394
	weldmetal @1.5 mm subsurface	246	232 – 254
	weldmetal @ t/2	277	271 – 283

FTL FLEET TECHNOLOGY LTD.

Charpy Impact Results

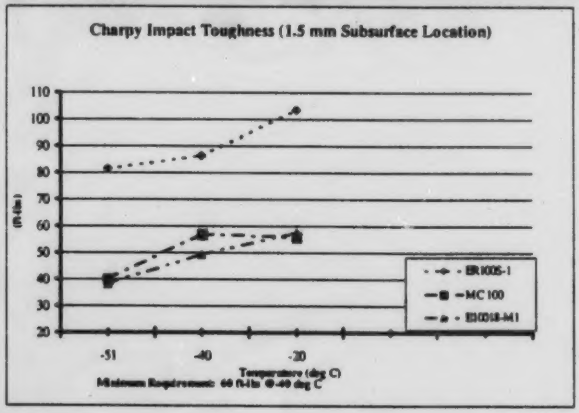

Minimum Requirement: 60 ft-lbs @-40 deg C

FTL FLEET TECHNOLOGY LTD.

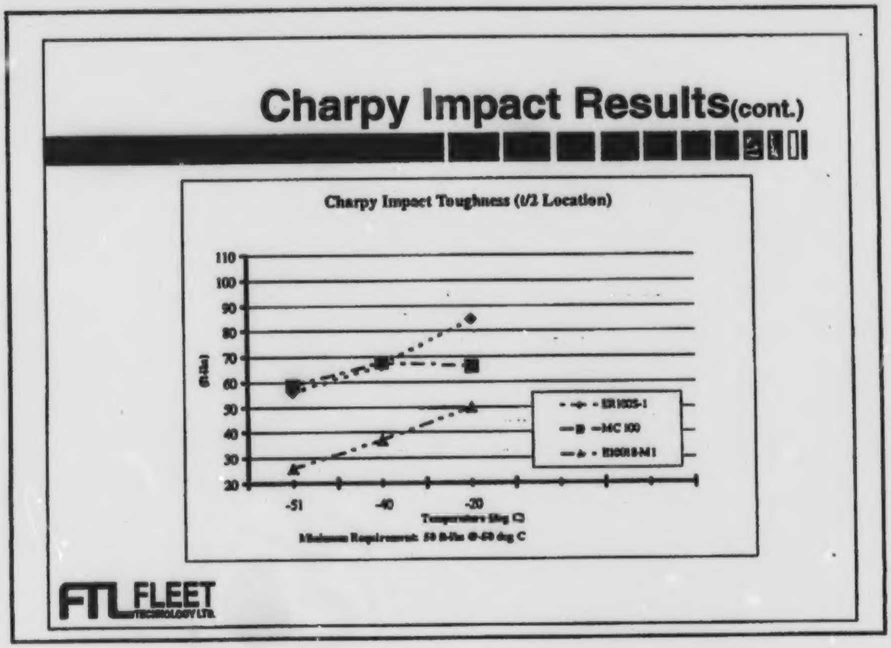

Charpy Impact Results(cont.)

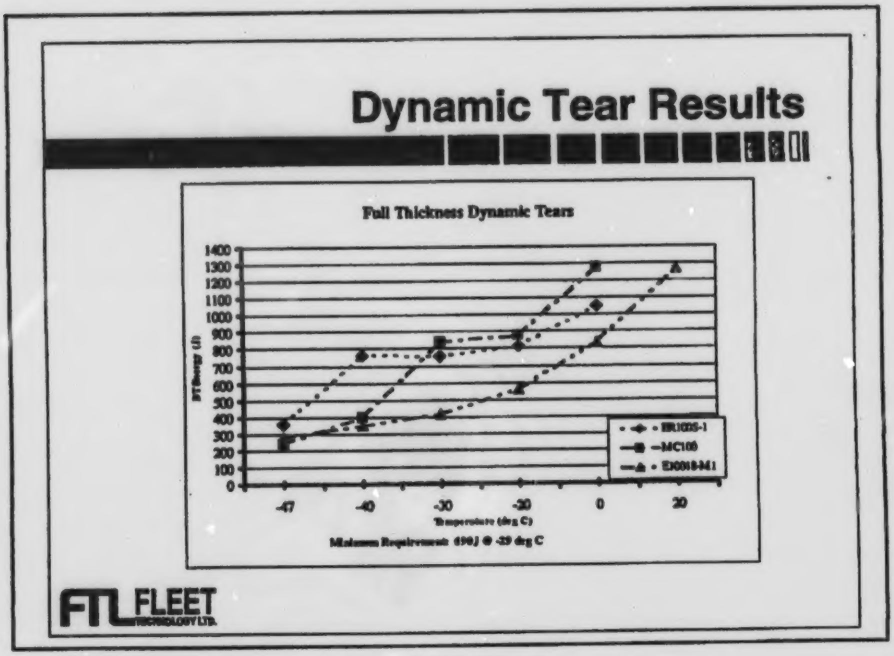

Dynamic Tear Results

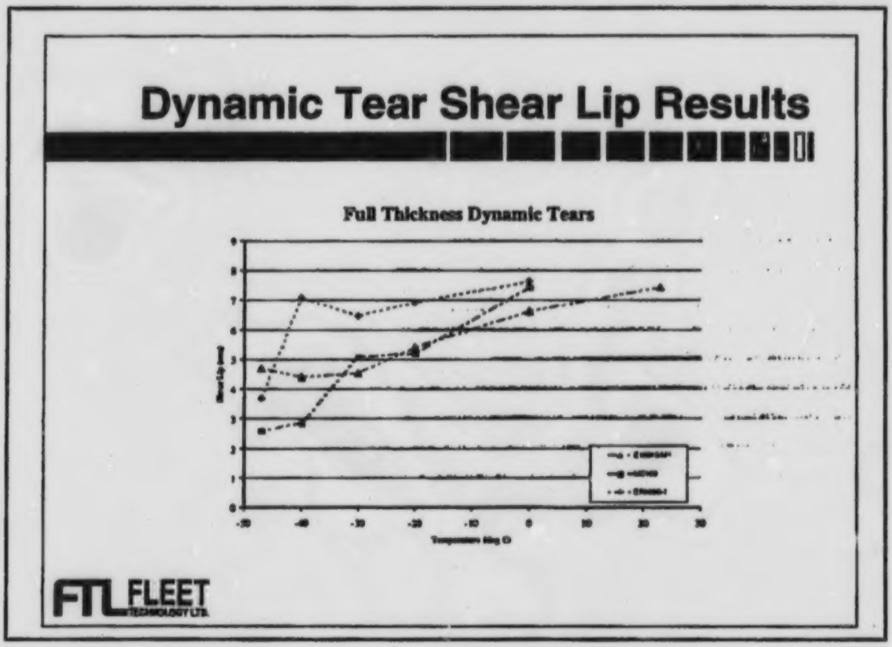

Dynamic Tear Shear Lip Results

Full Thickness Dynamic Tears

FTL FLEET TECHNOLOGY LTD.

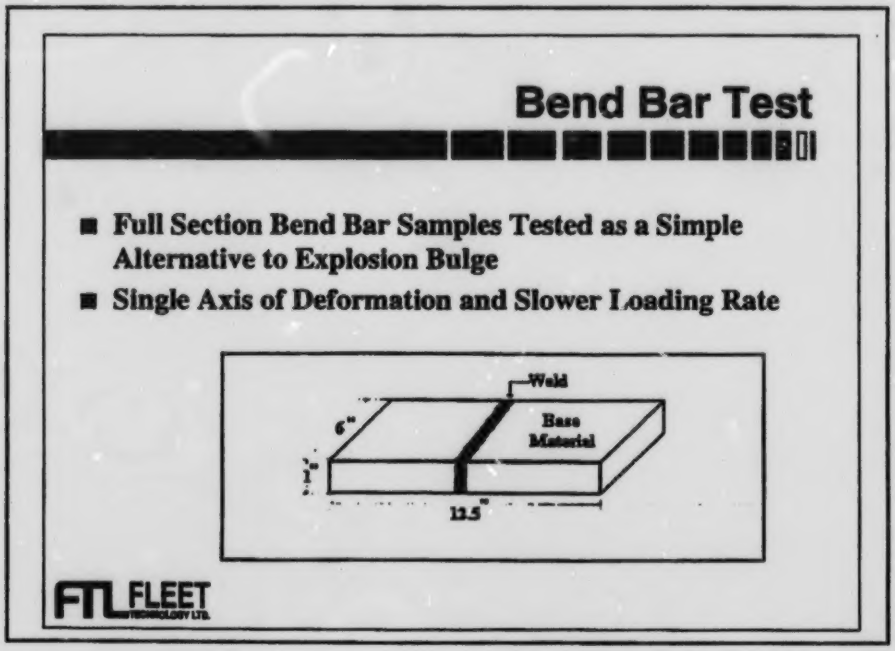

Bend Bar Test

- Full Section Bend Bar Samples Tested as a Simple Alternative to Explosion Bulge
- Single Axis of Deformation and Slower Loading Rate

Weld
Base Material
6"
1"
12.5"

FTL FLEET TECHNOLOGY LTD.

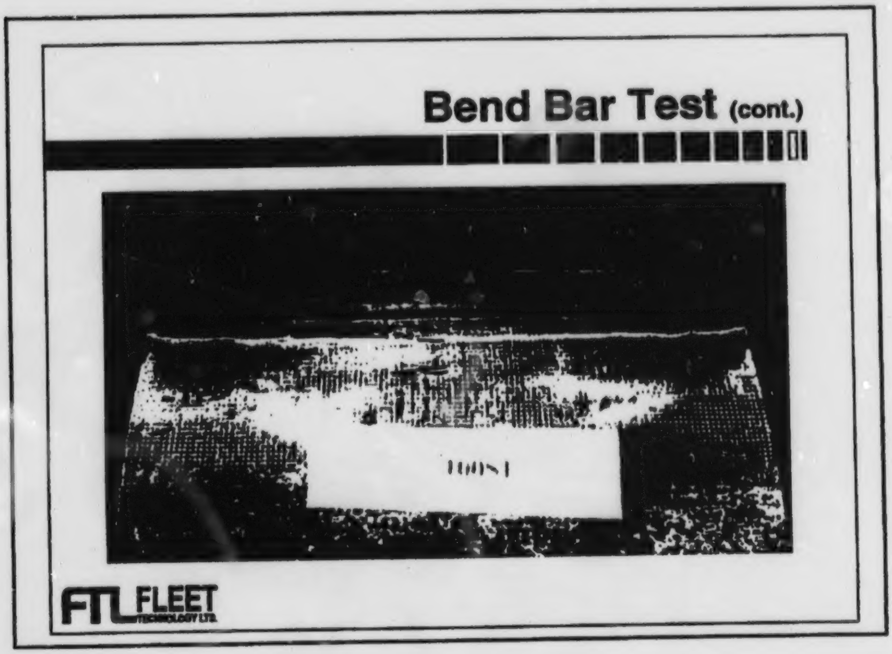

Bend Bar Test (cont.)

FTL FLEET TECHNOLOGY LTD.

Bend Bar Test(cont.)

FTL FLEET TECHNOLOGY LTD.

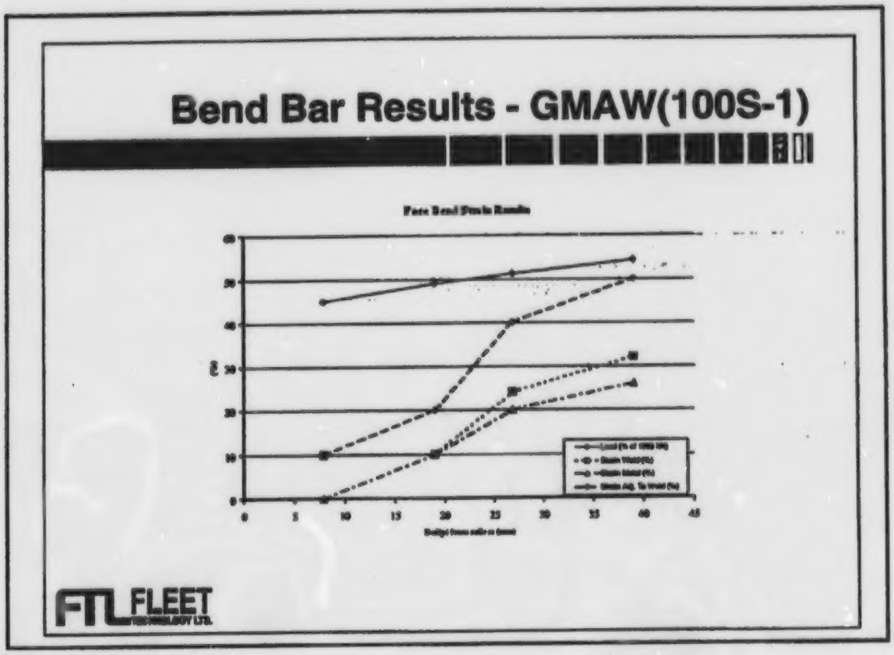

Bend Bar Results - GMAW(100S-1)

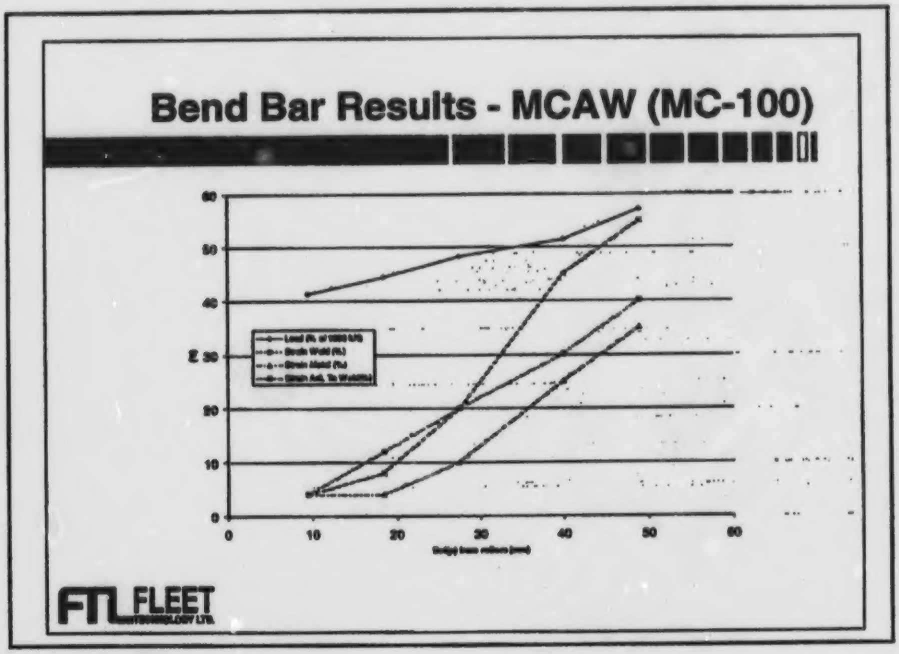

Bend Bar Results - MCAW (MC-100)

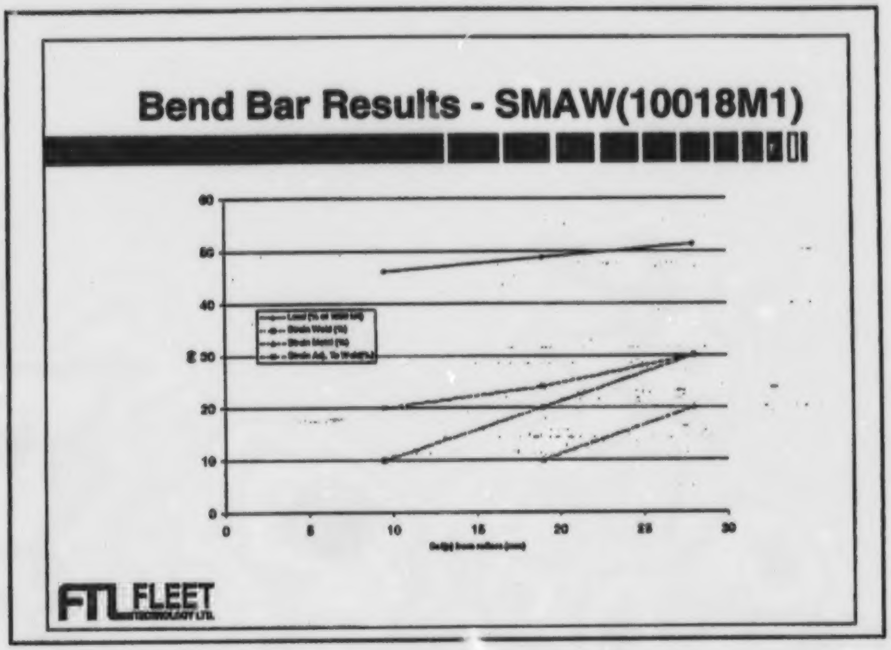

Bend Bar Results - SMAW(10018M1)

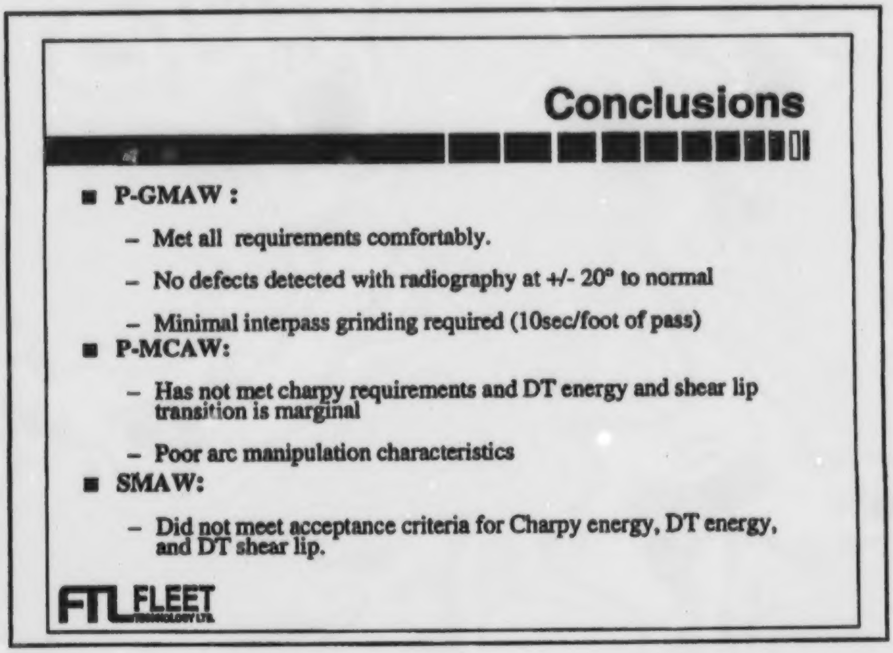

Conclusions

- **P-GMAW :**
  - Met all requirements comfortably.
  - No defects detected with radiography at +/- 20° to normal
  - Minimal interpass grinding required (10sec/foot of pass)
- **P-MCAW:**
  - Has not met charpy requirements and DT energy and shear lip transition is marginal
  - Poor arc manipulation characteristics
- **SMAW:**
  - Did not meet acceptance criteria for Charpy energy, DT energy, and DT shear lip.

FTL FLEET TECHNOLOGY LTD.

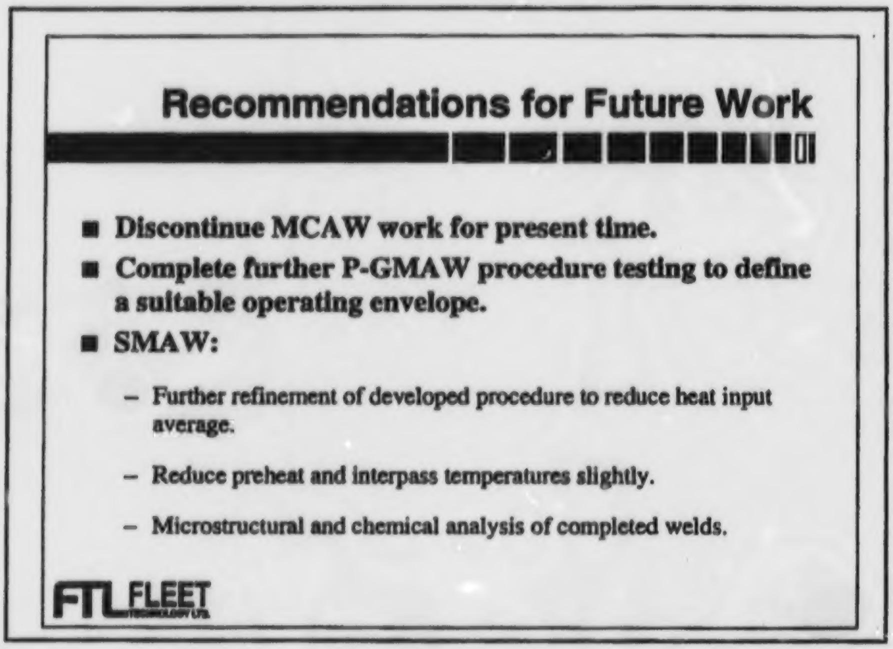

Recommendations for Future Work

- Discontinue MCAW work for present time.
- Complete further P-GMAW procedure testing to define a suitable operating envelope.
- SMAW:
  - Further refinement of developed procedure to reduce heat input average.
  - Reduce preheat and interpass temperatures slightly.
  - Microstructural and chemical analysis of completed welds.

FTL FLEET

#511881

Investigation of Plastic Zone Development in Dynamic Tear Test Specimens

T.S. Koko[1], J.R. Matthews[2], C.V. Hyatt[2] and V. Roy[2]

[1] Martec Limited, 400-1888 Brunswick Street, Halifax, N.S., B3J 3J8
[2]Dockyard Laboratory Atlantic, Defence Research Establishment Atlantic, P.O. Box 99000, Stn Forces, Bldg D17, Halifax, N.S., B3K 5X5

ABSTRACT

The J-integral is an elastic-plastic fracture criterion, which permits measurement of the fracture toughness of a specimen that has been fractured after general yielding. An understanding of the ratio of plastic zone size (radius) to the crack tip blunting (stretch zone) is required to determine the upper limit of temperature relative to full size transition curves where elastic plastic fracture becomes invalid. This study endeavours to acquire this ratio using finite element techniques. The development of the plastic zone in dynamic tear (DT) specimens and a non-standard three point bending fracture test specimen used to measure fracture properties was the main focus of the study. The ABAQUS finite element software was used to model the elastic-plastic behaviour of the specimens. For the DT specimen, a crack was induced by pressing the notch, followed by fatigue cracking at a limit load level of 40% of the specimen limit load, whereas, the crack shape for the non-standard specimen was a fatigue crack defined at approximately 30% of the limit load. The shapes of these cracks were adequately modelled in the finite element analysis. The specimens were made of 350WT steel and 304 stainless steel materials and were loaded until fixed amounts of permanent deformation were recorded. Results were obtained in the form of plots, showing the progression of the plastic zone around the crack tip. For each case, mid point plastic deflection, stretch zone width and plastic zone radius were computed. The finite element results obtained were compared to experimental elastic plastic testing where available, and reasonably accurate agreement was achieved.

INTRODUCTION

The J-integral is one of several criteria used to determine the fracture toughness of materials. This is a criterion that is suitable for measurement of fracture in the elastic-plastic regime of the full transition curve (Figure 1). It permits measurements of fracture toughness of specimens that have been fractured after general yielding, and assumes that onset of fracture is due to a critical level of stress or strain being achieved at or near the crack tip [1,2]. The J-integral is measured using three-point bend specimens, such as the dynamic tear (DT) test specimens. An understanding of the ratio of the plastic zone size (radius) to the crack tip blunting (stretch zone width) is required to determine the upper limit of temperature relative to the full size transition curves where elastic-plastic fracture (J-integral) becomes invalid.

Figure 2 shows a typical DT specimen and Figure 3 shows idealizations of the plastic zone around the crack tip. As shown in Figure 3, the plastic zone radius is the maximum extent of the plastic zone, and the stretch zone width (SZW) is the distance from the crack tip to the interface of the plastic zone with the side of the crack. The shear lip size is given by the distance from the yield surface to the original surface on the side of the specimen. The standard validity criterion stipulates that

$$a, b, B = 50J / \sigma_{flow} \tag{1}$$

This suggests that B should be greater than $50J/\sigma_{flow}$. But blunting is approximately $J/(2\sigma_{flow})$. Therefore the thickness B should be greater than 100 times the critical blunting for a valid test. Thus, if the ratio (β) of plastic zone size to blunting size is known, then the following relations will hold for a valid fracture test:

$$\begin{aligned} &B > 100SZW \\ &B > 100r_y/\beta \\ &B > 100s/\beta\ (or\ s < B\beta/100) \end{aligned} \tag{2}$$

where r_y (plastic radius) = s (shear lip size) [3,4,5], $\beta = r_y/SZW$, and the flow stress σ_{flow} is given by $\sigma_{flow} = (\sigma_y + \sigma_u)/2$, where σ_y is the yield stress and σ_u the ultimate stress. Accordingly, in the present study, the key is to identify the ratio of plastic zone size to stretch zone width. Four methods of verification are available:

(i) Analytical (after Rice[6], who suggested the ratio was as low as 5 and as high as 600);
(ii) Visual (after experiments on stainless steel at DREA);
(iii) Experience in valid J testing (after DREA investigations); and
(iv) By finite element (looking at plastic deformation of the center of the bar, stretch zone or blunting, plastic zone, and the parameter *s* which actually includes the shear lip and lateral contraction).

The focus of this study is to utilize the finite element methodology to investigate the plastic zone development in three point bend fracture specimens. The aim of the study is to provide an understanding of the ratio of the plastic zone size (radius) to crack tip blunting (stretch zone width), in order to be able to predict the upper limit where elastic plastic fracture becomes invalid. Of interest is the investigation of the plastic zone development in standard dynamic tear (DT) test specimens with 350WT or 304 stainless steel materials; and a non-standard (NS) three-point bend specimen made of 304 stainless steel material.

PROBLEM DESCRIPTION

Geometry

A schematic representation of the test specimen is shown in Figure 2. In the present study, three test specimens are analyzed. These include the following:

(i) DT specimen with 350WT steel, designated as DT-350WT;
(ii) DT specimen with 304 stainless steel, designated as DT-304SS; and
(iii) Non-standard specimen with 304 stainless steel, designated as NS-304SS.

The DT specimens (DT-350WT and DT-304SS) had the following geometric properties: L=181 mm; S=164 mm; a=12 mm plus .010 inches pressing followed by fatigue extension of 13 to 20 mm; W=41 mm; and B=8 mm. The non-standard specimen had the following configuration: L=125 mm; S=100 mm; a=12.5 mm fatigue crack produced by rigorous process; W=25 mm; and B=12.5 mm, where L=length of beam; S=span of beam between supports; W=width of beam; B=thickness of beam; and a=notch size (fatigue sharpened).

Crack Tip Shape

The crack tip shape is that of a fatigue crack initially and a blunted fatigue crack thereafter. For the DT specimen the notch is first machined with an included angle of 60° followed by a pressing process that extends the notch 0.254 mm (0.010) with an included angle of 40° and a resulting crack tip radius of 0.254 mm (0.001). This is followed by fatigue cracking at a load level of no more than 40% of the current specimen limit load. This produces a sharp fatigue crack of definable dimensions, which is used in the FE simulation. This pre-cracking extends the pressed notch by at least 1 mm. The crack tip shape for the non-standard specimen is that of a well established fatigue crack whose maximum loading has been defined by careful laboratory fatiguing (maximum load approximately 30% of the limit load). The shape of the resulting crack tip and the configuration of the crack along its entire length were acquired by sectioning. Detailed descriptions of the precracking process are available in Reference [7].

FINITE ELEMENT MODEL

Finite Element Approach

The prediction of the response behaviour of the DT specimen requires a tool that accounts for large geometry changes and plasticity effects in the crack tip region. There are several commercial FEA tools that can be employed or adapted for calculating the stresses and strains needed. In this study the ABAQUS finite element software [8] was used to model the elastic-plastic behaviour of the DT specimen. The software has a wide range of non-linear material models and can account for large strains and displacements. Moreover, it has been successfully used for the analysis of similar problems [9-11]. However, the HyperMesh [12] general-purpose pre- and post-processing program was used for model generation and results processing.

Finite Element Meshes

As stated, the HyperMesh code was used to generate the finite element models of the DT and non-standard specimens, which were then translated to ABAQUS input files. The exact shapes of the crack were obtained from DREA to enable accurate modelling of the structural configuration. Figure 4 shows the shape of the fatigue crack in the DT specimen. This shape had to be modelled accurately to provide meaningful results. Detailed 2-D finite element models of the specimen were developed. In order to reduce the problem size only one-half of the structure was modelled. The finite element models of the DT and non-standard (NS) specimens are as shown in Figures 5 and 6, respectively. Plane strain elements were used to model the structure. These elements allow for the treatment of large displacements, finite strains and plasticity, which are expected to occur in the specimen.

Material Models

An incremental rate independent plasticity theory available in the ABAQUS finite element program [8] was used for the material constitutive model. This standard model for plasticity is summarized here for completeness. The total multi-axial strain state ε_{ij}, expressed in terms of elastic and plastic components is given by

$$\in_{ij} = \in_{ij}^{e} + \in_{ij}^{p} \tag{3}$$

The total logarithmic uniaxial strain, ε, consistent with the integration of the rate of deformation tensor for a multiaxial strain state, is decomposed as

$$\in = \in^{e} + \in^{p} \tag{4}$$

where $\in^{e}, \in^{p}$ are the elastic and plastic strain vectors, respectively. The yield function f is related to uniaxial tension by

$$f(\tau_{ij}) = \tau(\in^{p}), \tag{5}$$

where τ_{ij} and τ are the multiaxial Kirchoff and uniaxial stress states, respectively. The von Mises yield criterion and an associated flow rule is used for the incremental analysis, where the von Mises yield function is given by

$$f(\tau_{ij}) = \left(\frac{3}{2}(S_{ij}S_{ij})\right)^{1/2}, \tag{6}$$

where S_{ij} is the deviatoric component of stress. The Kirchoff stress and logarithmic strain measures are employed because of computational convenience. The Kirchoff stress tensor, τ_{ij}, is approximately equal to the Cauchy stress tensor, σ_{ij}, for deformations involving only small changes in volume [10,11]. This condition is assumed in the elastic-plastic analysis. The uniaxial Cauchy stress-logarithmic strain constitutive relations of the material are input, in multilinear form, as Cauchy stress and logarithmic plastic strain pairs for the ABAQUS program. The constitutive parameters for the 350WT and 304SS materials are described below.

350WT Steel

The material for the first DT specimen was 350WT steel. The engineering stress-strain curve for this material was obtained from DREA. This curve terminated at a strain of 25%. However, from experimental investigations by DREA [13], strains as high as 250% were observed around the crack tip of the specimen. A method for defining the stress-strain behaviour beyond 25% strain was therefore required. Two possible stress-strain curves, as illustrated in Figure 7, were considered. In the first model (Figure 7(a)), the stress was assumed to be constant at the maximum stress level from 25% to 250% strain. This case is referred to as the flat curve model. In the second constitutive model (Figure 7(b)), the stress was assumed to rise from the maximum uniaxial test stress of about 600 MPa to 1100 MPa from 25% to 250% strain. The maximum stress value was determined from experimental observation and intuition [13]. This second case is referred to as the rising curve model.

304 Stainless Steel

The second DT specimen and the non-standard specimens were made of 304 stainless steel material. The stress strain curve for the material was obtained from the literature [14]. This curve terminated at a strain of about 80%. However, from experimental investigations by DREA [13], strains as high as 1000% were observed around the crack tip of the specimen. In this case only the rising curve model was used beyond the 80% strain level. The possible stress-strain curve is illustrated in Figure 8. In this constitutive model the stress was assumed to rise from the maximum uni-axial test stress of about 600 MPa to 1000 MPa from 80% to 1000% strain. The maximum stress value was determined from experimental observation and intuition [13].

Boundary Conditions and Loading

The following boundary conditions were applied:

At the support: $v = 0$
Along the center line: $u = 0$;

Where, u, v are the displacements components in the longitudinal and transverse directions. The load was applied as a concentrated load at the top middle point of the beam.

RESULTS AND DISCUSSIONS

The finite element results obtained for the three specimen configurations are discussed in this section. For each specimen, results of the midpoint displacement, plastic zone development and stretch zone width are provided.

DT Specimen with 350 WT Steel Material

Midpoint Displacements

The predicted load-displacement response of the midpoint of the beam is shown in Figure 9. In the figure, DL refers to the displacement of the top midpoint with respect to the top left end point, and DS refers to the bottom midpoint with respect to the support point. The results obtained from using the flat and rising stress-strain curves are all presented in the figure. It is seen that the use of a flat or rising stress-strain curve does not have any significant effect on the midpoint displacement responses. The applied load has been non-dimensionilized with respect to the limit load P_L, which is given by

$$P_L = \frac{4}{3}\left(\frac{Bb^2\sigma_y}{S}\right) \tag{7}$$

where B is the thickness, b is the untracked ligament (b=W-a), σ_y is the yield strength and S is the span between the supports.

Plastic Zone Development

The shape of the plastic zone was similar for both the flat and rising stress-strain models. However, the stress and strain levels beyond the 25% strain level were quite different for the two cases because of the different load paths. Figure 10 shows the development of the von Mises stresses and equivalent plastic strains in the DT-350WT material with the rising curve model, at different load levels. For the von Mises stress plots, all regions with stresses above the yield stress of 450 MPa are shown in red, and the area that has not yielded is shown in blue. For the equivalent plastic strain plots, all areas with plastic strains greater than 0.01% are shown in red and all other areas are shown in blue. Also, the same view is used for all the figures so a direct comparison of the shape and size of the plastic zone can be made. It is seen that the shapes and size, of the plastic zones using the von Mises stress or equivalent plastic strain are very similar. Also, as expected, the plastic zone size increased with load. In addition, the plastic zone tends to rise upwards from the tip of the crack, which is similar to the experimentally observed behaviour [2].

Figure 11 shows the plastic zone that has strained over 15% (when necking starts) of two load levels. In comparison with the plastic zones at the corresponding load levels in Figure 11, it is seen that necking occurs in only a small area around the crack tip.

Plastic Zone Radius (r_y) Stretch Zone Width (SZW) and Ratio r_y/SRW

The plastic zone radius, r_y, and the stretch zone width (SZW) at various load levels were measured from the plastic zone configurations. The plastic zone was given by the distance from the crack tip to the farthest point of the plastic zone. The stretch zone width (SZW) was given by the distance from the crack tip to the interface of the plastic zone with the side of the crack (see Figure 3). Figures 12 and 13 respectively show the variation of the plastic radius and SZW with load, for the flat and rising stress-strain curve models of the DT-350WT specimen. The figures show that the plastic zone radii and stretch zone widths obtained from the two models are almost identical as for the shapes of the plastic zones, as discussed above. The ratios of the plastic zone radius to stretch zone width (r_y/SZW) were also computed and presented in Figure 14. Again, the responses from the two constitutive models are very similar, and the ratios vary from 50 to 90. Due to the fact that the configurations of the plastic zone predicted by the flat and rising curve constitutive models were similar, only the rising curve (strain hardening) model was used for the remaining specimens, as this provided more realistic strain levels.

DT Specimen with 304 Stainless Steel Materials

Midpoint-Displacement

The predicted load-displacement response of the midpoint of the beam is shown in Figure 15. The displacements of the DT-304SS specimen are smaller than those of the DT-350WT specimen. For instance, at $1.1P_L$, the midpoint displacement with respect to the end point, DL, is approximately equal to 0.3mm compared to 0.63mm for the DT-350WT specimen (see Figure 9), since the applied load for the DT-304SS specimen (7.49 kN) was less than the load applied to the DT-350WT specimen (16 kN).

Plastic Zone Development

Figure 16 shows the development of the von Mises stresses in the DT-304SS specimen. In the plots, all regions with stress above the yield stress of 240 MPa are shown in red and the area that has not yielded is shown in blue. As before, the same view is used for the plots to facilitate direct comparison. The plastic zone configurations at various load levels follow the same pattern as described for the DT-350WT specimens. The area around the crack tip that was strained by more than 15% was insignificant.

Plastic Zone Radius (r_y), Stretch Zone Width (SZW) and Ratio r_y/SZW

The plastic zone radius and SZW at various loads were measured as described above. Figure 17 shows the variation of plastic radius with load. For comparison, the plastic zone radii of the DT-350WT specimen are also shown. As shown, the plastic radii for the DT-304SS specimen follow the same trend as for the DT-350WT specimen, and the plastic radii for the two specimens are very close, with those of the DT-304SS specimen being slightly larger. Figure 18 shows the variation of SZW with load. Again, the trends of the results for the DT-304SS and DT-350WT specimens are similar. However, the values of the SZW for the DT-304SS specimen are generally smaller than those of the DT-350WT specimen. The variation of the ratio of the plastic radius to the stretch zone width is shown in Figure 19, where a plot of the ratio for the DT-350WT specimen is also shown. Both ratios increase slightly with load, however, the range of the r_y/SZW for the DT-304SS specimen is 140-150 compared to 50-90 for the DT-350WT specimen, this is expected, since the 304SS material was more ductile than the 350WT steel.

NS Specimen with 304 Stainless Steel Material

Midpoint Displacement

The predicted load-displacement response of the midpoint of the beam is presented in Figure 20. The computed midpoint displacement of the last load step (1.044PL) was 0.18 mm compared to 0.23 mm obtained experimentally [7,15].

Plastic Zone Development

The predicted von Mises stresses and equivalent plastic strains at various load levels for the NS-304SS specimen are shown in Figure 21. The plastic zones are defined by the regions with stresses over 240 MPa or over 0.01% plastic strain. It is observed that the plastic zones predicted by using the stress or strain criterion are very similar. The same view is used for all the plots to facilitate direct comparison.

Plastic Zone Radius (r_y), Stretch Zone Width (SZW) and Ratio r_y/SZW

The variations of plastic zone radius and stretch zone with (SZW) with load, for the NS-304SS specimen are presented in Figures 17 and 18, respectively. For comparison, the corresponding results for the DT-350WT and DT-304SS specimens are also shown in the figures. It is observed that the plastic radius and SZW for the NS-304SS specimen are generally smaller than those of the DT-350WT and DT-304SS specimens. The variation of the ratio of plastic radius to stretch zone width is shown in Figure 19 along with the corresponding results for all the other specimens. The r_y/SZW ratio for the NS-304SS specimen fall generally between those of the DT-350WT and DT-304SS specimens.

SUMMARY, CONCLUSIONS AND RECOMMENDATIONS

This paper focussed on a study to investigate plastic zone development in three point bend fracture specimen. The finite element methodology was utilized to provide an understanding of the plastic zone size (radius) to crack tip blunting (stretch zone width), in order to be able to predict the upper limit where elastic plastic fracture becomes invalid. Finite element analysis of three test specimen configurations were performed. The test specimens were (i) a standard dynamic tear (DT) test specimen with 350WT steel; (ii) another standard DT specimen with 304 stainless steel; and (iii) a non-standard three point bend specimen with 304 stainless steel. The ABAQUS finite element code was used to perform incremental elastic-plastic analysis of the specimens. Intuition and experimental observation were used to develop approximate stress-strain curves for the materials beyond the points where uniaxial stress-strain data were available for the 350WT steel and 304 stainless steel materials.

The results computed for each analysis included the midpoint displacement; development of the plastic zone around the crack tip with progression of load; the plastic zone radius r_y; stretch zone width (SZW); and the ratio of plastic zone radius to SZW. The results were presented in the form of contour plots and charts for comparison with experiments being performed concurrently. It was found that the plastic zone radius r_y and stretch zone width SZW increased parabolically with load, up to 1.1 P_L, where P_L is the limit load. On the other hand, the variation of the ratio r_y/SZW with load fitted a linear distribution for all cases. This ratio was found to vary from 50-90 for the DT specimen with 350WT steel; 140-150 for the DT specimen with 304 stainless steel and 90 -140 for the non-standard specimen with 304 stainless steel.

The experimental results were not fully available to this study, as they were being performed concurrently. It is recommended that the results of this study be compared to the experimental results when they are available. Based on these comparisons it might be necessary to refine the stress-strain relations beyond the points where uniaxial test data available, to obtain better accuracy. Once a good level of accuracy has been achieved with the finite element model, it is further recommended that the analysis be applied to several other specimen configurations to enable a parametric study to be performed. Such a study would lead to the generation of generalized charts that can be used for fracture measurements and design.

REFERENCES

[1] Matthews, J.R. Porter, J.F. and Hyatt, C.V. "Fracture Control for Submarine Pressure Hulls II." 3rd Meeting of the TTCP PTP1 Operating Assignment on Fracture Control of Naval Structures, Annapolis, Maryland 1-3 May 1991.

[2] Matthews, J.R., Porter, J.F., Hyatt, C.V. and KarisAllen, K.J. "A General Discussion of Short Crack Fracture." proceedings of the Conference on Shallow Crack Fracture Mechanics Tests and Applications, Cambridge UK, 23-24 Sept, 1992.

[3] Matthews, J.R., Hyatt, C.V., Porter, J.F., and KarisAllen, K.J. "Effect of Thickness On The Relationship Between Shear Lip and Energy In Dynamic Tear Specimens", Engineering Fracture Mechanics, Vol 60, No.5-6, August 1998.

[4] Matthews, J.R. "On The Relationship Between Shear Lip, Shear Index and Energy In Dynamic Tear Specimens", Engineering Fracture Mechanics, 31 May 1996.

[5] Matthews, J.R., "On The Relationship Between Shear Index and Energy in Dynamic Tear Specimens," Engineering Fracture Mechanics, Vol 39, No.1, 1991.

[6] Rice, J.R. in Journal of Applied Mechanics Series E of Transactions of the ASME,

Vol., 90, June 1968.

[7] Roy, V. Hyatt, C.V. and Matthews, J.R. "Precracking Stainless Steel 304 for Notch Tip Plastic Zone Studies." DREA Note No. DL(A)/98/1, 1998.

[8] Hibbitt, H.D. Karlsson, B.I. and Sorensen, E.P. ABAQUS User's Manual, 1990.

[9] DeGiorgi, V.G., Kirby III, G.C. and Jones, M.I. "Prediction of Classical Fracture Initiation Toughness." Engineering Fracture Mechanics, Vol. 33, No. 5, pp. 773-785, 1989.

[10] DeGiorgi, V.G. and Matic, P. "A Computational Investigation of Local Material Strength and Toughness on Crack Growth." Engineering Fracture Mechanics, Vol. 39, No. 5, pp. 1039-1058, 1990.

[11] DeGiorgi, V.G., Matic, P., Bar-on, I. and Lee, G.M.C. "An Experimental and Computational Investigation of Crack Growth Initiation in Three-Point Bend Fracture Specimens." Engineering Fracture Mechanics, Vol. 50, No. 1, pp. 1-9, 1995.

[12] HyperMesh User's Manual.

[13] Matthews, J.R. Private comunications, 1999.

[14] Boyer, H.E. Atlas of Stress-Strain Curves. ASM International, Metals Park, Ohio.

[15] Koko, T.S., Gallant, B.K. and Tobin, S.B. "Investigation of Plastic Zone Development in Dynamic Tear Test Specimens", Martec Report TR-99-16, June 1999.

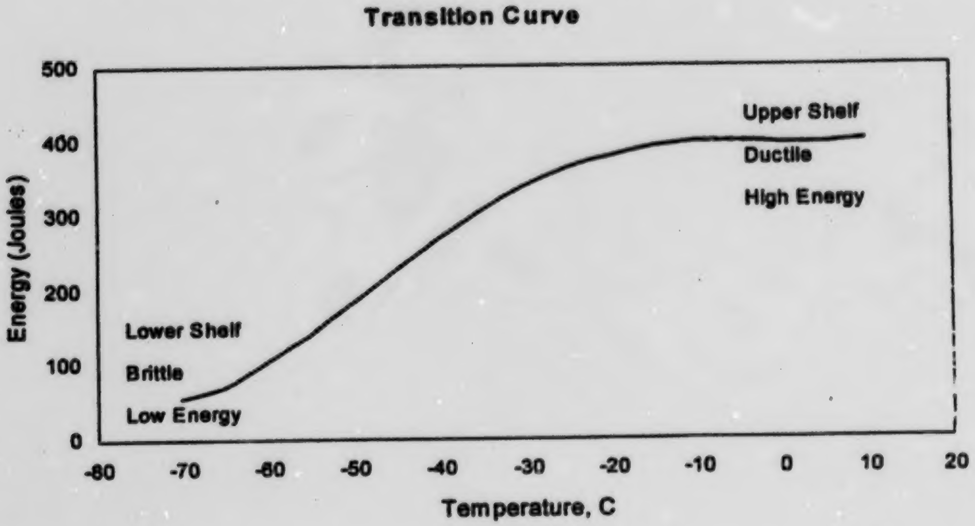

Figure 1: Typical Transition Curve

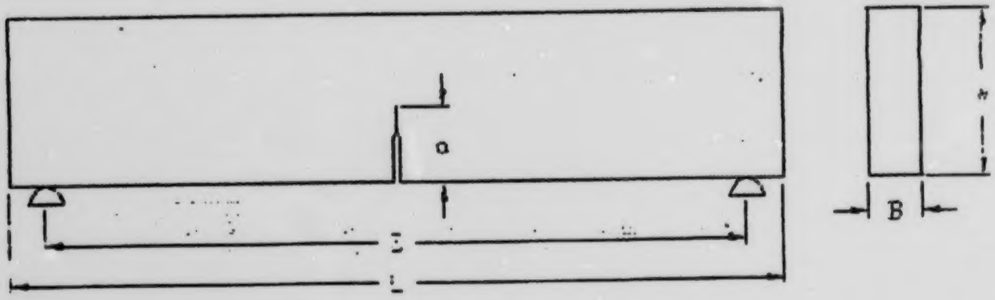

Figure2: Configuration of DT Specimen

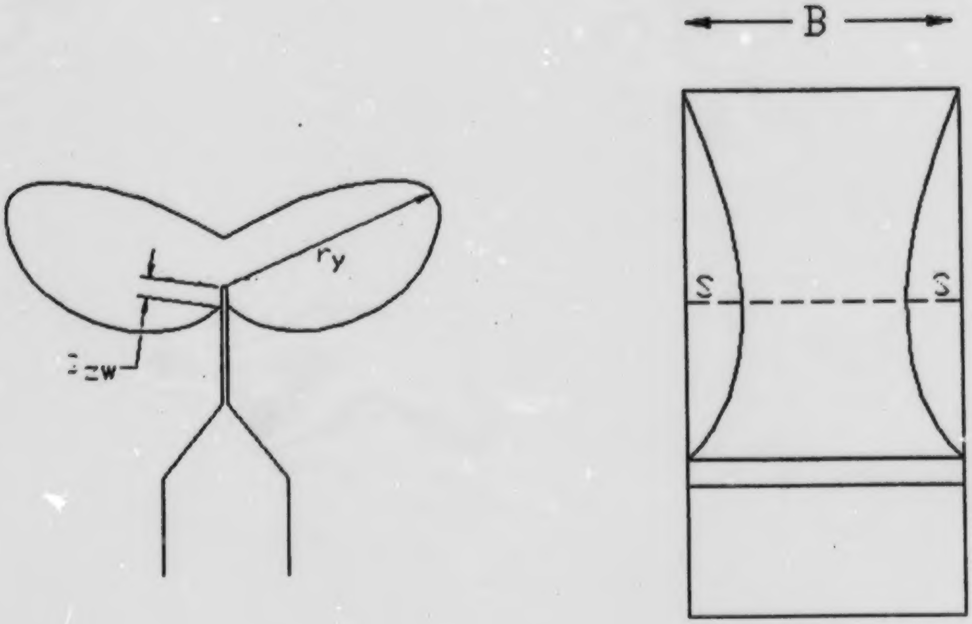

(a)

(b)

Figure 3: Idealization of Plastic Zone around Crack Tip

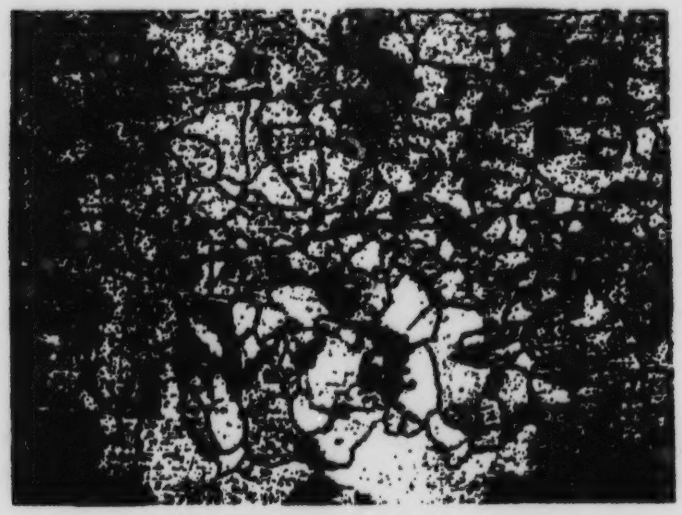

Figure 4: Shape of Fatigue Crack in DT Specimens

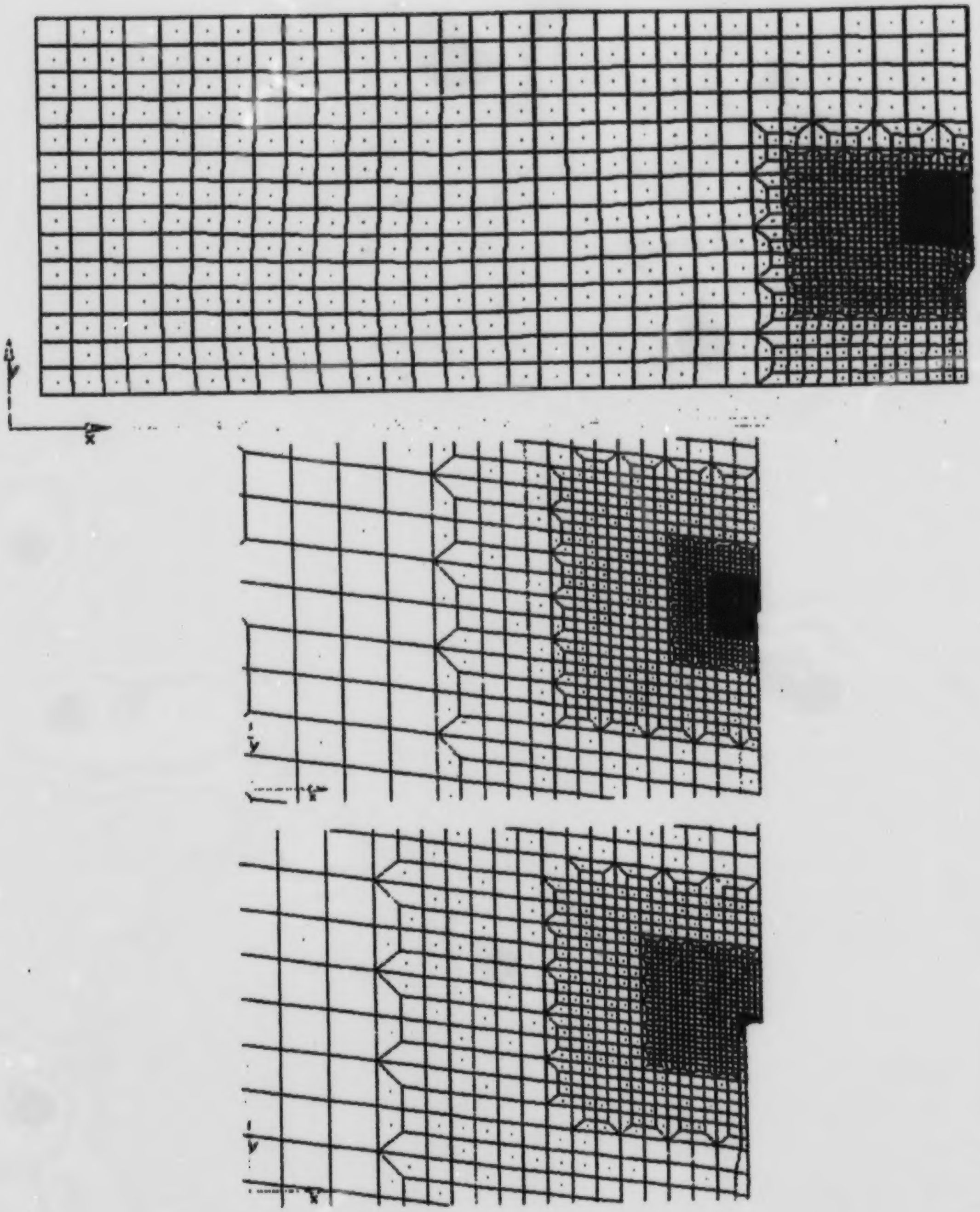

Figure 5: FE Mesh of DT Specimens

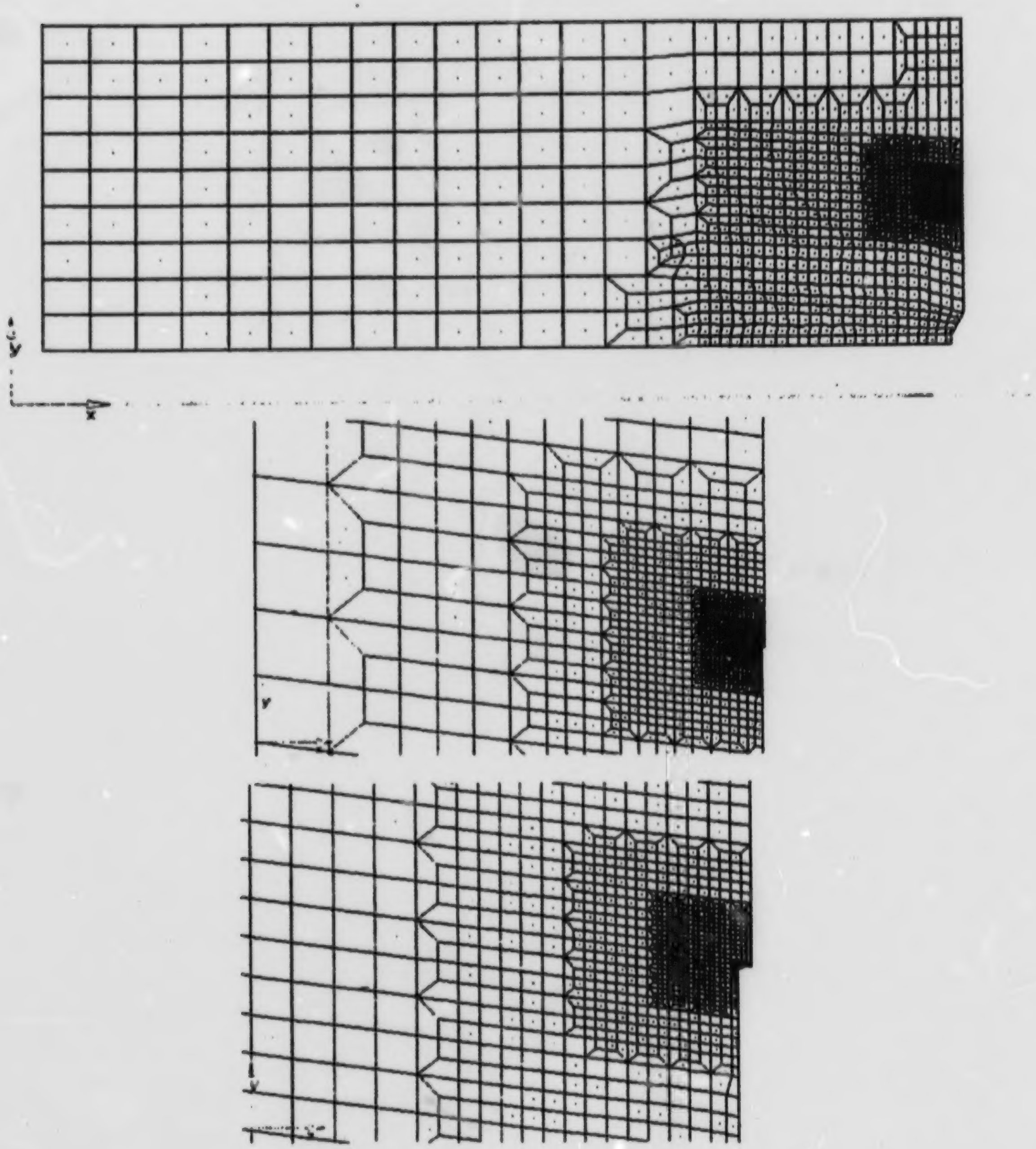

Figure 6: FE Mesh of Nonstandard (NS) Specimens

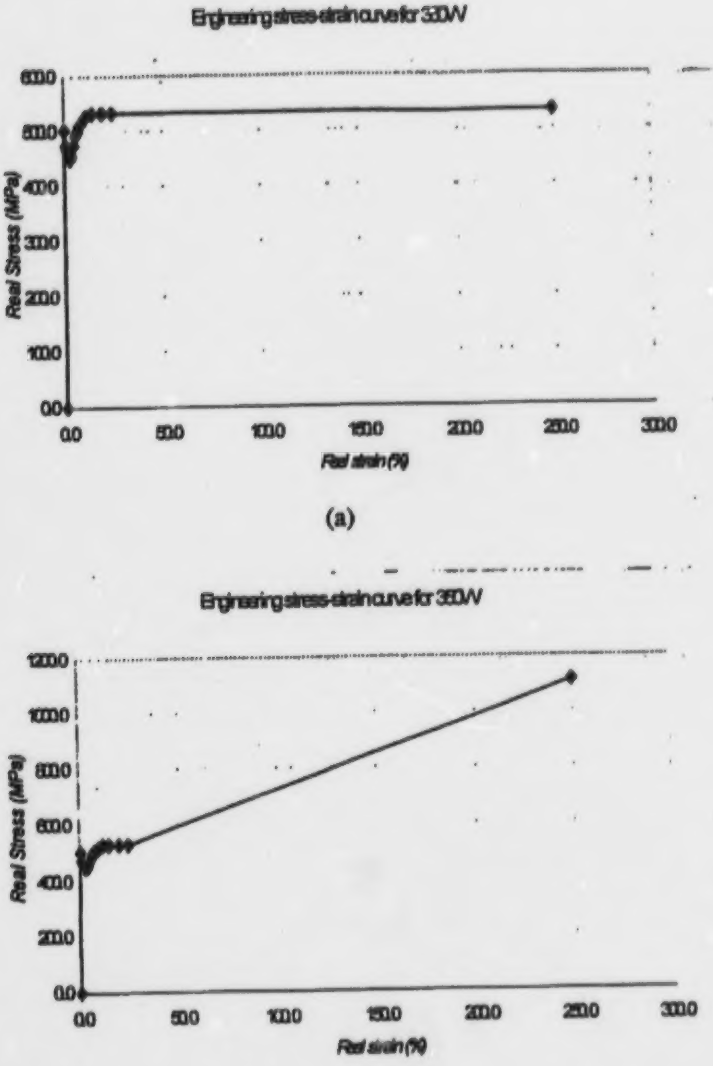

(a)

(b)

Figure 7: Stress-Strain Curves for 350WT Steel

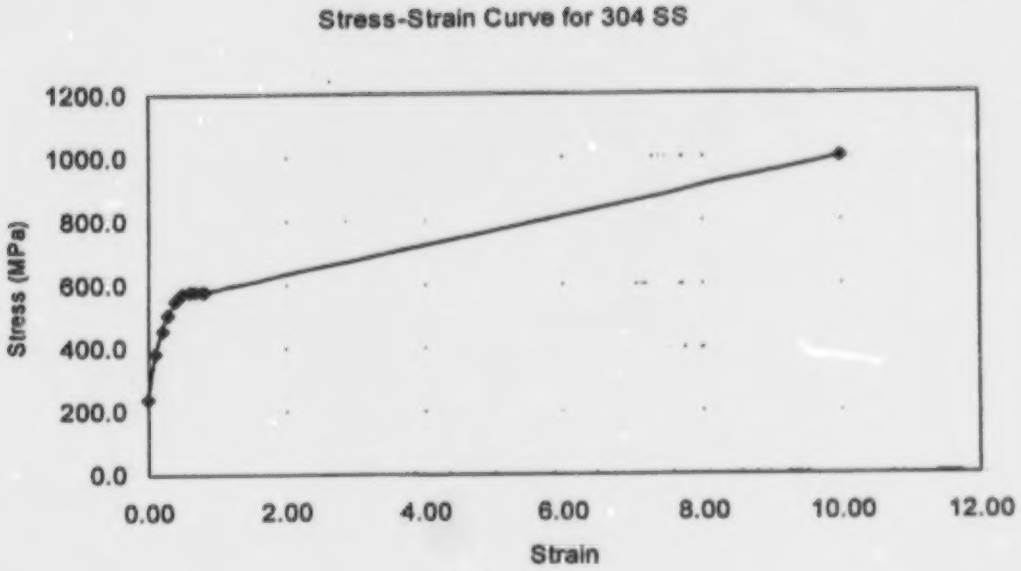

Figure 8: Stress-Strain Curves for 304 Stainless Steel

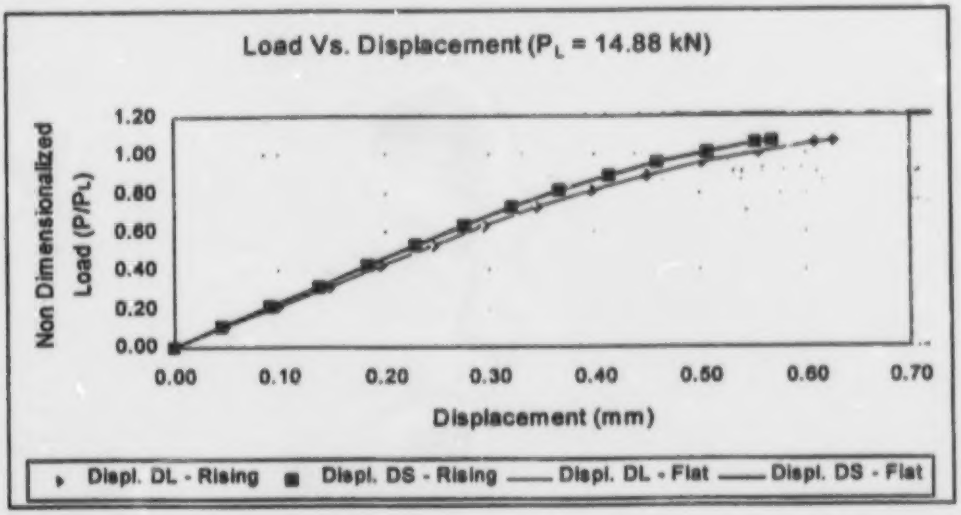

Figure 9: Midpoint Displacement Responses of DT-350WT Specimen, with Flat and Rising Stress-Strain Curve Models

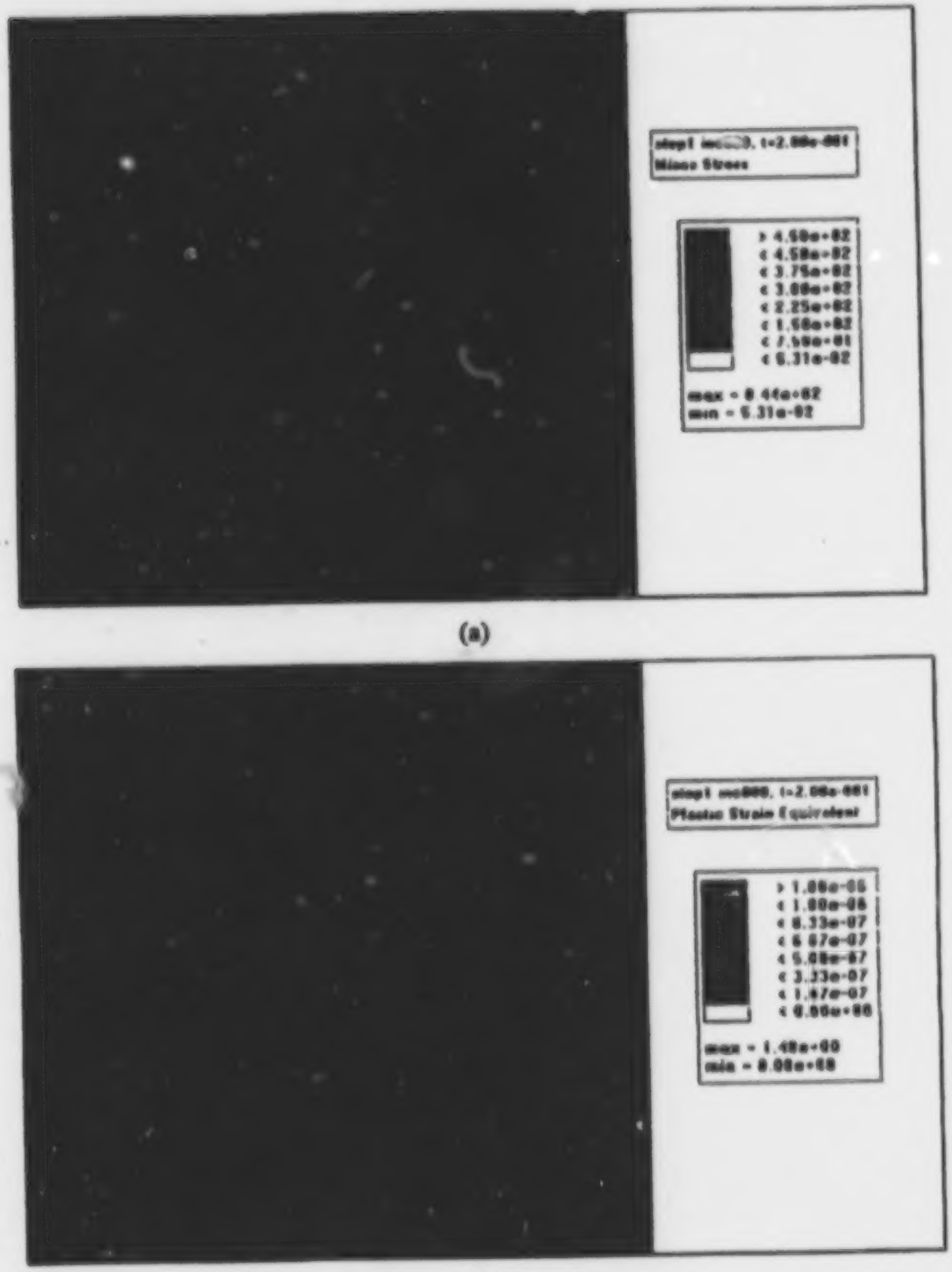
step1 inc000, t=2.00e-001
Mises Stress
> 4.50e+02
< 4.50e+02
< 3.75e+02
< 3.00e+02
< 2.25e+02
< 1.50e+02
< 7.50e+01
< 5.31e-02
max = 8.44e+02
min = 5.31e-02
(a)
step1 inc000, t=2.08e-001
Plastic Strain Equivalent
> 1.00e-06
< 1.00e-06
< 8.33e-07
< 6.67e-07
< 5.00e-07
< 3.33e-07
< 1.67e-07
< 0.00e+00
max = 1.48e+00
min = 0.00e+00

(b)

Figure 10: von Mises Stress and Equivalent Plastic Strain Development, in DT-350WT Specimen with Rising Stress-Strain Curve Model
(a) von Mises Stress and (b) Plastic Strain at 3.19 kN (0.21 P_L)

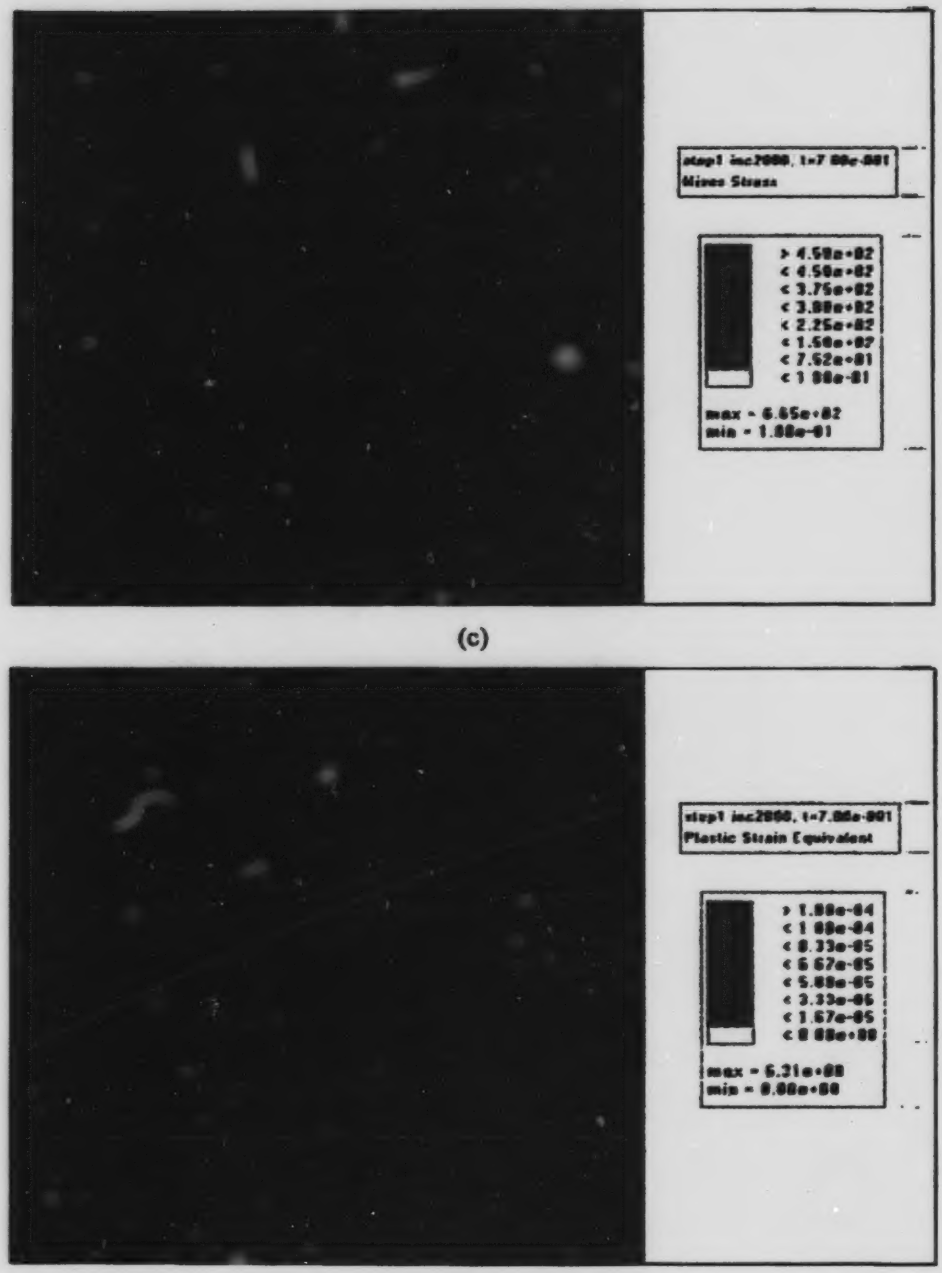
step1 inc2000, t=7.00e-001
Mises Stress
> 4.50e+02
< 4.50e+02
< 3.75e+02
< 3.00e+02
< 2.25e+02
< 1.50e+02
< 7.52e+01
< 1.00e-01
max = 6.65e+02
min = 1.00e-01
step1 inc2000, t=7.00e-001
Plastic Strain Equivalent
> 1.00e-04
< 1.00e-04
< 8.33e-05
< 6.67e-05
< 5.00e-05
< 3.33e-06
< 1.67e-05
< 0.00e+00
max = 6.31e+00
min = 0.00e+00

(c)

(d)

Figure 10 Continued: von Mises Stress and Equivalent Plastic Strain Development, in DT-350WT Specimen with Rising Stress-Strain Curve Model
(c) von Mises Stress and (d) Plastic Strain at 10.81 kN (0.73 P_L)

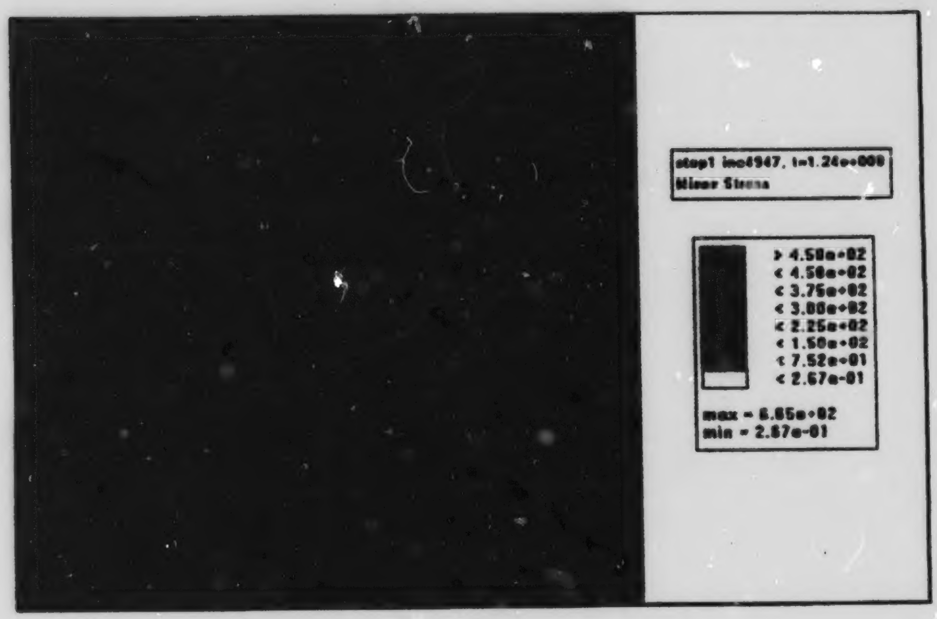
step1 inc4947, t=1.24e+000
Mises Stress
> 4.50e+02
< 4.50e+02
< 3.75e+02
< 3.00e+02
< 2.25e+02
< 1.50e+02
< 7.52e+01
< 2.67e-01
max = 6.65e+02
min = 2.67e-01

(e)

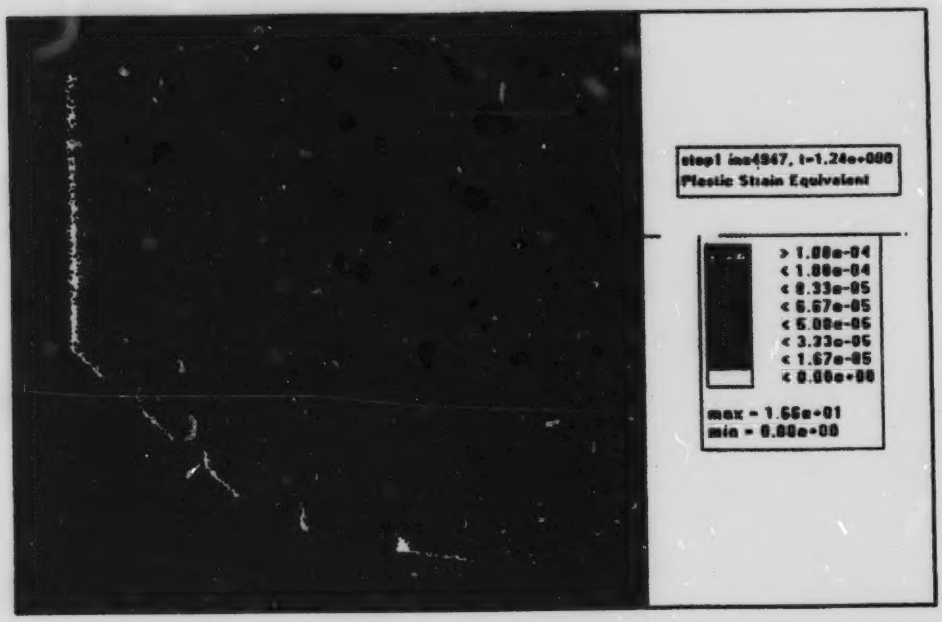
step1 inc4947, t=1.24e+000
Plastic Strain Equivalent
> 1.00e-04
< 1.00e-04
< 8.33e-05
< 6.67e-05
< 5.00e-05
< 3.33e-05
< 1.67e-05
< 0.00e+00
max = 1.66e-01
min = 0.00e+00

(f)

Figure 10 Continued: von Mises Stress and Equivalent Plastic Strain Development, in DT-350WT Specimen with Rising Stress-Strain Curve Model
(e) von Mises Stress and (f) Plastic Strain at 16.00 kN (1.08 P_L)

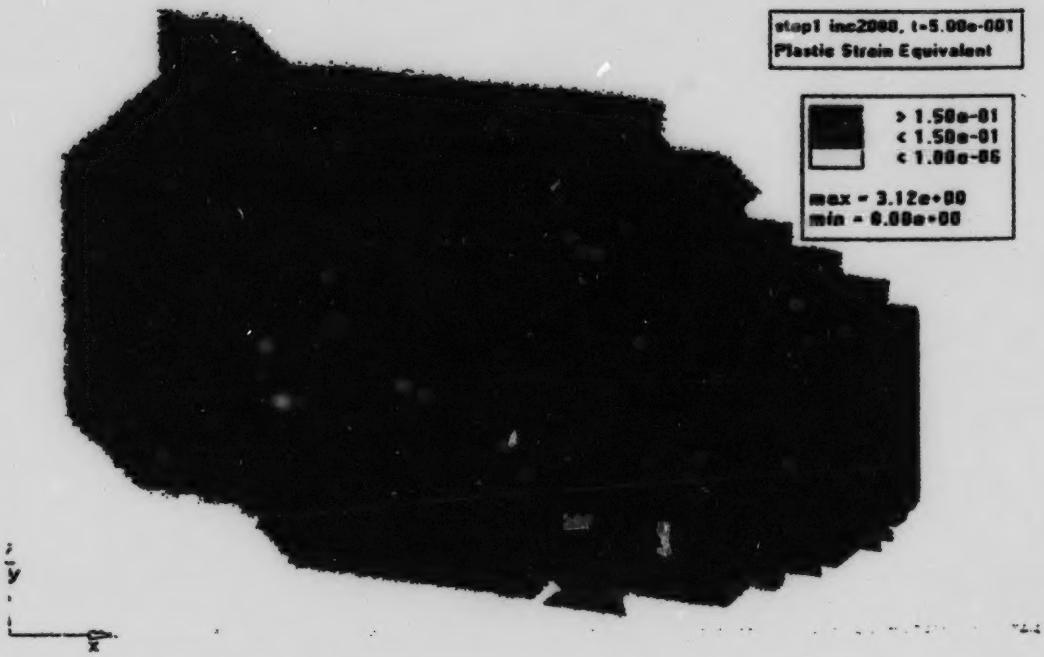
step1 inc2000, t=5.00e-001
Plastic Strain Equivalent
> 1.50e-01
< 1.50e-01
< 1.00e-06
max = 3.12e+00
min = 0.00e+00
y
x

Figure 11: Plastic Zone Configuration of DT-350WT Specimen Showing Area with Greater than 15% Plastic Strain at 7.87 kN (0.53 P_L)

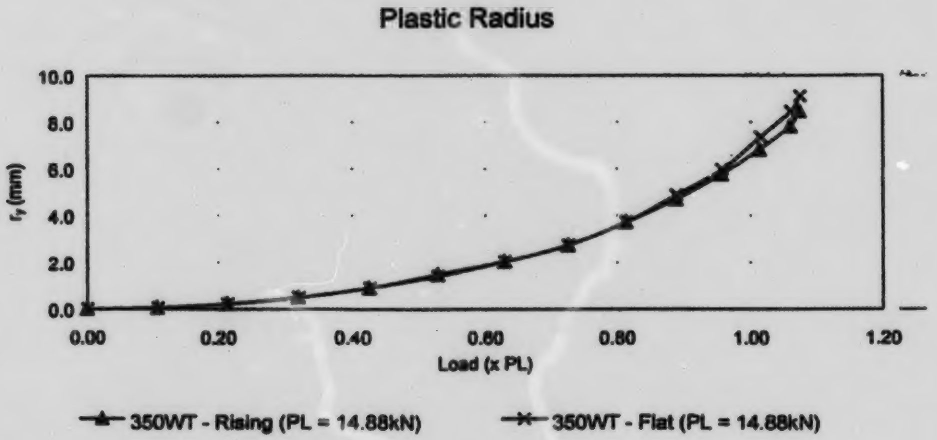

Figure 12: Plastic Radius of DT-350WT Specimen

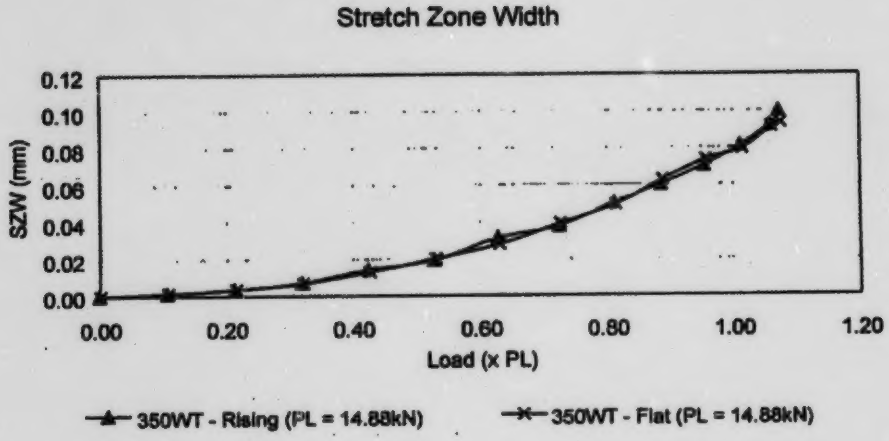

Figure 13: Stretch Zone Width of DT-350WT Specimen

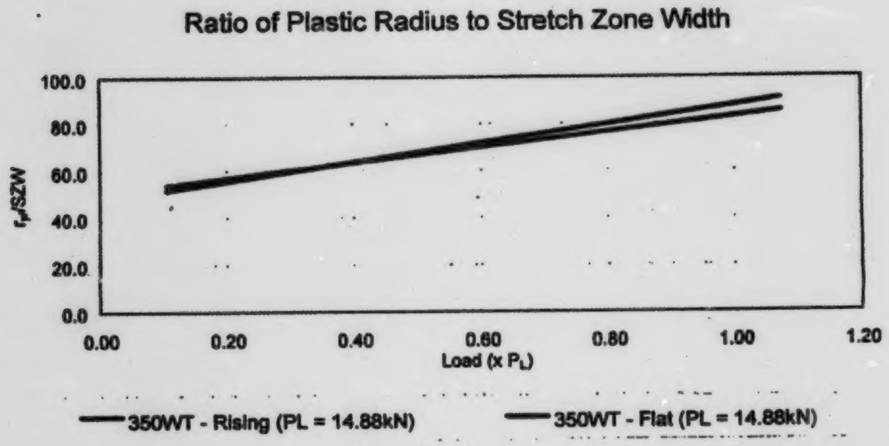

Figure 14: Ratio of Plastic Radius to Stretch Zone Width of DT-350WT Specimen

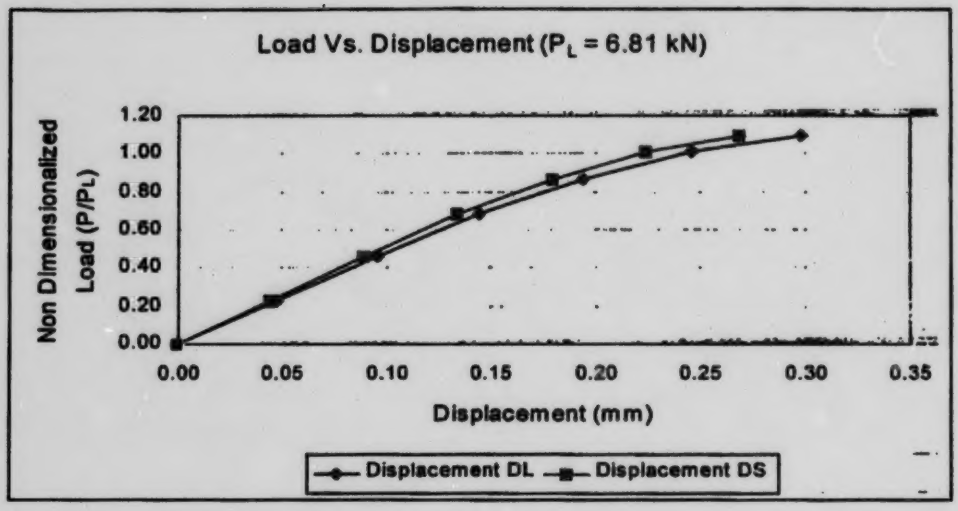

Figure 15: Midpoint Displacement Response of DT-304SS Specimen, Rising Curve Model

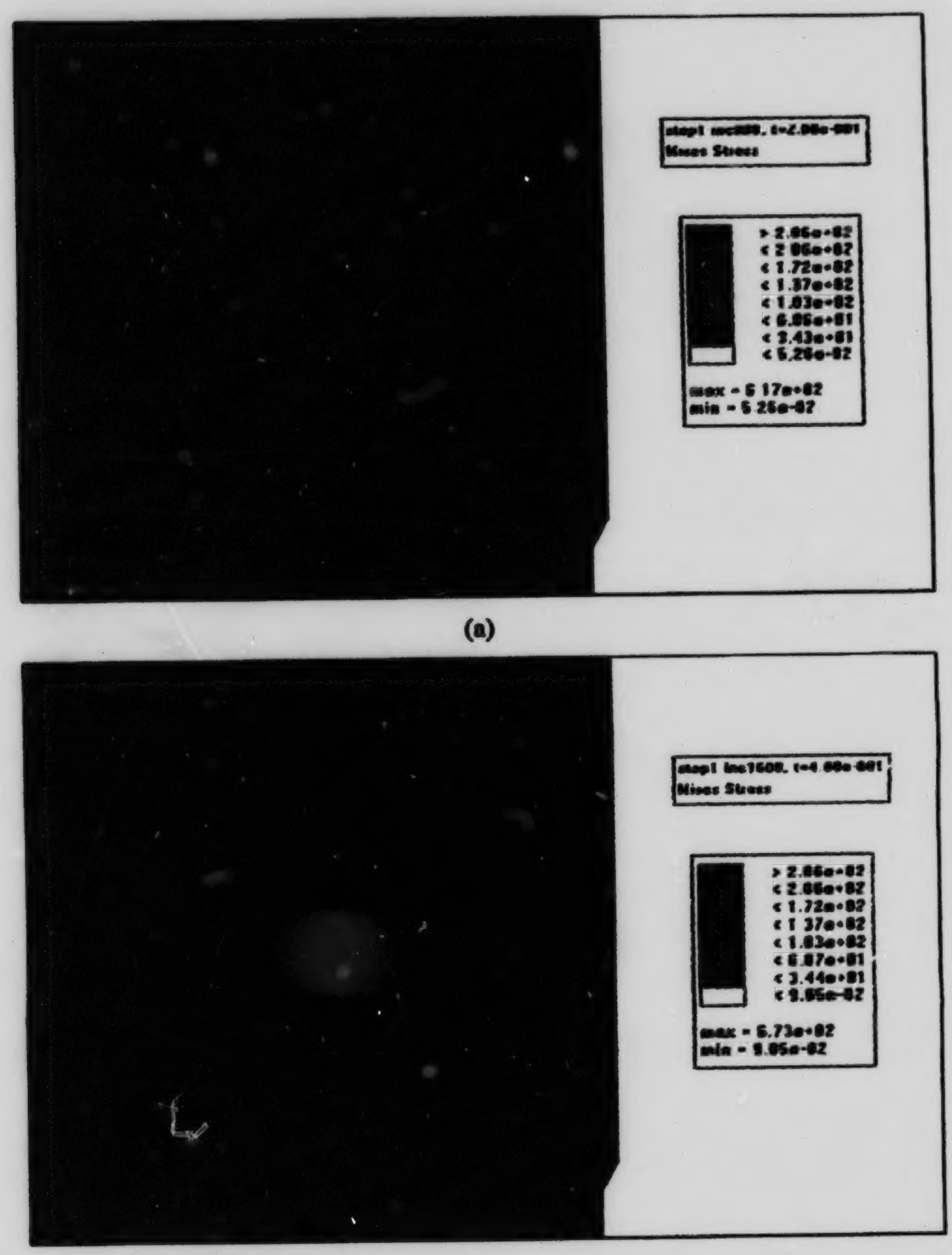

(a)

(b)

Figure 16: von Mises Stress Development in DT-304SS Specimen with Rising Stress-Strain Curve Model: (a) at 3.16 kN (0.46 P_L) and (b) at 5.92 kN (0.87 P_L)

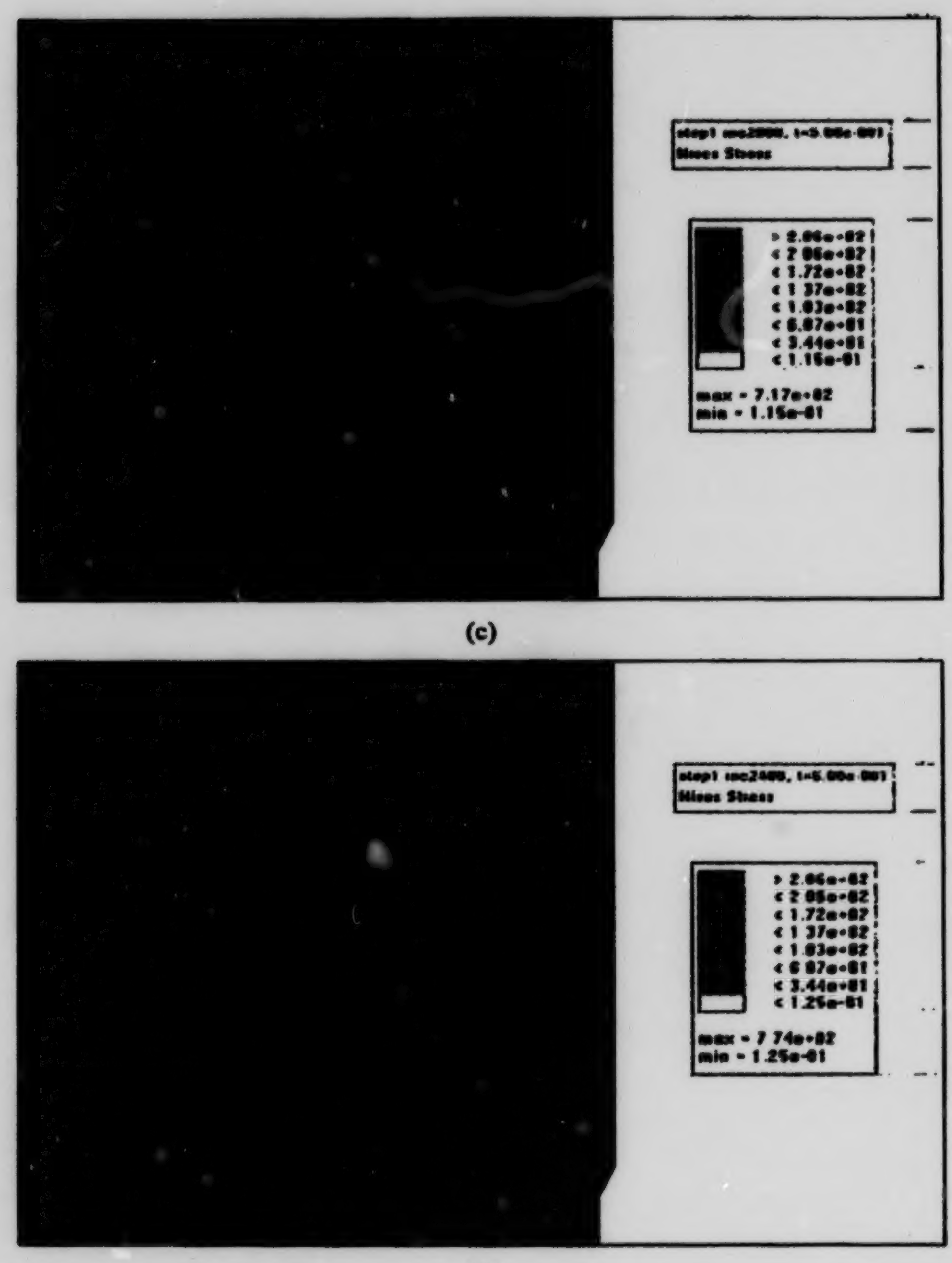
step1 inc2000, t=5.00e-001
Mises Stress
> 2.06e+02
< 2.06e+02
< 1.72e+02
< 1.37e+02
< 1.03e+02
< 6.87e+01
< 3.44e+01
< 1.15e-01
max = 7.17e+02
min = 1.15e-01
step1 inc2400, t=6.00e-001
Mises Stress
> 2.06e+02
< 2.06e+02
< 1.72e+02
< 1.37e+02
< 1.03e+02
< 6.87e+01
< 3.44e+01
< 1.25e-01
max = 7.74e+02
min = 1.25e-01

(c)

(d)

Figure 16 Continued: von Mises Stress Development in DT-304SS Specimen with Rising Stress-Strain Curve Model: (c) at 6.88 kN (1.01 P_L) and (d) at 7.48 kN (1.10 P_L)

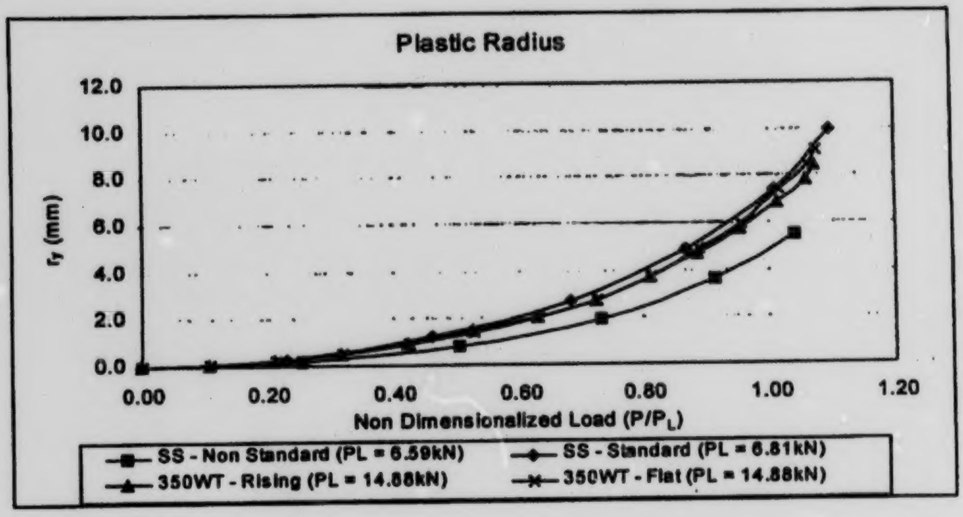

Figure 17: Comparison of Plastic Zone Radius

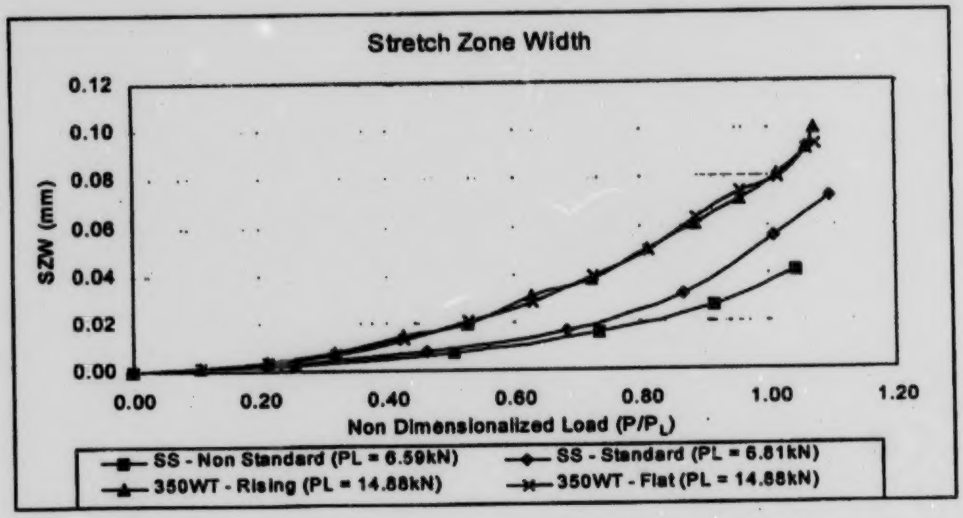

Figure 18: Comparison of Stretch Zone Width

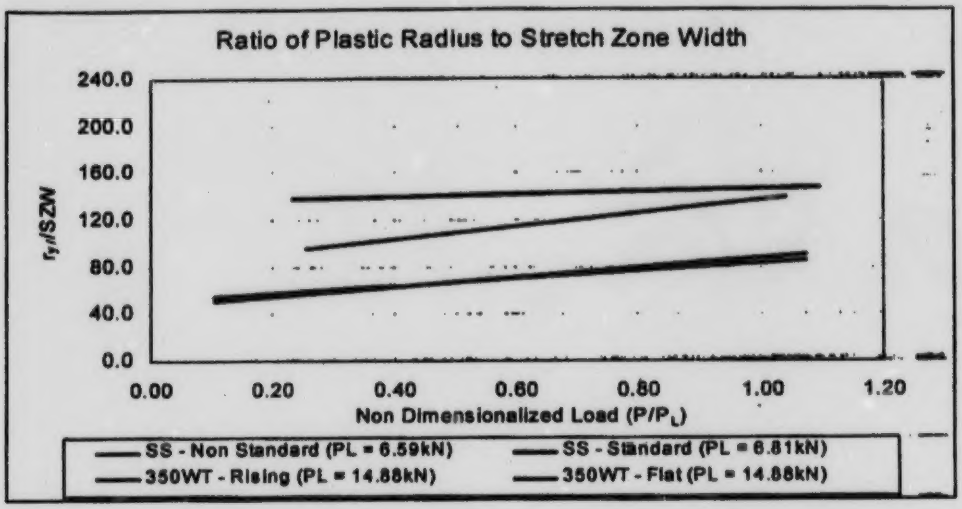

Figure 19: Comparison of Plastic Radius to Stretch Zone Width

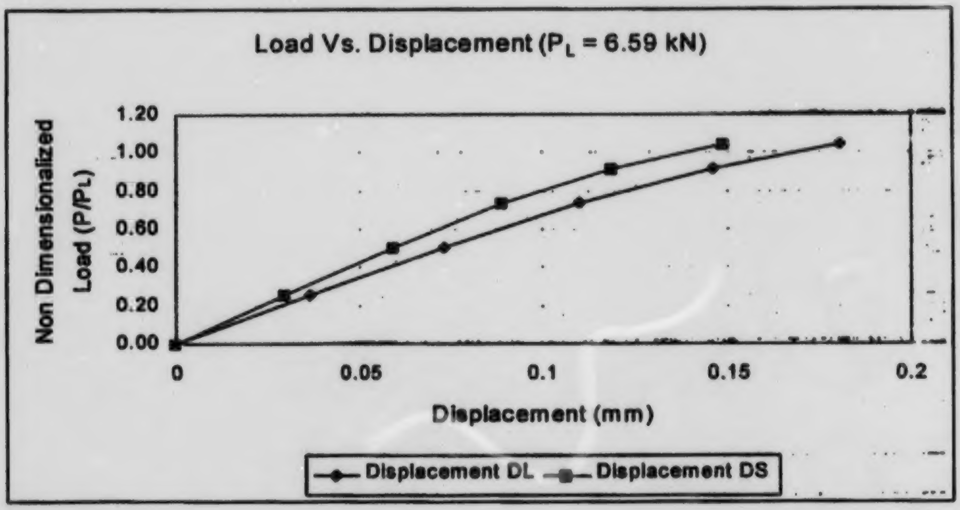

Figure 20: Midpoint Displacement Response of NS-304SS Specimen With Rising Stress-Strain Curve

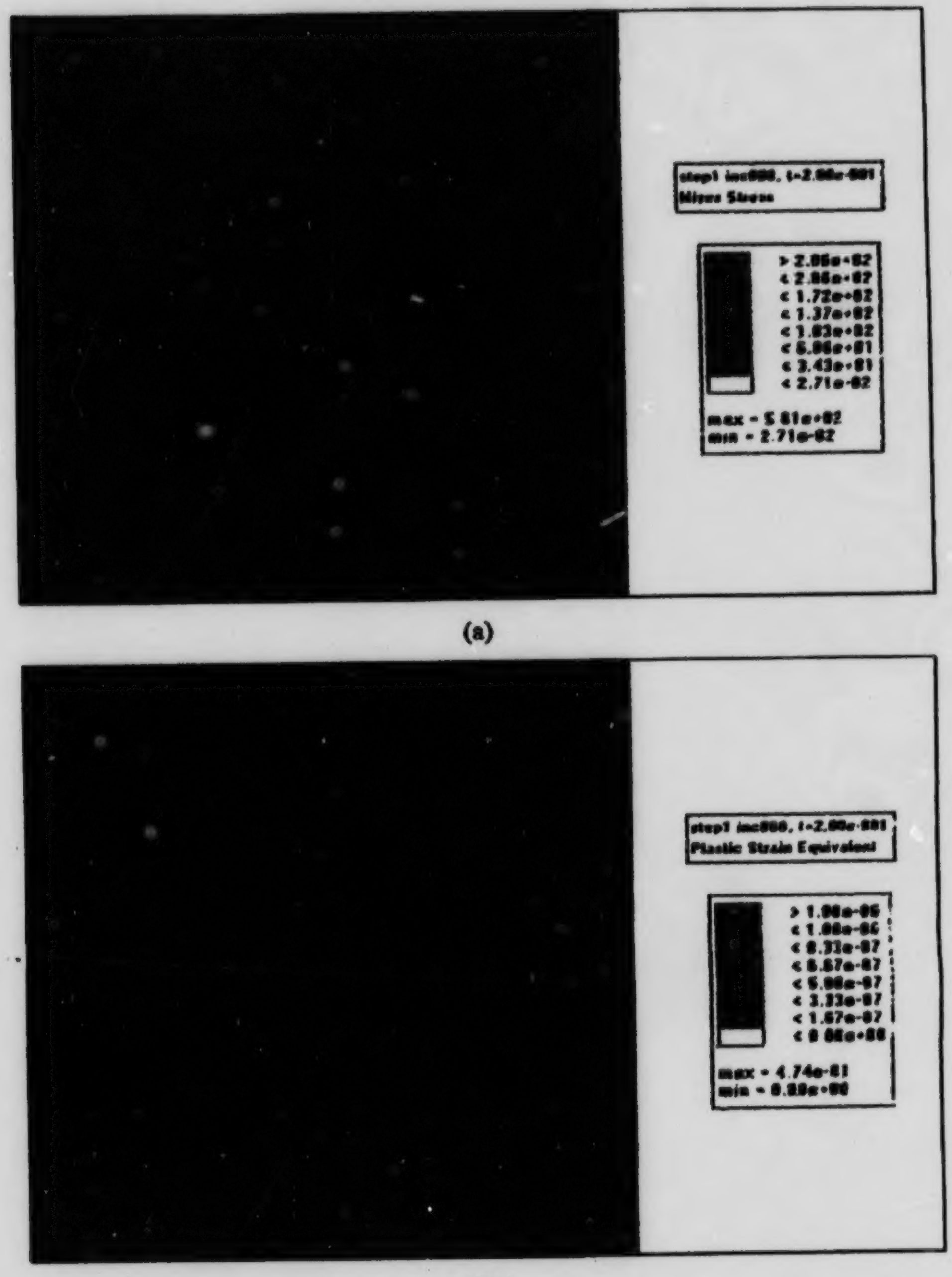

(a)

(b)

Figure 21: Plastic Zone Configurations of NS-304SS Specimens With Rising Stress-Strain Curve Model: (a) von Mises Stress and (b) Plastic Strain at 1.69 kN (0.26 P_L)

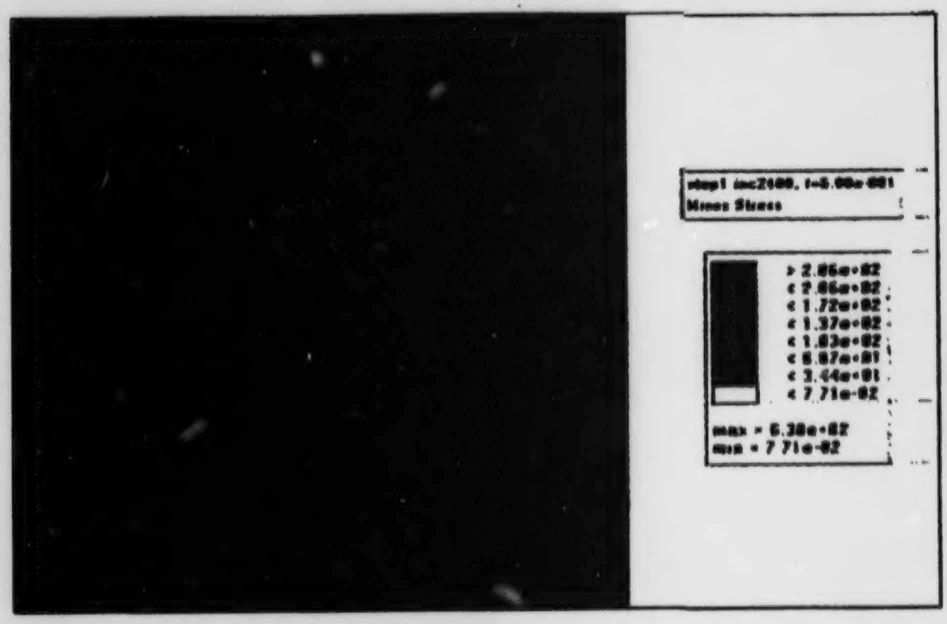

(e)

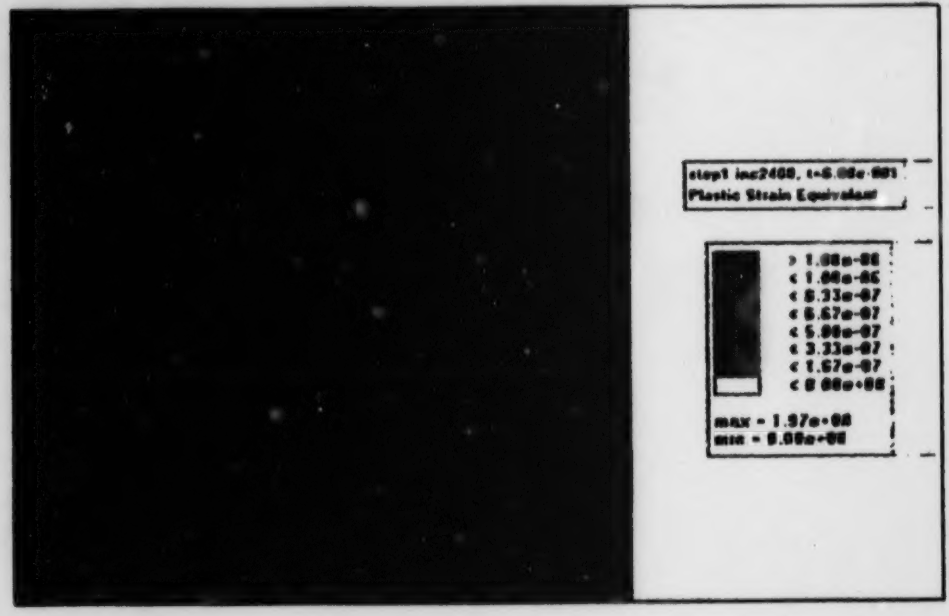

(f)

Figure 21 Continued: Plastic Zone Configurations of NS-304SS Specimens With Rising Stress-Strain Curve Model: (e) von Mises Stress and (f) Plastic Strain at 4.85 kN (0.74 P_L)

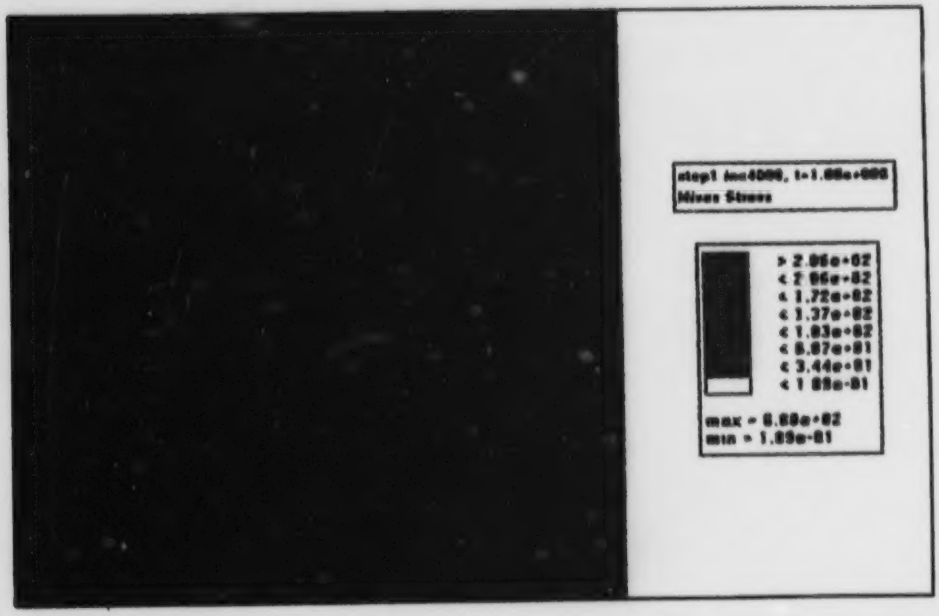
step1 inc4000, t=1.00e+000
Mises Stress
> 2.06e+02
< 2.06e+02
< 1.72e+02
< 1.37e+02
< 1.03e+02
< 6.87e+01
< 3.44e+01
< 1.89e-01
max = 6.80e+02
min = 1.89e-01

(i)

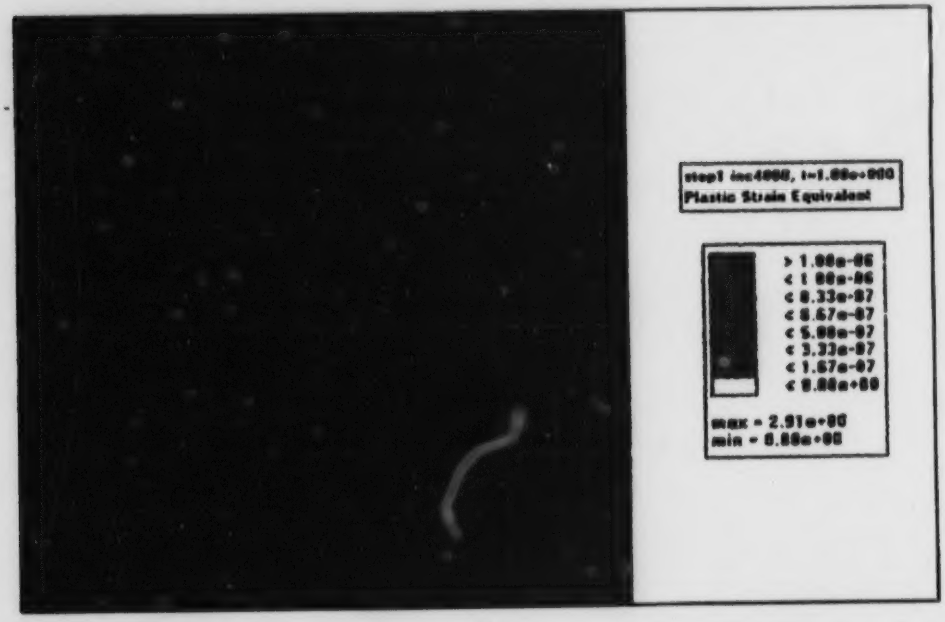
step1 inc4000, t=1.00e+000
Plastic Strain Equivalent
> 1.00e-06
< 1.00e-06
< 8.33e-07
< 6.67e-07
< 5.00e-07
< 3.33e-07
< 1.67e-07
< 0.00e+00
max = 2.91e+00
min = 0.00e+00

(j)

Figure 21 Continued: Plastic Zone Configurations of NS-304SS Specimens With Rising Stress-Strain Curve Model: (i) von Mises Stress and (j) Plastic Strain at 6.88 kN (1.04 P_L)

#511882 ⑧

Brittle Bead Weld Selection for Crack Arrest Toughness Tests

by L.N. Pussegoda*, L. Malik* and J. Morrison⁺

***Fleet Technology Ltd., Kanata, Ontario**

⁺Dockyard Laboratory Pacific, Victoria, British Columbia

ABSTRACT

In compact specimens used to measure crack arrest toughness, fast running cracks are usually initiated from either weld bead deposits or strain age embrittled notches. In previously reported work, tests were carried out on 15 mm thick 350WT grade steel plate specimens with strain aged chevron notches. Crack arrest toughness (K_v) varied between 155 to 95 MPa√m over the temperature range –15 to -40°C. The steels NDTT was -40°C.

The results also indicated that for optimum performance the crack starter needed to have different degrees of embrittlement depending on the specimen size and/or test material toughness. For a successful test, the higher the material crack arrest toughness level the larger is the required specimen size, and the higher the stored energy needed before crack initiation. As a result in this case the crack starter material needs to be capable of delaying the triggering of the crack run event. Similarly, smaller specimens designed to determine lower toughness need a lower stored energy prior to crack initiation.

The suitability of several weld electrodes with different hardness and toughness levels has been assessed in terms of their ability to initiate running cracks at various temperatures.

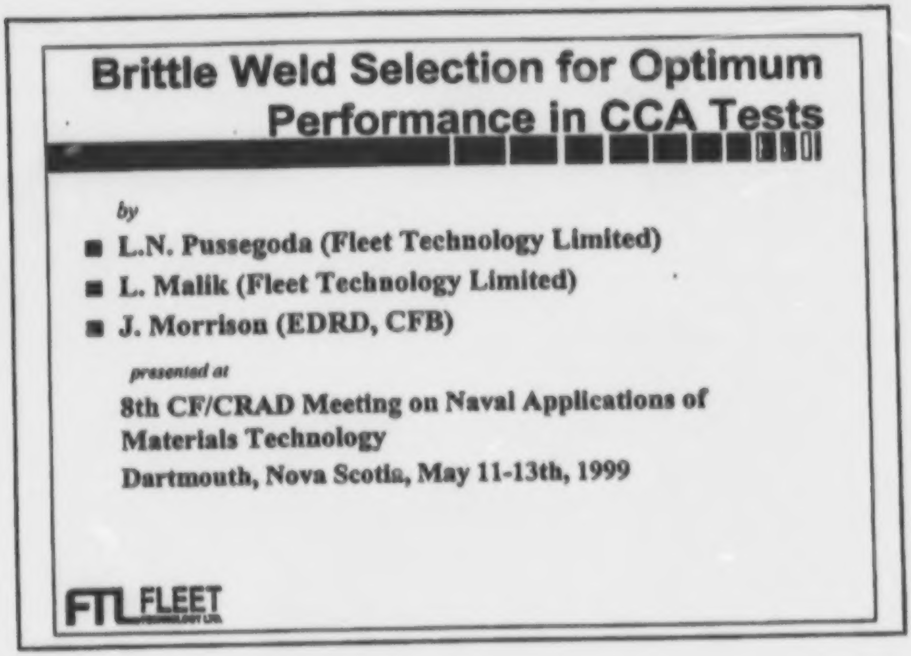

Brittle Weld Selection for Optimum Performance in CCA Tests

by

- **L.N. Pussegoda (Fleet Technology Limited)**
- **L. Malik (Fleet Technology Limited)**
- **J. Morrison (EDRD, CFB)**

presented at

8th CF/CRAD Meeting on Naval Applications of Materials Technology
Dartmouth, Nova Scotia, May 11-13th, 1999

FTL FLEET TECHNOLOGY LTD.

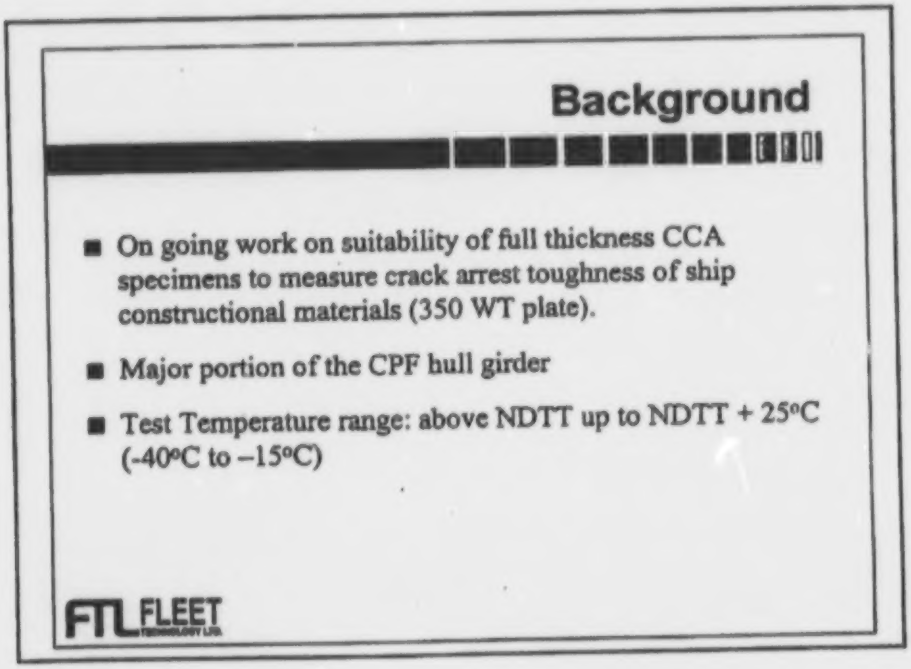

Background

- On going work on suitability of full thickness CCA specimens to measure crack arrest toughness of ship constructional materials (350 WT plate).
- Major portion of the CPF hull girder
- Test Temperature range: above NDTT up to NDTT + 25°C (-40°C to –15°C)

FTL FLEET TECHNOLOGY LTD.

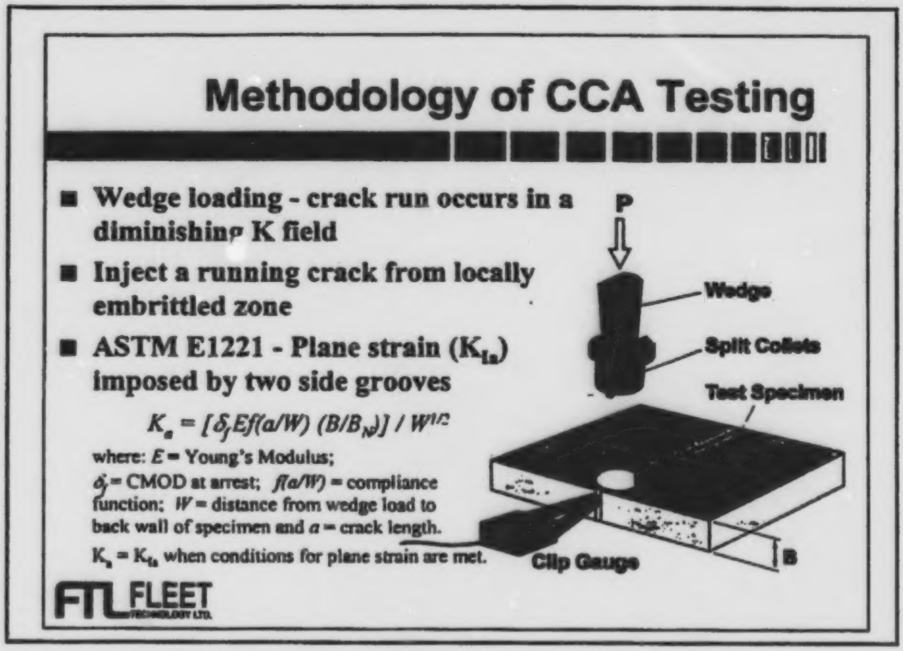

Methodology of CCA Testing

- Wedge loading - crack run occurs in a diminishing K field
- Inject a running crack from locally embrittled zone
- ASTM E1221 - Plane strain (K_{Ia}) imposed by two side grooves

$$K_a = [\delta_f E f(a/W)\,(B/B_N)] \,/\, W^{1/2}$$

where: E = Young's Modulus;
δ_f = CMOD at arrest; $f(a/W)$ = compliance function; W = distance from wedge load to back wall of specimen and a = crack length.

$K_a = K_{Ia}$ when conditions for plane strain are met.

P
Wedge
Split Collets
Test Specimen
Clip Gauge
B

FTL FLEET TECHNOLOGY LTD.

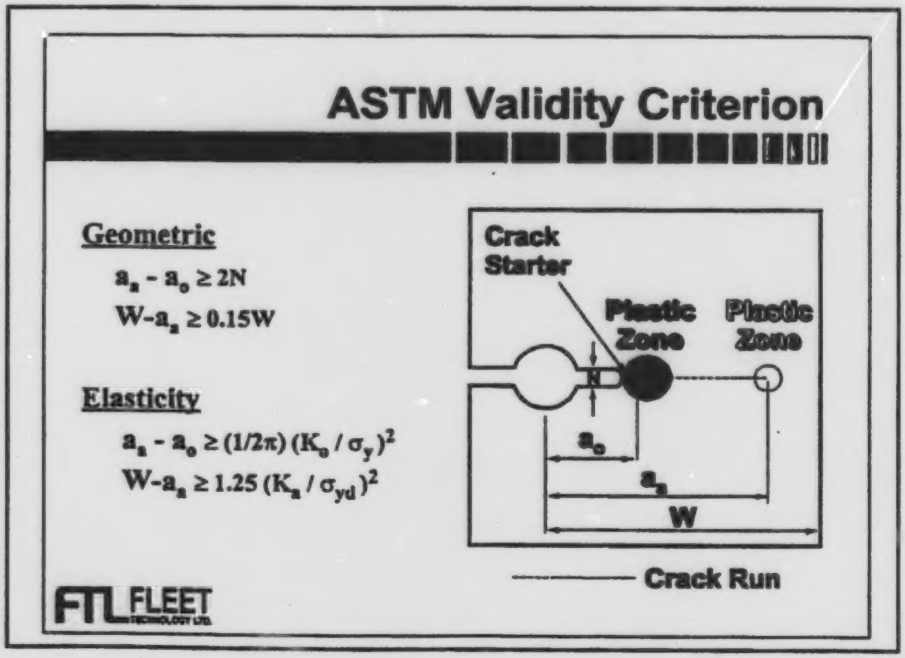

ASTM Validity Criterion

Geometric

$a_a - a_o \geq 2N$
$W - a_a \geq 0.15W$

Elasticity

$a_a - a_o \geq (1/2\pi)\,(K_o / \sigma_y)^2$
$W - a_a \geq 1.25\,(K_a / \sigma_{yd})^2$

Crack Starter
Plastic Zone
Plastic Zone
N
a_o
a_a
W
Crack Run

FTL FLEET TECHNOLOGY LTD.

Methodology of CCA Testing (cont)

- Non-plane Strain CCA Specimen Design Crosley & Ripling

$W \geq 2.83\,(K_v / \sigma_y)^2$

Where: K_v = is the "anticipated" crack arrest toughness - typically the minimum required for quality control purposes; σ_y = yield strength.

As test temperature is raised in-plane dimensions (W) increase - no limit for specimen size.

Validity requirements less stringent than ASTM - no check for plane strain.

Specified CMOD limits within which the run-arrest event should occur

- lower limit is based on a minimum crack length (0.5W)
- upper limit is based on a maximum crack length (0.8W)
- if arrest length is below or above these values a lower bound or upper bound estimate of K_a is realized.

FTL FLEET TECHNOLOGY LTD.

Procedure

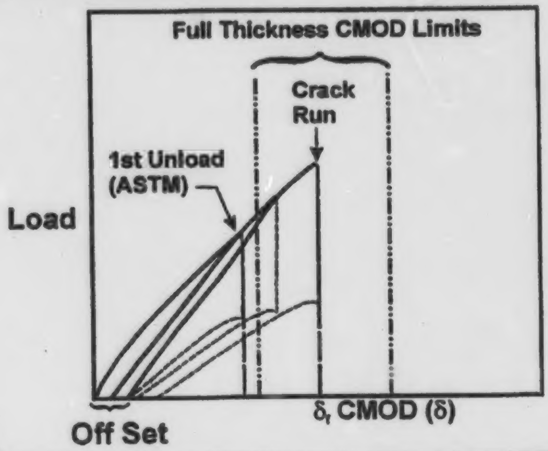

FTL FLEET TECHNOLOGY LTD.

Procedure

- ASTM experimental set up
- Multiple load cycle test (accordance with ASTM E1221). This method partially removes the plasticity component of the CMOD used for calculating K_a and thus reduces the arrest toughness compared to the single cycle approach of Crosley & Ripling.

FTL FLEET

Background (cont.)

- Previous work (presented at CRAD'97) showed the successful adaptation of the Full Thickness approach (Crosley & Ripling) for the base plate and HAZ.
- Crack starter - Strain age embrittled chevron notch. Success rate high (80%) at –15°C and no successful tests at -40°C for the base plate in the L-T orientation.
- Issue – the matching of degree of starter embrittlement with the level of arrest toughness of the test material.

FTL FLEET

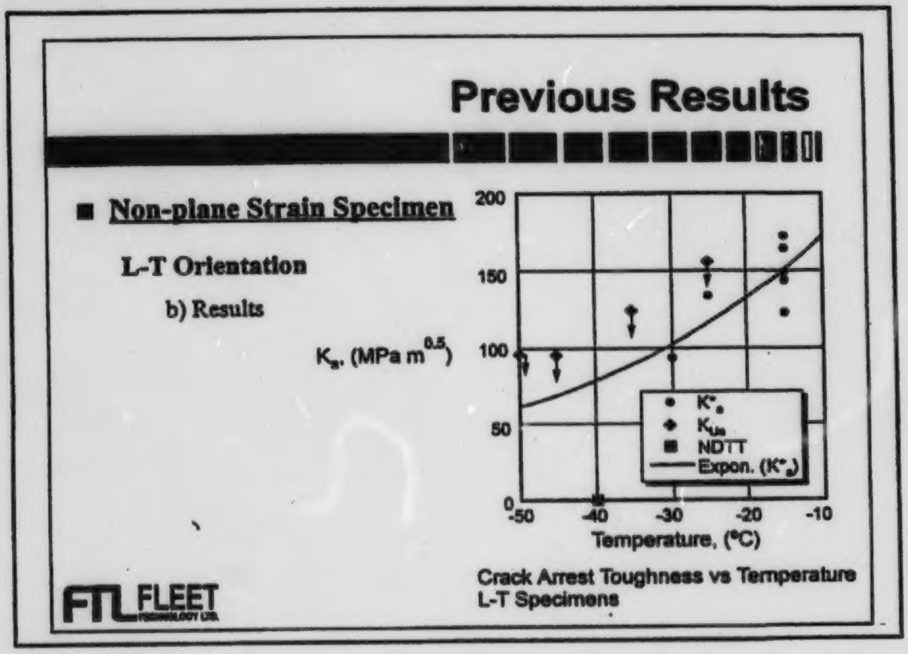

Previous Results

- **Non-plane Strain Specimen**

L-T Orientation

b) Results

Crack Arrest Toughness vs Temperature
L-T Specimens

FTL FLEET TECHNOLOGY LTD.

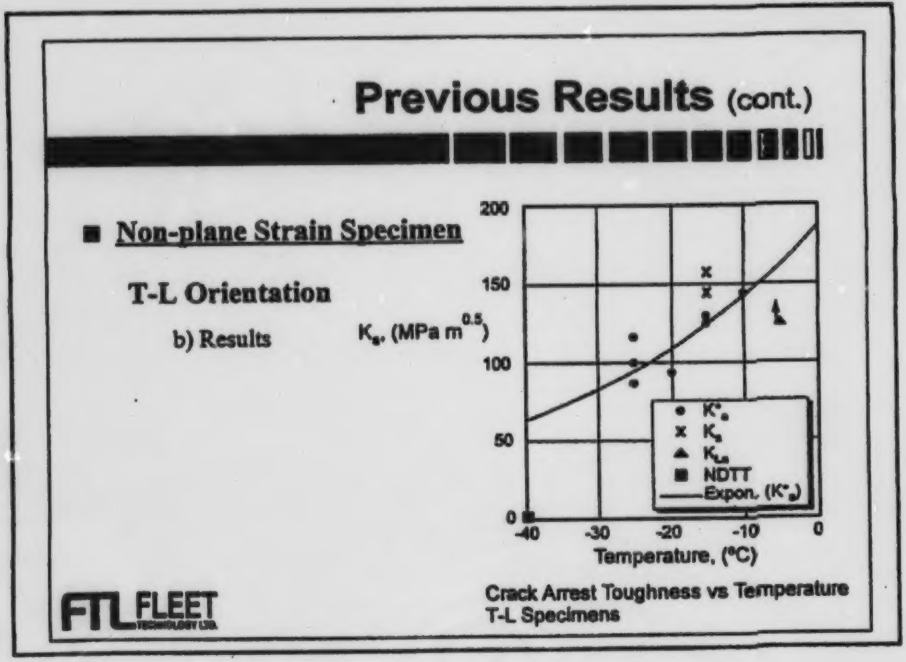

Previous Results (cont.)

- **Non-plane Strain Specimen**

T-L Orientation

b) Results

Crack Arrest Toughness vs Temperature
T-L Specimens

FTL FLEET TECHNOLOGY LTD.

Previous Results (cont.)

- **Previous work - single load cycle (Strain aged embrittled starter)**

  2 plots of K_a vs. T (L-T, T-L)

  - **L-T orientation**
    - **i) Success rate low at low temperatures**
    - **ii) Insufficient embrittlement of starter**
  - **T-L orientation**
    - **i) Premature initiation at higher temperatures.**
    - **ii) Excessive embrittlement of starter**
  - **A case of matching K_o (the degree of embrittlement) with K_a (and hence W).**

FTL FLEET TECHNOLOGY LTD.

Crack Starter

- Requirement: starter initiation toughness $K_o > K_a$ (because of decreasing K field)

  Options:

  a) brittle weld bead, b) chevron notch ($K_o >> K_a$), c) EDM notch ($K_o >> K_a$), d) strain age embrittled Chevron notch (mid-plane splitting) and e) fatigue crack ($K_o >> K_a$). ***The last 4 options are using the test material itself under different conditions.***

  Objective:

  Matching of K_o to K_a to get a single crack run event using the brittle weld bead.

FTL FLEET TECHNOLOGY LTD.

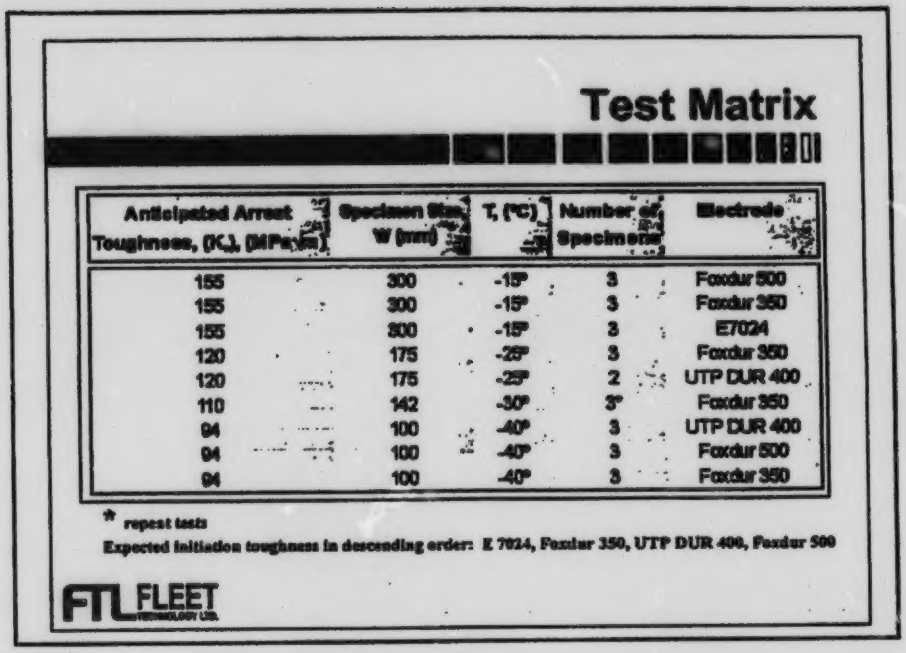

Test Matrix

Anticipated Arrest Toughness, (K_a), (MPa$\sqrt{m}$)	Specimen Size W (mm)	T, (°C)	Number of Specimens	Electrode
155	300	-15°	3	Foxdur 500
155	300	-15°	3	Foxdur 350
155	300	-15°	3	E7024
120	175	-25°	3	Foxdur 350
120	175	-25°	2	UTP DUR 400
110	142	-30°	3*	Foxdur 350
94	100	-40°	3	UTP DUR 400
94	100	-40°	3	Foxdur 500
94	100	-40°	3	Foxdur 350

* repeat tests

Expected initiation toughness in descending order: E 7024, Foxlar 350, UTP DUR 400, Foxdur 500

FTL FLEET TECHNOLOGY LTD.

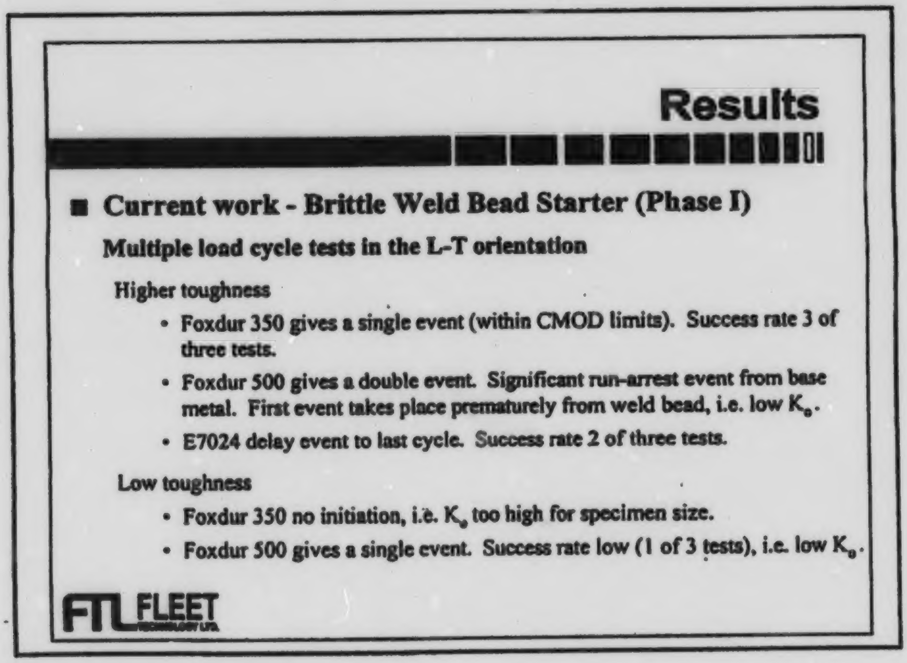

Results

- **Current work - Brittle Weld Bead Starter (Phase I)**

Multiple load cycle tests in the L-T orientation

Higher toughness
- Foxdur 350 gives a single event (within CMOD limits). Success rate 3 of three tests.
- Foxdur 500 gives a double event. Significant run-arrest event from base metal. First event takes place prematurely from weld bead, i.e. low K_o.
- E7024 delay event to last cycle. Success rate 2 of three tests.

Low toughness
- Foxdur 350 no initiation, i.e. K_o too high for specimen size.
- Foxdur 500 gives a single event. Success rate low (1 of 3 tests), i.e. low K_o.

FTL FLEET TECHNOLOGY LTD.

Results (Cont.)

- **Current work - Brittle Weld Bead Starter (Phase II)**

Intermediate toughness

- Foxdur 350 single event (within CMOD limits). Smaller specimen size compared to higher toughness tests. Success rate 6 of six tests. In two tests the crack run was sufficient, whereas in the other four the crack run was insufficient, indicating higher toughness than the anticipated value for this specimen size. Issue of material toughness variability at the edge of controlled rolled plate. A lower bound can be determined for latter specimens.
- UTP DUR 400 gives a single event prematurely (below the lower CMOD limit), i.e. low K_o.

Low toughness

- UTP DUR 400 gives a single event prematurely (below the lower CMOD limit), i.e. K_o too low for specimen size.

FTL FLEET

Results

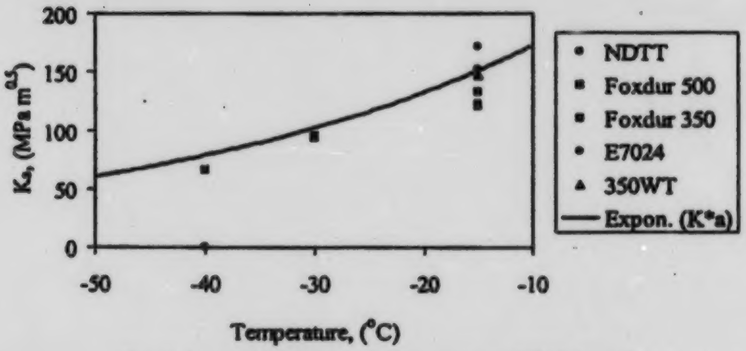

Crack Arrest Toughness vs Temperature - LT Orientation
(current - data points, previous - trend curve)

FTL FLEET

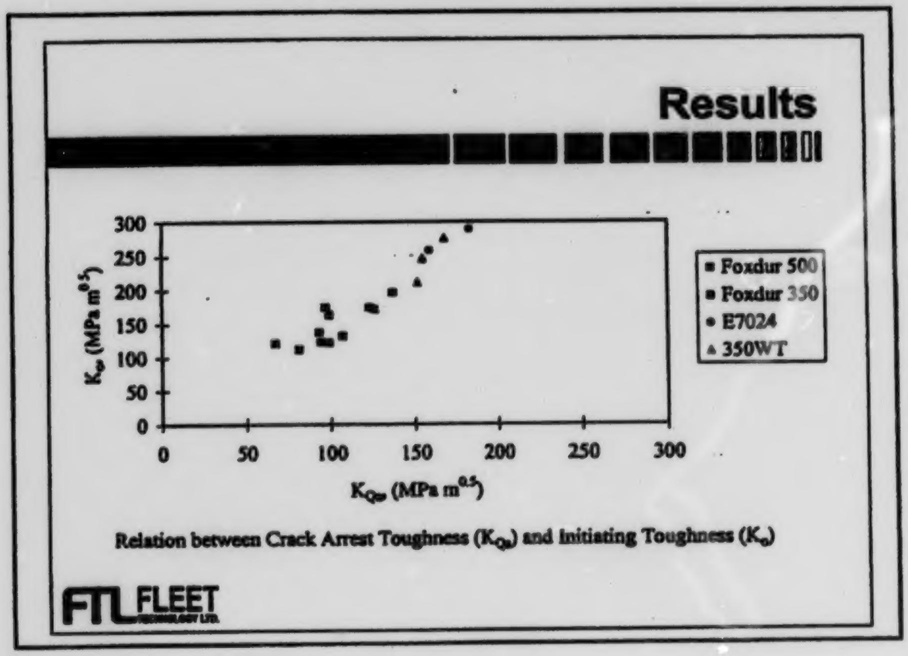

Results

Relation between Crack Arrest Toughness (K_{Qa}) and Initiating Toughness (K_o)

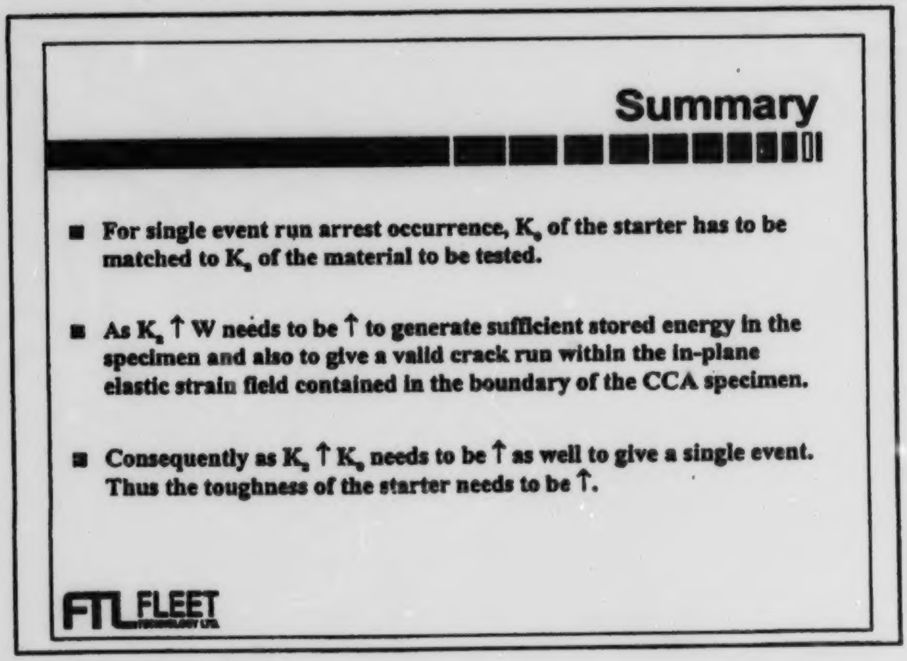

Summary

- For single event run arrest occurrence, K_s of the starter has to be matched to K_a of the material to be tested.
- As K_a ↑ W needs to be ↑ to generate sufficient stored energy in the specimen and also to give a valid crack run within the in-plane elastic strain field contained in the boundary of the CCA specimen.
- Consequently as K_a ↑ K_s needs to be ↑ as well to give a single event. Thus the toughness of the starter needs to be ↑.

#511883 (9)

Advanced Lithium Ion Super Polymer Rechargeable Batteries

by S. Das Gupta, J.K. Jacobs and D. Murdoch

Electrofuel Inc., 21 Hanna Avenue, Toronto, Ontario M6K 1W8

ABSTRACT

Electrofuel has recently developed a Lithium Ion Super polymer rechargeable battery. The Electrofuel battery has energy density of 470Wh/litre and 175 Wh/kg, which is the highest energy density of all lithium ion batteries in the world. Presently 98% of the world's Lithium Ion batteries are supplied by Japanese companies such as Sony, Panasonic and Toshiba with battery performance around 300Wh/litre and 120 Wh/kg. The Electrofuel battery is produced in a flat format, and can be produced in most shapes and sizes. Typical cells available from Electrofuel range from 1Ah to 12Ah. A new battery pack of 150Wh at 14.8V and 10.2Ah will be announced at this conference. This battery pack is compatible with portable computers and other uses. Electrofuel has a production plant in Toronto.

Introduction

Electrofuel, Inc. has developed a new type of Lithium Ion SuperPolymer battery which has the world's highest energy density of greater than 450 W/l and 190 W/ Kg.

The battery consists of a graphite negative electrode and a Lithium-Cobalt Oxide positive electrode, with the Lithium Ion shuttling between the electrodes. Typical average cell voltage is 3.75V.

The cells are charged to 4.2 volts through a constant current, constant voltage regime and typically discharged to 3.0 volts.

Applications

Electrofuel's SuperPolymer battery exceeds the following targets for different applications:

Name	**Target Market**	**ENERGY DENSITY Wh/liter**
1. Japan's Sunshine Program targets 2001	Alternate energy	360
2. USABC: long term target 2003	Transportation	250
3. NEMI : future energy requirements 2008	Electronic devices	400
4. **Electrofuel: 1999**		**450**
5. **Electrofuel: target for 2001**		**600**

The Electrofuel battery exceeds the performance of the above and therefore can be amply used in areas such as:

- Notebook Computer
- Personal Digital Assistance
- Cellular Telephones
- Portable Telecommunication Devices
- Electric Cars

- Power Assisted Bicycles
- Hybrid Vehicles
- Medical Devices
- Defense Power sources
- Aerospace Power sources

Product Performance

Electrofuel has developed a battery pack named the PowerPad 160. This pack has a capacity of 11 Ah and gives an average output of 15 volts and. Four 11 Ah cells are connected in series with the following configuration:

Dimensions: 3/8" thin by 8.75" x 11.75"
Weight: 2 lbs
Fuel Gauge: 5 LED Fuel Gauge with low battery alarm alert

The PowerPad 160 is designed specifically to provide external, long-lasting power for portable notebook computers.

Conclusion

The SuperPolymer battery appears to have many applications and the battery can be tailored to each application with respect to shape, size, capacity, voltage, configuration and discharge rates.

Electrofuel Vision

IT Markets

Portable Computers

Cellular Phones

Integrated Communication Devices

Energy & Other Markets

Medical Devices
Power Assisted Bicycles
Strategic Power Sources
Hybrid Electric Vehicles
Full Electric Vehicles
Energy Storage for Alternative Energy Solar, & Wind
Aerospace, Defense
Mini Disks
Load Leveling

electrofuel

ELECTROFUEL: Life Cycle Profile

Cell Capacity(nominal): 11,000 mAh

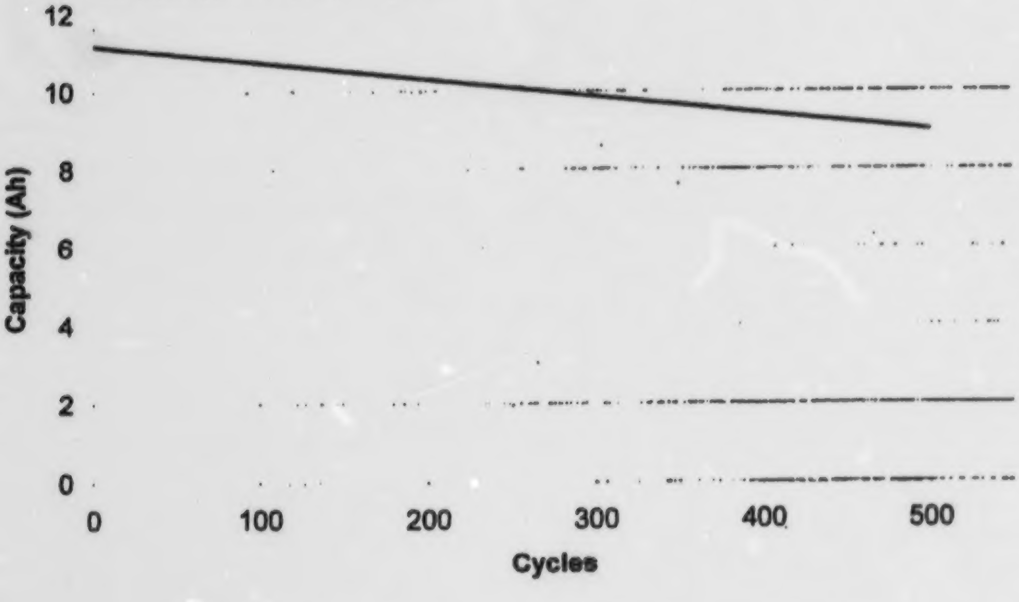

ELECTROFUEL: Charge - Discharge Profile

Cell Capacity (nominal): 11,000 mAh

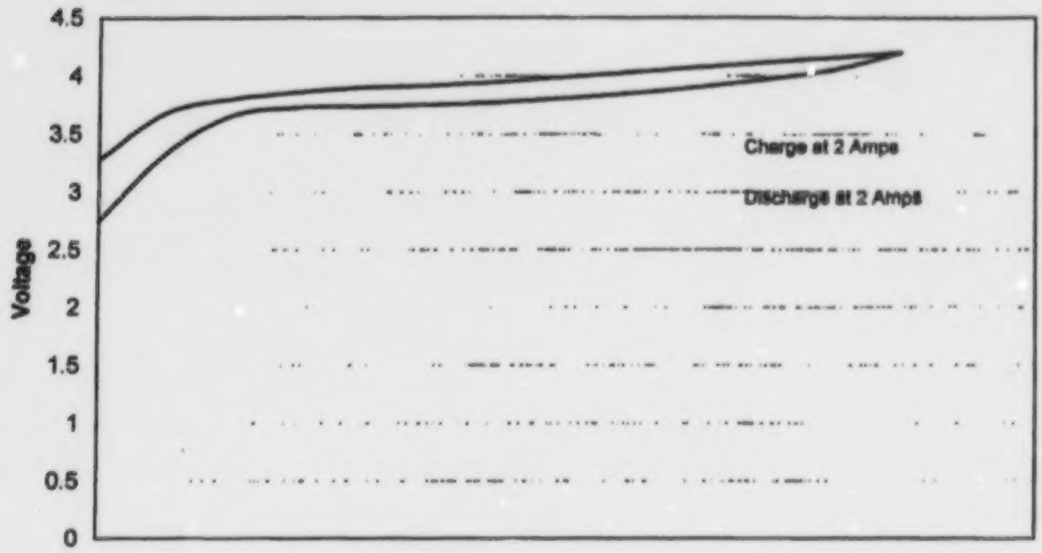

ELECTROFUEL: Discharge Characteristics

Cell Capacity (nominal): 11000 mAh

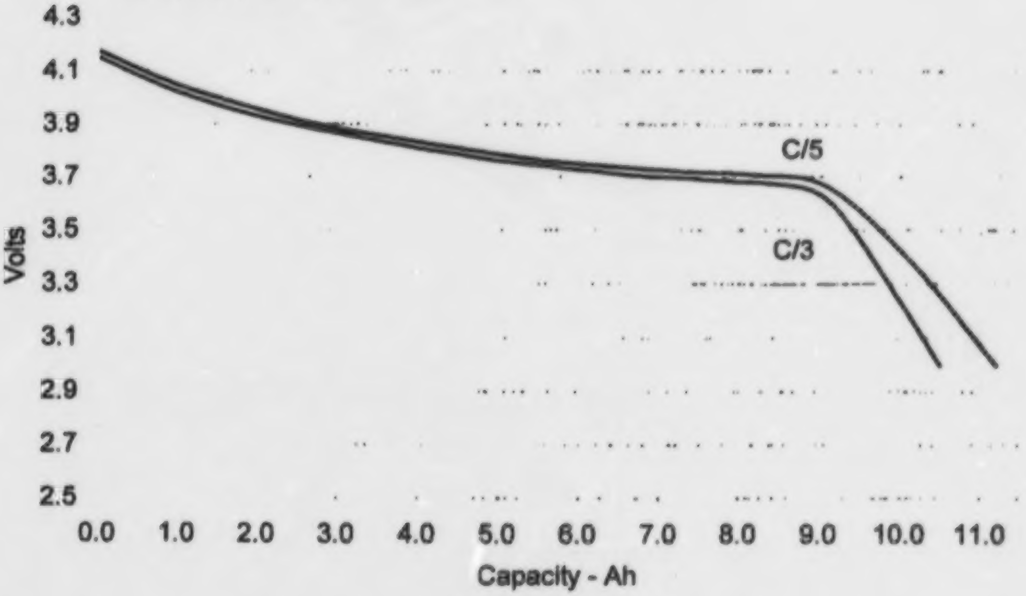

ELECTROFUEL: Discharge Profile

Cell Capacity (nominal): 11,000 mAh

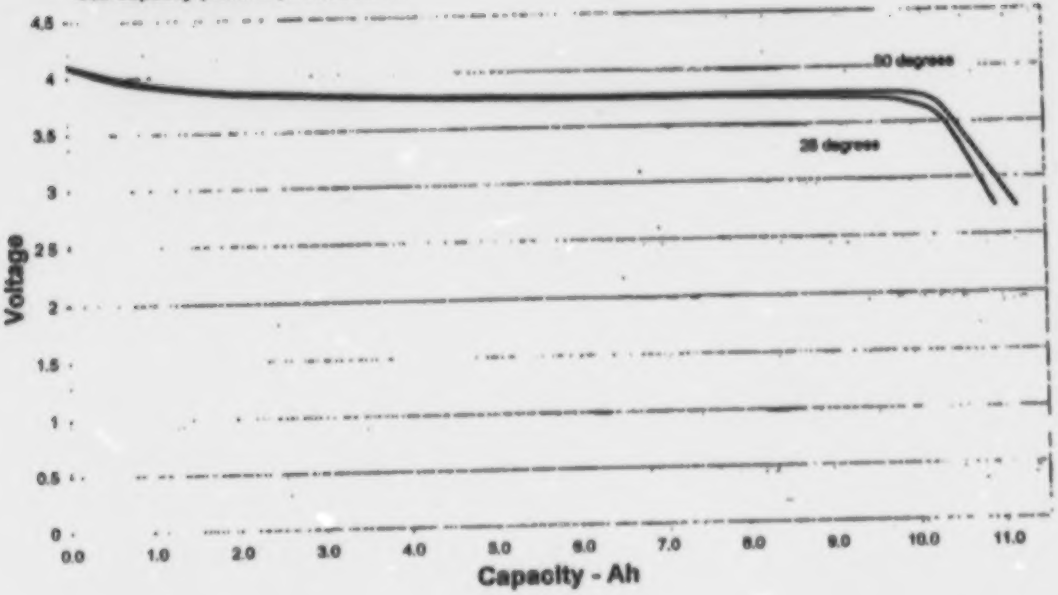

Performance Comparison

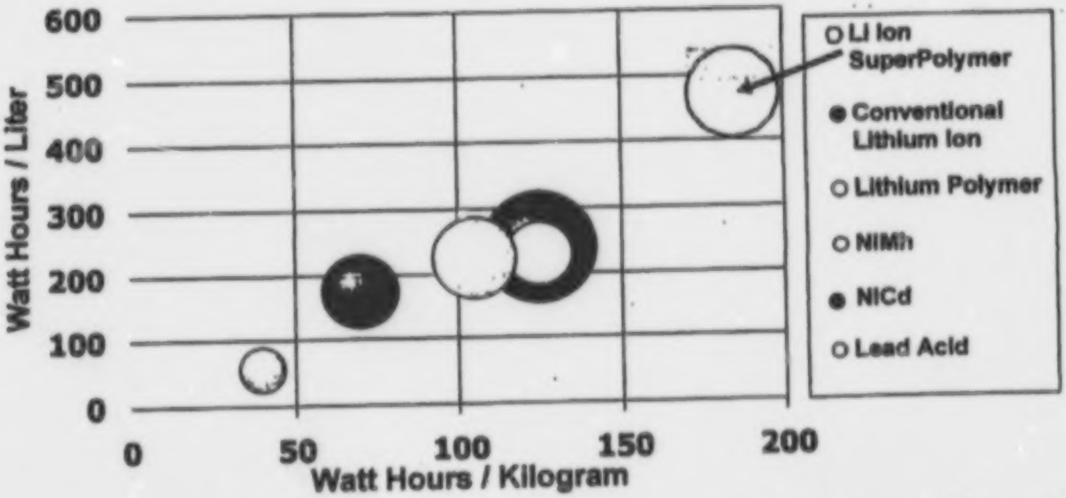

electrofuel

PowerPad™

electrofuel's extended life battery

Capacity:
14.8 V, 11Ah, 160 Wh
Run-time:
Up to 16 hrs from full charge
Ultra-Thin and Compact:
3/8" thin (9.5mm)
by 8.75 x 11.75"
(220 x 295mm)
Lightweight:
approximately 2 pounds
Rugged Design:
Titanium case
Fuel Guage:
5 LED Fuel Guage with low battery alarm alert
Fast Charge:
80% charge in less than 4 hours
Convenient to Use:
Can use portable computer's AC adapter

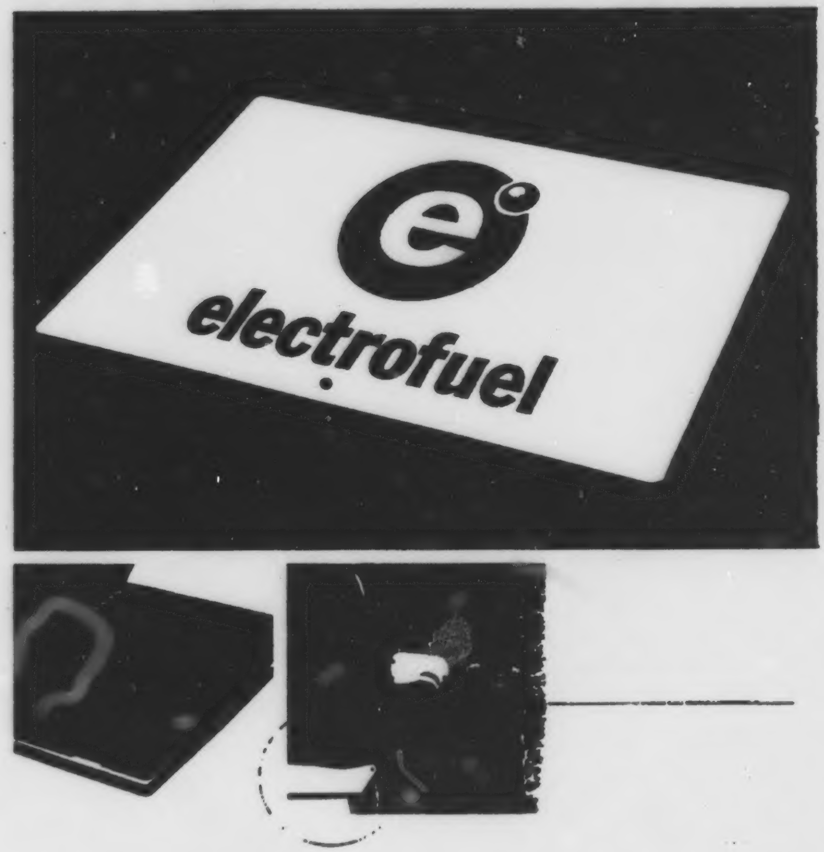

electrofuel

21 Hanna Avenue
Toronto, Ontario
Canada, M6K 1W9
T: 416.535.1114
F: 416.535.2361
E: www.electrofuel.com

[illegible]

PowerPad™

electrofuel's extended life battery

PowerPad 160™ with Electrofuel's Lithium Ion SuperPolymer.

WORLD'S HIGHEST ENERGY DENSITY BATTERY

The ultimate Portable Computer Battery...16 hours of power!... 160 Watt Hours.

Powering the 21st Century

Never be short of energy when you need it most. Order your PowerPad today.

Up to 10 times the run-time for some notebook computers.

In a lightweight and ultra-thin titanium clad pack !

Never worry about running out of battery life for those ....

- Long-haul flights overseas
- Extended presentations with no accessible outlet
- Weekends at the cottage or out in the boat with no power outlets
- Road warriors with no opportunities for recharge during the day

Imagine using your notebook computer for a full day and not having to worry about recharging. This in a light-weight and compact package no larger than a paper notepad. Easily stored away.

The pack is convenient to use with a universal cord with detachable connectors to fit most portable computers.

How can this be possible? Using Electrofuel's patented revolutionary new Lithium Ion SuperPolymer batteries, Electrofuel can deliver double the capacity in a thinner package than conventional lithium ion batteries or up to 5 times that of lead acid batteries. This is the battery technology of the 21st century available now in a titanium, ultra-thin pack.

Be the first to own this new battery technology, which will change the world of portable computing. Why use an internal battery pack, which forces you to choose between inserting your floppy drive or your CD-ROM? Why use an internal battery pack, which only delivers two-hours of run-time or less?

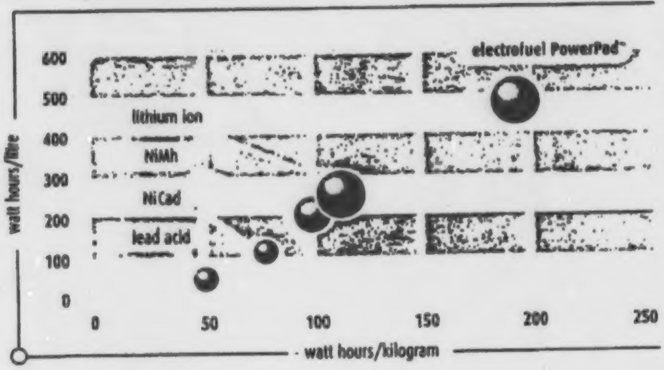

electrofuel

21 Hanna Avenue
Toronto, Ontario
Canada, M6K 1W9
T: 416.535.1114
F: 416.535.2361
E: www.electrofuel.com

[illegible]

electrofuel

Lithium ion super polymer battery

world's highest energy density

Applications:

- Portable
- Personal Digital Assistants
- Electric Vehicles
- Storage Systems
- Medical Devices Aerospace

500Wh/L, 180Wh/kg

- Cellular Phones
- PCS/PHS
- Camcorders
- Load leveling
- Defence
- Power Assisted Bicycles

electrofuel

21 Hanna Avenue
Toronto Ontario
Canada, M6K 1W9
T: 416 535 1114
F: 416.535.2361
E: dmurdoch@electrofuel.com

[illegible]

#511884 ⑩

Is There an Effective and Environmentally Friendly Way to Control Microbiological Contamination in Distillate

by R. D. Haggett

Defence Research Establishment Atlantic, Dockyard Laboratory (Atlantic)
P.O. Box 1012, Dartmouth, Nova Scotia, Canada B2Y 3Z7

ABSTRACT

Defence Research Establishment Atlantic (DREA) has been involved, since 1984, with research into the control and/or elimination of microbiological contamination (MBC) in distillate fuels and fuel systems. The purpose of this research is to determine the most effective and environmentally friendly way to combat MBC. The research included long term laboratory trials to determine the most effective biocide available, the investigation of alternative chemical, mechanical and physical methods of control and the design and development of an innovative flow-through ultrasonic system for the control of microbiological contamination in distillate fuels. All the above control methods will be discussed with particular emphasis on the use of biocides and ultrasonic energy in terms of efficacy and environmental impact.

Is There an Effective and Environmentally Friendly Way to Control Microbiological Contamination in Distillate Fuels?

By

Randall D. Haggett
Defence Research Establishment Atlantic

Introduction

Microbiological contamination in hydrocarbon fuels presents a variety of problems to the operators of land based and marine equipment as well as aircraft. The causative organisms are fungi, yeast and bacteria. Free water must be present in a fuel tank for these organisms to grow and proliferate. When water is present, conditions are favourable for fungal spores (dormant phase) to become viable. The fungi and yeast grow at the fuel/water interface by extracting oxygen from the water and nutrients from the fuel and water layers. The organisms reproduce by cell division creating branching chains (hyphae) which form an interlocking mat at the fuel/water interface. It is this mat which coats fuel tank walls, plugs filters, fouls injectors in diesel engines and causes coking of fuel control nozzles and hot spotting in gas turbine engines. Hot spotting in a gas turbine usually results in catastrophic failure requiring engine replacement. As the organisms grow and reproduce, biosurfactants are produced which reduce the interfacial tension in the fuel and allow water and debris to be suspended in a stable suspension in the fuel layer. This biosurfactant also wets coalescer elements and Teflon coated water separators allowing suspended water and debris to pass through and into the engine.

Defence Research Establishment Atlantic (DREA) has been involved, since 1984, with research into the control and/or elimination of microbiological contamination (MBC) in distillate fuels and fuel systems. The purpose of this research is to determine the most effective and environmentally friendly way to combat MBC. The research included long term laboratory trials to determine the most effective biocide available, the investigation of alternative chemical, mechanical and physical methods of control and the design and development of an innovative flow-through ultrasonic system for the control of microbiological contamination in distillate fuels.

TECHNIQUES FOR THE CONTROL AND/OR ELIMINATE MBC

Limited Effect but Environmentally Friendly

Ultraviolet Treatment

Ultraviolet (UV) treatment can be effective in destroying microorganisms. Wavelengths below 290 nanometers (nm) are usefully antimicrobial with an optimum wavelength being approximately 260 nm. Unfortunately the kill effectiveness is inversely proportional to the distance from the UV source and requires a relatively long exposure time. In addition, the effectiveness of ultraviolet disinfection is greatly reduced (due to absorption and screening effects) in media containing suspended matter. The safety of this method is also a concern. For UV to be effective in a fuel system, the light source must be in the fuel system (inside the fuel tank), or the fuel must pass in close proximity to the UV light. This creates the danger of fire or explosion of fuel or fuel vapours, should the media separating the fuel from the light source be breached. Personnel must be protected from direct exposure to the UV radiation. It has also been noted that UV radiation will excite atoms and may cause chemical reactions, which could affect fuel quality.

Thermal Treatment

Thermal treatment is a technique, which has been proposed for the control of MBC in fuels, lubricating oils and metalworking fluids. The application of heat above the optimum growth temperature can destroy microorganisms. Unfortunately the destruction is not instantaneous, due to difference in heat stability of different microbial populations and the amount of growth present. Although this process may be applicable to lubricating oils and metalworking fluids, the temperatures required for pasteurization and effective kill of microbial growth are too high for most fuels (65°C for 100 seconds).

Again, the primary concern is the increased risk of fire or explosion of fuels or fuel vapours.

Magnetic Treatment

Exposing contaminated fuel to, or passing fuel through, a strong magnetic field is commercially reported to be an effective method of destroying microbial growth. It is claimed that when microorganisms are subjected to a specific magnetic flux field, the ability of the protein channels to maintain the electrical and chemical potential across the cell's membrane is greatly affected and the organism is torn apart and destroyed. The manufacturer claims a kill efficiency of 97.6 percent in one pass. Several commercial units are being marketed in North America and Europe. However, the reported results have yet to be duplicated by a reputable research institution.

Fuel System Design and Maintenance

One of the greatest contributing factors to fuel and fuel system contamination, with microbial growth, is the lack of thought that goes into fuel tank design and construction. Marine fuel tanks are very seldom designed with bottom drains or a stripping system that reaches the tank bottom. Structural members, piping and conduits usually transit marine fuel tank walls. Fuel tanks in commercial vessels are generally not epoxy coated which leads to corrosion problems when water is present. It seems that the location of marine fuel tanks is dictated more by the space available than need for an efficient fuel system.

Some of the more obvious features that must be incorporated into fuel tank design if the effects of microbiological growth are to be minimized are:

(a) The walls and bottoms of storage tanks should slope to give a positive fall to a single low point sump for easy removal of any residual water by either a drain or a suction system.

(b) Marine fuel tanks should have smooth epoxy coated walls free of longitudinal and frame braces. This would prevent the trapping of water in the fuel layer and allow any accumulated water to be removed from the sump.

(c) Fuel tank air vents should be fitted with filters to prevent the ingress of air born organisms.

(d) Fuel tanks should be fitted with floating suction, which would greatly reduce the chances of contaminating the fuel system with bottom debris.

Marine fuel tanks should undergo regular inspections and cleaning if required. The argument often made against this practice is the expense and downtime required. In response to this argument, the expense and downtime incurred for periodic maintenance is minimal compared to the cost of a destroyed gas turbine or diesel engine.

An important part of any maintenance program is the practice of good fuel husbandry. This involves the regular stripping of water bottoms and fuel interfaces as well as regular cleaning of fuel filters, centrifuges, coalescer vessels and delivery lines. The removal of water bottoms is perhaps the single most important factor in the prevention of microbial contamination of fuels. Unfortunately, because of poor tank design it is virtually impossible to remove all water from a system.

Effective but Not Environmentally Friendly

Biocides

There is no doubt that the most effective way to control and/or eliminate microbiological growth in a fuel system is with the use of a biocide or biocidal agent. DREA has evaluated the efficacy of selected biocides and biocidal agents, which were reported in the literature to be the most effective in controlling MBC. These evaluations have shown that biocides containing chlorinated and non-chlorinated isothiazalon-3-one, as the active ingredient, were the most effective in eliminating the mixed populations of organisms commonly found in contaminated distillate fuel. The least effective biocides overall were those which contain organo-borates. These products not only appear to be ineffective against pure and mixed cultures but were found to actually stimulate growth when used in concentrations greater than the recommended dosage.

The primary concerns with the use of any biocide are the environmental effects of the active ingredients when present in discharged water bottoms and the effect on the health of personnel who may come in contact with treated fuel and fuel tank water bottoms.

Effective and Environmentally Friendly

Ultrasonic Energy

Ultrasonic energy has been used for several decades in the medical field for cleaning and sterilizing instruments and for destroying certain types of cells. The cavitation produced by ultrasonic energy can be applied for the destruction of microbial cells. Cavitation occurs when bubbles, created by ultrasonic energy, collapse. The collapse of these bubbles will produce shock waves and turbulence, which causes fractures in the cell walls of microorganisms.

Since 1993 DREA Dockyard Laboratory has been conducting research to development a flow-through system for the ultrasonic destruction of microorganisms in distillate fuels. The work consisted initially of the proof of concept of the process, then the design, development and testing of a full-scale flow through Ultrasonic Fuel Conditioner (UFC).

The UFC being constructed is a four cavitator unit with each cavitator unit made up of 16 stacked piezoceramic rings. Each cavitator has an optimum flow rate of 60 gallons per hour with a power consumption of approximately 500 Watts. Depending on the flow-through volume required the unit could be run with one to four cavitators in place. The frequency which produces the optimum cavitation, resulting in maximum kill rate is 23.5 kHz.

The test results using both water and distillate fuel show that ultrasonic energy does kill some portion of the population of all exposed microorganisms. Although the kill rate was not dramatic (45-70 percent in a single pass with a four second residence time) it was encouraging. Test results indicate that with, more work and refinement, the application of ultrasonic energy has the potential of becoming an environmentally friendly and effective way to control microbiological growth in distillate fuels.

Conclusion

Many methods have been proposed for the control and/or elimination of microbiological contamination in distillate fuels. The use of biocides or biocidal agents is an effective means to control or eliminate MBC in distillate fuels. Unfortunately the use of biocides presents some serious health and safety concerns. The use of UV radiation or the application of heat may have limited success and be environmentally friendly but the safety of these techniques with distillate fuel is an issue. The use of magnetic energy and the practice of good fuel husbandry are both safe and environmentally friendly but the effectiveness of these techniques is either questionable (magnetic treatment) or of limited success (fuel husbandry). The application of ultrasonic energy for the control and/or elimination of microbiological contamination in distillate fuel is not only safe and environmentally friendly but has the potential to be a very effective technique.

DEFENCE R&D DÉFENSE

Is There an Effective and Environmentally Friendly Way to Control Microbiological Contamination in Distillate Fuels?

Randall D. Haggett
Defence Research Establishment Atlantic

National Defence Défense nationale

Canada

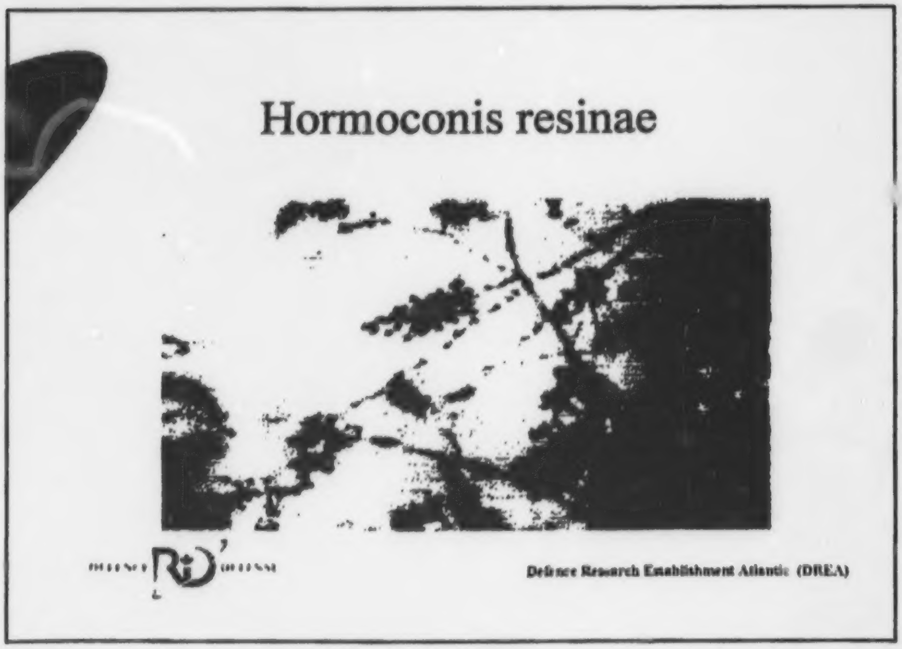

Hormoconis resinae

DEFENCE R&D DÉFENSE

Defence Research Establishment Atlantic (DREA)

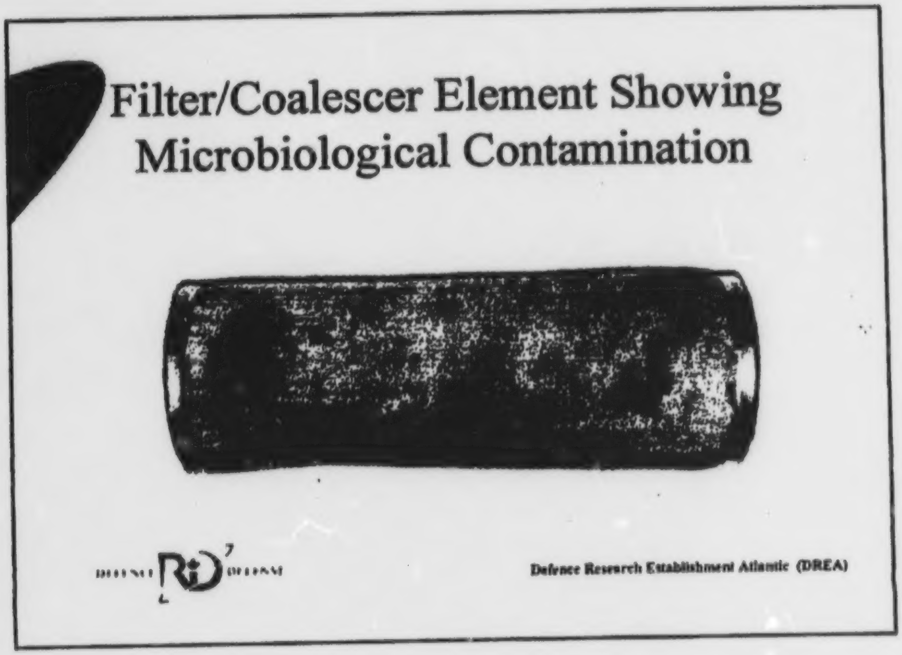

Filter/Coalescer Element Showing Microbiological Contamination

Defence Research Establishment Atlantic (DREA)

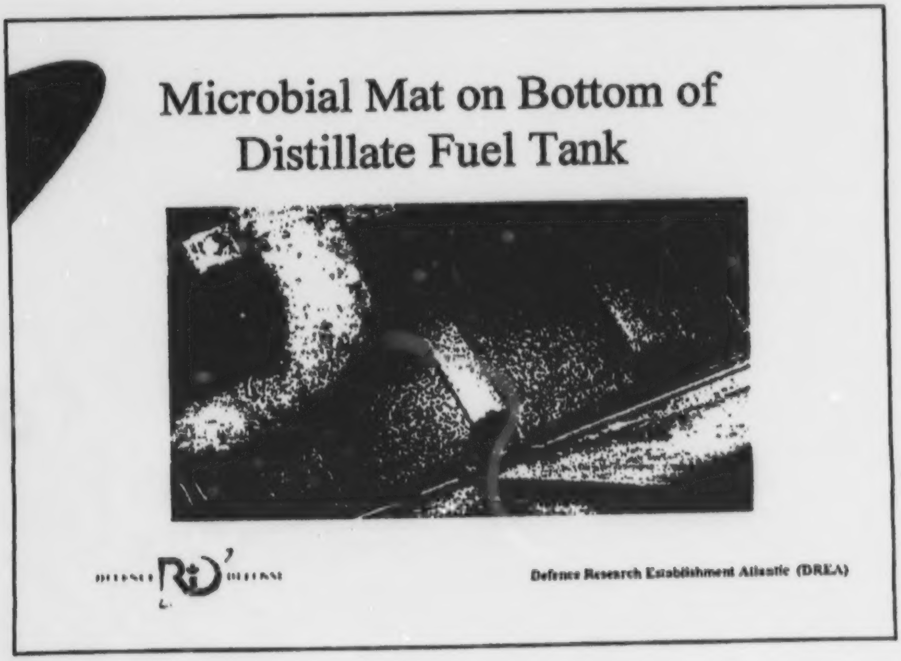

Microbial Mat on Bottom of Distillate Fuel Tank

Defence Research Establishment Atlantic (DREA)

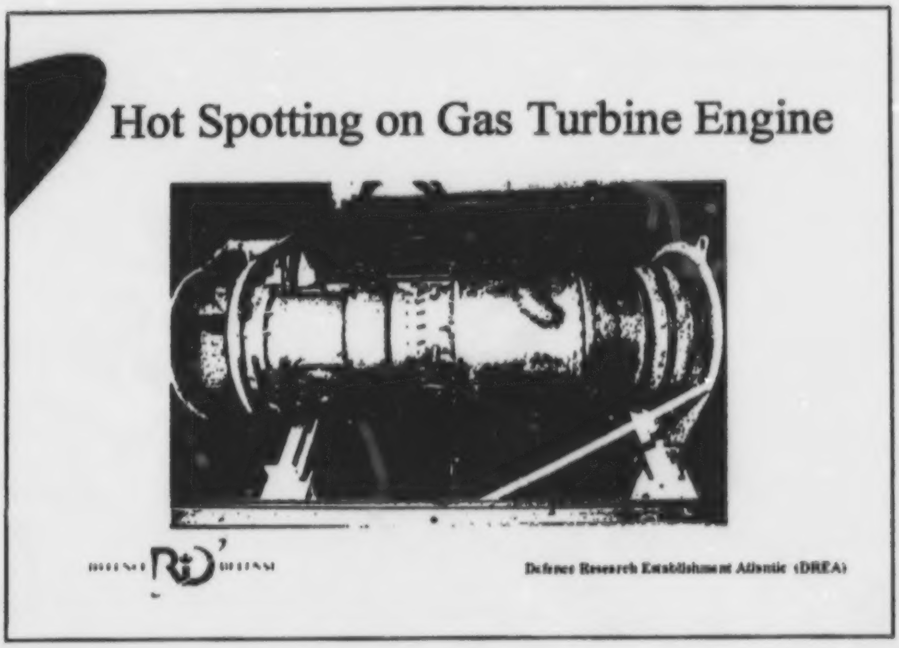

Hot Spotting on Gas Turbine Engine

Defence Research Establishment Atlantic (DREA)

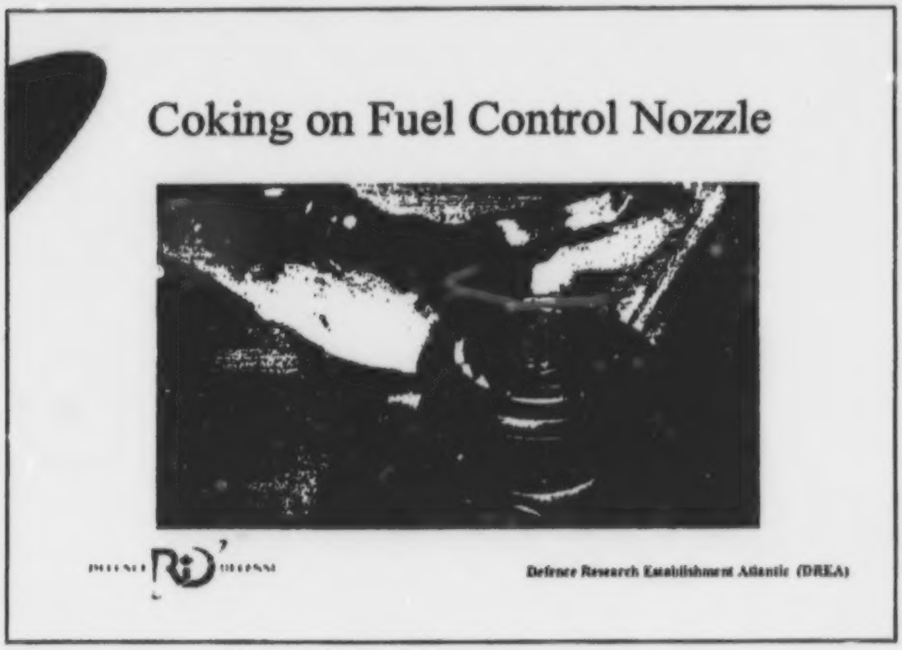

Coking on Fuel Control Nozzle

Defence Research Establishment Atlantic (DREA)

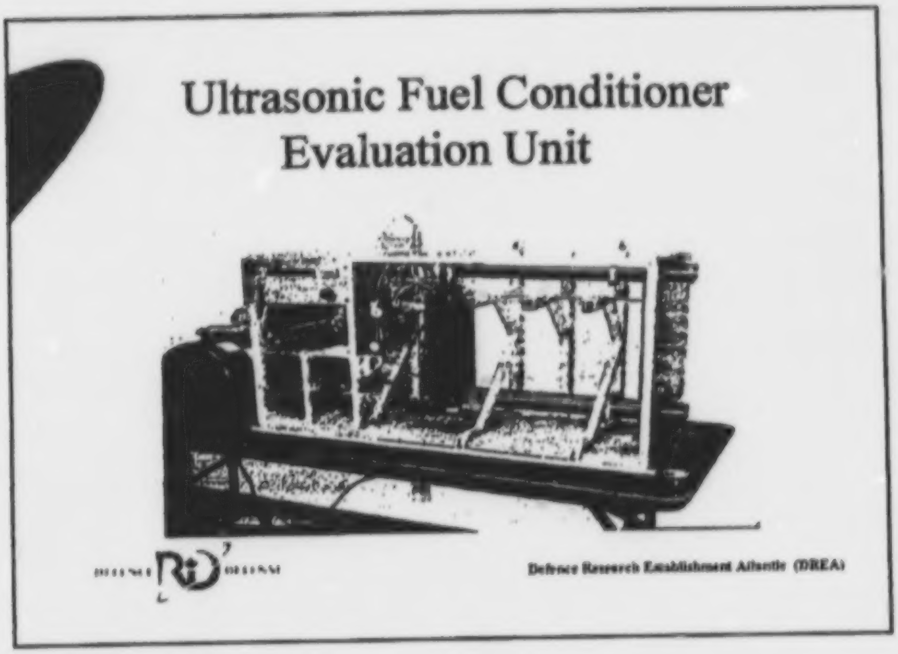

Ultrasonic Fuel Conditioner Evaluation Unit

Defence Research Establishment Atlantic (DREA)

Treatment Methods to Control and/or Eliminate MBC

- Ultraviolet Radiation
- Thermal Treatment
- Magnetic Treatment
- Fuel Husbandry and Fuel Tank Design
- Biocide Treatment
- Ultrasonic Energy

Defence Research Establishment Atlantic (DREA)

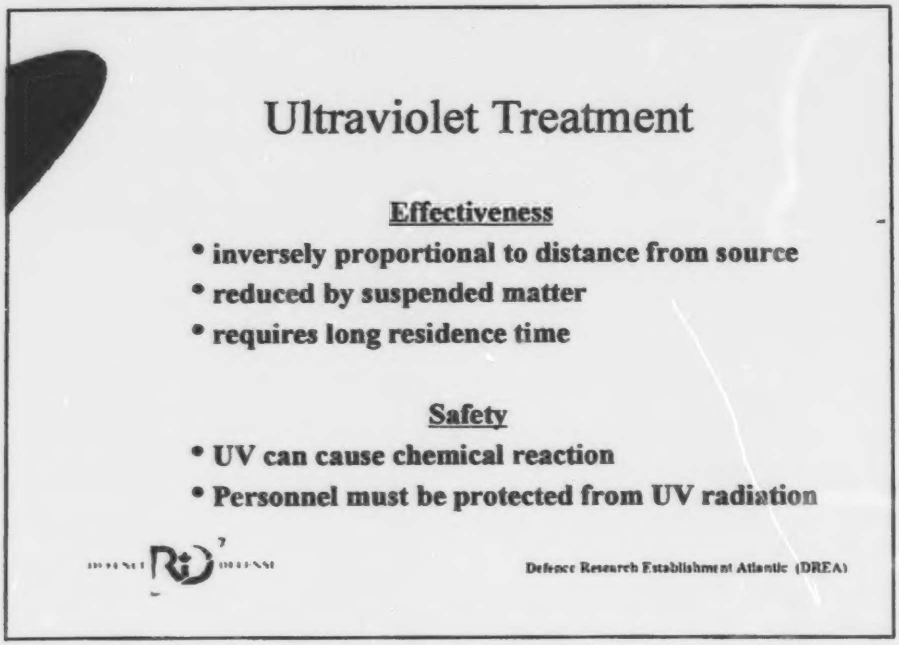

Ultraviolet Treatment

Effectiveness

- inversely proportional to distance from source
- reduced by suspended matter
- requires long residence time

Safety

- UV can cause chemical reaction
- Personnel must be protected from UV radiation

Defence Research Establishment Atlantic (DREA)

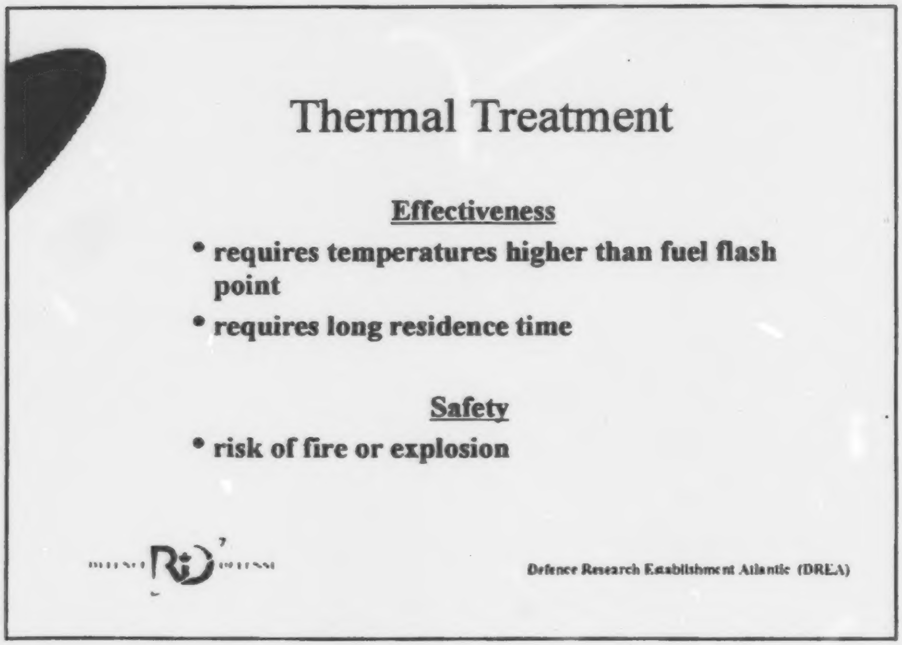

Thermal Treatment

Effectiveness

- requires temperatures higher than fuel flash point
- requires long residence time

Safety

- risk of fire or explosion

Defence Research Establishment Atlantic (DREA)

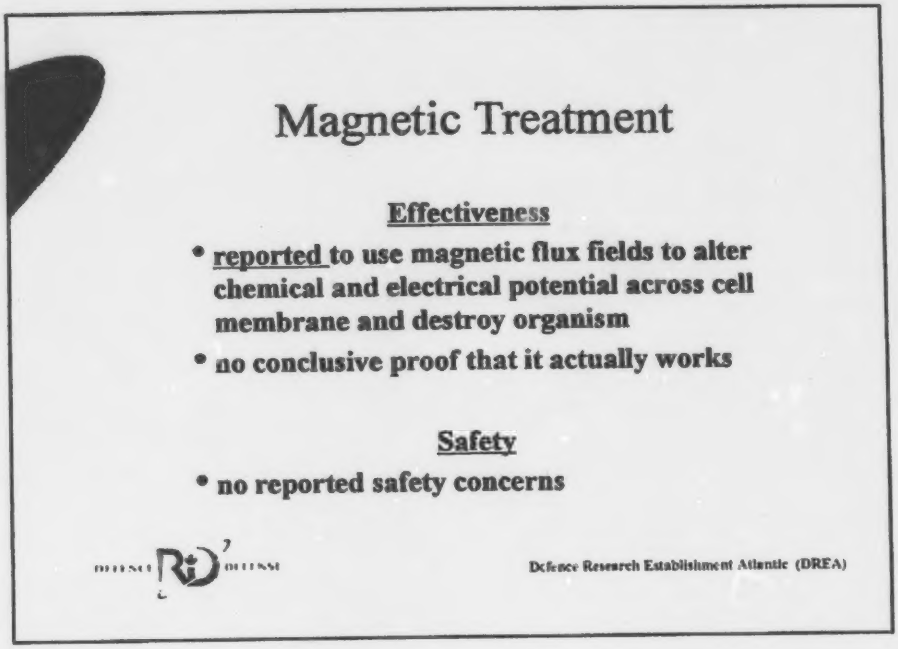

Magnetic Treatment

Effectiveness

- **reported to use magnetic flux fields to alter chemical and electrical potential across cell membrane and destroy organism**
- **no conclusive proof that it actually works**

Safety

- **no reported safety concerns**

Defence Research Establishment Atlantic (DREA)

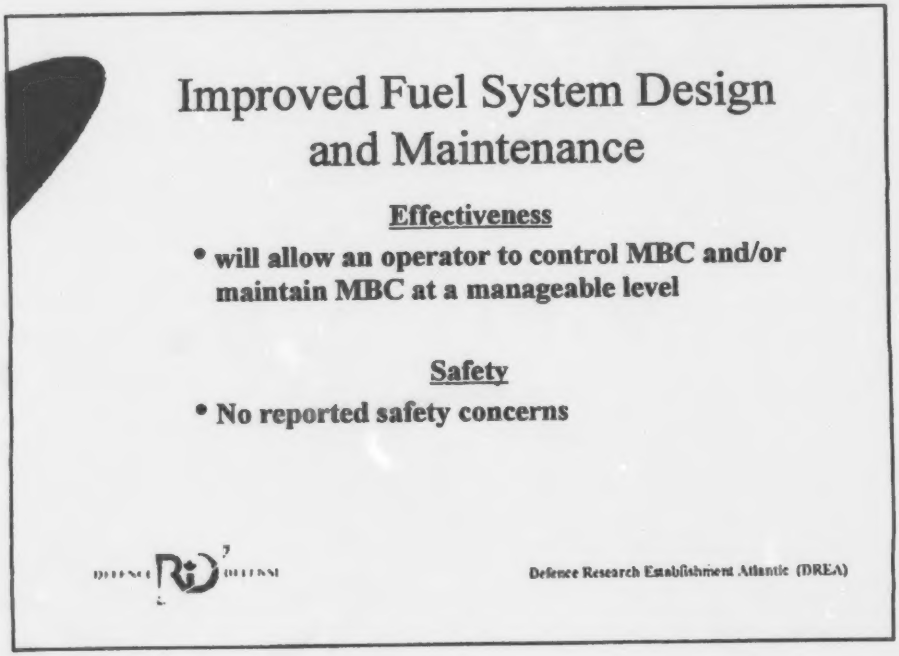

Improved Fuel System Design and Maintenance

Effectiveness

- **will allow an operator to control MBC and/or maintain MBC at a manageable level**

Safety

- **No reported safety concerns**

Defence Research Establishment Atlantic (DREA)

Biocides

Effectiveness

- **most effective way to control/eliminate MBC**
- **partitions in both the fuel and water layer**

Safety

- **untreated water bottoms are toxic to marine organisms**
- **hazard to personnel working with fuel system**

Defence Research Establishment Atlantic (DREA)

Ultrasonic Energy

Effectiveness

- **used for decades in medical field to destroy cells**
- **cavitation fractures cell membrane**

Safety

- **no reported safety concerns**

Defence Research Establishment Atlantic (DREA)

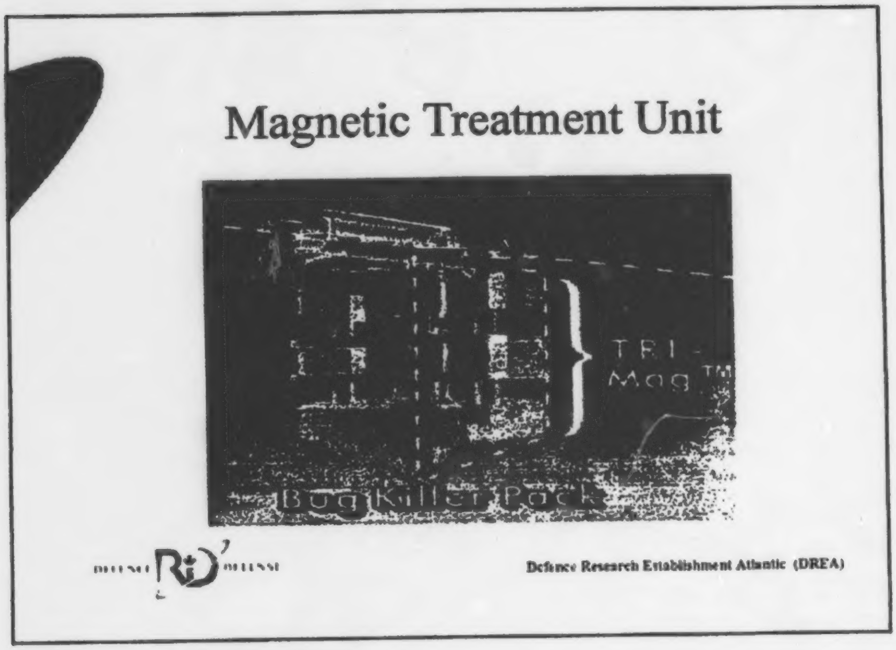

Magnetic Treatment Unit

TRI-
Mag™
Bug Killer Pack

Defence Research Establishment Atlantic (DREA)

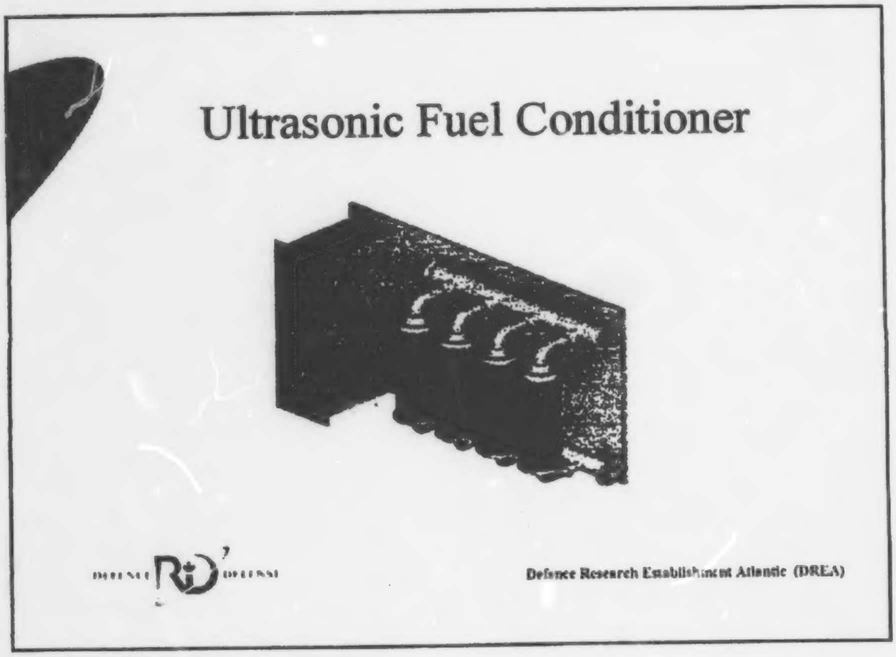

Ultrasonic Fuel Conditioner

Defence Research Establishment Atlantic (DREA)

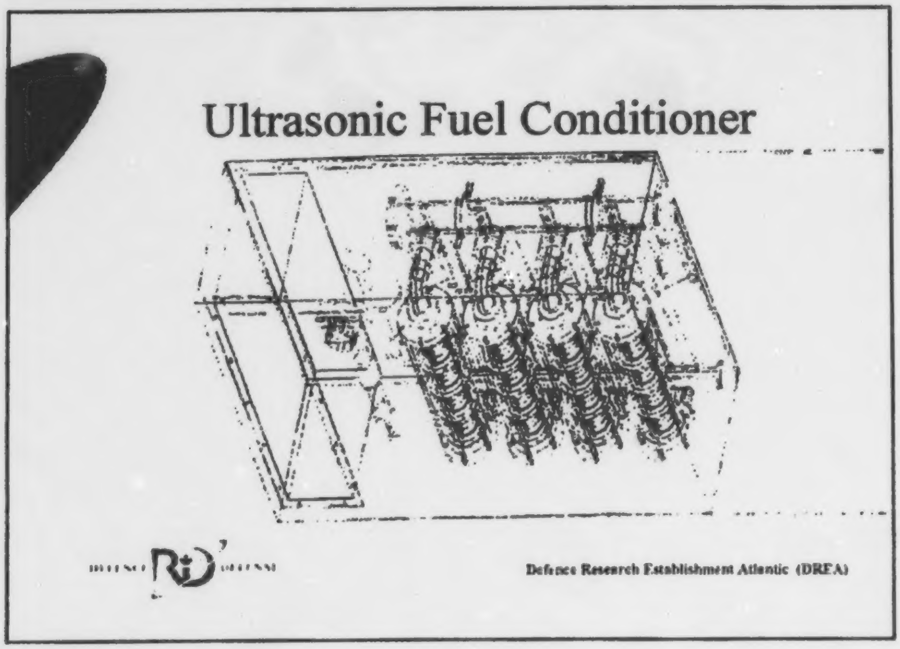

Ultrasonic Fuel Conditioner

DEFENCE DÉFENSE

Defence Research Establishment Atlantic (DREA)

The Defence Research
and Development Branch
provides Science and
Technology leadership
in the advancement and
maintenance of Canada's
defence capabilities.

DEFENCE DÉFENSE

#511885 ⑪

Application of Ultraviolet Spectroscopy for Monitoring Oil in Water

by Clive MacGregor
Seatech Ltd.
and
Dwight Veinot
Defence Research Establishment Atlantic, Dockyard Laboratory (Atlantic)
Dartmouth, Nova Scotia, Canada B2Y 3Z7

ABSTRACT

This paper will discuss the usefulness of ultraviolet spectroscopy for determination of low levels of oil in water. The presentation will include the findings of a laboratory study and relate this work to the use of ultraviolet spectroscopy in the detection of oil in water from oil rig discharges, tanker discharges and oil spills at sea.

The test program was essentially a matrix test where different types of oil (diesel, naval distillate, lubricating oil and hydraulic oil) were mixed at concentrations from 0 to 100 ppm and detected using various wavelengths for ultraviolet absorbance and ultraviolet fluorescence. Limits of detection, linearity, interference, and phase effects (ie. dissolved versus particulate oil) were assessed.

The results indicated that both ultraviolet absorbance and fluorescence could detect oil in water at 1 ppm, though experience indicated that fluorescence was about one order of magnitude more sensitive. The linearity of response was acceptable for both detection methods over the range 0 to 25 ppm. Beyond this range both methods tended to significantly under report the oil present. Interference from bilge cleaners, solids and other chemicals were very pronounced for ultraviolet absorbance, but were almost non existent for ultraviolet fluorescence. These interference results were consistent with previous site experiences testing Oil Detection Monitors on various oil tankers and in other similar applications.

The major problem with all Oil Detection Monitors with regard to calibration was reconfirmed for these detection formats. The response of the detector varies depending on the type of oil present. Thus the calibration of a unit to produce accurate readout of part per million oil in water is very problematic. Experience in the field with existing oil tanker or rig discharges show that where a variety of oils may be present the Oil Detection Monitors are often inaccurate, and generally under report significantly. Thus a simple colorimetric detector tube which could measure total oil in water at part per million levels would be a useful addition to any onboard monitoring equipment. This presentation will conclude with some preliminary results on the development of such a device.

METHODS FOR DIRECT CONTINUOUS MONITORING OF OIL IN DISCHARGED WATERS

1) WHITE LIGHT SCATTERING

-based on scattering by oil droplets of a light beam, measure back scatter or loss of light transmittance.
Advantages: robust, rugged & inexpensive.
Disadvantages: not specific to oil, does not detect dissolved oil, interference from solids in discharge, high error at 15 ppm oil in water.

2) INFRA RED DETECTION

-based on infrared light absorption by C-H bond vibration, thus less IR light transmittance more oil in the water.
Advantages: specific to organics, detects dissolved oil in water
Disadvantages: will detect other organics as oil (eg sewage), some interference from solids but less than white light, limit of detection is approx. 5 ppm or worse, more technically demanding to operate.

3) ULTRAVIOLET DETECTION

-based on either absorption of UV light exciting conjugated double bonds (ie aromatic fraction), or absorbance and fluorescence in the UV from excited conjugated double bonds.
Advantages: more specific to oil, detects dissolved oil in water, low level of detection to 1 ppm or less.
Disadvantages: more expensive and technically demanding to operate, UV absorption affected by additives (eg soaps)

LEGISLATIVE REGIME

International Maritime Organization (IMO) and Canada Shipping Act

Effective July, 1998 new oil in water discharge levels from vessels in coastal waters regulated.
-applies to all oil tankers over 150 GRT & all vessels over 400 GRT
-there are four allowed levels: 5 ppmv in Inland waters
15 ppmv in specified coastal waters
100 ppmv 12 nautical miles
30L/nm 50 nautical miles

-there are two levels of monitors specified, those for 15 ppmv and 5 ppmv (some vessels allowed 15 ppmv discharge will need 5 ppmv monitors)
-the regulation specifies control systems, separation and filtration equipment for any ship discharges.
-specifies records be kept of discharges, maintenance and calibration, and annual steamship inspector inspections.

What determines exceedance of this criteria?

Sample collected and analyzed in a lab, or a visible sheen coming from the suspect vessel with concurrent oil identification (comparison of oil on water sample with samples from suspect vessel). To varying degrees the results from the oil detection monitor will be accepted as proof of compliance (obviously good records of calibration and maintenance, or some independent test would be useful).

OBJECTIVE

Determine the generic capability of Ultraviolet spectroscopy to detect oil in Canadian Naval vessel discharges at levels of 1 ppmv.

White light scattering and Infra Red were eliminated from consideration due to lack of ability to readily detect dissolved oil, the effect of interferences, and insufficiently low level of detection.

A review of the literature indicated that several UV Fluorescence detector systems existed, but there were few scientific evaluations (not including the manufacturer). Several other types of commercial detectors using technologies noted above also existed.

The assessment was designed to test response from lab UV spectrometers for both UV absorption and UV fluorescence. The tests were undertaken on five oils:

Diesel Fuel
Naval Distillate
Diesel Motor Oil
Synthetic Lube Oil
Hydraulic Fluid

Over the range 0 to 100 mg/L.

Note: 0.7 mg/L = 1 ppmv.

UV SPECTRAL ANALYSIS OF THE OILS IN WATER

1) Is there a single wavelength which might be on average be appropriate to use for reliable detection of oil in discharged water ?

2) What was the variation of response with oil type and might there be an average oil mixture to use ?

3) What amount of oil was dissolved in the water, as this is much harder to remove than oil droplets (particulate oil) ?

4) What factors cause interferences in the detection of oil in water ? (Not a topic of this study but reviewed outside this work).

5) What is a reasonable limit of detection based on these laboratory tests and is there linear response around 20 ppmv ?

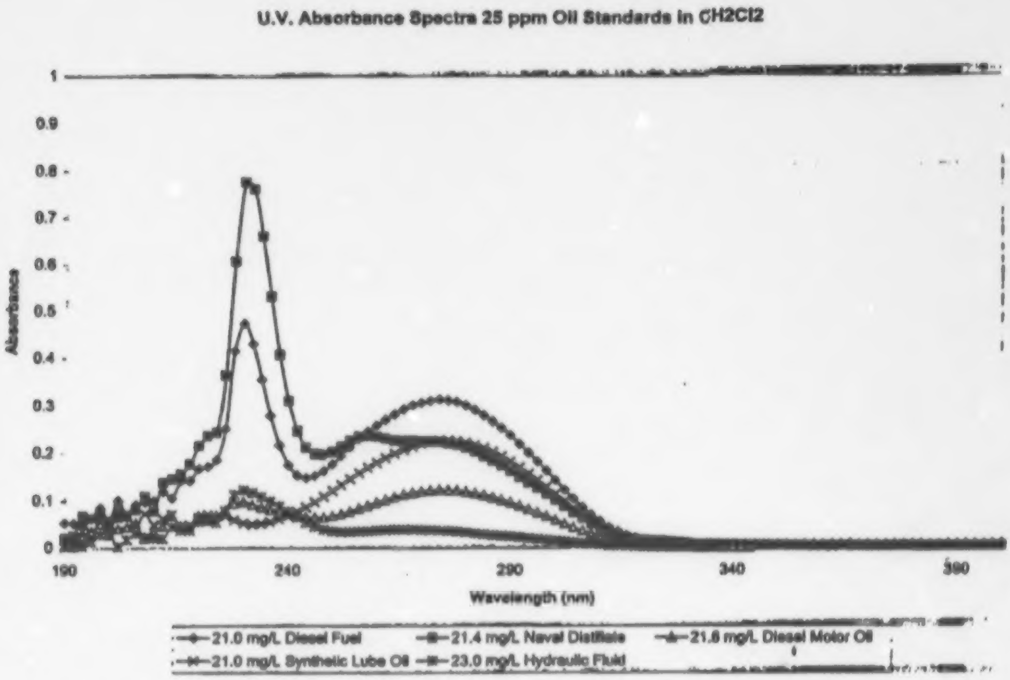

Figure 3.2.1

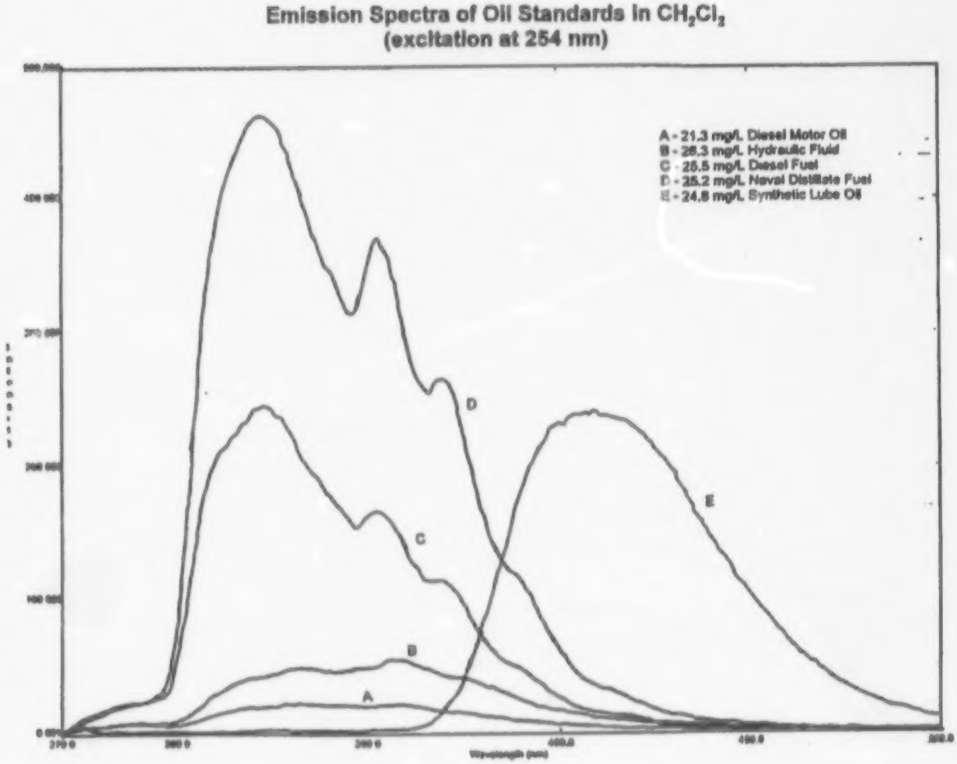

Figure 3.2.2

PERCENT DISSOLVED OIL FOR
OIL AT APPROXIMATELY 20 MG/L

OIL TYPE	PERCENT DISSOLVED
Diesel Fuel	75-80
Diesel Motor Oil	5-15
Hydraulic Fluid	15-60
Naval Distilate	10-70
Synthetic Lube	30-80

Variability caused by effect of different agitation times, and potentially some wall effects.

INTERFERENCES ON UV OIL DETECTION
(Based on literature and other knowledge)

UV ABSORBANCE

-soaps (degreasers) could cause up to 100%+ positive error in determination of oil in discharge water.
-solids (eg rust) caused some positive reading effects.

UV FLUORESCENCE

-soaps and chemicals had little effect on the determination of oil in discharge water.
-solids had very little effect on readings.

LIMIT OF DETECTION AND LINEARITY

Limits of detection were calculated using a twice baseline noise response criteria at 1 to 10 ppmv.

UV ABSORPTION	**1.4 mg/L**	**+-0.7 mg/L**
UV FLUORESCENCE	**0.3 mg/L**	**+-0.13 mg/L**

Note this is laboratory best case, and may not represent field capability

Linearity can best be descibed by a least squares regression calculation R^2 (over the range 0 - 100 mg/L).Better linearity is described by

UV ABSORPTION	**0.58**	**(Hydraulic was 0.01)**
UV FLUORESCENCE	**0.94**	

CONCLUSIONS

1) To ensure there is no discharge above limits there is no simple electronic detection system that will reliably determine mixtures of oil in discharge water.

This fact is not due to lack of capabilities of the detectors but rather the variability of the potential discharge mixtures (ie lubes in with Naval Distillate,etc).

A unit calibrated on Naval Distillate at that wavelength will under report Lubricating oil by over a factor of ten.

These systems work very well in situations where the oil is of one type such as for a production platform on a specific field (eg the Cohasset field off Sable Island).

2) UV Fluorescence is the preferred method for oil detection and is presently in use at many locations, but some of the units used in oil fields offshore may be inappropriate for vessels with a lot of movement. This is because the units use “falling stream detection” to prevent fouling of detector windows. Some other changes to UV Fluorescence specific to the offshore oil production may not be needed or may be counter productive for shipboard use (eg size, falling stream, etc).

3) Electronic units always carry a higher cost of maintenance and calibration and the need for independent checks on performance (lab samples or other test methods).

#511886 (12)

Effect of Particulate Size on Membrane Performance in Bilge Water Treatment Systems

by M. Nottegar and A.Y. Tremblay

University of Ottawa
Department of Chemical Engineering
161 Louis Pasteur St., P.O. Box 450, Station A
Ottawa, Ontario K1N 6N5

ABSTRACT

Environmental regulations now preclude all ships, including naval vessels, from the direct overboard discharge of bilge water, primarily owing to hydrocarbon contamination. Acceptable limits for hydrocarbon contamination levels for overboard discharge in various areas have been established. However, due to the complex composition of bilge water and onboard restrictions, including available space and ship's motion, the identification of purification systems that can produce discharge fluids which meet these new acceptable low limits of contamination is extremely difficult. Many different types of systems have been tried, including coalescers and parallel plate separators, but all have problems purifying the discharge to the new low levels of contamination required. Membrane based systems can surmount these difficulties and provide an effective onboard bilge water treatment system.

A major factor affecting the quality and quantity of a membrane's permeate is the presence of emulsified oil and particulates in bilge water. Specifically, emulsions and particulates in the 0.01 to 0.1 micrometer size range accumulate readily at the surface of the membrane. In this range, particles are too large to back diffuse and too small to be swept away from the surface of the membrane. They accumulate in a layer on the surface of the membrane and greatly reduce its flux. Additionally the type of oil present in the bilge water (that is new versus used oil) can also affect membrane performance. This is related to the difference in the size and quantity of particulate in new and used oils. Used oil often contains particulate originating from oxidized hydrocarbons, carbonaceous debris, and metallic wear particles, etc. which are not likely present in new oils.

This paper will focus on the performance of various membranes in terms of separation and flux as functions of particulate loading in laboratory prepared bilge water mixtures produced using new and used oil as contaminants. The interaction of the membrane material with these different particulate contaminants and the potential effectiveness of membrane system operational parameters, such as backpulsing, to optimize separation, flux and useful lifetime will also be discussed.

Introduction

- Problem Definition
  - Environmental (Oil Discharge) Regulations
  - Shipborne Constraints
  - Bilge Water Composition
- Membrane System
  - Pre & Post Treatment
  - Membrane Selection
  - Membrane Gel Layer & Fouling
  - Effect of Operational Parameters

Problem Definition

- Environmental Regulations
  - Beyond 12 nautical miles - 100 ppm oil
  - Within 12 nautical miles - 15 ppm oil
  - Within Canadian waters - 10 ppm oil
  - Within Internal waters - 5 ppm oil
  - Arctic - 0 ppm oil

While these are the current discharge regulations it is highly preferable for a system to have the possibility of achieving increased discharge limits, due to ever increasing environmental concerns. In this vein, the Canadian Government and the International Maritime Organization (IMO) are currently examining the possibility of increasing these regulations.

One 'easy' method in which a membrane based system, could achieve more stringent discharge limits it to use membranes that have a smaller pore size.

Shipborne Constraints

- Bilge Water Concentration - 16 to 27 X
- Physical Space Constraints
  - 1.7m wide X 1.0m deep X 1.5m high
- System Automation
- Bilge Water composition will vary

An average daily bilge water production for Canadian warships – IROQUOIS and HALIFAX Classes – is approximately 3 tonnes per day. Based on this quantity a concentration approaching 30X is a minimum requirement.

The physical constraints on a ship are obvious; these particular constraints are to allow installation into the footprint of the current Oily Water Separator (SAREX Coalescer) system.

Another obvious shipborne constraint is automation. Bilge water treatment is at best a secondary requirement and therefore cannot unduly task engineering personnel.

Bilge Water Composition

- Total Oils and Greases - 2000 ppm
  - Fuel Oil - 1000 ppm
  - Lubricating Oil (New or Used) - 800 ppm
  - Hydraulic Oil - 200 ppm
- Total Suspended Solids - 500 ppm
- Total Dissolved Solids - 18 000 ppm
- Detergents - 500 ppm
- Remainder is Fresh & Sea Water

In accordance with NETE Study IT1082 – Bilge Water Characterization Study and Bilge Fluid Production Estimates - bilge water contains, on average approximately 1300 ppm oil and grease. However, this quantity can vary widely – bilge waters can contain up to 10,000 ppm oil and grease.

New vs. Used Lubricating Oil

- Approximately equal particulate size distribution
- Oxidation of Used Lubricating Oil
- Stronger Emulsion with the Used Lubricating Oil

An analysis of new and used naval diesel lubricating oil revealed a virtually identical particle size distribution. However, there exists a very real difference between the two lubricating oils. An obvious difference stems from the extreme conditions used lubricating oil has experienced. This appears to be manifested in used lubricating oil since it created a more stable oil emulsion than the new lubricating oil.

Membrane Pre & Post Treatment

- Pre Treatment:
  - Coarse Filtration
  - Hydrocyclone
  - MF Coalescence
- Post Treatment:
  - Adsorption

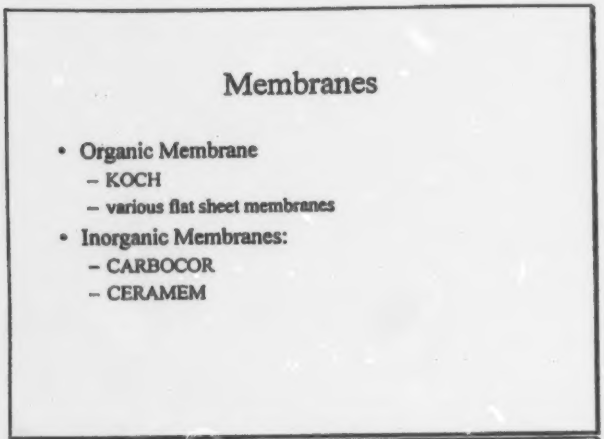

Membranes

- Organic Membrane
  - KOCH
  - various flat sheet membranes
- Inorganic Membranes:
  - CARBOCOR
  - CERAMEM

KOCH: Fabricated from polyacrylo nitrile (PAN) polymer. It has a molecular weight cut-off of 50,000 Daltons, which relates to a nominal pore size of roughly 0.003 microns.

CARBOCOR: Fabricated from a carbon-graphite composite material. It has a nominal pore size of 0.05 microns.

CERAMEM: A ceramic (silica) membrane. It has a nominal pore size of 0.005 microns.

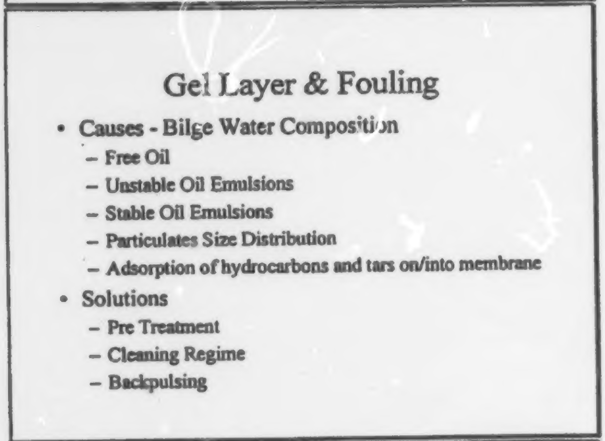

Gel Layer & Fouling

- Causes - Bilge Water Composition
  - Free Oil
  - Unstable Oil Emulsions
  - Stable Oil Emulsions
  - Particulates Size Distribution
  - Adsorption of hydrocarbons and tars on/into membrane
- Solutions
  - Pre Treatment
  - Cleaning Regime
  - Backpulsing

The oils found in the bilge water can be present either as a free oil or as an emulsion – stable and/or unstable emulsion. The free oil and unstable emulsion can be fairly easily separated from the bilge water. Therefore, to be effective, a membrane must be able to treat stable oil-water emulsions.

The following two pictures depict the emulsions created by new and used lubricating oil found in bilge water.

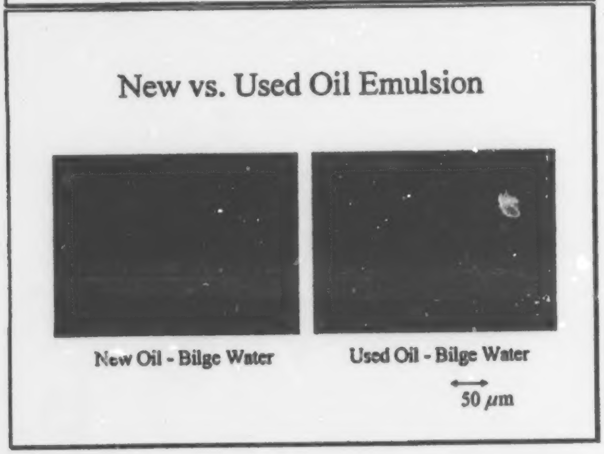

New vs. Used Oil Emulsion

New Oil - Bilge Water

Used Oil - Bilge Water

The oil-water emulsion created with 'New' bilge water is a simple oil/water emulsion. Accordingly, the specific density difference between the water and oil emulsion is quite distinct.

The oil-water emulsion created with 'Used' bilge water is a more complex water in oil in water emulsion. This causes the specific gravity differential between the water and the oil emulsion to be reduced – hence it produces an emulsion which is more difficult to separate. Additionally, this emulsion appears to be more turbid – i.e. a more stable emulsion.

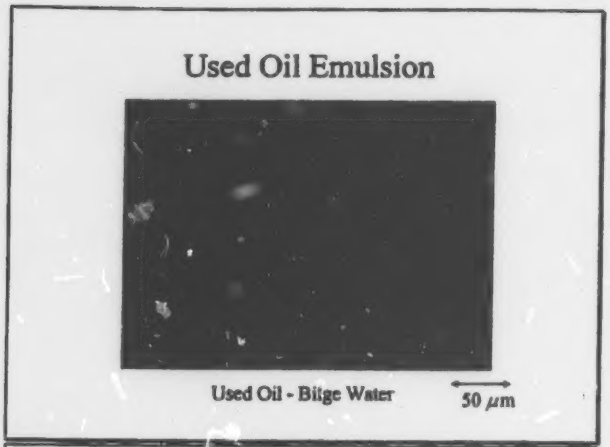

Used Oil Emulsion

Used Oil - Bilge Water

Another picture of the 'used' bilge water oil emulsion.

In this picture the water in oil in water nature of the emulsion is very apparent.

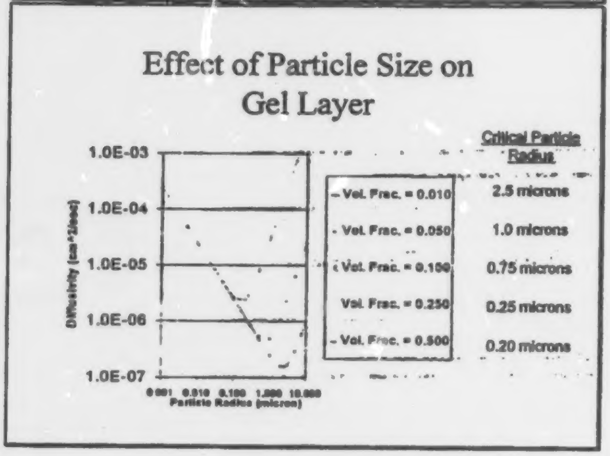

Effect of Particle Size on Gel Layer

	Critical Particle Radius
Vol. Frac. = 0.010	2.5 microns
Vol. Frac. = 0.050	1.0 microns
Vol. Frac. = 0.100	0.75 microns
Vol. Frac. = 0.250	0.25 microns
Vol. Frac. = 0.500	0.20 microns

In membrane applications a particulate 'gel' layer forms on the membrane surface. This 'gel' layer acts as an additional filter.

This graph depicts the relationship between the oil content (volumetric fraction) in the bilge water near the surface of the membrane and the critical oil emulsion (particle) radius. This critical radius is the size of oil emulsions which would form the 'gel' layer.

Noting these critical radii and the nominal pore sizes of the membranes it can be seen that membrane pore plugging is unlikely to result.

Operational Parameters

- Pressure
- Cross-flow velocity
- Backpulsing
- Composition
- Temperature

The following operational parameters were examined for their effects on permeate quantity and quality.

Membrane theory predicts that initially permeate flux is linearly dependent on pressure. However, a point exists where the flux becomes pressure independent – due to gel polarization. As pressure is increased the permeate quality should also decrease.

Permeate flux is dependent upon cross-flow velocity. However, its effect varies depending upon laminar or turbulent flow. An increase in cross-flow velocity should result in an increase in permeate flux, but a decrease in quality.

Backpulsing – reversing permeate (clean water) flow at higher than normal system pressure – allows for the gel layer to be lifted off the membrane surface. It is expected that this would increase permeate flux and decrease quality.

The composition of the bilge water – composed of new or used lube oil – results in a difference in permeate flux and quality.

Temperature is well documented to increase permeate flux by approximately 3% per degree Celsius.

Results

- Effect of Pressure
- Effect of Cross-Flow Velocity
- Effect of Backpulsing
- Composition: New vs. Used Lubricating Oil

Effect of Pressure
CARBOCOR Membrane

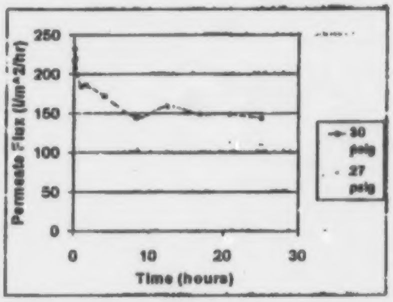

Bilge Water composed of used lube oil
Backpulsing: 5 seconds every 2 minutes

The effect of pressure is shown to be quite important – a 3 psi increase resulted in an increased flux of 40-50%. However, this increased flux was achieved with a noticeable, but not great, degradation in permeate quality.

For the pressure range tested (10-32 psi) the membrane showed no sign of entering into the pressure independent region.

Effect of Cross-Flow Velocity
CERAMEM Module

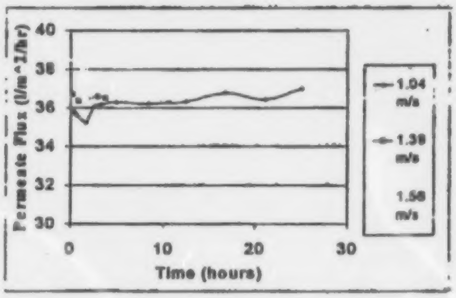

Bilge Water composed of new lube oil
Operating Pressure = 30 psig

This and the following chart show that the cross-flow velocity has little impact on flux. However, increasing the cross-flow velocity did have a very significant negative impact on permeate quality.

Effect of Cross-Flow Velocity
KOCH Membrane

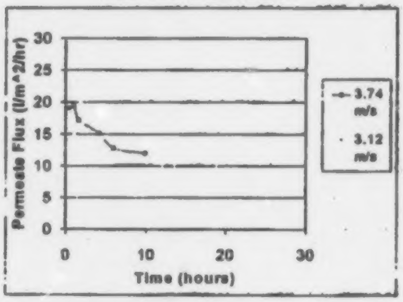

Bilge Water composed of used lube oil
Operating Pressure = 30 psig

Effect of Backpulsing
CERAMEM Module

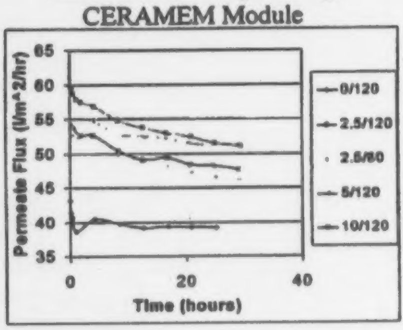

Bilge Water composed of new lube oil
Operating Pressure = 32 psig

As seen from the accompanying chart utilizing backpulsing results in a substantial flux improvement – 20 to 40%. Surprisingly, this increased flux was accompanied by little, if any, degradation in permeate quality.

Effect of Composition
KOCH M-100 Flatsheet Membrane

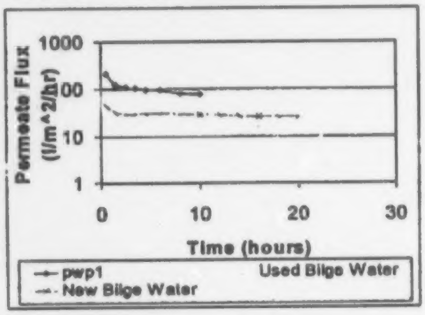

MWCO of Membrane = 30,000 Daltons

Early testing was conducted with flatsheet or membrane coupons. These early tests revealed differences in fluxes when treating bilge water comprised of new or used lubricating oil – with the flux of 'used' bilge water being lower than the 'new' bilge water.

Note: Tests with the membrane modules revealed that this flux degradation did not occur with the inorganic membranes.

Notes

- Fouling & subsequent cleaning requirements for organic (KOCH) membrane
- Membrane surface area
  - CERAMEM > KOCH > CARBOCOR

Organic membranes are much more susceptible to fouling than inorganic membranes and their subsequent cleaning is more cumbersome.

Membrane surface area is critical when designing membrane systems as experimental / pilot plant fluxes are expressed in volume per area per time. Scaling membrane requirements to actual system needs requires determining the overall quantity of permeate needed and then dividing the membrane flux rate into this requirement to determine the number of membranes needed. Accordingly the fact that the CERAMEM module has the greatest surface area per volume is important for optimizing space requirements - a very important shipborne variable.

CONCLUSIONS

- Membrane based systems offer a good solution to the Navy's bilge water treatment problem.
- Operators must become familiar with the effects of operational parameters.
- Bilge water composition is very important. Particularly the variance in lubricating oils.
- Membranes will foul (espically inorganic). Accordingly cleaning regime is critical.
- Membrane selection is important.

#511887 ⑬

Mineralogical Characterization of Airborne Industrial Pollutants

by Gary Fisher

Defence Research Establishment Atlantic, Dockyard Laboratory (Atlantic)
P.O. Box 99000, Stn Forces, Halifax, Nova Scotia, Canada B3K 5X5

ABSTRACT

Increased awareness of environmental and health-related issues has lead to heightened concern about air quality in industrial and office settings. Often the airborne pollutants that cause personnel complaints of eye, nose and throat irritation are inorganic particulates released by industrial processes, dirty or inadequate ventilation systems, or poor housecleaning practices. Identification of these particulates and their source is a necessary first step to improving industrial air quality. However, due to the small quantities of airborne material available in even the dirtiest of samples, standard analytical techniques are not practical for such identification. This paper describes the use of transmission polarized light microscopy, both alone and in conjunction with scanning electron microscopy/energy dispersive x-ray microanalysis, as a means of identifying airborne inorganic particulates at the picogram level.

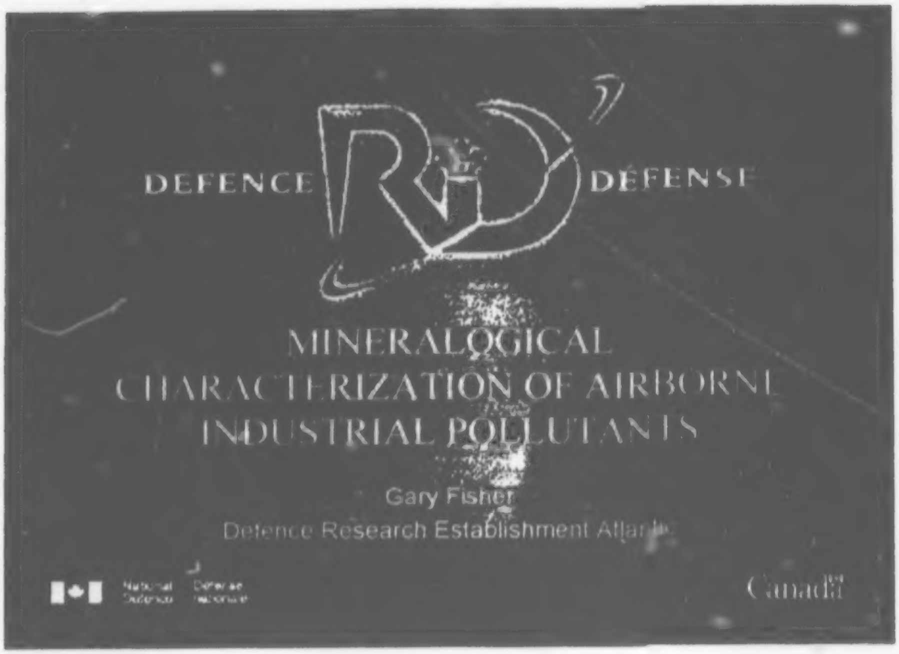

DEFENCE DÉFENSE

MINERALOGICAL CHARACTERIZATION OF AIRBORNE INDUSTRIAL POLLUTANTS

Gary Fisher

Defence Research Establishment Atlantic

National Defence Défense nationale

Canada

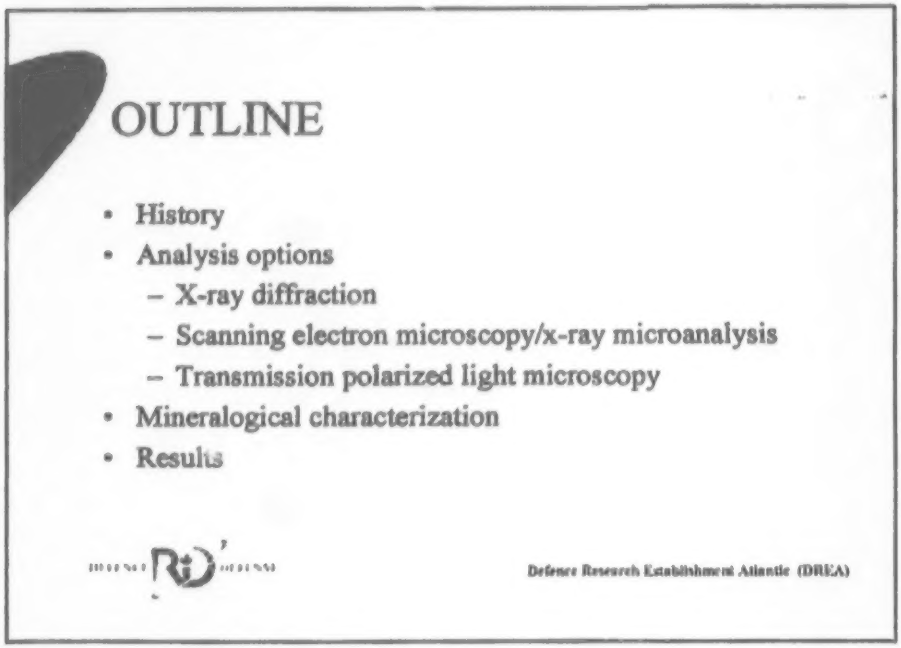

OUTLINE

- History
- Analysis options
  - X-ray diffraction
  - Scanning electron microscopy/x-ray microanalysis
  - Transmission polarized light microscopy
- Mineralogical characterization
- Results

Defence Research Establishment Atlantic (DREA)

HISTORY

- Industry/government respond to health & safety and political issues of the day
- 1970's - reduction in use of toxic industrial materials
  - asbestos, lead, PCBs
- 1980's - global environment
  - recycling, eco-products, spill prevention
- 1990's - personal working environment
  - ventilation issues, fugitive emissions, allergens, individual sensitivities

Defence Research Establishment Atlantic (DREA)

HISTORY

- Increase in general health complaints
  - eye/nose/throat irritations
  - headaches
  - nausea/drowsiness/general malaise
  - transitory

Defence Research Establishment Atlantic (DREA)

HISTORY

- Air quality issues
  - fumes, fugitive emissions, particulates
- Airborne particulate content is recognized as a health & safety issue
  - 50 μg/m³ particles < 10 μm proposed limit

Defence Research Establishment Atlantic (DREA)

ANALYSIS OPTIONS

- Require a technique able to identify airborne particulates
  - Natural:
    - minerals, pollen, plant fibers
  - Synthetic:
    - fibers, soot (fly ash), minerals

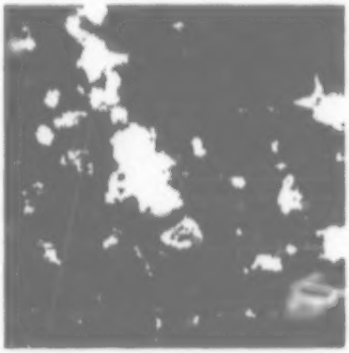

Defence Research Establishment Atlantic (DREA)

ANALYSIS OPTIONS

- X-ray diffraction
  - identify crystallographic species
  - problems with polymers and natural materials
  - insensitive: 5% detection limit
- Microscopic technique
  - Scanning electron microscopy/energy dispersive x-ray microanalysis (SEM/EDX)
  - Transmission polarized light microscopy

SEM/EDX

- Superior resolving power and depth of focus
- Non-conductive samples problematic
- No colour

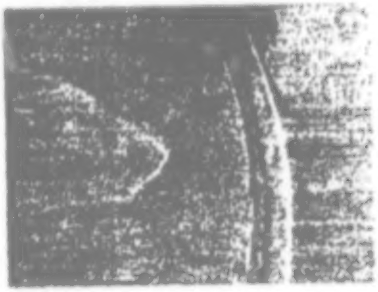

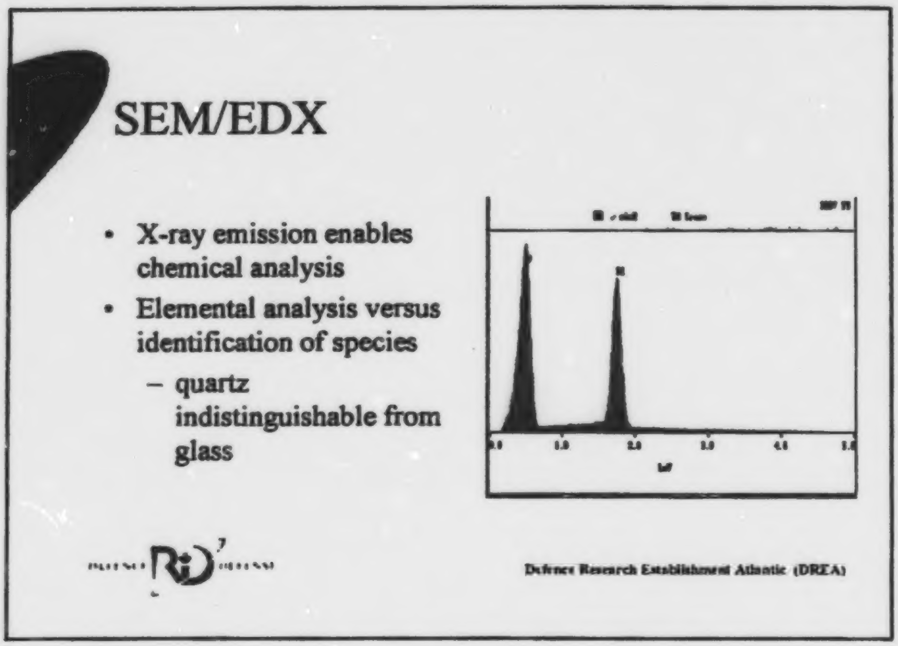

SEM/EDX

- X-ray emission enables chemical analysis
- Elemental analysis versus identification of species
  - quartz indistinguishable from glass

Defence Research Establishment Atlantic (DREA)

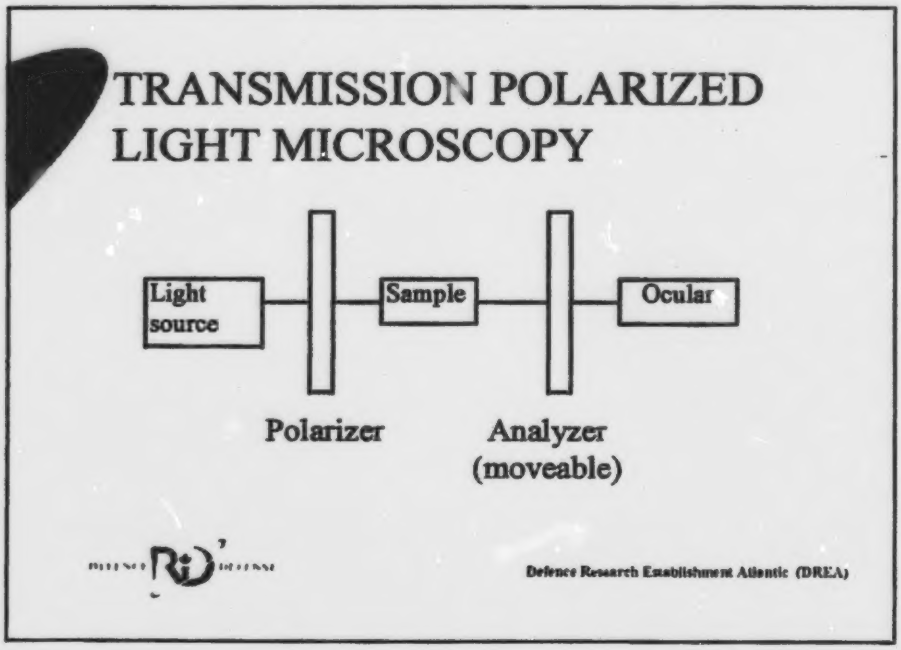

TRANSMISSION POLARIZED LIGHT MICROSCOPY

Light source
Sample
Ocular
Polarizer
Analyzer (moveable)

Defence Research Establishment Atlantic (DREA)

F3

TRANSMISSION POLARIZED LIGHT MICROSCOPY

Sample Preparation

- Examined using stereomicroscope to select particle types and/or representative sample
- Sieved and/or crushed
- Sample mounted in refractive index fluid, $n_D = 1.550$
- Examined at low magnification (10X objective) to determine particle types

Defence Research Establishment Atlantic (DREA)

POLARIZED VS. UNPOLARIZED

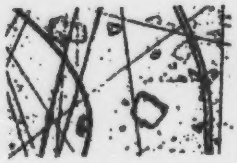

Unpolarized

Polarized

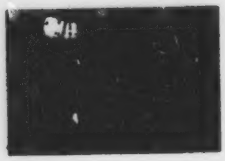

Crossed polars

Defence Research Establishment Atlantic (DREA)

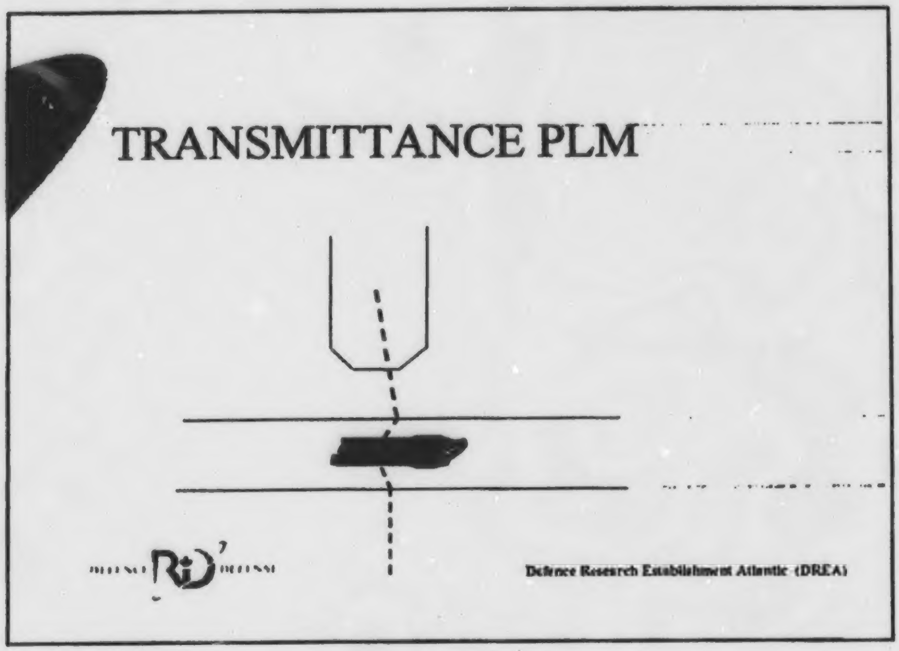

TRANSMITTANCE PLM

Defence Research Establishment Atlantic (DREA)

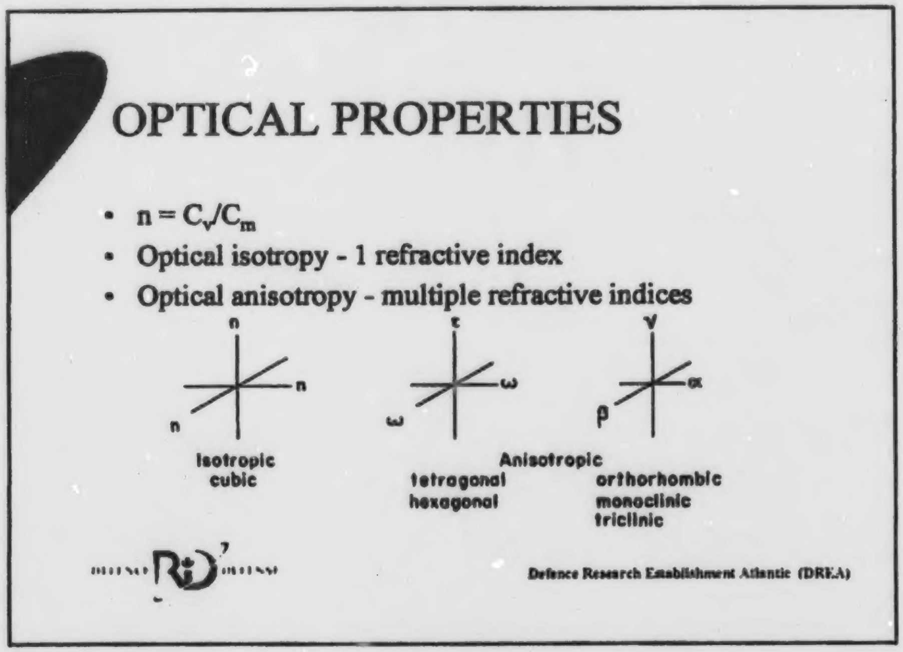

OPTICAL PROPERTIES

- $n = C_v/C_m$
- Optical isotropy - 1 refractive index
- Optical anisotropy - multiple refractive indices

Isotropic
cubic

Anisotropic
tetragonal
hexagonal

orthorhombic
monoclinic
triclinic

Defence Research Establishment Atlantic (DREA)

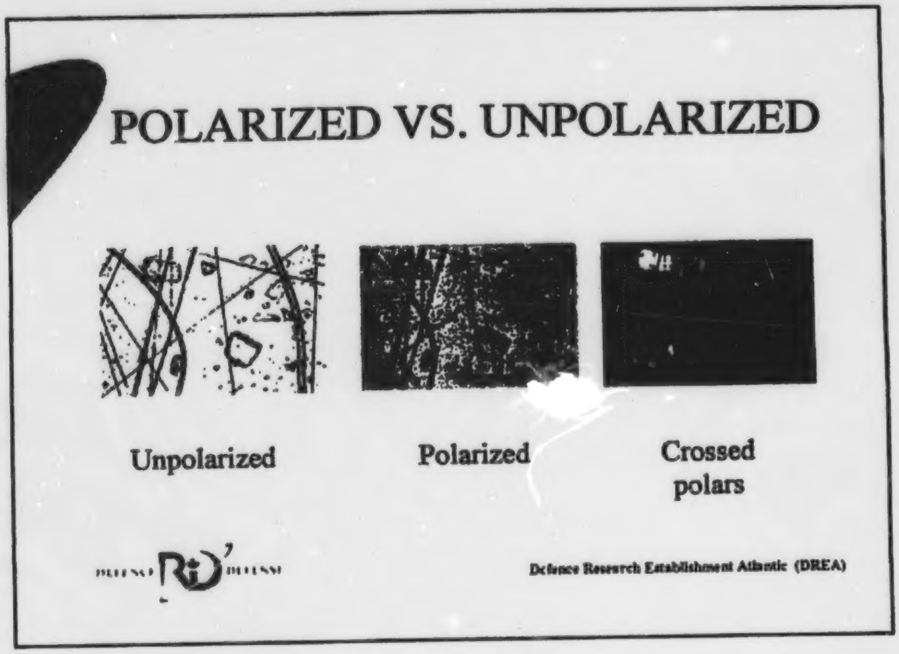

POLARIZED VS. UNPOLARIZED

Unpolarized

Polarized

Crossed polars

Defence Research Establishment Atlantic (DREA)

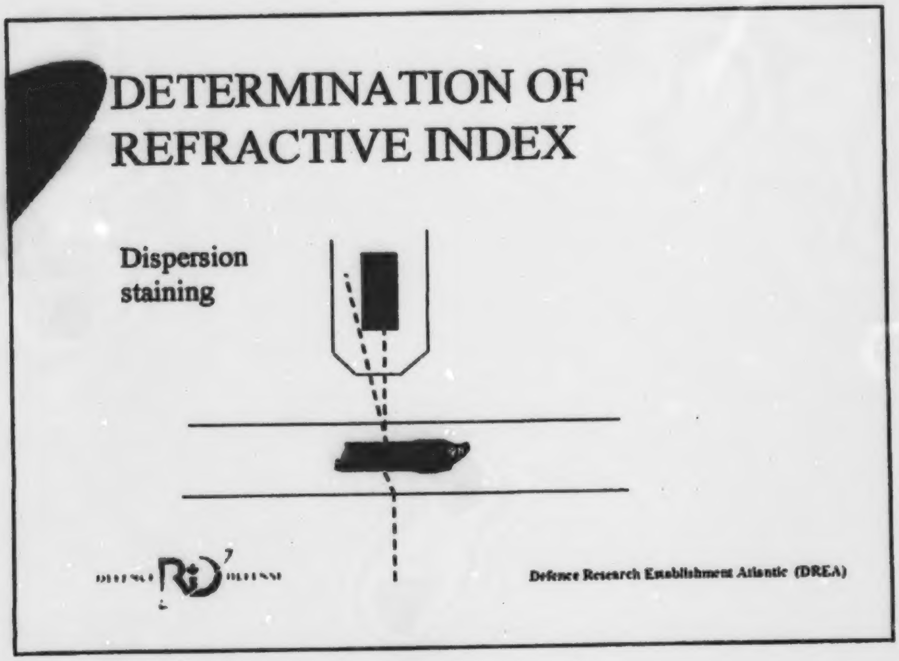

DETERMINATION OF REFRACTIVE INDEX

Dispersion staining

Defence Research Establishment Atlantic (DREA)

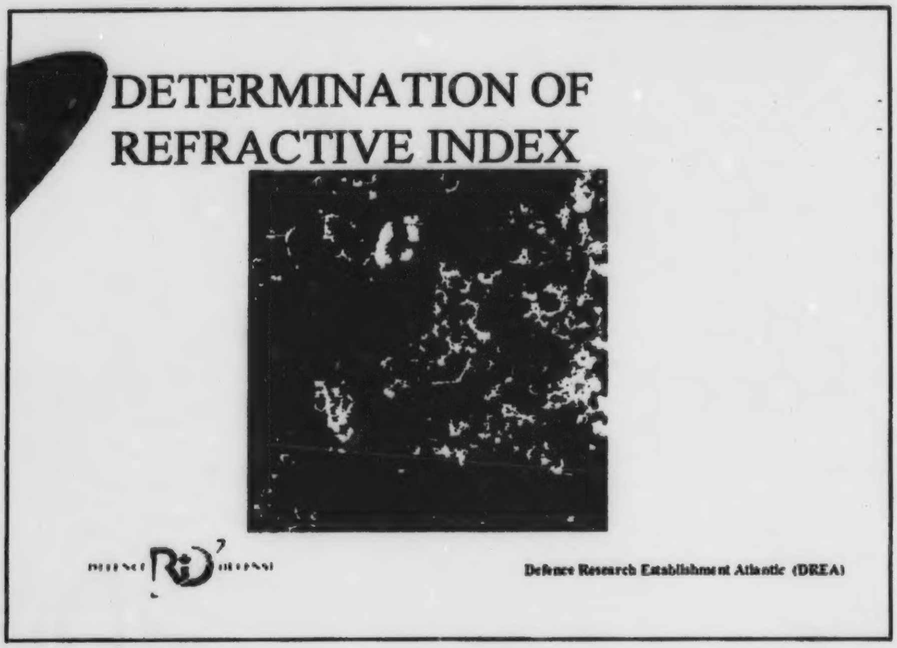

DETERMINATION OF REFRACTIVE INDEX

Defence Research Establishment Atlantic (DREA)

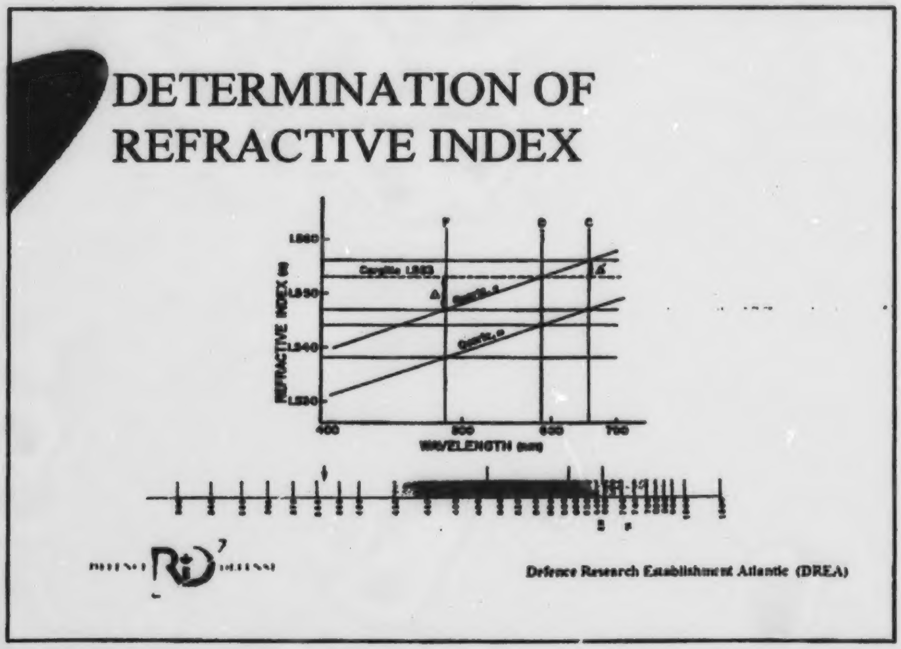

DETERMINATION OF REFRACTIVE INDEX

Defence Research Establishment Atlantic (DREA)

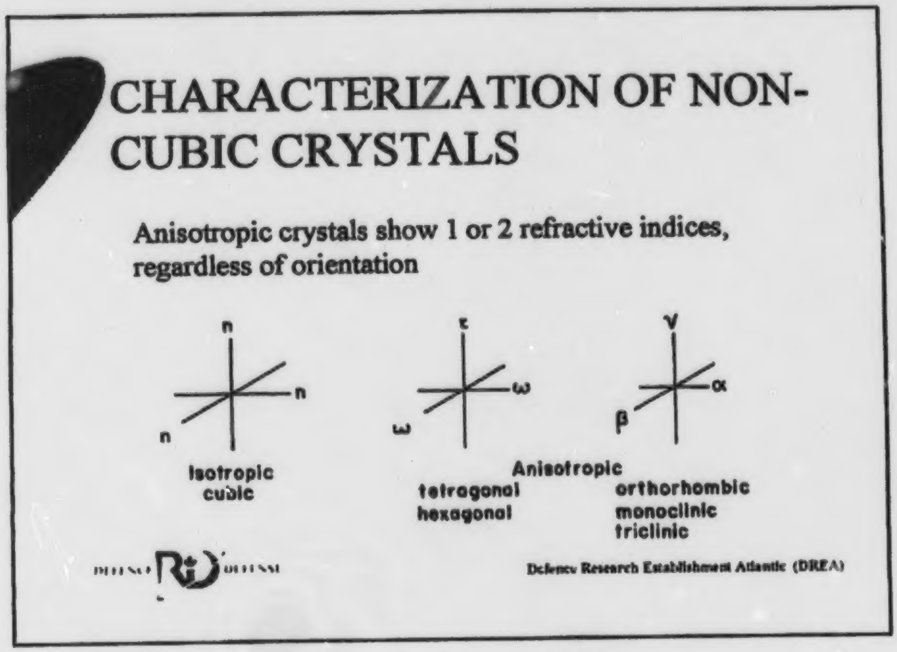

CHARACTERIZATION OF NON-CUBIC CRYSTALS

Anisotropic crystals show 1 or 2 refractive indices, regardless of orientation

Isotropic
cubic

Anisotropic

tetragonal
hexagonal

orthorhombic
monoclinic
triclinic

Defence Research Establishment Atlantic (DREA)

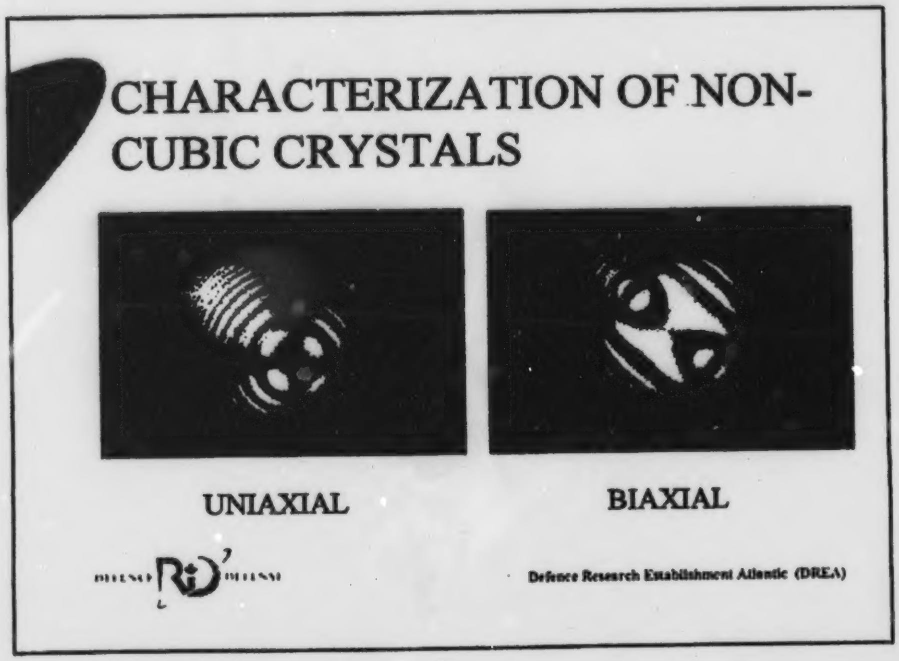

CHARACTERIZATION OF NON-CUBIC CRYSTALS

UNIAXIAL

BIAXIAL

Defence Research Establishment Atlantic (DREA)

CHARACTERIZATION OF NON-CUBIC CRYSTALS

BIREFRINGENCE

- Light exiting one axis is "retarded" relative to the other
- Yields interference colors

$$B = \frac{\text{retardation (nm)}}{\text{thickness (nm)}}$$

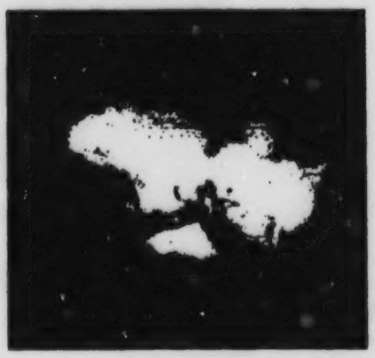

Defence Research Establishment Atlantic (DREA)

CHARACTERIZATION OF NON-CUBIC CRYSTALS

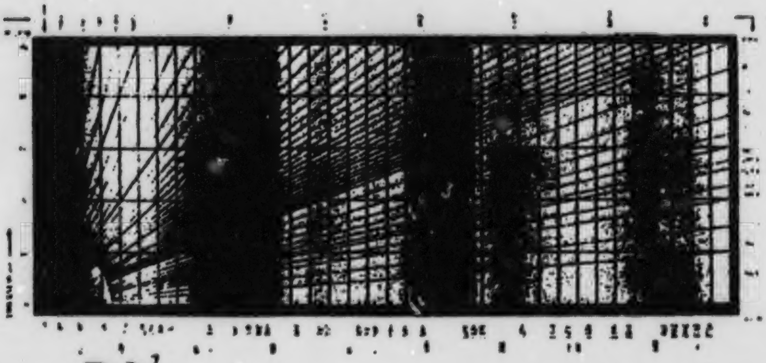

Defence Research Establishment Atlantic (DREA)

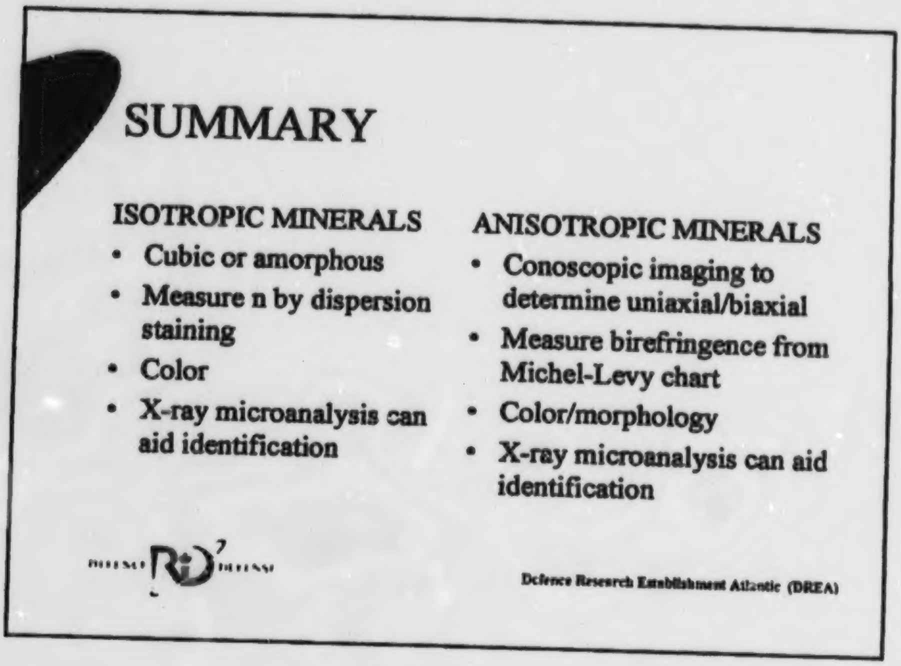

SUMMARY

ISOTROPIC MINERALS
- Cubic or amorphous
- Measure n by dispersion staining
- Color
- X-ray microanalysis can aid identification

ANISOTROPIC MINERALS
- Conoscopic imaging to determine uniaxial/biaxial
- Measure birefringence from Michel-Levy chart
- Color/morphology
- X-ray microanalysis can aid identification

Defence Research Establishment Atlantic (DREA)

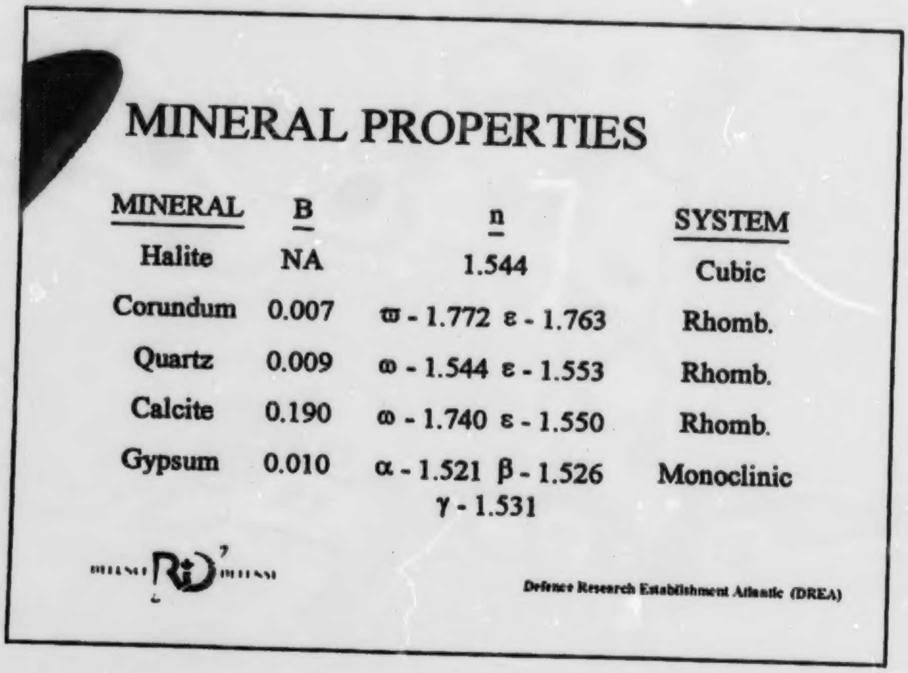

MINERAL PROPERTIES

MINERAL	B	n	SYSTEM
Halite	NA	1.544	Cubic
Corundum	0.007	ϖ - 1.772 ε - 1.763	Rhomb.
Quartz	0.009	ω - 1.544 ε - 1.553	Rhomb.
Calcite	0.190	ω - 1.740 ε - 1.550	Rhomb.
Gypsum	0.010	α - 1.521 β - 1.526 γ - 1.531	Monoclinic

Defence Research Establishment Atlantic (DREA)

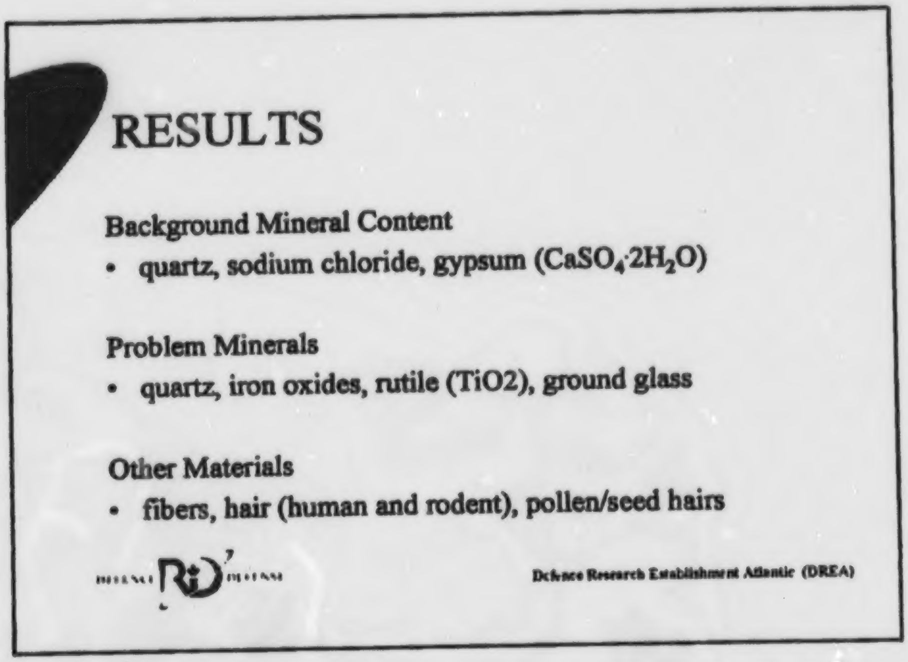

RESULTS

Background Mineral Content

- quartz, sodium chloride, gypsum ($CaSO_4 \cdot 2H_2O$)

Problem Minerals

- quartz, iron oxides, rutile (TiO2), ground glass

Other Materials

- fibers, hair (human and rodent), pollen/seed hairs

DEFENCE R&D DEFENSE

Defence Research Establishment Atlantic (DREA)

The Defence Research
and Development Branch
provides Science and
Technology leadership
in the advancement and
maintenance of Canada's
defence capabilities.

DEFENCE R&D DEFENSE

#511888 (14)

Applications of High-Frequency Pulsed Water Jets for the Removal of Marine Coatings

by M.M. Vijay[1], W. Yan[1], A. Tieu[1] and S. Pecman[2]

[1]VLN Advanced Technologies, Inc
P.O. Box 27076, Gloucester Centre Postal Outlet
Gloucester, ON., Canada, K1J 9L9

[2]DMSS 2-4-2, Department of National Defence
LSTL Building, Hull, Quebec, Canada, K1A 0K2

ABSTRACT

Experiments are in progress on the removal of several types of marine coatings with ultrasonically modulated high frequency pulsed water jets. Following an extensive laboratory investigation, a pre-commercial prototype has been manufactured. The machine has been tested for the removal of several types of marine coatings. Removal rates typically of the order of 50 ft^2/hr were obtained at water pressures as low as 5,000 psi. Although continuous water jets are becoming increasingly popular for the removal of hard coatings, the magnitude of pressure employed is well above 15,000 psi. Thus, pulsed water jets offer distinct advantages compared to continuous water jets and conventional removal systems such as sand blasting, needle gun techniques, etc. Since low pressures are involved, compact portable machines which are safe, user and environmentally friendly, can be manufactured at competitive costs. The paper will discuss the fundamentals of pulsed water jet technology followed by experimental results on the removal of several types of marine coatings.

#511889 ⑬

Copper Nickel Chromium for Marine Applications

by J.C. Galsworthy[1] and J. Bird[2]

**[1]Defence Evaluation and Research Agency,
Farnborough, Hampshire, GU14 OLX, UK**

**[2]Directorate of Naval Architecture, Defence Procurement Agency,
Ministry of Defence, Abbey Wood, Bristol, BS12 7DU, UK**

ABSTRACT

The use of a Copper Nickel Chromium Alloy to replace the current Nickel Aluminum Bronze in naval seawater systems and other marine applications is being pursued in the UK. This has been principally implemented to avoid the selective phase corrosion problems encountered in NAB, but other advantages may exist. This paper will present details of recent studies conducted in the UK on the Copper Nickel Chromium alloy to NES824.

A series of full sized cast components have been procured to confirm the supply of seawater system components. The acceptability of these components for naval use has been established through chemical analysis, mechanical property tests and non destructive testing. Destructive evaluation of one component has been conducted to compare properties with the test bars separately cast but used in the acceptance documentation.

INTRODUCTION

The background to high strength copper nickel alloys stem from the work conducted on these alloy types in the 1960's. It was at this time that the use of gunmetal castings for submarine seawater systems was questioned. Gunmetal suffered from corrosion problems and was not really adequate with respect to the 0.2% proof stress requirement. Consequently the various components made in this alloy tended to be heavy and thus the shock resistance was questionable, especially the inherent toughness which was not ideal. These concerns regarding the strength and particularly the shock resistance of the gunmetal castings employed in submarine seawater systems prompted the search for a replacement alloy.

High strength copper nickel alloys with resistance to seawater corrosion were under development with a view to developing an all welded seawater system of castings and pipes. However, concerns over the weldability of these copper nickel alloys and other varied reasons led to the eventual selection of nickel aluminium bronze (NAB) as the replacement for the gunmetal castings at that time.

In the 1970's NAB castings were found to be suffering from severe selective phase attack after relatively short periods of service in submarine seawater systems. This occurred in the cast matrix but was more severe in the heat affected zones of the welds. Welding had been used to fabricated complex structures or to repair defective regions of the castings. Amendments to the NAB material specifications, particularly heat treatments, were made to improve the material and HAZ performance, and welding on the wetted faces was restricted. This has enabled the seawater systems to be effectively managed in recent years. However management of the system is tiresome, labour intensive and costly. One is never sure if the described procedure will work in all circumstances. In addition, some weld repaired castings are too large to be effectively heat treated and thus circumstances exist where severe corrosion can be expected to occur.

Developments in welding techniques, such as low heat input welding, to control the HAZ microstructure and size, have helped but their control is costly and effectiveness still questionable. Developments in NDE techniques and procedures for the detection of selective phase corrosion have been progressed but are not yet effective in the inspection of in-service items in situ. Seawater systems must be dismantled for revalidation.

HIGH STRENGTH COPPER NICKEL ALLOY

There was understandably a renewed interest in an alternative material, particularly to reduce the overall maintenance costs of these seawater systems. A review of candidate materials, based on strength, corrosion resistance and shock behaviour, identified niobium and chromium strengthened copper nickel alloys as leading contenders. After some further development the chromium alloy, with reportedly greater resistance to impingement attack and slightly superior weldability, won the vote. This alloy, specified in NES824, became the selected alternative to NAB in the mid 1980s, for use in future submarines and at refit.

Considerable work was conducted on the castability of this alloy prior to commercial procurement of components, and recommendations on methodology were prepared. This was instigated to avoid the procurement problems encountered when NAB components were initially purchased and casting problems encountered by some foundries.

Despite these actions the first commercial NES824 castings showed the existence of what were described as linear defects, particularly in the larger castings. These linear defects have been attributed to the casting methodologies utilised by the suppliers. The defects were large entrapped oxides formed as a result of inadequate control and turbulence during casting. Mechanical properties of specimens containing these defects clearly showed the defective material to have effectively no strength. They needed to be considered as a potential starter crack in fracture mechanics based safety analyses, although the inherent toughness of the material usually prevented any crack extension occurring in practical fracture and fatigue testing. These oxide films were originally very difficult to identify. They were not detected by radiography, and only found by dye penetrant inspection when surface breaking. This posed problems, with defects only being identified when final machining actions were undertaken. An eddy current technique has now been developed to reliably identify such defects in the surface layer.

The presence of these linear defects delayed the introduction of the material into many new or refitted systems. Components with defects were initially quarantined, prior to revalidation when the inspection techniques were developed and acceptance criteria were reviewed. NAB components continued to be procured and utilised in the seawater systems.

COPPER NICKEL CHROMIUM COMPONENT EVALUATION

The two foundries approved for the supply of NES824 castings closed in 1994 preventing any further procurement of this material. To re-establish a procurement route, a review of copper alloy foundries in the UK was undertaken to determine candidate foundries for the future production of NES824 castings. Foundries were invited to tender for the production of five castings representing typical submarine designs in NES824, with the aim of proving their capability to supply to Class 1 standards. Three suppliers were contracted to supply the castings which covered a range of different sizes, ranging from 100-200 pounds to 1-1.5 tons. The components supplied were independently evaluated and assessed by DERA.

Each of the three foundries selected supplied an inlet T piece, a valve body, a filter body, a hull valve body, an inlet/outlet header and four test plates. The castings were to be in copper nickel chromium alloy to NES 824 Part 1 Issue 3. Three bars for tensile testing and an analysis sample were also cast for each separate melt used.

Each casting was evaluated by DERA against the requirements of NES 824 Part 1 Issue 3 for chemical composition, mechanical properties and structural integrity by non-destructive testing.

Chemical Composition

It has been identified that the chemical analysis of this material is not a simple matter. Considerable uncertainty in absolute composition existed in earlier studies. To facilitate conformance to the NES824 specification a number of analytical standards have been specially prepared for MoD to ensure that whatever the analytical method used it can be calibrated by use of the standard samples. For this independent evaluation the methods used were: X-ray fluorescence against standards for Ni, Cr, Fe, Mn, Si, Zr, Ti, P, and Co; inductively coupled plasma for B; furnace atomic absorption for Pb and Bi; combustion using carbon-sulphur analyser for C and S. The results of these analyses were compared with the chemical composition specified by NES 824 Part 1 Issue 3 in Table 1.

There were some indications of chemical compositions being outside the NES824 specification limits. In general, the extent of the differences in the analyses is to be expected. It has been shown that compositional variation in cast copper nickel chromium to NES824 will occur due to dendritic 'coring' and that nickel, chromium, iron, manganese, silicon and copper levels can vary considerably. Similarly, despite the use of the analytical standards, different test methods can still generate different compositional results. However, some results were clearly shown to be outside the limits for certain elements by a large amount. Two analytical samples from one supplier appeared to be supplied without Zr and Ti additions. One sample was found to have three times the phosphorous limit and another twice the boron limit. Confirmatory tests on the actual castings may be possible in future.

Mechanical Properties

The three cast bars supplied from each casting were machined into tensile test pieces and tested in accordance with BS EN10002. The average values of room temperature Ultimate Tensile Strength (UTS), 0.2% Proof Stress (PS) and % Elongation compare with the specification values are presented in Table 2.

The mechanical properties determined showed individual test UTS values ranging from 500 to 584 MPa, 0.2%PS values from 319 to 387 MPa, and elongations from 16 to 24% across the tests conducted on each of the 15 casts. It is not surprising that some variation in elongations were observed given the large grain size existing in some of the test bars.

Subsequent work on an inlet T piece has enabled the testing of the tensile properties of the actual component for comparison with the results from the test bars from the same cast. It has long been a concern that the results from these test bars do not truly represent the cast component which are invariably lower being part of a larger casting. The results obtained from flange and body specimens are compared with the test bar results in Table 3.

The values obtained to date confirm these concerns and have results below those within the specification. From fractography the lower strength values have been found to be associated with areas of shrinkage and interdendritic porosity within the test specimens machined from the component.

Whilst it is evident that the UTS and 0.2% PS properties of the specimens machined from the actual casting are slightly below the material property minima stated in the NES, it must be considered that the 0.2% PS for this material is greater than the 270 MPa value for NAB which it is planned to replace. (This NAB figure is itself based on test bars and there is evidence that actual castings in this material also shows reduced property levels.) It is likely that within the casting there would be a range of properties dependent on such aspects as section size, casting methodology, grain size, etc. Some areas being above and a few below the specified minima. Sufficient safety factors are used in the design of these components to allow for this observed reduction in tensile behaviour.

Non Destructive Evaluation

Each casting was subjected to non-destructive examination by each supplying foundry in accordance with the current NES 824 Part 1 specification requirements. This covered liquid penetrant examination, eddy current inspection and radiographic examination. The NES allows for a degree of rectification of defects. In this trial a condition of the contracts was that no weld repairs were to be conducted but castings rejected by the foundry but considered repairable in accordance with the NES could be supplied

Defects identified by the three NDE techniques used were reported by the suppliers in some castings but they considered them acceptable or rejectable but repairable within the specification e.g. linear defects revealed by liquid penetrant inspection of an inlet/outlet header, a surface breaking defect revealed by eddy current inspection of an inlet T piece, and shrinkage identified by radiography in a valve body and header. There was general agreement in the interpretation of the radiographs by the foundries and the independent assessor. Although one supplier sent components with known defects that he deemed repairable but some of these were rejected by the independent assessor. In a true procurement scenario the supplier would be conducting the weld repair and to conduct this he would be grinding out the defect and would be able to confirm whether the casting was actually acceptable at that point.

It is planned that some of these casting will be used in the development and evaluation of weld repair techniques and these studies will confirm the acceptability of these types of components.

CONCLUSIONS

The reported studies have been part of an exercise to re-establish an UK production base for submarine seawater system components manufactured in the copper nickel chromium alloy to NES824.

The assessment has shown that acceptable castings over a range of sizes can be supplied that conform to the requirements of NES824 Part 1 Issue 3.

The cost benefits and improved corrosion performance identified in the use of this copper nickel chromium alloy for submarine seawater systems can now be realised in future RN vessels and in current vessels at refit.

ACKNOWLEDGEMENTS

The authors wish to acknowledge the assistance of colleagues in this work, particularly Colin Roberts and Tim Shucksmith at DERA.

© British Crown Copyright 1999 / MOD. Published with the permission of the Controller of Her Britannic Majesty's Stationary Office.

Chemical Composition

		Ni	Cr	Fe	Mn	Si	Zr	Ti	Cu
NES824 Part 1 Issue 3	min	29.00	1.6	.5	.5	.20	.05	.05	—
	max	32.00	2.0	1.0	1.0	.40	.15	.15	rem

		Pb	P	Bi	S	C	Co	B	Total Impurities
NES824 Part 1 Issue 3	min	—	—	—	—	—	—	—	—
	max	.005	.005	.001	.005	.020	.050	.001	.070
	target max	.0015		.0005	.0030	.006			

		Se	Te	As	Zn
NES824 Part 1 Issue 3	target max	.0005	.0005	.0010	.0030

Table 1. ***Chemical composition requirements from NES824 Part 1 Issue 3.***

Casting		Mechanical Properties		
		Tensile Strength (UTS) MPa	0.2% Proof Stress (PS) MPa	Elongation %
	Supplier			
Inlet T Piece	A	529	351	18
	B	584	386	21
	C	521	338	20
Valve Body	A	525	342	21
	B	543	352	22
	C	528	347	21
Filter Body	A	547	362	21
	B	551	355	20
	C	528	347	21
Hull Valve Body	A	529	342	21
	B	531	344	21
	C	504	331	19
Inlet/Outlet Header	A	562	383	18
	B	543	366	18
	C	507	331	19
NES824 Pt1 Iss3		480 min	300 min	18 min

Table 2. Mechanical properties of cast test bars.

COMPONENT	UTS MPa	0.2% PS MPa	% Elongation
Test Bar	516	351	16.5
	535	350	19.5
	537	352	19.5
Ave	529	351	18.5
Casting Flange	445	296	14.1
	411	295	18.0
Ave	428	295.5	16.0
Casting Body	459	287	23.1
	481	294	27.3
Ave	470	290.5	25.2
NES824 Pt1 Iss3	480 min	300 min	18 min

Table 3. Comparison of tensile properties of inlet T piece test bars and actual casting.

#511890 (16)

Corrosion Problems with Copper-Nickel Components in Sea Water Systems

by D. R. Lenard and R. R. Welland

Defence Research Establishment Atlantic, Dockyard Laboratory (Pacific)

Esquimalt Defence Research Detachment
CFB Esquimalt, PO Box 17000 Stn Forces
Victoria, British Columbia V9A 7N2

ABSTRACT

Recent changes in construction techniques and operational practice have resulted in a number of failures of copper-nickel components in sea water systems. These failures include erosion corrosion of welded 90/10 copper-nickel pipe, erosion corrosion of 90/10 copper-nickel heat exchanger tubes, "hot-spot" corrosion of 70/30 copper-nickel tubes and denickelification of 70/30 copper-nickel tubes. Case histories describing examples of each of these problems are presented. Factors contributing to these failures, such as welds protruding into the flow stream, tight bends, contamination by marine organisms, unusual flow patterns and exposure to sulfide-polluted, stagnant sea water, are discussed. Methods to prevent or reduce the future occurrence of these problems are also presented.

INTRODUCTION

Several significant changes in fabrication technology and operational use of sea water systems have recently been introduced during the construction, modernization and maintenance of Canadian naval vessels. These changes include the use of welded copper-nickel piping, modular construction and the supply of "water on demand" instead of continuous flow. While these changes provide some notable benefits, they have also contributed to a number of rapid failures of copper-nickel components in sea water. In this paper, a brief history of the experience with copper-nickel alloys prior to these changes will be provided. This will be followed by several recent case histories involving erosion corrosion and denickelification. Methods to prevent the future occurrence of these problems will also be discussed.

HISTORICAL PERFORMANCE OF COPPER-NICKEL ALLOYS

Sea water systems using 90/10 copper nickel (UNS C70600) piping have provided many years of reliable service in surface ships operated by the Canadian Forces over the past forty years. Very few failures of this piping have been brought to the attention of either of the Dockyard Laboratories (this one in Esquimalt, BC or the other in Halifax, NS). Most of these failures have involved erosion corrosion caused by unintentional obstructions at flanges or by modifications to the piping systems to accommodate new equipment or operational procedures. An example of the latter involves a blackwater piping system that had been in service since 1964. The 90/10 copper nickel pipe shown in Figure 1 perforated in 1992 as a result of erosion corrosion near the exit of the small discharge pipe from one of the crew's heads. The system had originally been designed for sea water-flushed overboard discharge. However, in 1985, the blackwater system was adapted to accommodate vacuum collection into a holding tank. The changes in velocities and composition of the effluent resulting from this conversion caused erosion corrosion of the original copper nickel collection pipes.

Heat exchangers using sea water as a coolant have been used extensively in ships of the Canadian Forces. In the past, most of these heat exchangers have been fabricated with 90/10 copper nickel tubes and Naval brass (UNS C46400) tube plates. These systems have provided excellent service as long as the alloys have been protected against corrosion by the use of sacrificial steel anodes. When these anodes have not been properly utilized, failure of the 90/10 tubes and erosion corrosion of the Naval brass tube plates has occurred (Figure 2).

The performance of copper nickel alloys in sea water continues to be the subject of a substantial amount of research. For example, at CORROSION/97, three of the papers presented at the Symposium on Marine Corrosion were specifically devoted to these alloys[1-3]. This research is driven, in part, by efforts to understand the differences in the relative behavior of 90/10 and 70/30 (UNS C71500) copper-nickel alloys in different environments. There is, for example, general agreement that sulfides liberated from decaying organic matter can cause accelerated corrosion of both alloys. However, in one study, Popplewell[4] determined that 70/30 was substantially more susceptible to localized corrosion in flowing sea water than 90/10, whereas Todhunter[5] reported that tubes made of 70/30 had a lower incidence of failure in sulfide polluted Los Angeles harbor water than those made of 90/10. Gudas and Hack[6] found that 70/30 and 90/10 were both susceptible to sulfide-induced pitting, but higher sulfide concentrations were required to trigger the attack of 70/30. Our own work in flowing sea water suggested that these contradictory reports in the literature could be related to the nature of the corrosion product films that had developed on the components in question and that these films were very dependent on the sea water chemistry and the length of exposure[7].

EROSION CORROSION OF COPPER-NICKEL SEA WATER PIPING

The extensive use of welded copper-nickel sea water piping has recently been introduced. Welded systems offered the advantage of reducing the cost and weight of flanged elbows and cast T fittings. A reduction in the number of flanged joints also allowed pipe runs to be situated closer together, thereby saving space. Furthermore, welded systems held the promise of removing some of the shock resistance problems associated with the brazed joints that had previously been used. Finally, the use of welded systems was intended to reduce the problems with leaks that were associated with brazed joints and bolted connections.

A section of piping which increased the diameter of a sea water system from 150 mm to 200 mm is shown in Figure 3. The pipe developed a leak in this transition section just downstream from a circumferential weld. Depending on the rate of flow through the pipe, the change in diameter alone could create enough turbulence to cause erosion. However, a cross-section of the transition piece revealed that the circumferential weld protruded into the flow stream and contributed to the erosion corrosion (Figure 4). The eroded section of piping was also found to have an iron content of 1.11% (Table 1). Although this iron content was within the required specification for the 90/10 copper nickel piping (United States Department of Defense specification MIL-S-16420 alloy C70600 Class 200), a content of at least 1.4% is recommended for sea water service[8]. The importance of iron additions in improving resistance to flowing sea water has been known for many years. For example, in 1972, Pearson[9] published a review which included references to comprehensive studies of copper-nickel alloys that were conducted in the early 1950's[10-12].

This piping system was also found to contain a number of seamed elbows with a very tight radius of curvature (Figure 5). The welds in these elbows which ran parallel to the direction of flow had been carefully ground out, but the circumferential welds, which

Table 1. Chemical Composition of Transition Section (weight percent)

Element	Cu	Ni	Fe	Pb	Zn	Mn	Al	Si
Percent	rem	9.58	1.11	0.03	0.02	0.34	<0.01	0.04

connected the elbows to the rest of the piping system, protruded into the flow stream (Figure 6). The resulting turbulence gave rise to erosion corrosion (Figure 7) similar to that observed in the transition section. Also like the transition section, the material in the bend had a lower iron content (1.10%) than that recommended for sea water service. The turbulence cause by the tight radius led to impingement attack in the classic "horse walking upstream" pattern[13] (Figure 8). Prevention of the corrosion problems observed in the bends could be achieved by tighter quality control of the welding, by using an alloy with a higher iron content and by using bends with larger radii. LaQue[14] has recommended bends with a minimum radius of three pipe diameters. This is the minimum radius specified in the piping standard that is normally applicable to Canadian naval vessels. However, in a few cases, exemptions were granted in order to solve some pipe routing problems. Similarly, the welding specification allowed a maximum root concavity of 1.5 mm. This specification could be achieved during the fabrication of individual modules but proved difficult to meet in some of the field welds that tied the modules together. These welds were located in areas that made electrode manipulation awkward and efficient argon purging difficult, with excessive weld penetration as a result. In the future, the selection of locations for field tie-ins should be made with accessibility for welding and the sea water flow conditions in mind.

In an effort to reduce staffing requirements, remotely operated flow control systems have been incorporated into new or updated sea water systems. Complicated arrangements of cross-over pipes and valves, intended to provide redundant flow paths to important pieces of equipment, have also been utilized. These factors have led to some unusual flow conditions within the piping systems. For example, a section of firemain failed in a cross-over pipe that was nominally upstream from a butterfly valve. The erosion corrosion was very localized (Figure 9), suggesting that the valve had been left slightly open, creating an eddy in the "upstream" pipe.

EROSION CORROSION OF COPPER-NICKEL HEAT EXCHANGERS

The redundant sea water flow paths mentioned earlier, along with a new philosophy of supplying water on demand, have given rise to another problem that had only been observed on a few isolated occasions in the past. The gentle flow of sea water in some pipe runs has provided an ideal environment for the attachment of marine organisms. As a result, these pipes have become heavily fouled (Figure 10). For a number of reasons, including visits to fresh water ports, the colonies can die off. When this happens, particularly in the case of hydroid colonies, parts of the colonies break off in chunks and become lodged in the orifices in the tube plates of heat exchangers. Figure 11 shows the extent of the blockage that occurred on the supply side of a heat exchanger just three months after it had been completely cleaned. The mass of dead hydroids provides an ideal home for other organisms and thriving colonies of mussels and barnacles have been observed (Figure 12).

With so many tubes blocked, the flow through the remaining tubes occurred at a higher velocity than that assumed in the original design. As a result, erosion corrosion of the tube ends has occurred (Figure 13). The altered flow patterns have also caused erosion of the divider plate (Figure 14). The installation of sacrificial steel anodes in the end bells would increase the resistance to erosion corrosion. Ship staff and the Fleet Maintenance Facilities have been installing these anodes as opportunities arise. While anodes will help to reduce the extent of erosion corrosion, elimination of the problem will require removal of the marine growth throughout the ships. Under current operating conditions, this will be very difficult to achieve.

DENICKELIFICATION OF 70/30 COPPER-NICKEL TUBES

Several 70/30 copper-nickel tubes in a sea water-cooled heat exchanger for engine oil were found to have perforated near a baffle plate. Splitting these tubes lengthwise revealed that the perforations had resulted from deep pits (Figure 15) which had been initiated on the sea water side of the tubes. When the tube wall became thin enough due to this corrosion, the oil (under pressure) ruptured the tubes inward. Other tubes that were removed at random from this heat exchanger were also found to be pitted, with most of the damage concentrated in areas corresponding to the locations of the baffle plates.

This heat exchanger was mounted on the engine block, with one of the support angles quite close to the baffle plate that was near to the perforated tubes. When the engine was shut down, the pump which delivered sea water to the heat exchanger was shut off as well, leaving quiescent sea water inside the tubes. Furthermore, an oil circulation pump was then turned on, which kept hot oil flowing through the heat exchanger and thereby maintained a high temperature for the sea water trapped in the tubes for an extended period of time after the engine was shut off. These conditions gave rise to a particularly severe form of denickelification, known as "hot-spot" corrosion. "Hot-spot" corrosion has been reproduced in the laboratory[15-16] but reports of in-service problems seem to be quite rare, as the general industry approach seems to be to avoid the conditions known to cause this form of corrosion[17].The laboratory investigations indicated that "hot-spot" corrosion occurred at temperatures between 90° and 170°C and that the corrosion was intensified in the presence of sulfides.

As noted earlier, some sea water supply lines are heavily fouled, so the presence of sulfides from decaying marine organisms in the sea water trapped in the heat exchanger during shut-downs is very likely. The temperature of the sea water will remain within the studied region for some time after the engine is shut down. Finally, the proximity of the baffle plate to the engine mount could lead to localized conductive transfer of engine heat.

A number of steps can be taken to prevent future "hot-spot" corrosion in this system. The simplest, and most effective, action is to keep sea water flowing through the heat exchanger at all times. Ideally, when not in use for extended periods of time, the heat exchangers should be drained, flushed and ventilated. Sacrificial steel anodes should also be installed in the end bells and replaced as required. Although these anodes only provide cathodic protection within a few tube diameters, the ferrous ions that they release have been shown to be beneficial to the development and maintenance of protective films throughout the tubes[7]. The heat exchangers should also be relocated to alleviate any problems with the residual heat.

The precise mechanism of denickelification is still a matter of some controversy. However, the end result is a pit with associated deposits of copper. Some of this copper can be found in locations downstream from the original pit (Figure 16). Denickelification has also been observed under conditions that are less severe than those known to cause "hot-spot" corrosion. For example, a leak developed in a hydraulic oil cooler after it had been in operation for 15 months. Examination of the failed 70/30 copper-nickel tube (Figure 17) revealed a deep pit that had been initiated on the sea water side. There were several other pits containing deposits of copper. The hydraulic oil normally bypasses this cooler until the oil reaches a temperature of 30°C, so the temperature of the oil entering the cooler is normally between 30°and 40°C. If the temperature reaches 65°C, an alarm is activated. Sea water flows constantly through the cooler while the ship is at sea, but flow to the cooler is shut down while the ship is in port, leaving the cooler full of stagnant sea water. Because this tube had been cleaned prior to delivery to the Dockyard Laboratory, it was not possible to determine the exact sequence of events that led to the perforation. Almost certainly, the pit was initiated during a shut-down period as a result of contact with sulfide-polluted, stagnant sea water. It could not be determined whether the ensuing corrosion occurred only during shut-downs or also continued under a deposit which shielded the pit from flowing sea water while the ship was at sea.

A final example indicates the role that operational practice can have on the corrosion of 70/30 copper-nickel tubes. A tube from an air cooler perforated as a result of pitting that had been initiated on the sea water side (Figure 18). Discussions with crew members on different ships revealed that there was no set routine for the operation of this cooler. Some ships closed the valves to the coolers during periods of inactivity while others left them open, thereby allowing the sea water to flow through them continuously. These coolers were also not fitted with sacrificial steel anodes. To date, those ships which maintained continuous flow have not reported any problems with these coolers. The manual supplied by the manufacturer for this cooler recommends that it be completely drained and vented when not in use. Although this would be an acceptable alternate to the installation of anodes and maintenance of continuous flow, this recommendation appears to have been overlooked in the overall design of the ship, as provisions for easy draining and venting do not exist.

SUMMARY

The case histories of several failures involving copper-nickel sea water piping or heat exchangers were presented. These failures were attributed to problems with construction techniques and operational practices that have recently been introduced. The erosion corrosion that has been observed in the welded 90/10 copper-nickel piping system was caused by circumferential welds that protruded into the flow stream, by bends that were tighter than the recommended minimum of three pipe diameters or by unusual flow patterns near cross-over valves. A new philosophy involving redundant pipe runs which supply water on demand, instead of the continuous flow used previously, has led to the creation of an ideal environment for the attachment of marine organisms. Masses of dead organisms have become trapped at the entrances to heat exchangers, providing a base for subsequent generations and altering the flow patterns in the heat exchangers. This has led to erosion corrosion of the tube plates. Sacrificial steel anodes should be installed in all heat exchangers to reduce the extent of corrosion. Removal of the existing biological contamination will be difficult but, if successful, subsequent fouling can be substantially reduced by maintaining flow rates that are sufficiently high to prevent the initial attachment of marine organisms.

One heat exchanger was located and operated in such a manner that its 70/30 copper-nickel tubes suffered a particularly severe form of denickelification known as "hot-spot" corrosion. This problem could be prevented by maintaining a continuous flow of sea water, installing anodes and relocating the unit. Denickelification was also observed in 70/30 tubes under less severe conditions. In these cases it had been initiated during periods of exposure to sulfide-polluted sea water during shut-downs. Prevention of biological contamination and maintenance of continuous flow of sea water would reduce or eliminate these corrosion problems as well.

REFERENCES

1. R. M. Kain and B. E. Weber, "Effects of Alternating Seawater Flow and Stagnant Layup Conditions on the General and Localized Corrosion Resistance of CuNi and NiCu Alloys in Marine Service", CORROSION/97, Paper No.422, NACE International, Houston, TX (1997)
2. P. T. Wojcik and M. E. Orazem, "Experimental Study of the Erosion-Corrosion of Copper and Copper-Nickel Alloys Using a Submerged Impinging Jet", CORROSION/97, Paper No. 435, NACE International, Houston, TX (1997)
3. A. Al-Hashem, J. A. Carew and A. Al-Sayegh, "The Sacrificial Protection of UNS C71500 Heat Exchanger Tubes in Arabian Gulf Sea Water", CORROSION/97, Paper No. 414, NACE International, Houston, TX (1997)
4. J. M. Popplewell, CORROSION/80, Paper No.180, NACE International, Houston, TX (1980)
5. H. A. Todhunter, *Power*, Vol.. 111, No. 3, p. 57 (1967)
6. J. P. Gudas and H. P. Hack, *Corrosion*, Vol. 35., No. 2, p. 67 (1979)
7. D. R. Lenard, J. G. Moores and G. E. Morin, *Br. Corros. J.*, Vol. 24, No. 1, p. 19 (1989)
8. C. P. Dillon & Associates, Materials Technology Institute Publication No.26, St. Louis, MO (1987)
9. C. Pearson, *Br. Corros. J.*, Vol. 7, No. 2, p. 61 (1972)
10. G. L. Bailey, *J. Inst. Metals*, Vol. 79, p. 243 (1951)
11. E. W. Palmer and F. H. Wilson, *J. Metals*, Vol. 4, p. 55 (1952)

12. W. C. Stewart and F. L. LaQue, *Corrosion*, Vol. 8, p. 259 (1952)
13. T. H. Rogers, "The Marine Corrosion Handbook", p. 172, McGraw-Hill, Toronto (1960)
14. F. L. LaQue, "Marine Corrosion", p. 257, Wiley & Sons, New York (1975)
15. C. Breckon and P. T. Gilbert, "Corrosion of Condenser Tubes under Conditions of Local High Temperature", Proc. 1st International Congress of Metallic Corrosion, p. 624, Butterworths, London (1962)
16. R. S. Bem and H. S. Campbell, "Laboratory Hot Spot Corrosion Tests of Condenser Tube Alloys", ibid., p.630
17. A. H. Tuthill, *Mat. Perf.*, Vol. 26, No. 9, p.12 (1987)

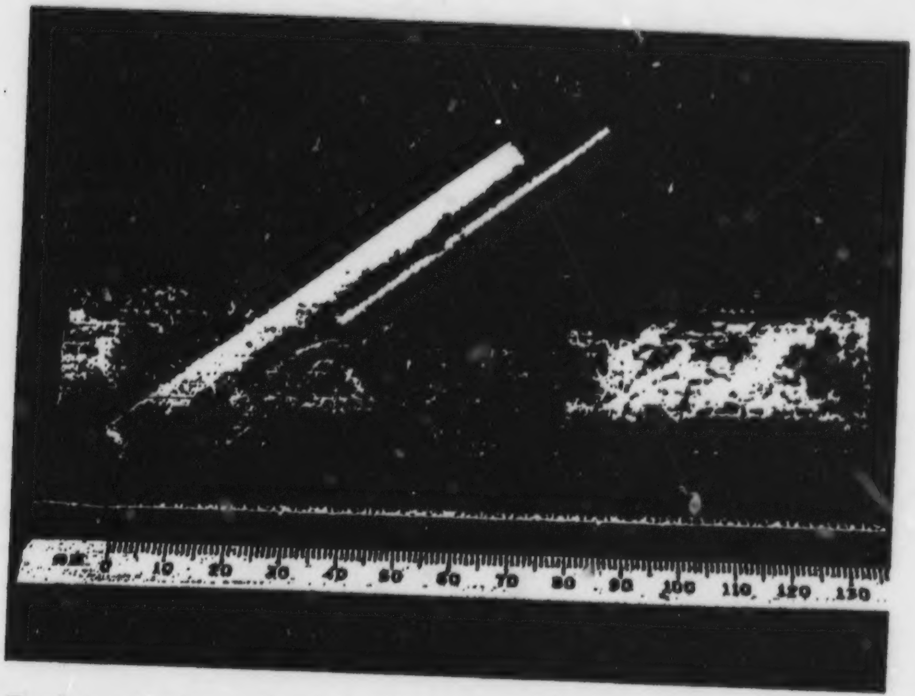
0
10
20
30
40
50
60
70
80
90
100
110
120
130

Figure 1. Erosion corrosion of 90/10 Cu-Ni pipe in blackwater system on HMCS Annapolis

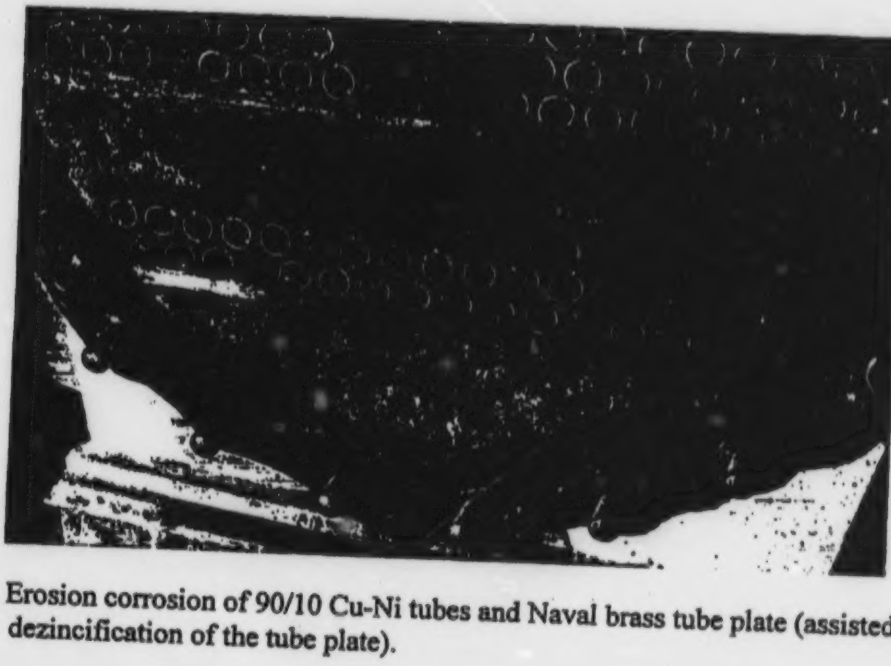

Figure 2. Erosion corrosion of 90/10 Cu-Ni tubes and Naval brass tube plate (assisted by dezincification of the tube plate).

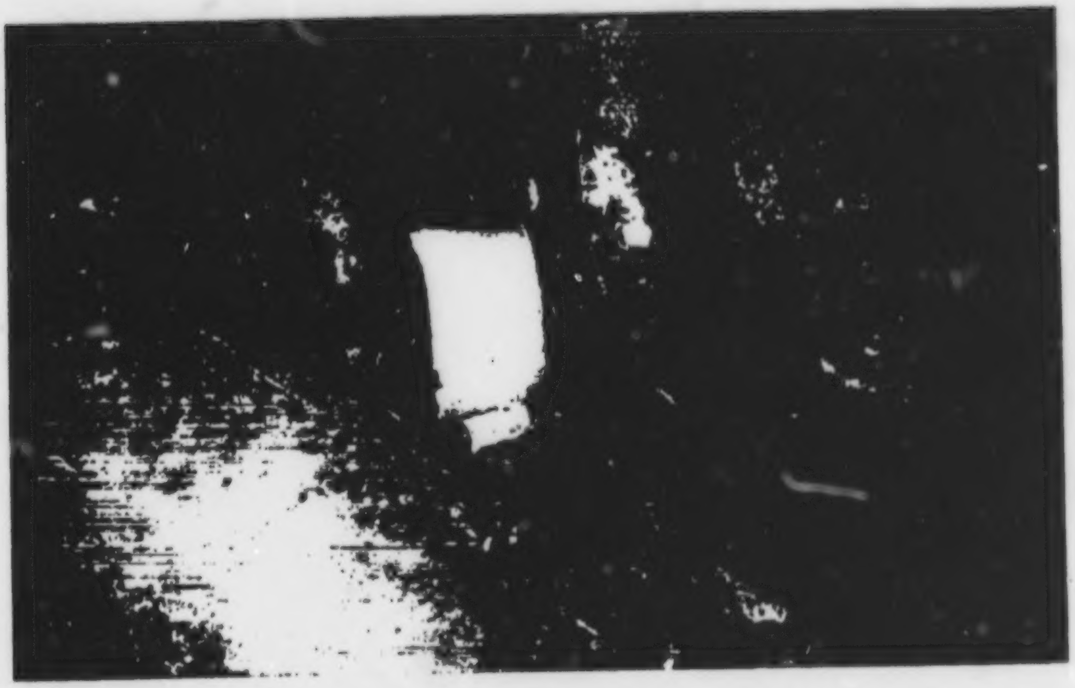

Figure 3. Transition section of 90/10 Cu-Ni pipe that increases the diameter of the pipe run from 150 mm to 200 mm.

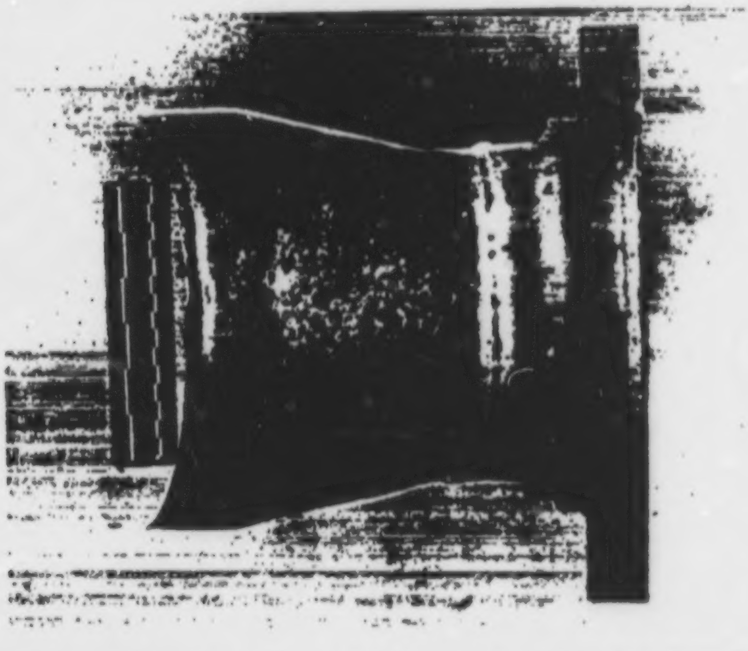

Figure 4. Cross-section of transition piece showing erosion corrosion downstream from a circumferential weld.

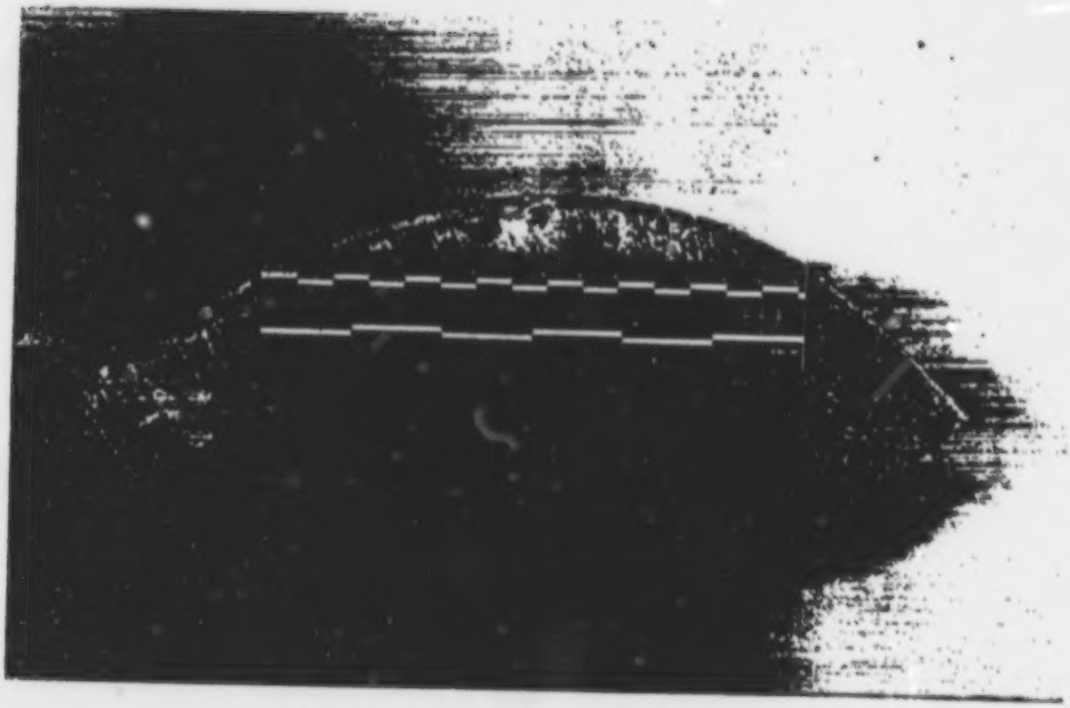

Figure 5. Seamed elbow with tight radius of curvature. This elbow was bisected in the direction of flow prior to this photograph.

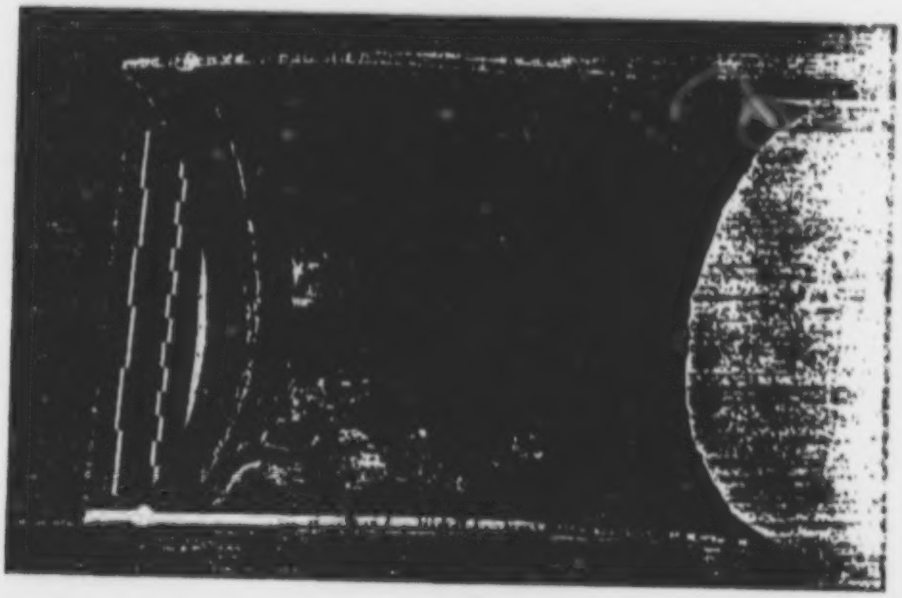

Figure 6. Seamed elbow with weld in direction of flow ground out. Circumferential weld protrudes into flow stream.

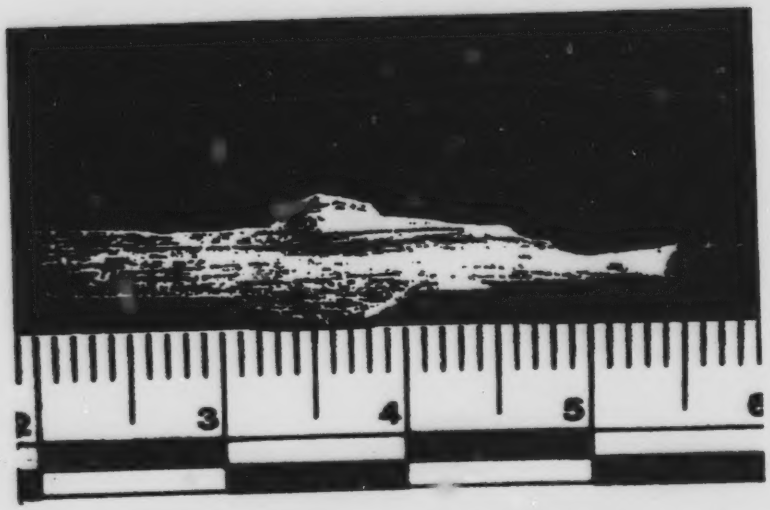

Figure 7. Cross-section showing erosion corrosion downstream from a weld.

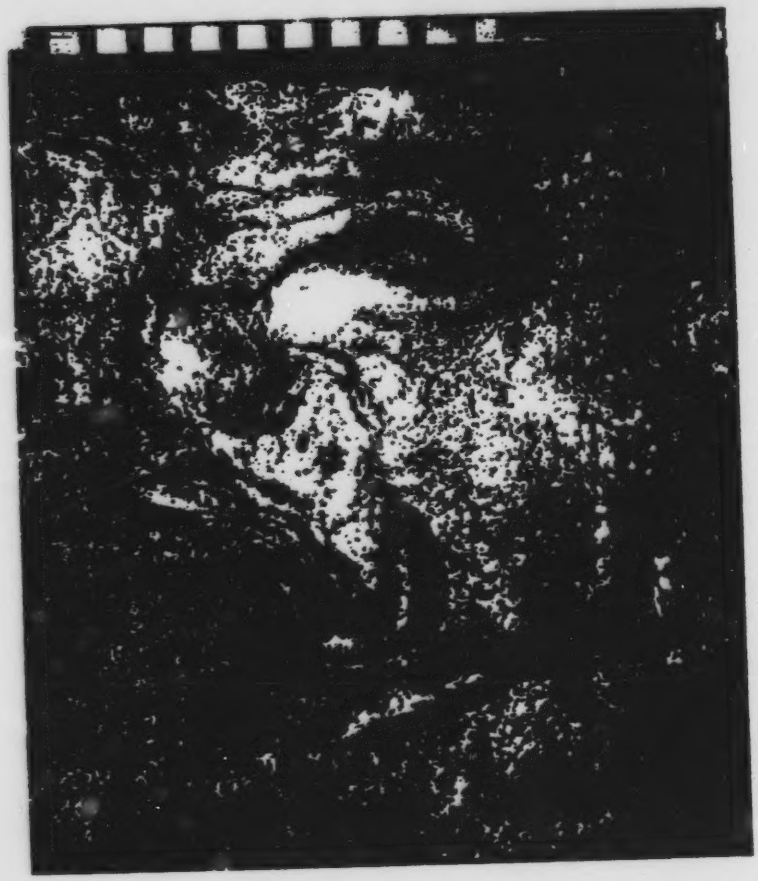

Figure 8. Horseshoe pattern typical of impingement corrosion in a tight bend.

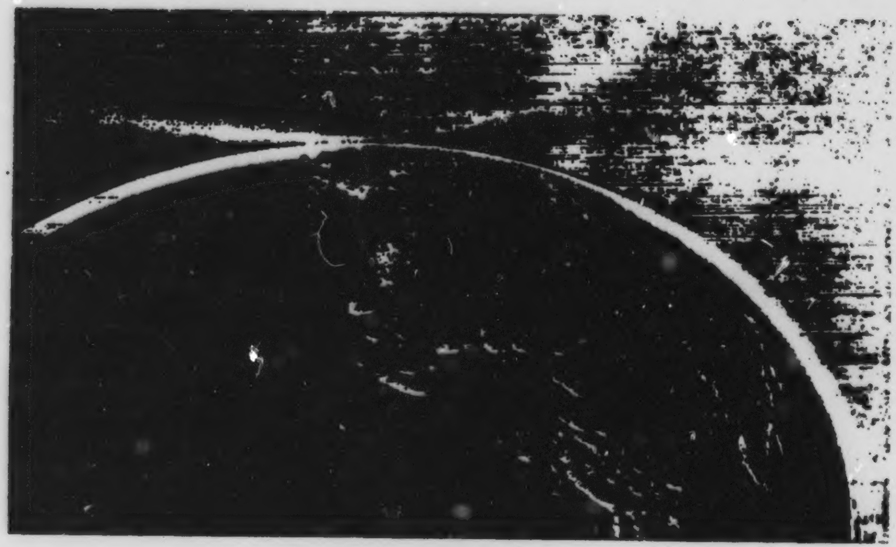

Figure 9. Erosion corrosion near a cross-over valve.

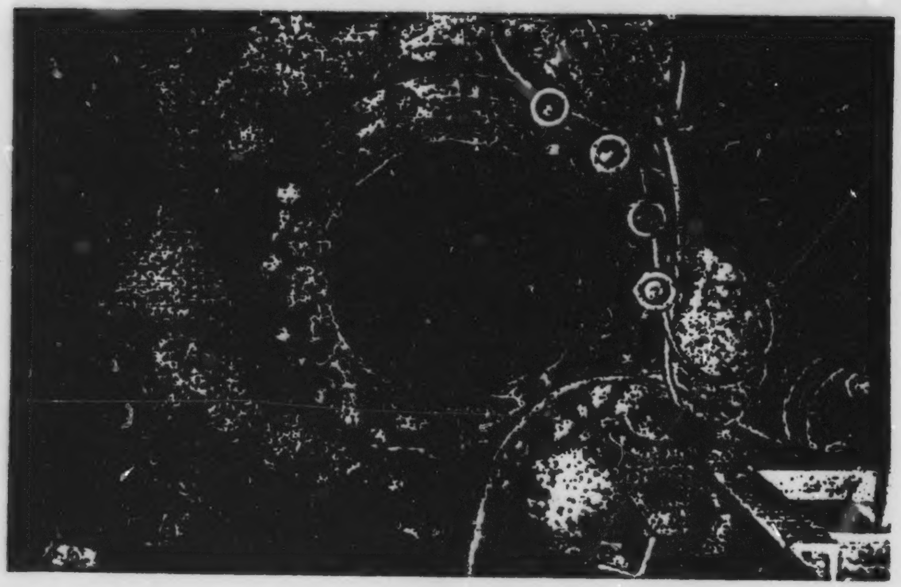

Figure 10. Firemain fouled with marine organisms.

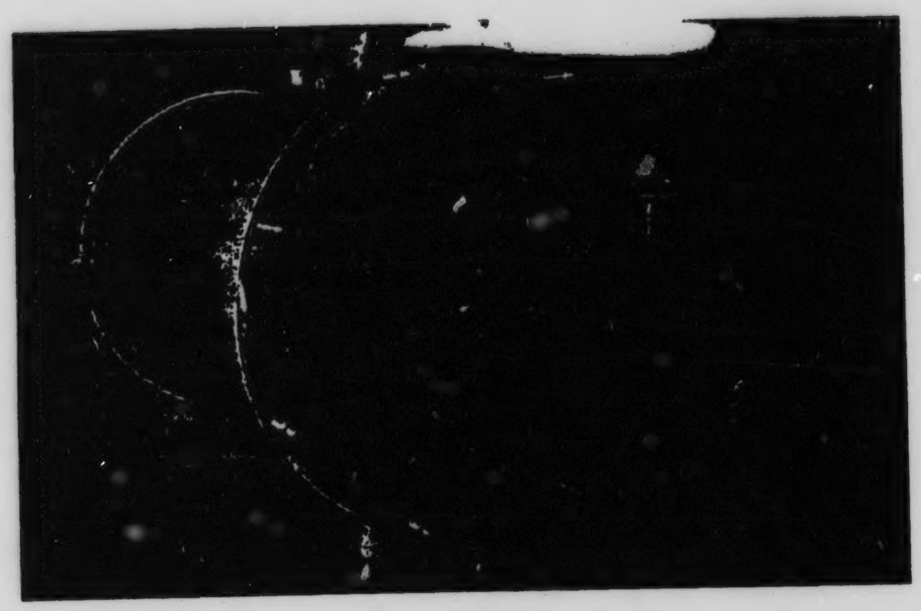

Figure 11. Extent of blockage in a chiller 3 months after cleaning.

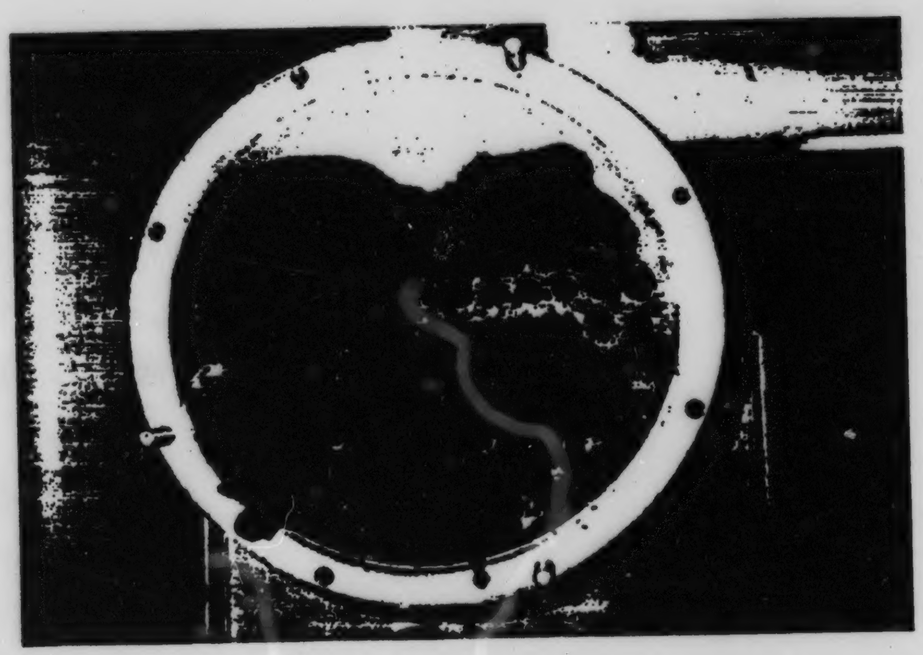

Figure 12. Mussels and other marine organisms blocking a chiller that had been in service without cleaning longer than the chiller shown in Figure 11.

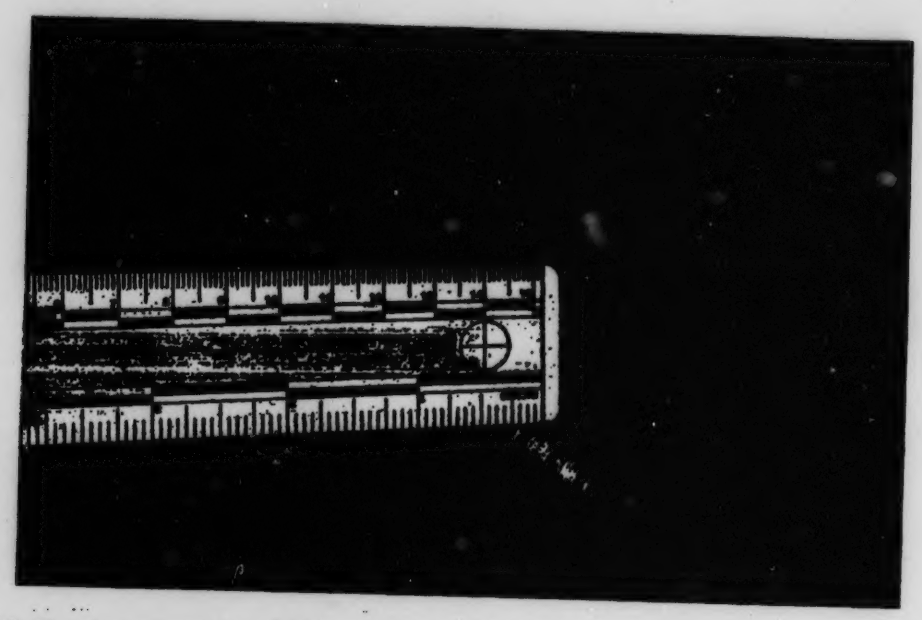

Figure 13. Erosion corrosion of 90/10 Cu-Ni tube ends resulting from blockage.

Figure 14. Erosion corrosion of divider plate resulting from blockage.

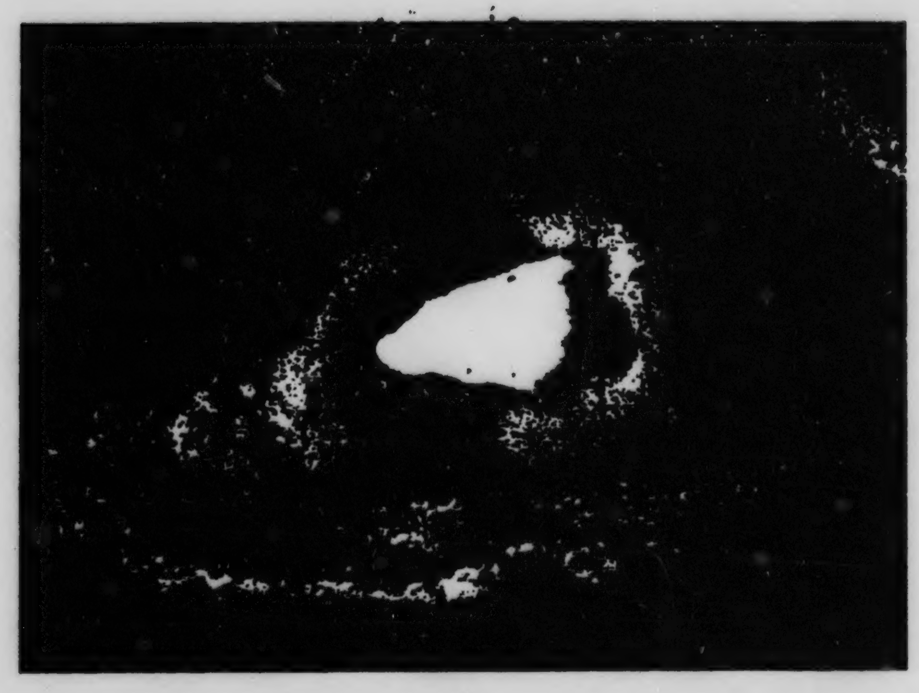

Figure 15. Pit initiated on sea water side of 70/30 Cu-Ni tube. 18x.

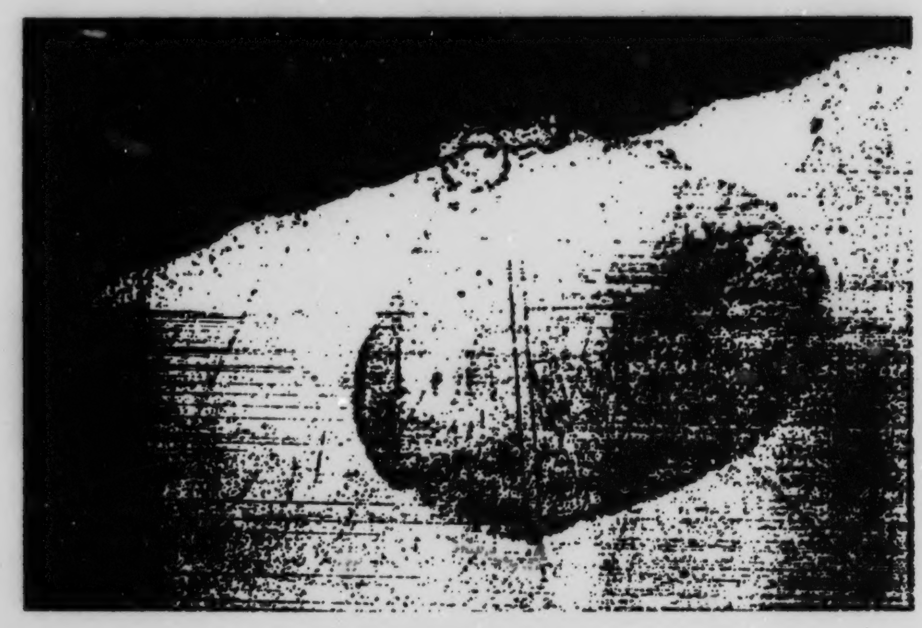

Figure 16. Copper particle downstream from a pit. An alcohol stain is also visible. 450x.

DIRECTION OF FLOW

Figure 17. Pit initiated on the sea water side of a 70/30 tube in a hydraulic oil cooler.

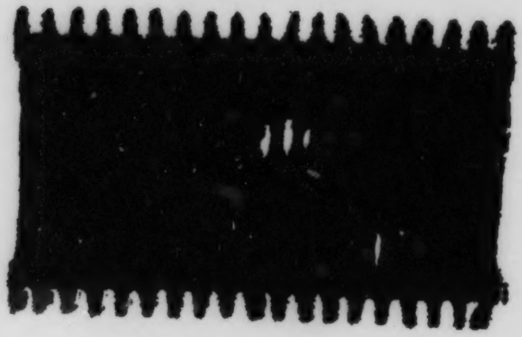

Figure 18. Pits initiated on the sea water side of a 70/30 tube in an air cooler.

#511891 (17)

Effect of Impurity Elements on the Mechanical Properties of Aluminum Bronze Alloy C95800

by M. Sadayappan, R. Zavadil and M. Sahoo

Materials Technology Laboratory
568 Booth Street, Ottawa, Ontario

ABSTRACT

At present there is no consensus on the maximum allowable limits for impurity elements such as Pb,Zn,Sn,Cr,Be,Bi and Se in aluminum bronze castings. These impurities could adversely affect mechanical properties and promote cracking during welding and heat treatment. This project was undertaken to evaluate the effect of such impurity elements on the mechanical properties, heat treatment and weldability of the most popular aluminum bronze, alloy C95800. To date, mechanical properties of single and two element additions have been completed. UTS and Ys values were in excess of the minimum specified in ASTM B148. However, the % elongation was reduced to below or just above the specified minimum in a few cases. Weldability evaluation and addition of three element combination are in progress.

Effect of Impurity Elements on the Mechanical Properties of Aluminum Bronze Alloy C95800

M.Sadayappan, R.Zavadil and M.Sahoo
Materials Technology Laboratory, CANMET
Ottawa, Canada

Introduction

- Three year project (Dec. 1996 - Dec.1999)
- Sponsored by U S Department of Energy, through Cast Metal Coalition (CMC)
- The limits on impurity elements to be included in ASTM specification

Current Standard

CDA C95800 and ASTM B148-95

Limits for major alloying elements

Al	Fe	Ni	Mn
8.5 - 9.5	3.5 - 4.5	4.0 - 5.0	0.8 - 1.5

Limits for impurity elements

Pb	Si
0.03 max	0.10 max

Literature Review

- Si, Pb, Sn, Mg, Bi, Sb and Cd reduce ductility.
- Only Si and Sn increase strength.
- No agreement on safe limits.
- Zn has no significant effect on mech. properties.
- Some elements promote cracking in heat affected zone of weld or during heat treatment.

Experimental Ranges

- C95800 9%Al - 4.5%Fe - 4.5%Ni - 1%Mn
- Impurities

Lead	0.01 - 0.2%	Zinc	0.1 - 1.0%
Tin	0.01 - 0.25%	Bismuth	0.005 - 0.1%
Selenium	0.005 - 0.1%	Silicon	0.01 - 0.25%
Chromium	0.01 - 0.1%	Beryllium	0.01 - 0.1%

Two Element Combinations

- Combinations selected by the monitoring committee:

Lead-Zinc	Lead-Bismuth
Lead -Tin	Bismuth-Selenium

Evaluation

- Microstructure
- Properties
  Tensile strength, Yield strength
  Ductility (% Elongation and Reduction in Area)
  Hardness
- Heat Treatment
  C95800, 700C for 6hrs, air cool
- Weldability
  Gleeble analysis

Procedure

- 100kW, 3000Hz pushup type induction furnace
- Charge material: pure copper, aluminum, Cu-10%Fe, Cu-28% Ni and Cu-35% Mn
- Degassed with dry nitrogen
- Pouring temperature 1160 - 1180°C
- Green sand molds
  - Keel blocks for tensile testing
  - 12"x6"x0.75" plate castings for weldability testing

C95800 - Base Composition

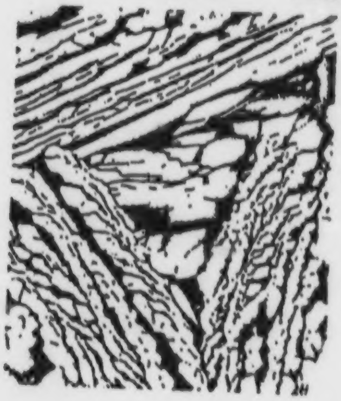

As - cast 100x

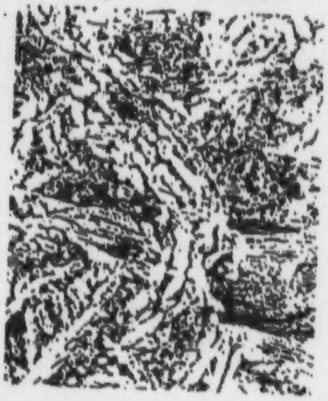

Heat treated 100x

C95800 - Cr added

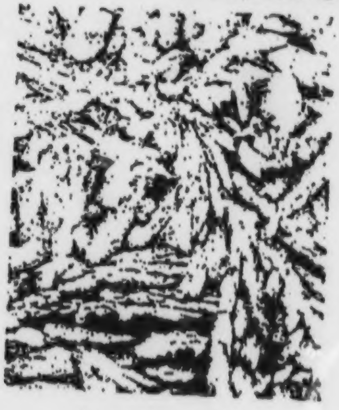

As - cast 100x

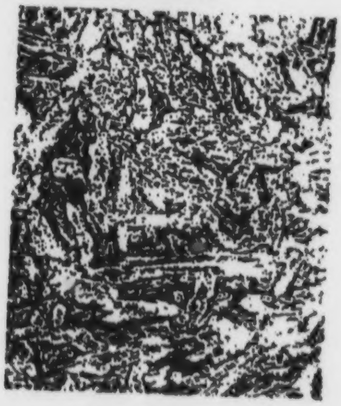

Heat treated 100x

C95800 - Si added

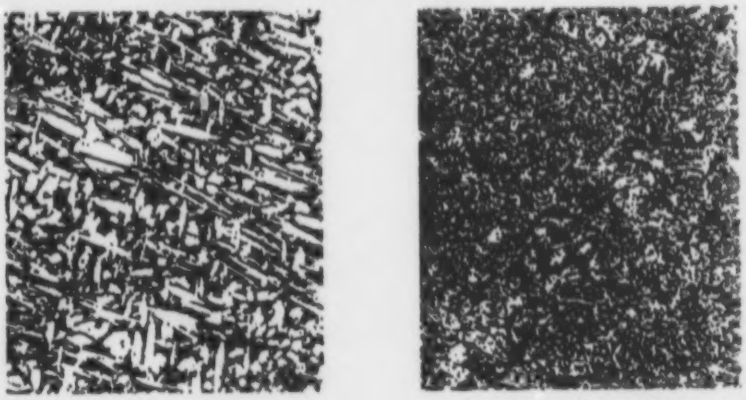

As - cast 100x

Heat treated 100x

C95800 - Be added

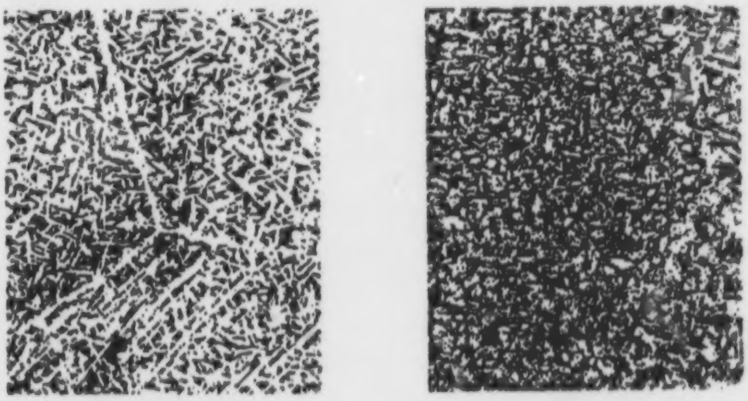

As - cast 100x

Heat treated 100x

C95800 - Tensile Strength
Single Element

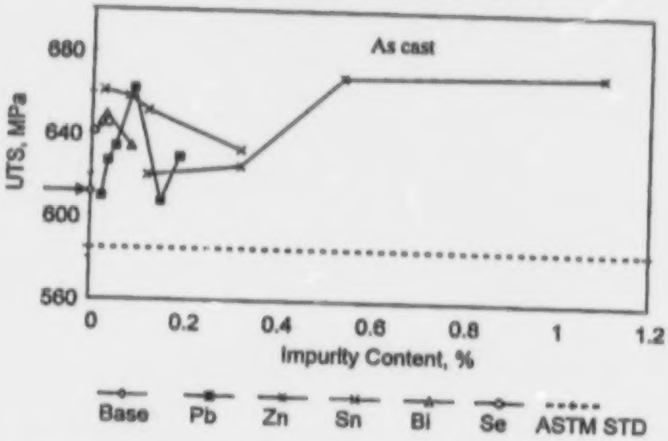

C95800 - Elongation
Single Element

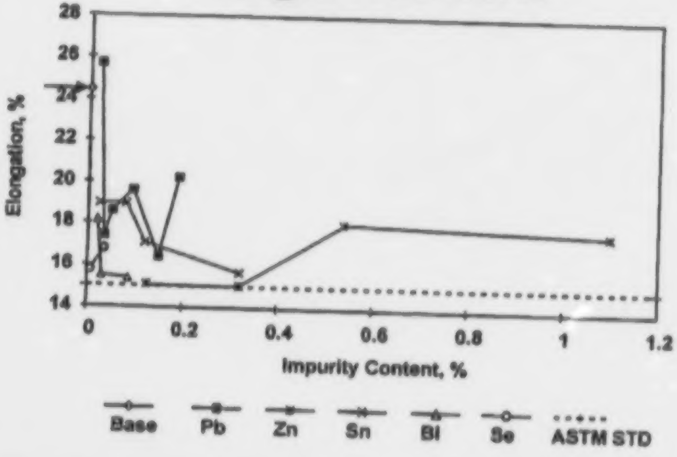

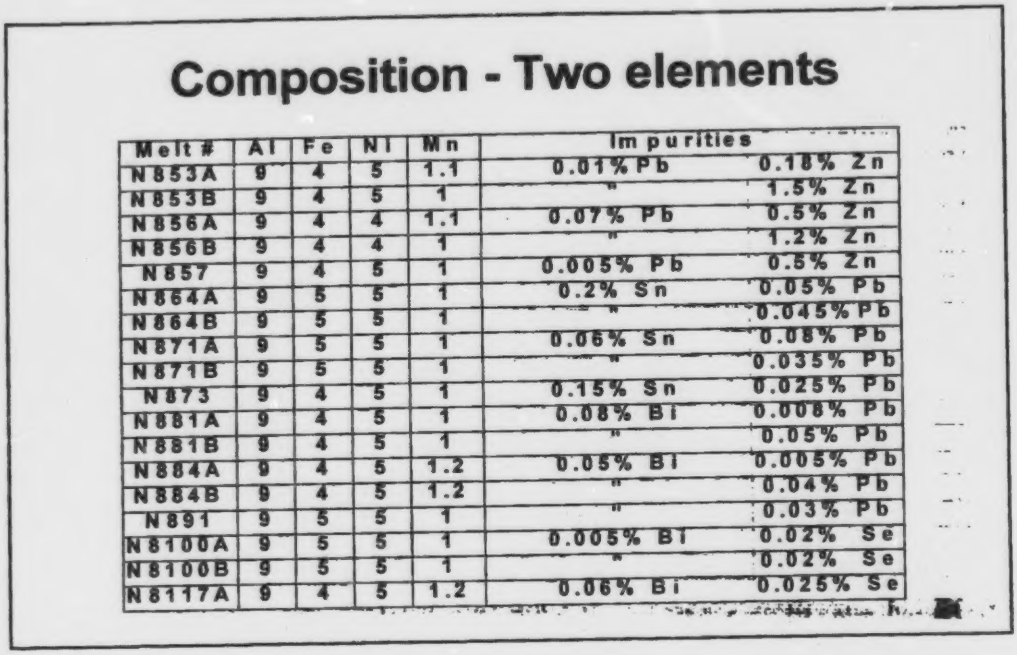

Composition - Two elements

Melt #	Al	Fe	Ni	Mn	Impurities	
N853A	9	4	5	1.1	0.01%Pb	0.18% Zn
N853B	9	4	5	1	"	1.5% Zn
N856A	9	4	4	1.1	0.07% Pb	0.5% Zn
N856B	9	4	4	1	"	1.2% Zn
N857	9	4	5	1	0.005% Pb	0.5% Zn
N864A	9	5	5	1	0.2% Sn	0.05% Pb
N864B	9	5	5	1	"	0.045%Pb
N871A	9	5	5	1	0.06% Sn	0.08% Pb
N871B	9	5	5	1	"	0.035% Pb
N873	9	4	5	1	0.15% Sn	0.025% Pb
N881A	9	4	5	1	0.08% Bi	0.008% Pb
N881B	9	4	5	1	"	0.05% Pb
N884A	9	4	5	1.2	0.05% Bi	0.005% Pb
N884B	9	4	5	1.2	"	0.04% Pb
N891	9	5	5	1	"	0.03% Pb
N8100A	9	5	5	1	0.005% Bi	0.02% Se
N8100B	9	5	5	1	"	0.02% Se
N8117A	9	4	5	1.2	0.06% Bi	0.025% Se

Tensile Strength - Two element

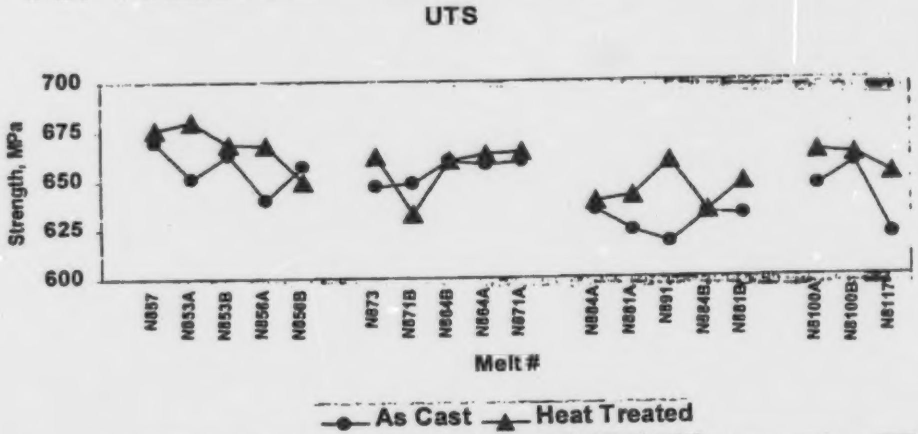

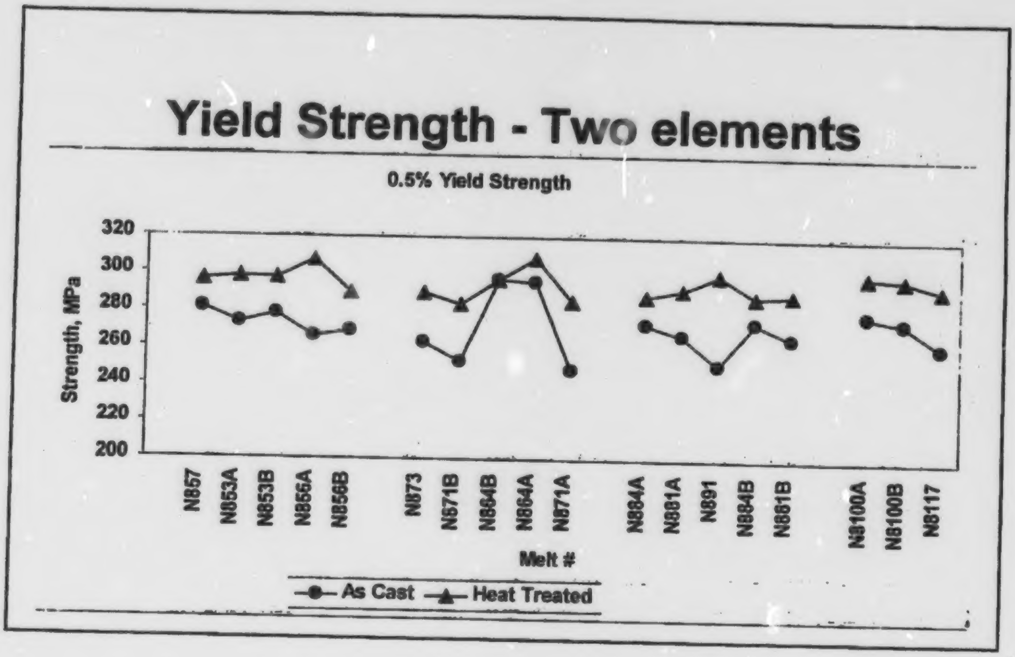

Yield Strength - Two elements

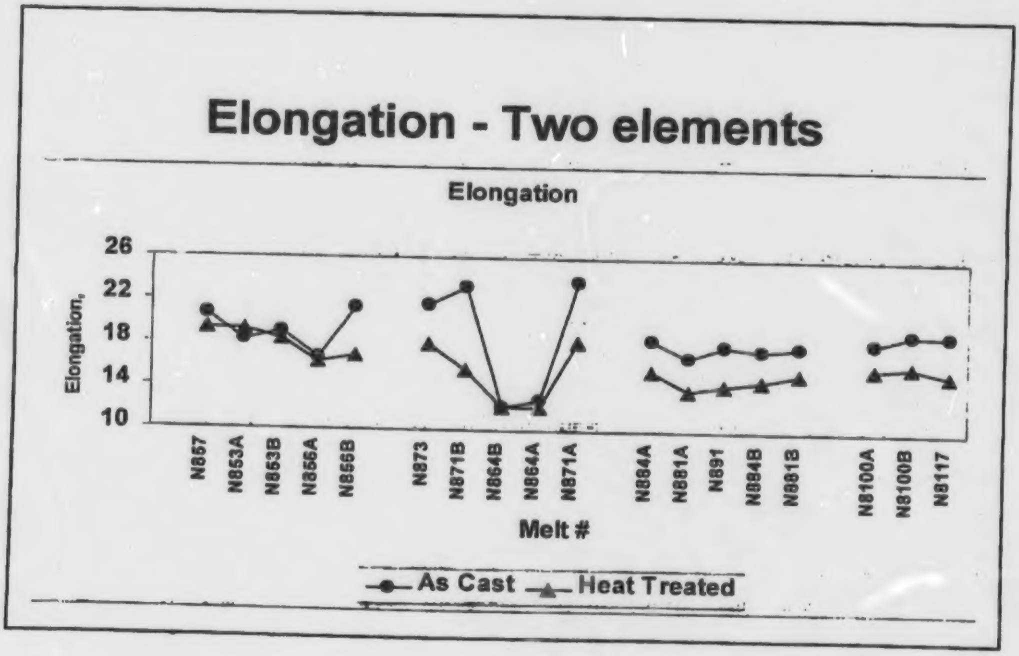

Elongation - Two elements

Weldability

- Cracking in the heat affected zones during welding
- Impurities such as lead, silicon and bismuth are considered to be the cause of cracking
- The lead content is restricted to 0.03% to prevent cracking

Weldability

- Bend tests to evaluate the weld strength
- The plate specimen for testing is selected to be 175x25x15mm.
- The mandrel diameter was 50mm.
- The thickness reduced to 9.8mm and the mandrel daimeter was increased to 62.5mm to obtain as cast specimens free of cracks.

Weldability

- Three weld beads were deposited on the plate using stick electrodes (Ampco Trode 10)
- Bend test specimens were machined with the weld beads in the center of the plates.
- All the welded specimens were broken during testing
- It was necessary to develop a test method to evaluate the weldability

Weldability - Testing

- Heat affected zone simulation using Gleeble
- Specimens were of 75x10x10 mm size
- Preheat the specimen at 140C for 5 seconds
- Heat to the required operating temperature, in this case 950, 980 and 1020C.
- Cool the specimen - air cool and water cool
- analyze the specimen for cracking in the HAZ

Weldability - Results

- Lead and bismuth containing alloys reveal cracks even when heated to 900C and air cooled
- Heating to higher temperatures, some of these specimens rupture
- All other elements, Zn, Sn, Se, Si, Cr or Be have no effect and the HAZ remain crack free.
- In two element combination melts, alloys having Pb-Zn, Pb-Sn and Pb-Bi, show cracking.

Conclusions

- The UTS of C95800 was above minimum ASTM value - 585 MPa.
- All impurity elements improved yield strength in as-cast condition (except low Pb, 0.028%).
- Yield strength improved after heat treatment.
- Ductility was reduced by impurity elements but remained above the 15% minimum in most cases.

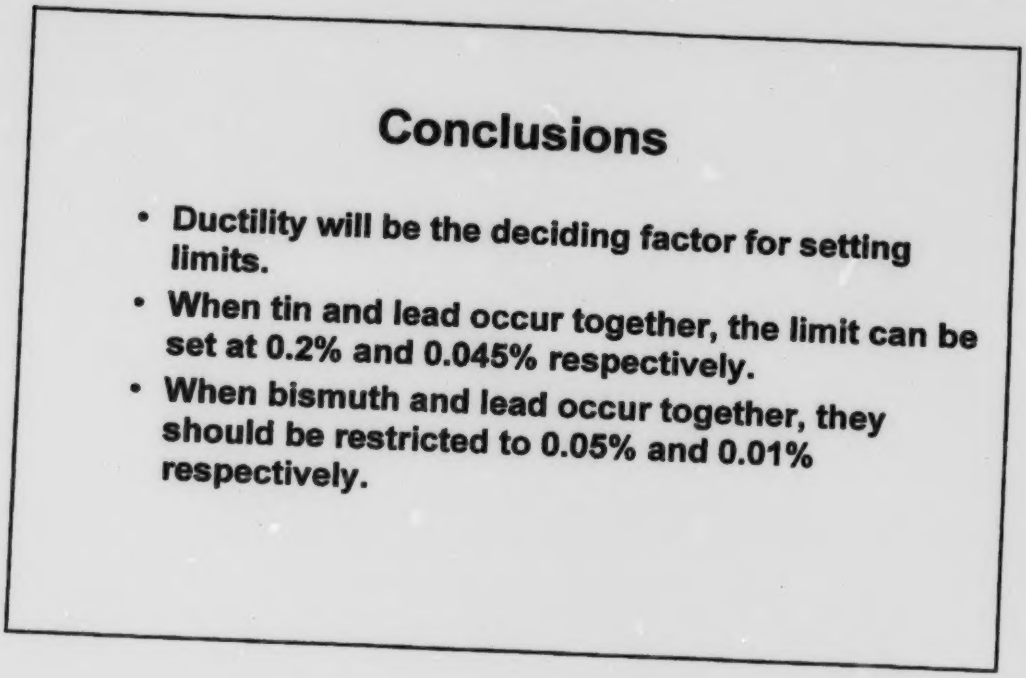

Conclusions

- Ductility will be the deciding factor for setting limits.
- When tin and lead occur together, the limit can be set at 0.2% and 0.045% respectively.
- When bismuth and lead occur together, they should be restricted to 0.05% and 0.01% respectively.

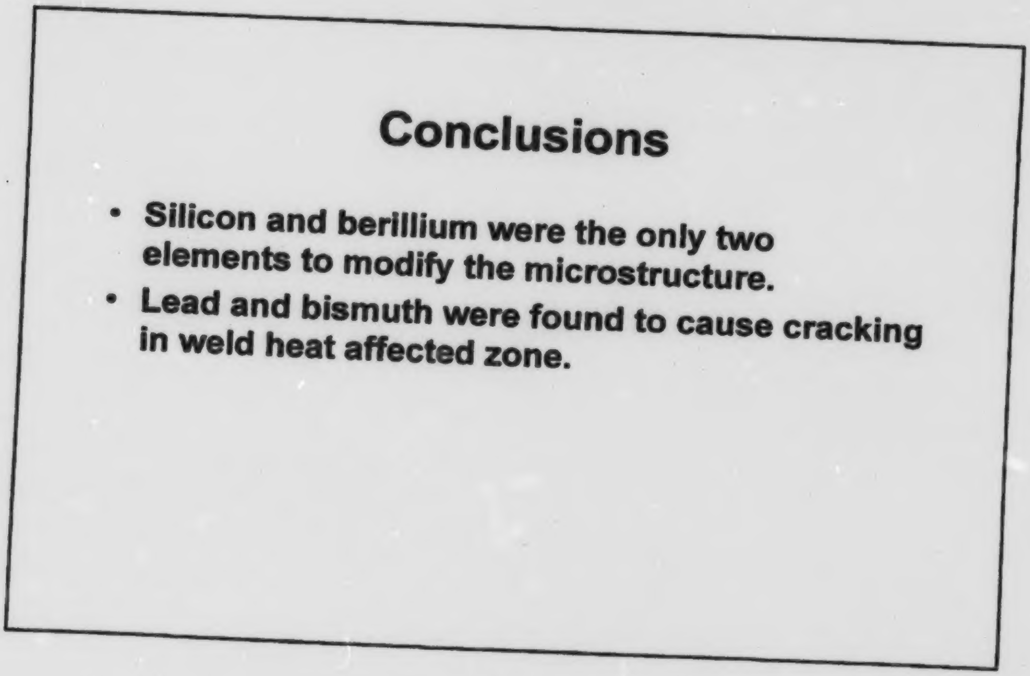

Conclusions

- Silicon and berillium were the only two elements to modify the microstructure.
- Lead and bismuth were found to cause cracking in weld heat affected zone.

#571842

Chemical Analysis of Nickel Aluminum Bronze Alloys

by Gary Fisher

Defence Research Establishment Atlantic, Dockyard Laboratory(Atlantic) P.O. Box 99000 Stn Forces, Halifax, Nova Scotia B3K 5X5

ABSTRACT

A modern laboratory involved in the quantitative chemical analysis of metal alloys has a variety of methodologies from which to select. These methods range from the destructive techniques of traditional wet chemistry and spectrometric methods to the nondestructive optical emission or x-ray techniques that have recently come into vogue. Non-destructive methods are attractive, both in terms of sample integrity and their ability to yield quick results. This paper compares the abilities of destructive techniques (atomic absorption and inductively coupled plasma) with some currently available nondestructive methods (energy dispersive x-ray analysis and spark emission).

DEFENCE R&D DEFENSE

CHEMICAL ANALYSIS OF NICKEL ALUMINUM BRONZE ALLOYS

[illegible] Fleet & SLt [illegible]

[illegible] Establishment

Canada

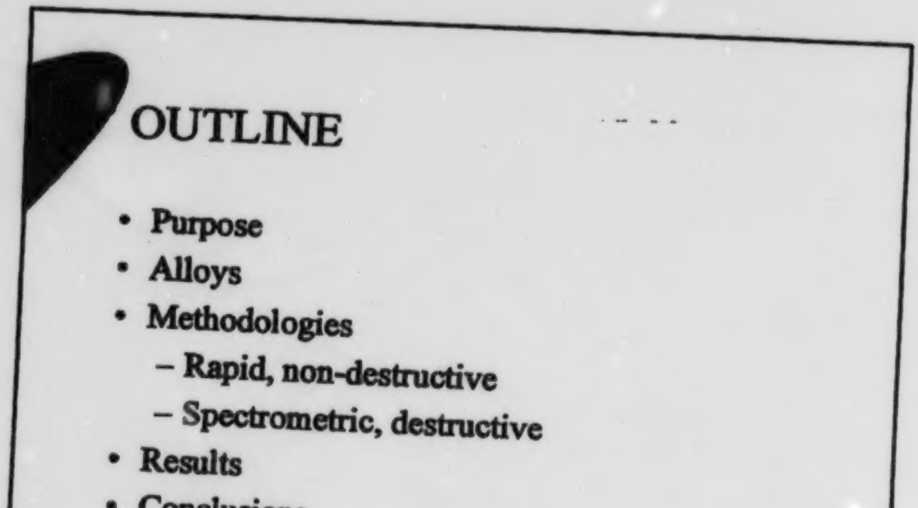

OUTLINE

- Purpose
- Alloys
- Methodologies
  - Rapid, non-destructive
  - Spectrometric, destructive
- Results
- Conclusions

DEFENCE R&D DEFENSE

Defence Research Establishment Atlantic (DREA)

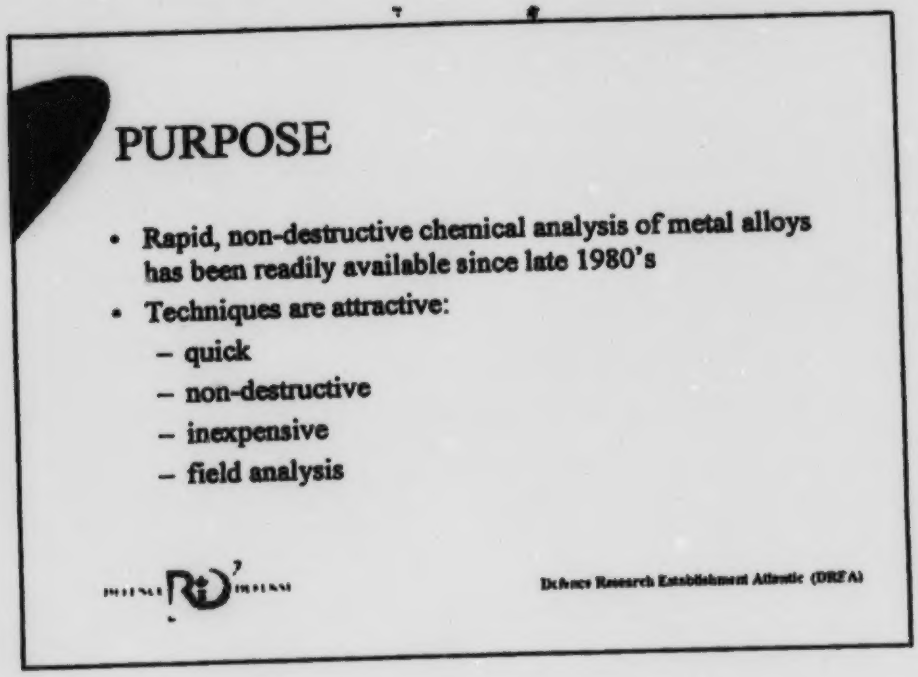

PURPOSE

- Rapid, non-destructive chemical analysis of metal alloys has been readily available since late 1980's
- Techniques are attractive:
  - quick
  - non-destructive
  - inexpensive
  - field analysis

Defence Research Establishment Atlantic (DREA)

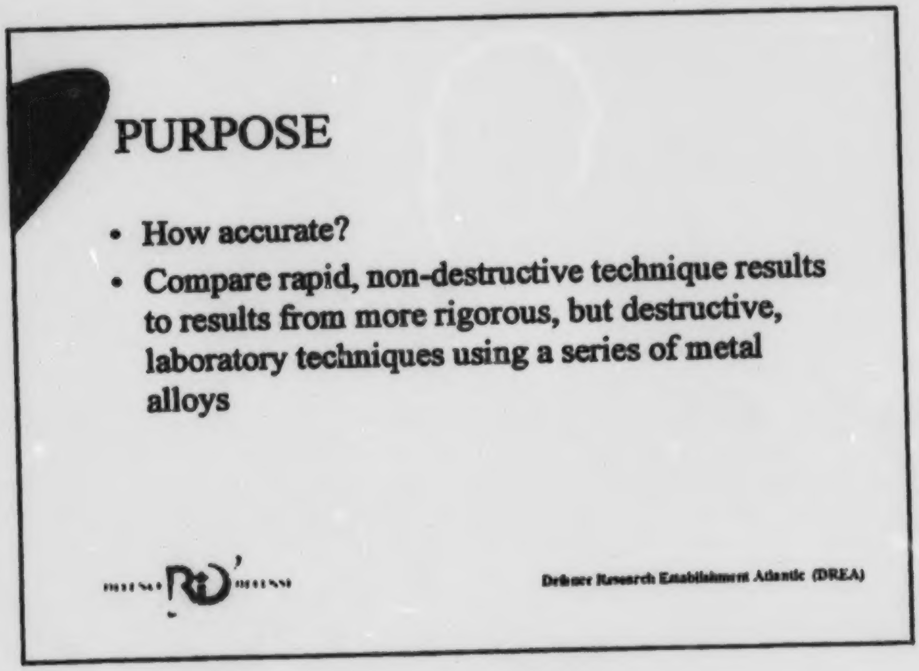

PURPOSE

- How accurate?
- Compare rapid, non-destructive technique results to results from more rigorous, but destructive, laboratory techniques using a series of metal alloys

Defence Research Establishment Atlantic (DREA)

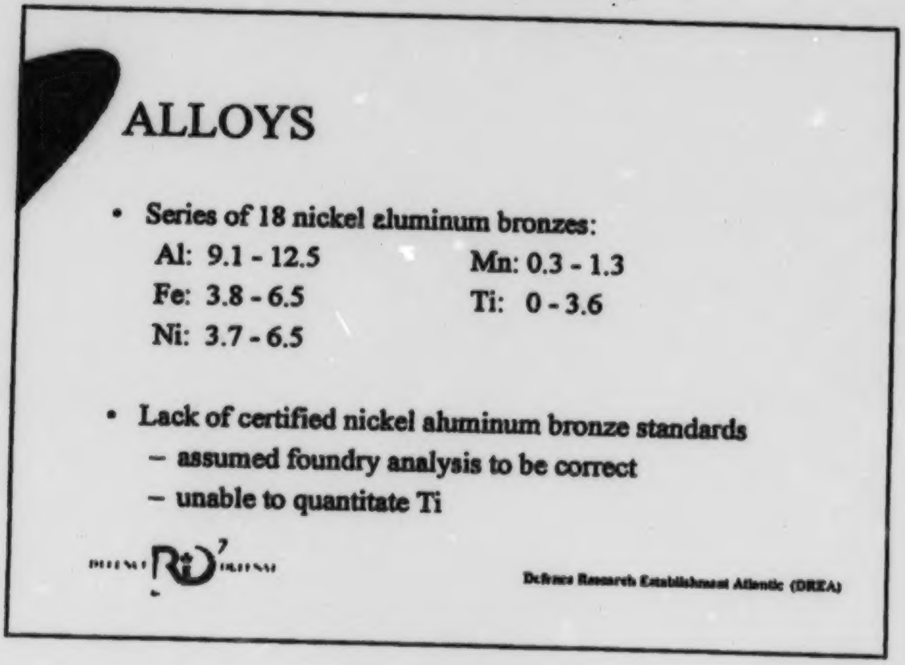

ALLOYS

- Series of 18 nickel aluminum bronzes:

Al: 9.1 - 12.5	Mn: 0.3 - 1.3
Fe: 3.8 - 6.5	Ti: 0 - 3.6
Ni: 3.7 - 6.5	

- Lack of certified nickel aluminum bronze standards
  - assumed foundry analysis to be correct
  - unable to quantitate Ti

Defence Research Establishment Atlantic (DREA)

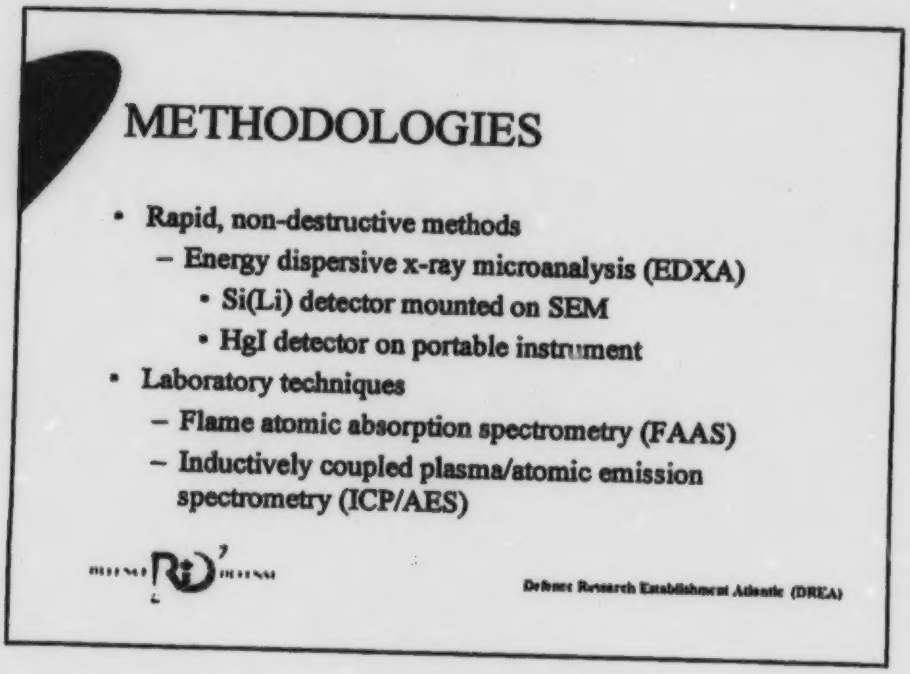

METHODOLOGIES

- Rapid, non-destructive methods
  - Energy dispersive x-ray microanalysis (EDXA)
    - Si(Li) detector mounted on SEM
    - HgI detector on portable instrument
- Laboratory techniques
  - Flame atomic absorption spectrometry (FAAS)
  - Inductively coupled plasma/atomic emission spectrometry (ICP/AES)

Defence Research Establishment Atlantic (DREA)

RAPID METHODS

- EDXA relies on x-ray generation by bombardment of sample by incident particles
- Si(Li) detector system used beam electrons
- HgI detector system utilized radiation from Cd109 and/or Fe55 sources

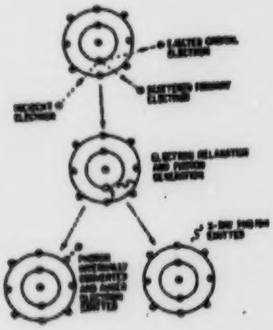

Defence Research Establishment Atlantic (DREA)

RAPID METHODS

HgI Detector

- Predetermined methods
  - Intermediate level
- Orientation less critical
  - flat surface, 600 grit
- Standardless ZAF calculations

- Si(Li) Detector
- Beam energy variable
  - 20 KV accelerating voltage
  - 100 sec count at ~3000 cps
- Orientation critical
  - 30 mm working distance
  - 37.5° take-off angle
- Standardless ZAF calculations

Defence Research Establishment Atlantic (DREA)

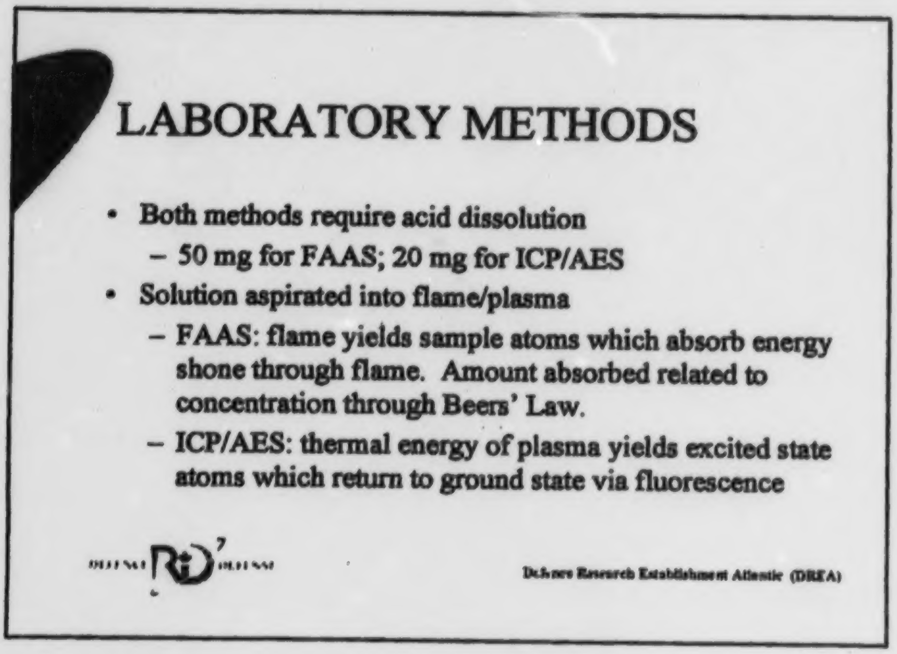

LABORATORY METHODS

- Both methods require acid dissolution
  - 50 mg for FAAS; 20 mg for ICP/AES
- Solution aspirated into flame/plasma
  - FAAS: flame yields sample atoms which absorb energy shone through flame. Amount absorbed related to concentration through Beers' Law.
  - ICP/AES: thermal energy of plasma yields excited state atoms which return to ground state via fluorescence

Defence Research Establishment Atlantic (DREA)

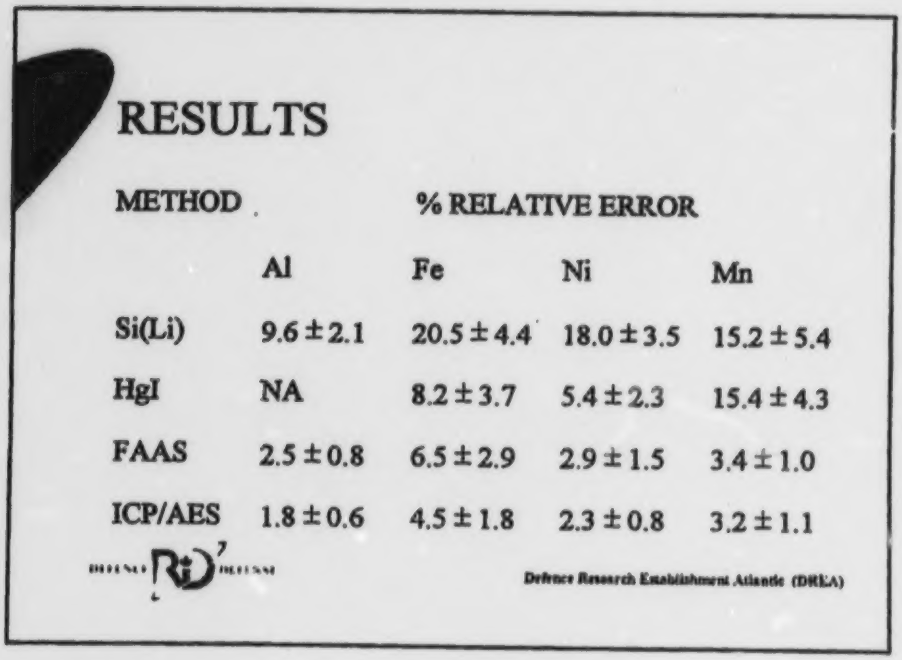

RESULTS

METHOD	% RELATIVE ERROR			
	Al	Fe	Ni	Mn
Si(Li)	9.6 ± 2.1	20.5 ± 4.4	18.0 ± 3.5	15.2 ± 5.4
HgI	NA	8.2 ± 3.7	5.4 ± 2.3	15.4 ± 4.3
FAAS	2.5 ± 0.8	6.5 ± 2.9	2.9 ± 1.5	3.4 ± 1.0
ICP/AES	1.8 ± 0.6	4.5 ± 1.8	2.3 ± 0.8	3.2 ± 1.1

Defence Research Establishment Atlantic (DREA)

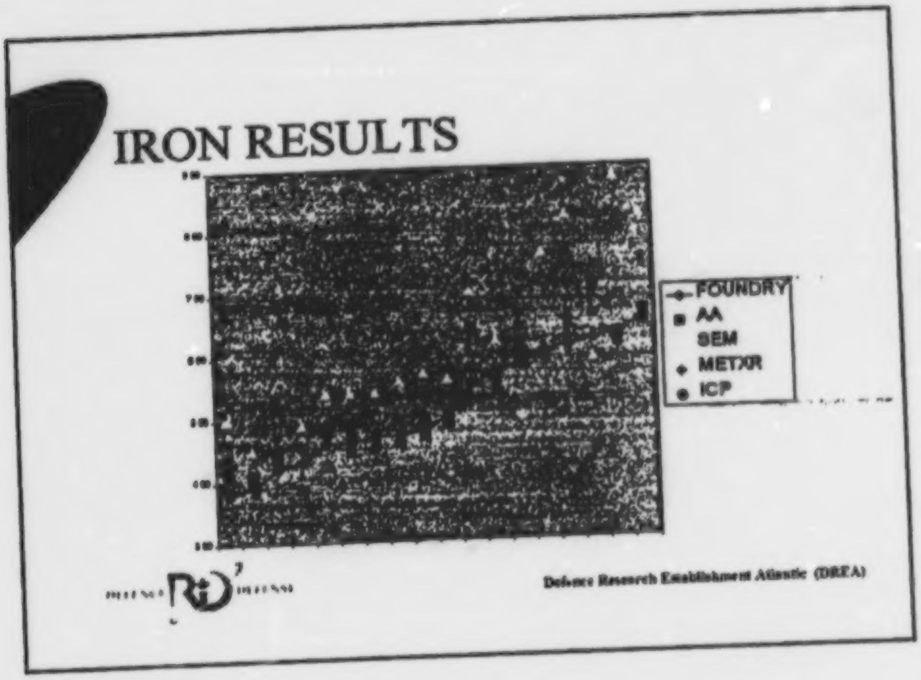

IRON RESULTS

Defence Research Establishment Atlantic (DREA)

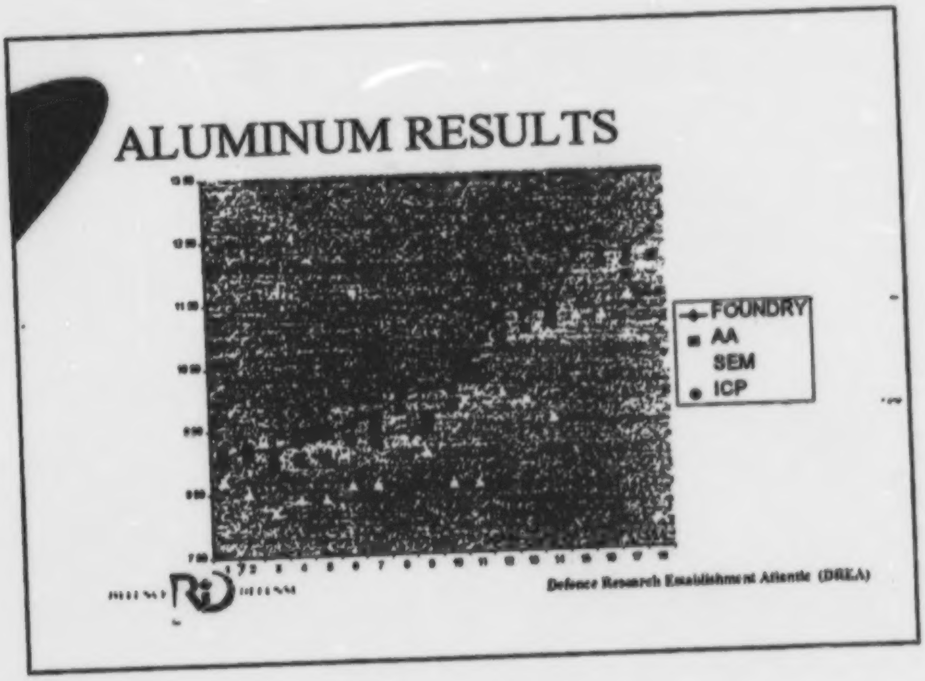

ALUMINUM RESULTS

Defence Research Establishment Atlantic (DREA)

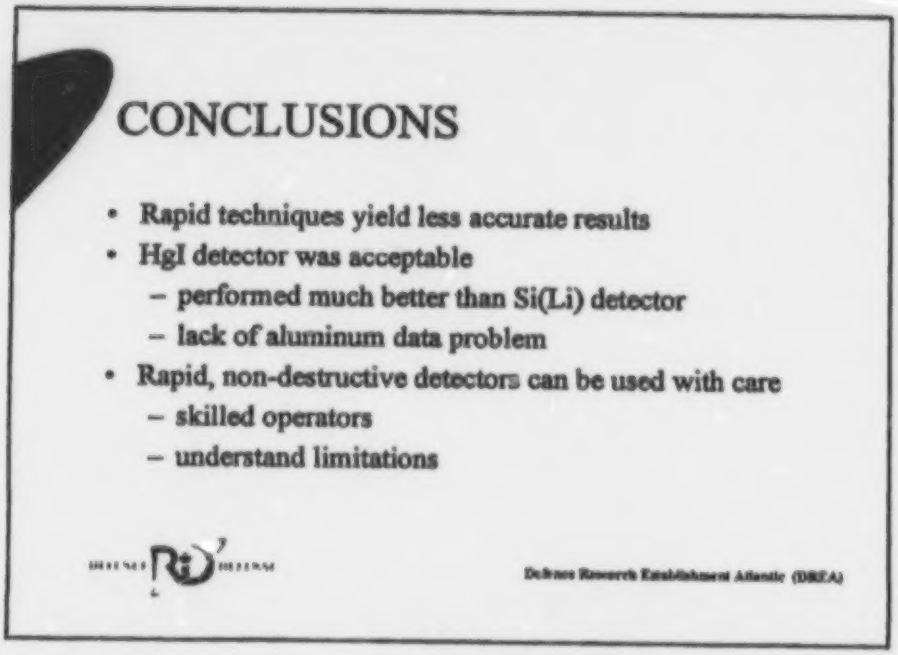

CONCLUSIONS

- Rapid techniques yield less accurate results
- HgI detector was acceptable
  - performed much better than Si(Li) detector
  - lack of aluminum data problem
- Rapid, non-destructive detectors can be used with care
  - skilled operators
  - understand limitations

Defence Research Establishment Atlantic (DREA)

The Defence Research
and Development Branch
provides Science and
Technology leadership
in the advancement and
maintenance of Canada's
defence capabilities.

DEFENCE DEFENSE

#511893

Characterization of a Nickel Aluminum Bronze Laser-Clad Weldment

by J.A. Gianetto and R.H. Packwood

Materials Technology Laboratory-CANMET
Ottawa, Ontario, Canada

ABSTRACT

The microstructural and compositional variations that exist across a laser-clad weldment produced with a heat input of 150 J/cm and filler wire composition Cu-9.0% Al, 4.6% Ni, 3.9% Fe and 1.2% Mn have been characterized. The weld metal, heat-affected zone and casting base metal structures and elemental distributions were evaluated using light optical microscope and electron microprobe, respectively. The results show that a considerable range of microstructures and some significant compositional variations are present in the laser-clad weldment investigated.

CHARACTERIZATION OF A NICKEL ALUMINUM BRONZE LASER-CLAD WELDMENT

by

J.A. Gianetto and R.H. Packwood

Materials Technology Laboratory-CANMET
Ottawa, Ontario, Canada

Acknowledgments
Judith Price
Vera Weatherall
Catherine Bibby

Materials Technology Laboratory-CANMET

Objective

To characterize the microstructural features and corresponding elemental distributions that exist in a low heat input laser clad weldment.

Materials Technology Laboratory-CANMET

Reference Laser Weld Cladding

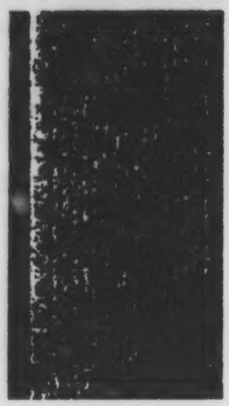

- Shielding Gas = Ar
- Laser Power = 3300 W
- Heat Input = 150 J/mm
- Wire Diameter = 0.25 mm
- Overlay consists of alternating as-deposited and reheated weld metal.

Materials Technology Laboratory-CANMET

Experimental Approach

- Characterize microstructure optically and
- Use the Cameca SX-51 EPMA to determine elemental distributions for:
  - as-deposited and reheated weld metal
  - fusion zone transition region (dendritic)
  - HAZ
  - casting base metal

Materials Technology Laboratory-CANMET

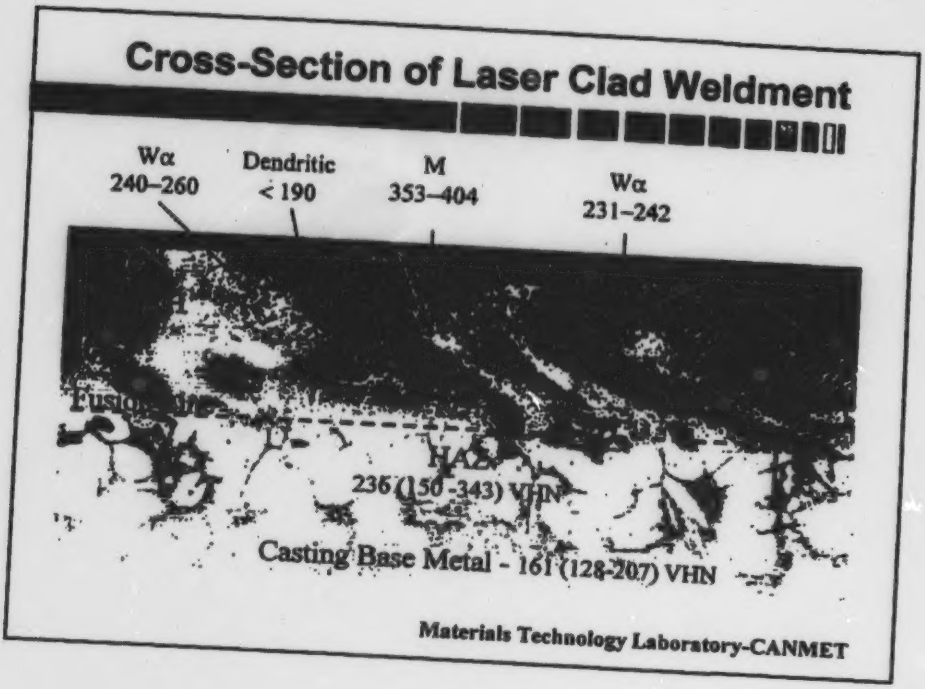

Cross-Section of Laser Clad Weldment

Wα
240–260
Dendritic
< 190
M
353–404
Wα
231–242
Fusion Line
HAZ
236 (150-343) VHN
Casting Base Metal - 161 (128-207) VHN

Materials Technology Laboratory-CANMET

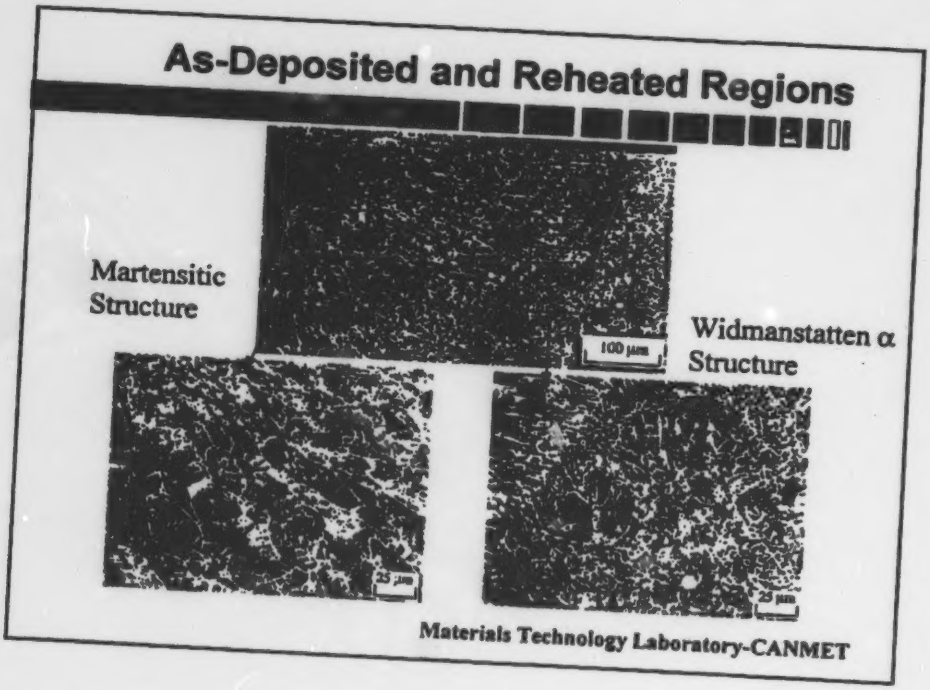

As-Deposited and Reheated Regions

Martensitic
Structure
Widmanstatten α
Structure
100 μm
25 μm
25 μm

Materials Technology Laboratory-CANMET

As-deposited and Reheated Regions

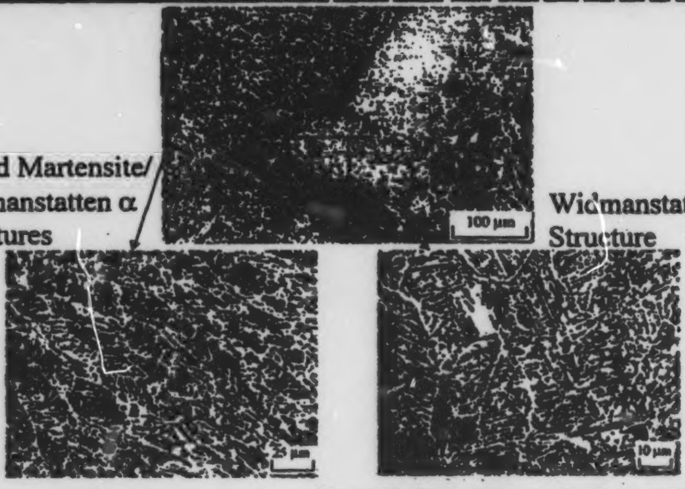

Mixed Martensite/
Widmanstatten α
Structures

Widmanstatten α
Structure

Materials Technology Laboratory-CANMET

HAZ and Base Metal Structures

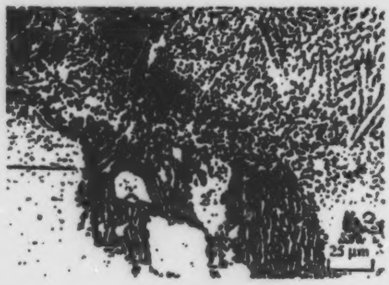

HAZ

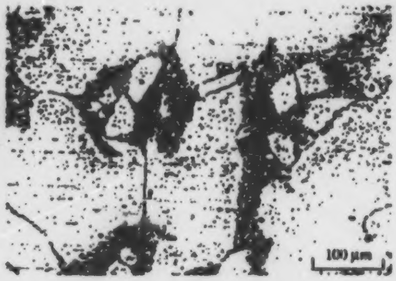

Base Metal

Materials Technology Laboratory-CANMET

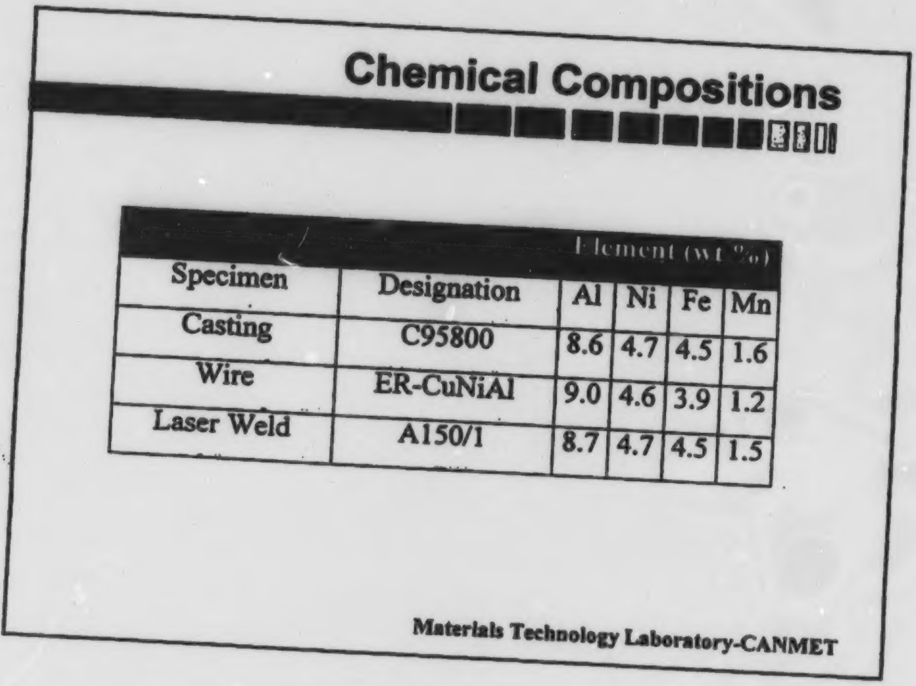

Chemical Compositions

		Element (wt %)			
Specimen	Designation	Al	Ni	Fe	Mn
Casting	C95800	8.6	4.7	4.5	1.6
Wire	ER-CuNiAl	9.0	4.6	3.9	1.2
Laser Weld	A150/1	8.7	4.7	4.5	1.5

Materials Technology Laboratory-CANMET

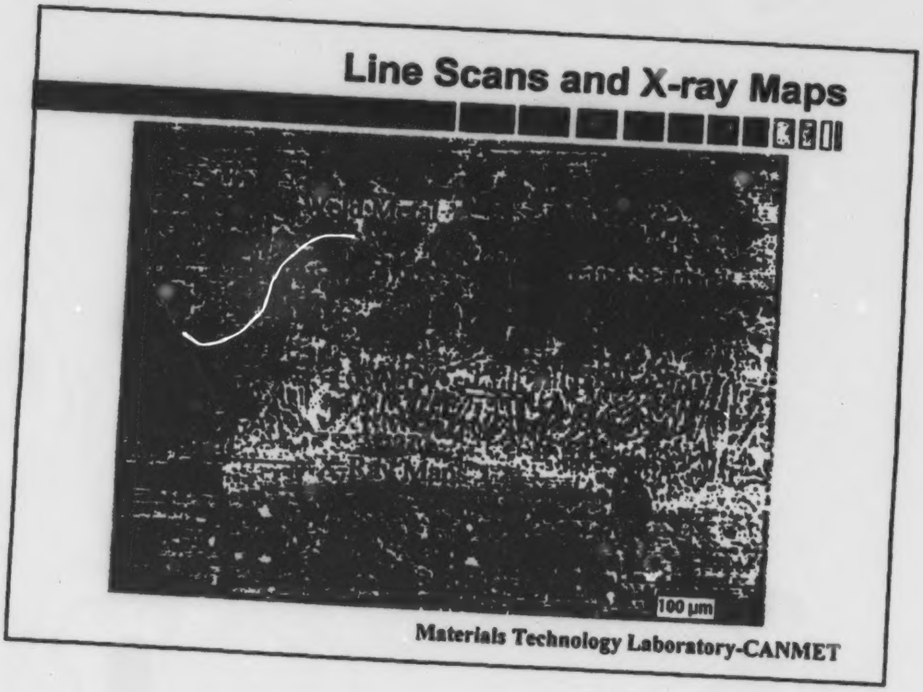

Line Scans and X-ray Maps

Materials Technology Laboratory-CANMET

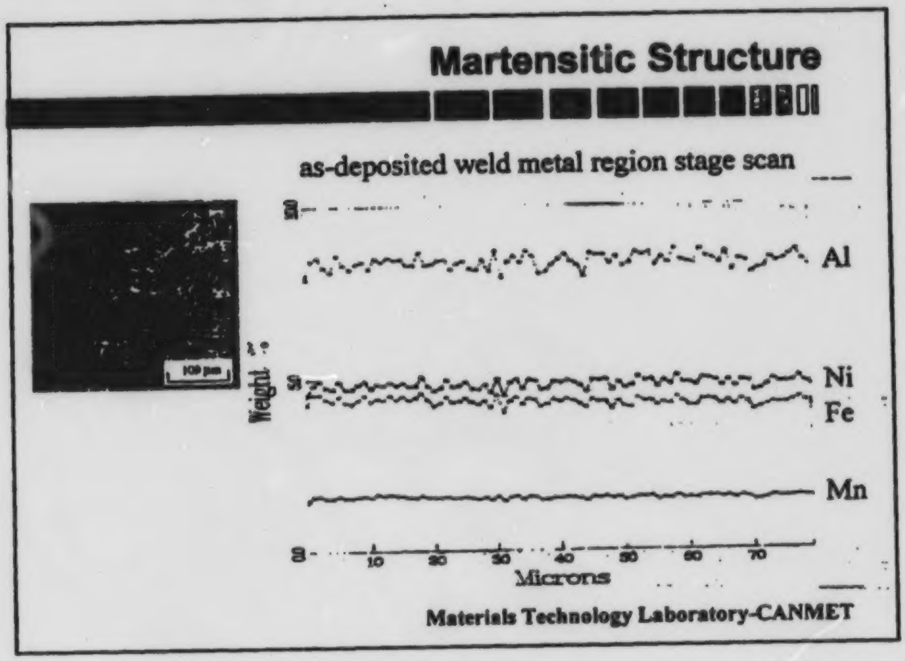

Martensitic Structure

as-deposited weld metal region stage scan

100 µm
100
Al
Weight %
50
Ni
Fe
Mn
0
10
20
30
40
50
60
70
Microns

Materials Technology Laboratory-CANMET

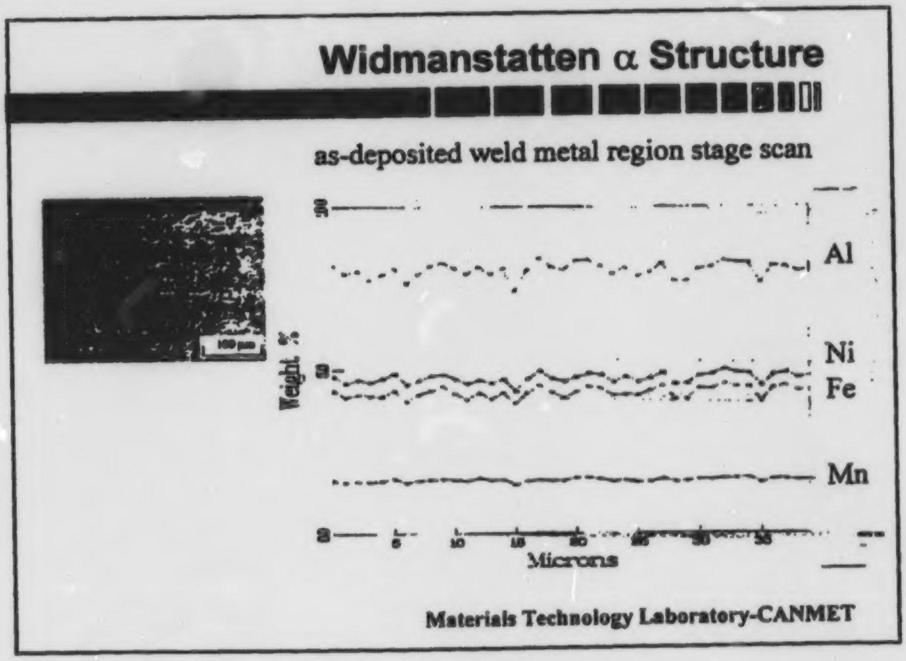

Widmanstatten α Structure

as-deposited weld metal region stage scan

100 µm
100
Al
Weight %
50
Ni
Fe
Mn
0
5
10
15
20
25
30
35
Microns

Materials Technology Laboratory-CANMET

Fusion Zone Dendritic Region

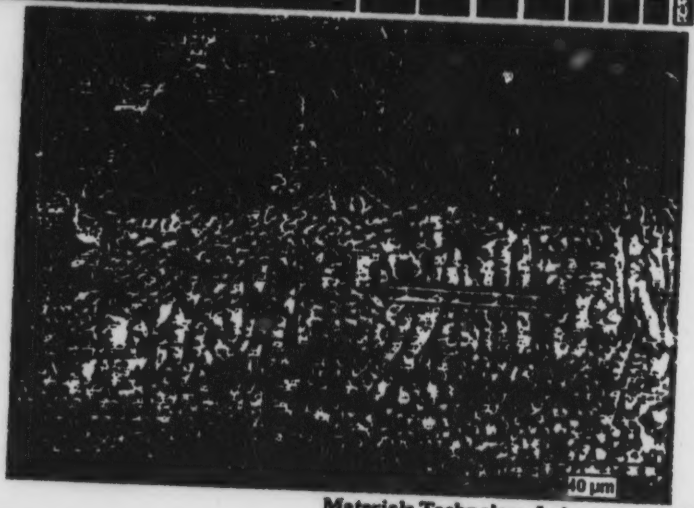

Materials Technology Laboratory-CANMET

Fusion Zone Dendritic Region

- peaks correspond to dark interdendritic regions

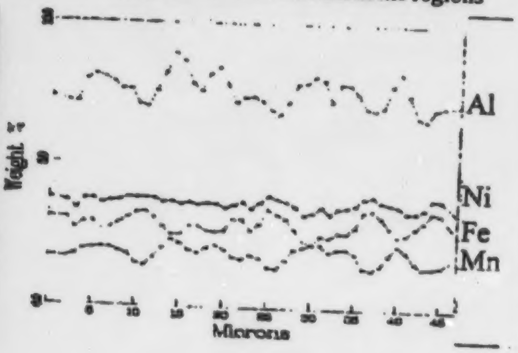

Materials Technology Laboratory-CANMET

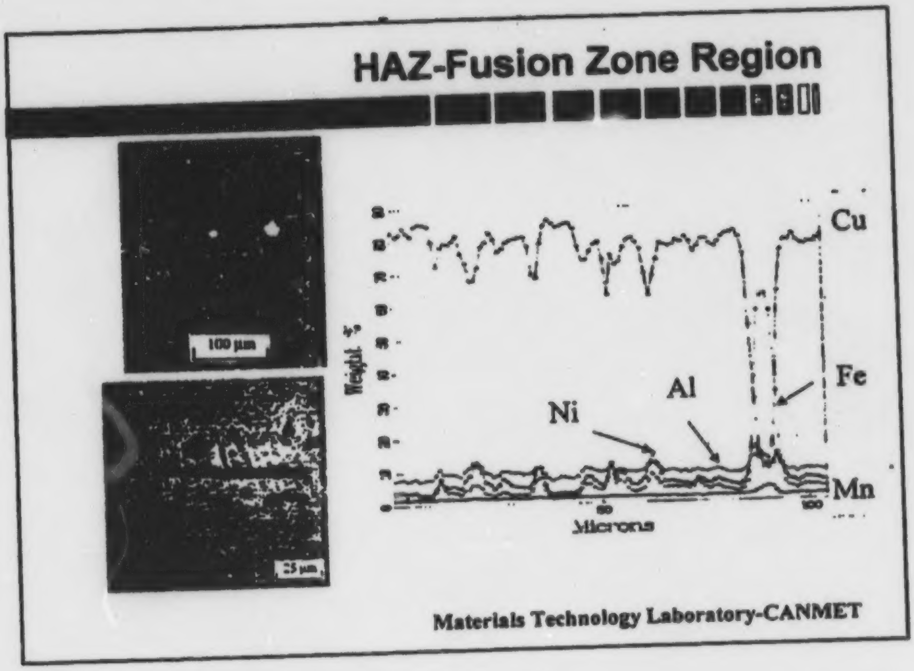

HAZ-Fusion Zone Region

Materials Technology Laboratory-CANMET

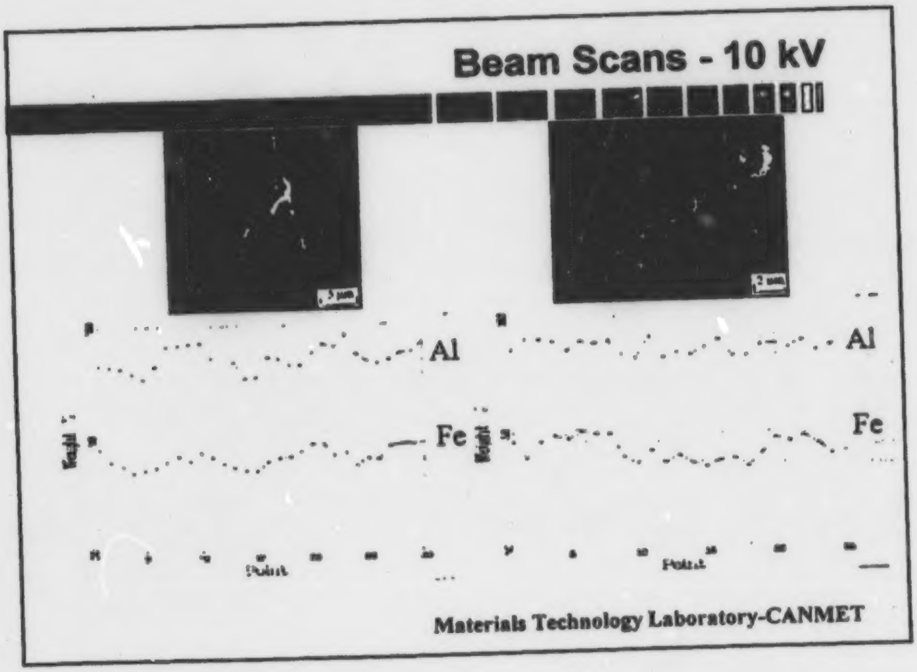

Beam Scans - 10 kV

Materials Technology Laboratory-CANMET

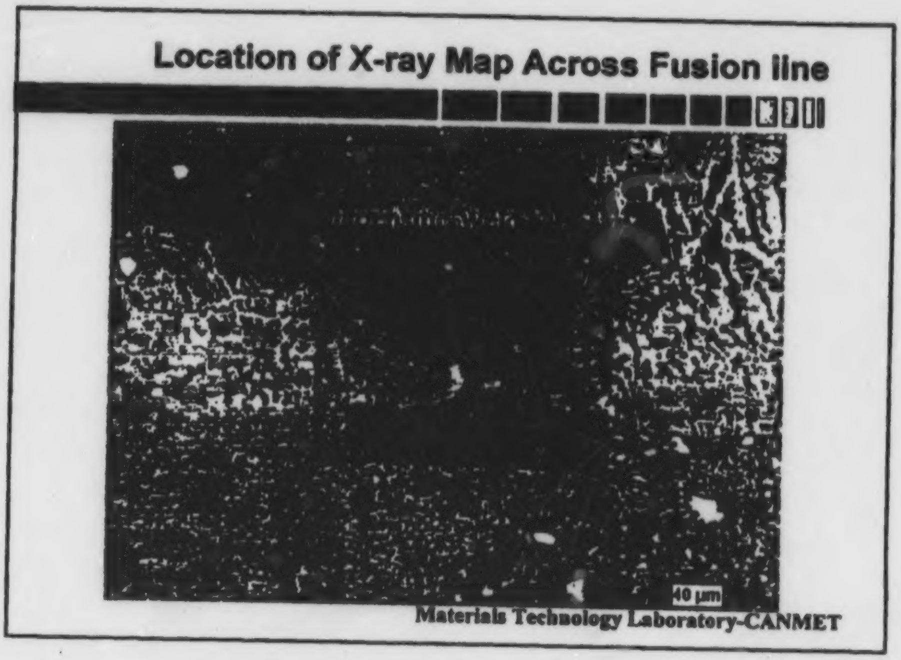

Location of X-ray Map Across Fusion line

Materials Technology Laboratory-CANMET

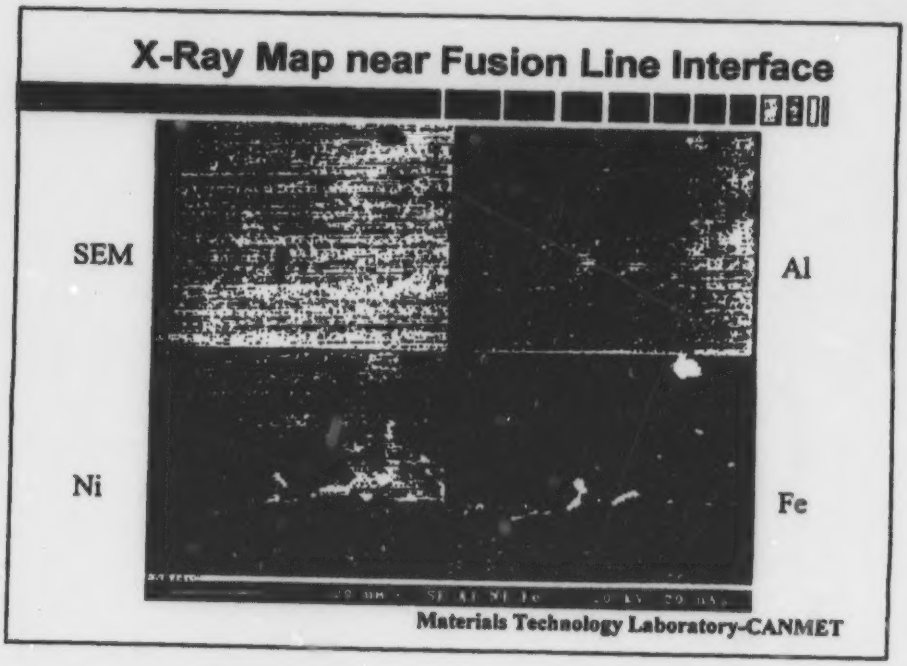

X-Ray Map near Fusion Line Interface

Materials Technology Laboratory-CANMET

X-Ray Map Below Fusion Zone

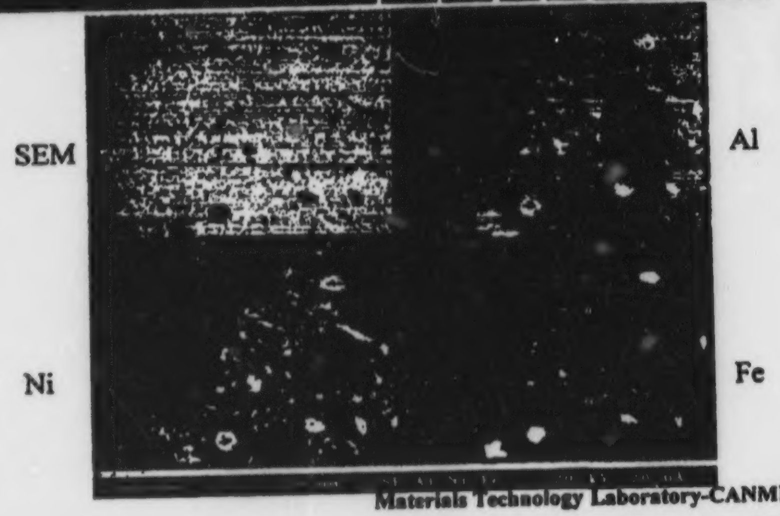

Materials Technology Laboratory-CANMET

Stage Scan X-ray Map

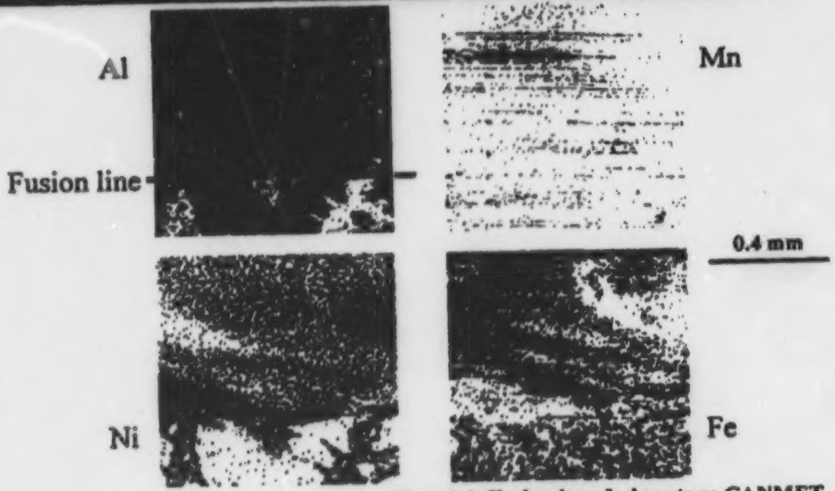
Al
Mn
Fusion line
0.4 mm
Ni
Fe

Materials Technology Laboratory-CANMET

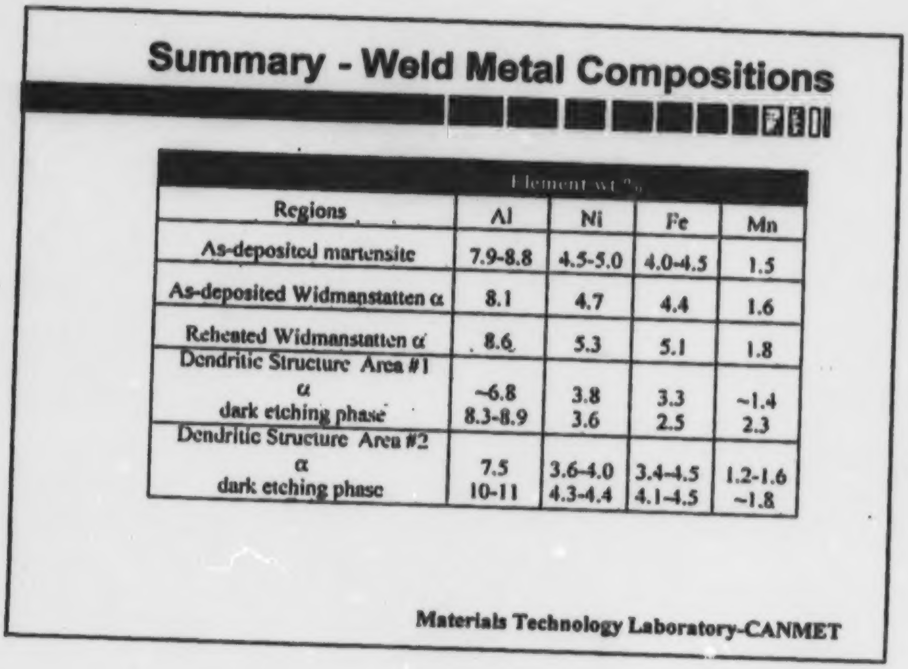

Summary - Weld Metal Compositions

	Element wt %			
Regions	Al	Ni	Fe	Mn
As-deposited martensite	7.9-8.8	4.5-5.0	4.0-4.5	1.5
As-deposited Widmanstatten α	8.1	4.7	4.4	1.6
Reheated Widmanstatten α'	8.6	5.3	5.1	1.8
Dendritic Structure Area #1				
α	~6.8	3.8	3.3	~1.4
dark etching phase	8.3-8.9	3.6	2.5	2.3
Dendritic Structure Area #2				
α	7.5	3.6-4.0	3.4-4.5	1.2-1.6
dark etching phase	10-11	4.3-4.4	4.1-4.5	~1.8

Materials Technology Laboratory-CANMET

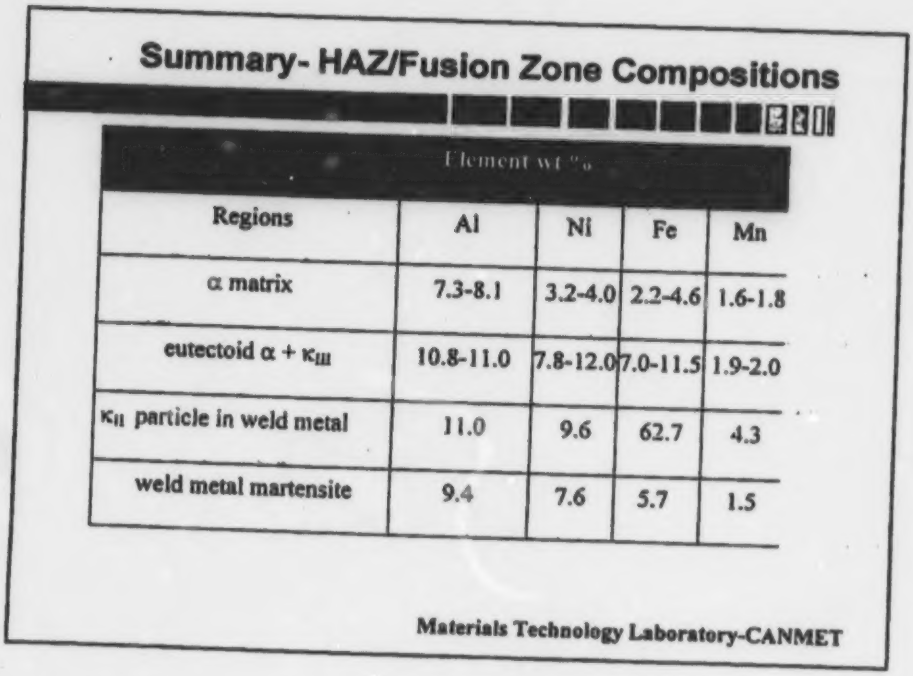

Summary- HAZ/Fusion Zone Compositions

	Element wt %			
Regions	Al	Ni	Fe	Mn
α matrix	7.3-8.1	3.2-4.0	2.2-4.6	1.6-1.8
eutectoid $\alpha + \kappa_{III}$	10.8-11.0	7.8-12.0	7.0-11.5	1.9-2.0
κ_{II} particle in weld metal	11.0	9.6	62.7	4.3
weld metal martensite	9.4	7.6	5.7	1.5

Materials Technology Laboratory-CANMET

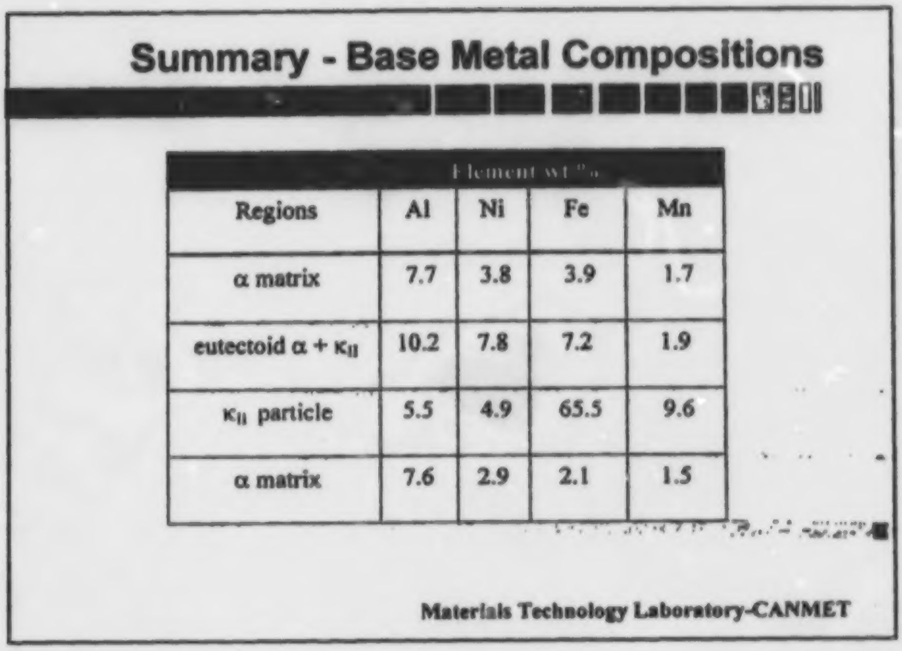

Summary - Base Metal Compositions

	Element wt %			
Regions	Al	Ni	Fe	Mn
α matrix	7.7	3.8	3.9	1.7
eutectoid α + κ_{II}	10.2	7.8	7.2	1.9
κ_{II} particle	5.5	4.9	65.5	9.6
α matrix	7.6	2.9	2.1	1.5

Materials Technology Laboratory-CANMET

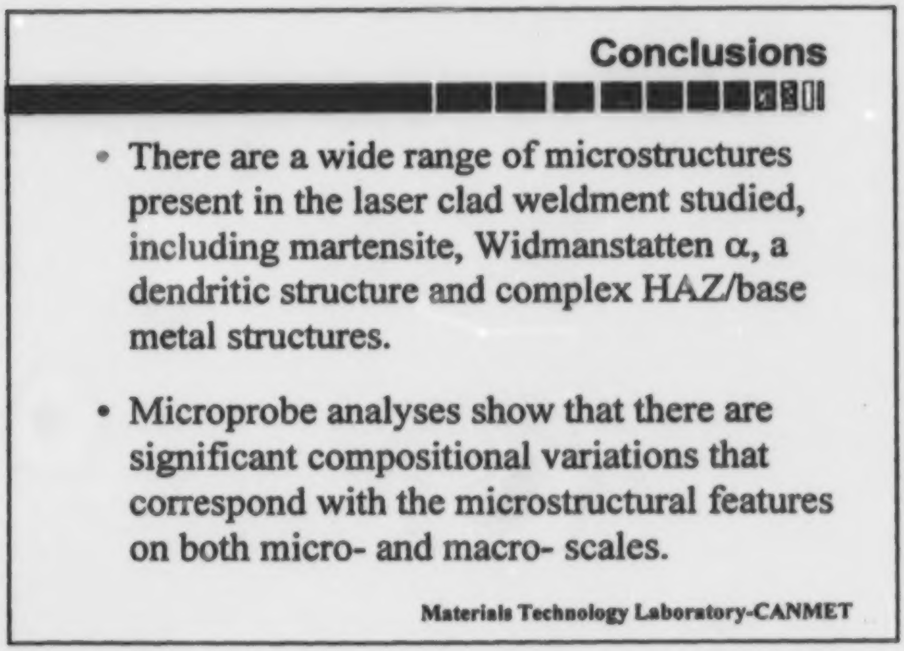

Conclusions

- There are a wide range of microstructures present in the laser clad weldment studied, including martensite, Widmanstatten α, a dendritic structure and complex HAZ/base metal structures.
- Microprobe analyses show that there are significant compositional variations that correspond with the microstructural features on both micro- and macro- scales.

Materials Technology Laboratory-CANMET

#511894

The Development of Microstructure in the Laser Cladding of Nickel Aluminum Bronze

by Calvin V. Hyatt[1], J. Craig Bennett[2] and J. Gianetto[3]

[1]Defence Research Establishment Atlantic, Dockyard Laboratory (Atlantic)
P.O. Box 99000 Stn Forces, Halifax, Nova Scotia, Canada B3K 5X5

[2]Acadia University, Wolfville, Nova Scotia, Canada

[3]Materials Technology Laboratory, Ottawa, Ontario, Canada

ABSTRACT

Laser Cladding with nickel aluminum bronze has much promise for the repair and surface engineering of components made from nickel aluminum bronzes and from other alloys. Until recently, comprehensive understanding of how microstructure develops in this alloy, under the rapid rates of cooling typical of laser methods, has been missing. This presentation will summarize our understanding of how microstructures develop in the as-deposited, re-heated and heat affected zones of laser clad nickel aluminum bronzes. Consideration of the effects of interpass temperature, nickel/iron ratio, and aluminum content will be given. The difficulties these microstructures impose for residual stress measurement and implications of these microstructures for properties will also be considered.

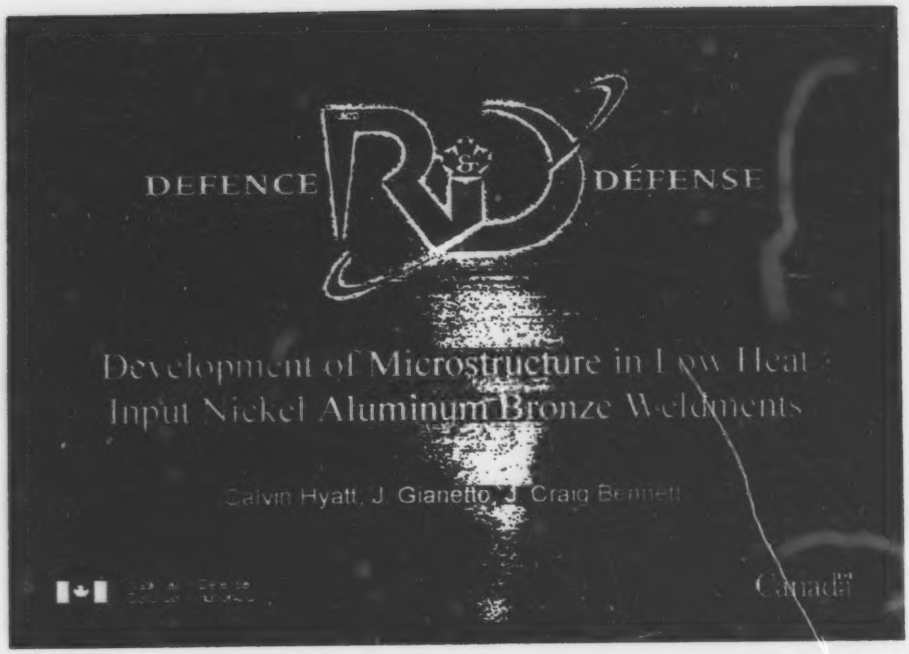

DEFENCE DÉFENSE

Development of Microstructure in Low Heat Input Nickel Aluminum Bronze Weldments

Calvin Hyatt, J. Gianetto, J. Craig Bennett

Canada

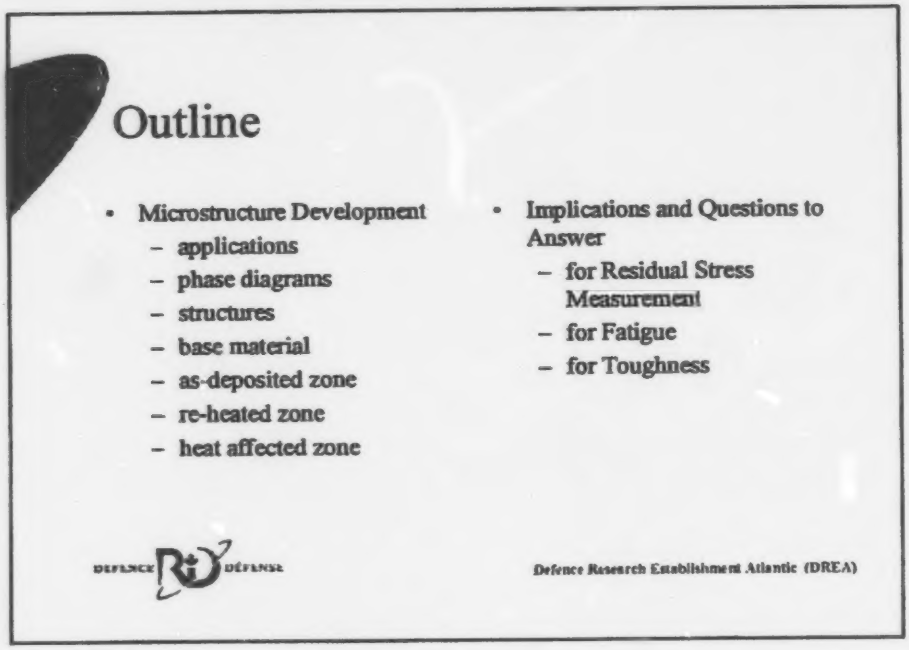

Outline

- Microstructure Development
  - applications
  - phase diagrams
  - structures
  - base material
  - as-deposited zone
  - re-heated zone
  - heat affected zone
- Implications and Questions to Answer
  - for Residual Stress Measurement
  - for Fatigue
  - for Toughness

DEFENCE DÉFENSE

Defence Research Establishment Atlantic (DREA)

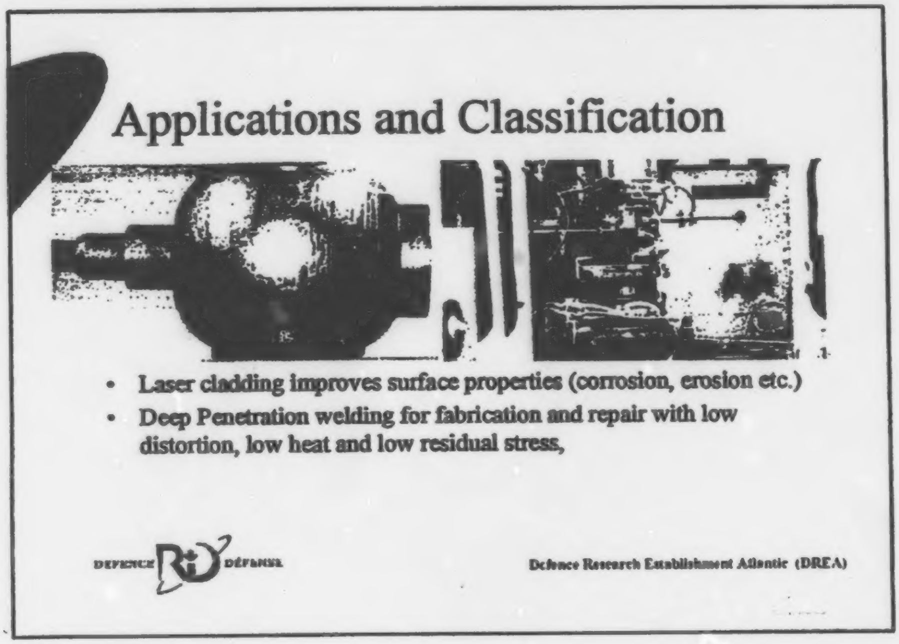

Applications and Classification

- Laser cladding improves surface properties (corrosion, erosion etc.)
- Deep Penetration welding for fabrication and repair with low distortion, low heat and low residual stress,

DEFENCE R&D DÉFENSE

Defence Research Establishment Atlantic (DREA)

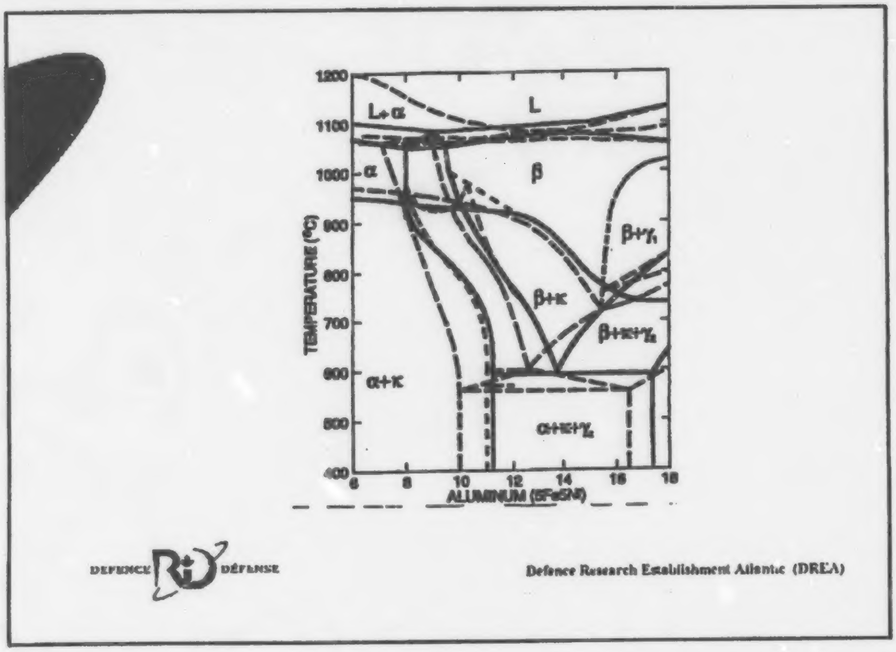

DEFENCE R&D DÉFENSE

Defence Research Establishment Atlantic (DREA)

Phases in nickel aluminum bronze

α	fcc	Cu solid solution
β, β'	bcc, ordered bcc	High temp phase
κ_I	Several structures	Cored, Fe rich, mel
κ_{II}	Fe_3Al	Fe rich, solid state
κ_{III}	NiAl	Ni rich, eutectoid
κ_{IV}	Fe_3Al	High Fe
Martensites	9R, (3R Cast),	Distorted, faulted fcc

DEFENCE RD DÉFENSE

Defence Research Establishment Atlantic (DREA)

Nickel Aluminum Bronze As-cast structure, Base Material

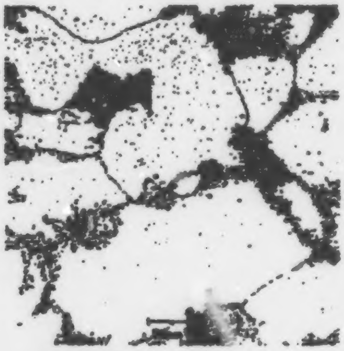

- Liquid to β to $\alpha+\kappa_I,+\kappa_{II},+\kappa_{III},+\kappa_{IV}$ + Martensite (β*)
- homogeneity determined by composition, casting size, cooling rate and heat treatment

DEFENCE RD DÉFENSE

Defence Research Establishment Atlantic (DREA)

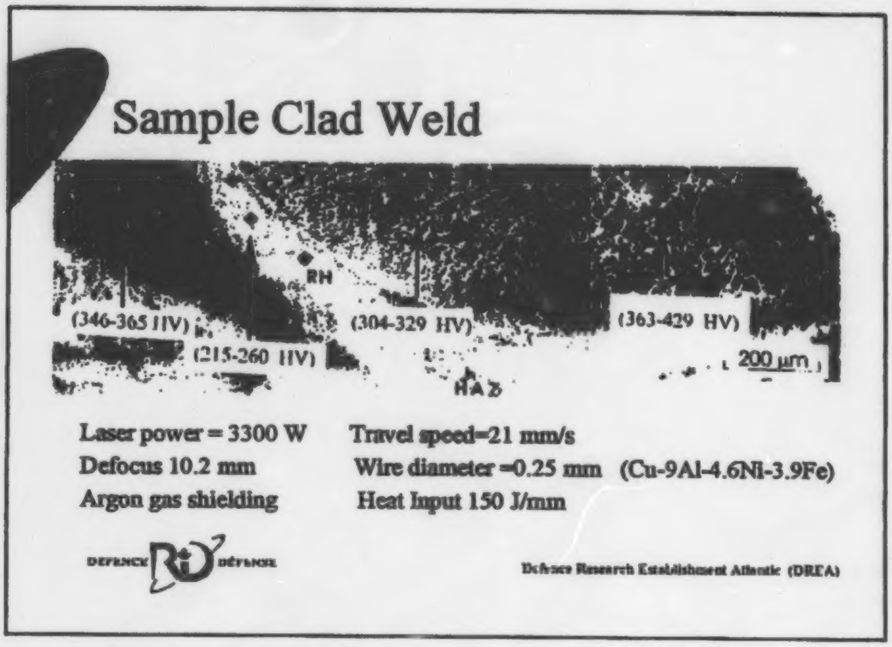

Sample Clad Weld

Laser power = 3300 W
Defocus 10.2 mm
Argon gas shielding

Travel speed=21 mm/s
Wire diameter =0.25 mm (Cu-9Al-4.6Ni-3.9Fe)
Heat Input 150 J/mm

DEFENCE DÉFENSE

Defence Research Establishment Atlantic (DREA)

Heat Affected Zone

- Transforms between 1040 and 400°C, $\Delta t_{800\text{-}500^{\circ}C} < 1$sec
- Prior cast structure not homogenized, little coarsening, even in small castings
- regions of α phase remain
- regions of κ_I, κ_{II}, κ_{III}, κ_{IV}, and martensite, undergo partial or complete retransformation to β followed by martensite formation at ~150°C (Widmanstattan α, κ, for higher heat inputs/interpass)
- Martensite in heat affected zone phases may cause trouble in fracture and fatigue of penetration welds (even low Al)

DEFENCE DÉFENSE

Defence Research Establishment Atlantic (DREA)

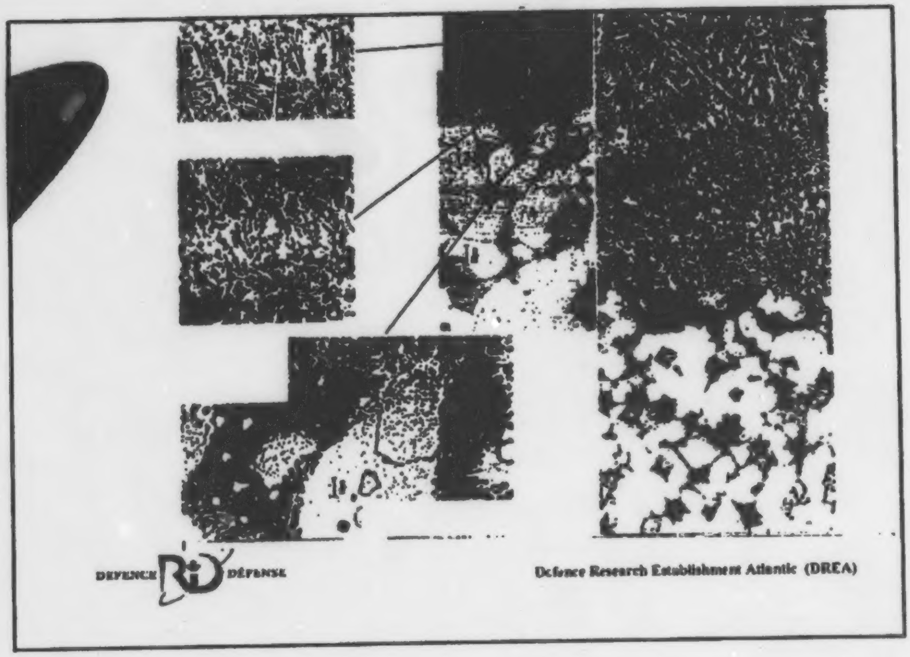

DEFENCE DÉFENSE

Defence Research Establishment Atlantic (DREA)

DEFENCE DÉFENSE

Defence Research Establishment Atlantic (DREA)

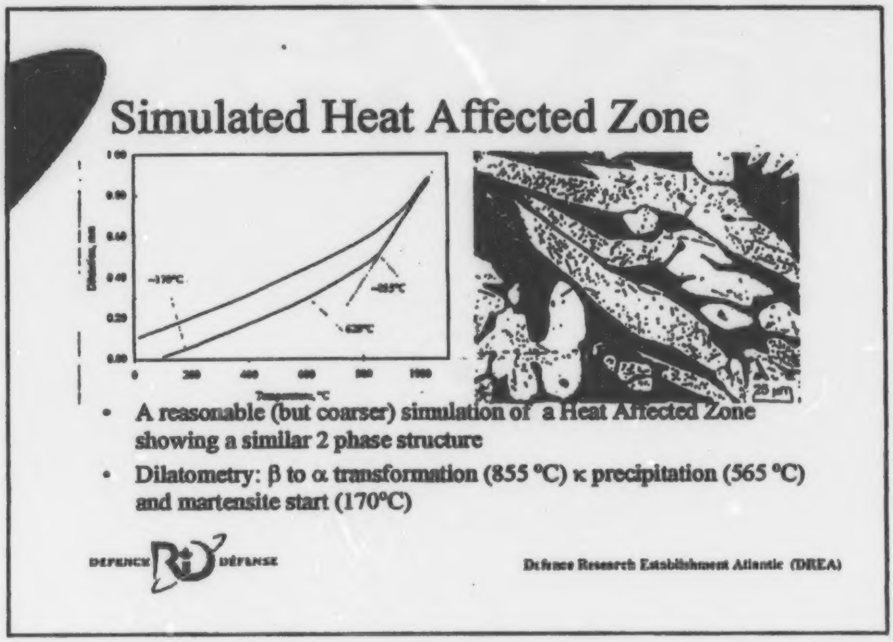
1.00
0.80
0.60
0.40
0.20
0.00
0
200
400
600
800
1000
Temperature, °C
~170°C
~855°C
25 µm

Simulated Heat Affected Zone

- A reasonable (but coarser) simulation of a Heat Affected Zone showing a similar 2 phase structure
- Dilatometry: β to α transformation (855 °C) κ precipitation (565 °C) and martensite start (170°C)

DEFENCE RD DÉFENSE

Defence Research Establishment Atlantic (DREA)

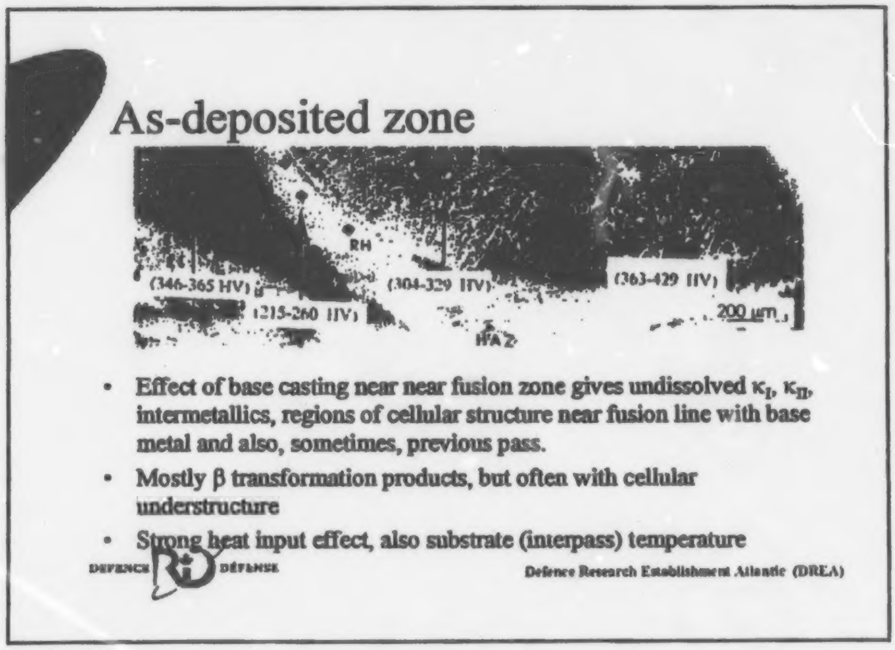
RH
(346-365 HV)
(304-329 HV)
(363-429 HV)
(215-260 HV)
HAZ
200 µm

As-deposited zone

- Effect of base casting near near fusion zone gives undissolved κ_I, κ_{II}, intermetallics, regions of cellular structure near fusion line with base metal and also, sometimes, previous pass.
- Mostly β transformation products, but often with cellular understructure
- Strong heat input effect, also substrate (interpass) temperature

DEFENCE RD DÉFENSE

Defence Research Establishment Atlantic (DREA)

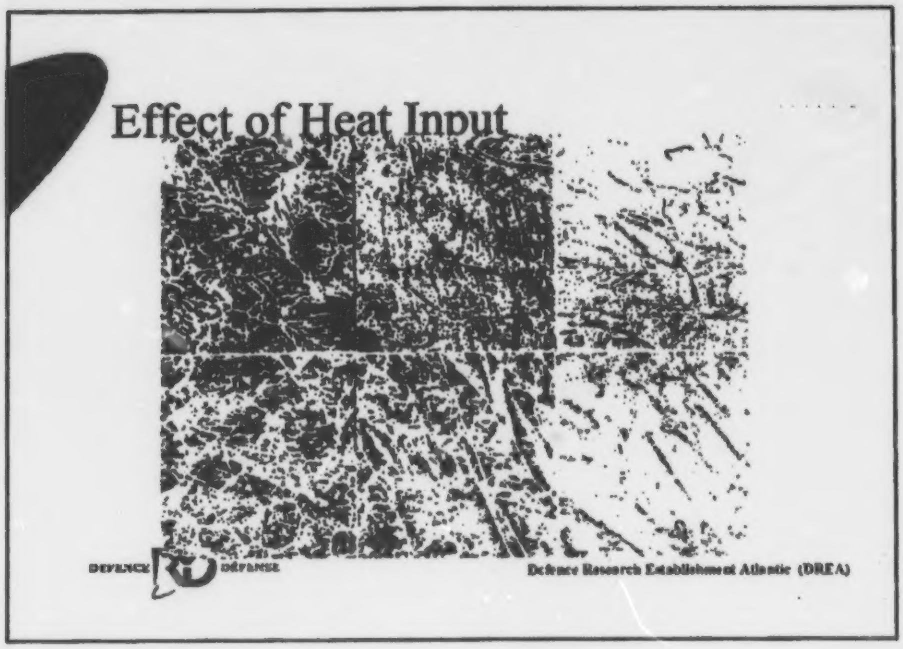

Effect of Heat Input

DEFENCE DÉFENSE

Defence Research Establishment Atlantic (DREA)

β transformation products in the as-deposited material

- Low heat input 9-R martensite plus strengthening κ_{IV} precipitates (42 J/mm, $\Delta t_{800\text{-}500°C}$<0.4s)
- Precipitates nucleate before martensite (600-400°C?)
- With Increased heat input, increasing amounts of allotriomorphic (prior β boundary) and Widmanstattan α form. Only slight differences in composition from martensite, but contain fewer precipitates. Also eutectoid.
- As heat input increases different martensite morpoholgy also forms (not a bainitic product)—order in β?
- Higher Ni, Al favor martensite; lower Al, higher Fe α

DEFENCE DÉFENSE

Defence Research Establishment Atlantic (DREA)

Reheated Zone

- Only scale depends strongly on heat input…near fusion line, structure consists of allotriomorphic (prior β boundary) and Widmanstattan α and martensite
- Differences in α and martensite compositions and diffusional coarsening kinetics. Only a few large pptes in α
- Hint of order in martensite,
- dominated by diffusional coarsening of pre-existing alpha between 800 and 1040°C

DEFENCE DÉFENSE

Defence Research Establishment Atlantic (DREA)

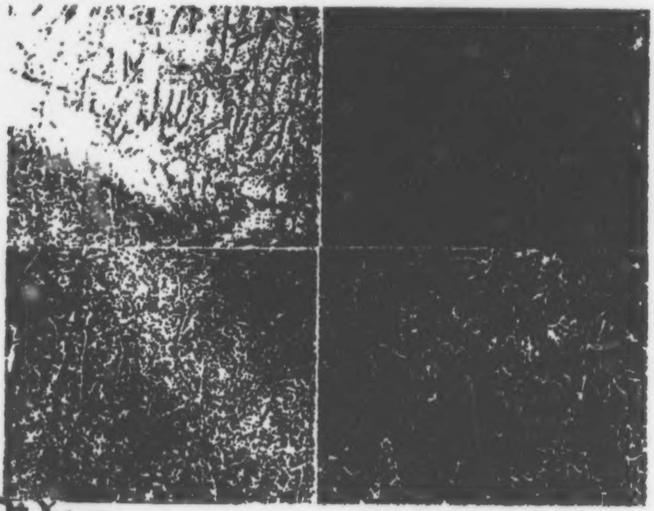

DEFENCE DÉFENSE

Defence Research Establishment Atlantic (DREA)

Implications and Questions to Answer

- How do we make x-ray residual stress measurements if α composition changes from deposit to reheated zone and β' has a faulted 9-R structure? Do we need to measure non-hardenable alloy
- Will martensitic regions of heat affected zone crack on cooling or in fatigue or fracture test? Something to look for in this years testing.
- What is the role of planar boundaries in fatigue?

Defence Research Establishment Atlantic (DREA)

Conclusions

- Heat affected zone structure influenced by prior cast structure
- As-deposited zone very sensitive to heat input (9-R martensites plus allotriomorphic and Widmanstattan α, precipitates and eutectoid)
- Reheated zone dominated by diffusional coarsening of α

Defence Research Establishment Atlantic (DREA)

#511895 (2

Passivation of Laser-Treated Nickel Aluminum Bronze as Measured by Electrochemical Impedance Spectroscopy

by R.D. Klassen[1], C. Hyatt[2] and P.R. Roberge[1]

[1]Dept. of Chem./Chem.Eng., Royal Military College of Canada
P.O.Box 17000 Stn Forces, Kingston, Ontario K7K 7B4

[2]Defence Research Establishment Atlantic, Dockyard Laboratory
P.O. Box 99000 Stn Forces, Halifax, Nova Scotia B3K 5X5

ABSTRACT

Although laser welding and cladding of nickel aluminum bronze (NAB) surfaces involves a fraction of the energy input of conventional welding, a heat affected zone (HAZ) is still formed as well as an as-deposited zone. The main objective of this work was to determine whether the corrosion resistance of the HAZ due to laser treatment was different from the as-deposited zone or a surface without laser treatment. Electrochemical impedance spectroscopy (EIS) was employed to measure the corrosion rates of samples immersed in 3.5% neutral saline. The following specimens of a nickel aluminum bronze (Alloy D) were tested over an immersion time of 50 hours: (i) polished (not laser treated), (ii) laser-treated and polished, (iii) the as-deposited region of laser-treated and polished specimen, (iv) the HAZ region of a laser-treated and polished specimen and (v) laser-treated and unpolished.

A pseudo steady-state level of passivation was reached in all the samples within 40 hours. As expected, laser treatment increased the short-term rate of passivation and therefore improves the long-term resistance to corrosion. The HAZ region clearly passivated more slowly than the as-deposited region. The long-term susceptibility of part of the HAZ to corrosion was confirmed with SEM micrographs. Electrochemical impedance data illustrated a transition during the passivation process of the polished specimens that is consistent with the development of a film layer that restricts mass transfer. The welding oxide from the laser treatment produced a passivation film that is indistinguishable from that which eventually develops on polished specimens.

Passivation of Laser-Treated NAB as Measured by Electrochemical Impedance Spectroscopy

Bob Klassen, Calvin Hyatt and Pierre Roberge

Previous work

- Schussler and Exner had found, via Auger analysis, that the passivation of a NAB (un-clad) was due a layer of disordered aluminum oxide that was about 9 nm thick.
- The passivation time for laser-clad NAB was shorter than for an un-clad NAB (Taylor et al.).

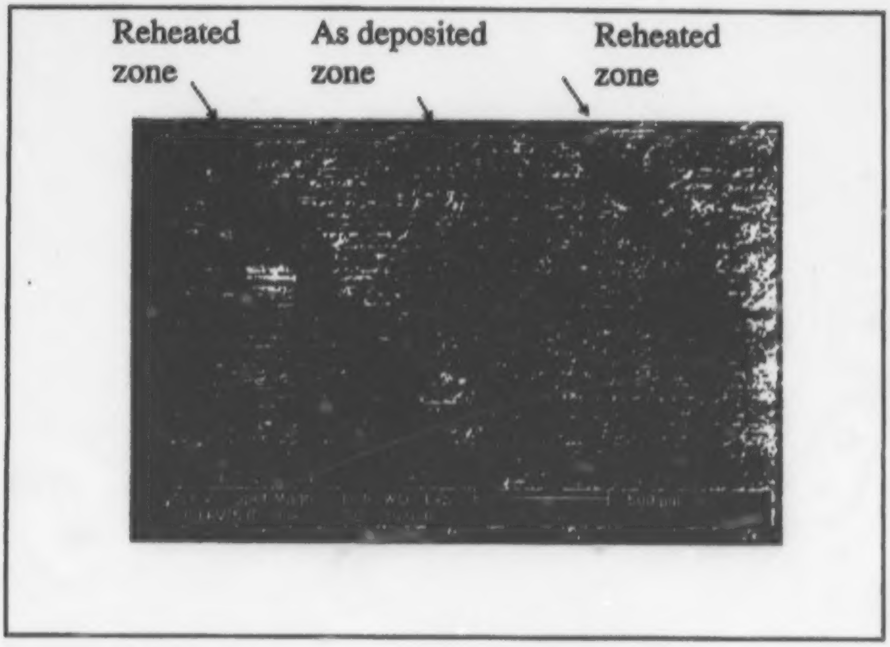
Reheated zone
As deposited zone
Reheated zone

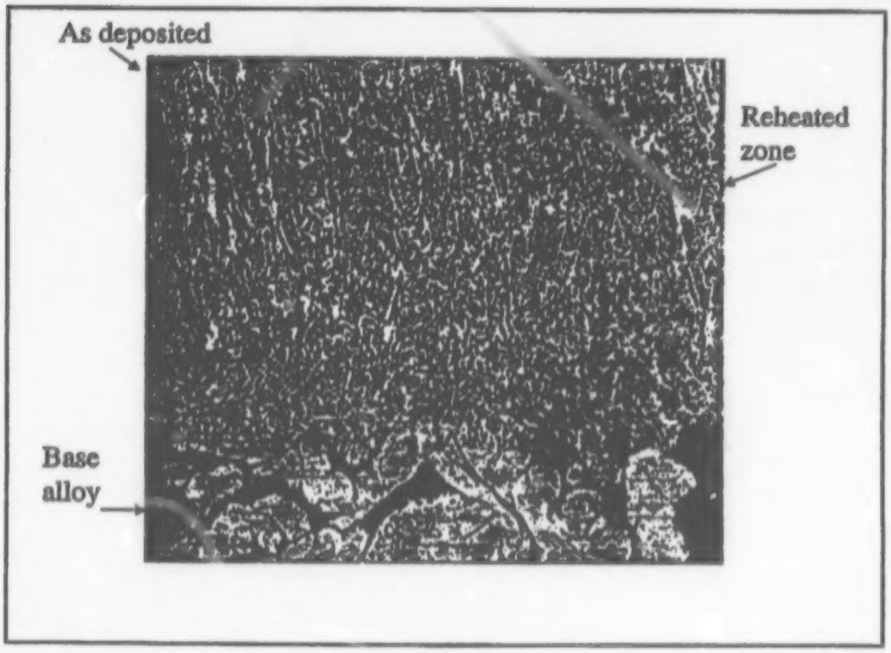
As deposited
Reheated zone
Base alloy

NAB samples

- base alloy, polished
- laser-clad, unpolished
- laser-clad, polished
- laser-clad, polished, as-deposited region only
- Gleeble specimen (reheated zone simulation), polished

Alloy	Designation (UNS)	Specimen Composition				
		Cu	Al	Ni	Fe	Mn
base	C95800	81	9.1	4.4	4.1	1.1
wire	CuNiAl	80.8	9.0	4.6	3.9	1.2
Gleeble	C95800		9.2	4.7	3.4	0.77

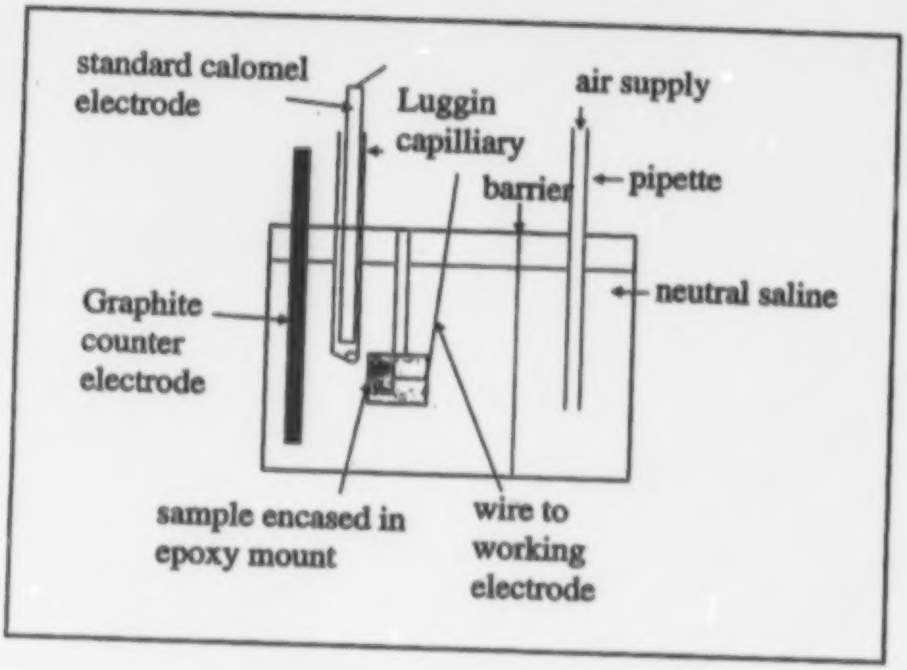
standard calomel electrode
Luggin capilliary
air supply
pipette
barrier
neutral saline
Graphite counter electrode
sample encased in epoxy mount
wire to working electrode

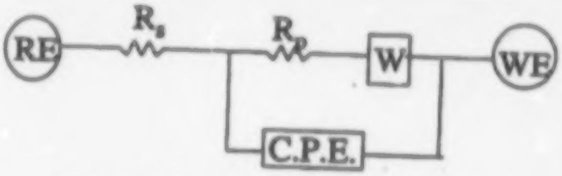
RE
R_s
R_p
W
WE
C.P.E.

Mixed kinetic and diffusion control circuit

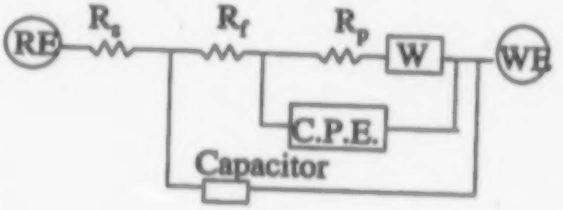
RE
R_s
R_f
R_p
W
WE
C.P.E.
Capacitor

Filmed metal circuit.

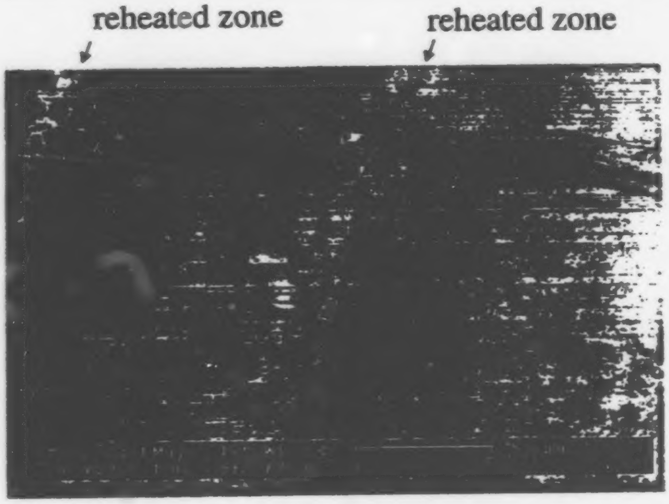
reheated zone
reheated zone

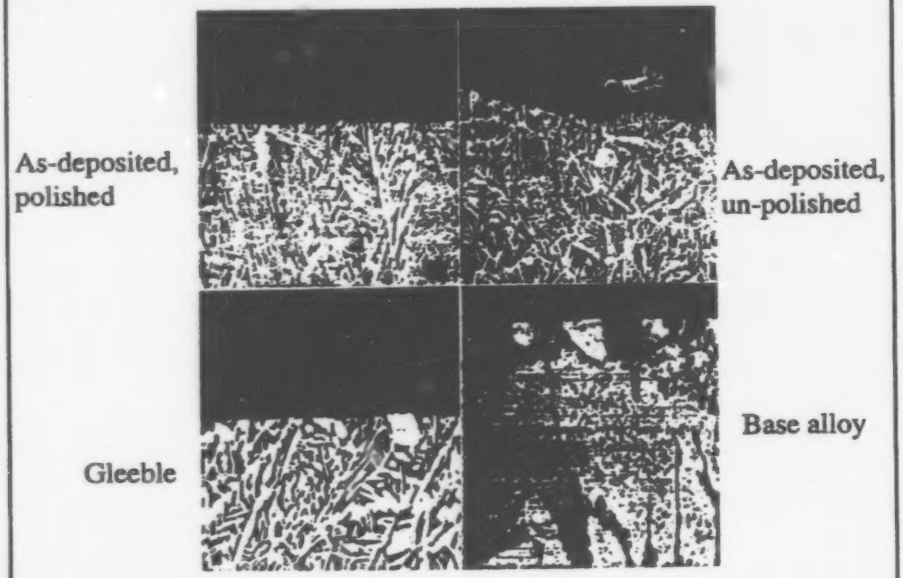
As-deposited, polished
As-deposited, un-polished
Gleeble
Base alloy

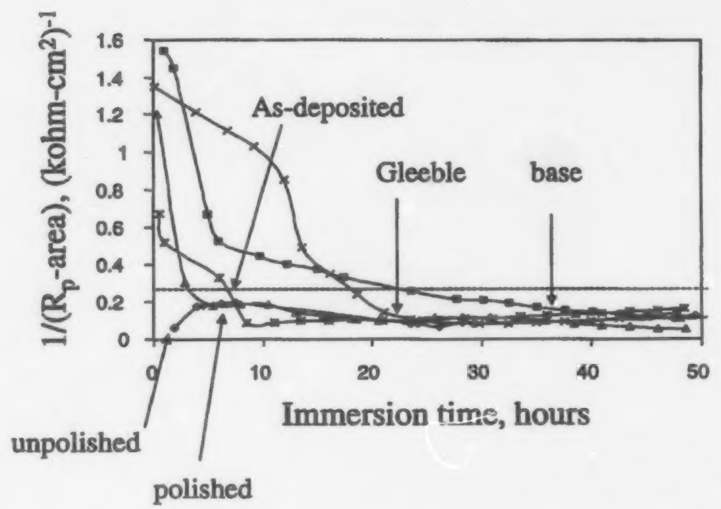
1/(R_p-area), (kohm-cm²)⁻¹
1.6
1.4
1.2
1
0.8
0.6
0.4
0.2
0
0
10
20
30
40
50
Immersion time, hours
As-deposited
Gleeble
base
unpolished
polished

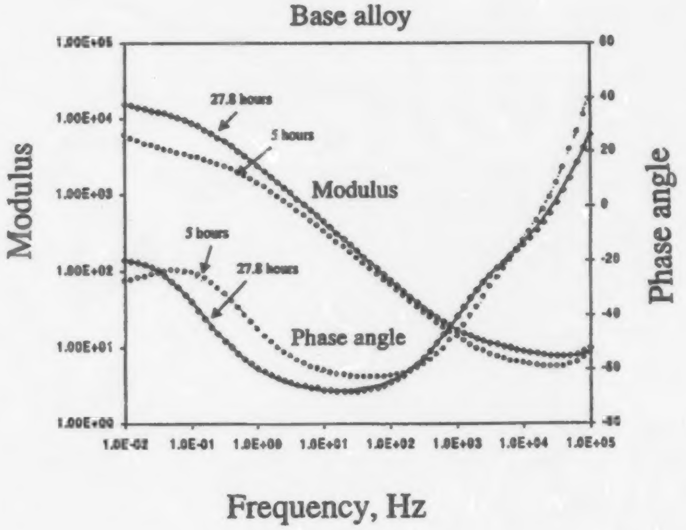
Base alloy
Modulus
Phase angle
1.00E+05
1.00E+04
1.00E+03
1.00E+02
1.00E+01
1.00E+00
60
40
20
0
-20
-40
-60
-80
27.8 hours
5 hours
Modulus
5 hours
27.8 hours
Phase angle
1.0E-02
1.0E-01
1.0E+00
1.0E+01
1.0E+02
1.0E+03
1.0E+04
1.0E+05
Frequency, Hz

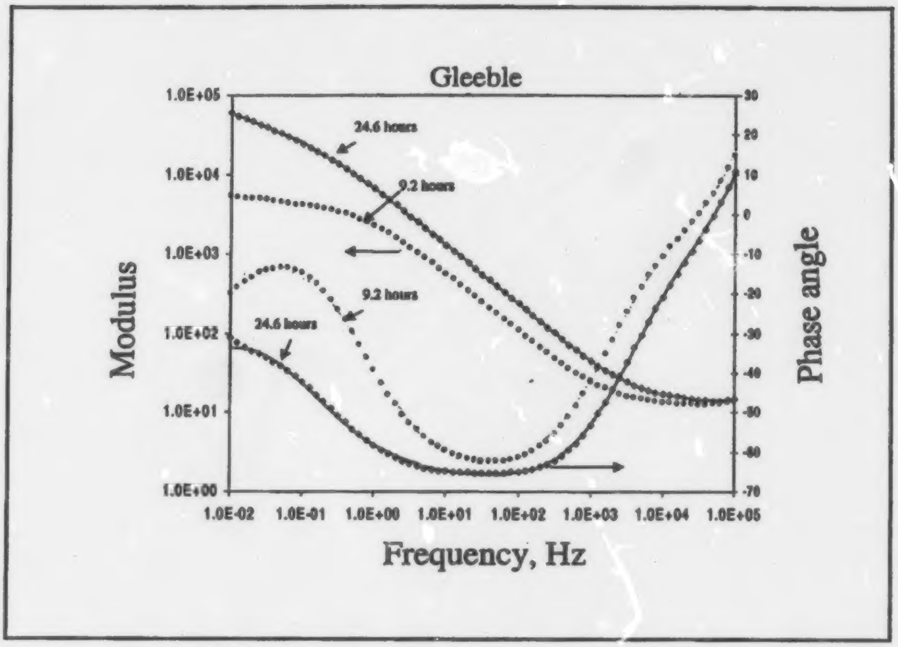
Gleeble
24.6 hours
9.2 hours
9.2 hours
24.6 hours
1.0E+05
1.0E+04
1.0E+03
1.0E+02
1.0E+01
1.0E+00
Modulus
30
20
10
0
-10
-20
-30
-40
-50
-60
-70
Phase angle
1.0E-02
1.0E-01
1.0E+00
1.0E+01
1.0E+02
1.0E+03
1.0E+04
1.0E+05
Frequency, Hz

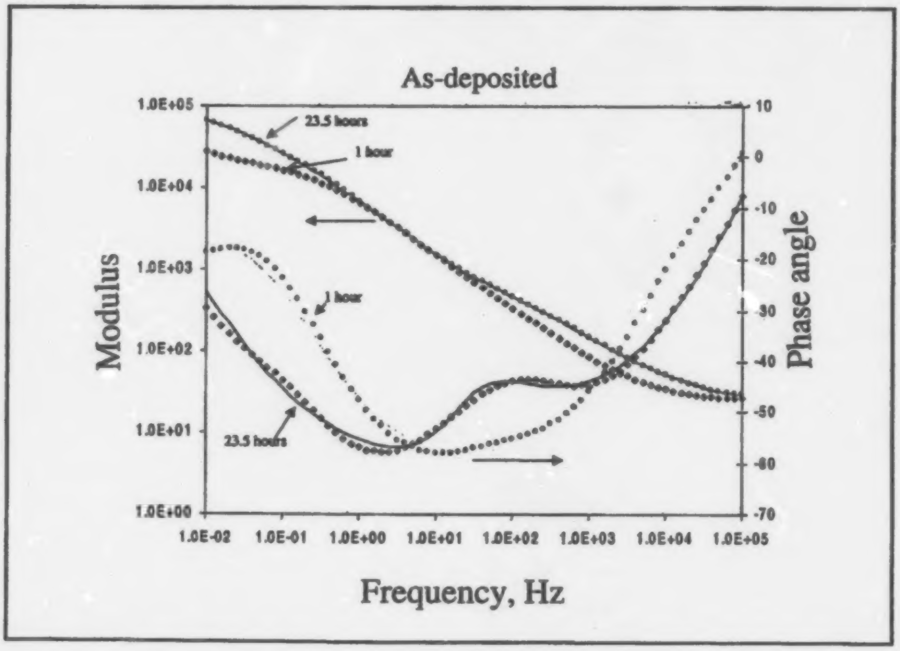
As-deposited
23.5 hours
1 hour
1 hour
23.5 hours
1.0E+05
1.0E+04
1.0E+03
1.0E+02
1.0E+01
1.0E+00
Modulus
10
0
-10
-20
-30
-40
-50
-60
-70
Phase angle
1.0E-02
1.0E-01
1.0E+00
1.0E+01
1.0E+02
1.0E+03
1.0E+04
1.0E+05
Frequency, Hz

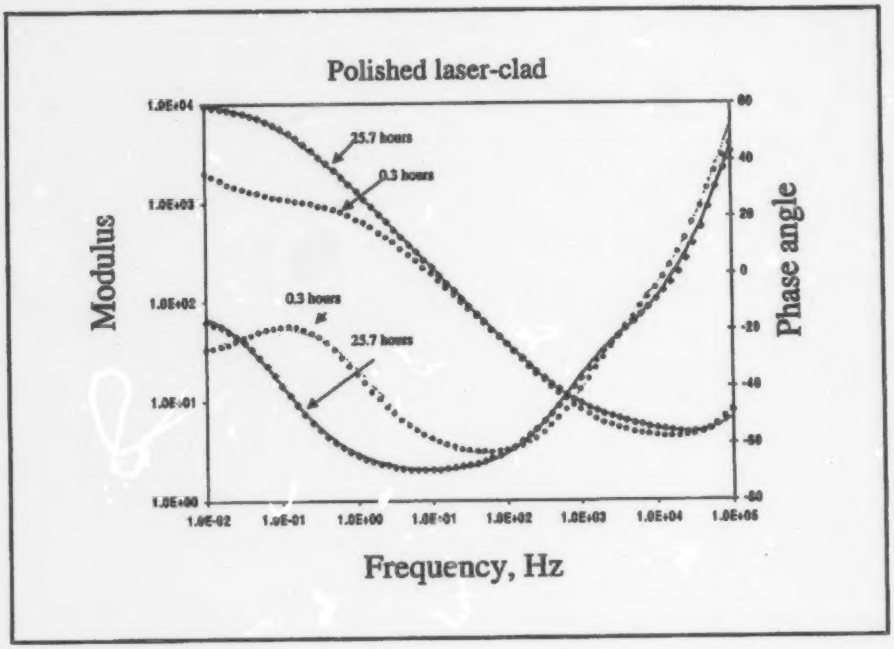
Polished laser-clad
Modulus
Phase angle
Frequency, Hz
25.7 hours
0.3 hours
0.3 hours
25.7 hours
1.0E+04
1.0E+03
1.0E+02
1.0E+01
1.0E+00
60
40
20
0
-20
-40
-60
-80
1.0E-02
1.0E-01
1.0E+00
1.0E+01
1.0E+02
1.0E+03
1.0E+04
1.0E+05

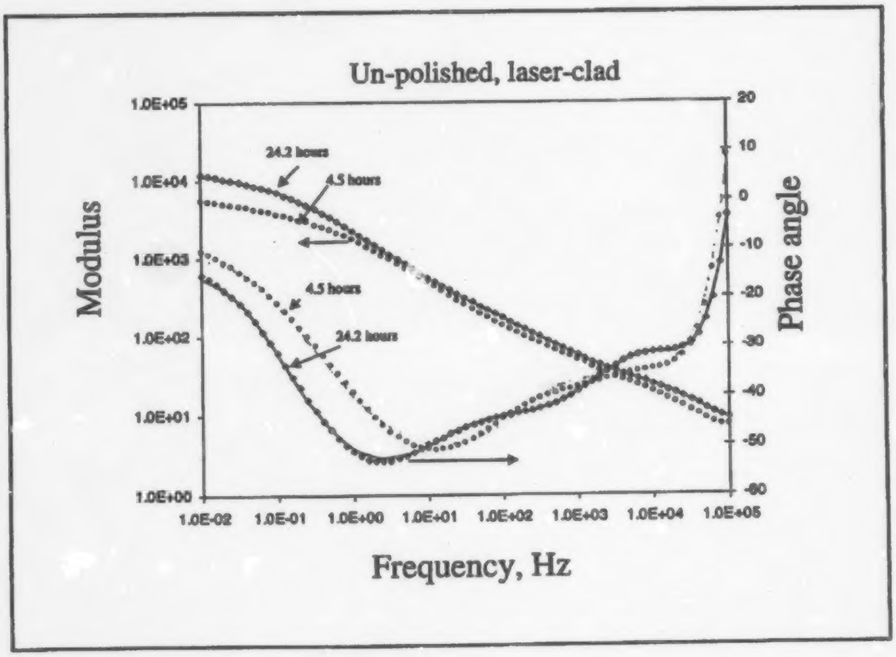
Un-polished, laser-clad
Modulus
Phase angle
Frequency, Hz
24.2 hours
4.5 hours
4.5 hours
24.2 hours
1.0E+05
1.0E+04
1.0E+03
1.0E+02
1.0E+01
1.0E+00
20
10
0
-10
-20
-30
-40
-50
-60
1.0E-02
1.0E-01
1.0E+00
1.0E+01
1.0E+02
1.0E+03
1.0E+04
1.0E+05

EIS curve fitting

- the value of the capacitance of the film was about 10 µF/cm2 for all of the runs below the dotted line
- this value corresponds to a thickness of 0.6 nm of ordered aluminum oxide which is fairly consistent with the thickness measured by Schussler and Exner (9 nm by Auger analysis)
- the Warburg element was consistently higher for the runs below the dotted line; this indicates that the mass transfer resistance increased during passivation
- these results are consistent with the development of a thin layer of aluminum oxide as the reason for the passivation

Conclusions

- Reheated zone passivates more slowly than as-deposited zone in neutral saline.
- Laser-clad surface passivates faster than base alloy.
- Martensitic region of reheated zone seems to be preferentially attacked.
- Passivation is consistent with the development of a thin layer of aluminum oxide that restricts mass transfer.
- The welding oxide behaved as a passivation film.

#511846 (22

Transmission Electron Microscopy of Laser Surface Melted Nickel Aluminum Bronze Alloys

by J.C. Bennett[1] and C.V. Hyatt[2]

[1]Department of Physics, Acadia University, Wolfville, Nova Scotia, B0P 1X0
[2]Defence Research Establishment Atlantic, Dockyard Laboratory, P.O. Box 99000
Stn Forces, Halifax, Nova Scotia B3K 5X5

ABSTRACT

Nickel aluminum bronze alloys are susceptible to a number of surface sensitive degradation processes during service in marine environments. Surface engineering using laser melting and cladding techniques has demonstrated a potential to substantially enhance performance, however little data is currently available on the microstructures developed in these materials. In this study, the microstructure of a series of experimental nickel aluminum bronze alloys containing from 8 to 12 wt. % Al, 3.8 to 6.5 wt. % Ni, 3.8 to 6.5 wt. % Fe, ~ 1 wt. % Mn plus additions of Ti and Zr was examined using transmission electron microscopy. The distributions, morphologies and crystal structures of the phases/precipitates present were found to vary significantly with the nominal alloy composition. For quaternary alloys having in excess of 11.30 wt. % Al, the microstructure mainly consists of martensitic β' plates containing a high density of small, Fe-rich precipitates of the κ_{IV} type. For lower Al contents, the proportion of proeutectoid α along the prior β grain boundaries and Widmanstätten α within these grains is observed to increase when the Ni/Fe ratio is below unity while β' appears to be stabilized for Ni/Fe ratios greater than unity. Additions of Ti and Zr lead to the formation of intermetallic precipitate phases and also appear to influence the relative stability of the α and β' phases. The observed microstructures will be discussed in terms of the phase relationships developed during cooling from the melt.

Transmission Electron Microscopy of Laser Surface Melted Nickel Aluminum Bronze Alloys

J.C. Bennett
Department of Physics, Acadia University

C.V. Hyatt
Defence Research Establishment Atlantic

Outline

- Nickel Aluminum Bronze Phase Diagram
- Objectives
- Experimental Technique: TEM
- Materials
- TEM Observations
- Conclusions and Future Work

Nickel Aluminum Bronze Phase Diagram

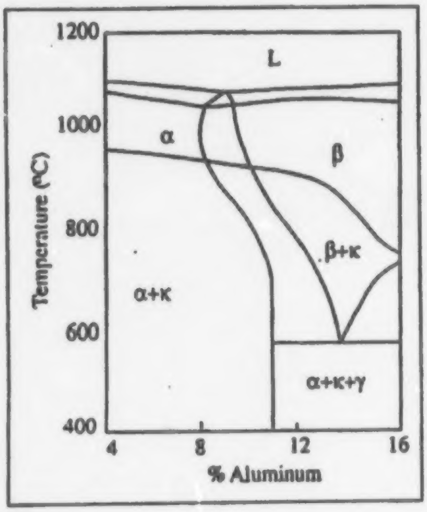

Typically contain 9 -12 wt. % Al

Al < ~11 wt. %:
α solid solution (fcc)
κ phases: κ_I, κ_{II}, κ_{IV} (Fe_3Al prototype)
κ_{III} (NiAl prototype)

Al > 11 wt. %:
β solid solution (bcc)
γ: martensite → 2H

Rapid cooling:
"retained β": martensite → 9R or 18R

Vertical Section of Cu-Al- 5 wt. % Ni -5 wt. % Fe Equilibrium Phase Diagram

---

Background

- Laser cladding techniques developed by DREA have demonstrated a potential to improve surface properties.
- Interest in developing an optimum consumable alloy with less sensitivity to heat input, better ductility, etc.

Problem:

- Melt cooling rates are inherently high in laser surface treatments → the microstructure forms far from equilibrium.
- Little data is currently available on microstructural development in NiAl bronzes under these conditions.

Objectives:

- Determine phase distributions, structural defects, etc., produced in several alloys under varying heat inputs.
- Improve understanding of the effects of the various microstructural features on the surface properties.

Transmission Electron Microscopy

Techniques:

- Selected area electron diffraction
- Convergent beam electron diffraction
  - *crystallographic information from matrix and precipitate phases as small as 10 nm^2*
- Diffraction contrast electron microscopy
- High resolution electron microscopy
  - *direct imaging of crystal structures and lattice defects (stacking faults, twins, dislocations) with near atomic resolution.*
- Energy dispersive x-ray microanalysis
  - *semi-quantitative elemental analysis from small volumes ~ 100 nm^3*

Materials

1.) NiAl Bronze Laser Cladding

Base casting: Cu-8.6 % Al-4.4 % Ni-4 % Fe-1.1 % Mn
Welding wire: Cu-9.0 % Al-4.6 % Ni-3.9 % Fe-1.2 % Mn
Laser heat input: 1.2 kJ/cm

2.) Gleeble Simulated NiAl Bronze Weldments

Base alloy: Cu-9.2 % Al-4.7 % Ni-3.4 % Fe-0.8 % Mn
Thermal Cycle: i) Peak temp 1040 °C → water quench (750 °C/s)
ii) Peak temp 1040 °C → air quench (188 °C/s)

3.) Experimental NiAl Surface Melted Alloys

Alloy	Cu	Ni	Fe	Mn	Al	Cr	Ti	Zr	Ni/Fe
1	76.45	5.06	6.20	0.35	9.70		2.24		0.82
2	79.60	3.80	5.50	1.00	10.10				0.69
4	81.20	3.80	3.90	1.00	10.10				0.97
5	78.60	6.50	4.60	1.10	9.20				1.41
7	77.95	4.00	5.80	0.95	11.30				0.69
9	77.30	4.60	4.60	1.00	12.50				1.00
12	79.30	4.10	4.30	1.00	11.30				0.95
23	78.95	4.70	5.00	1.00	8.90	0.60	0.44	0.41	0.94
24	80.60	3.70	4.40	0.91	7.80	1.12	0.79	0.68	0.84
27	78.63	4.90	5.3	1.10	9.30	0.31	0.23	0.23	0.92
CDA958		4.5	4.0	1.2	9.0				> 1

Experimental Details

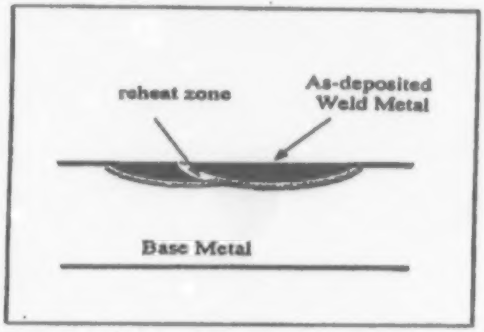

- Specimens prepared in plan view.
- Procedure: (i) weldment sectioned parallel to the clad surface
  (ii) mechanically back-thinned to 0.1 mm
  (iii) 3 mm diameter disks punched for TEM
  (iv) disks were ground to ~ 100 μm
  (v) electropolished (33% HNO3 in methanol, -30 °C, 10 V)

- Examined at 200 kV in Philips CM20 and 100 kV in Philips EM301

NiAl Bronze Laser Cladding

Optical micrograph

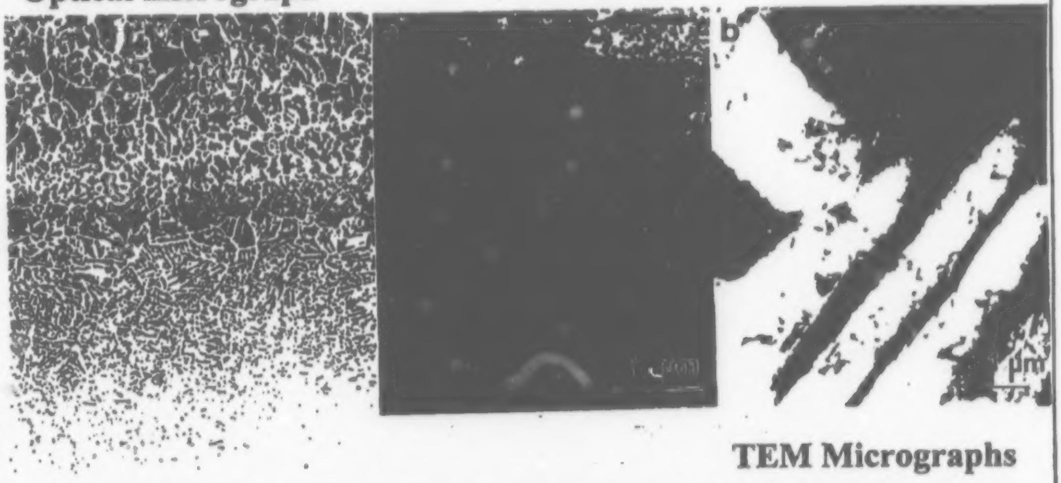

TEM Micrographs

(a) as-deposited: (i) light plates (basket-weave), (ii) dark irregular plates
(iii) high density of small (~20 nm) precipitates

(b) reheat zone: (i) light phase (plates and equiaxed), (ii) dark plates
(iii) high density of precipitates in the dark phase

Laser Clad *as-deposited* Region: Light Plates

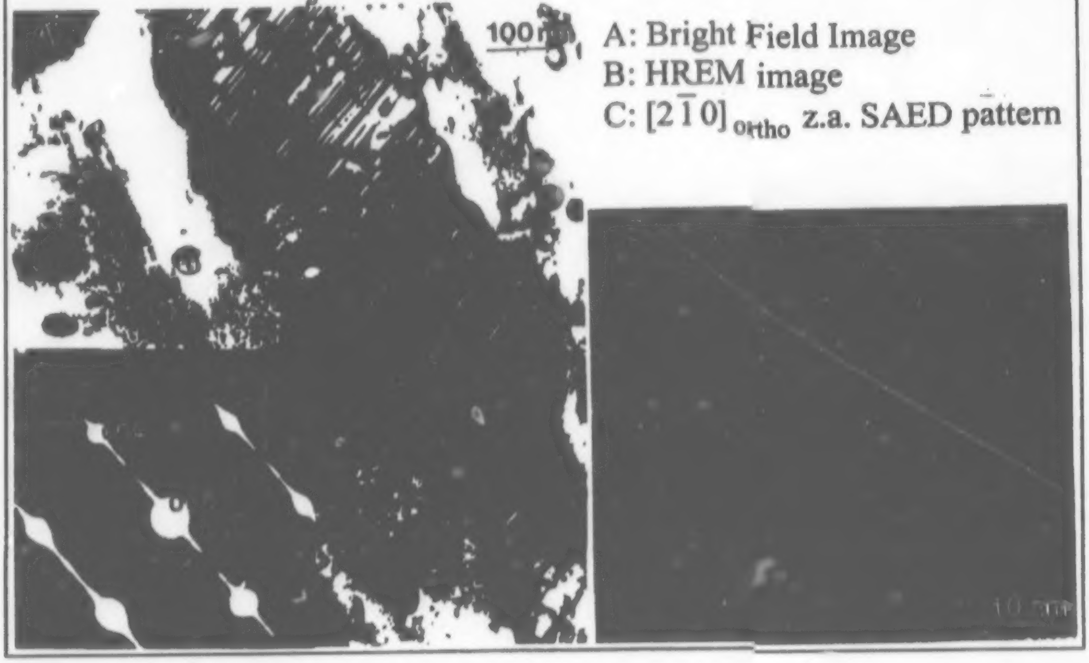

A: Bright Field Image
B: HREM image
C: $[2\bar{1}0]_{ortho}$ z.a. SAED pattern

CDA 95800
Cu-9 wt.% Al-4.5 wt.% Ni-4.0 wt. % Fe-1.2 wt.% Mn,
Heat Input 3000 J/cm

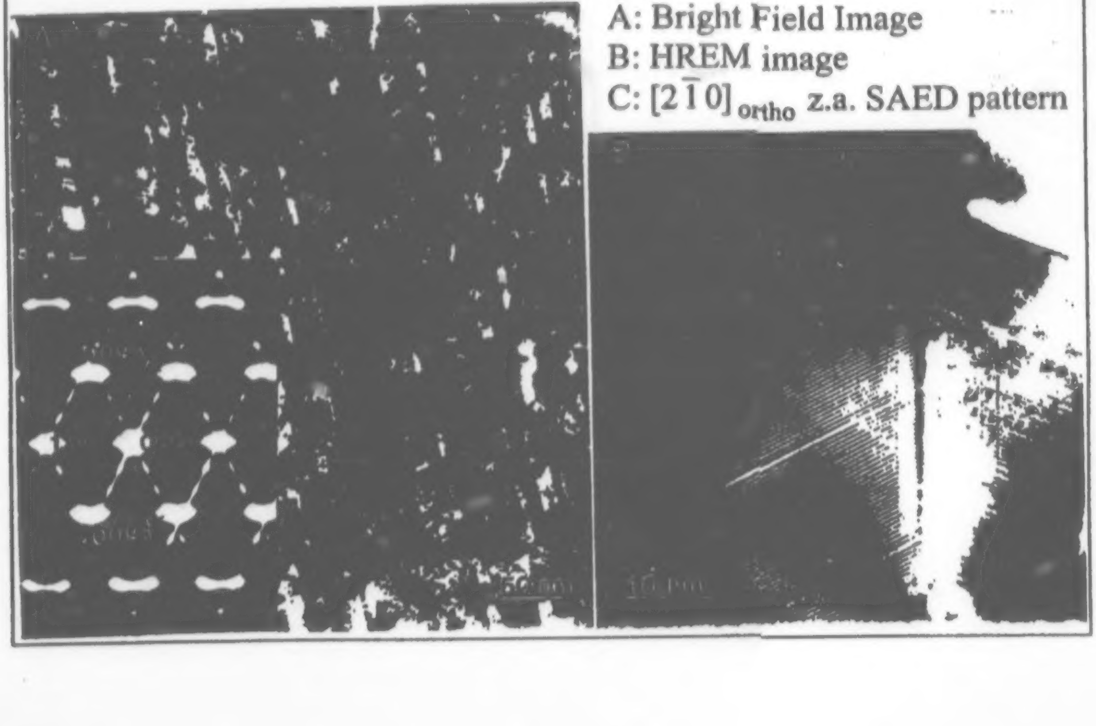

A: Bright Field Image
B: HREM image
C: $[2\bar{1}0]_{ortho}$ z.a. SAED pattern

Laser Clad NiAl Bronze Phase Distribution

as-deposited region

Light plates:
- *9R structure*: long-range ordering of close-packed $\{111\}_{fcc}$ layers
- average stacking order ABCBCACAB is disturbed by many random faults
- orthorhombic unit cell (a = 0.449 nm, b = 0.519 nm, c = 1.91 nm)

Dark Plates:
- *9R structure*: narrow (~ 20 nm) twin-related domains $(101)_{tp}$
- semi-coherent due to random faulting

The 9R structure occurs for martensites in related systems (e.g. Cu-Al).

Small precipitates (~ 20 nm diameter):
- numerous in both light and dark plates
- microdiffraction patterns consistent with Fe_3Al type structure (κ_{IV} precipitates)

reheat region

Light plates and grain boundaries: α phase (fcc, a = 0.365 nm)

Dark plates: similar to as-deposited region

Small precipitates: κ_{IV} type in martensite, few found in α

Gleeble Weld Simulations: Water quenched

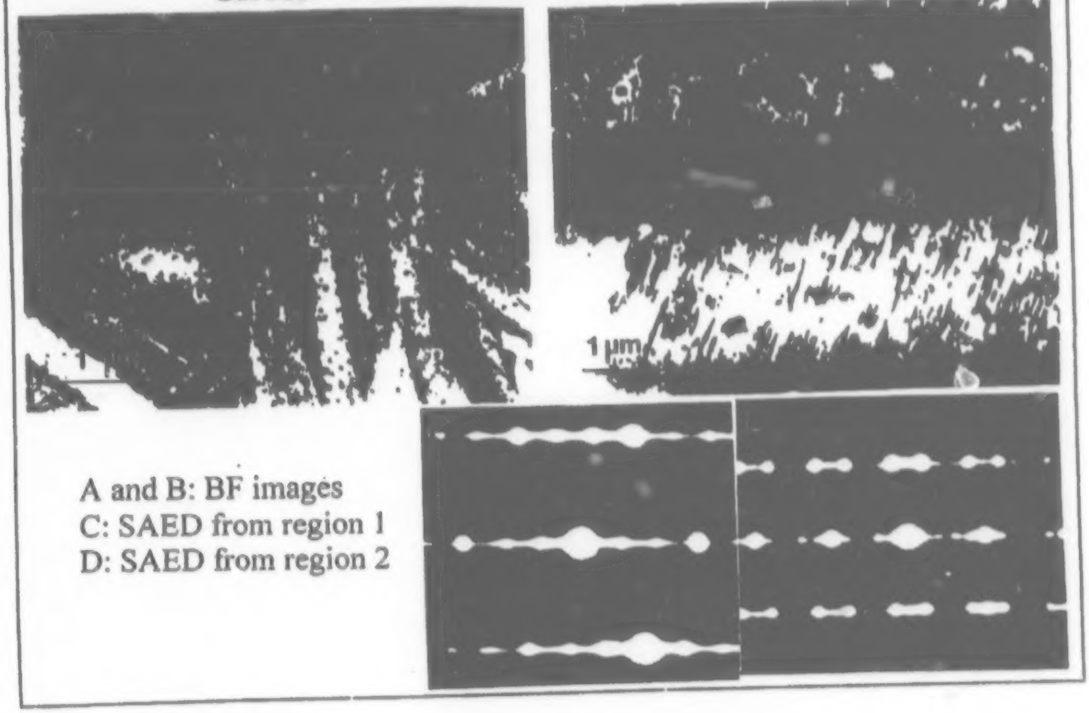

A and B: BF images
C: SAED from region 1
D: SAED from region 2

Gleeble Weld Simulations: air quenched

A: Bright field image of eutectoid region ($\alpha + \kappa_{III}$)

B: SAED pattern from elongated precipitate (NiAl, κ_{III} type)

Similar eutectoid regions are common in the reheat zone and less frequent in the as-deposited material.

CDA 95800
Cu-9 wt.% Al-4.5 wt.% Ni-4.0 wt. % Fe-1.2 wt.% Mn, Heat Input 25 J/cm

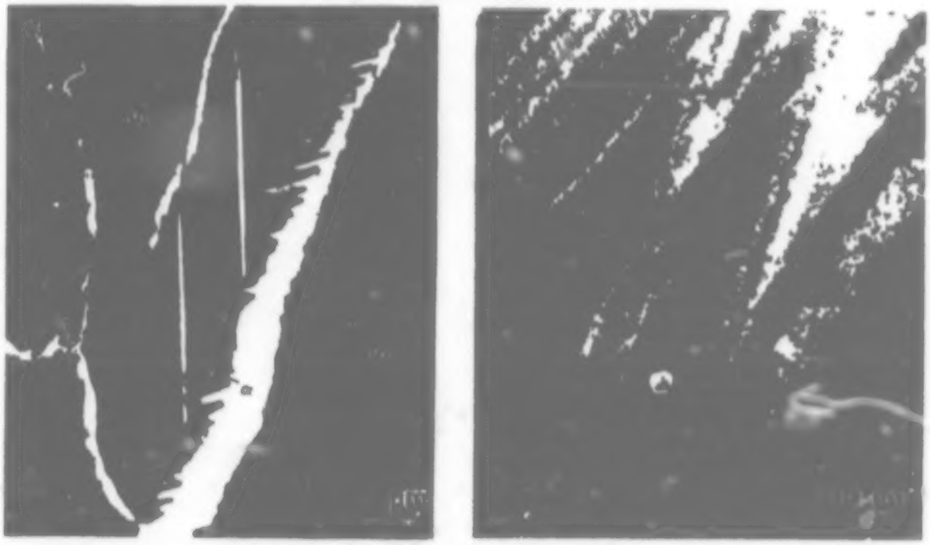

A: Low magnification BF image (M: martensite, a: α phase)

B: BF image of a typical grain interior showing *mottle* contrast

CDA 95800
Cu-9 wt.% Al-4.5 wt.% Ni-4.0 wt. % Fe-1.2 wt.% Mn,
Heat Input 25 J/cm

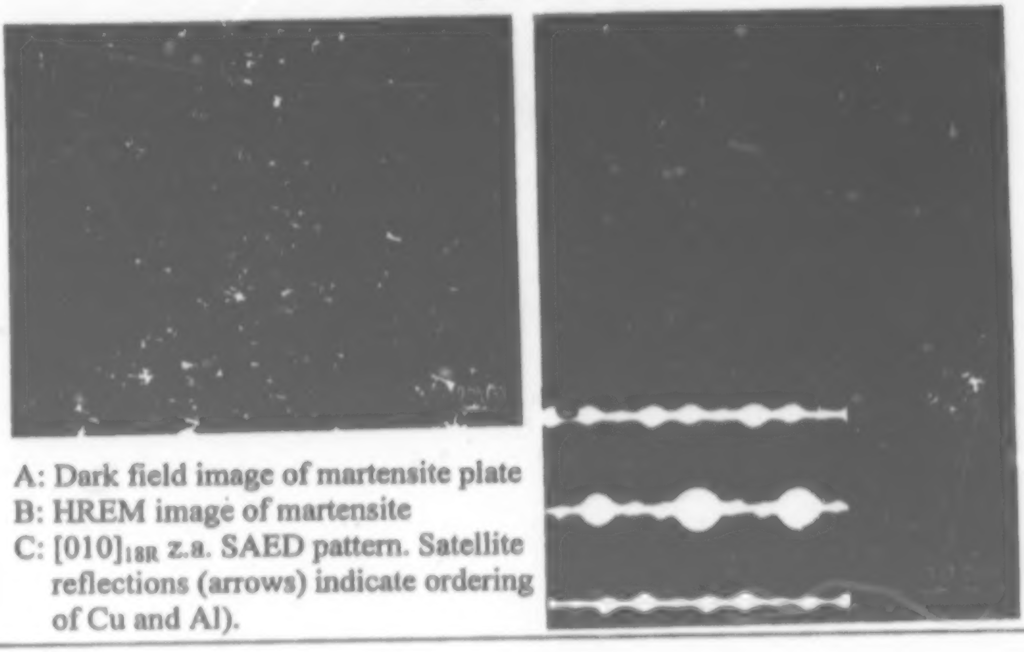

A: Dark field image of martensite plate
B: HREM image of martensite
C: [010]$_{18R}$ z.a. SAED pattern. Satellite reflections (arrows) indicate ordering of Cu and Al).

Cu-9.2 wt.% Al-6.5 wt.% Ni-4.6 wt. % Fe-1.1 wt.% Mn,
Heat Input 800 J/cm

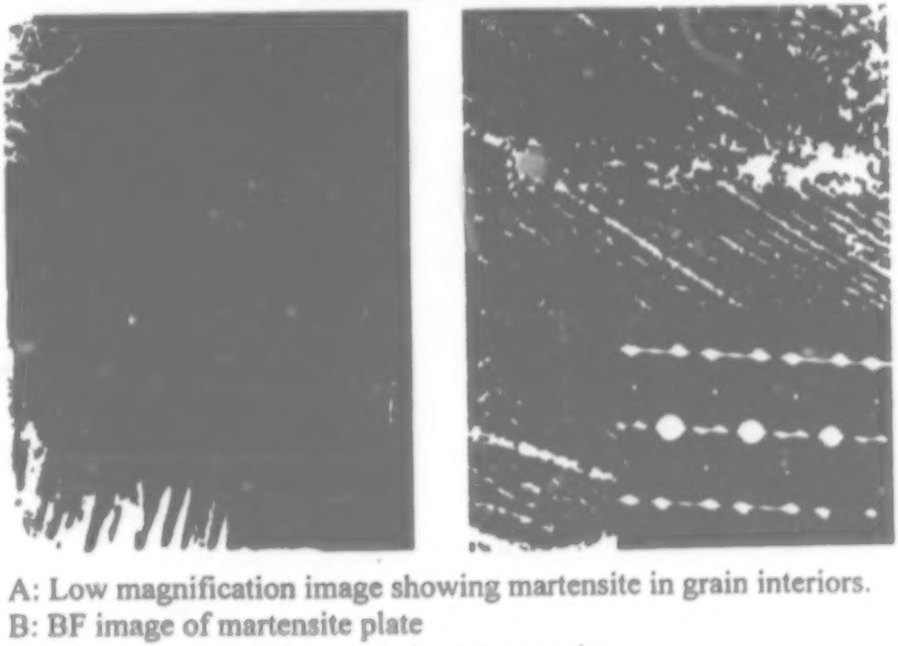

A: Low magnification image showing martensite in grain interiors.
B: BF image of martensite plate
C: [010]$_{18R}$ z.a. SAED pattern from martensite.

Cu-11.3 wt.% Al-4.0 wt.% Ni-5.8 wt. % Fe-0.9 wt.% Mn, Heat Input 3000 J/cm

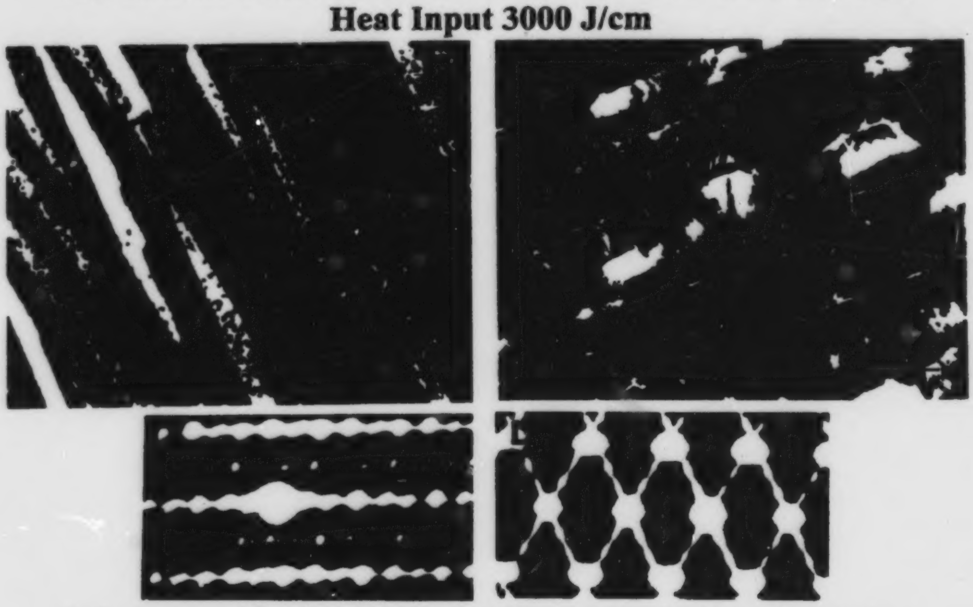

A: Low magnification image showing martensite in grain interiors.
B: [010] z.a. HREM image of martensite plate
C, D: $[010]_{18R}$ and [210] z.a. SAED patterns from martensite.

Cu-12.5 wt.% Al-4.6 wt.% Ni-4.6 wt. % Fe-1.0 wt.% Mn Heat Input 3000 J/cm

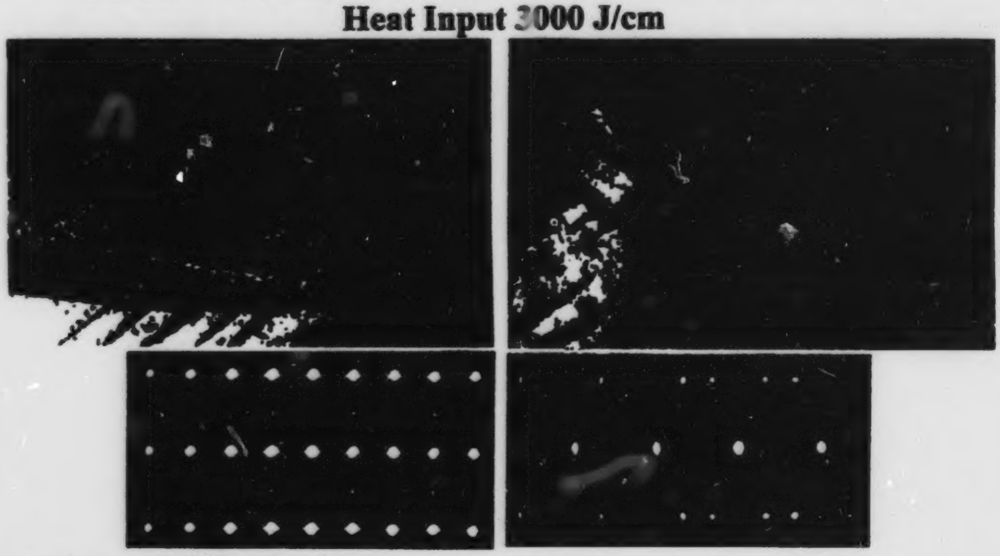

A: Low magnification image.
B: Bright field image of γ' martensite
C: $[010]_{18R}$ z.a. (equivalent to$[1\bar{1}00]_{2H}$) SAED pattern from γ' martensite.
D: $[2\bar{1}4]_{18R}$ z.a SAED twinned on the (121) plane.

Cr-Ti-Zr bearing Nickel Aluminum Bronze

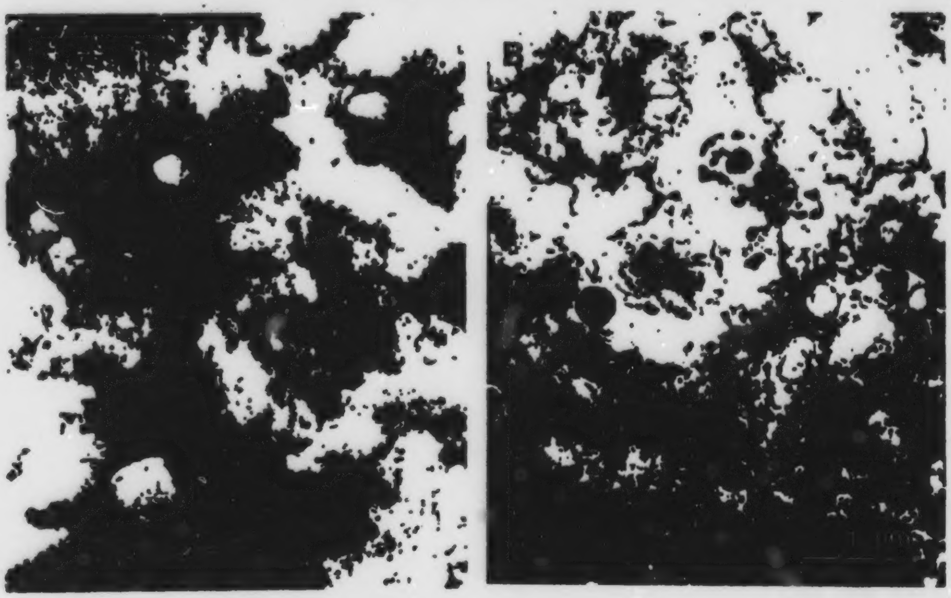

BF images: Cu:Al:Ni:Fe:Mn:Cr:Ti:Zr
A: 78.9:8.9:4.7:5.0:1.0:0.6:0.44:0.41; B: 80.6:7.8:3.7:4.4:0.9:1.1:0.8:0.7

Cr-Ti-Zr bearing Nickel Aluminum Bronze

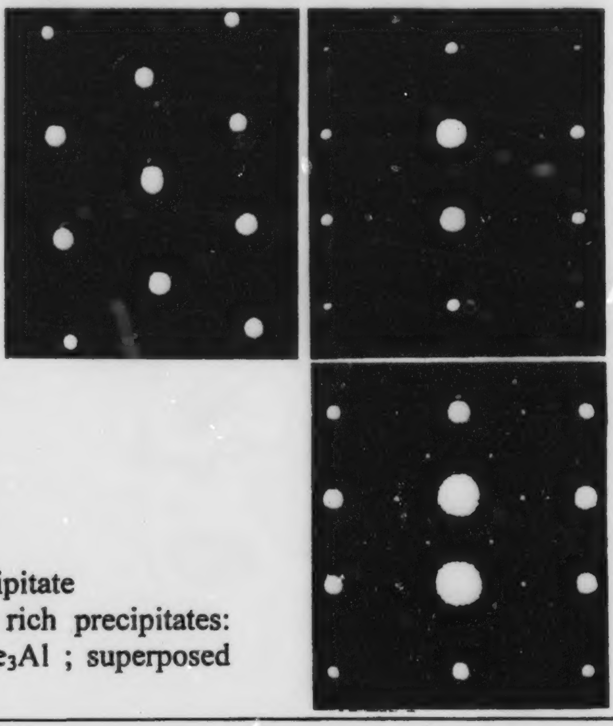

A: BF image of Fe rich precipitate
B, C, D: SAED from Fe rich precipitates: [111] z.a ; [100] z.a for Fe_3Al ; superposed [100] z.a and [110] z.a.

Conclusions

- TEM has been used to characterize the phase distribution developed in nickel aluminum bronze during laser cladding.
  - phases include α phase (allotriomorphic and Widmanstatten), two morphologies (i.e. plate sizes) with 9R structure, small Fe rich κ_{IV} precipitates, and (α + Ni rich κ_{III}) eutectoid.
- Simulated welds that were water quenched from 1040 °C developed a microstructure within the grains similar to that observed in the as-deposit region of the laser clads.
  - the large domain α plates adopt the 9R structure exclusively
- Simulated welds that were air cooled from 1040 °C developed a microstructure somewhat different than that observed in the reheat zone of the laser clads.
  - proportion of eutectoid appears to be increased
- Laser surface melting CDA 95800 with heat input 25 J/cm produced α at the grain boundaries and 9R martensite within the grains.
  - contain a very high density of small (< 10 nm) coherent precipitates

Conclusions

- A high density of Fe-rich precipitates was observed in all martensite phases.
- Ni content of 6.5 wt. % produced some ordering of the β' martensite (to 18R). Martensite predominates in the interior of the grains.
- Ordered β' martensite (18R) was observed for all samples studied with Al concentration exceeding 11 wt. % independent of Ni/Fe ratio. Again predominately martensite (both morphologies) within grains
- For the sample containing 12.5 wt. % Al, β' (majority phase) and γ' (minority phase) martensites were observed.
- Cr, Ti and Zr additions resulted in major microstructural changes. The α phase was found to be inter-dispered, irregular martensite plates. Large Fe rich κ_{II}/κ_{IV} type and irregular Zr rich precipitates were found to be numerous.

#511897 (23)

Laser Cladding of Ni-Al Bronze for Repairing Marine Components

by L. Xue*, J.-Y. Chen*, C.V. Hyatt and M. Islam***

***National Research Counc[illegible]anada
Integrated Manufacturing Technologies Institute
800 Collip Circle, London, Ontario N6G 4X8**

****Defence Research Establishment Atlantic, Dockyard Laboratory (Atlantic)
P.O. Box 1012, Dartmouth, Nova Scotia B2Y 3Z7**

ABSTRACT

Laser cladding of conventional Ni-Al bronze onto a bronze substrate by using welding wire has been investigated. The laser cladding was conducted with a 3 kW CO_2 laser with a simultaneous feeding of the Ni-Al bronze wire into the molten pool. The clad geometry and microstructure depended on the laser processing parameters. With optimized processing conditions, a relatively uniform and smooth clad layer was obtained. The hardness of clad layer was substantially higher than that of the substrate. The microstructure and composition of laser clad layer was studied with scanning electron microscope (SEM) and energy disperse spectroscopy of x-ray (EDS). The macro and micro stresses of laser clad layer were investigated with x-ray diffraction (XRD) technique. The electrochemical polarization testing in 3.5 % NaCl solution showed that the corrosion resistance of laser clad coating was similar to that of the substrate material.

Contents:

- *Introduction*
- *Experimental Details*
- *Results and Discussion*
- *Conclusions*

NRC · CNRC

Introduction

Laser Cladding:

- A process to create a layer of desired material on the substrate surface by melting the surface as well as the clad material with a focused laser beam.

Advantages:

- Produces a fully dense coating with metallurgical bonding to the substrate - no peeling or debonding problems.
- Modifies substrate surface composition selectively to improve its surface related properties.
- Can functionally repair local damage with minimised heat effect.

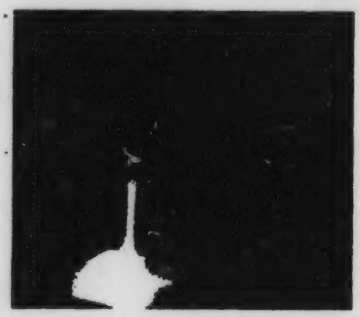

NRC · CNRC

Introduction

Supply of Clad Materials:

- Pre-placed thin strip or paste.
- Continuous feeding of powder or wire.

Continuous Wire Feeding Technique:

- Not widely investigated.
- Cleaner process compared to powder feeding method.
- Ni-Al welding wires are commercially available.

Objective:

- To investigate laser cladding process with continuous feeding of Ni-Al bronze wires for the repair of marine components.

NRC · CNRC

Experimental Details
- Materials

Substrate Material:

- UNS C95800 Cast Ni-Al Bronze (Cu8.6%Al-4.8%Ni4.0%Fe1.1%Mn)

Clad Material:

- Ni-Al Bronze welding wire (Cu9.0%Al4.6%Ni-3.9%Fe1.2%Mn), 0.254 mm in diameter.

NRC · CNRC

Experimental Set-Up

- 3 kw CO_2 laser with a 190 mm focal length lens.
- Power density: (6 - 9.5) x 10^4 w/cm^2.
- Traversing speed: 5 - 20 mm/s.
- Wire feeder rate: 50 - 200 mm/sec.
- 4-axis motion system: x, y, z and rotary.

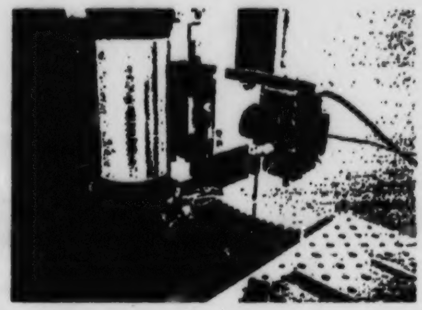

NRC · CNRC

Experimental Details - Specimen Evaluation

Metallurgical Evaluation

- Optical microscope, microhardness, SEM, EDS & XRD analysis.

XRD Residual Stress Measurement

- Conventional Sin$^2\Psi$ method.
- Measure (331) peak shift.
- Ni-filtered *CuK*α X-ray irradiation with 40 kV / 55 mA.

Corrosion Test

- Electrochemical polarization in 3.5% NaCl solutions at 1mV/sec scan speed.

NRC · CNRC

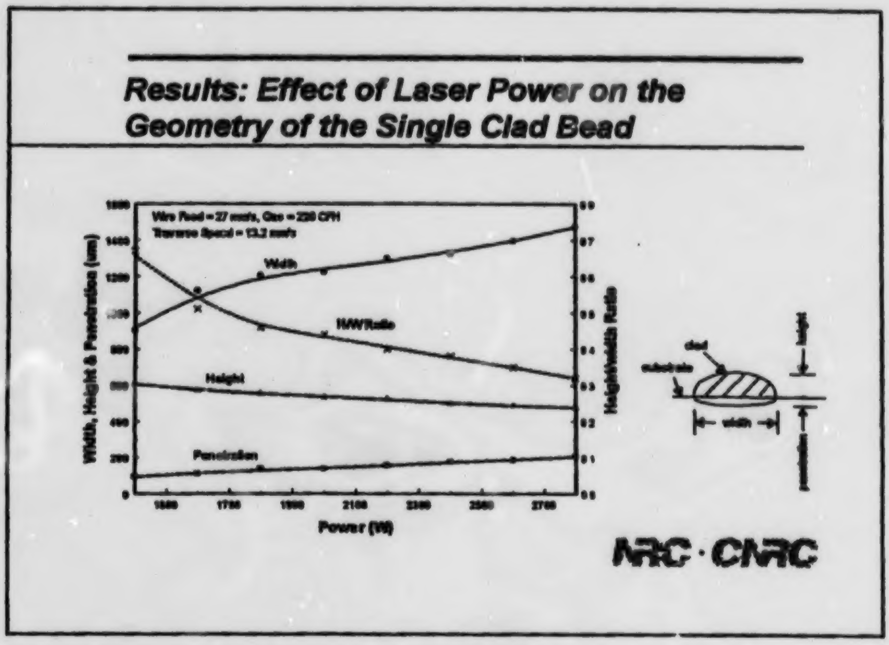

Results: Effect of Laser Power on the Geometry of the Single Clad Bead

NRC · CNRC

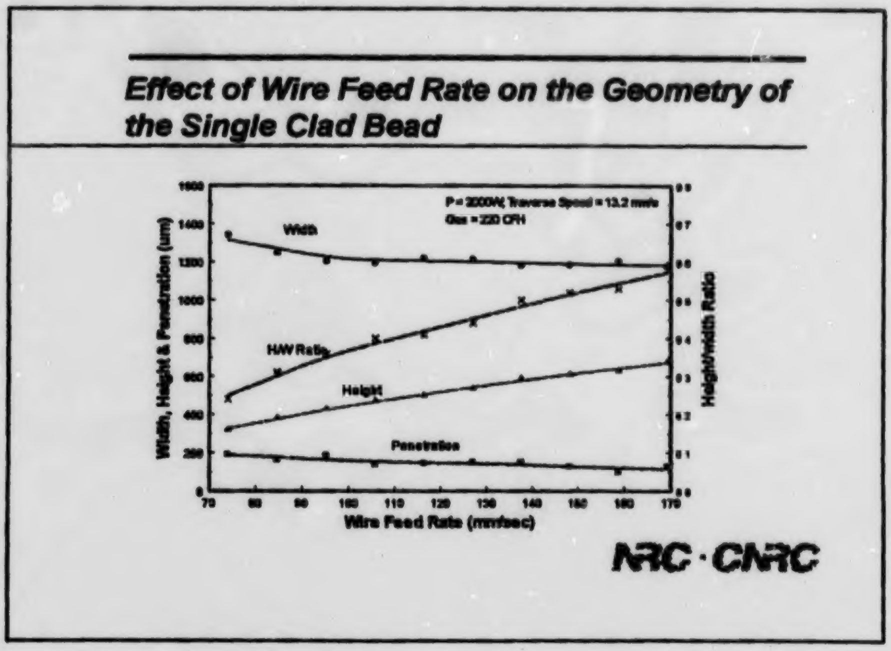

Effect of Wire Feed Rate on the Geometry of the Single Clad Bead

NRC · CNRC

Effect of Shielding Gas Flow on the Geometry of the Single Clad Bead

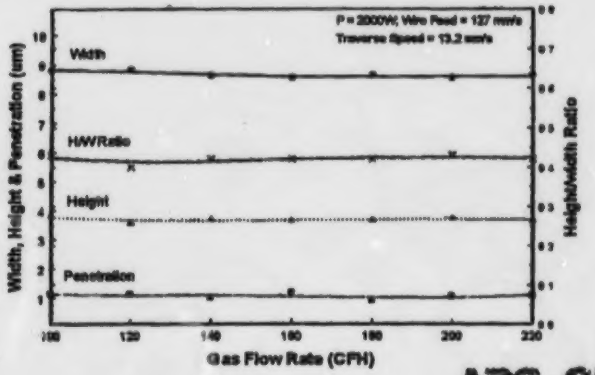

NRC · CNRC

Laser Clad Ni-Al Bronze Coating on Bronze Substrate

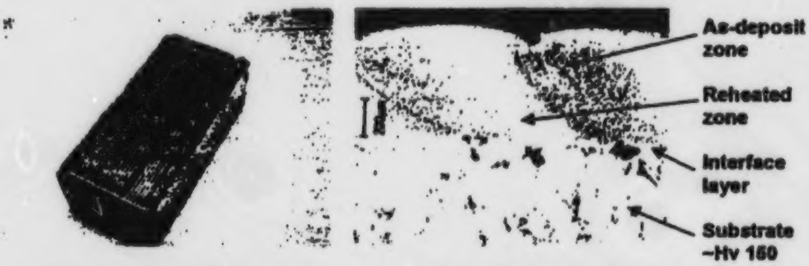
As-deposit zone
Reheated zone
Interface layer
Substrate ~Hv 150

(a) Overall View of Clad Layer

(b) Cross-Sectional View

NRC · CNRC

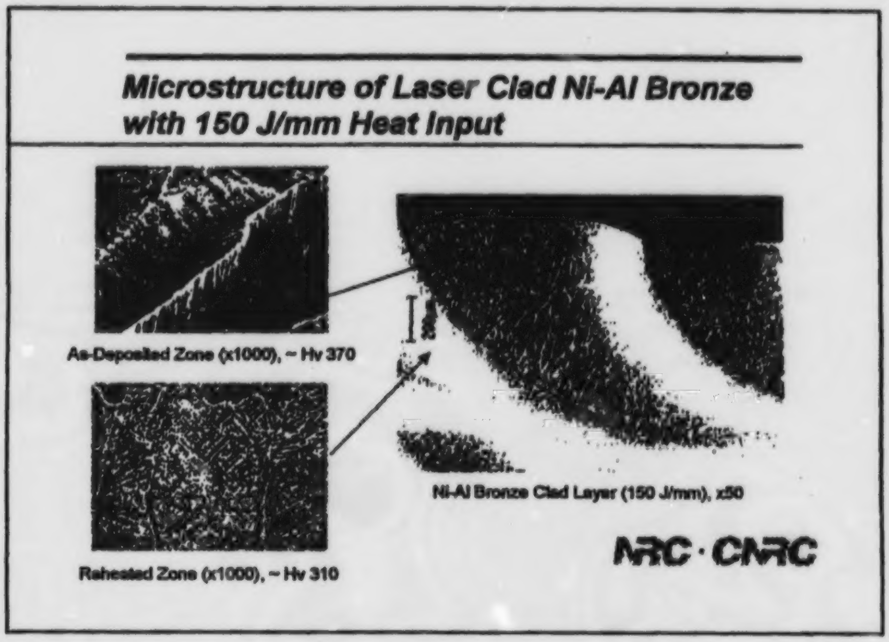

Microstructure of Laser Clad Ni-Al Bronze with 150 J/mm Heat Input

As-Deposited Zone (x1000), ~ Hv 370

Reheated Zone (x1000), ~ Hv 310

Ni-Al Bronze Clad Layer (150 J/mm), x50

NRC · CNRC

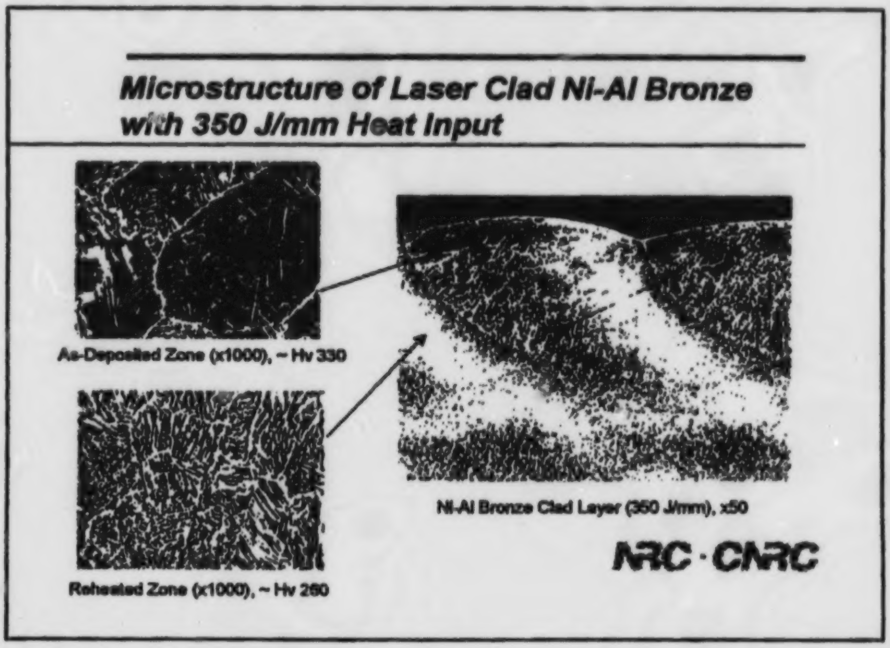

Microstructure of Laser Clad Ni-Al Bronze with 350 J/mm Heat Input

As-Deposited Zone (x1000), ~ Hv 330

Reheated Zone (x1000), ~ Hv 260

Ni-Al Bronze Clad Layer (350 J/mm), x50

NRC · CNRC

Comparison of Hardness in Laser Clad Coatings with Different Heat Input

Region	Average Micro-Hardness, Hv_{200}	
	150 J/mm Heat Input	350 J/mm Heat Input
As-Deposited Zone	370	330
Reheated Zone	310	280
Substrate	150	

- The laser clad Ni-Al bronze coating with 150 J/mm heat input has higher hardness compared with that with 350 J/mm heat input.

NRC · CNRC

Phase Identification of Laser Clad Ni-Al Bronze Coatings with X-Ray Diffraction

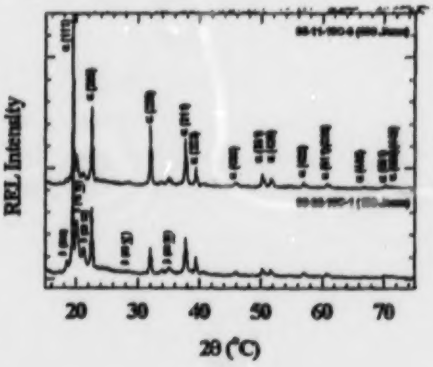

- Zr-filtered MoKα x-ray irradiation was used for the measurement.
- No significant difference in the x-ray diffraction patterns of two coatings with different heat inputs.
- Both have majority of α phase plus small amount of β* phase.

NRC · CNRC

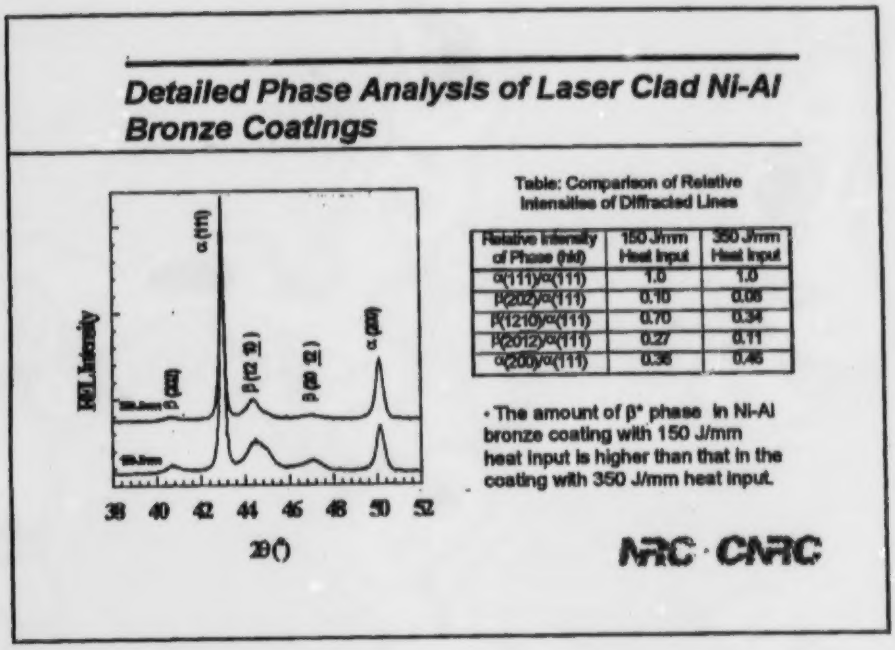

Detailed Phase Analysis of Laser Clad Ni-Al Bronze Coatings

Table: Comparison of Relative Intensities of Diffracted Lines

Relative Intensity of Phase (hkl)	150 J/mm Heat Input	350 J/mm Heat Input
α(111)/α(111)	1.0	1.0
β(202)/α(111)	0.10	0.06
β(1210)/α(111)	0.70	0.34
β(2012)/α(111)	0.27	0.11
α(200)/α(111)	0.36	0.46

- The amount of β' phase in Ni-Al bronze coating with 150 J/mm heat input is higher than that in the coating with 350 J/mm heat input.

NRC · CNRC

Comparison of Micro-Strains of Laser Clad Ni-Al Bronze Coatings

(hkl)	Lattice Strain (%)	
	150 J/mm Heat Input	350 J/mm Heat Input
α(200)	0.228	0.141
α(220)	0.146	0.107

- The lattice strain (micro-strain) is measured by x-ray diffraction method (peak broadening) with Zr-filtered *MoKα* radiation.
- The micro-strain of α phase in Ni-Al bronze coating clad with 150 J/mm heat input is higher than that in the coating with 350 J/mm heat input.

NRC · CNRC

Surface Macro Residual Stress Evaluation of Laser Clad Ni-Al Bronze with XRD

- $\sin^2\Psi$ method was used to measure the peak shift of (331) plane.
- Ni-filtered *CuKα* x-ray irradiation with 40 kV / 55 mA.
- Assuming bulk E ≈ 130 GPa, $\nu = 0.3$.

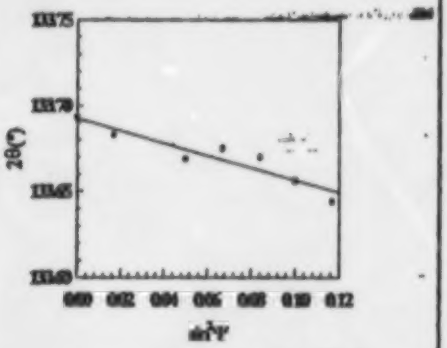

NRC · CNRC

Surface Residual Stress Measurements of Laser Clad Ni-Al Bronze with XRD

For 350 J/mm heat input:
$\sigma_1 = 149 \pm 26$ MPa
$\sigma_2 = 133 \pm 22$ MPa
For 150 J/mm heat input:
$\sigma_1 = 133 \pm 30$ MPa
$\sigma_2 = 138 \pm 28$ MPa

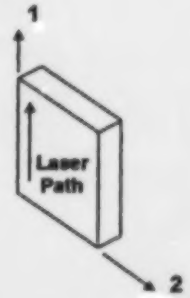

NRC · CNRC

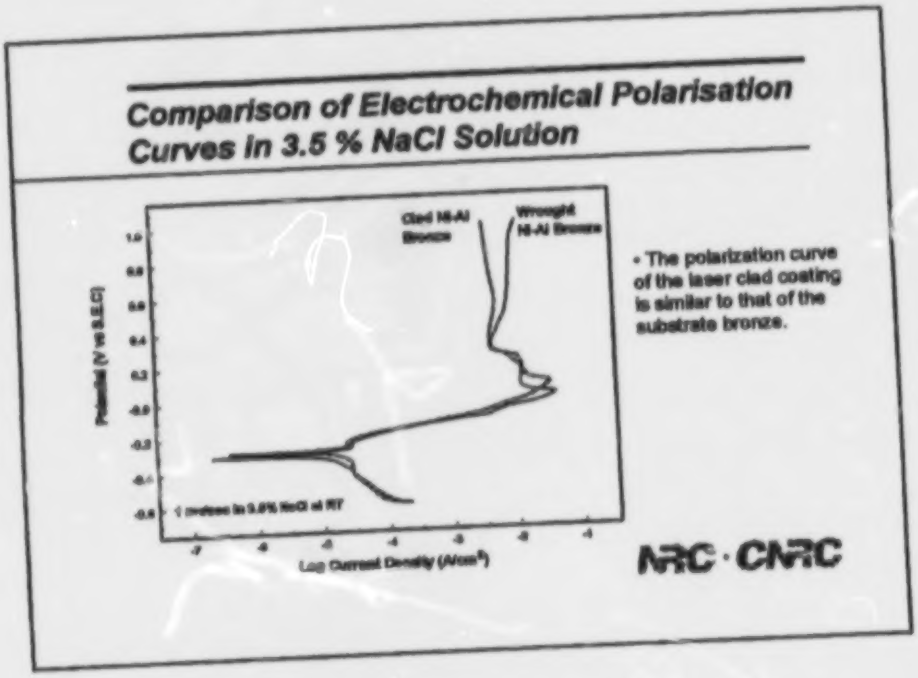

Comparison of Electrochemical Polarisation Curves in 3.5 % NaCl Solution

- The polarization curve of the laser clad coating is similar to that of the substrate bronze.

NRC · CNRC

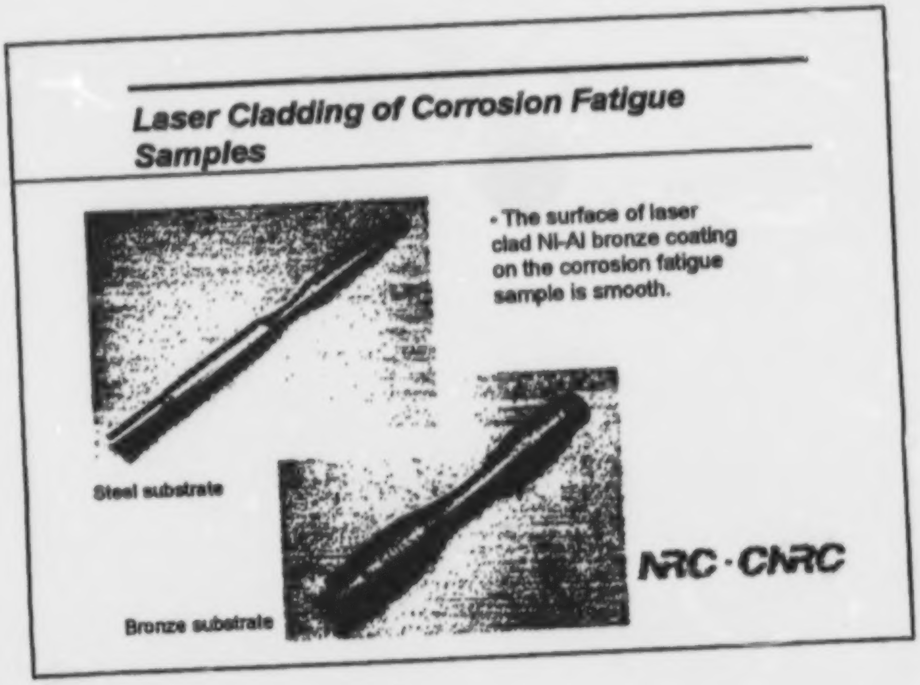

Laser Cladding of Corrosion Fatigue Samples

- The surface of laser clad Ni-Al bronze coating on the corrosion fatigue sample is smooth.

NRC · CNRC

Cross-Sectional Views of Clad Ni-Al Bronze Coating on Corrosion Fatigue Sample

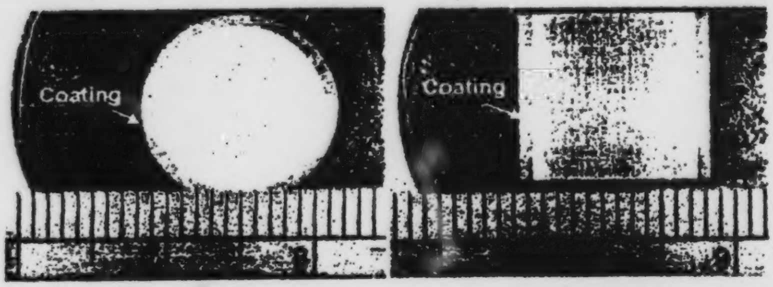

(a) Perpendicular direction

(b) Axial direction

- The Ni-Al bronze coating is uniform, free of porosity and cracking.

NRC · CNRC

Hardness of Ni-Al Bronze Coating on Corrosion Fatigue Samples

- The substrate dimension of the corrosion fatigue sample is relatively small.
- The hardness of Ni-Al bronze coating at the reduced section is significantly reduced due to the limited heat sink effect.
- The hardness of Ni-Al bronze coating at the area can increase with additional cooling methods.

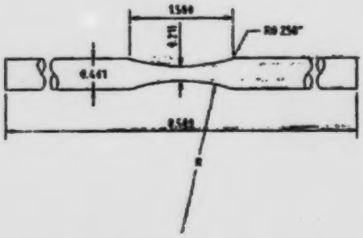

The substrate dimension of corrosion fatigue sample before cladding.

NRC · CNRC

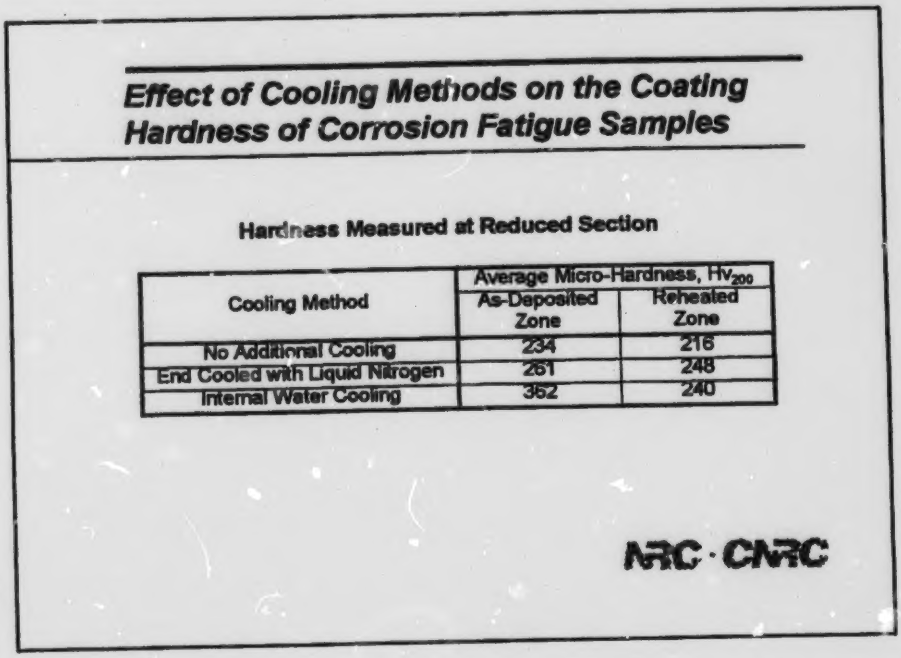

Effect of Cooling Methods on the Coating Hardness of Corrosion Fatigue Samples

Hardness Measured at Reduced Section

Cooling Method	Average Micro-Hardness, Hv_{200}	
	As-Deposited Zone	Reheated Zone
No Additional Cooling	234	216
End Cooled with Liquid Nitrogen	261	248
Internal Water Cooling	352	240

NRC · CNRC

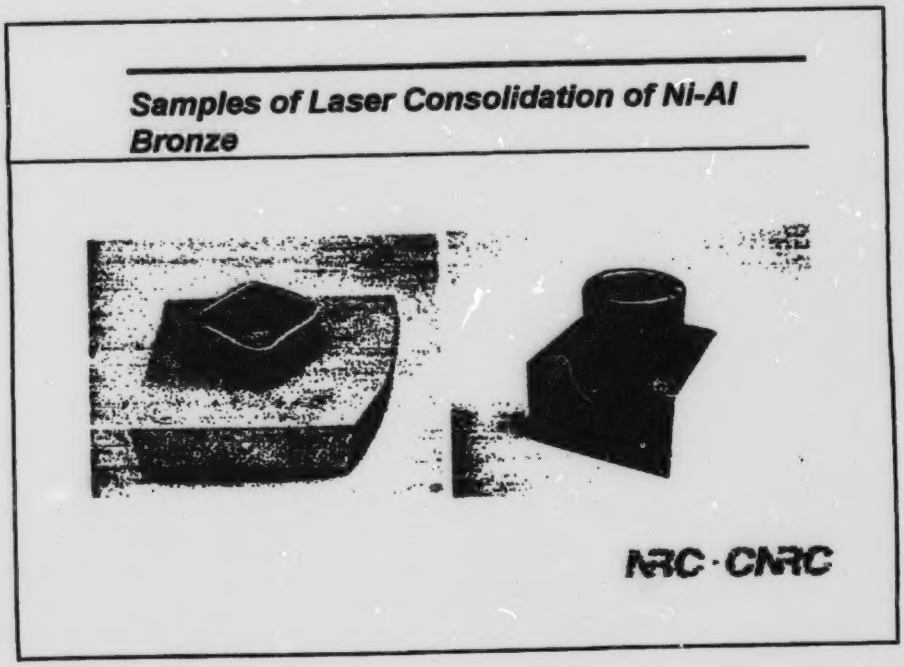

Samples of Laser Consolidation of Ni-Al Bronze

NRC · CNRC

Conclusions

- With optimized processing parameters, a uniform and crack-free Ni-Al bronze coating can be clad onto bronze substrate with a CO_2 laser and continuous wire feeding.
- The laser clad Ni-Al bronze coating is harder than substrate. However, the coating hardness is significantly affected by the laser heat input as well as the substrate cooling effect.

NRC · CNRC

Conclusions

- In 3.5% NaCl solution, the polarization curve of the laser clad coating is similar to that of the substrate bronze.
- The laser cladding process can be used for repairing marine components, while the laser consolidation process can be used to build features on the components or produce functional rapid prototype parts for marine applications.

NRC · CNRC

Acknowledgements

- The authors would like to thank Jon Fenner for his significant contribution in process development.
- Thanks are also expressed to Andrew Chen, Glen Campbell, Andre Theriault and Mike Meinert for their numerous contributions for the work.

#511898 - ㉔

Investigation of Cracked Propeller Blades on an Icebreaker

by L.N. Pussegoda and L. Malik

Fleet Technology Ltd., 311 Legget Drive, Kanata, Ontario K2K IZ8

ABSTRACT

Examination of two blades of a four bladed CP propeller, from the port shaft of an icebreaker that had through thickness fractures is discussed. The fractures propagated radially from the blade tip part way down the blade before arresting. The direction of the chevrons on the fracture surface indicated that the fracture initiation sites were located in the tip region of the blade. The other two port propeller blades with major portions lost in operation also had fracture initiation sites at the tip region.

Metallography revealed that extensive multi-pass weld build up and weld repairs had been carried out in the blade tip regions. These regions also displayed lack of fusion and porosity type flaws.

In the initiation region, the cracks propagated in stages displaying run-arrest events. The main through thickness crack did not occur until the crack propagation reached the un-refined as-cast microstructure. This is because of the superior toughness of the refined microstructure in the repair region.

The fracture features of the initiation region in blade 1 demonstrated loading from both sides of the CP blade. This opened up the possibility of fatigue crack propagation in that region. Finally, recommendations and suggestions were presented aimed at avoiding such failures in the future.

Investigation of Cracked Propeller Blade on an Icebreaker

L. N. Pussegoda, L. Malik *and* **B. Paterson**
Fleet Technology Limited

Presented at

8th CF/CRAD Meeting on Naval Applications of Materials Technology

Dartmouth, Nova Scotia, May 11-13th, 1999

FTL FLEET TECHNOLOGY LTD.

Site Investigation Findings 1

- **A Broken Blade (two out of four)**

  CP Port Propeller - damaged,

  Starboard - no damage,

  Material – Cunial (Ni-Ai-Bronze)

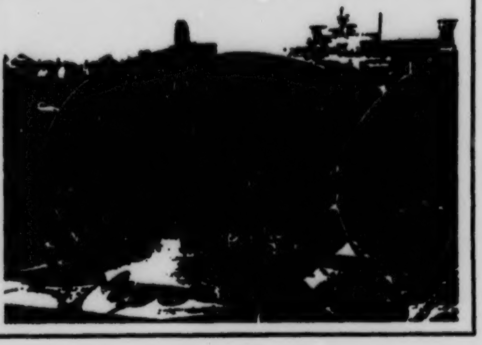

FTL FLEET TECHNOLOGY LTD.

Site Investigation Findings 2

No significant surface scratches or gouges

Significant loading from the HP side from relative movement.

All four blade cracks commencing from tips. Two stages of fracture.

Damage incident report 60 to 70% multi-year ice.

FTL FLEET TECHNOLOGY LTD.

Laboratory Investigation 1

Investigations Performed on the Two Cracked Blades

- Visual Examination
- Fractography
- Metallography
- Chemical Analysis

FTL FLEET TECHNOLOGY LTD.

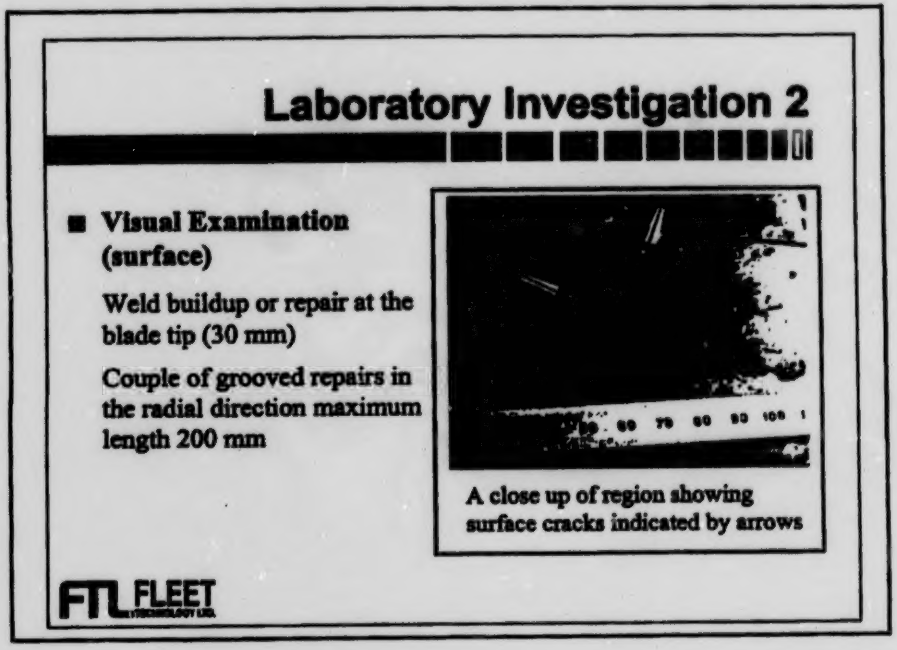

Laboratory Investigation 2

- **Visual Examination (surface)**

  Weld buildup or repair at the blade tip (30 mm)

  Couple of grooved repairs in the radial direction maximum length 200 mm

A close up of region showing surface cracks indicated by arrows

FTL FLEET TECHNOLOGY LTD.

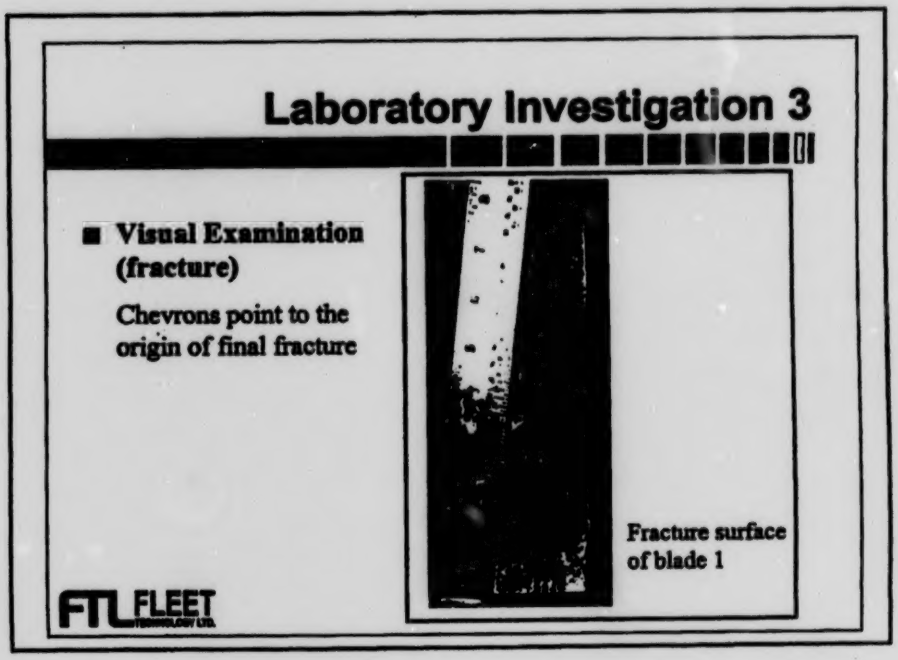

Laboratory Investigation 3

- **Visual Examination (fracture)**

  Chevrons point to the origin of final fracture

Fracture surface of blade 1

FTL FLEET TECHNOLOGY LTD.

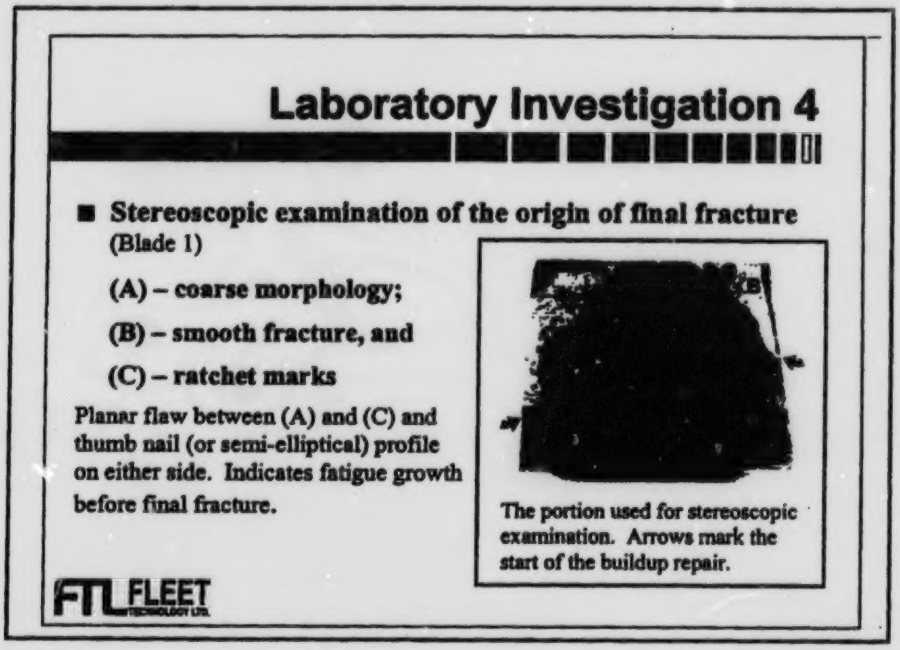

Laboratory Investigation 4

- **Stereoscopic examination of the origin of final fracture** (Blade 1)

  (A) – coarse morphology;

  (B) – smooth fracture, and

  (C) – ratchet marks

Planar flaw between (A) and (C) and thumb nail (or semi-elliptical) profile on either side. Indicates fatigue growth before final fracture.

The portion used for stereoscopic examination. Arrows mark the start of the buildup repair.

FTL FLEET TECHNOLOGY LTD.

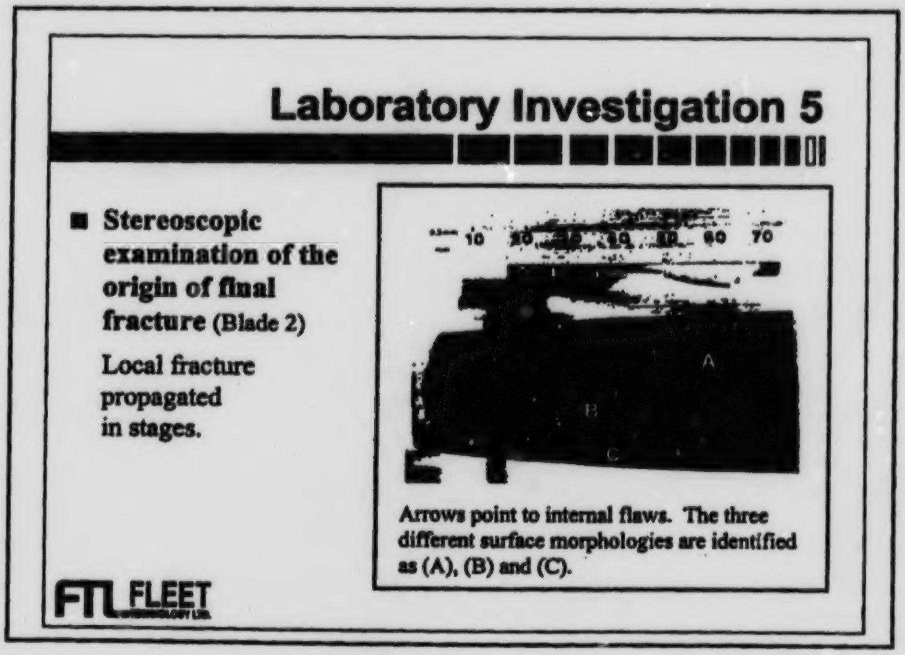

Laboratory Investigation 5

- **Stereoscopic examination of the origin of final fracture** (Blade 2)

  Local fracture propagated in stages.

10
20
30
40
50
60
70
A
B
C

Arrows point to internal flaws. The three different surface morphologies are identified as (A), (B) and (C).

FTL FLEET TECHNOLOGY LTD.

Laboratory Investigation 6

- **SEM examination**

  Objective: examine fracture facets in regions (A), (B) and (C) at high magnification.

  Cleaning in 50/50 (vol.) HCl and distilled water to remove surface oxides. Propagation region displays underlying features found in brittle fracture of bronze castings (flat facets bounded by ductile tear regions).

FTL FLEET TECHNOLOGY LTD.

Laboratory Investigation 7

- **Metallography**

  Through thickness repair

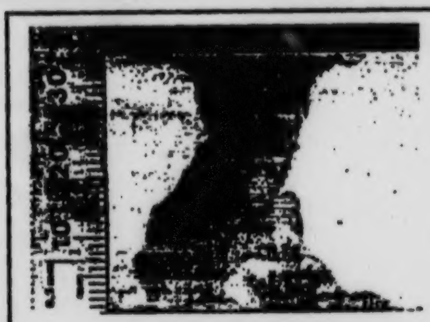

Full thickness cross-section showing a weld repair in blade 2. Alcoholic ferric chloride etch.

FTL FLEET TECHNOLOGY LTD.

Laboratory Investigation 8

- **Metallography**

  Buildup performed by multiple weld passes through the entire thickness.

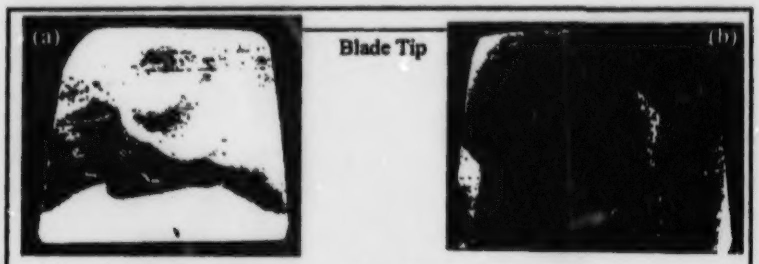

Macrographs from blade 1(a), blade2 (b) behind the fracture faces.

FTL FLEET TECHNOLOGY LTD.

Laboratory Investigation 9

- **Chemical Analysis (wt%)**

Element	C95800 (Ni-Al-Bronze)	Built Up Region	As-cast Region
Cu	remainder	81.17	79.92
Fe	3.5 to 4.5	3.66	4.67
Mn	0.8 - 1.5	1.48	1.15
Ni	4 - 5	4.38	4.33
Al	8.5 - 9.5	9.27	9.5

FTL FLEET TECHNOLOGY LTD.

Discussion

- Origin for the final fracture point to the blade tip. In this region flaws are associated with repairs/buildup with weld passes.
- Were there previous growth events locally before final failure?

Blade 2

- Fracture surface morphology indicates crack propagation in buildup areas caused by discrete loading events
- Arrest of cracks in this region; a) unloading, b) encountering higher toughness region (refined microstructure in the buildup region), c) at a boundary of a weld pass, and d) encountering an internal flaw with different orientation

FTL FLEET TECHNOLOGY LTD.

Discussion (cont.)

- **Blade 1**
  - Fracture in the origination region in one plane, in contrast to several planes in blade 2.
  - Arrest of crack in this region; a) unloading, b) encountering higher toughness region.
  - Metallography performed X-section normal to planar flaw showed refined structure in region (C) compared to as-cast structure in (A).
  - As propagation events occurred on both sides of planer flaw the explanation for arrest is the unloading option from both sides. Fatigue loading cycles are the most probable.

FTL FLEET TECHNOLOGY LTD.

Recommendations

- Proper methods of buildup by welding need to be developed, documented, and implemented to avoid unexpected costly failures.
- Any buildup or repairs need to be qualified by radiography or ultrasonic inspection to verify soundness.
- Blade tips need to be examined for planar defects during maintenance.
- Before repairs are carried out on cracked blades, investigations will be useful to obtaining a historical background with a view to creating a database on damage to CP propeller blades.

FTL FLEET

511899

Linear Elastic Fracture Toughness (K_{Ic}) and Dynamic Tear Transition

by Vincent Roy[1], Ken KarisAllen[2] and J.R. Matthews[1]

[1]Defence Research Establishment Atlantic, Dockyard Laboratory
P.O. Box 99000 Stn Forces, Halifax, Nova Scotia B3K 5X5

[2]Facts Engineering, P.O.Box 20039 Halifax, Nova Scotia B3R 2K9

ABSTRACT

The design of a modern warship is a very complex task. Some of the greatest concerns in the design are the selection of proper materials and welding techniques. The aim of the selection is to reach a design, which enables the whole structure to have a ductile behaviour under all operating conditions.

This report concentrates on Linear Elastic (K type) tests at temperatures where the Dynamic Tear energy was less than 133 joules for a 16 mm specimen. 133 joules was selected since it has been suggested that nil ductility occurs at that point for a standard Dynamic Tear Specimen.

A background on the subject at hand and a proposed new transition curve interpretation is given. The materials composition and the dynamic tear transition behaviour of three weldments and a Grade A steel chosen for testing are shown. Precracking and fracture toughness procedures are given. The fracture toughness experimental results are shown for all temperatures. A proposed relationship between the shear lip size and the critical plastic zone size is used to determine the validity of the results.

The results show that the transition curve is a useful guide to establish a temperature range where a valid plane strain test will exist. Lower shelf is not necessarily plane strain. Using the shear lip size it is possible to establish a new criteria for a valid plane strain test (i.e. shear lip size (*s*) less than thickness (B) divided by 50)

$$s < \frac{B}{50}$$

Finally, it will be shown that the measured stress intensity at fracture, K_Q, only becomes a valid K_{Ic} at a temperature below the inflection point on the K_Q versus temperature graph.

INTRODUCTION

The design of a modern warship is a very complex task. Some of the greatest concerns in the design are the selection of proper materials and welding techniques. The aim of the selection is to reach a design, which enables the whole structure to have a ductile behaviour under all operating conditions. The prediction of the performance in welded structures requires the following knowledge: Structural transition behaviour for steels and weldments, environmental conditions such as temperatures, and external influences such as insulation and heat sources [1].

The transition curves of steels and welds are a good guideline to help the designer select the proper materials. If the minimum operating temperature corresponds with the upper shelf of the transition curve the structure will have a ductile comportment and this is a desirable situation for all ships. Designers should be concerned about steels and welds, which lie in the lower shelf section of the transition curve.

Dynamic Tear (DT) Transition Curves [1,2] were completed for a grade A steel and three welds examined in this paper in order to establish the appropriate temperature for quantitative fracture tests. This report concentrates on Linear Elastic (K type) tests at temperatures where the Dynamic Tear energy was less than 133 joules for a 16 mm specimen. 133 joules was selected since a report [3] suggested that nil ductility occurs at that point for a standard DT Specimen.

It was expected that valid linear elastic fracture toughness would occur near this nil ductility temperature point but as will be seen in this paper plane strain fracture toughness would be measurable only at a much lower temperature than anticipated.

The paper is divided into distinct sections. First, a background on the subject at hand and a proposed new transition curve interpretation is given. Second, the materials composition and the dynamic tear transition behaviour for the three weldments and the steel chosen for testing is shown. Third, the precracking procedure is given. Fourth, the procedure for the fracture toughness test is given. Fifth, a proposed relationship between the shear lip size and the critical plastic zone size is discussed. Sixth, the fracture toughness experimental results are shown for all temperatures. Seventh, the validity of the results are discussed by using the shear lip size and the critical plastic zone size. Eighth, a final discussion and overview graphs are given.

BACKGROUND

The plane strain linear elastic toughness (K_{Ic}) characterizes the resistance of a material to fracture in a neutral environment in the presence of a sharp crack under severe tensile constraint. The K_{Ic} value represents a limiting value of fracture toughness [4]. This property is used to estimate the relation between failure stress and defect size for materials in a high constraint condition.

The transition curve represented in Figure 1 shows the energy transition behaviour in relation to the temperature. The top shelf where there is full plastic shear, the material behaves in a ductile manner. The relevant material property in this top shelf zone is the flow stress in shear. The flow stress in shear($\hat{k}$) is approximately half the yield strength. In the elastic-plastic zone, failure can be evaluated using the J_{Ic} equations. In transition, the most relevant property, for shear lips between B/20 and B/2, is strain to fracture. Finally, the lower shelf corresponds to an elastic behaviour. This report focuses on determining the highest temperature at which a valid K_{Ic} value can be determined for 3 different weldments and a UK supplied Grade A steel and thus the establishment of the fracture transition elastic point on the transition curve. From our results it will be apparent that the temperature range for a valid K_{Ic} is much lower than initially thought. This is also true for J_{Ic} [5] and therefore the transition curve quantitative relationships are redefined.

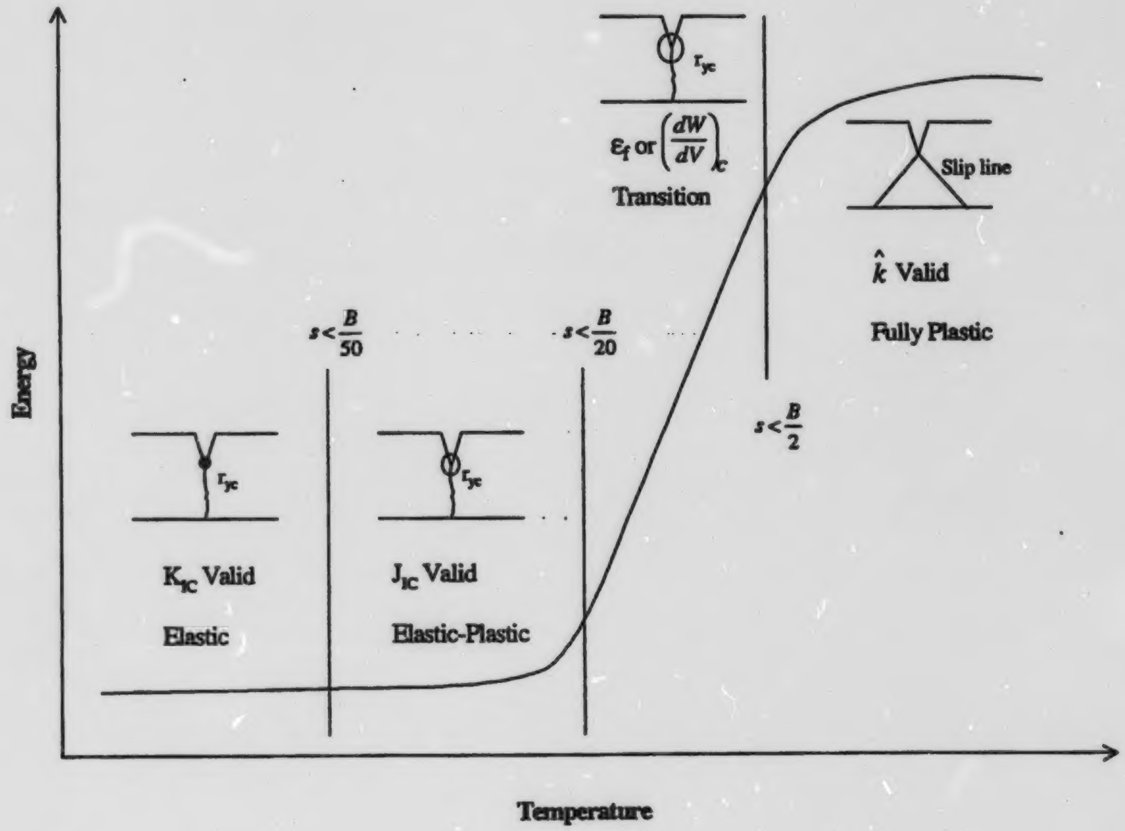

r_{yc}
ε_f or $\left(\frac{dW}{dV}\right)_c$
Transition
Slip line
$\hat{k}$ Valid
Fully Plastic
$s<\frac{B}{50}$
$s<\frac{B}{20}$
$s<\frac{B}{2}$
Energy
r_{yc}
r_{yc}
K_{IC} Valid
Elastic
J_{IC} Valid
Elastic-Plastic
Temperature

Figure 1. Transition curve.

MATERIAL

The materials mentioned in this paper include three weldments of a CSA G40.21 Gr 350WT steel and a British Grade A steel plate. Table 1a describes these three weldments and Table 1b describes the Grade A steel.

Table 1a. Weldment description for samples tested.

	Weldment #3	Weldment #11	Weldment #12
Base Material	350WT	350WT	350WT
Thickness	8 mm (0.31 in)	12 mm (0.47 in)	12 mm (0.47 in)
Weld Process	SAW	SAW	FCAW
Position	1G Ceramic	1G	1G Ceramic
Joint	SQ	SQ	SV
Root opening	0 mm (0 in)	0 mm (0 in)	6-8 mm (0.24 in)
Root Face	8 mm (0.31 in)	12 mm (0.47 in)	1 mm (0.04 in)
Bevel Details	Square	Square	60° included

Table 1b. Chemical composition of British Grade A Steel.

C	Mn	Si	P	S
0.15-0.16	0.85-0.90	0.20-0.27	0.016-0.025	0.017-0.020

The lower shelf K_{Ic} testing was performed on the three weldments with the worst transition performance in a series of 21 weldments in a materials data base study [1]. The lower shelf K_{Ic} testing was performed on the steel because it exhibited poor transition performance.

DYNAMIC TEAR TRANSITION BEHAVIOUR

The dynamic tear test results for the 3 weldments [1] studied in this paper are shown in Figure 2a. The results for the Grade A Steel, for both T-L and L-T directions, are shown in Figure 2b. For the K tests, the L-T direction was selected. Figures 2a and b are critical since the results helped select temperatures for the fracture toughness tests performed in this work. The dynamic tear tests were completed with ASTM E604 specimens in a drop tower.

From Figure 2a, it is evident that the 3 weldments tested are lower shelf below about 0°C according to the dynamic tear transition curve. It is evident that in the L-T direction, British Grade A Steel at 10 °C is lower shelf according to the dynamic tear transition curve. Does lower shelf mean valid K_{Ic}? This report attempts to answer that question.

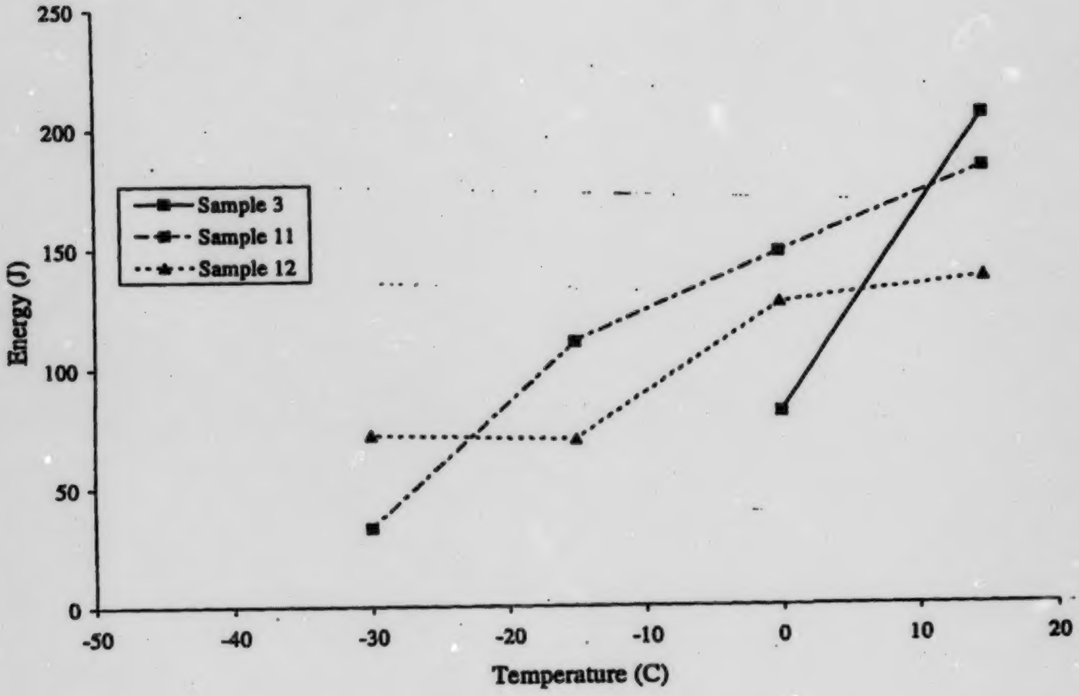

Figure 2a. Dynamic Tear Transition of Simulated Weldments #3, #11 and #12 [1].

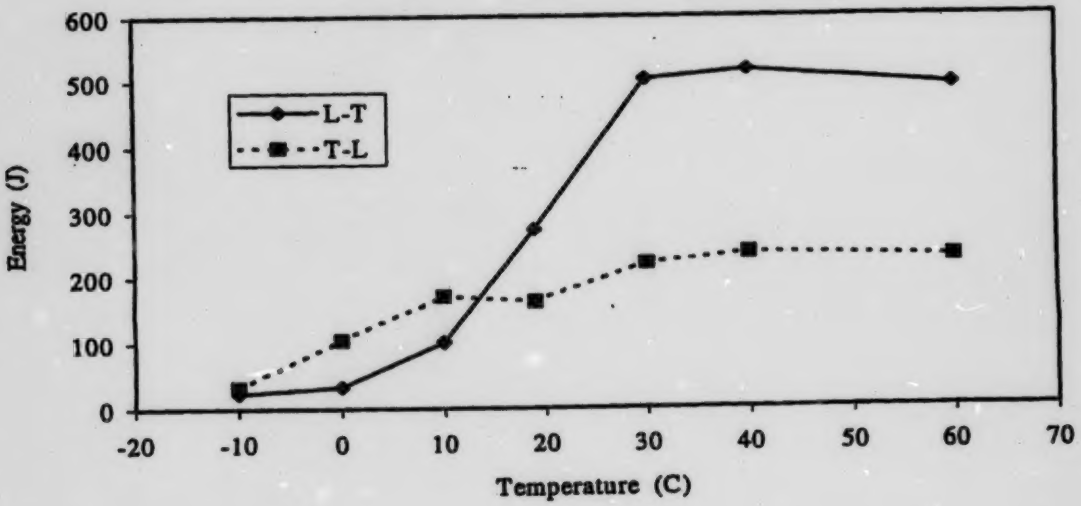

Figure 2b. Dynamic Tear Transition Curve of British Grade A Steel.

PROCEDURE FOR SPECIMEN PRECRACKING

Carefully controlled fatigue precracking [6] was used to obtain reproducible sharp cracks in well defined plastic zones for each K test [4]. Figure 3 represents the parameters for the specimens and also the sample configuration for the 3 point bend test [3].

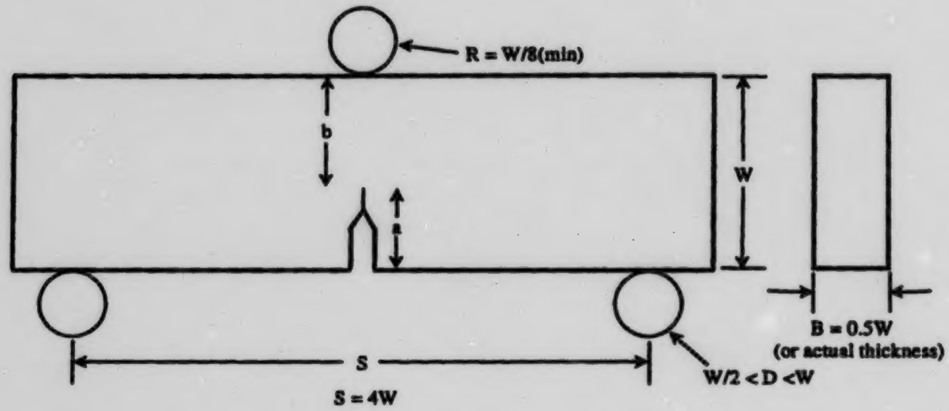

Figure 3. Set up for the 3 point bend with parameter representation.

The parameters of importance are defined as:

P_L	limit load (load at which permanent bending will occur)
a	crack length
W	specimen width
b	uncracked ligament (b = W - a)
B	thickness
σ_Y	yield strength
S	span between bottom rollers (4W)

The load ratio (min load/max load) R=0.1 was used to fatigue all the specimens. A fraction of the load P_L was used during the weldment precracking. For three point bend specimens Equation 1 was used to determine the P_L values [5].

$$P_L = \left[\left(\frac{4}{3}\right)\left(\frac{Bb_o^2\sigma_Y}{S}\right)\right] \qquad (1)$$

The yield strength values for the welds were determined from tensile tests performed by Fleet Technologies Limited [7]. The quasi-static yield stress at 0 °C averaged 469 MPa. The reported yield strength value for the British Grade A Steel is approximately 350 MPa (50.7 ksi). Since the yield strength does not vary much within our temperature testing range, these values were used for all tests.

The values of P_L were calculated for different crack lengths as the crack advances since P_L is crack length dependent. The P_L value had to be evaluated for each sample since the thickness and yield strength varies for each. Detailed information on precracking values can be found in references 6 and 8.

The maximum stress intensity level must not exceed 60% of the K_{Ic} value in the last 2.5 % of the fatigue crack length to have a proper precracking of the sample. If the fatigue level exceeds this value the K_{Ic} will not be valid.

Standard specimens have a crack length, a, equal to the thickness, B (but can be greater), and a/W is between 0.45 and 0.55. The ratio W/B is nominally equal to two [4]. Acceptable alternative samples are $1 \leq W/B \leq 4$. The dimensions for weldment specimen #3 is given in Table 2a. The dimensions for weldment specimens #11 and 12 and the grade A steel are given in Table 2b.

Table 2a. Specimen Dimensions (Weldment #3).

Width (W)		Thickness (B)		Crack Length (a)		Uncracked Ligament (b)	
(mm)	(in)	(mm)	(in)	(mm)	(in)	(mm)	(in)
40.6	1.6	8.9	0.35	12.7	0.5	27.9	1.1

Table 2b. Specimen Dimensions (Weldments #11 and #12 and grade A steel).

Width (W)		Thickness (B)		Crack Length (a)		Uncracked Ligament (b)	
(mm)	(in)	(mm)	(in)	(mm)	(in)	(mm)	(in)
40.6	1.6	12.7	0.5	12.7	0.5	27.9	1.1

PROCEDURE FOR FRACTURE TOUGHNESS (K_{IC}) TEST

The test method used for the determination of the plane strain fracture toughness (K_{Ic}) is covered in ASTM E399 [4]. The testing involves notched samples which are precracked in three point bend fatigue loading. During the test of a specimen, the load versus the displacement across the notch is measured. The point at which the load versus the displacement ceases to be linear (P_Q) can be established as the point representing a 2 % increase in crack length. This load is recorded and is used to determine the fracture toughness value. The equations established to calculate the K_{Ic} value are based on elastic stress analysis.

A sharp-crack condition at the tip of the notch had to be present in order to have a valid K_{Ic} test. Therefore the stress intensity level at which the specimen was fatigue cracked had to be limited to a relatively low value.

Specimens were loaded in a testing machine that had a proper fixture in order to minimize the frictional contribution to the measured load. The displacement gauge was installed to indicate the relative displacement of two precisely located gauge positions spanning the crack starter notch mouth [4]. Figure 4 gives a representation of the setup used in the K_{Ic} test.

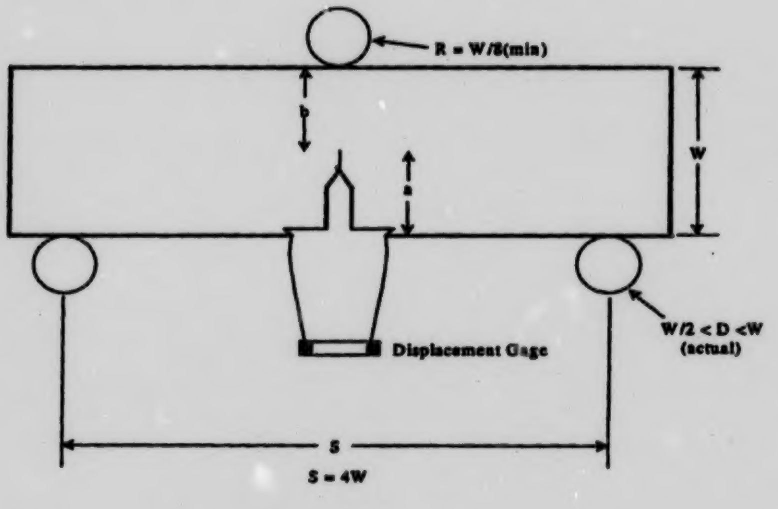

Figure 4. Bend Test Configuration.

Each gauge was checked for linearity using an extensometer calibrator. The gauge employed during the test was provided by Instron and had an initial gauge width of 7.5 mm. It was capable of measuring a displacement, from its initial position, to approximately 3 mm.

In order for the results to be valid Equations 2 and 3 must be satisfied [4]:

$$B \geq 2.5\left(\frac{K_{Ic}}{\sigma_{YS}}\right)^2 \qquad (2)$$

$$a \geq 2.5\left(\frac{K_{Ic}}{\sigma_{YS}}\right)^2 \qquad (3)$$

where σ_{YS} is the 0.2 % offset yield strength of the material for the temperature and loading rate of the test [4]. Normally, the initial size of the specimen is selected so that valid results will be obtained. For this work the samples were already defined so it therefore remained to verify the results with Equations 2 and 3.

For the calculation of the plane strain toughness three measurements are necessary (B, a and W). The thickness of the three specimens was measured to the nearest 0.025 mm (0.001 in) and the average was calculated; the resulting value was B. The nine crack lengths were measured to the nearest 0.5 % on both sides of each specimen. A difference of more than 10 % on each side of a specimen was unacceptable [4]. Again, the average was calculated; the resulting value was a.

In order to establish if the results from a specimen were valid, it was necessary to calculate conditional results. P_Q is determined graphically from the output collected during the experiment. First, a tangential line is drawn from the linear part of the graph, ensuring it passes through the origin. The slope was then calculated. 95 % of the slope was calculated and was drawn on the same graph and the point at which it crossed the output was identified as P_Q. The procedure to find P_Q is demonstrated in Figure 5.

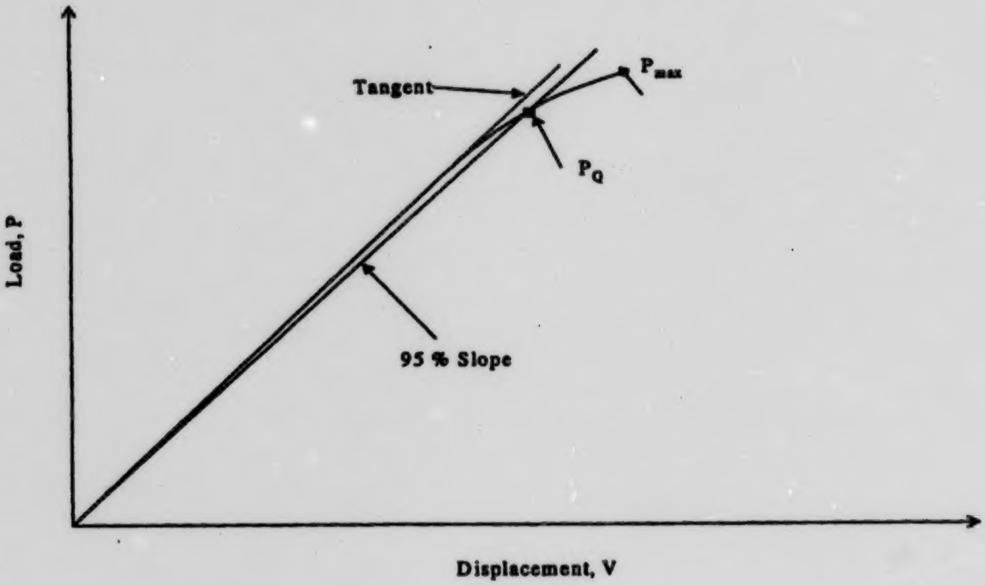

Figure 5. Graphical representation of P_Q.

If the ratio P_{max}/P_Q exceeded 1.1, then the test was not a valid K_{Ic} [4]. If the ratio was less than 1.1 then Equations 2 and 3 were used to confirm the validity of the test. If the test is valid then K_Q is equal to K_{Ic}. Accordingly, the plane strain fracture toughness, K_{Ic}, was calculated using Equations 4 and 5 [4].

$$K_Q = \left(\frac{P_Q S}{B W^{3/2}} \right) \cdot f\left(a/W \right) \tag{4}$$

$$f\left(a/W \right) = \frac{3\left(a/W \right)^{1/2} \left[1.99 - \left(a/W \right)\left(1 - a/W \right) \cdot \left(2.15 - 3.93\, a/W + 2.7\, a^2/W^2 \right) \right]}{2\left(1 + 2\, a/W \right)\left(1 - a/W \right)^{3/2}} \tag{5}$$

The shear lip was also measured [9] for each sample at closest point of contact (x) of the two lips.

$$s = \frac{B - x}{2} \tag{6}$$

SHEAR LIP SIZE AND CRITICAL PLASTIC ZONE SIZE

The critical plastic zone size (r_{Yc}) can be calculated with Equation 7 to give the size of the plastically deformed zone.

$$r_{Yc} = \frac{1}{6\pi} \left(\frac{K_{Ic}}{\sigma_Y} \right)^2 \tag{7}$$

In order to have a valid test it is well known that a, b, and B must be greater than 50 times the critical plastic zone radius. For the plane strain case, Equation 8 shows that Equation 2 is found again.

$$a, b, B \geq \frac{50}{6\pi} \left(\frac{K_{Ic}}{\sigma_Y} \right)^2 = 2.5 \left(\frac{K_{Ic}}{\sigma_Y} \right)^2 \tag{8}$$

According to Matthews [9], it is estimated that the shear lip size, s, is approximately equal to the critical radius, r_{Yc}, in the elastic range. Using the previous relationship in Equation 8, it is therefore possible to establish Equation 9 as a requirement for a valid plane strain test.

$$s < \frac{B}{50} \tag{9}$$

FRACTURE TOUGHNESS (K_{Ic}) TEST RESULTS

The fatigued weldments were tested in the CO_2 cold chamber at various temperatures to give broad results in the elastic-plastic zone. The specimens were preloaded to 200 kg to ensure that the clip gauge was properly set in.

It was verified experimentally that one hour was sufficient time to assure that the core temperature was equal to the ambient chamber temperature at -40 °C.

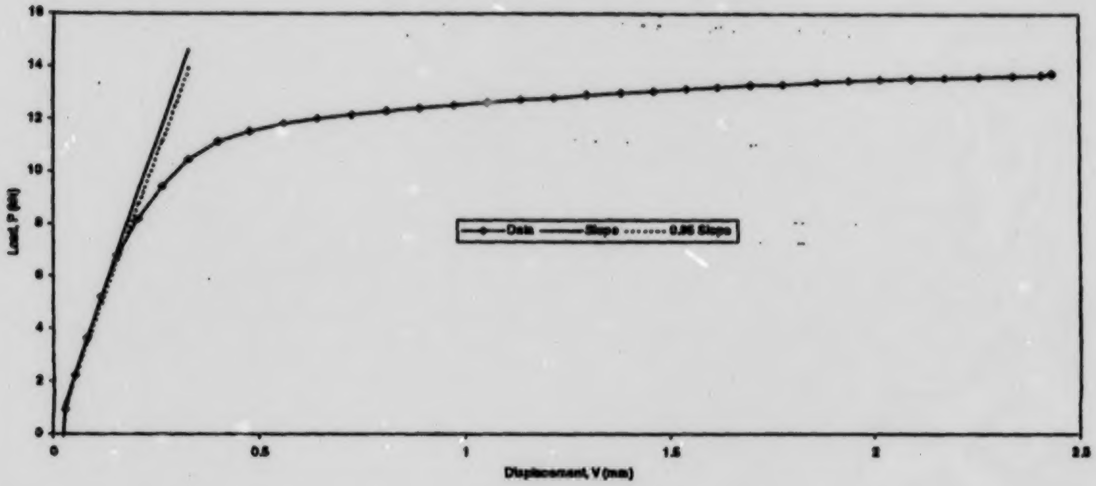

Figure 6a. Weldment #3 at Room Temperature (18 °C).

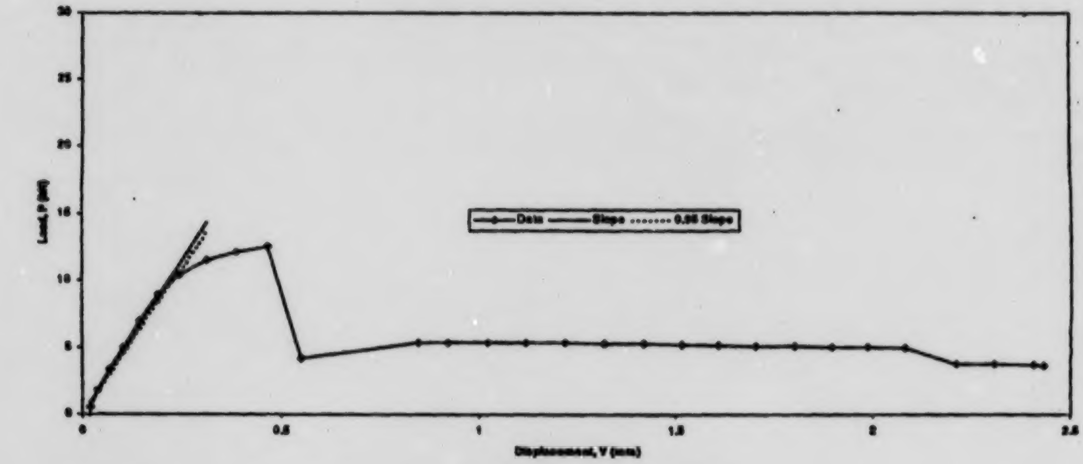

Figure 6b. Weldment #3 at -20 °C.

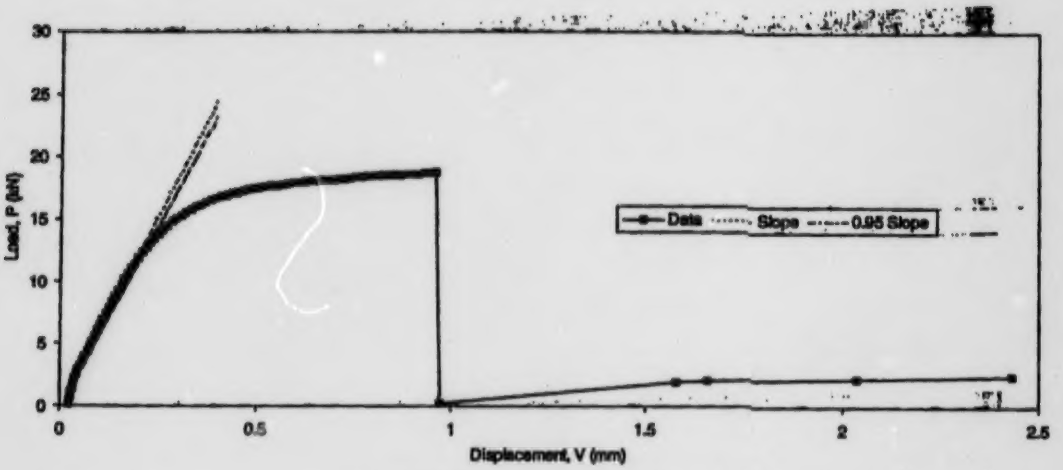

Figure 6c. Weldment #3 at -40 °C.

Figures 6a, b and c show the load in kilonewtons versus displacement in millimeters at various temperatures. The displacement V is the clip gauge opening. Two slopes are shown on each graph; the slope of the initial data points and the second slope 95% of that value. Also, the information in Table 3a was gathered from Figures 6a to c.

Table 3a. Calculated results from Weldment #3

Temperature (°C)	18	-20	-40
a/W	0.54	0.55	0.49
P_Q (kN)	7.25	10.0	13.1
P_{max} (kN)	13.5	12.5	18.8
P_{max}/P_Q	1.86	1.25	1.44
K_Q (MPa $m^{1/2}$)	49.2	69.4	76.3
$2.5(K_Q/\sigma_y)^2$ (mm)	27.6	54.7	66.2
B/50 (mm)	0.178	0.178	0.178
s (mm)	4.5	0.75	0.36

From the results at 18, -20 and -40 °C it is obvious that the tests were not valid K_{Ic}. The P_Q and P_{max} ratio, as shown in Table 3a, exceeds the allowed value in the ASTM standard. Weldment #3 displayed no ductility at -20 °C and below. This indicates that the material should have behaved elastically.

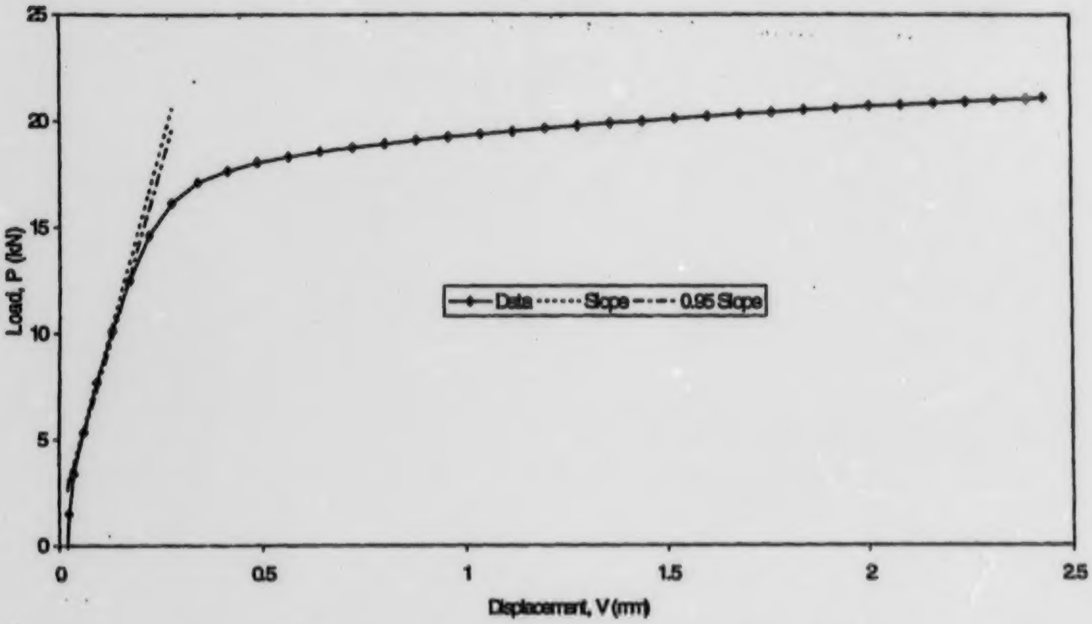

Figure 7a. Weldment #11 at Room Temperature (18 °C).

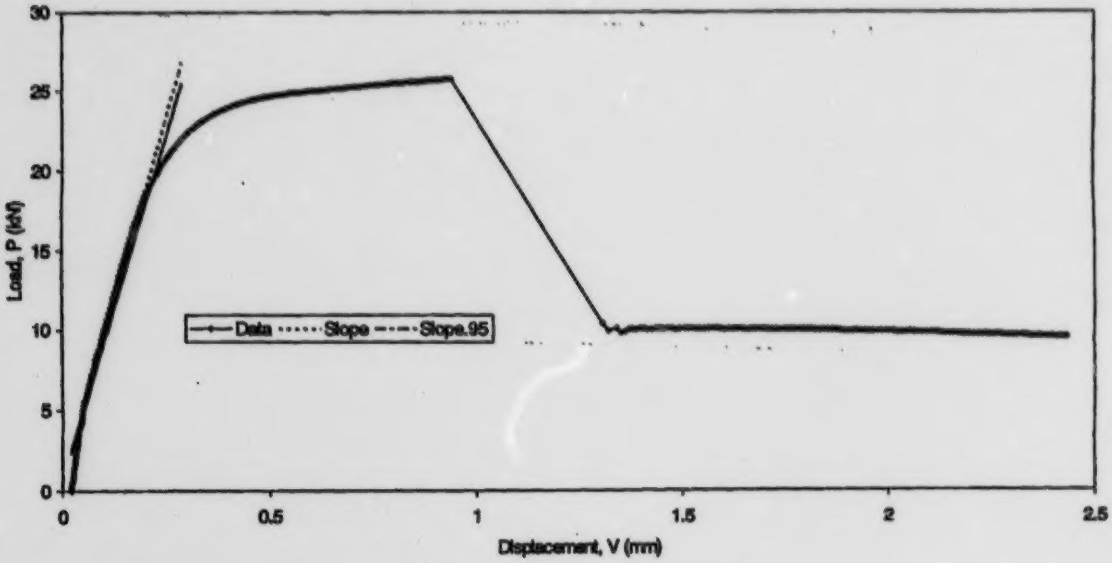

Figure 7b. Weldment #11 at -20 °C.

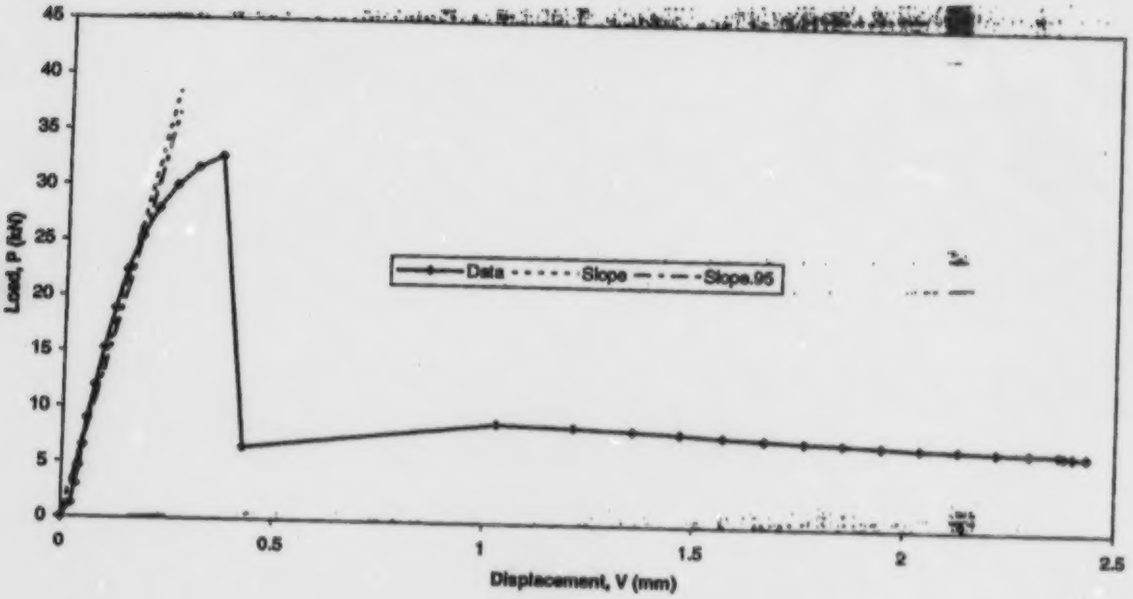

Figure 7c. Weldment #11 at -40 °C.

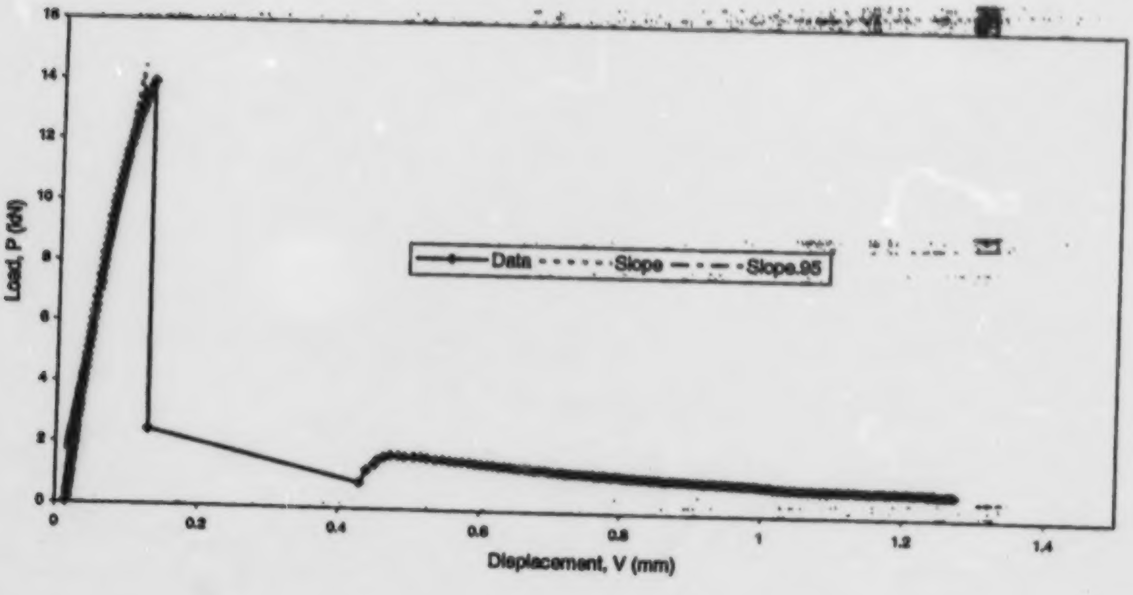

Figure 7d. Weldment #11 at -45 °C.

Figures 7a, b, c and d show the load in kilonewtons versus displacement in millimeters at various temperatures for Weldment #11. The displacement V is the clip gauge opening. Two slopes are shown on each graph; the slope of the initial data points and the second slope is 95% of that value. Also, the information in Table 3b was gathered from Figures 7a to d.

Table 3b. Calculated results from Weldment #11

Temperature (°C)	18	-20	-40	-45
a/W	0.53	0.47	0.43	0.41
P_Q (kN)	12.5	19.2	25.5	12.7
P_{max} (kN)	21	25.8	32.71	13.9
P_{max}/P_Q	1.7	1.3	1.3	1.1
K_Q (MPa $m^{1/2}$)	59.3	76.2	89.4	41.8
$2.5(K_Q/\sigma_y)^2$ (mm)	40.0	66.0	90.9	19.8
B/50 (mm)	0.244	0.244	0.244	0.244
s (mm)	4.45	1.0	0.64	0.3

From the results at 18, -20 and -40 °C it is obvious that the tests were not valid K_{Ic}. The P_Q and P_{max} ratio, as shown in Table 3b, exceeded the allowed value in the ASTM standard. Weldment #11 displayed no ductility at -20 °C and below. This indicates that the material should have behaved elastically. The fatiguing on the weldments at -40 and -45 °C did not meet the standard's requirements for shape but at -45 °C, the weldment displayed a fully elastic behaviour and met the P_Q and P_{max} ratio of 1.1.

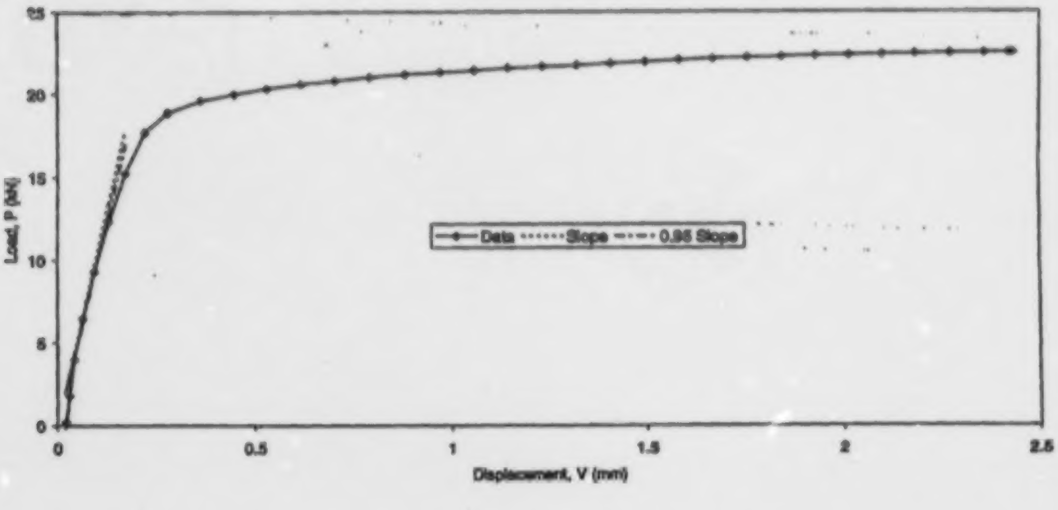

Figure 8a. Weldment #12 at Room Temperature (18 °C).

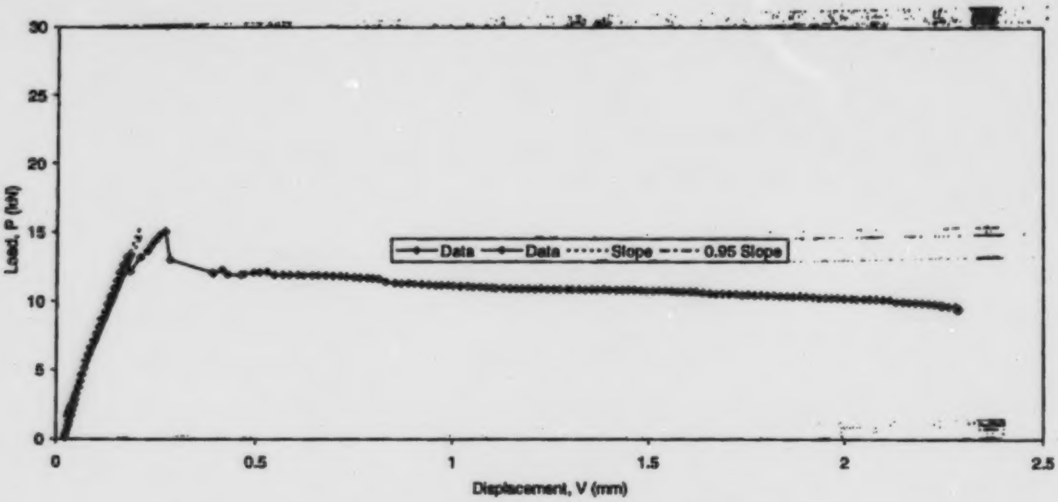

Figure 8b. Weldment #12 at -30 °C.

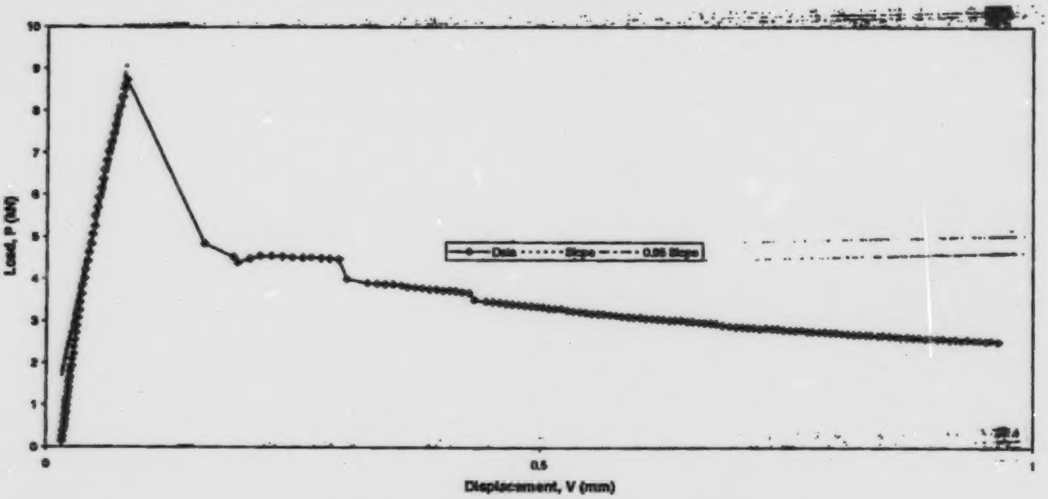

Figure 8c. Weldment #12 at -45°C.

Figures 8a, b and c show the load in kilonewtons versus displacement in millimeters at various temperatures for Weldment #12. The displacement V is the clip gauge opening. Two slopes are shown on each graph; the slope of the initial data points and the second slope is 95% of that value. Also, the information in Table 3c was gathered from Figures 8a to c.

Table 3c. Calculated results from Weldment #12

Temperature (°C)	18	-30	-45
a/W	0.49	0.51	0.42
P_Q (kN)	9.2	13.2	8.0
P_{max} (kN)	22.5	15.1	8.7
P_{max}/P_Q	2.5	1.14	1.1
K_Q (MPa $m^{1/2}$)	39.1	58.5	27.3
$2.5(K_Q/\sigma_y)^2$ (mm)	17.6	39.4	8.6
B/50 (mm)	0.244	0.244	0.244
s (mm)	2.7	1.9	0.45*

*At a/W = 0.5. At a/W = 0.7, the shear lip size was 1.54mm.

From the results at 18 and -20 °C it is obvious that the tests were not valid K_{Ic}, according to the ASTM standard. The P_Q and P_{max} ratio, as shown in Table 3c, exceeds the allowed value in the ASTM standard, although not much in the case at -30 °C. Weldment #12 displayed no ductility at and below -30 °C, and except for crack shape met the validity requirements at -45 °C.

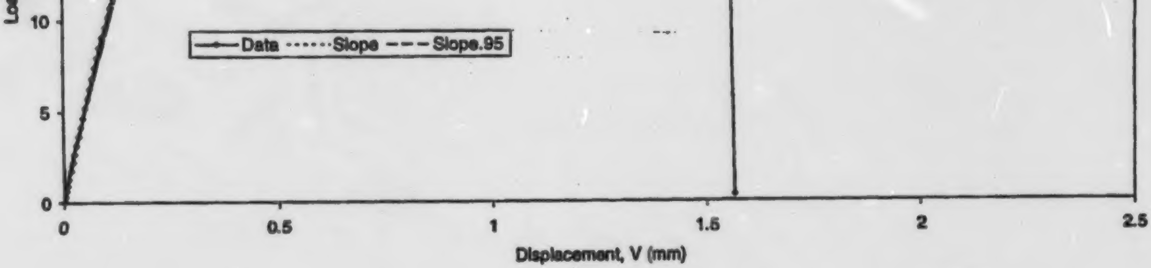

Figure 9a. Steel Specimen #15 at –40 °C.

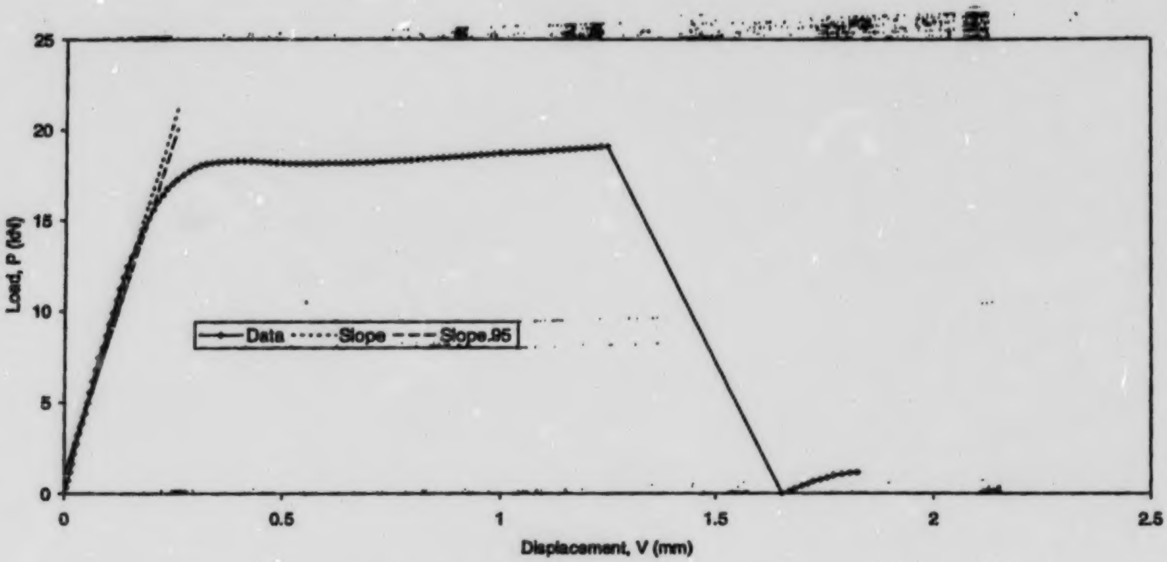

Figure 9b. Steel Specimen #18 at -55 °C.

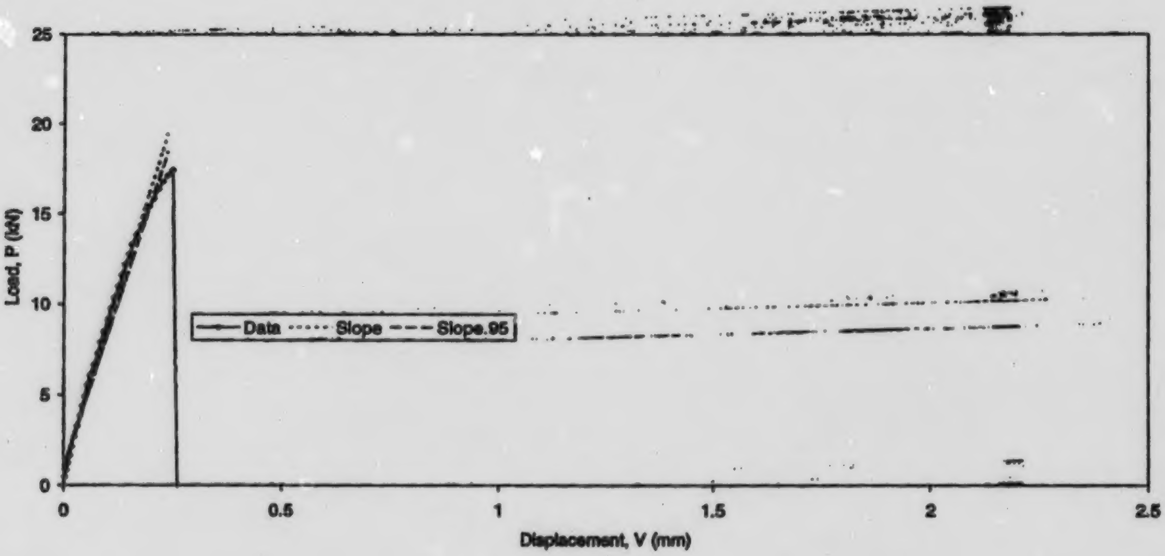

Figure 9c. Steel Specimen #17 at -65 °C.

Figures 9a, b and c show the load in kilonewtons versus displacement in millimeters at various temperatures for the Grade A steel. The displacement V is the clip gauge opening. Two slopes are shown on each graph; the slope of the initial data points and the second slope 95% of that value. Also, the information in Table 4 was gathered from Figures 9a to c.

Table 4a. K_Q vs Temperature results for British Grade A Specimens.

Temperature (°C)	-70	-65	-55	-40	-20	0
K_Q	52.6	63.4	62.4	51.0	48.7	48.6

Table 4b. Detailed results from select British Grade A specimens (near inflection point).

Temperature (°C)	-40	-55	-65
a/W	0.46	0.48	0.48
P_Q (kN)	13.5	15.6	15.9
P_{max} (kN)	20.1	19.1	17.4
P_{max}/P_Q	1.49	1.22	1.10
K_Q (MPa m$^{1/2}$)	51.0	62.4	63.4
$2.5(K_Q/\sigma_y)^2$ (mm)	53.2	79.5	82.2
B/50 (mm)	0.25	0.25	0.25
s (mm)	0.42	0.33	0.04

From the results at -40 and -55 °C it is obvious that the tests were not valid K_{Ic}. The P_Q and P_{max} ratio, as shown in Table 4b, exceeded the allowed value in the ASTM standard. British Grade A displayed no evident ductility except for a small band near the fracture initiation area at -40 and -55 °C. At -65 °C, the band was non-existent, which perhaps explains the lower P_{max}/P_Q ratio and why the specimen displayed a fully elastic behaviour.

VALIDITY OF PLANE STRAIN FRACTURE TOUGHNESS RESULTS

According to [9], shear lip size, s, is approximately equal to the critical radius, r_{Yc}, in the data range. Based on this relationship, Equation 9 can be a criteria to determine the validity of a test. Tables 5a and b evaluate B/50 and give the results on the Equation 9 criteria.

Table 5a. Validity of Plane strain Fracture Toughness Based on Shear Lip Size for Weldments.

Weldments	Temperature (°C)	Shear Lip Size (mm)	B/50 (mm)	S ≤ B/50
#3	18	4.5	0.178	NO
	-20	0.75		NO
	-40	0.36		NO
#11	18	4.45	0.244	NO
	-20	1.0		NO
	-40	0.64		NO
	-45	0.3		YES*
#12	18	2.7	0.244	NO
	-30	1.9		NO
	-45	0.45		NO

* Within 20% of B/50.

Table 5b. Validity of Plane Strain Fracture Toughness Based on Shear Lip Size for Steel.

Specimens	Temperature (°C)	Shear Lip Size (mm)	B/50 (mm)	s ≤ B/50
Steel 15	-40	0.42	0.25	NO
Steel 18	-55	0.33		NO
Steel 17	-65	0.04		YES

DISCUSSION

There is some ambiguity in the E399 standard for line construction used to determine P_Q. Determining the correct secant line through the origin is very difficult when the initial slope is curved. It is stated in the ASTM standard that the slope has to be determined with high precision. This of course is essential to obtain meaningful results. The results can vary greatly as a function of choice of line position and it was chosen for this report to be conservative with the choice of the secant line positioning, passing close to the origin.

It is well known that by making thicker (larger B) specimens constraint and brittleness is increased. This was verified with Weldments #11 and #12 when they were compared with Weldment #3. This fact was also confirmed by using the B/50 ratio to evaluate the validity of plane strain fracture toughness. As shown in Table 5a, the size of the shear lips required for a valid test with Weldment #3 are much smaller than with Weldments #11 and #12.

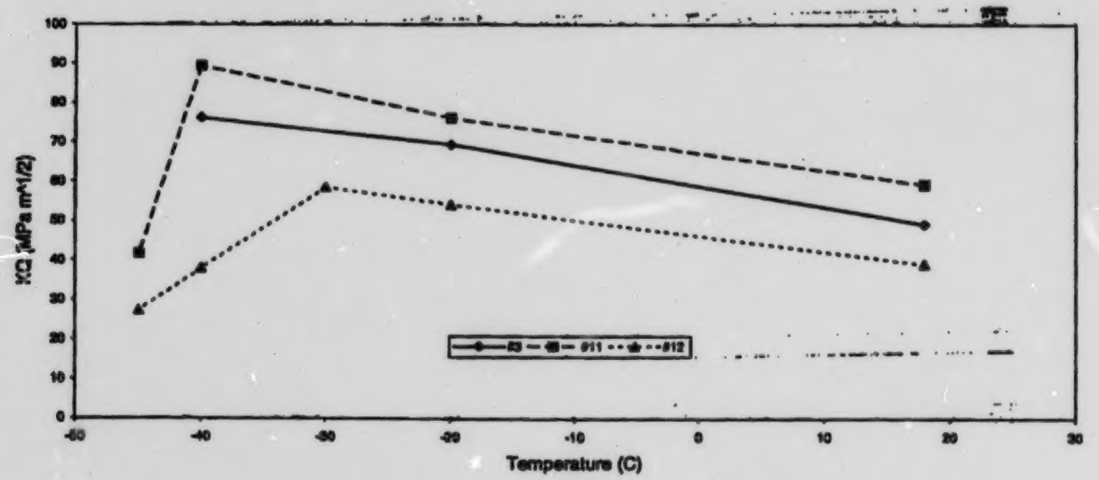

Figure 10a. K_Q Results as a Function of Temperature for the Weldments.

The plot of K_Q with temperature, Figure 10a, shows increasing K_Q with decreasing temperature until the point of inflection is reached. Below this point the K_Q value decreases. At -45 °C, Weldments #11 and #12 both displayed valid or very near valid testing. This suggests that for a temperature colder than the inflection point the test is valid. For a temperature warmer than the inflection point the test is not valid and is indicative of testing outside the valid range. What is seen is a phenomenon of size effect and decreasing constraint opposing one another.

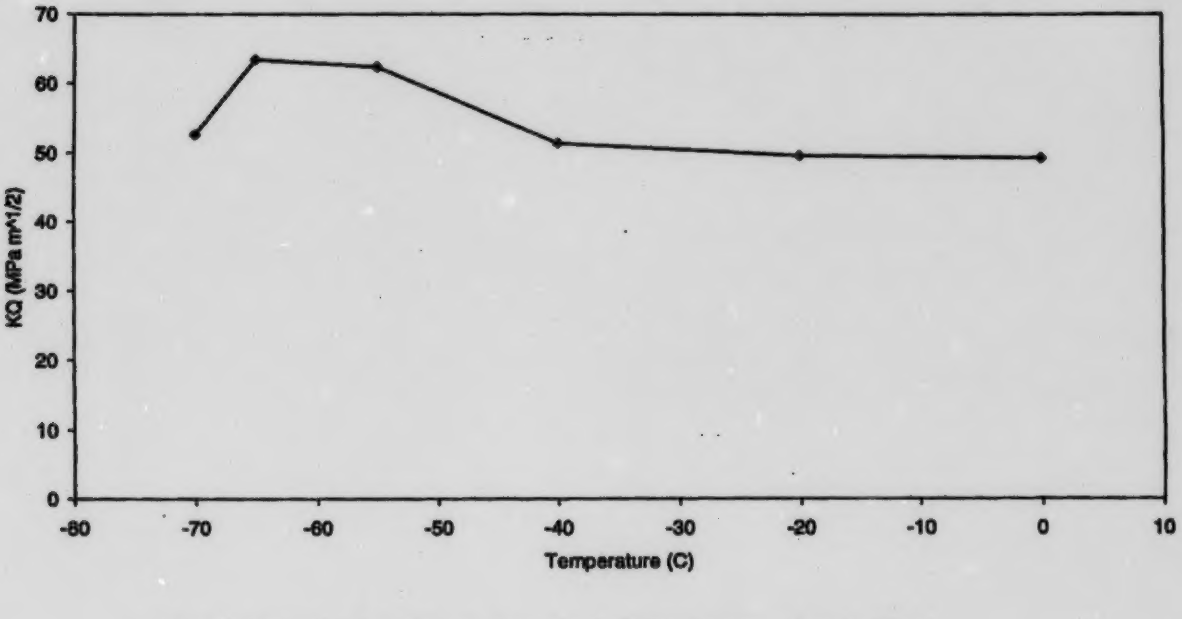

Figure 10b. K_Q Results as a Function of Temperature for the Steel.

The plot of K_Q with temperature, Figure 10b, for the steel, also shows increasing K_Q with decreasing temperature until the point of inflection is reached. Below this point the K_Q value decreases. At -65 °C, Specimen #17 displayed a valid K_{Ic} test. This suggests, as in the case for the weldments above, that for a temperature colder than the inflection point the test is valid. For a temperature warmer than the inflection point the test is not valid and is indicative of testing outside the valid range.

The goal, as depicted in Figures 10a and b, is to decrease testing temperature until elastic conditions prevail and a valid K_{Ic} result occurs. When this point is reached the maximum valid K_{Ic} value is found and the K_{Ic} value will decrease thereafter as the test temperature is lowered.

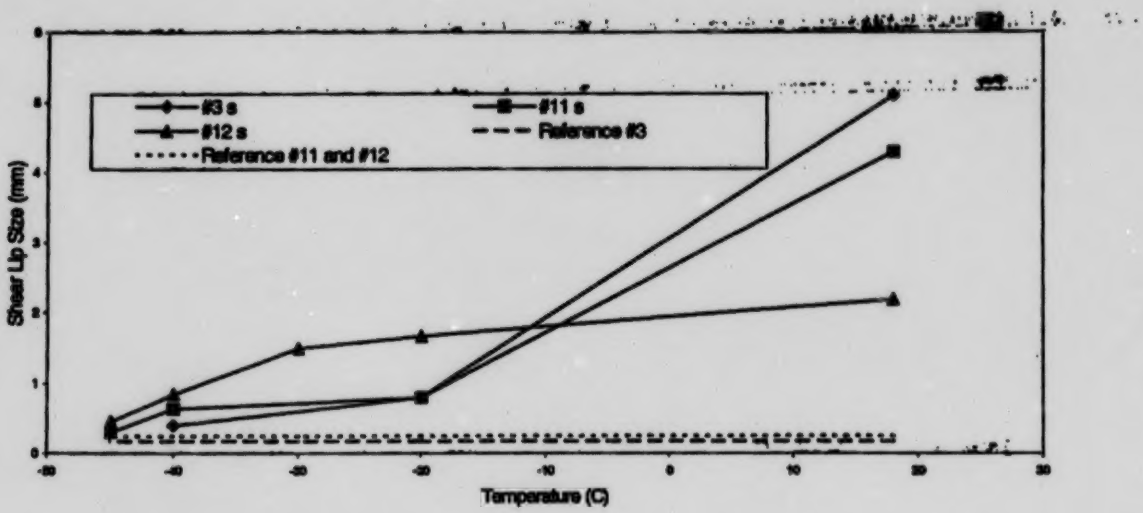

Figure 11a. Shear Lip Size as a Function of Temperature from K Tests on the Weldments.

The results of Figure 11a clearly show the decreasing toughness and increasing constraint with lowering temperature. It also shows that it was not possible to get a valid plane strain toughness test above a temperature of -45°C. At that temperature the shear lip sizes of Weldments #11 and #12 reached or were very close to their respective reference levels (B/50 lines). Using the B/50 reference lines, the test becomes valid at -45°C.

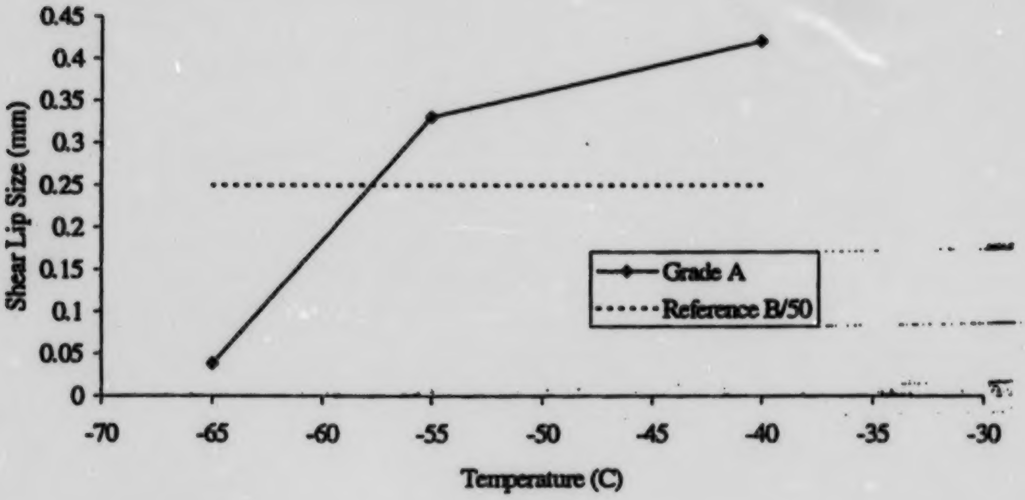

Figure 11b. Shear Lip Size as a Function of Temperature from the K Tests on the Steel.

The results of Figure 11b clearly show the decreasing toughness with lowering temperature (smaller shear lips equate to smaller plastic zones which give rise to greater constraint). It also shows that it was not possible to get a valid plane strain toughness test above a temperature of -55°C. At -65 °C the shear lip size of Specimen #17 was smaller than the reference level (B/50 dashed line). Using the B/50 reference line, the test becomes valid at -57°C.

CONCLUSIONS

1. The transition curve is a useful guide to establish a temperature range where a valid plane strain test will exist. Lower shelf is not necessarily plane strain.

2. The method suggested in reference [9] to estimate the critical plastic zone size from shear lip size seems very dependable. Using this relationship it is possible to establish a new criteria for a valid plane strain test.

$$s < \frac{B}{50} \qquad (9)$$

3. The measured stress intensity at fracture, K_Q, only becomes a valid K_{Ic} at a temperature below the inflection point on the K_Q versus temperature graph.

4. The technique proposed in the ASTM standard [4] to determine P_Q is imprecise.

REFERENCES

1. J.R Matthews and J.F. Porter, Dynamic Tear Curves for Materials Data Base, Defence Research Establishment Atlantic, Halifax, Nova Scotia, DREA DL(A) Research Note, DREA RN DL/97/7, November 1997, informal report
2. G. Pelletier, V. Roy, J.F. Porter and J.R. Matthews, Dynamic Tear and Charpy Transition Curves for British Grade A Steel, DREA Note No. DL/98/4, July 1998, informal report.
3. S.T. Rolfe, D.M. Rhea, B.O. Kuzmanovic, Fracture-Control Guidelines for Welded Ship Hulls, University of Kansas, 1974.
4. ASTM E399, Plane strain Fracture Toughness of Metallic Materials, American Society of Testing Materials, Volume 3.01, Philadelphia (1987).
5. ASTM E813, J_{Ic} A measure of Fracture Toughness, American Society of Testing Materials, Volume 3.01, Philadelphia (1987).
6. V. Roy and J.R. Matthews, Correlation of Linear Elastic Toughness (K_{Ic}) with the Lower Shelf of the Dynamic Tear Transition Curve, DREA TN 1999-014, January 1999.
7. Fleet Technology Limited, Tensile Properties of CPF Structural Materials, Kanata, Ontario, June 1997.
8. V. Roy, Ken KarisAllen and J.R. Matthews, Correlation of Linear Elastic Toughness (K_{Ic}) with the Lower Shelf of the Dynamic Tear Transition Curve, for British Grade A Steel, DREA TN 1999-056, May 1999.
9. J.R. Matthews, On the Relationship Between Shear Lip, Shear Index and Energy in Dynamic Tear Specimens, Engineering Fracture Mechanics, May (1996).

#511900 (26)

Dynamic and Static Fracture Toughness Measurement

by K.J. KarisAllen[1] and J.R. Matthews[2]

[1]FACTS Engineering Inc., P.O. Box 20039, Halifax, N.S. Canada, B3R 2K9

**[2]Defence Research Establishment Atlantic, Dockyard Laboratory (Atlantic),
P.O. Box 99000 Stn Forces, Halifax, N.S. B3K 5X5**

ABSTRACT

Two unique measurement systems for generating toughness parameters will be detailed during this presentation. The first is an ACPD Crack measurement system which has been integrated into an instrumented impact test system. This system can be utilized to generate dynamic J-resistance curve information. The second system is a specialized differential extensometer which can be used to accurately measure axial strain in tension specimens experiencing plastic necking. This system can be used for experimentally generating the data necessary for conducting a strain energy density analysis of a material system. This device may alternatively be used to characterize the partitioning of strain across a weldment in uniaxial tension.

OVERVIEW

DYNAMIC J-R CURVE

- THE PROJECT OBJECTIVE WAS TO DEVELOP AN INTEGRATED HARDWARE/SOFTWARE SYSTEM CAPABLE OF GENERATING DYNAMIC J-RESISTANCE TOUGHNESS INFORMATION
- DETAIL THE INTEGRATION OF AN ACPD CRACK MONITORING HARDWARE INTO AN INSTRUMENTED IMPACT TEST SYSTEM
- EVALUATE THE ACCURACY OF THE SYSTEM

DIFFERENTIAL AXIAL STRAIN

- THE PROJECT OBJECTIVE WAS TO DESIGN AND DEVELOP A SYSTEM CAPABLE OF MONITORING DIFFERENTIAL AXIAL STRAIN AT MULTIPLE POINTS OVER THE GAUGE LENGTH OF A TENSION SPECIMEN
- DETAIL THE DESIGN OF THE SYSTEM DEVELOPED TO MEET THE OBJECTIVES
- EVALUATE THE ACCURACY OF THE SYSTEM

TECHNIQUES FOR GENERATING J-R CURVE DATA

FORCE

- NORMALLY GENERATED DIRECTLY FROM A CALIBRATED FORCE TRANSDUCER

DISPLACEMENT

- LINEAR VARIABLE DISPLACEMENT TRANSDUCERS
- RESISTIVE ELEMENTS
- OPTICAL METHODS
- INDIRECT METHODS

CRACK EXTENSION

- MULTI SPECIMEN
- UNLOADING COMPLIANCE
- ELECTRICAL RESISTANCE
- NORMALIZATION (KEY CURVE TECHNIQUES)
- POTENTIAL DIFFERENCE METHODS

SYSTEM FORCE- DISPLACEMENT MEASUREMENT

FORCE - DIRECT
DISPLACEMENT - INDIRECT

$$m\int V\,dV + mg\int dh - \int P_a V_a\,dt = 0$$

$$V_o = \sqrt{2gh_o}$$

SYSTEM CRACK EXTENSION MEASUREMENT

DIRECT ACPD

$$\frac{a}{W} = \left[0.2864\left(\frac{U}{U_0} - 0.5\right)\right]^{0.3506}$$

$$U_0 = \frac{U_B}{3.4916\left(\frac{a_o}{W}\right)^{2.851} + 0.5}$$

HARDWARE REQUIREMENTS

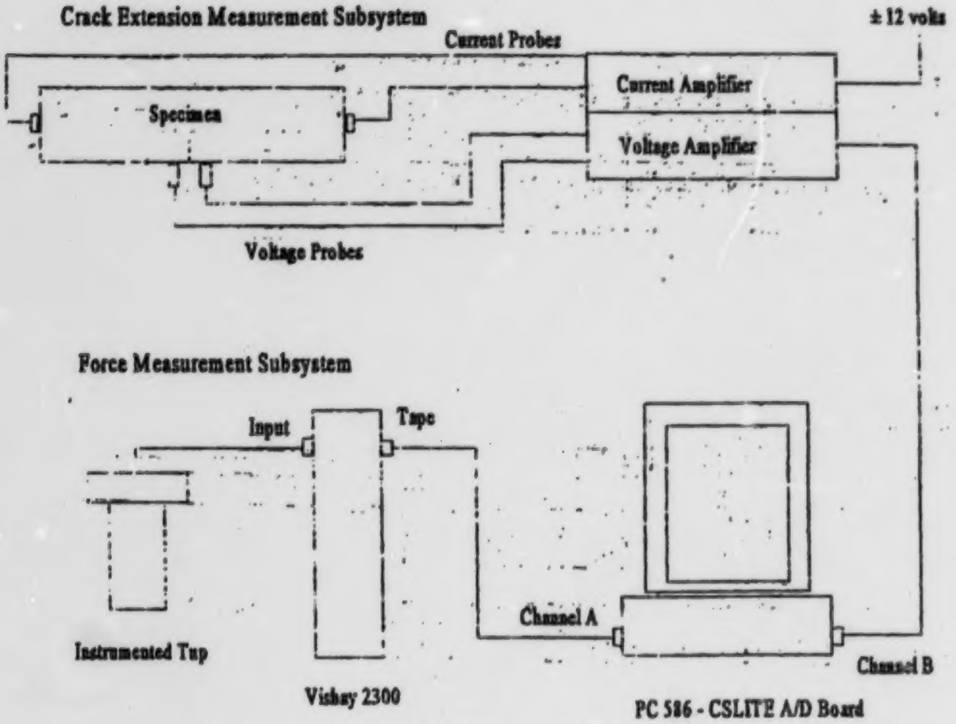
Crack Extension Measurement Subsystem
± 12 volts
Current Probes
Current Amplifier
Specimen
Voltage Amplifier
Voltage Probes
Force Measurement Subsystem
Input
Tape
Instrumented Tup
Vishay 2300
Channel A
Channel B
PC 586 - CSLITE A/D Board

SOFTWARE INTERFACE

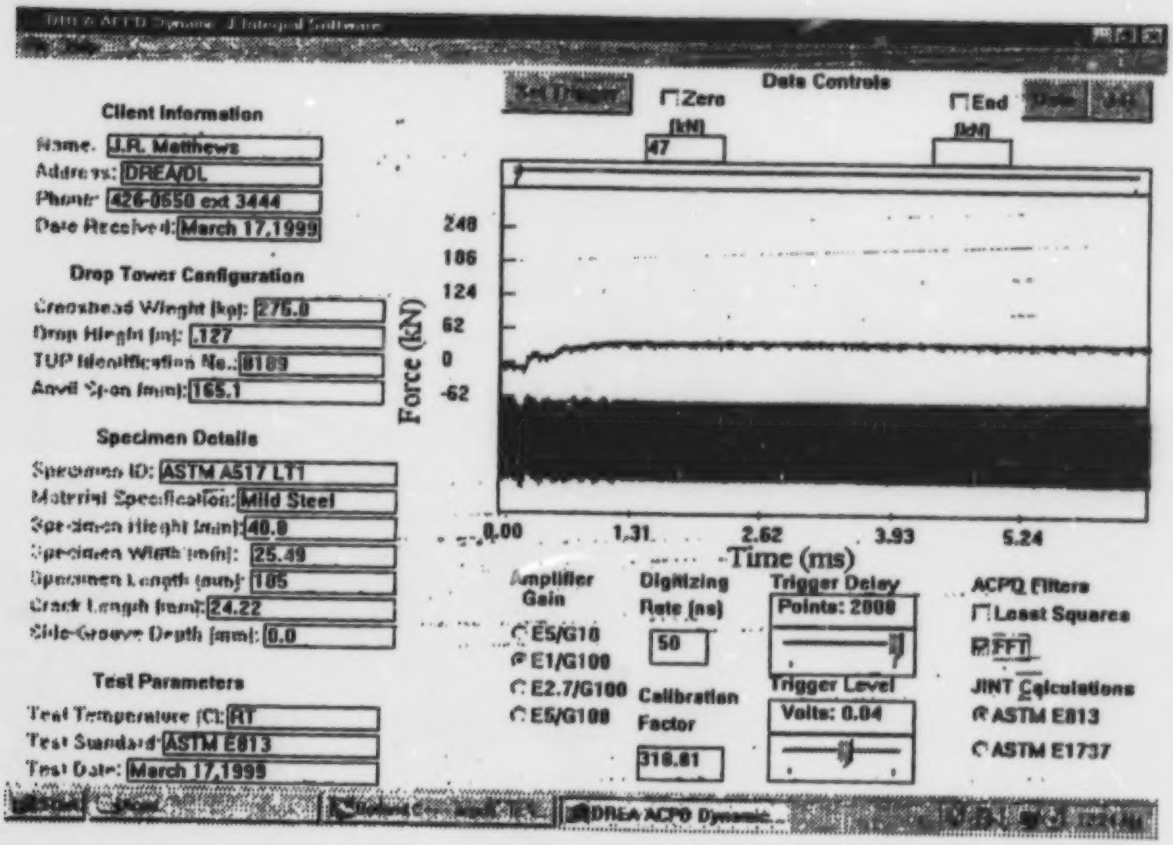
DREA ACPD Dynamic J Integral Software
Set Trigger
Data Controls
☐ Zero
(kN)
47
☐ End
(kN)
248
186
124
62
0
-62
Force (kN)
0.00
1.31
2.62
3.93
5.24
Time (ms)
Start
DREA ACPD Dynamic...

Client Information

Name: J.R. Matthews
Address: DREA/DL
Phone: 426-0650 ext 3444
Date Received: March 17,1999

Drop Tower Configuration

Crosshead Weight (kg): 275.0
Drop Height (m): .127
TUP Identification No.: 8189
Anvil Span (mm): 165.1

Specimen Details

Specimen ID: ASTM A517 LT1
Material Specification: Mild Steel
Specimen Height (mm): 40.8
Specimen Width (mm): 25.49
Specimen Length (mm): 185
Crack Length (mm): 24.22
Side-Groove Depth (mm): 0.0

Test Parameters

Test Temperature (C): RT
Test Standard: ASTM E813
Test Date: March 17,1999

Amplifier Gain

○ E5/G10
● E1/G100
○ E2.7/G100
○ E5/G100

Digitizing Rate (ns): 50

Calibration Factor: 318.81

Trigger Delay

Points: 2000

Trigger Level

Volts: 0.04

ACPD Filters

☐ Least Squares
☑ FFT

JINT Calculations

● ASTM E813
○ ASTM E1737

EXPERIMENTAL VERIFICATION

SPECIMEN PREPARATION

- MATERIAL - QUENCHED AND TEMPERED ALLOYED STEEL
- GEOMETRY - 25 mm x 50 mm x 181 mm
- NOTCH ORIENTATION L-T
- PRECOMPRESSED TO 0.4 PL AND PRECRACKED TO BETWEEN .45 AND .55 a/W
- TEST TEMPERATURE - AMBIENT
- SPECIMENS IMPACTED AT BETWEEN 1.4 m/s AND 1.7 m/s WITH A 275 kg CROSSHEAD (LOW BLOW TEST).
- AFTER TESTING SPECIMENS WERE HEAT TINTED AND INITIAL FATIGUE CRACK AND FINAL CRACK EXTENSION WERE MEASURED.

SPECIMEN PROBE ATTACHMENT POSITIONS

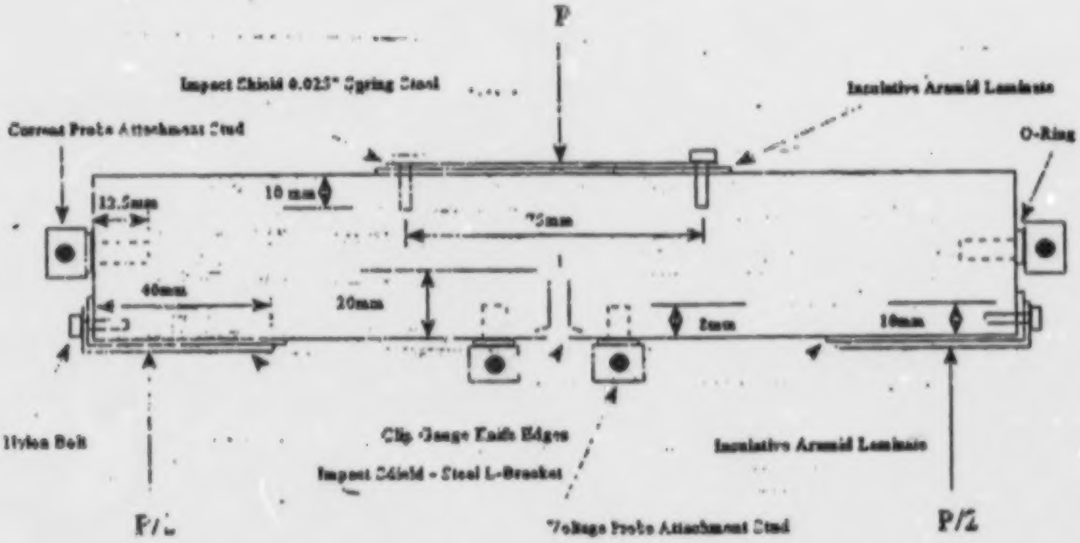
P
Impact Shield 0.025" Spring Steel
Insulative Aramid Laminate
Current Probe Attachment Stud
O-Ring
10 mm
12.5mm
75mm
40mm
20mm
8mm
10mm
Nylon Bolt
Clip Gauge Knife Edges
Impact Shield - Steel L-Bracket
Insulative Aramid Laminate
P/2
Voltage Probe Attachment Stud
P/2

FORCE AND ACPD TEST DATA

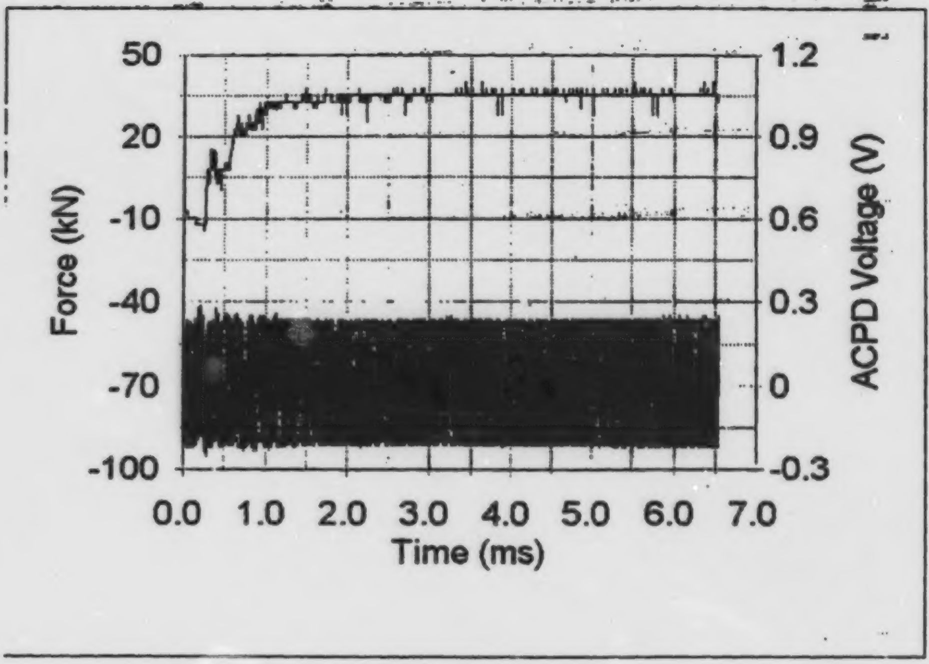

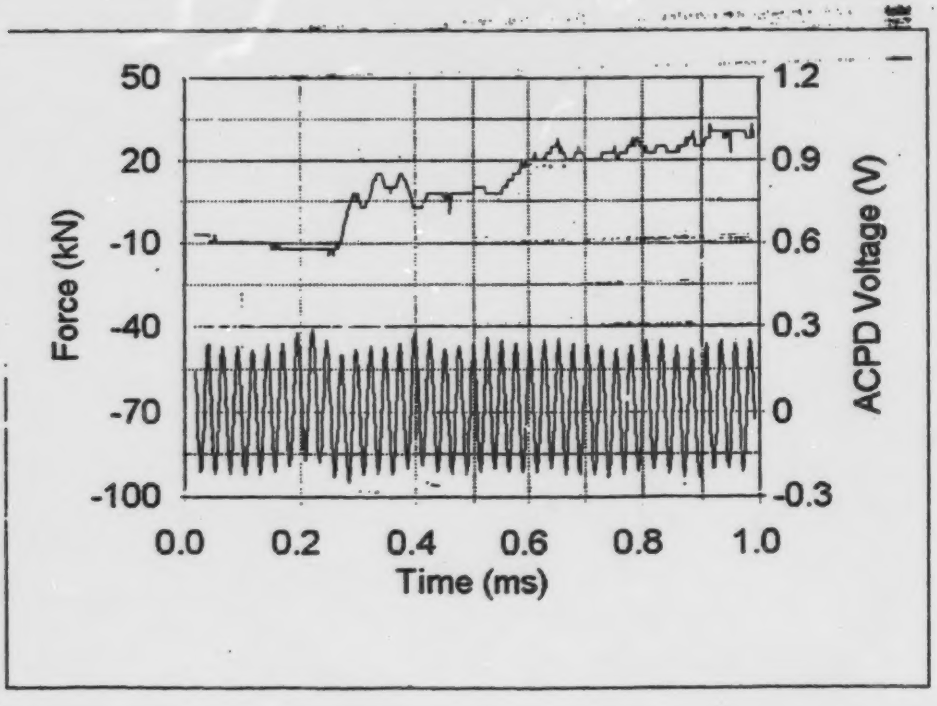

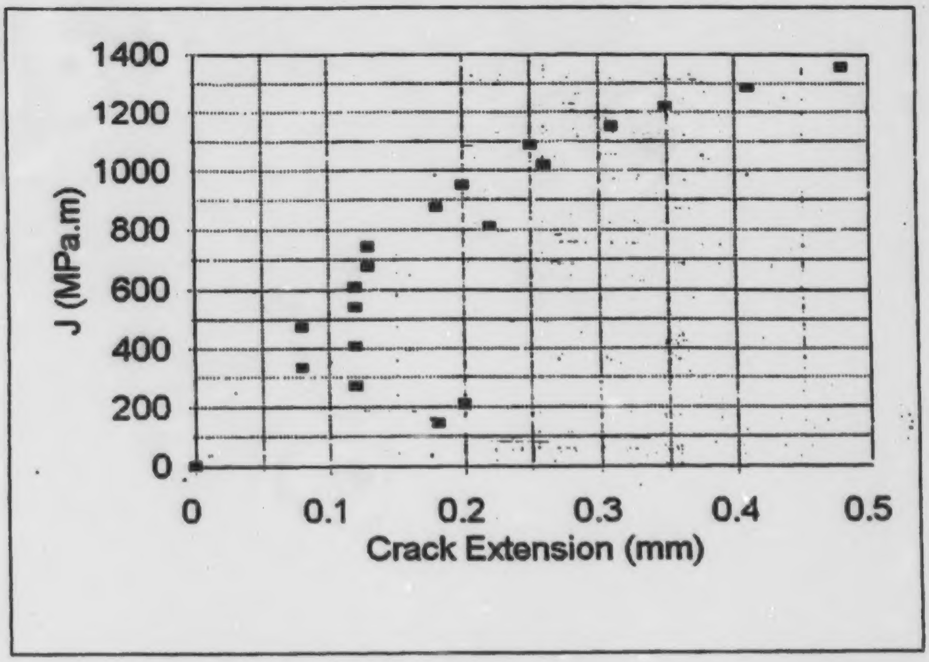

FORCE AND ACPD TEST DATA

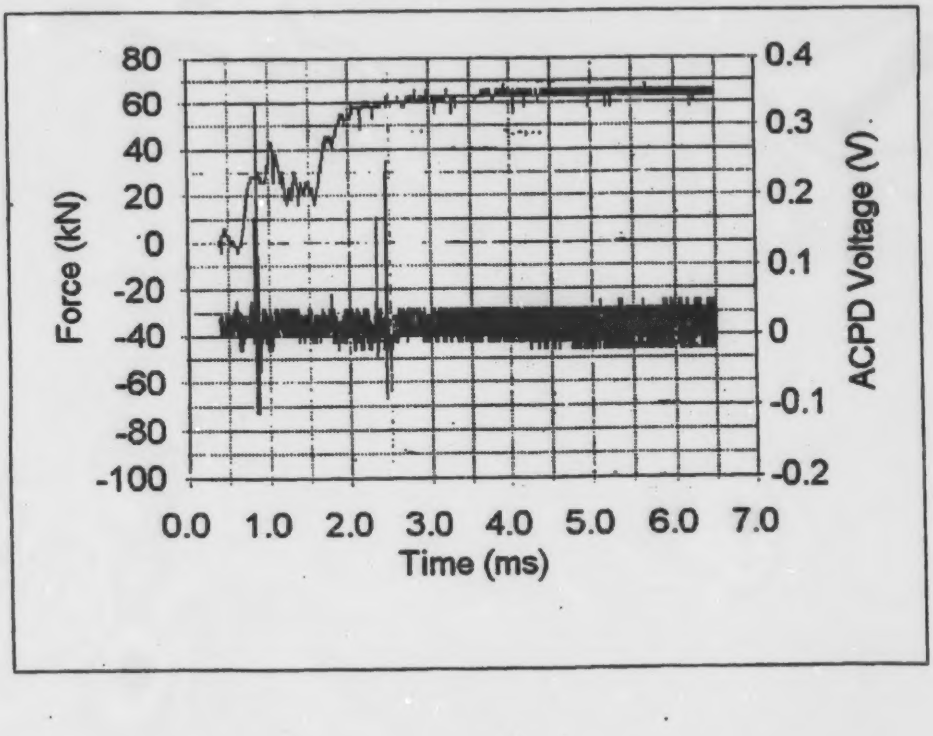

J-RESISTANCE DATA

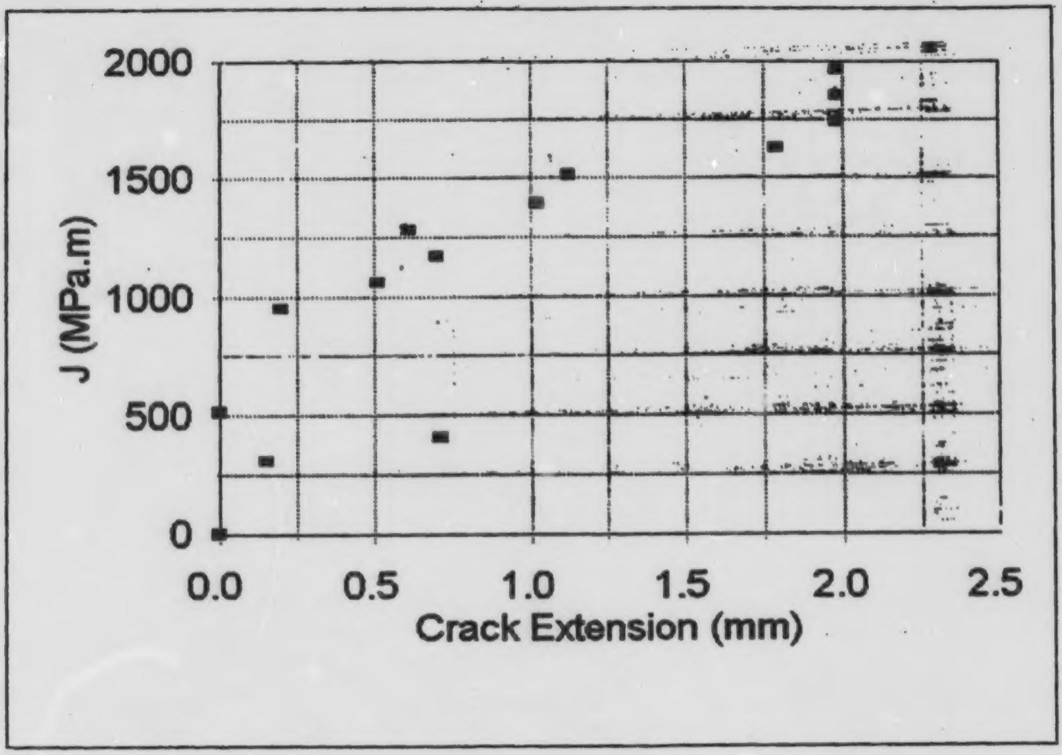

CONCLUSIONS

- THE EXPERIMENTALLY DERIVED EQUATION PUBLISHED IN ASTM E-1737 PROVIDES ACCEPTABLE ACCURACY FOR THE DETERMINATION OF CRACK EXTENSION FOR THE ACPD SYSTEM DEVELOPED. CALCULATED CRACK LENGTHS ARE IN CLOSE AGREEMENT WITH VISUALLY MEASURED CRACK LENGTHS.
- THE SPECIMEN INERTIAL EFFECTS GENERATE LOW FREQUENCY BACKGROUND NOISE INTO THE ACPD SIGNAL.
- SPECIMENS WHICH L OSE ELECTRICAL ISOLATION FROM THE LOAD TRAIN DURING THE IMPACT EVENT PRODUCE ACPD DATA WHICH GENERATES ERRONEOUS ESTIMATES OF CRACK LENGTH.

#511901 (27)

Fracture Properties of 350 WT Steel at Very High Loading Rates

by M.N. Bassim* and J. R. Matthews**

***University of Manitoba**

****Defence Research Establishment Atlantic, Dockyard Laboratory (Atlantic) P.O. Box 1012, Dartmouth, Nova Scotia B2Y 3Z7**

ABSTRACT

Fracture studies were conducted on 12.7 mm thick compact tension specimens of 350 WT steel at very high loading rates. The equipment used in the studies consisted of a specially designed Split Hopkinson Bar system capable of delivering sufficient energy to fracture the specimens on impact. Projectile speeds in the Split Hopkinson Bar were in excess of 50m/s.

Following fracture, the extent of the shear lip as well as the stretch zone width which occurs before crack extension, were measured in all the specimens tested. Test temperatures ranged from -45 to 15C. It was found that above 0C, fracture is ductile with a shear lip extending across the fracture surface for the specimens with no fatigue precrack. For those with a fatigue precrack, the shear lips are smaller.

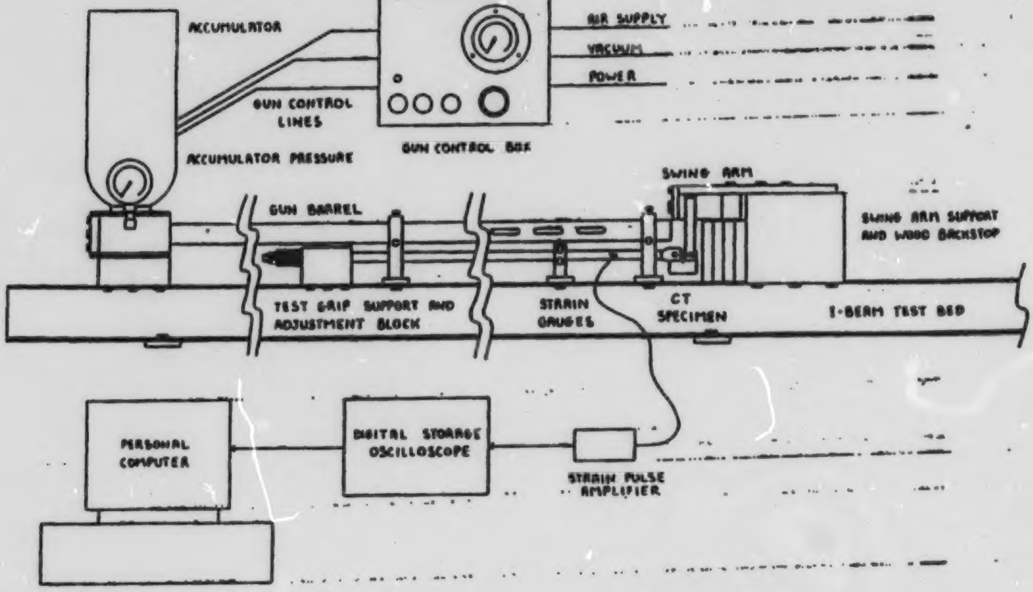
ACCUMULATOR
GUN CONTROL LINES
ACCUMULATOR PRESSURE
GUN CONTROL BOX
AIR SUPPLY
VACUUM
POWER
SWING ARM
GUN BARREL
SWING ARM SUPPORT AND WOOD BACKSTOP
TEST GRIP SUPPORT AND ADJUSTMENT BLOCK
STRAIN GAUGES
CT SPECIMEN
I-BEAM TEST BED
PERSONAL COMPUTER
DIGITAL STORAGE OSCILLOSCOPE
STRAIN PULSE AMPLIFIER

Figure 1a: Split Hopkinson Bar Assembly For CT Specimen Testing.

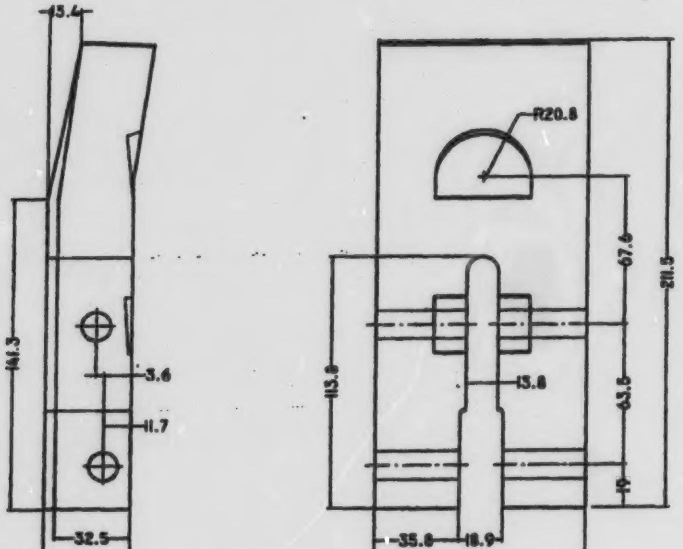
15.4
141.3
3.6
11.7
32.5
37
R20.8
67.6
211.5
115.8
13.8
63.5
19
35.8
18.9
90.5

All dimensions are in mm

. Figure 1b: Swing Arm Assembly Mechanism.

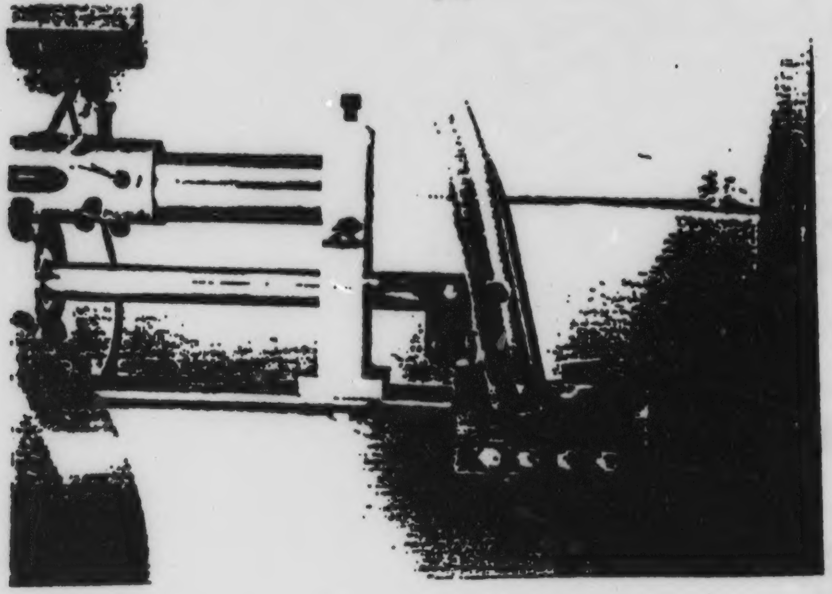

(a)

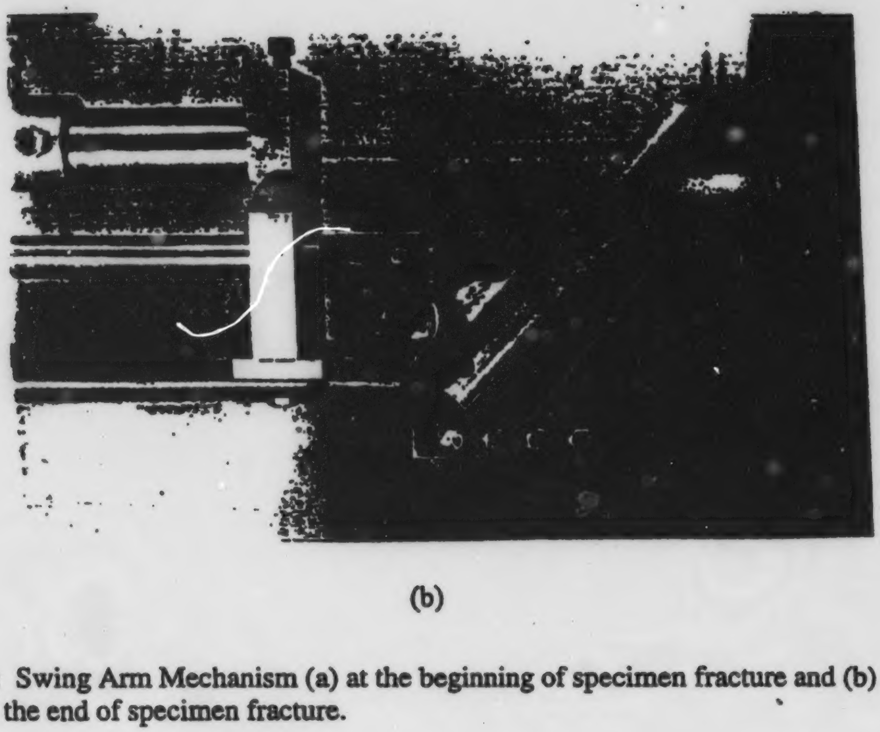

(b)

Figure 1c: Swing Arm Mechanism (a) at the beginning of specimen fracture and (b) at the end of specimen fracture.

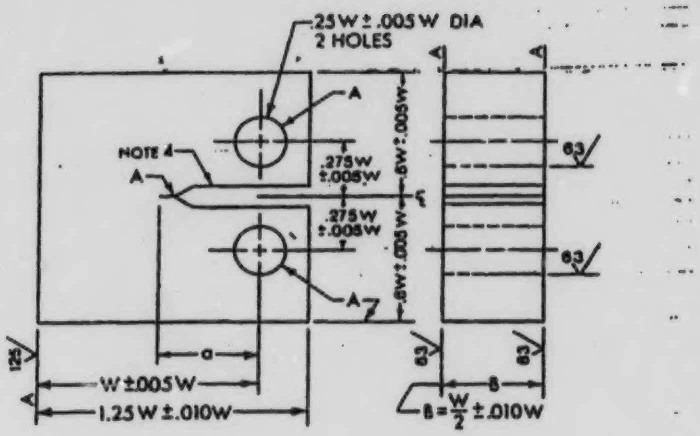
.25W ± .005W DIA
2 HOLES
A
NOTE 4
A
.275W ±.005W
.275W ±.005W
.6W ±.005W
.6W ±.005W
A
63
63
125
a
W ±.005W
1.25W ±.010W
63
63
B
B = $\frac{W}{2}$ ±.010W

W = 50 mm
B = 12.7 mm
a/W = 0.5

Figure 2a: Compact Tension Specimen Dimensions.

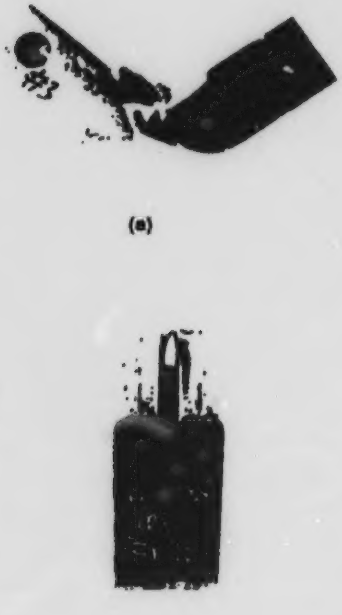

(a)

(b)

Figure 2b: (a) Broken Specimen and (b) Fracture Surface

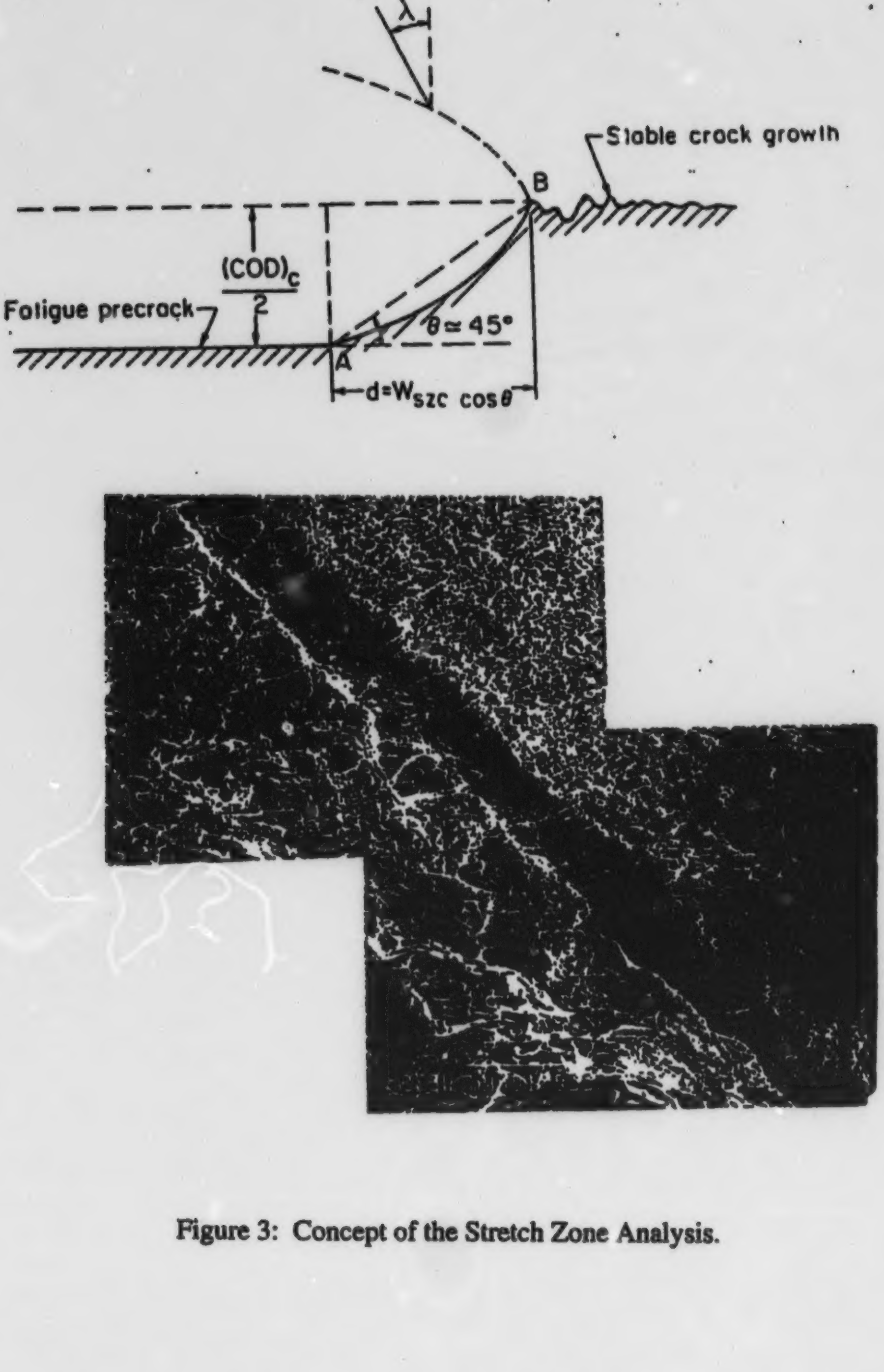
λ
Stable crack growth
B
(COD)c / 2
Fatigue precrack
θ ≃ 45°
A
d=W szc cos θ

Figure 3: Concept of the Stretch Zone Analysis.

Table 1: Stretch Zone Width (SZW) measurements of fatigue precracked specimens from 1998 contract.

ID	Temperature Deg. C	Orientation	Notch	SZW	SZW Value Microns	Shear Lip Mm
II-1	15	L-T	Pressed			6.1
II-2	15	T-L	Pressed			6.0
II-3	0	L-T	Pressed			6.1
II-4	0	T-L	Pressed			6.0
II-5	15	L-T	Fatigue Precracked			6.0
II-6	0	L-T	Fatigue Precracked			6.0
II-7	15	L-T	Fatigue Precracked	Yes	1080[1]	5.5
II-8	15	T-L	Fatigue Precracked	Yes	990[1]	6.0
II-9	0	L-T	Fatigue Precracked	Yes	863[1]	3.0
II-10	0	T-L	Fatigue Precracked	Yes	975[1]	3.8

Table 2: Summary of testing results of 350WT steel (1999)

Temperature Deg. C	Orientation	Notch	SZW	SZW Value Microns	Shear Lip Mm
-45	T-L	Fatigue Precracked	Yes	147	1.5
-45	L-T	Fatigue Precracked	Yes	210	2.0
-45	T-L	Pressed			2.0
-45	T-L	Pressed			2.0
-30	T-L	Fatigue Precracked	Yes	343	2.5
-30	L-T	Fatigue Precracked	Yes	450	2.0
-30	T-L	Pressed			2.0
-30	T-L	Pressed			6.0
-15	T-L	Fatigue Precracked	Yes	812	6.0
-15	L-T	Fatigue Precracked	Yes	1177	6.0
-15	T-L	Pressed			5.5
-15	T-L	Pressed			3.5

Table 3: Shear Lip and Stretch Zone Width (SZW) measurements of fatigue precracked and pressed specimens from 1997 contract (slowed tests).

ID	Temperature Deg. C	Orientation	Notch	SZW	SZW Value Microns	Shear Lip Mm
APA	-45	T-L	Pressed			0.39
APB	-30	T-L	Pressed			0.64
APE	15	T-L	Pressed			2.58
ATE	15	L-T	Pressed			2.8
BPA	-45	T-L	Fatigue Precracked	Yes	56	0.39
BPB	-30	T-L	Fatigue Precracked	Yes	83	0.79
BPC	-15	T-L	Fatigue Precracked	Yes	97	1.31
BPD	15	T-L	Fatigue Precracked	Yes	175	2.21
BPE	0	T-L	Fatigue Precracked	Yes	600	3.08
BTA	-45	L-T	Fatigue Precracked	Yes	46	.24
BTB	-30	L-T	Fatigue Precracked	Yes	55	.3
BTC	-15	L-T	Fatigue Precracked	Yes	69	1.11
BTD	0	L-T	Fatigue Precracked	Yes	140	1.96
BTE	15	L-T	Fatigue Precracked	Yes	500	2.80

Note: all specimens a/W of 0.55

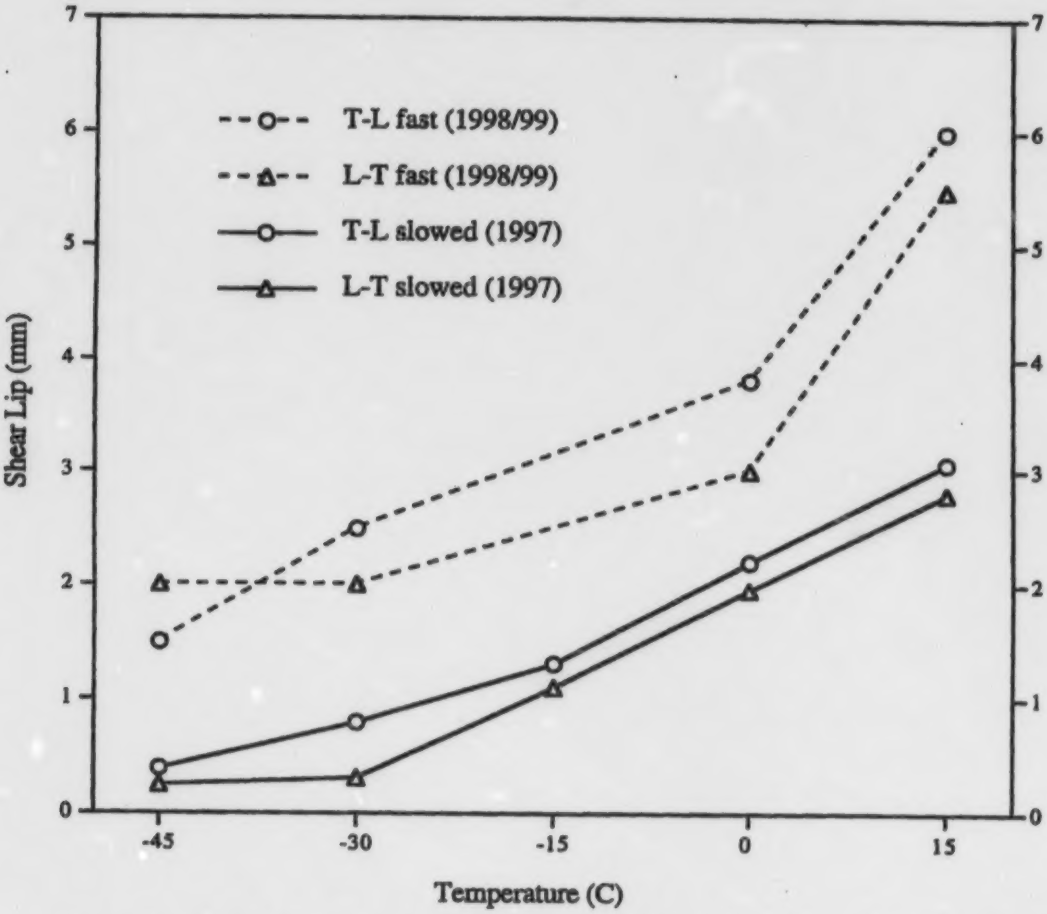

Figure 4: Comparison of the results for the unmodified Splt Hopkinson Bar (1997) which slowed considerably during the test and actually stopped at 0 and 15°C and results with the modified Split Hopkinson Bar (1998 and 1999). Graph shows variation of Shear Lip with Temperature for Fatigue Pre-Cracked Specimens.

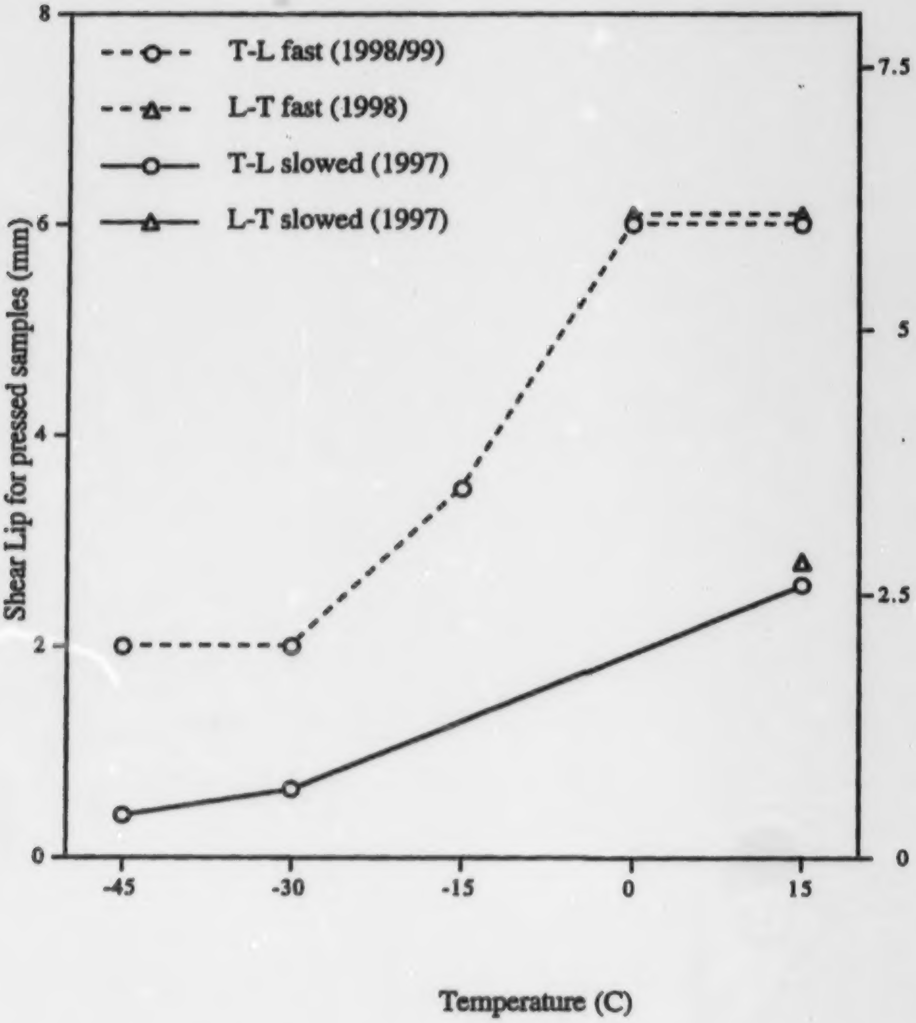

Figure 5: Graph shows variation of Shear Lip with Temperature for Pressed Notched Specimens.

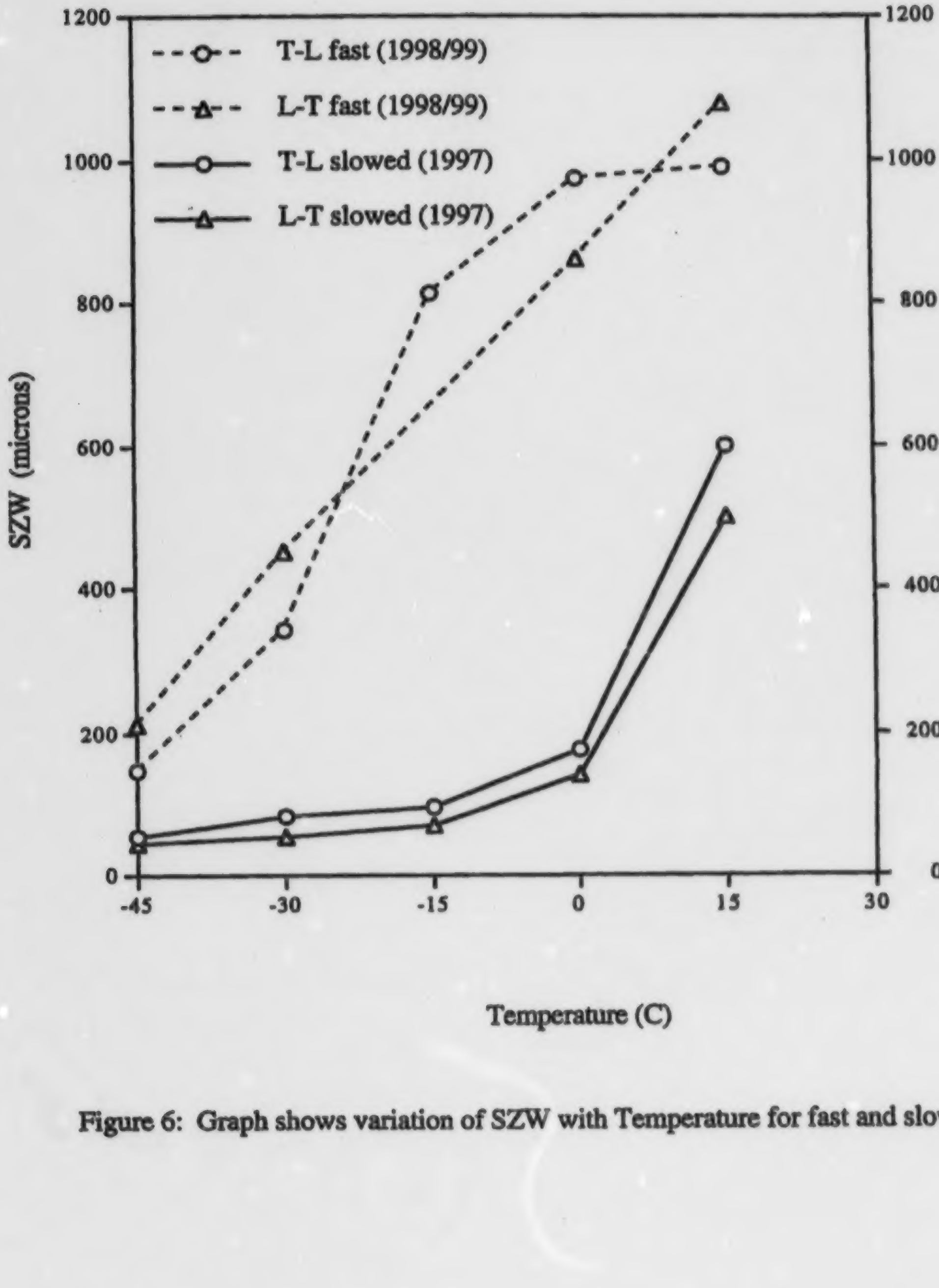

Figure 6: Graph shows variation of SZW with Temperature for fast and slowed.

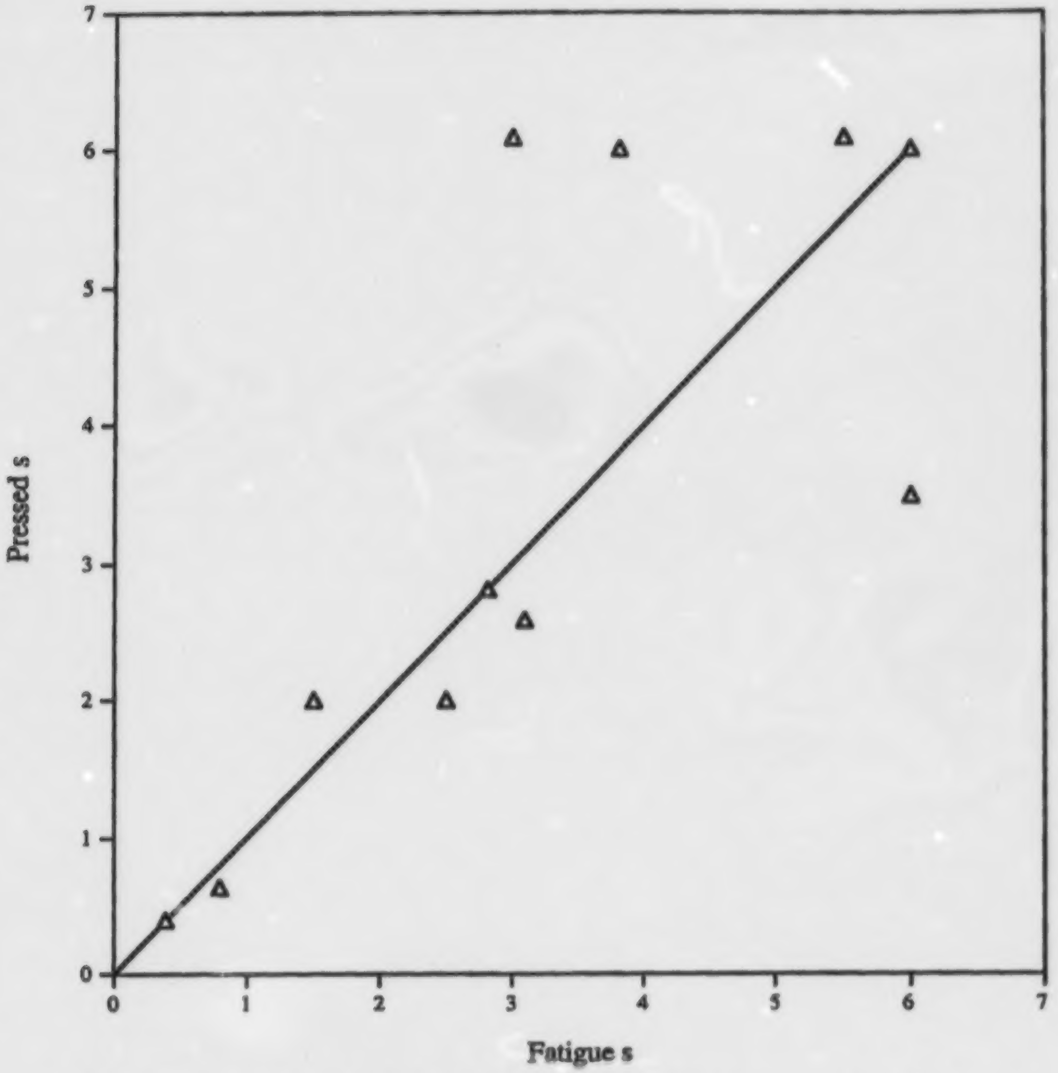

Figure 7: Graph shows relationship between Shear Lip for Pressed Notched Specimens and Fatigue Pre-Cracked Specimens.

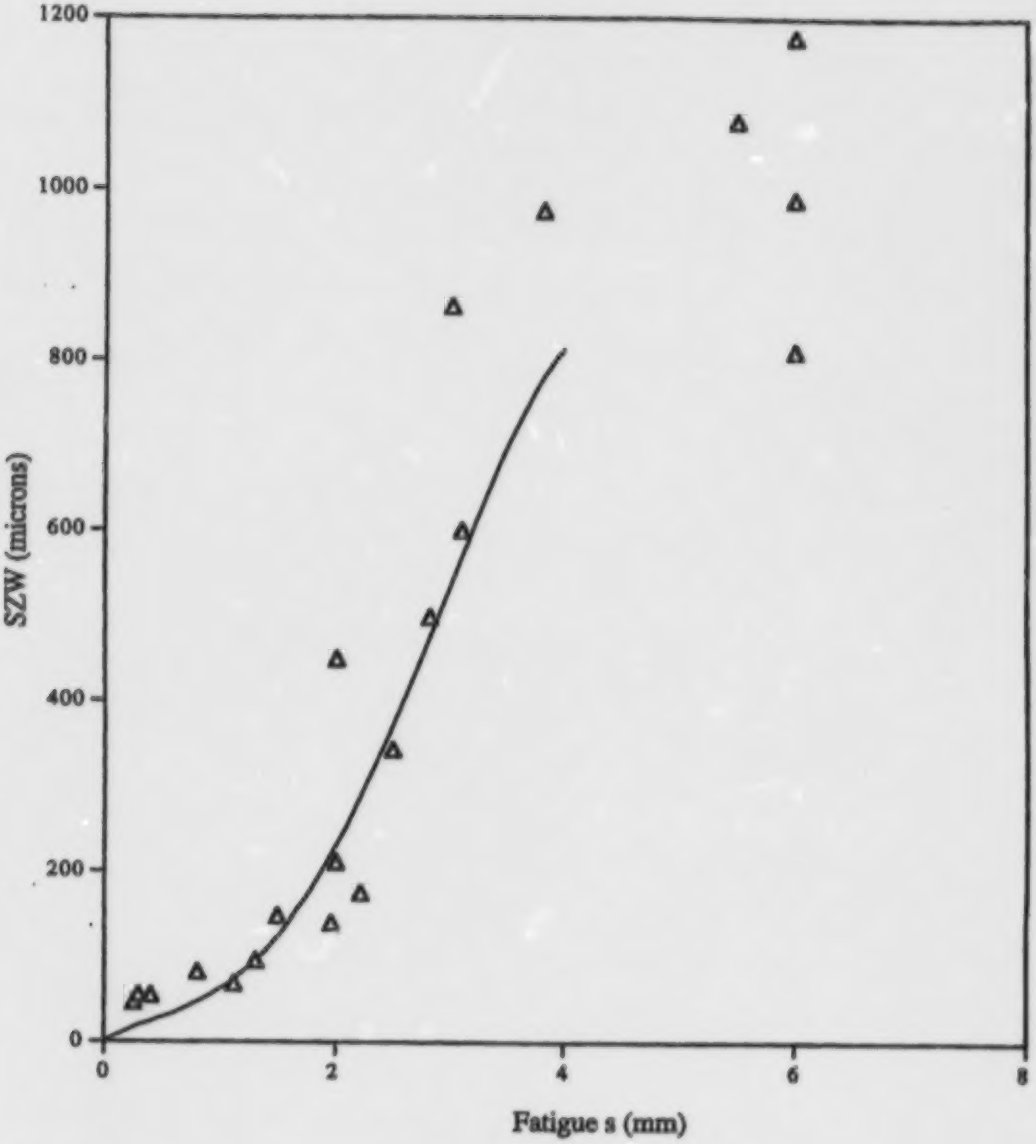

Figure 8: SZW vs shear lip on fatigue pre-cracked specimens.

#511902 ②

Critical Strain Energy Density from Tensile Specimens

by G.R. Pelletier and J.R. Matthews

Defence Research Establishment Atlantic
P.O. Box 1012, Dartmouth, Nova Scotia, B2Y 3Z7

ABSTRACT

Fracture has always been a serious concern in the design and repair of steel structures such as ships. Because of these concerns, much research has been ongoing in the causes of fractures and in ways which they could be predicted and thus prevented.

The objective of this study was to find, test and evaluate a method for measuring the critical strain energy density with tensile specimens.

Plastic strain at fracture (real strain) was measured for gauge lengths of 1.25 mm and 1.125 cm using an etched grid. Real stress, the force divided by the reduced area, was also measured. Complexities in these two measurements were dealt with by detailed numerical analysis resulting in approximate average real stress - real strain curves that, in the transition zone, displayed decreasing strain energy density with temperature.

1.0 Introduction

Fractures in ships, buildings and bridges have always been a serious concern. Especially, in the areas of design and repair. Because of this, much research has been ongoing in the causes of fractures and in ways which they could be predicted and thus prevented.

This report will concentrate on techniques by which fractures can be predicted and thus prevented. The objective of this study was to find, test and evaluate a method for measuring the critical strain energy density with tensile specimens.

There are an alarming amount of failures occurring in ships, bridges and buildings. These failures have motivated extensive investigations in various countries. It was observed in the early 1940's that fractures were occurring more frequently at low temperatures. Many fractures occurred suddenly, without warning, at low nominal stresses. Investigations into these fractures revealed that the steels experienced states of extreme brittleness.

It was slowly recognized that there existed service temperatures where the structures were susceptible to brittle fractures even though the material was thought to be ductile. Included in this report are discussions of some of these failures and the result of their respective inquiries.

Tensile tests were performed to obtain data so that the strain to fracture (plastic and total), and the critical strain energy density could be evaluated in the transition zone.

2.0 Background

The background section discusses the various investigations that occurred as a consequence of certain steel failures. Presented herein are some of the conclusions and recommendations from the formal inquiries that took place as a result of the failures.

2.1 Boston Molasses Tank

One of the most famous tank failures was that of the Boston molasses tank, which failed in January 1919. The tank contained 2,300,000 gallons of molasses when it failed. Twelve people were drowned, 40 were injured and several horses were drowned. Houses were damaged, and a portion of the Boston Elevated Railway structure was knocked over.

An extensive lawsuit followed, and many well-known engineers and scientist were called to testify. After years of testimony, the court appointed auditor handed down the decision that the tanks failed by over-stress. When the auditor was asked to comment on the conflicting technical testimony, he was quoted as saying " amid this swirl of polemical scientific waters…[he] at times felt that the only rock to which he could safely cling was the obvious fact that at least one half of the scientists must be wrong" [1]. His comment summarized the state of knowledge among engineers regarding brittle fractures. At times, it seems that the statement is still true today.

2.2 Liberty Class & T-2 Tankers

Over twenty-five hundred Liberty Class Ships were produced between 1941 and 1945 for the Second World War [2]. The mass produced Liberty Ships were the first all-welded ships. These cargo ships were designed for a service life of five years, and took less than 60 days to construct [3]. One yard actually built a Liberty ship in four days, 15 hours and 30 minutes [4]. Figure 1a is a photograph of a Liberty Ship.

Welding provided savings in time, manpower and training [5]. Without welding, it would have been impossible to build, at such speeds, the enormous merchant fleet of Liberty Class Ships.

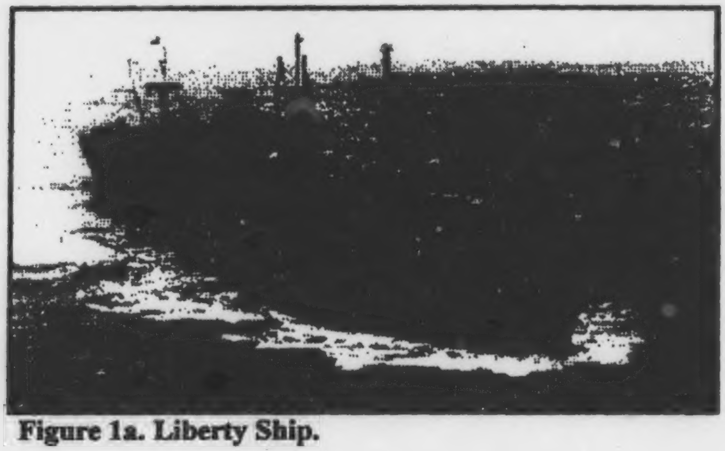

Figure 1a. Liberty Ship.

Many of the Liberty Ships failed. Over a thousand ships suffered from cracks in varying degree, 190 ships sustained serious fractures, and twelve ships broke in two [6]. Design errors and inferior workmanship were shown to be factors in these failures [7]. However, the Liberty ships were made from steel that had low toughness [8]. Shown in Figure 1b are Charpy transition curves for the Liberty ship, SS Simon Willard, the SS Warrior, and the average results from 26 Liberty ships.

The SS Simon Willard was one of the worst case scenarios. The midpoint Charpy transition temperature for the Liberty ships was found to be approximately 32°C, while the midpoint Charpy transition temperature for the SS Simon Willard was found to be approximately 50°C. The midpoint Charpy transition temperature for the SS Warrior was –5C°. Many failures were initiated by fatigue cracks which nucleated at the corner of square hatches [2]. In the earlier riveted ships, the riveted plates acted as crack arresters, preventing catastrophic fractures from occurring, but the overall incidence when size was factored in, was no better.

The T-2 tanker SS Schenectady was the first all-welded tanker built by the Kaiser Company. She was launched in late 1942. While the Schenectady was afloat at dock in early 1943, she broke in two. Figure 2 is a photograph of the SS Schenectady.

The night of the failure the air temperature had fallen from 3°C to -5°C. The ship broke in two, in a brittle manner, across the deck at a point abaft of midship. The ship jack-knifed, leaving a gap 10 feet wide in the deck. The vessel was ballasted as for the trial trip, the bending moment was about half the maximum designed bending moment [5].

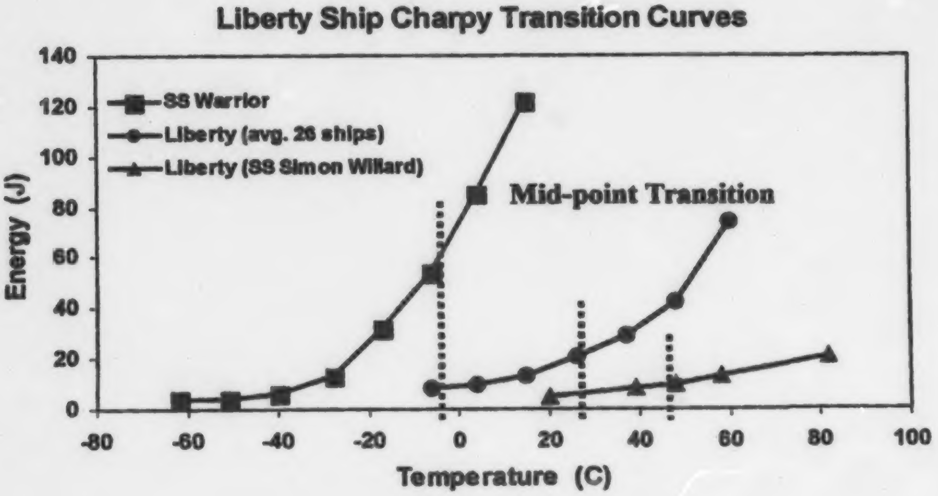

Figure 1b. Liberty Ship Charpy V-Notch Transition Curves.

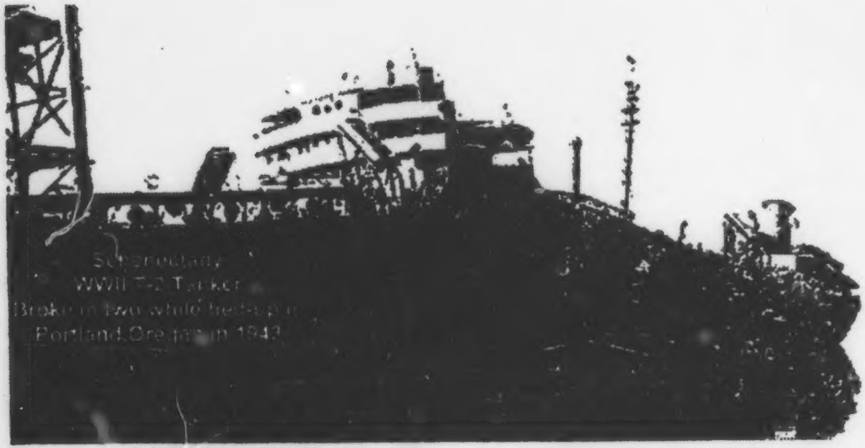

Figure 2. SS Schenectady.

The investigation into the failure found that there was a lack of uniformity in the quality of steel used for the hull. Low impact values at room temperature were obtained in impact tests, while complete brittleness occurred at -6°C. There were no specifications in place at this time which required impact tests on the steel.

In 1943, the Admiralty Ship Welding Committee was formed in England [9]. The committee's prime directive was to investigate and find solutions to the failure problems occurring in welded ships. Ships where breaking in two for reasons other than war, collision, or stranding. The failure of the all-welded American tanker, the Schenectady, was a significant catalyst for the committee formation. The committee sponsored several experiments. The objective of these experiments was to measure stresses and deflections in critical locations in both riveted and welded construction. Several features emerged from these experiments:

- Notches and sharp changes in sections should be avoided;
- There was a tendency for fractures to occur more frequently when the ship operated at low temperatures;
- Fractures in welded ships were occurring suddenly, they were sharp and accompanied by very little deformation or reduction in thickness at the fractured edges;
- Few fractures followed the weld. When the fracture started at a faulty weld, it proceeded into virgin plate;
- Most serious fractures in welded ships have been brittle. Notched tensile test samples taken from the vicinity of fractures have displayed the property of notch brittleness at temperatures within service range; and
- An increase in plate thickness tends to increase the possibility of a brittle type fracture.

It was concluded by the Committee that a remedy to the welded ship fracture problem was to eliminate the use of notch brittle steel in ship construction.

In 1946 the Secretary of the U.S. Navy assembled a Board of Inquiry into welded ship failures. Several relevant features emerged from this inquiry, they are as follows:

- All fractures investigated started at a discontinuity involving design or workmanship;
- Statistically, the age of the ship had no appreciable influence ;
- Steel from the fractured plates complied with the test requirements for ship steel (tensile strength);
- Fractures occurred more frequently at low temperatures;
- Killed steel is less susceptible to failure than semi-killed steel; and
- Metallurgical variables, such as grain size, deoxidization and plate thickness are important.

Sadly, the Admiralty Committee and the US Navy Inquiry, failed to appreciate the significance of their observations. This was perhaps due to the non-conservative nature of the Charpy test (structural transition is much worse than Charpy transition).

3.0 Fracture Control Theory

Material testing involves methods for systematic measuring and evaluation of the mechanical properties of materials. The properties measured in this report include strength and toughness.

The strength properties are related to the ability of a material to resist applied forces. Toughness measurements are related to the ability of a material to carry a load in the presence of a defect [10]. The toughness exhibited by steel is a weak function of the rate of loading and a strong function of temperature.

Steel structures that operate safely in warmer climates can suddenly fail in a brittle manner under colder conditions. This type of failure has been termed "brittle fracture". It was slowly recognized in the late 1940's that there existed service temperatures where the structure experienced brittle fracture even though the material was thought to be ductile. The antonym of a brittle fracture is a ductile fracture. Ductile fractures are characterized by their plastic deformation when a load is applied. The surface of a fractured ductile material has a fibrous texture with silky, dull-grey appearance, while the surface of a fractured brittle material has a bright granular appearance. The likelihood of a brittle fracture occurring increases as the temperature decreases. Thicker and wider sections and the presence of defects also reduce the capacity for plastic deformation to occur before fracture.

Brittle fractures have been, and still are one of the leading sources of steel casualties. Because of this, much time and effort has gone into the research of brittle fracture. Three conditions must be present for a brittle fracture to occur: i) stresses must be present; ii) there must be a crack forming flaw; and iii) structural transition must be lower shelf. The stresses may be present in the form of applied stresses, an example being wave action on a ship, or as residential stresses. Residential stresses are stresses that can not be measured non-destructively with the aid of strain gauges, these include hydrostatic stresses, welding residual stresses, fabrication restraint stresses, and thermal stresses. The crack forming flaw may be in the form of a welding defect such as lack of fusion, slag, porosity, fatigue cracking from applied cyclic strain, and geometric discontinuities.

Transition curves can be constructed from data obtained from Charpy V-Notch Impact (C_V) and Dynamic Tear (DT) tests. The most effective way of predicting structural performance of a given material is through dynamic tear testing. The results obtained with DT specimens are much more meaningful than those obtained with the Charpy specimen. Past tests have shown that transition behaviour for a Charpy size specimen can be approximately 50°C to 100°C below the larger DT specimens [11]. Figure 3 is a schematic representation of the Charpy V-notch, the dynamic tear, and the estimated structural transition curves. In designing against brittle fractures it is of extreme importance that the minimum service temperature of the structure's steel must coincide with the upper shelf of the structural transition curve. It is therefore necessary to determine the structural transition of the steel and to design within the minimum service temperature of the surroundings and selected materials. From the structural transition curve it is possible to determine if the structure will exhibit ductile behaviour under all service conditions. Structures are subjected to a wide range of loading conditions and service temperatures. Service loading conditions can be significantly different for structures that are placed on land as compared to those that are located in water.

Structures immersed in seawater have a minimum service temperature of approximately –2.5°C, while structures that are exposed to the air and wind may be subjected to service temperatures as low as –50°C [6].

The Charpy V-Notch impact test has limitations. The small specimen used in the test lacks the constraint and the degree of triaxiality that exists in a larger structure. The Charpy test specimen is too small in size. Because of this small size it does not mimic the structure's behaviour. Therefore, the Charpy test requirements can not guarantee ductile behaviour. G. E. Dieter [12] outlined that the chief deficiency of the Charpy impact test is that the small specimen is not always a realistic model of the actual structure. At a particular service temperature the standard Charpy specimen shows high shelf energy, while the actual structure exhibits low toughness at the same temperatures.

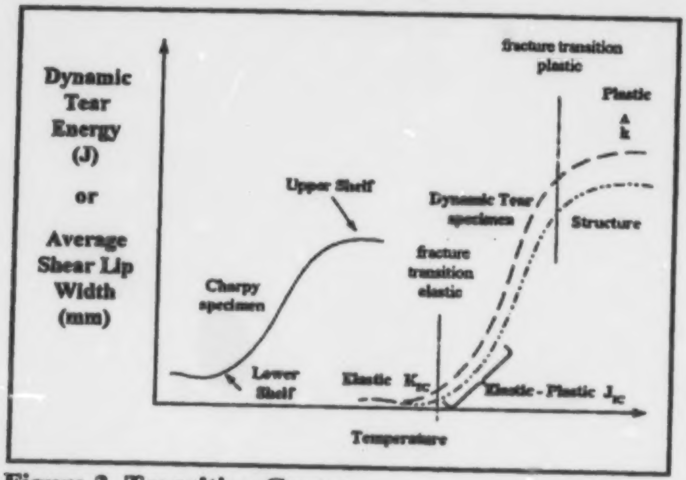

Figure 3. Transition Curves.

Transition curves can also be constructed from the shear lip width measurements obtained from the tested DT specimens. The shear lip information is equivalent to the energy information for characterizing the toughness of carbon and low alloy steels and their weldments [13]. Because the shear lip data is always available for re-examination and inexpensive to obtain, it is the preferred method for evaluating the transition behaviour of steels and weldments.

Analysis methods and formula also vary depending on the constraint and the degree of plasticity [10]. There exists different analysis for linear elastic fractures, elastic plastic fractures, transition fractures, and fully plastic fractures. Serious errors occur when the analysis of one level is applied to that of a different level. Errors can be avoided by staying within the bounds of the analysis listed in Table 1 and illustrated in Figure 4. There exists no accepted formula, nor method of analysis for the transition zone shown in Figure 4. The primary objective of this research report is to attempt to measure strain to fracture and critical strain energy density with the use of tensile specimens and to determine if these properties are relevant in transition.

Table 1. Constraints and Formulas.

Condition	Formula
Plane strain linear elastic	a, b, B > 50ry a, b, B > $50/6\pi (K_Ic/\sigma y)^2$
Plane stress linear elastic	a, b > 50ry a, b > $50/2\pi (Kc/\sigma y)^2$
elastic-plastic	a, b, B > $50J/\sigma y$
between elastic-plastic & fully plastic	ε_f *or* $(dW/dV)_c$
fully plastic	$\hat{k} = \sigma y/2$

Where a is the crack length; b is the length of the un-cracked ligament; B is the specimen thickness; K_{Ic} is the plane strain fracture toughness; J_{Ic} is the elastic plastic fracture toughness; $\hat{k}$ is the flow stress in shear; ε_f is the fracture strain; $(dW/dV)_c$ is the critical strain energy density; s is the shear lip width; and σy is the yield strength [10].

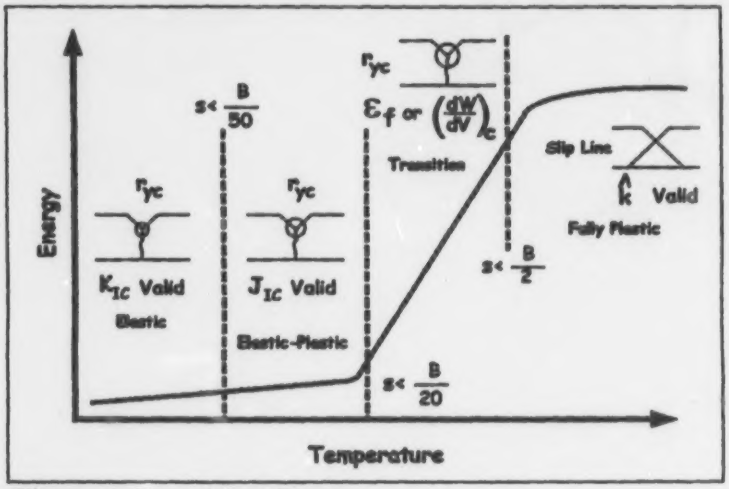
Energy
Temperature
r_{yc}
K_{IC} Valid
Elastic
$s < \frac{B}{50}$
r_{yc}
J_{IC} Valid
Elastic-Plastic
r_{yc}
ε_f or $\left(\frac{dW}{dV}\right)_c$
Transition
$s < \frac{B}{20}$
Slip Line
$\hat{k}$ Valid
Fully Plastic
$s < \frac{B}{2}$

Figure 4. Transition Curve.

4.0 Stress Strain Curve: Theory and Practice

Data obtained through tensile testing can be used to plot stress-strain curves. The engineering stress-strain curve is constructed by computing stress in terms of load divided by the original cross-sectional area, and the strain as the extension divided by the original gauge length over which the extension is measured. Figure 5 illustrates an engineering stress-strain curve. The elastic regime represents the area where a material will recover its original shape when a deforming load is removed. The elastic regime is a linear relationship where Hooke's law applies. A material in this region will relax to its initial form when the load is released. The yield stress represents a critical stress above which deformation will be permanent. Relaxing the load in this region will not allow the material to return to its initial form. The point marked "fracture" gives the fracture stress (fracture load divided by the original cross-section). This is one of the real short comings of the engineering stress strain curve (force divided by the cross section at fracture is more significant).

The strain at fracture is represented by equation 1. The equation takes into account the original length and the length at fracture.

$$\varepsilon_f = \frac{L_f - L_i}{L_i} \qquad (1)$$

The strain necessary to deform the specimen from maximum load to fracture is called the necking strain, as necking usually begins at maximum load for most metals. The location of the maximum load on a stress-strain diagram is shown in Figure 6. After maximum load the specimen experiences an increase in stress. This increase is the result of a decrease in the cross sectional area of the specimen due to necking. Materials that show permanent necking before fracture do not have a uniform strain distribution along the length of the tensile specimen. The exact distribution of strain is a function of the metal, the gauge length, and the cross-sectional area of the specimen. Figure 8a illustrates that the area under the stress-strain curve will be lower for a less ductile material than a highly ductile material. The same is true of a material with less strain hardening, it will have a smaller area under the curve than a highly strain hardened material. The more strain hardened a material, the greater the amount of deformation away from the necking region. The shorter the gauge length, the greater the percentage elongation. Specimens that are to be compared must be geometrically similar. Therefore, the ratio of gage length to diameter must be a constant. The American convention is to have a tensile specimen with an L/D ratio of 4. The German standard calls for a L/D ratio of 10, while the British standard calls for a ratio of 3.54.

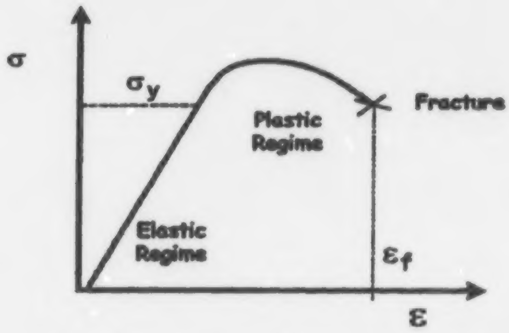

Figure 5. Typical Engineering Stress-Strain Diagram. (In this schematic the fracture stress is load divided by original cross-sectional area)

By increasing the thickness of a specimen, while maintaining a constant gauge length, the fracture elongation will increase until the length divided by the diameter reaches unity. Once unity has been obtained, the fracture elongation will decrease as the specimen thickness increases. This can be seen in Figure 8b. This data was obtained from research preformed by the United States Naval Research Laboratory (NRL) in

Washington, DC [14]. NRL investigated the possibility of using tensile specimen size and geometry effects to accurately and uniquely assess the uniaxial continuum stress- strain curve. Reduction of tensile specimen load-displacement data to uniaxial continuum stress- strain data valid at large deformation is thought not to be possible for continuum material specimens which exhibit necking [14]. Valid uniaxial continuum stress-strain data is required for accurate finite element analysis, deformation prediction and design application. The necking phenomenon in specimens has been a difficult barrier to overcome so that accurate characteristics of a given material can be found. Focusing on real stress - real strain may be the answer.

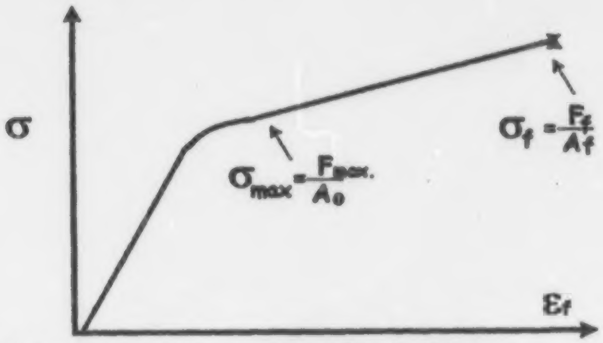
σ
$\sigma_{max} = \frac{F_{max.}}{A_0}$
$\sigma_f = \frac{F_f}{A_f}$
ε_f

Figure 7. Real Stress - Real Strain Diagram.

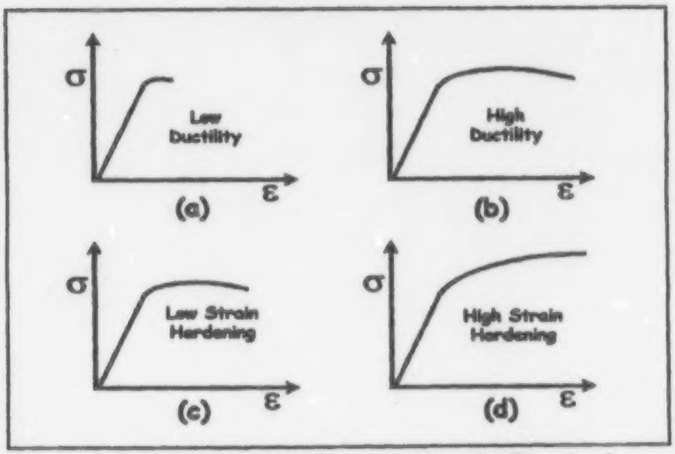

Figure 8a. Effect of Ductility and Strain Hardening on Engineering Stress-Strain Diagram.

The area under the stress-strain curve at fracture represents the critical strain energy density $(dW/dV)_{critical}$. This area is an indication of the amount of work per unit volume which can be done without failure occurring. The area under the stress-strain curve can also be referred to as the toughness of a material. The form of the stress-strain curves (engineering stress-strain versus real stress - real strain) is critical to succeed in determining $(dW/dV)_{critical}$.

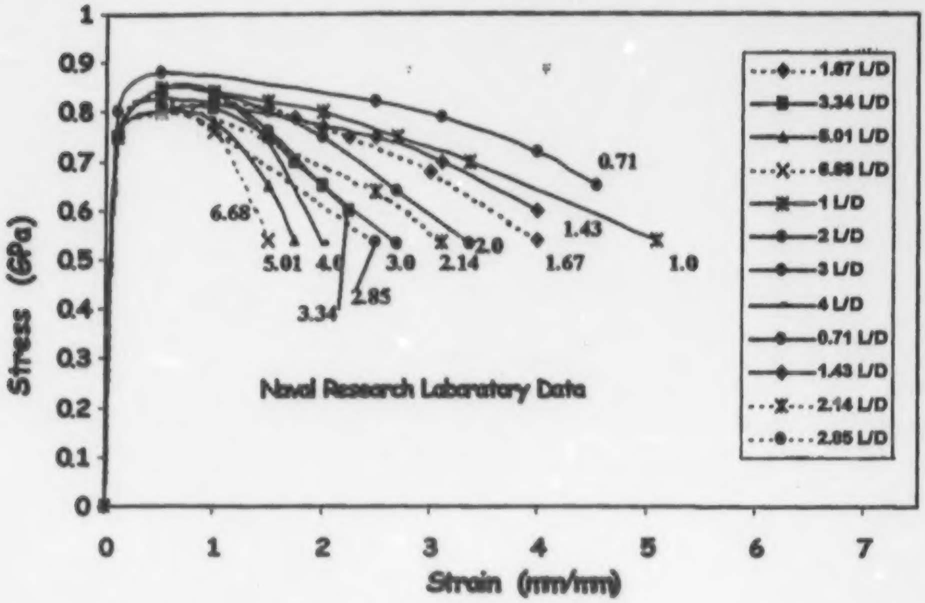

Figure 8b. Effects of Length/Diameter on Stress-Strain Diagram.

5.0 Material & Method

5.1 Materials

Structural quality steel plates used for general engineering purposes must comply with the requirements set forth by CSA Standard CAN3-G40.20-M, General Requirements for Rolled or Welded Structural Quality Steel. This Standard specifies specific requirements for analysis, number of tests, test preparation, methods of tests, permissible variations in dimensions and mass, repair, marking, inspection, re-tests, rejections, reports, packaging and loading.

The steel used in this research report was 350WT. The plate was a Fleet Maintenance facility (FMF) stores item. This item was stocked following the construction of the Canadian Patrol Frigates. The Stelco Steel Plant in Canada certified that the Canadian plate was made of Can/CSA-G40.21-M92 GRD 350 WT Category 5 steel. The "WT" indicates that the steel is weldable and has a toughness requirement. Steels of this type are required to meet specific strength and Charpy V-Notch impact requirements and are suitable for welded construction where notch toughness at low temperature is a design requirement.

Outlined in Table 3 are the chemical compositions set forth by the Standard. According to the Standard, materials that differ from the requirements of Table 3 (except for carbon, manganese, phosphorus, and sulphur contents) may be considered as meeting the requirements of the Standard, provided that all of the specified mechanical properties have been obtained. Included in the table are two independent analyzes which were done on portable analytical instruments.

Table 3. Chemical Composition of 350WT Steel.

	C	Mn[1]	P	S	Si	Cr	Ni	Cu
Standard	0.22 max.	0.80-1.50	0.03 max.	0.04 max.	0.15-0.40			
Spectro Port	0.054	1.17	0.018	0.012	0.210	0.029	<0.005	0.010
Metallurgist XR	na	1.45	na	na	na	0.21		

	Al	Co	Nb	Ti	V[2]	W	Pb	Mo	Fe
Standard					0.10 max.[3]				98.70 max.
Spectro Port	0.049	0.150	0.022	0.024	0.069	0.004	<0.0009	<0.010	98.2
Metallurgist XR	na		0.03		0.07				97.93

[1] The manganese content may be increased provided the sum of the carbon content plus 1/6 of the manganese content does not exceed 0.40% for Grade 350WT.

[2] Aluminum may be used as a grain refining element, however it shall not be included in the summation of grain refining elements. The elements columbium and vanadium may be used singly or in combination up to the total percentage indicated.

[3] A nitrogen content of 0.01-0.02% may be used if the nitrogen content does not exceed ¼ of the vanadium content.

5.1.1 Tensile Specimens

Twelve tensile specimens were machined from the 350WT plate. The specimen dimensions are shown in Figure 9. The specimens were machined in accordance to ASTM Standard E8. Six specimens were cut with a width (W) of ¼ inch, and six specimens were cut with a width of ½ inch. The specimens were cut in the L-T direction (length parallel to rolling direction). The specimens were marked with an electro-etch grid of 1.25 mm.

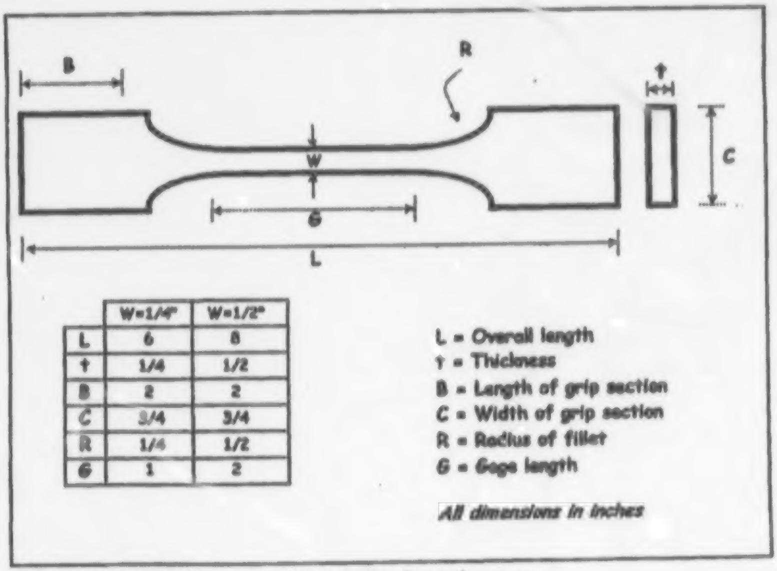

	W=1/4"	W=1/2"
L	6	8
t	1/4	1/2
B	2	2
C	3/4	3/4
R	1/4	1/2
G	1	2

L = Overall length
t = Thickness
B = Length of grip section
C = Width of grip section
R = Radius of fillet
G = Gage length

All dimensions in inches

Figure 9. Schematic of Tensile Specimen.

6.0 Testing

Tension tests were performed on an Instron interfaced with "daqware" software. Figures 10a & b are photographs of the apparatus. The specimens were fractured inside an enclosed compartment so that the temperature could be controlled. The specimens were cooled with CO_2 gas. Specimens with two different gauge lengths (1 & 2 inch) were tested at five different temperatures (-40 to 10°C). Three different parameters were recorded during testing: strain, stroke, and load. The computer was set for analog input, at a maximum (100%) of 10 volts. This related 10 volts to 22000 lb. load, 2-inch stroke, ½-inch strain. The strain was recorded with the use of an extensometer gauge. One hundred data points were recorded per second. Conversion of the data was necessary from volts to pounds and inches.

Figure 10a. Tensile Test Set-up.

Figure 10b. Grips with Specimen & Extensometer.

7.0 Results

Two sets of data were generated. The first set was the extensometer and applied load readings, while the second set was the grid spacing measurements. Shown in Figure 11 is the stress-strain curve for the 2 inch gauge length specimens.

Figures 12a & b represent the grid extension after testing (plastic strain) versus the fracture location on the specimen. Position 5 is where the specimens fractured. From these graphs, it appears that there was no direct relationship with temperature. However, it became apparent that the magnitudes of the curves were influenced by the position where failure occurred with respect to the grid line. The unsymmetrical points of each curve provided this clue. What is meant by unsymmetrical, is that the relative points on the opposite sides of the individual curves experienced different strains. For example, specimen 5a, from Figure 12a, had a distance of 0.275 mm from the first grid-line to the fracture on the left side of the fractured specimen. The right side of the fractured specimen had a distance of 0.125 mm from the first grid-line to the fracture. The red line on Figure 12a indicates this difference.

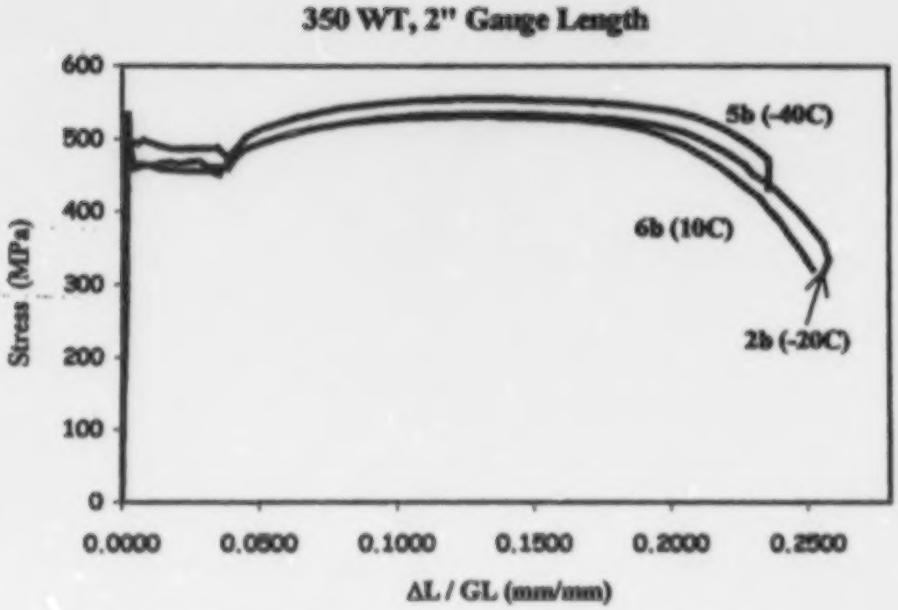

Figure 11. Two Inch Gauge Length Tensile Test Data.

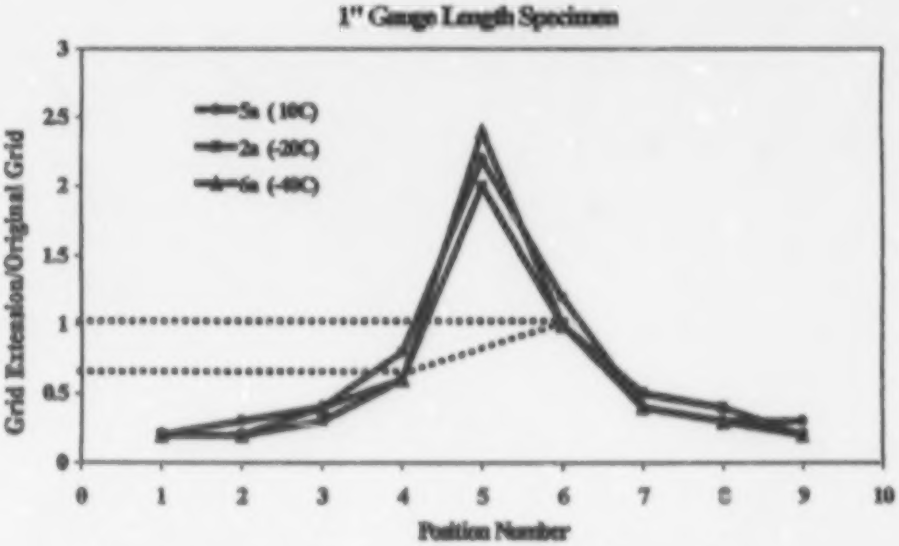

Figure 12a. One Inch Gauge Length Grid Extensions.

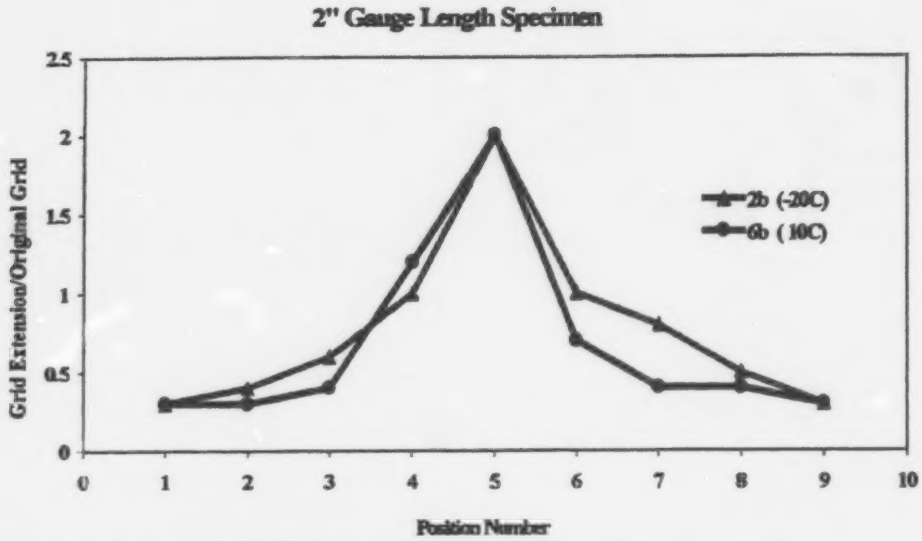

Figure 12b. Two Inch Gauge Length Grid Extensions.

Figure 13 illustrates the distance from the fracture to the closest grid-line. The thick vertical line represents the location of the fracture. The 1" specimens are identified by the *a* suffix, while the 2" specimens are identified by the *b* suffix. The rectangle represents the distance from the fracture to the grid-line. The best result occurred with specimen 6a, the distance to the nearest grid-line, from the fractured end, on both pieces were very close in length. For example, on side A the grid-line was found to be 0.25 mm from the fracture, while on side B the grid-line was found to be 0.175 mm from the fracture.

Specimen 5a and 2b also had lengths that were fairly similar in their distances from the fractured end to the nearest grid-line. Specimen 6b fractured on the grid-line, it was the only specimen to do so.

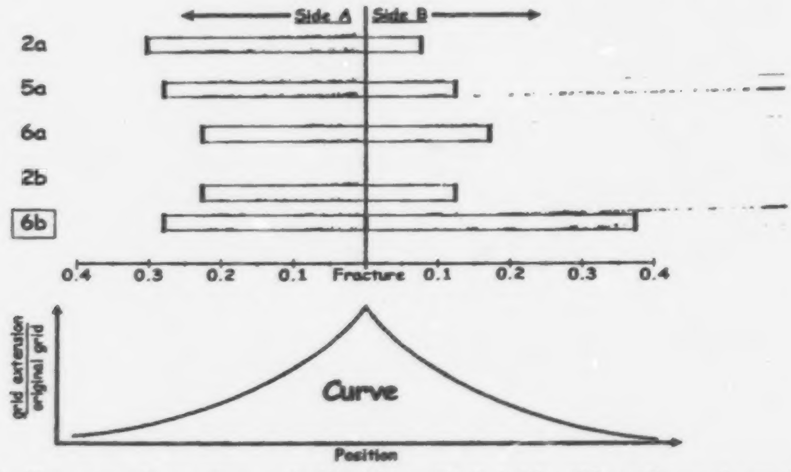

Figure 13. Fracture Locations. (a identifies 1" & b identifies 2" specimens)

The five closest grids on both sides of the fractured specimens were measured, and the percent strain calculated. Figure 14a displays the stress versus percent strain for the tested specimens. The areas under these curves are the critical strain energy density for the tested specimens. It is difficult to obtain relevant information from these curves. However, averaging the stress and the percent strain for the 1 and 2 inch specimens at each temperature results in the graph shown Figure 14b. It is apparent from this graph that there is a direct relationship with temperature. The area under the curve for the specimen tested at -40°C was approximately 53000, the area under the curve for the specimens tested at -20°C was approximately 61000, and the area under the curve for the specimens tested at 10°C was approximately 64000. As the temperature increased so did the area under the curves.

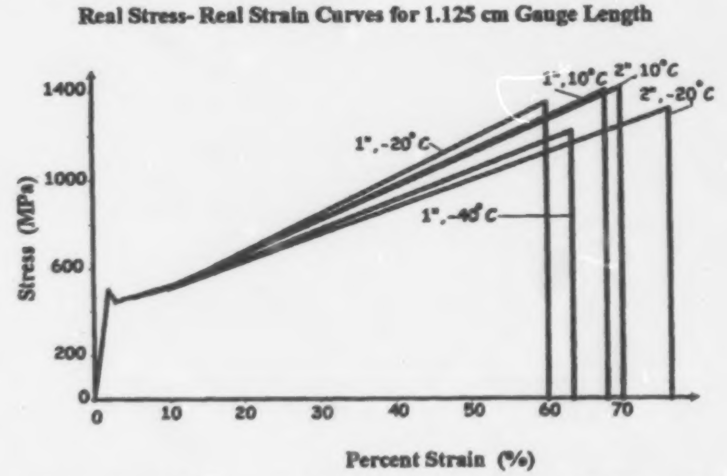
Real Stress- Real Strain Curves for 1.125 cm Gauge Length

Figure 14a. Real Stress - Real Strain Curves for 1.125 cm Gauge Lengths.

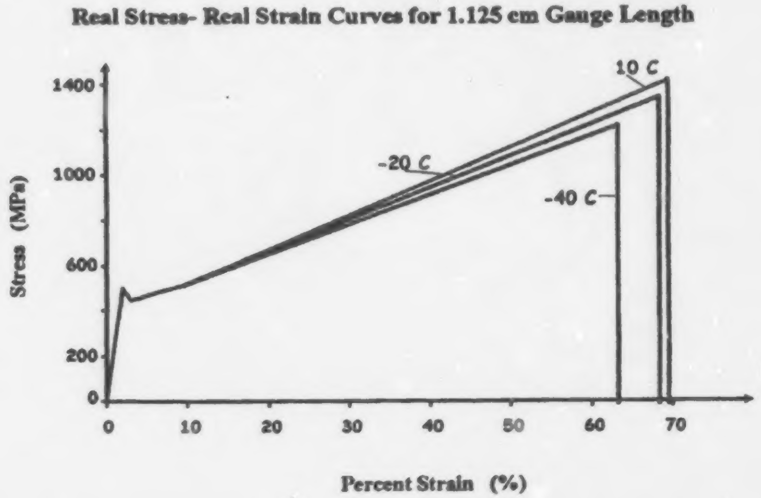
Real Stress- Real Strain Curves for 1.125 cm Gauge Length

Figure 14b. Averaged Real Stress – Real Strain Curves for 1.125 cm Gauge Lengths.

8.0 Conclusions

In this study the focus was on critical strain energy density and strain to fracture for the transition zone. In the transition zone, a direct relationship between the critical strain energy density and the plastic strain over 1.125 cm, was found with temperature.

9.0 Recommendations

The real stress - real strain test procedure must be improved to acquire real stress and real strain of at least 10 points along the curve.

The grid should be etched onto all four sides of the specimens. To increase accuracy in determining fracture strain, the grid on one face of the specimen should have an offset to the adjacent face.

Techniques to accurately acquire strain to fracture over smaller and smaller gauge lengths, need to be developed. Ideally, it may be necessary to match the specimen gauge length with finite element mesh size.

10.0 References

1. Rolfe S.T., Barsom J.M., Fracture and Fatigue Control In Structure: Applications of Fracture Mechanics, Prentice-Hall, USA 1987, pp. 2.

2. Manchester Material Science Center, www/umist.ac.uk/MatSc/liberty.

3. H.C. Campbell, “Brittle Fracture and Structural Failure of the Liberty Ships”, 1967.

4. American Bureau of Shipping, “Surveyor”, Democrat Press, Vol. 23, No. 2, June 1992, pp.32.

5. Biggs W.D., The Brittle Fracture Of Steel, MacDonald & Evans, Great Britain, 1960.

6. Thomson R. & Champion C.S., “Fracture Toughness Evaluation of Steels for Arctic Marine Use”, CANMET, Canada, 1983.

7. Lawn B.R., Wilshaw T.R., Fracture of Brittle Solids, Cambridge University Press, Cambridge, 1975.

8. Http://ranger.eng.tau.ac.il/history

9. Admiralty Ship Welding Committee, “First and Second Interim Reports”, Great Britain, 1946 and 1948.

10. J.R. Matthews, J. F. Porter and C.V. Hyatt, "Fracture Control for Submarine Pressure Hulls II", Prepared for the third meeting of the TTCP PTP1 Operating Assignment on Fracture Control of Naval Structures, Annapolis Maryland, May 1-3, 1991.

11. J.R. Matthews, "Ship Fracture", Paper Presented at the 3rd CF/CRAD Meeting on Naval Applications of Material Technology, Halifax, NS. April 22-24, 1997, pp. 409-29.

12. G. E. Dieter, Mechanical Metallurgy, 2nd ed., McGraw-Hill, New York, 1976.

13. J. R. Matthews, "Prediction of Ductile Behaviour in Welded Structures (Transition Behaviour, Shear Lip, Notch Acuity and Specimen Size)"., The Minerals, Metals & Material Society, 1997.

14. P. Matic, G.C. Kirby III and M.I. Jolles, "The Relationship of Tensile Specimen Size and Geometry Effects to Unique Constitutive Parameters for Ductile Materials", NRL Memorandum Report 5936, Office of Naval Research, Arlington, VA, 1987.

#511903 ②

The Fracture Toughness Transition Curve for a 350WT Plate

by Jack Morrison[+], J Xiaozhu Wu[+] and Al Hull[++]

[+]Dockyard Laboratory(Pacific), Victoria, British Columbia
[++]Engineering Material Research, Downsview, Ontario

ABSTRACT

Quantitative measurements of cracking resistance are needed to assess the risk of brittle fracture under service conditions in warships. This requires laboratory toughness testing at the minimum service temperature and at loading rates equivalent to hull impact events such as wave slamming and minor collisions. A technique has recently been standardized by ASTM for determining the variation of fracture toughness with temperature of ferritic steels and welds in the transition fracture range. Using ASTM E1921 K_{Jc} toughness transition curves are generated statistically from the analysis of toughness data populations using a Master Curve concept. An experimental program is underway to establish whether Master Curve technology will provide an effective way of quantifying hull toughness for warship fracture control. CSA G21 350WT steel plate has been evaluated using this approach, and the toughness data generated met all of the validity requirements of the standard. This work is being extended to include loading rate and plate orientation effects, and the determination of weld fracture transition behaviour.

15 mm 350WT Plate

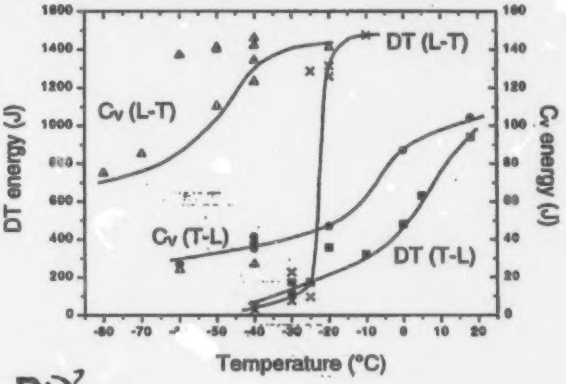

DEFENCE R&D DÉFENSE

Outline

- Reference Temperature and Master Curve concepts.
- Summary of ASTM E1921 procedure.
- Scope of the DL(P) program.
- Material.
- Test results and data analysis.
- Conclusions.

DEFENCE R&D DÉFENSE

Master Curve Assumptions

- Temperature dependence of median toughness is the same for all ferritic steels.
- Crack front behavior can be described using weakest link model.
- Toughness variation about the median follows a Weibull Distribution with a slope of 4.

An index temperature is then sufficient to describe the transition behavior.

Cleavage Fracture

- Fracture control of ferritic structures is aimed at avoiding unstable cleavage.
- The relative ease of crack nucleation and propagation depends on the crack tip stress distribution.
- A statistical model is needed to quantify the probability of cleavage fracture.

Statistical Model

- Assumes a distribution of potential initiation sites for cleavage.
- Under specified conditions each initiator has a certain probability of being critical.
- If fracture is initiated there is a further probability that propagation can occur.
- "Weakest link" approach assumes that failure probability is initiation controlled.

- Probability of cleavage initiation under small scale yielding conditions:

$$P_f = 1 - \exp\left(- \frac{B}{B_0} \left(\frac{K_1}{K_0} \right)^4 \right)$$

where K_0 is the scale parameter

- Cumulative failure probability (incorporating propagation effects):

$$P_f = 1 - \exp\left(- \frac{B}{B_0} \frac{A}{K_0^4} (K_1 - K_{min})^4 \right)$$

where A is a propagation constant

- This combined failure probability can be rearranged in the form of a three parameter Weibull expression:

$$P_f = 1 - \exp\left(-\frac{B}{B_0}\left(\frac{K_1 - K_{min}}{K_0 - K_{min}}\right)^4\right)$$

where K_{min} is the shift parameter

- This probability curve provides a fracture mechanics description of cleavage transition.
- The shift parameter (K_{min}) in the Weibull curve provides a lower bound toughness.
- An empirical estimate for K_{min} in ferritic steels is 20 MPa√m.
- The scale parameter K_0 has an exponential temperature dependence.

The Master Curve

- The “Master Curve” describes the temperature dependence of cleavage fracture toughness for a wide range of ferritic steels.
- A “Reference Temperature” T_0 provides an index at which the median toughness for a 25 mm specimen thickness is 100 MPa√m.

ASTM Standard E1921

- Uses replicate K_{Jc} tests (minimum 6) to obtain K_0 and calculate median toughness.
- Test temperature estimated from Charpy.
- Cleavage must occur before a K_{limit} reached.
- Results adjusted to 1T equivalent thickness.
- Data analysis is provided for both the Reference Temperature and Master Curve.
- Currently excludes HAZ and dynamic testing.

Data Analytical Procedures

- Determine K_o from Weibull analysis.
- Calculate $K_{Jc(med)}$ from K_o

  $K_{Jc(med)} = (K_o - K_{min})(\ln 2)^{1/4} + K_{min}$
- Calculate T_0 from $K_{Jc(med)}$.
- Master Curve

  $K_{Jc(med)} = 30 + 70 \exp[0.019(T - T_0)]$

  Lower tolerance bound

  $K_{Jc(05)} = 25.4 + 37.8 \exp[0.019(T - T_0)]$

Objectives of DL(P) Work

- Using ASTM E1921 determine T_0 and the Master Curve for marine steels and welds.
- Examine orientation and loading rate effects.
- Compare with existing fracture data bases.
- Evaluate implications for fracture mechanics based structural integrity assessments.

Current Status

- Completed: 350WT plate L-T & T-L (QS)
- Underway: 350WT plate L-T & T-L (D)
  350WT weld (QS & D)
  A517 weld (QS &D)
- Planned: X80 steel

350WT Plate

- 15 mm Stelco plate 0.16C 1.4Mn 0.07V
- Yield Strength 460 MPa @ 20°C,
  630 MPa @ -96°C
- Charpy V-notch
  L-T: 120 J @ -40°C, 70J @ -80°C
  T-L: 38J @ -40°C, 27J @ -60°C
- CTOD @ -20°C L-T: 0.55 mm
  T-L: 0.42 mm
- NDTT -40°C

Test Parameters

- Test specimen:
  15 mm x 30 mm SENB
  a/W = 0.5
- Test Temperatures:
  -96°C (L-T), -50°C (T-L)
- Specimen K_{Jc} limits:
  237 - 250 MPa√m

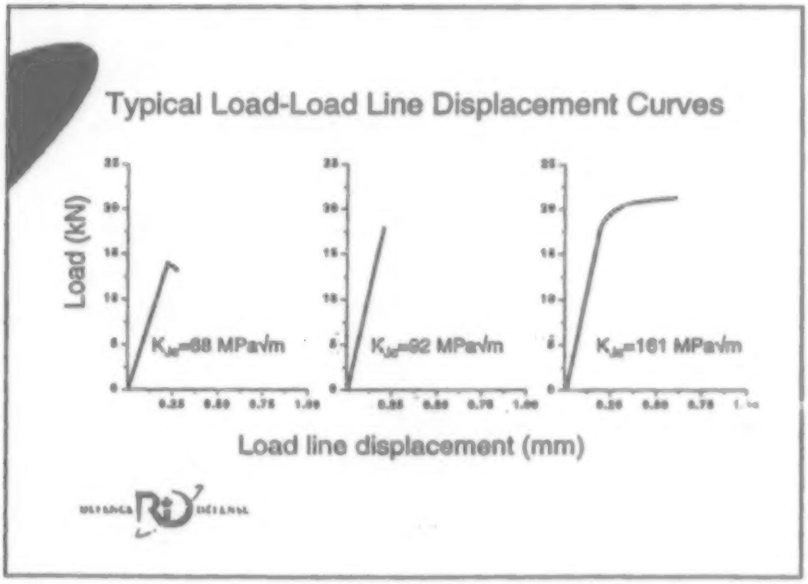

Typical Load-Load Line Displacement Curves

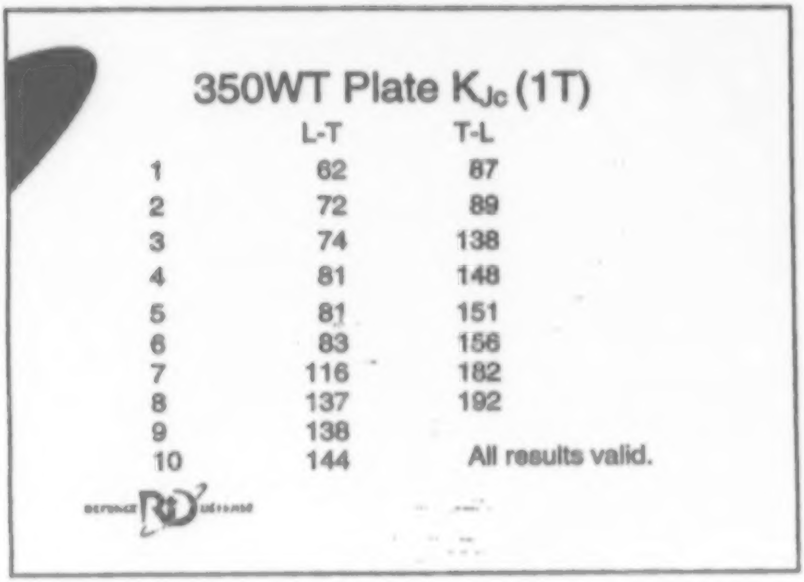

350WT Plate K_{Jc} (1T)

	L-T	T-L
1	62	87
2	72	89
3	74	138
4	81	148
5	81	151
6	83	156
7	116	182
8	137	192
9	138	
10	144	

All results valid.

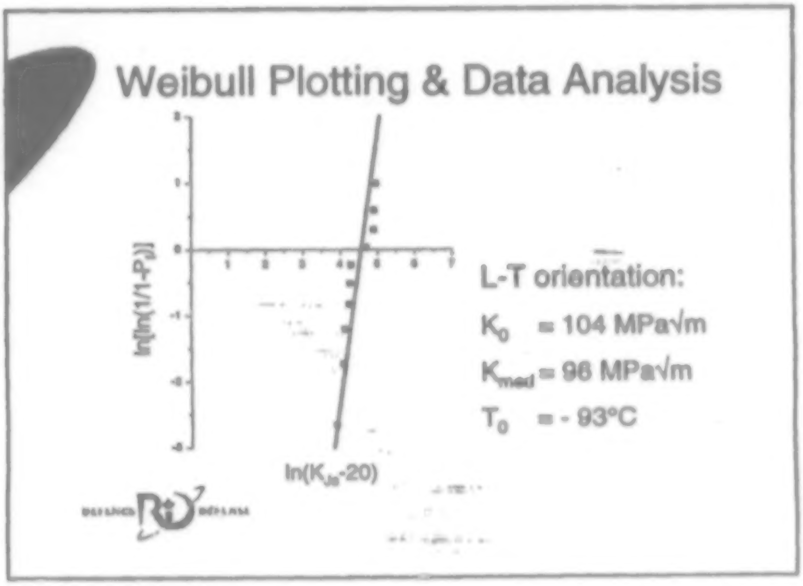

Weibull Plotting & Data Analysis

L-T orientation:

K_0 = 104 MPa√m

K_{med} = 96 MPa√m

T_0 = - 93°C

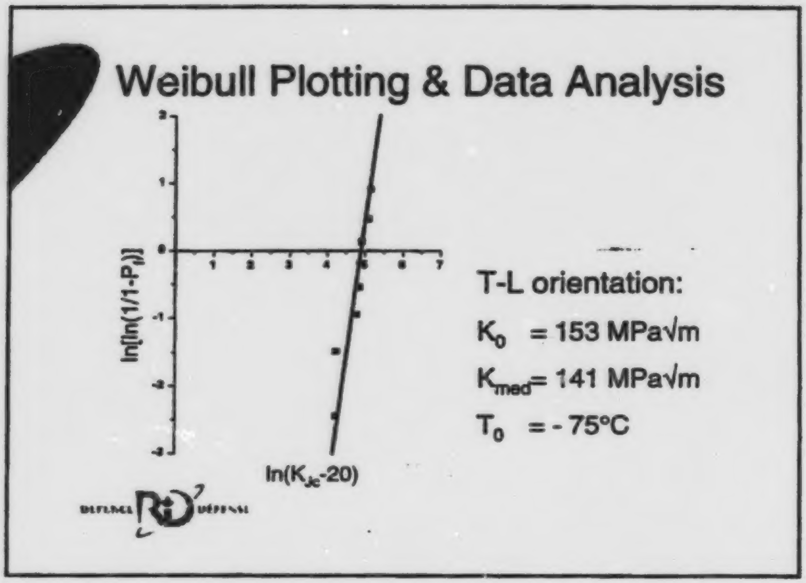

Weibull Plotting & Data Analysis

T-L orientation:

$K_0 = 153$ MPa√m

$K_{med} = 141$ MPa√m

$T_0 = -75$°C

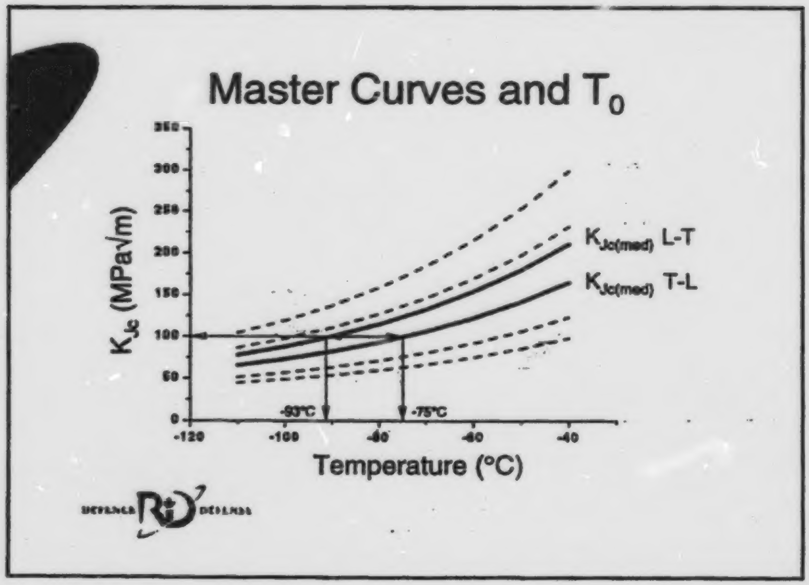

Master Curves and T_0

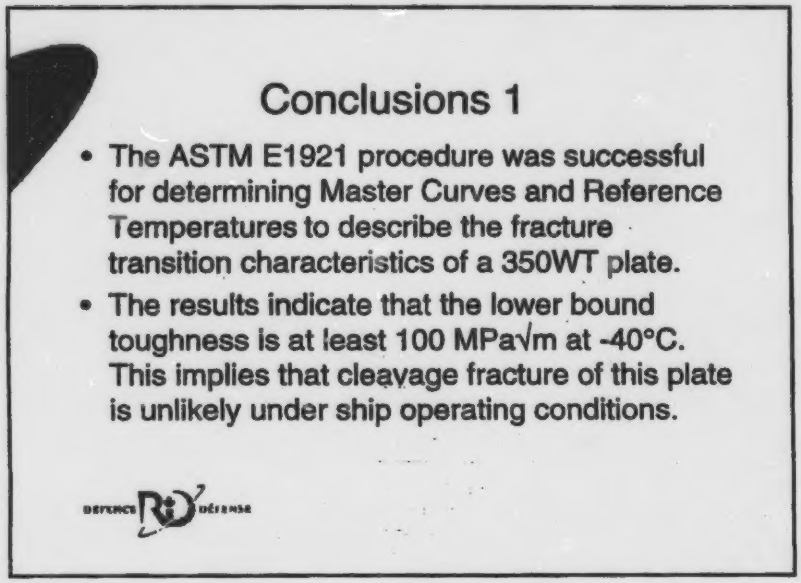

Conclusions 1

- The ASTM E1921 procedure was successful for determining Master Curves and Reference Temperatures to describe the fracture transition characteristics of a 350WT plate.
- The results indicate that the lower bound toughness is at least 100 MPa√m at -40°C. This implies that cleavage fracture of this plate is unlikely under ship operating conditions.

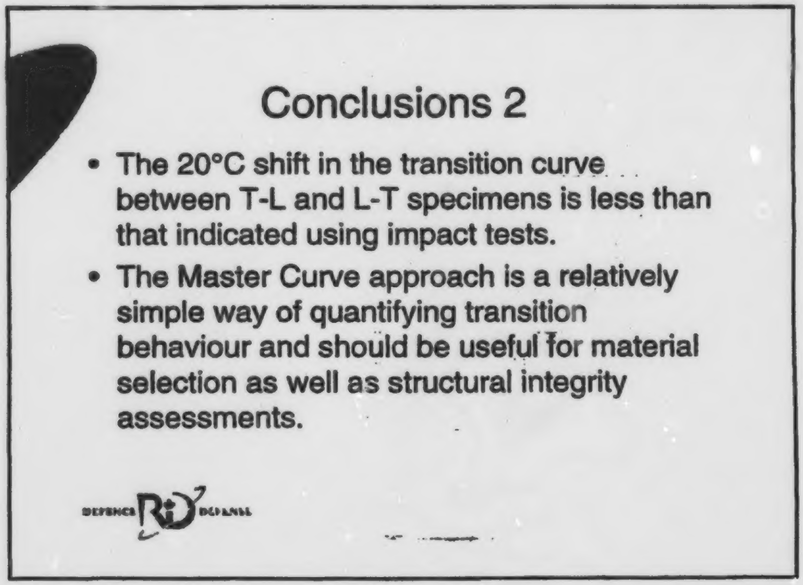

Conclusions 2

- The 20°C shift in the transition curve between T-L and L-T specimens is less than that indicated using impact tests.
- The Master Curve approach is a relatively simple way of quantifying transition behaviour and should be useful for material selection as well as structural integrity assessments.

#511904 (30)

Dynamic Mechanical Property Prediction by Group Contribution Analysis

by J.P. Szabo and J.C. Roberts

Defence Research Establishment Atlantic, Dockyard Laboratory (Atlantic)
P.O. Box 1012, Dartmouth, Nova Scotia B2Y 3Z7

ABSTRACT

Vibroacoustic materials play a key role in signature control of military platforms, and their performance is related to the frequency dependence of the modulus and loss factor of the polymers from which they are fabricated. The height, width, and position (fmax) of the loss factor peak varies from polymer to polymer, as does the rubbery and glassy plateau moduli. This paper presents work in progress on a TTCP operating assignment whose goal is to extend and validate models which relate a polymer's dynamic mechanical properties to its chemical structure. The complex modulus of polymeric materials may be described by the Havriliak-Negami (HN) equation. Group contribution analysis (GCA) was used to derive contributions to the five parameters of the HN equation for a set of polyurethanes. Use of the calculated contributions gave HN parameters which show good agreement with experimental values when used on the training set, but had high error when tested on other polymers. Redefining the groups used for GCA show significantly improved results. The use of a new training set of polymers and the use of different structure descriptors is also discussed.

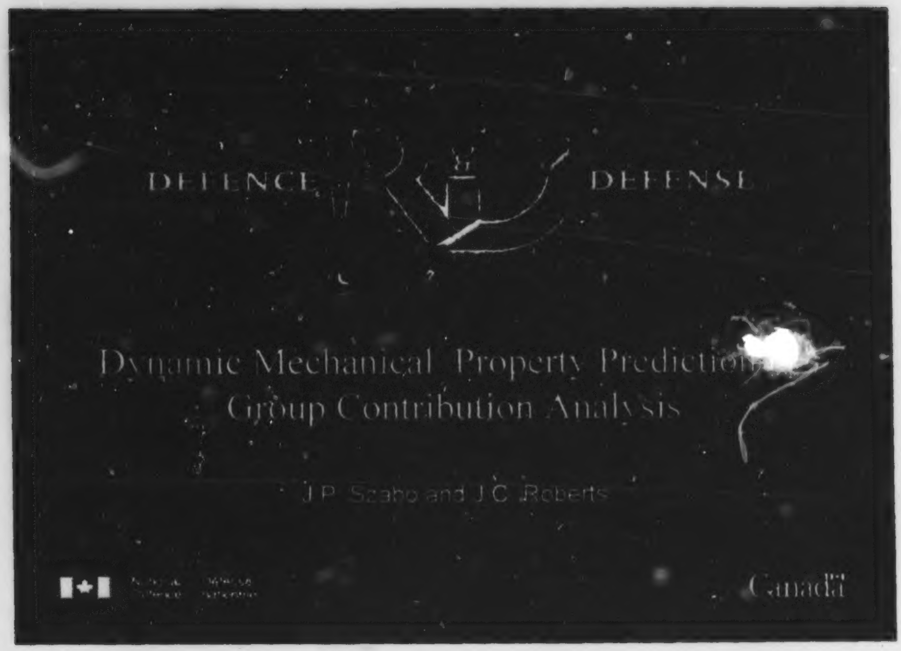

DEFENCE DEFENSE

Dynamic Mechanical Property Prediction: Group Contribution Analysis

J.P. Szabo and J.C. Roberts

Canada

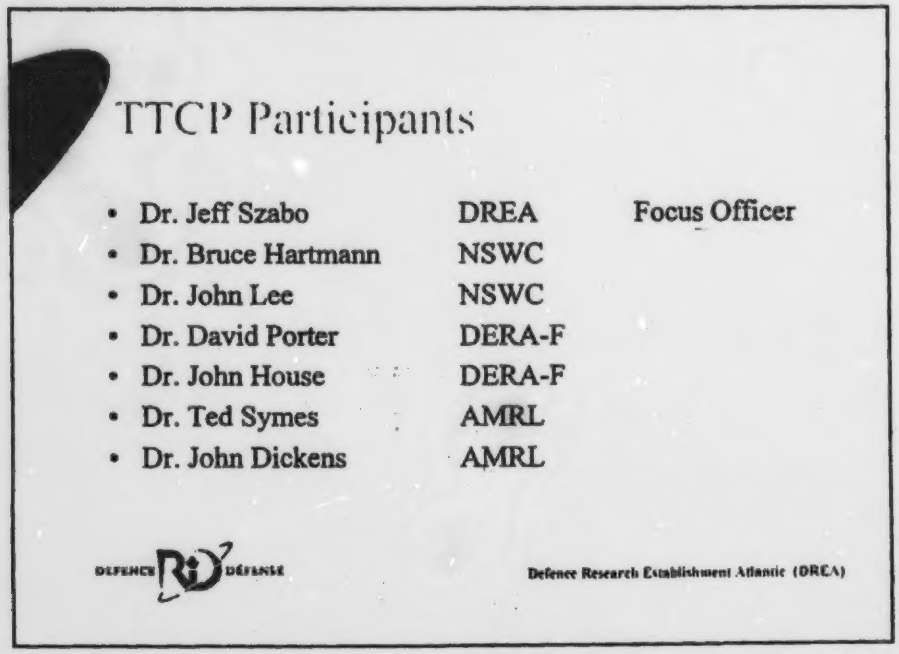

TTCP Participants

Dr. Jeff Szabo	DREA	Focus Officer
Dr. Bruce Hartmann	NSWC	
Dr. John Lee	NSWC	
Dr. David Porter	DERA-F	
Dr. John House	DERA-F	
Dr. Ted Symes	AMRL	
Dr. John Dickens	AMRL	

DEFENCE R&D DEFENSE

Defence Research Establishment Atlantic (DREA)

TTCP-MAT-TP-6-09

- The goal is to develop methods to predict the dynamic mechanical properties of polymers from their chemical structures.

Chemical Structure → **Polymer Properties** → **System Performance**

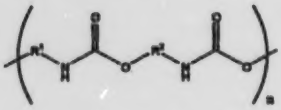

$E^*(\omega,t)$

$G^*(\omega,t)$

Vibration Isolators

Decoupling Tiles

Anechoic Tiles

Structural Damping

DEFENCE R&D DÉFENSE

Defence Research Establishment Atlantic (DREA)

Assignment Tasks

- Preliminary modelling using data from the literature
  - Group Interaction Modelling (GIM)
  - Group Contributions
- Synthesis, characterization, and modelling of 20 phase mixed polyurethanes.
- Effect of static load on dynamic mechanical properties
- Phase morphology effects (blends, block copolymers)

DEFENCE R&D DÉFENSE

Defence Research Establishment Atlantic (DREA)

Dynamic Mechanical Properties

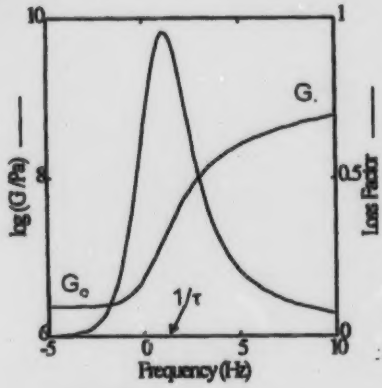

$$G^* = G' + i\,G''$$

$$\tan\delta = G''/G'$$

Structure controls:

- **Limiting moduli** G_0, G_∞
- **Peak height, width** β
- **Peak shape** α
- **Peak position** $1/\tau$

$$\boxed{G^* = \frac{G_0 - G_\infty}{\left[1+(i\omega\tau)^\alpha\right]^\beta} + G_\infty}$$

Havriliak - Negami Eqn

Defence Research Establishment Atlantic (DREA)

Group Contribution Analysis

- **Based on the assumption that each chemical group contributes a certain amount to a given property, eg density**

$$\rho = \sum_j W_j \rho_j$$

- **Can GCA be applied to HN parameters: α, β, τ, G_0, G_∞ ?**

1) Took a number of polymers with known $G^*(\omega)$, solved for HN parameters "Training Data"

2) Broke down monomer structures into groups, e.g. $-CH_2-$, $-O-$, phenyl, urethane,...

Defence Research Establishment Atlantic (DREA)

3) Calculated weighting factors for each group i and polymer j:

$$W_{i,j} = N_{i,j}\frac{M_{i,j}}{M_j}$$

4) Solved for coefficients A, B, C, D, E which satisfy matrix equations:

$$\log(\tau) = W\,C$$

$$\alpha = W\,A \qquad \log(G_0) = W\,D$$

$$\beta = W\,B \qquad \log(G_\infty) = W\,E$$

Can now use coefficients to calculate dynamic mechanical properties of other polymers with same groups

DEFENCE R&D DEFENSE

Defence Research Establishment Atlantic (DREA)

Polyurethane Structures

GENERAL POLYURETHANE:

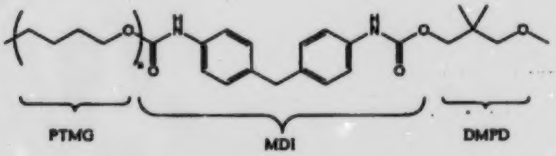
PTMG
MDI
DMPD

CHAIN EXTENDERS:

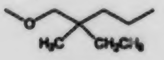

EMPD

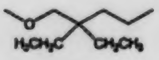
H_3CH_2C
CH_2CH_3

DEPD

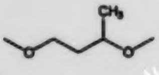

1,3 BDO

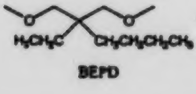
H_3CH_2C
$CH_2CH_2CH_2CH_3$

BEPD

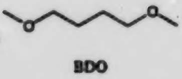

BDO

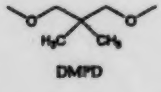

DMPD

Preliminary GCA Study

- Selected a set of 14 polyurethanes for which dynamic mechanical properties were known (literature)
- Divided repeat structure up small groups:

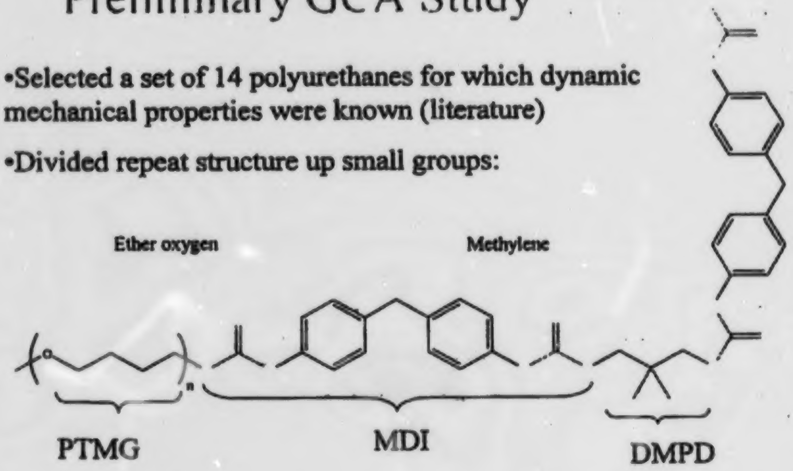

Number of Groups per Monomer (N)

Monomer	MW	Methylene 14.027	Oxygen 15.999	Phenyl 76.098	cyclohexane 82.146	urethane 59.025	DMPD 42.081	EMPD 56.108	BEPD 98.189	DEPD 70.135
ptmg2000/3mdi/2dmpd	2995	119	27	6	0	6	2	0	0	0
ptmg2000/4mdi/3dmpd	3350	122	27	8	0	8	3	0	0	0
ptmg2000/6mdi/5dmpd	3958	128	27	12	0	12	5	0	0	0
ptmg1000/3mdi/2dmpd	1987	63	13	6	0	6	2	0	0	0
ptmg1000/3mdi/2depd	2043	63	13	6	0	6	0	0	0	2
ptmg2000/3mdi/2depd	3051	119	27	6	0	6	0	0	0	2
ptmg1000/3mdi/2 13bdo	1959	65	13	6	0	6	0	0	0	0
ptmg1000/3mdi/2empd	2015	63	13	6	0	6	0	2	0	0
ptmg2000/3mdi/2empd	3023	119	27	6	0	6	0	2	0	0
ptmg1000/3mdi/2bepd	2099	63	13	6	0	6	0	0	2	0
ptmg2000/3mdi/2bepd	3107	119	27	6	0	6	0	0	2	0
ptmg650/3 h12mdi/2bdo	1546	47	8	0	6	6	0	0	0	0
ptmg1000/3mdi/2bdo	1870	67	13	6	0	6	0	0	0	0
ptmg1430/3mdi/2bdo	2303	91	19	6	0	6	0	0	0	0

DEFENCE DÉFENSE

Defence Research Establishment Atlantic (DREA)

Results: Group Contributions

Contributions to HN Parameters:

Group	alpha	beta	log(tau)	log(Go)	log(Ginf)
Methylene	-24.9	15.1	-330.9	64.8	-8
Ether Oxygen	89	-52.4	1093.4	-199.2	70.9
phenyl	11.8	-6.1	146.6	-12	23.1
cyclohexane	11.8	-6.1	156.1	-12.7	21.8
urethane	0	0	0	0	0
DMPD	-9	5.5	-102.2	28	2.4
EMPD	-5.4	4.2	-65.2	21.4	-0.1
BEPD	-2	2.8	-36.4	15.5	2
DEPD	-4.2	3.1	-61.5	16.8	4

- Note urethane coefficients are zero
- Note strange values for some coefficients

DEFENCE R&D DÉFENSE

Defence Research Establishment Atlantic (DREA)

Results: Training Set

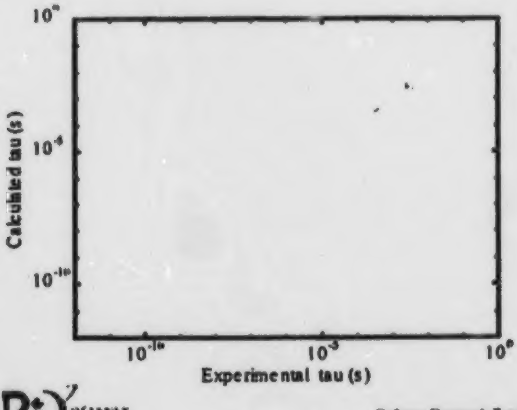

DEFENCE R&D DÉFENSE

Defence Research Establishment Atlantic (DREA)

Polymer in Training Data Set

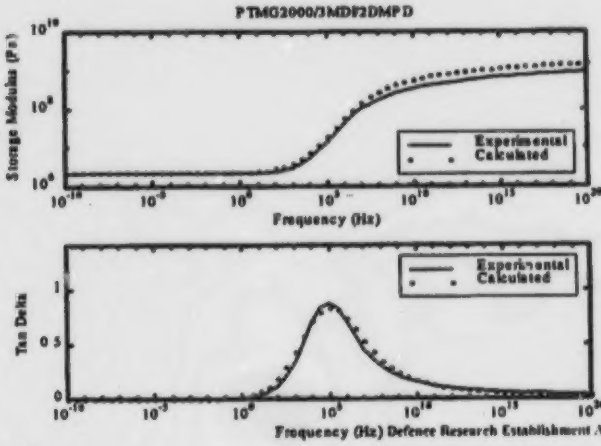

DEF

Defence Research Establishment Atlantic (DREA)

[illegible]

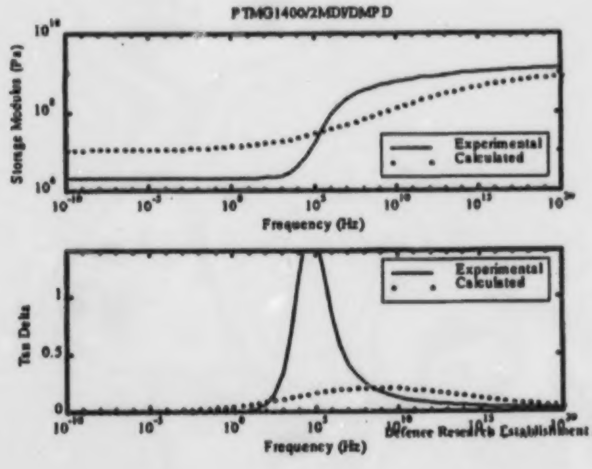

DEFE

Defence Research Establishment Atlantic (DREA)

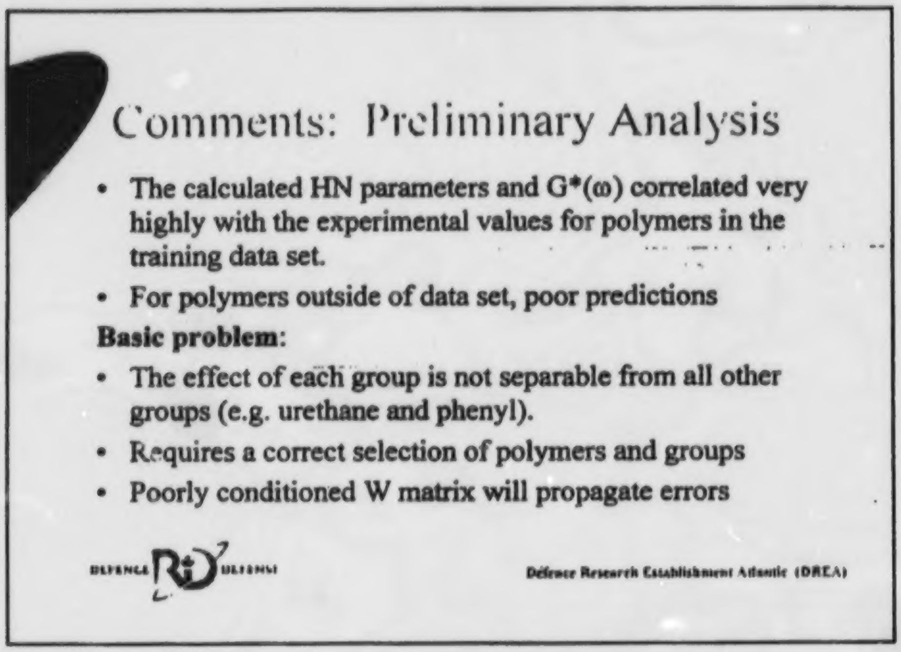

Comments: Preliminary Analysis

- The calculated HN parameters and $G^*(\omega)$ correlated very highly with the experimental values for polymers in the training data set.
- For polymers outside of data set, poor predictions

Basic problem:

- The effect of each group is not separable from all other groups (e.g. urethane and phenyl).
- Requires a correct selection of polymers and groups
- Poorly conditioned W matrix will propagate errors

Defence Research Establishment Atlantic (DREA)

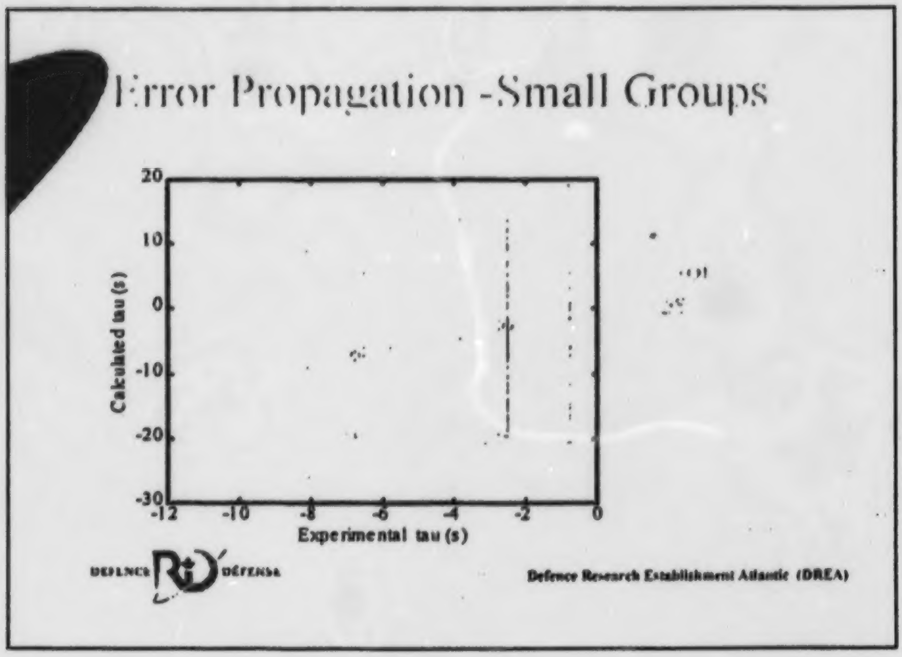

Error Propagation -Small Groups

Defence Research Establishment Atlantic (DREA)

Possible Solutions

1) Synthesize a set of polymers that contain a small number of groups, designed with low propagation error in W matrix.

   This should be completed by Fall 1999:

   20 polyurethanes containing 5 groups

2) Using existing polyurethane dataset from literature, represent structures in terms of larger groups such as tetamethylene glycol or MDI segments.

DEFENCE DÉFENSE

Defence Research Establishment Atlantic (DREA)

Larger Groups

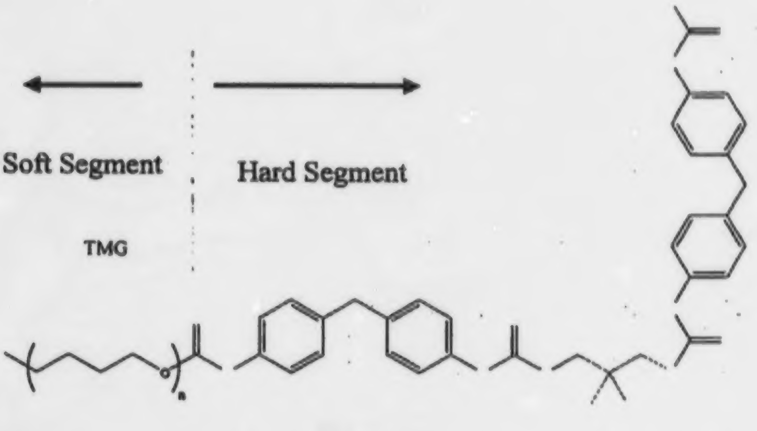

Results from Large Group Analysis

Group	alpha	beta	log(tau)	log(Go)	log(Ginf)
TMG	0.37	0.10	-15.09	6.26	9.5
MDI	1.11	0.23	10.78	6.63	5.3
HDI	-0.21	-1.16	3.00	5.44	24.1
DMPD	1.57	-0.05	22.47	5.39	5.3
DEPD	0.30	-0.94	-0.51	4.52	20.9
EMPD	0.29	-0.69	5.96	5.43	21.0
BEPD	0.97	-0.40	4.79	6.03	16.2
BDO	-5.19	1.36	-70.87	16.27	26.5
1,3 BDO	-0.16	-1.59	-6.57	4.76	29.6

- Correlations between the experimental HN parameters for the data set and those calculated using the values above:

log(Go)	log(Ginf)	log(Tau)	alpha	beta
0.989	0.820	1.000	0.991	0.764

DEFENCE DÉFENSE

Defence Research Establishment Atlantic (DREA)

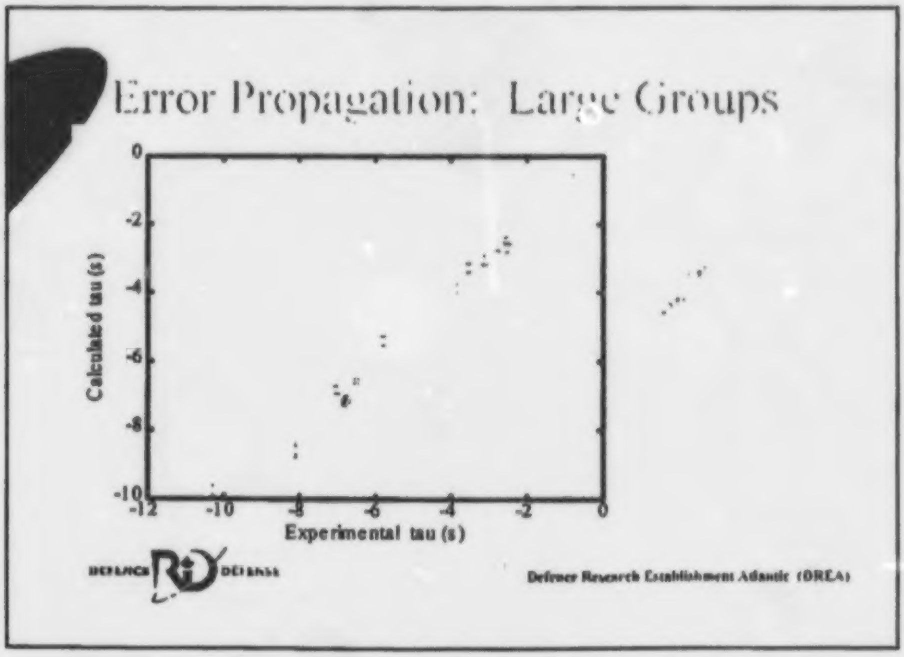

Error Propagation: Large Groups

DEFENCE DÉFENSE

Defence Research Establishment Atlantic (DREA)

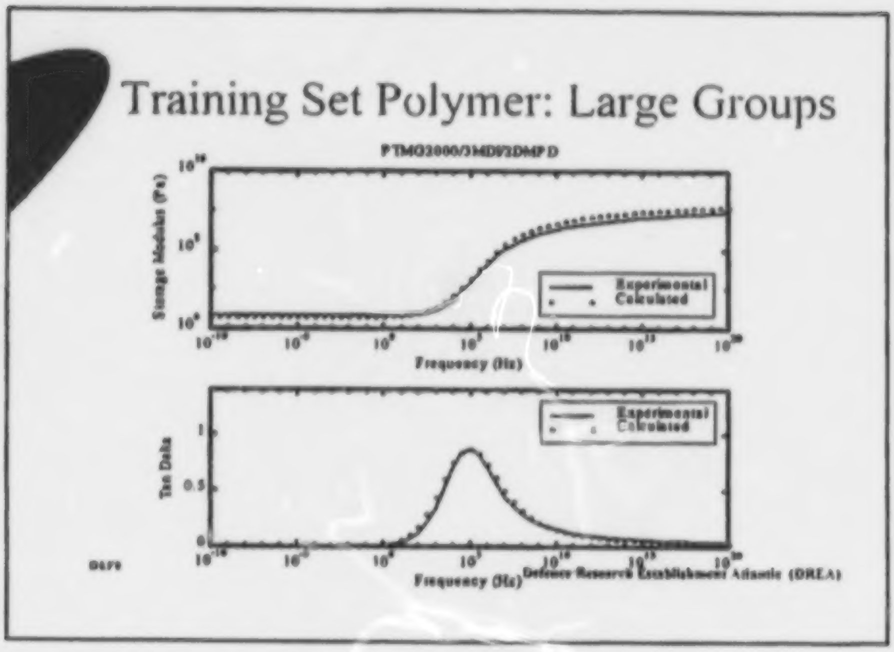

Training Set Polymer: Large Groups

Defence Research Establishment Atlantic (DREA)

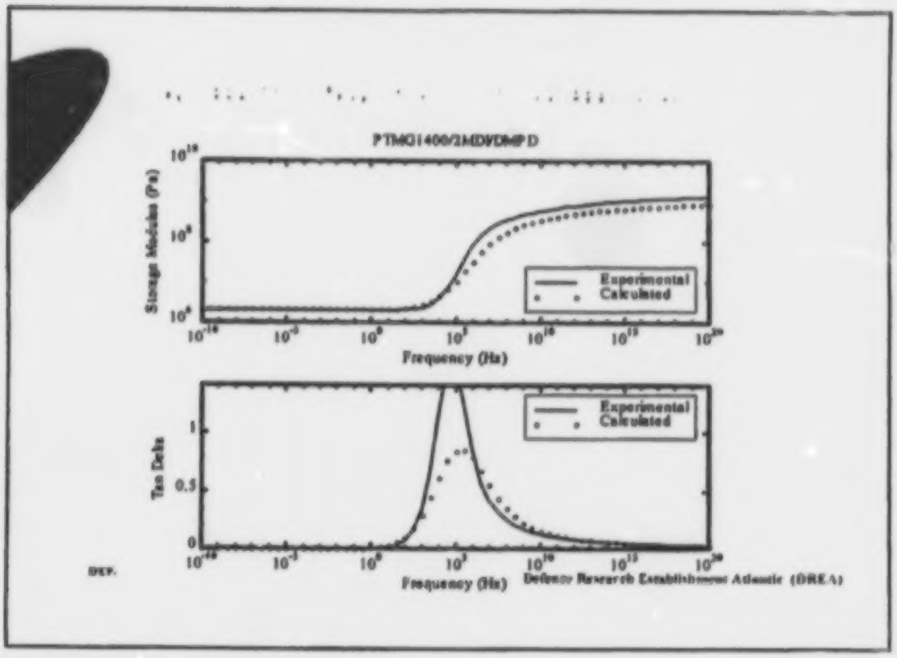

[illegible]

Defence Research Establishment Atlantic (DREA)

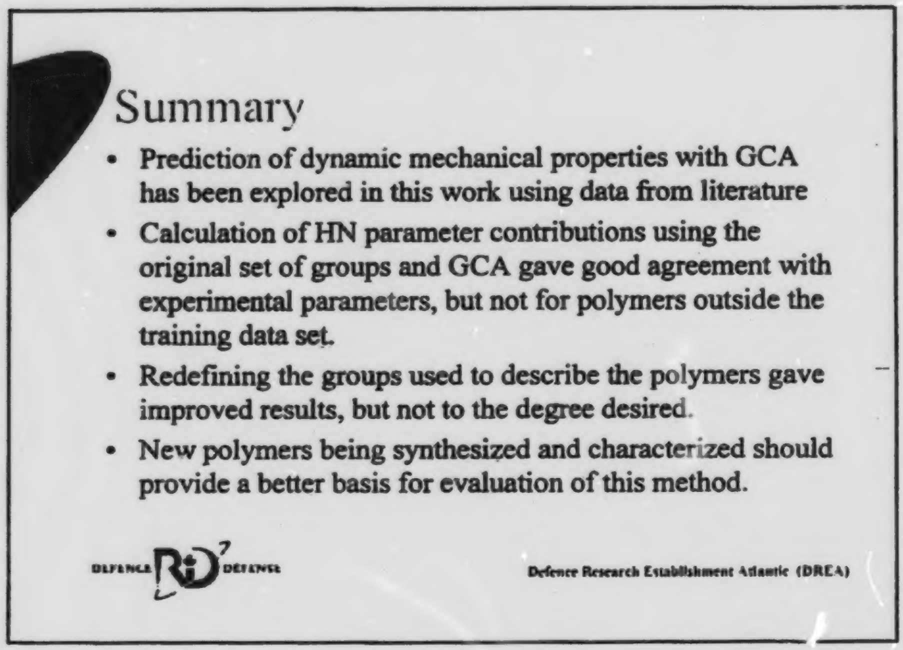

Summary

- Prediction of dynamic mechanical properties with GCA has been explored in this work using data from literature
- Calculation of HN parameter contributions using the original set of groups and GCA gave good agreement with experimental parameters, but not for polymers outside the training data set.
- Redefining the groups used to describe the polymers gave improved results, but not to the degree desired.
- New polymers being synthesized and characterized should provide a better basis for evaluation of this method.

Defence Research Establishment Atlantic (DREA)

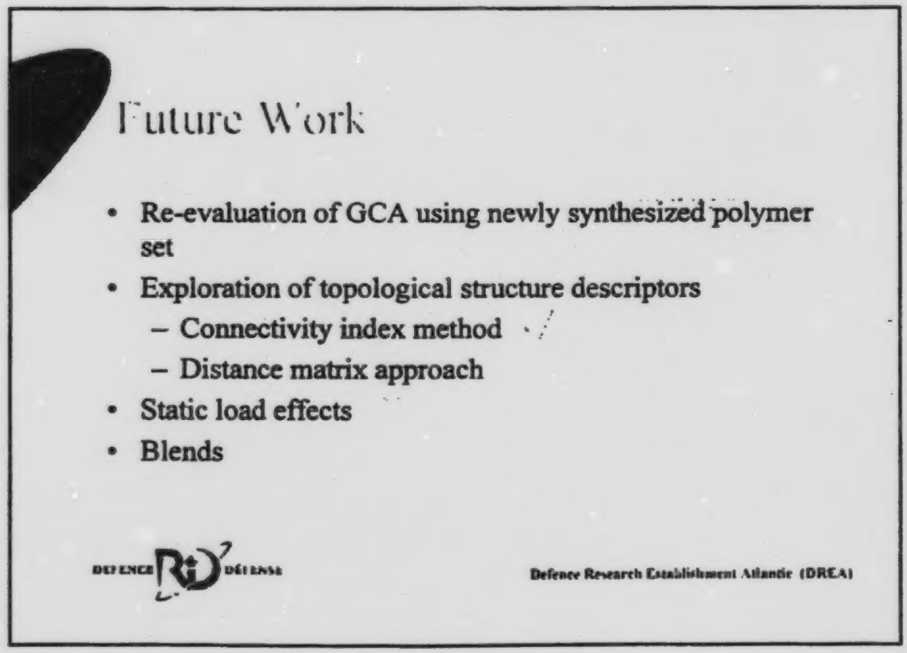

Future Work

- Re-evaluation of GCA using newly synthesized polymer set
- Exploration of topological structure descriptors
  - Connectivity index method
  - Distance matrix approach
- Static load effects
- Blends

Defence Research Establishment Atlantic (DREA)

#511905 (31)

Failure Analysis of Polymeric Materials

By

John A. Hiltz and Gary C. Fisher

Defence Research Establishment Atlantic, Dockyard Laboratory, PO Box 99000,
Station Forces, Halifax, Nova Scotia, B3K 5X5

Abstract

The use of polymeric materials on naval vessels continues to increase. At present most of the applications are non-structural, but structural applications should increase as topside weight reduction becomes critical and concerns about fire and flammability properties are addressed. Concomitant with the increased use of these materials are increased in-service failures. In this paper an approach to the study of polymer failures is discussed. It includes material identification, consideration of the in-service environment, and the study of fracture surfaces to determine the cause of the failure. Several polymer failures are discussed to illustrate the applicability of the technique to the analysis of failures.

Introduction

The production and use of plastics continues to increase. In 1992 production reached 110 million m^3 and was valued at \$300 billion (US). To put this in perspective, steel production in 1992 was 50 million m^3 and was valued at \$125 billion (US). By 1994 production of plastics had increased to 110 million metric tons and would suffice to pave a strip around the world a mile wide and an inch thick[1].

The increased use of plastics has been paralleled by an increase in in-service failures. These failures result from a number of factors including chemical attack, thermal and thermal oxidative degradation, in-service mechanical stresses, changes in properties with temperature and poor part design.

The analysis of in-service failures can provide valuable information on how and/or why the part failed. The how and why of the failure enable the scientist to make recommendations on materials and design changes that will eliminate further failures.

In this paper several polymer failures are discussed. Particular emphasis is placed on the approach used to study the failures. This approach includes material identification, assessment of degradation caused by the in-service environment and failure surface analysis to determine the cause of the failure.

Polymeric Materials

As the volume of plastics produced has increased, so have the number and types of polymeric materials. There are two major types of polymers, thermoplastics and thermosets. Thermoplastic and thermoset polymers differ in that thermoplastic polymers can be reshaped following heating while thermoset polymers degrade upon heating. Thermoplastics range from commodity plastics like poly(ethylene), poly(styrene) and poly(methylmethacrylate) to engineering thermoplastics such as poly(etheretherketone), poly(phenylene sulfide) and poly(amideimide). Thermosets include epoxies, phenolics, and poly(imides).

Polymers are blended, copolymerized, toughened, and reinforced to reduce costs, improve performance, or alter chemical and physical properties. Additives such as antioxidants, flame retardants, uv stabilizers and plasticizers improve/alter the oxidative, thermal, ultraviolet (uv) resistance and dynamic mechanical properties of a polymer.
The thermal history and processing conditions of a polymer can affect the degree of crystallinity and phase structure of a polymer. This in turns changes the chemical and mechanical properties of the polymer.

Material Identification

Material identification is the first step in any failure analysis. Knowledge of the identity of the material is important for two reasons; first, it indicates whether or not the material was specified for and had the necessary properties for the application, and second, if it is the specified material whether or not its properties changed while in service. Identification techniques include pyrolysis gas chromatography/mass spectrometry (py-GC/MS), infrared (IR) spectrometry, differential scanning calorimetry (DSC) and dynamic mechanical analysis (DMA).

Py-GC/MS and IR Spectrometry

Py-GC/MS and IR spectrometry are two powerful polymer identification techniques. These techniques can differentiate between the various types of polymers and in some instances can differentiate between the various grades of a particular polymer.

Pyrograms of three rubber samples are shown in Figure 1. Comparison of the pyrograms indicates that they are different and therefore the rubber samples are different. When the thermal degradation mechanisms of a polymer are known, mass spectral analysis of the pyrolytic degradation products can be used to identify compounds characteristic of that polymer and allow positive identification. This analysis identified the elastomers as chloroprene rubber, natural rubber and poly(acrylonitrile-butadiene) rubber.

Py-GC/MS can also be used to differentiate between various grades of the same polymer. The pyrograms of two samples of poly(ethylene) (PE) cable sheathing are shown in Figure 2. One of the samples of sheathing failed (Figure 2a) when wound onto a cable spool while the other did not (Figure 2b). Pyrograms of PE are characterized by a series of triplets. These are shown in Figure 3. Comparison of the pyrograms indicates that the failed sheathing had no smaller peaks between the characteristic triplets while the unfailed sheathing did. These smaller peaks are characteristic of branched PE. The branched structure reduces the density of the polymer by reducing the crystallinity of the sample. This information suggested that the sheathing failure was related to its microstructure.

Infrared spectra of two poly(ether)urethane thermoplastic elastomers are shown in Figure 4. The spectra indicate that these are diphenylmethanediisocyanate/poly(oxytetramethylene)/1,4-butanediol based poly(ether)urethanes. However, comparison of the ratios of the peaks at 1730 cm^{-1} and 1703 cm^{-1} and 1110 cm^{-1} and 1080 cm^{-1} indicates that these two elastomers are different and the differences can be attributed to different amounts of diisocyanate, polyol and diol used in the synthesis of these elastomers.

DSC

DSC measures changes in the heat capacity and heat flow to and from a sample as temperature is scanned. An abrupt change in heat capacity is indicative of a glass transition, while heat flow to and from semicrystalline polymers is characteristic of melting and crystallization taking place in the sample. The glass transition temperature and melting point are in and of themselves useful in identifying or differentiating between different polymers. However, they are often more useful in assessing differences in grades of the same polymer or changes introduced by environmental exposure, thermal or processing history.

DSC thermograms of the failed and unfailed poly(ethylene) cable sheathing are shown in Figure 5. The thermograms show an endothermic peak at approximately 130C which corresponds to the melt temperature for PE. The areas of the endotherms are directly related to the percent crystallinity of the two samples and calculations indicated that the failed sample was approximately 65% crystalline while the unfailed sample was approximately 49% crystalline.

DSC thermograms of two samples of thermoplastic elastomers, Texin 970D and Elastollan 1164D, are shown in Figure 6. Although Py-GC/MS and IR analysis of these elastomers indicated that they had similar compositions, the thermograms are very different. Interpretation of the thermograms indicates that the two elastomers have different amounts of phase mixing and that this can be attributed to the methods used to synthesize the polymers.

DMA

Dynamic mechanical analysis measures the real and imaginary components of the storage modulus, E' and E" respectively, and tan δ (E"/E') of a polymer as a function of temperature. As E' changes abruptly and E" and tan δ go through maxima at the glass transition, this technique is very useful in measuring the glass transition temperature (T_g) of polymers and changes in the glass transition brought about by in-service conditions. The T_g of a polymeric material is important as it defines the temperature where its properties change from hard and glassy to soft and rubbery.

DMA plots of loss modulus versus temperature for samples of poly(amideimide) containing between 0% and 4.25% absorbed water are shown in Figure 7. The temperature of the maximum in the plots of E" versus T decreases as the percent absorbed water increases. In fact, the T_g decreases by approximately 80C as the absorbed water content increases to 4.25%. This is an example of water acting as a plasticizer and altering the properties of the material.

Service Conditions

Once a failed material has been identified, the in-service conditions the material was exposed to must be investigated to determine if these were the cause of the failure. In-service conditions include the environment, temperature changes, loads and loading rates.

The chemical environment can include exposure to solvents, fuels and lubricants, visible light and ultraviolet radiation, ozone, moisture, and corrosives. Exposure to solvents, fuel and lubricants, and corrosives can result in complete dissolution of the polymer through degradation or alteration of mechanical properties to reduced operational lifetime.

The effect of temperature changes is twofold. An increase in temperature will accelerate thermal and thermal-oxidative degradation. Changes in temperature will also have a large effect on the modulus of polymeric materials, especially in the area of the glass transition. For a glassy polymer, an increase in temperature through the glass transition will result in the material changing from glass-like to rubbery, while for a rubbery material a decrease in temperature through the glass transition will result in the material changing from rubbery to glass-like.

The Torlon samples discussed in the DMA section illustrate the effect of environment and temperature on a polymeric material. Figure 8 shows four Torlon samples following heating to 300C. As the % absorbed water increases, so does the distortion of samples. This results from the vaporization of the absorbed water as the sample is heated. As the sample nears the glass transition temperature it softens and the pressure of the water vapor is high enough to form voids. A scanning electron micrograph showing the interior of a distorted Torlon sample is shown in Figure 9. Flow of the sample and voiding caused by absorbed water can be seen.

The selection of a polymeric material for a particular application will include consideration of the loads that the material will be exposed to in-service. If the material fails, and factors such as the chemical environment, temperature, and thermal and oxidative degradation have been ruled out, the failure most likely can be related to the effect of loading, loading rates, and/or defects arising from processing or design. Defects, such as voids, inclusions, sharp corners, and machine marks, act as stress risers and are often the initiation sites for failures.

Fractography

The study of the failure surface can often reveal a wealth of information on the factors leading to the failure of a polymeric material. This information can include the site of initiation of the failure and the failure mode of the polymer. As the failure mode can often be related to the loading and loading rates, this information can be used to comment on the conditions under which the part failed.

CIWS Dummy Round

The fracture surface of the plastic portion of a CIWS dummy round, reported to have fractured when dropped, is shown in Figure 10. Analysis of the plastic indicated that it was poly(phenylene sulfide) (PPS), a crystalline engineering thermoplastic with a melting point of 290C. A large number of voids can be seen in the center of the fracture surface (Figure 10a). This area is enlarged in Figure 10b.

The voids act as stress risers, and when the round was dropped were the site of the initiation of the failure. The voids arose during processing of the polymer. The most likely cause is trapped water. Although PPS absorbs very little water, water can be present on the surface of the polymer. In fact, the recommended procedure for processing this plastic includes drying at 150C for 6 hours prior to thermoforming[2]. If the polymer is not dried prior to processing, the water vaporizes as the polymer is heated to processing temperature (>300C). If it cannot diffuse from the polymer during processing the water vapor expands and leaves voids in the polymer.

PE Cable Sheathing

The fracture surface an aluminum wire rope PE cable sheathing is shown in Figure 11. Figure 11a shows a low magnification scanning electron micrograph of the fracture surface through the thickness of the sheathing. The U-shaped depressions at the top of the micrograph result from the strands of the aluminum wire rope. Figures 11b and 11c are higher magnification images of the fracture surface towards the outer and inner surfaces of the sheathing respectively. The morphology of the fracture surface near the inner and outer surfaces of the cable sheathing is quite different. Figure 12a shows a higher magnification of the fracture surface shown in Figure 11c. The fracture surface near the inner part of the sheathing has a fibrillar structure. Figure 12b shows the fracture surface of a PE sample that failed by a slow brittle crack growth mechanism[3]. Comparison of the micrographs in Figure 12 suggests that the PE sheathing failed in this manner.

In the section on Polymer Identification the differences in the crystallinity of this sheathing sample and another sample that did not fail were discussed. The failed sheathing was a higher density (more crystalline) PE than the unfailed sample. Recent research[4-6] has shown that the resistance of PE samples to slow crack growth, as measured by time to failure, can vary by more than a factor of million depending on molecular and morphological structure. The superior resistance to slow crack growth of low density PE has been attributed to a larger tie molecule density relative to high density PE.

Plastic Component 76 mm Cartridge Lifting Mechanism

A schematic of the 76 mm cartridge lifting mechanism, including the plastic component, is shown in Figure 13. The plastic component failed as indicated in the drawing, that is, directly through the pin holes used to secure the component to the chain lifting mechanism.

Several questions were asked concerning the failure. DREA was asked to identify the material, comment on its suitability for this application, and comment on the failure mechanism. In particular, there was interest in whether or not the failure was related to normal operating conditions or arose due to an isolated incident. Discussions indicated that a round had dropped approximately 5 inches onto plastic component.

Chemical analysis indicated that the plastic component was fabricated from the specified material, Nylon 11.

The fracture surface is show in Figure 14. Two fracture initiations sites, designated D and C, were found on the fracture surface. Chevrons on the fracture surface can be seen pointing back to the initiation sites. The fracture initiation site and fracture surfaces of Nylon 11 samples failed in fatigue and impact modes are shown in Figure 15. Comparison of these with the fracture surface of the actual component indicates that the component did not fail by a fatigue mechanism. The impact fracture surface is characterized by steps and facets and more closely resembles the fracture surface of the failed component.

It was concluded that the failure resulted from the impact of the round falling 5 inches onto the plastic component. The initiation at the pin hole closest to the chain mechanism is consistent with an impact on the outer top edge of the plastic component.

Conclusions

A failure analysis method that incorporates material identification, consideration of in-service environment, and fracture surface analysis to investigate polymer failures has been described. Identification of the cause(s) of the failure of a polymeric material allow changes to be made that reduce or prevent reoccurrence of the failure. In the case of the CIWS dummy round, the analysis led to the selection of another engineering plastic (Nylon 6,6) for the application. This led to reduced cost and easier processing without a loss in mechanical properties. The cable sheathing analysis led to two recommendations. Specify low density polyethylene for cable sheathing applications or handle the cable sheathed with high density polyethylene in a way that does not subject it to high stresses during storage. The cartridge lifting mechanism failure was not due to either material selection ir degradation in-service. It was the result of an impact from a round falling five inches onto the outer edge of the Nylon component.

Failure analysis and subsequent recommendations on material suitability for an application reduce maintenance and repair costs and increase the operational readiness of the system in which the material is used.

References

1. L. A. Utracki, Polymer Engineering and Science, 35, 1 (1995).
2. D. G. Brady, Polyphenylene Sulfides, page 189, in Engineered Materials Handbook, Volume 2, Engineering Plastics, ASM International, Metals Park, Ohio (1988).
3. A. Lustiger, 'Environmental Stress Cracking: The Phenomenon and its Utility', Chapter 16 in **Failure of Plastics**, edited by W. Brostow and R. D. Corneliussen, Hanser Publishers, New York, 1986.
4. Y-L. Huang and N. Brown, "Slow crack growth in blends of HDPE and UHMWPE, Polymer, 33, 2989 (1992).
5. Z. Zhou, X. Li and N. Brown, The effect of blending high-density and linear low-density polyethylenes on slow crack growth", Polymer, 34, 2520 (1993).
6. Z. Zhou and N. Brown, "Slow crack growth of blends of high density and linear low density polyethylenes as influenced by morphology", Polymer, 35, 3619 (1994).

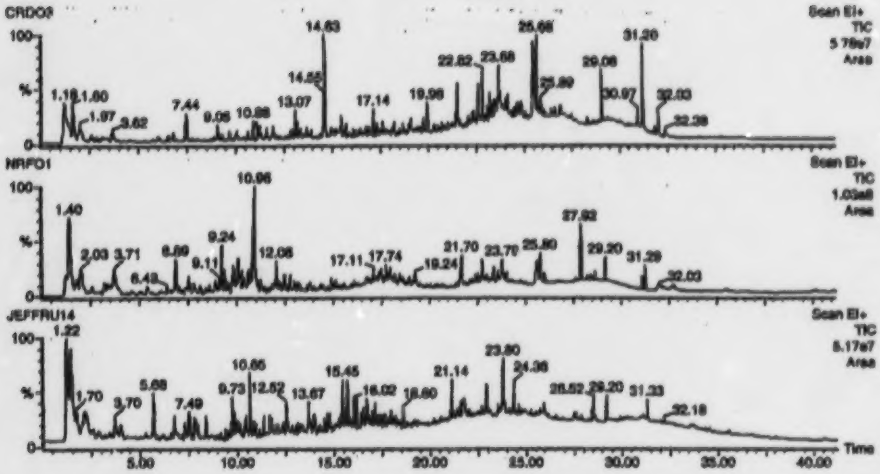

Figure 1 – Pyrograms of, from top to bottom, chloroprene, natural and nitrile rubbers.

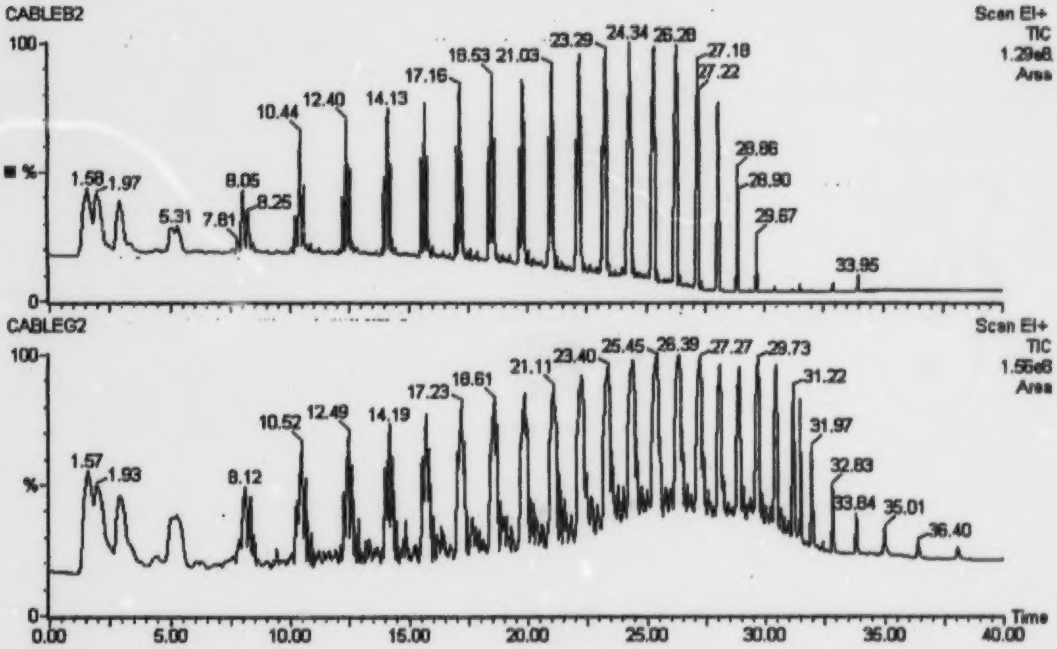

Figure 2 – Pyrograms of top) failed polyethylene cable sheathing and bottom) good polyethylene cable sheathing.

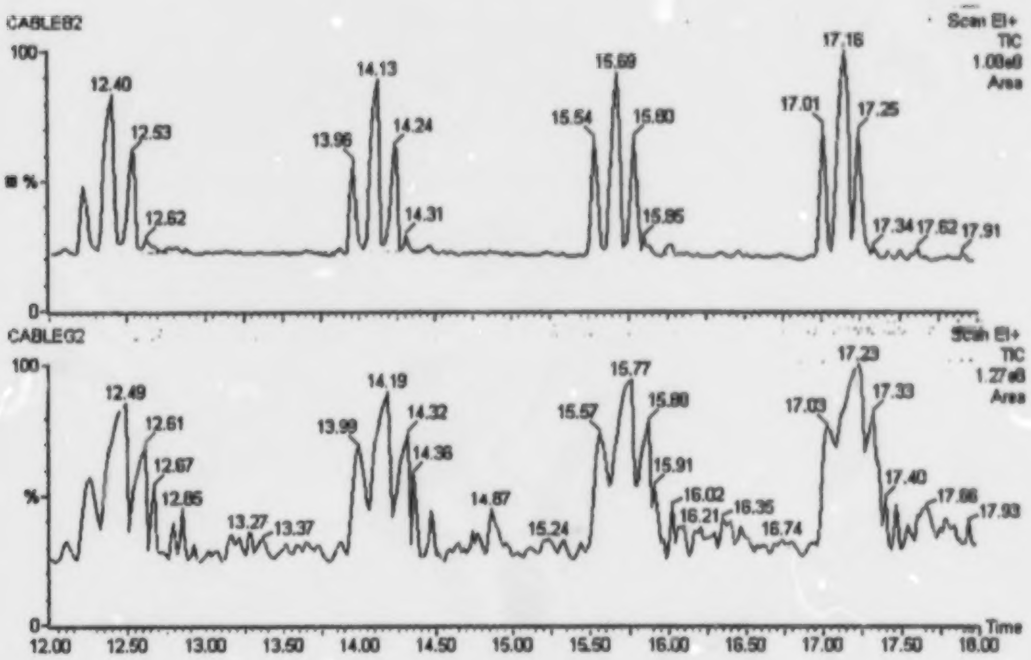

Figure 3 – Expansion of the pyrograms shown in Figure 2 between 12 and 18 minutes retention time. Notice the peaks between the triplets in the good polyethylene cable sheathing sample (lower trace). These are indicative of a branched low density polyethylene.

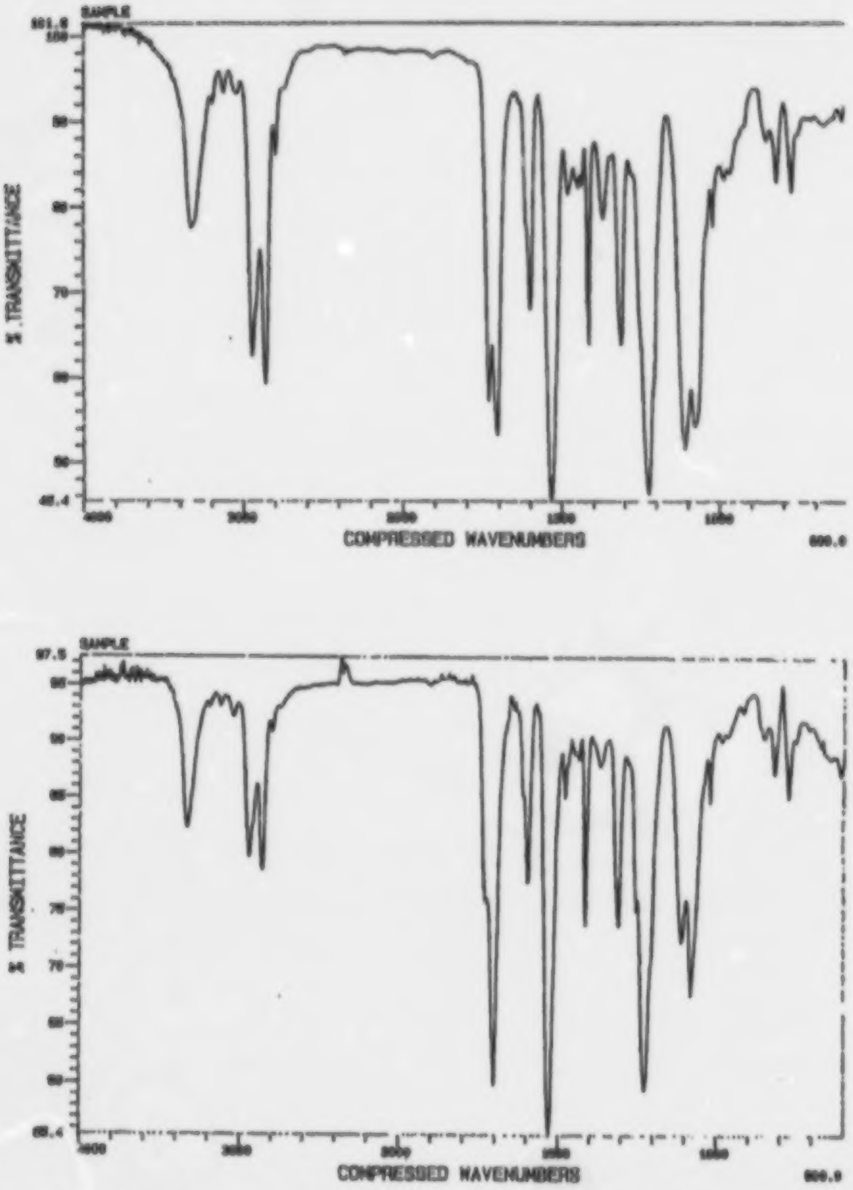

Figure 4 – Infrared spectra of top) Texin 990A poly(ether)urethane and bottom) Texin 970D poly(ether)urethane thermoplastic elastomers. Notice the difference in the relative intensities of the carbonyl peaks at 1730 cm^{-1} and 1703 cm^{-1} and 1110 cm^{-1} and 1080 cm^{-1}.

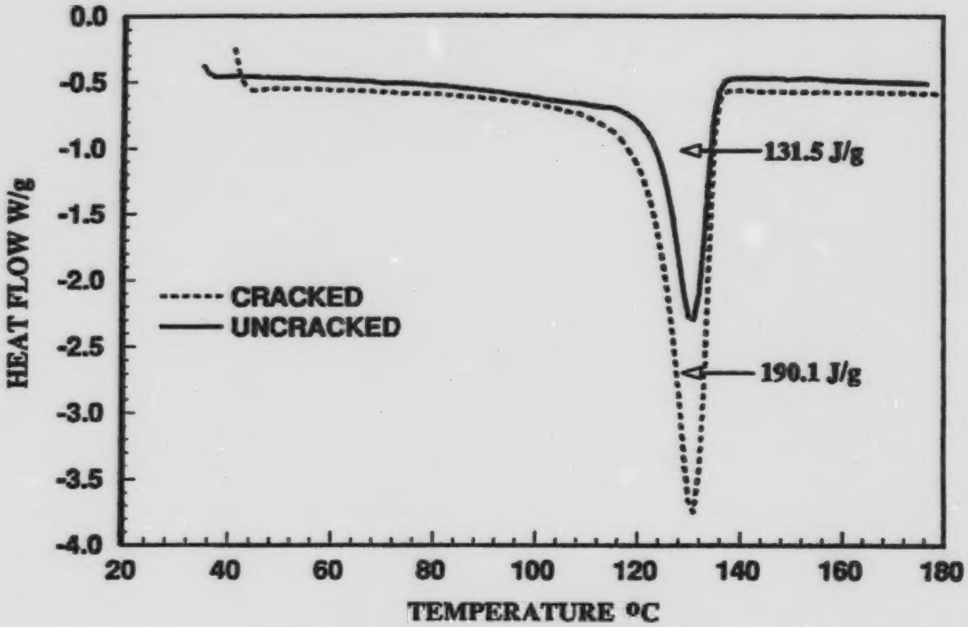

Figure 5 – DSC thermograms of cracked and uncracked polyethylene cable sheathing. The heat (J/g) required to melt the samples is proportional to the percent crystallinity in the sample.

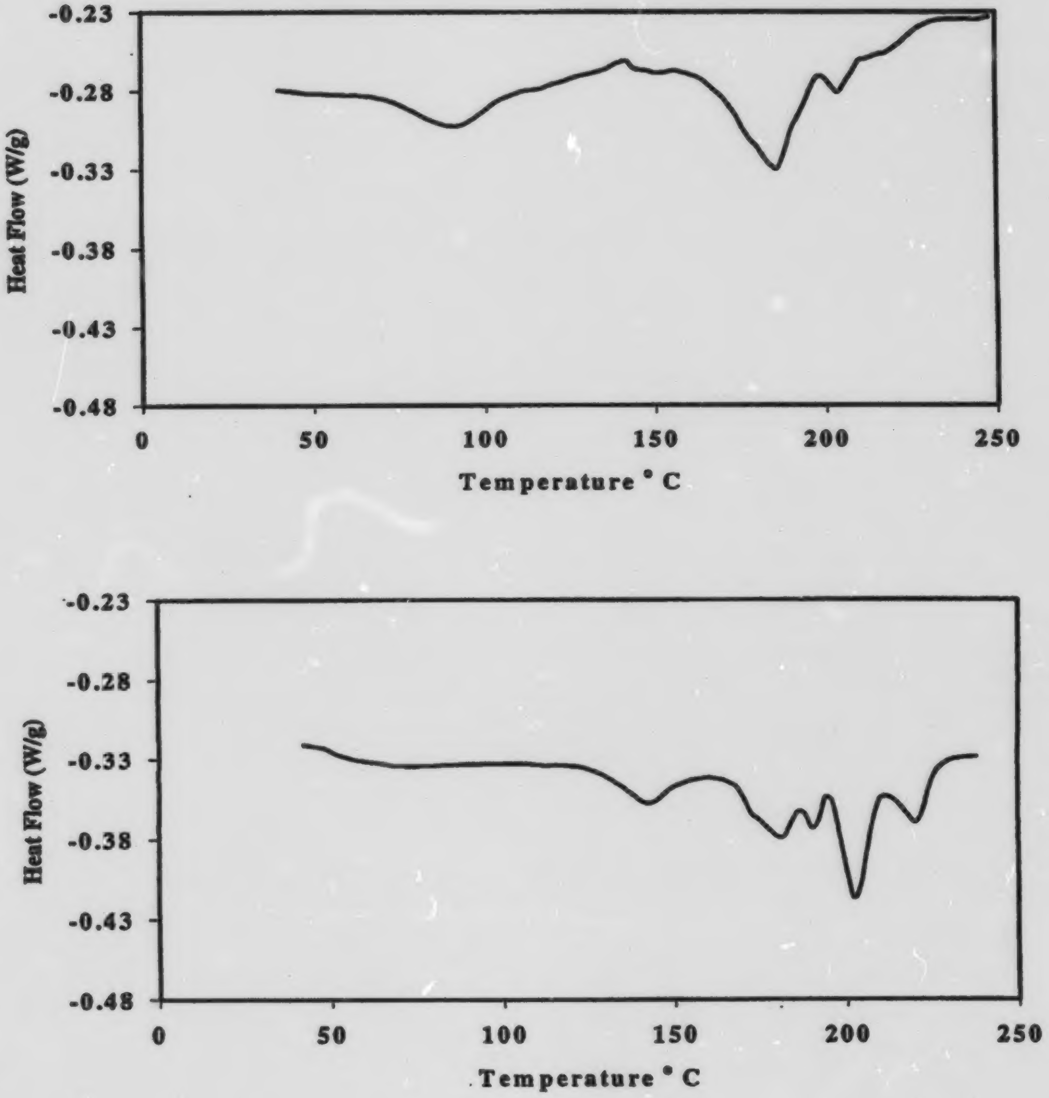

Figure 6 – DSC thermograms of top) Texin 970D and bottom) Elastollan 1164D. The differences in the thermograms are indicative of differences in the microstructures of these poly(ether)urethanes.

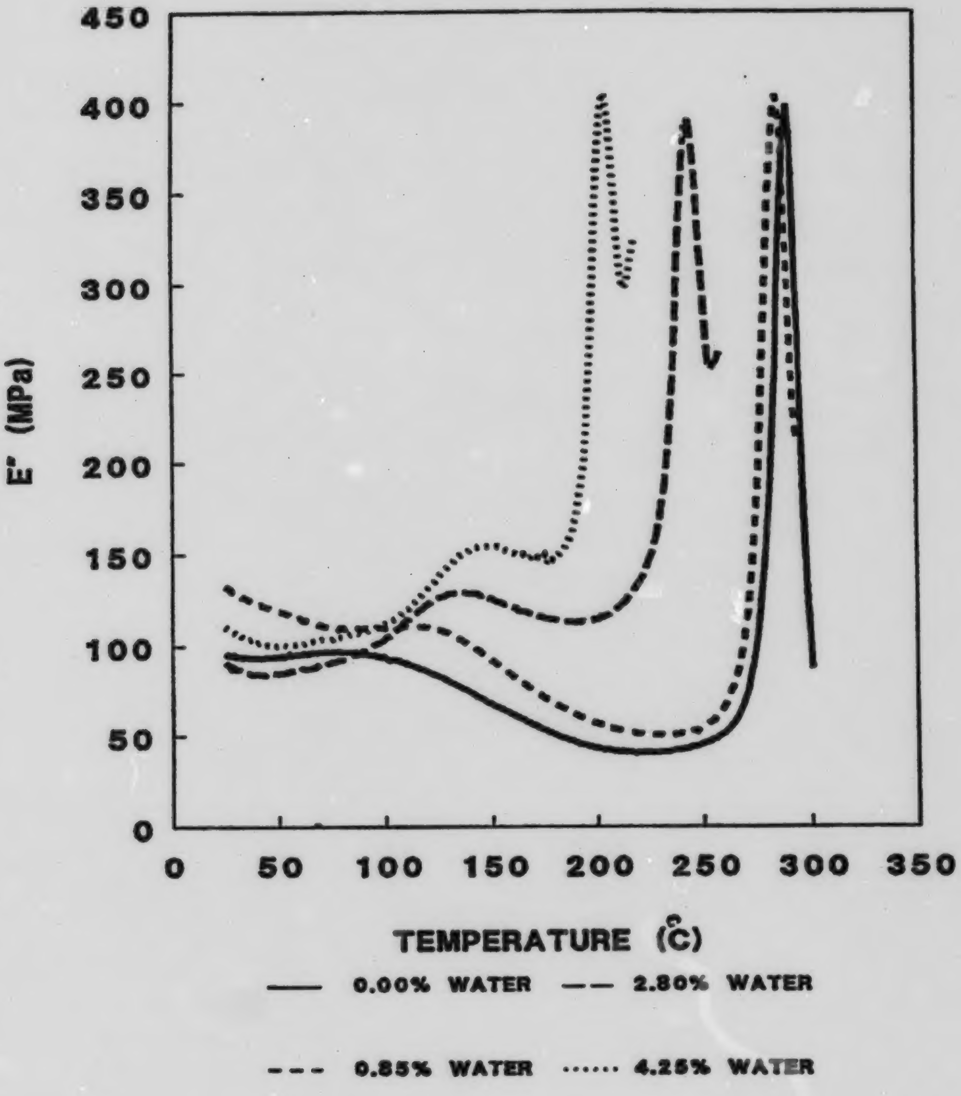

Figure 7 – Plot of loss modulus (E") versus temperature for Torlon samples containing 0%, 0.85%, 2.80% and 4.25% absorbed water. The glass transition temperature (maximum in a plot of E" versus T) decreases with increasing water content indicating that water plasticizes this polymer.

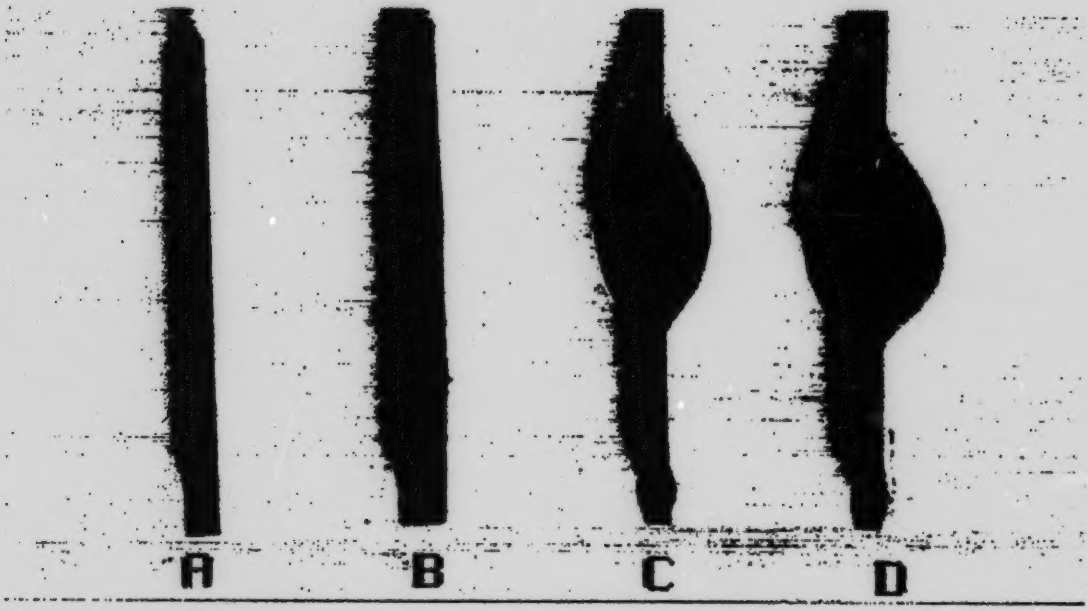

Figure 8 – Torlon samples containing a) 0%, b) 0.85%, c) 2.80% and d) 4.25% absorbed water after heating to 300C.

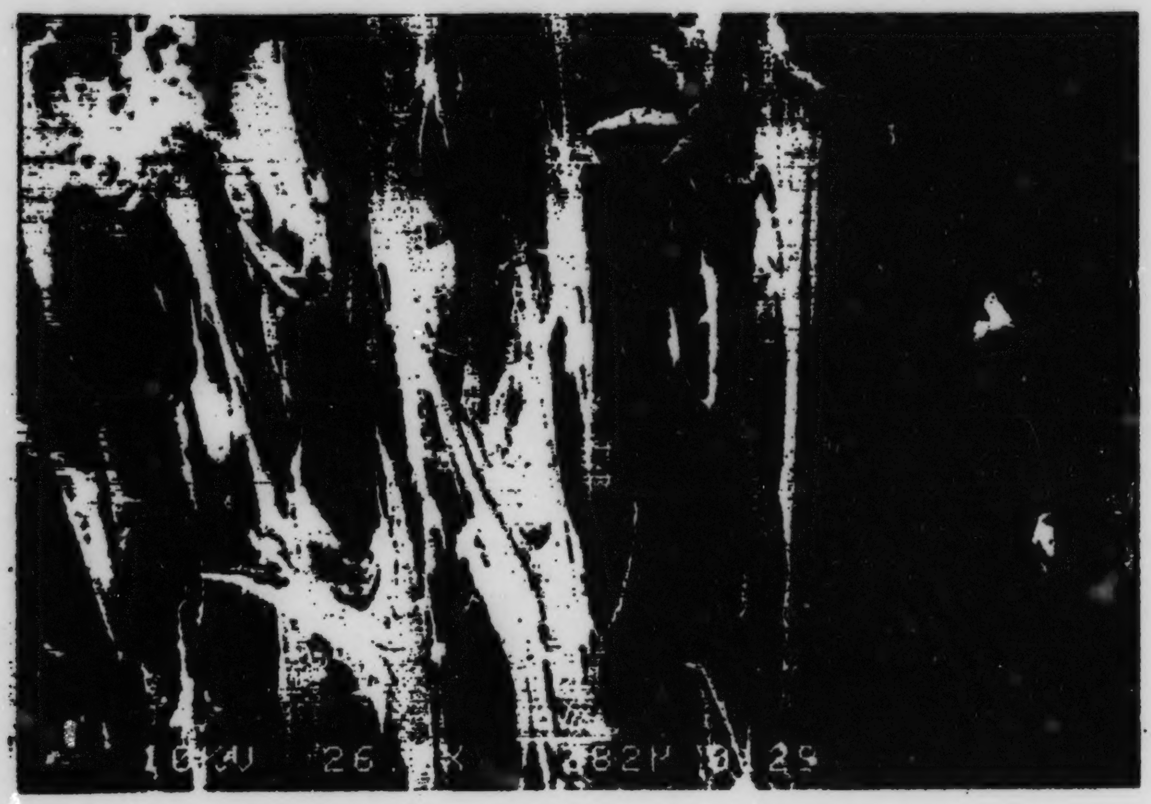

Figure 9 – Scanning electron micrograph of the interior of the Torlon sample containing 4.25% absorbed water and heated to 300C. Trapped water vaporized and, as the polymer softened, expanded causing flow and distortion of the sample.

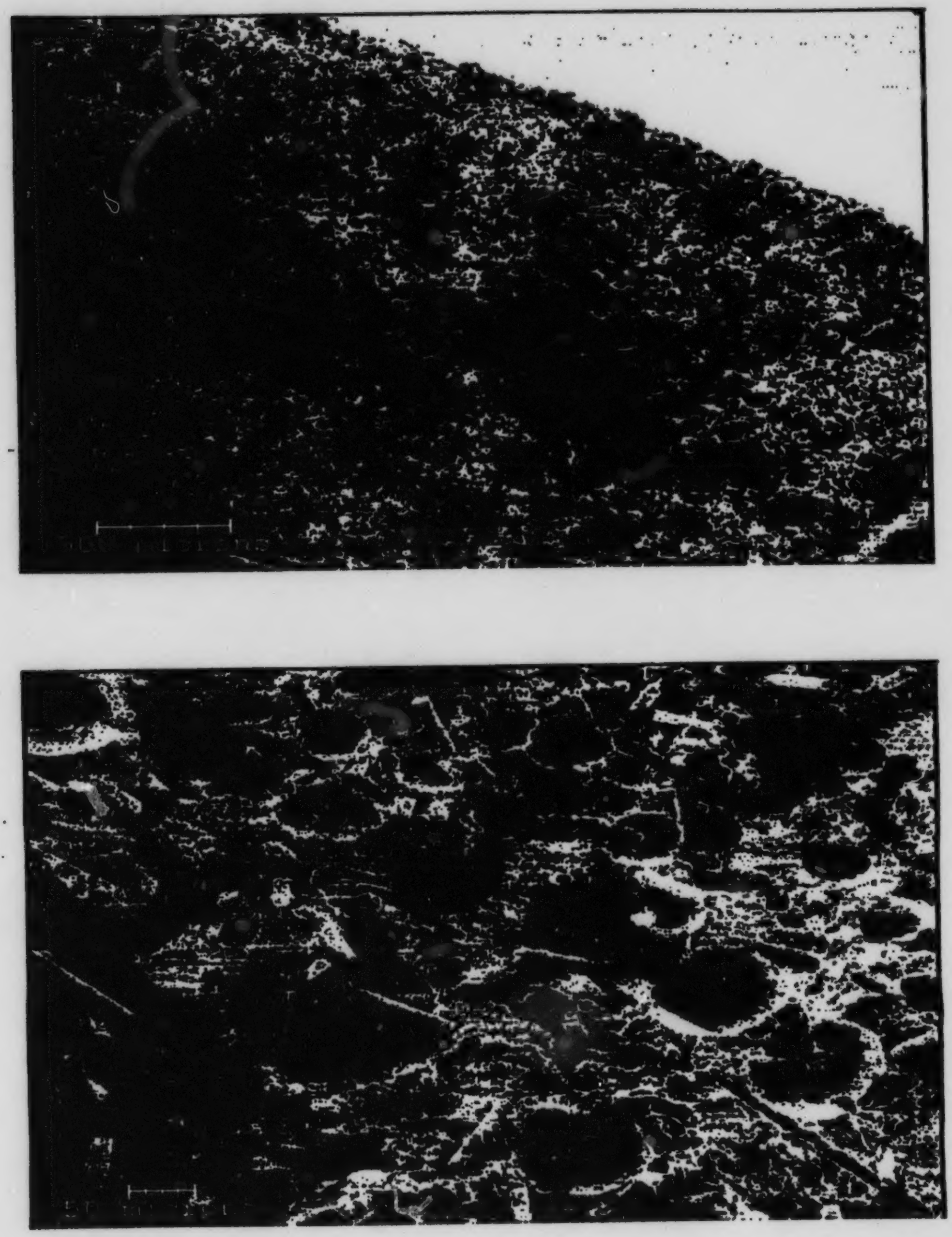

Figure 10 – Top) Scanning electron micrograph of the fracture surface of a CIWS dummy round. The failure occurred in a poly(phenylene)sulfide portion of the round. Bottom) Enlargement of an area in the top micrograph. Voids caused by trapped moisture are clearly visible.

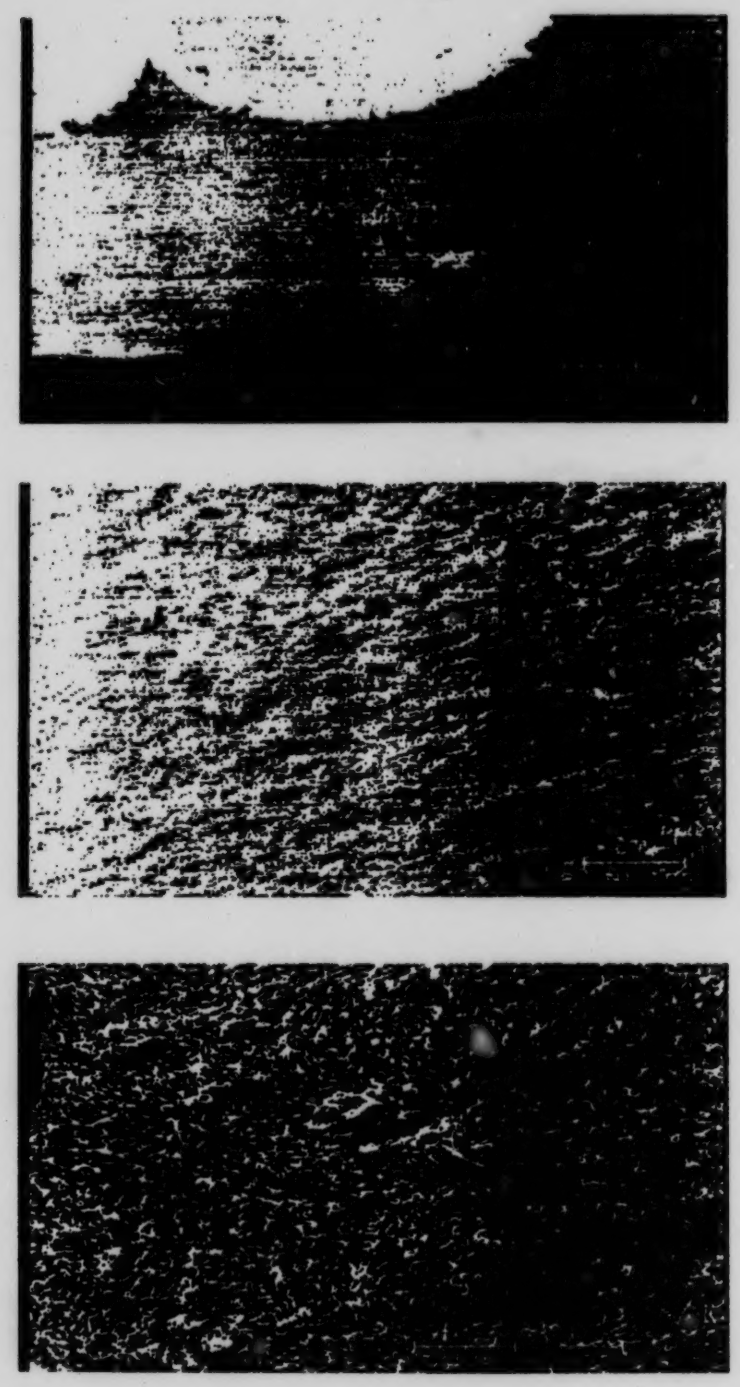

Figure 11 – Scanning electron micrographs of top) fracture surface of failed cable sheathing, middle) fracture surface towards the outer surface of the cable, and bottom) fracture surface towards the inner surface of the sheathing.

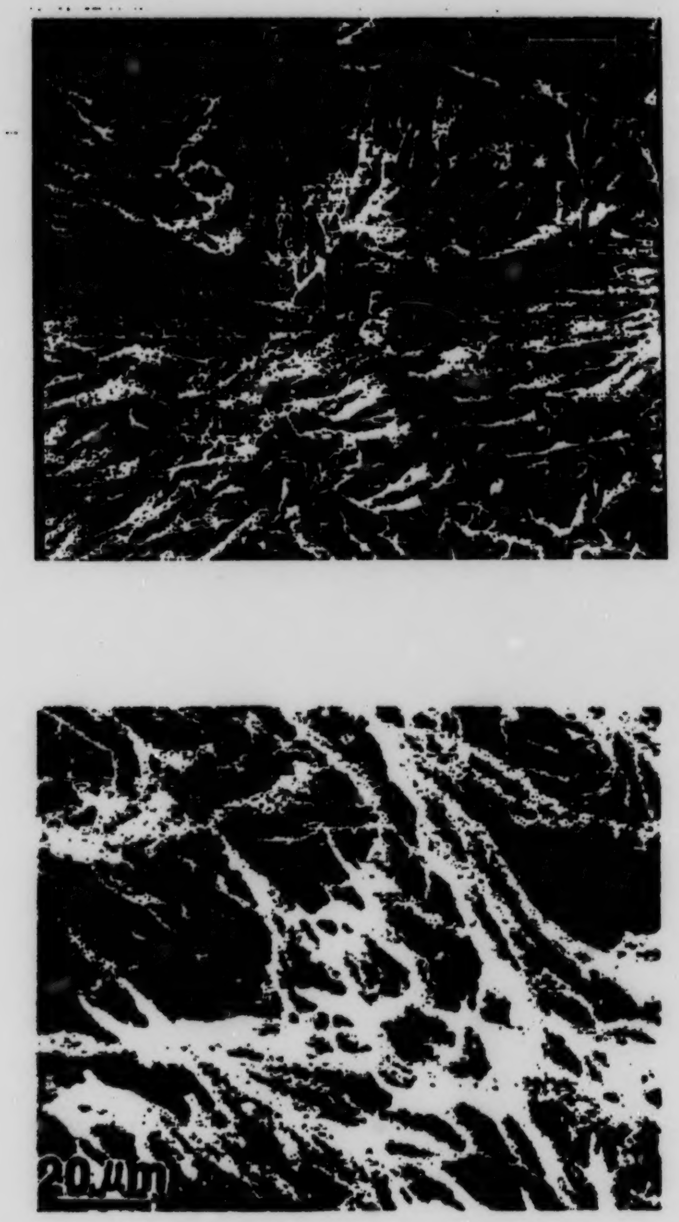

Figure 12 – Top) Magnification of cable sheathing fracture surface towards the inner side of the sheathing. Bottom) Fracture surface of a polyethylene sample that failed by a brittle, slow crack growth mechanism (**Failure of Plastics**, edited by W. Brostow and R. D. Corneliussen, Hanser Publishers, New York, 1986).

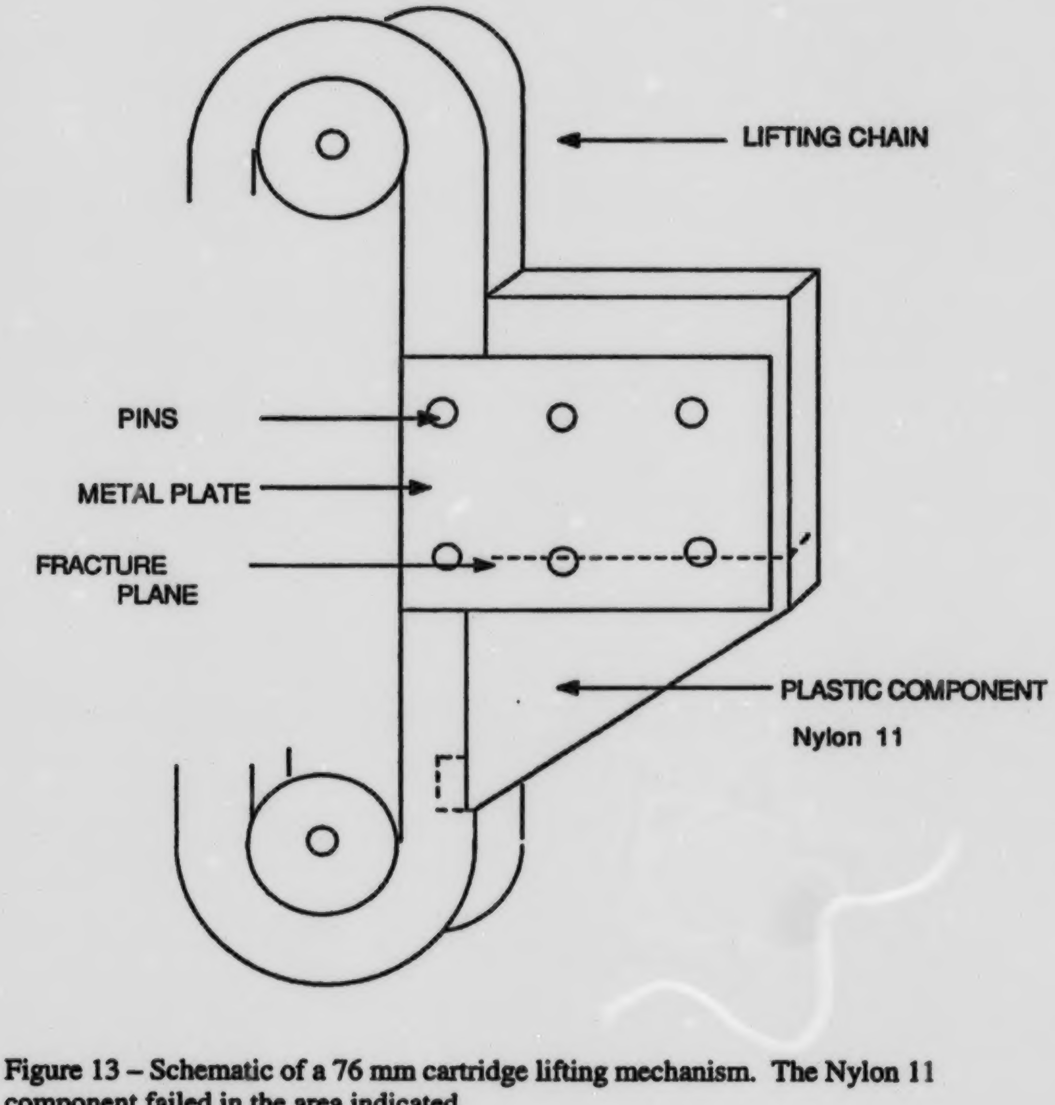
LIFTING CHAIN
PINS
METAL PLATE
FRACTURE PLANE
PLASTIC COMPONENT
Nylon 11

Figure 13 – Schematic of a 76 mm cartridge lifting mechanism. The Nylon 11 component failed in the area indicated.

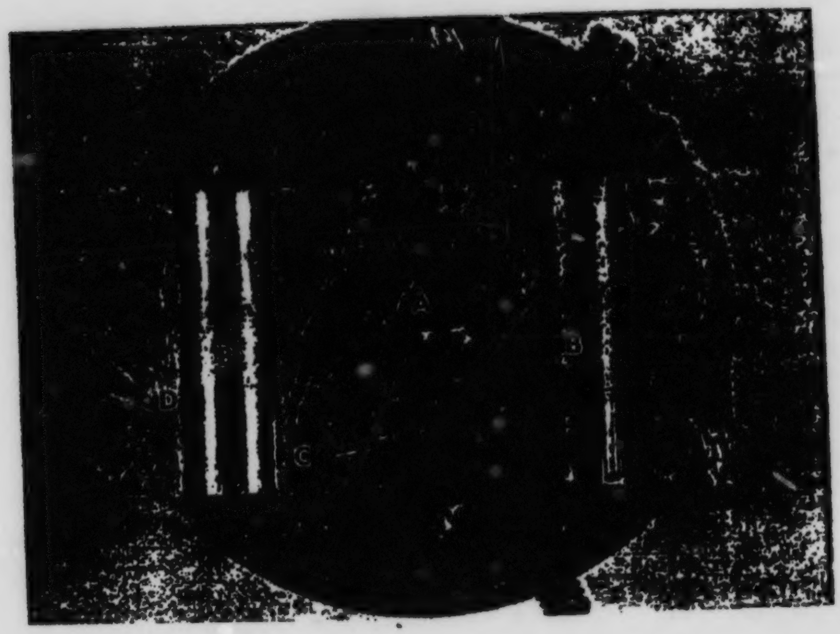

Figure 14 – Photograph of Nylon 11 component fracture surface. A indicates a large void in the component, B are the holes for attachment pins, and C and D are failure initiation sites.

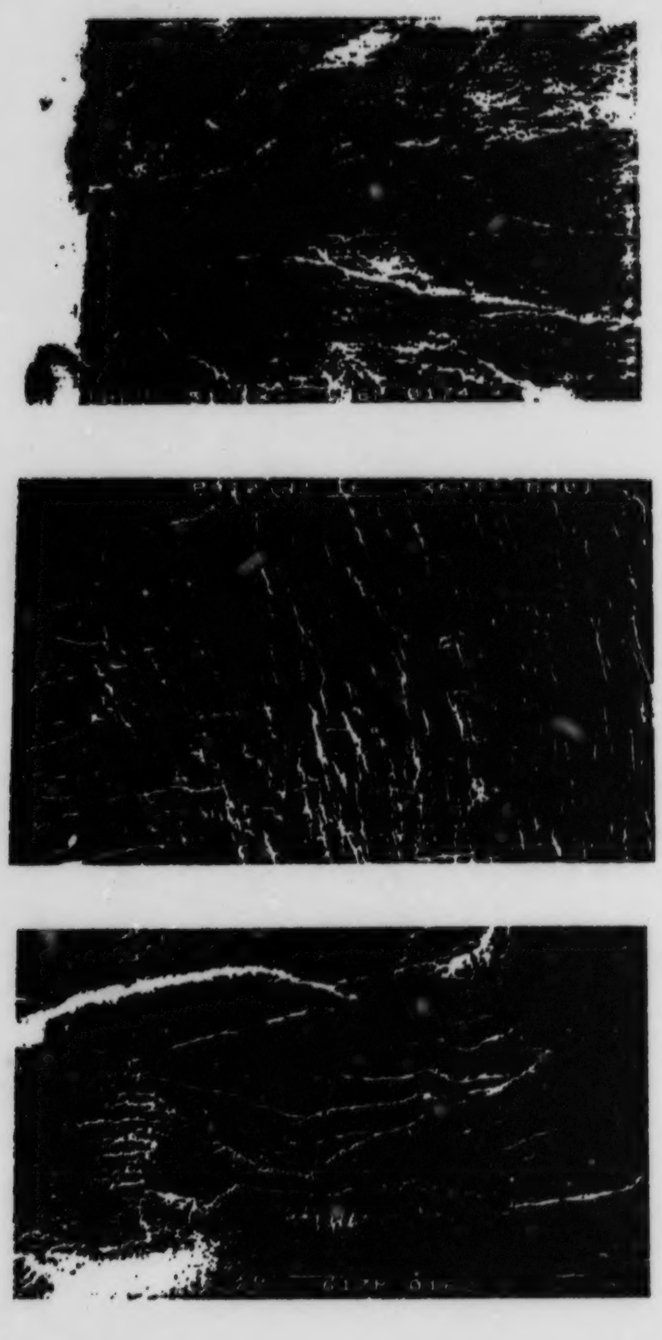

Figure 15 – Micrographs of top) failure initiation site of Nylon 11 component of cartridge lifting mechanism, middle) fracture surface of Nylon 11 failed in fatigue mode, and bottom) fracture surface of Nylon 11 failed in impact mode.

#511906

Evaluation and Application of GRP Composite Fasteners for Sonar Dome Components

by T.S. Koko[1], K.D. MacKay[1] and G.V. Corbett[2]

[1] Martec Limited, 400-1888 Brunswick Street, Halifax, NS, Canada, B3J 3J8
[2]Directorate Maritime Ship Support, DMSS 7-3-5, National Defence Headquarters, Ottawa, ON, Canada, K1A 0K2

ABSTRACT

This paper presents a study to evaluate the mechanical properties of commercially available GRP composite fasteners for the fairing band assembly components of the hull mounted sonar domes on Canadian frigates. The study was undertaken as part of an effort to develop an all-composite fairing band assembly for a stainless steel sonar dome, to eliminate corrosion problems that occur with the use of stainless steel bolts which result in loss of the fairing band assembly at sea [1]. The assembly consists of two bands and a tail-cap which were changed from stainless steel to GRP composite material. The stainless steel bolts used to fasten the fairing band assembly to the mild steel ship hull were replaced with GRP fasteners to eliminate the corrosion of the mild steel structure [1]. The experimental investigations performed to evaluate commercially available GRP fasteners and the application of the bolts are presented in this paper

INTRODUCTION

This paper presents a study to evaluate the mechanical properties of commercially available GRP composite fasteners for the fairing band assembly components of the hull mounted sonar domes on Canadian frigates. The study was undertaken as part of an effort to develop an all-composite fairing band assembly for a stainless steel sonar dome, to eliminate corrosion problems that occur with the use of stainless steel bolts which result in loss of the fairing band assembly at sea [1]. The fairing band assembly is used to wrap around the dome-hull interface in order to provide a smooth surface, to reduce turbulence and flow-noise. The assembly consists of two bands and a tail cap which were changed from stainless steel to GRP composite material. The stainless steel bolts used to fasten the fairing band assembly to the mild steel ship hull were replaced with GRP fasteners to eliminate the corrosion of the mild steel structure [1]. The experimental investigations performed to evaluate commercially available GRP fasteners and their application for the assembly are presented in this paper.

The GRP fasteners were obtained from various suppliers and fasteners of three standard diameters: 6.3 mm, 9.53 mm and 12.70 mm were considered. Tests were performed to determine the tensile, shear and torque properties of each set of fasteners following procedures similar to the ASTM F606 standard. At least three samples were used for each test in order to provide good statistical averages. The details of the experimental setup and the test results are presented. The properties of the 9.53-mm bolts were found to be adequate for fastening the fairing band assembly and were recommended for the application.

EXPERIMENTAL PROGRAM

Fasteners Tested

Several manufacturers of composite fasteners in the USA were contacted in order to obtain information on commercially available composite fasteners (see Koko et al. 1998). Information was obtained from the following suppliers: (i.) Craftech Industries Inc., Hudson, New York; (ii) McMaster Carr, New York; (iii) Textron Aerospace Fasteners, Santa Ana, California; and (iv) Tiodize Co. Inc., Huntington Beach, California. From the information obtained it was obvious that the composite fasteners could not be used for highly loaded components due to torque limitations. Consequently, the decision was made to use the fasteners for lightly loaded components, which were also the components that had the most significant corrosion problems. Materials were obtained from Craftech Industries and McMaster Carr, which had lower priced products. It should be mentioned that fasteners manufactured by Textron Aerospace Fasteners and Tiodize Co. appeared to be of higher quality (see for instance Cherry Textron (1996)) then those manufactured by the companies selected. However, the cost of the materials was a deciding factor because of limited budget. The tests were performed to ensure that the quality of the cheaper materials was adequate for the application.

Table 1 shows the properties of the four fasteners and their designations. All fasteners were made of GRP material. Fasteners A, B and C, having diameters of 6.35 mm (¼"), 9.53 mm (0.375") and 12.7 mm (½"), respectively, had hexagonal socket heads and were obtained from Craftech Industries. Fastener D with a diameter of 9.53-mm (0.375") had a hexagonal bolt head and was obtained from McMaster Carr. Pictures of the four fasteners are shown in Fig. 1.

Tests Performed

Experiments were conducted to evaluate the tensile, shear and torque properties of the different types of fasteners considered in this study. The tests were performed in the *as received condition* and after soaking in water at 50 °C for periods of 24 and 72 hours, respectively. The latter tests were conducted to determine the effects of moisture on the mechanical properties of the fasteners.

The tension tests were performed on the four types of fasteners following the ASTM F606 standard (1995). Fig. 2 shows the set-up for the tension tests. Tests were performed in the "as received condition" as control. Table 2 shows the number of samples tested for each fastener type. The samples were tested in an Instron machine. The load was applied slowly, at the rate of 9 mm/min and the load displacement behaviour was measured by using an extensometer that was connected to a data acquisition system. The tests were terminated after failure of the fastener occurred.

The four types of fasteners were also tested in shear following the ASTM F606 standard (1995). Fig. 3 shows the setup for the shear tests.. Table 2 also shows the number of samples tested in shear for each fastener type. The samples were tested in an Instron machine. The load was applied slowly, at the rate of 9 mm/min and the load displacement behaviour was measured by using an extensometer that was connected to a data acquisition system.

Torque tests were performed using the test fixture shown in Fig. 4 and a torque meter. The torque meter was constructed using a 3/8" drive ratchet extension instrumented with two 90° strain gage rosettes. The bolts were held in the test fixture using steel nut and spacer blocks. The bolts were loaded by hand using a ratchet at a rate of approximately 9 degrees/second. The torque meter was connected to a data acquisition system to record the torque during the tests. As in the two previous cases, tests were performed in the "as received condition", and after soaking in 50°C for periods of 24 and 72 hours, respectively. Table 2 also shows the number of samples tested in torsion for each fastener type.

RESULTS AND DISCUSSIONS

Tension Test Results

The tensile failure loads for the four fasteners under the various test conditions were obtained by taking the average of the failure loads for all the samples in that test condition. The tensile strength was obtained by dividing the average failure load by the nominal fastener cross sectional area. Fig. 5 summarizes the tensile test results, including the effect of exposure to the hot-wet conditions. The tensile strengths of the fasteners range from 45.5 MPa (6.6 ksi) to 88.3 MPa (12.8 ksi), with the 3/8-16 UNC fasteners (Type B) having the highest strengths and the 1/2-13 UNC fasteners (Type C) having the lowest tensile strength values. Soaking the fasteners in hot water does not have any significant effect on the tensile strength properties of the fasteners, for the test conditions considered. Fig. 6 shows a typical load-displacement curve for the tensile tests.

Shear Test Results

The shear failure loads for the four fasteners under the various test conditions were obtained by averaging the failure loads for all the samples in that test condition as described above. The shear strength was obtained by dividing the average failure load by the nominal fastener cross sectional area. Fig. 7 summarizes the shear test results, including the effect of exposure to the hot-wet conditions. The shear strengths of the fasteners range from 29.7 MPa (4.3 ksi) to 51.7 MPa (7.5 ksi). Again, the 3/8-16 UNC fasteners (Type B) had the highest shear strengths and the 1/2-13 UNC fasteners (Type C) had the lowest shear strength values. Also, soaking the fasteners in hot water does not have any significant effect on the tensile strength properties of the fasteners, for the test conditions considered.

Torque Test Results

The torque strengths of the four fasteners under the various test conditions were obtained by averaging the torque capacities of all the samples in that test condition. Fig. 8 summarizes the torque test results, including the effect of exposure to the hot-wet conditions. The torque capacities of the fasteners range from 1.8 Nm (1.3 ft-lb) to 15.9 Nm (11.7 ft-lb). The torque capacities increase with fastener diameter, such that the 1/2-13 UNC fasteners (Type C) have the highest torque capacity. This is an important result because the torque capacity can indeed limiting factor in the design of composite fasteners. Consider for instance the 1/4-20 UNC fastener (Type A). Even though its tensile and shear strengths are higher than those of the 1/2-13 UNC fastener (Type C), its torque capacity is so low that the tensile and shear capacities may not be realized in any design. Soaking the fasteners in hot water does not have any significant effect on the torque capacities for the conditions considered.

Application of the Fasteners

The fasteners have been applied for fastening the fairing band components in non-load bearing situations. In this condition, the fasteners are designed only for nominal shear and tensile loads. The ranges of tensile and shear strengths of the bolts (45-88 Mpa (6.6-12.8 ksi); and 30-52 Mpa (4.3-7.5 ksi), respectively) are sufficient to sustain the nominal loads. However, the limiting factor in the use of the fasteners is the torque capability. It was recommended that the torque applied to the fasteners be limited to about 4.4 Nm (6 ft-lb). The 9.53 mm (3/8") and 12.70 mm (½") bolts were recommended for the application, with the 12.70 mm (½") bolts being the most preferred option, because of its size (easier to handle for divers).

SUMMARY AND CONCLUSIONS

This paper has presented an experimental study to determine the mechanical properties of commercially available GRP composite fasteners. Accelerated testing, involving exposure to hot water was used to evaluate the effect of moisture on the mechanical properties of the fasteners. Fasteners of three standard diameters: 6.3 mm (¼"), 9.53 mm (3/8") and 12.70 mm (½") were tested. The tensile strengths of the fastener ranged from 46-88 MPa (6.6-12.8 ksi); the shear strengths were typically in the range of 30-52 MPa (4.3-7.5 ksi); and the torque capacities range from 2-16 Nm (1.3-11.7 ft-lb). The influence of moisture absorption on the material properties was not significant for the test conditions used in this study. The GRP composite fasteners are being used to fasten none load bearing composite sonar dome components to a ship hull.

ACKNOWLEDGEMENTS

This work was partially funded under contract with the Canadian Department of National Defence. Martec also provided support thorough its corporate research program. The use of test facilities at Dalhousie University of Technology, Halifax is also acknowledged.

REFERENCE

ASTM Standard F606 (1995). "Test Methods for Determining the Mechanical Properties of Externally and Internally Threaded Fasteners, Washers and Rivets". Annual book of ASTM Standards Vol. 15-08.

Cherry Textron Technical Data on Advanced Composite Products, Santa Anna, California, (1996).

Koko, T.S., Connor, M.J. and Corbett, C.V. (1997). "Development of a Composite Fairing Band Assembly for A Stainless Steel Sonar Dome". Proceedings of ICCM-11, Gold Coast Australia, pp. I-426 - I-435.

Koko, T.S. (1998). "Development of Prototype Composite Fairing Band Assembly Components for the C-5 Sonar Dome". Martec Technical Report, in preparation, 1998.

Table 1: Identification of Fastener Types

PROPERTIES	FASTENER TYPES			
	A	B	C	D
Dimensions*	¼-20 UNCx1	• -16 UNCx1½	½-13 UNCx1½	• -16 UNCx1½
Head Type	Hex Cap Screw	Hex Cap Screw	Hex Cap Screw	Hex Bolt Head
Material System	40% Long Glass Epoxy	40% Long Glass Epoxy	40% Long Glass Epoxy	Glass Epoxy
Colour	White	White	White	Black
Unit Cost (1997 US$)**	1.85	2.85	3.4	1.43
Supplier	Craftech	Craftech	Craftech	McMaster-Carr

* Imperial Designations

** Based on minimum order quantities

Table 2: Matrix of Composite Bolt Tests

TYPE OF TEST	TEST CONDITION	NUMBER OF SAMPLES FOR FASTENER TYPES			
		A	B	C	D
Tension	As Received	3	2	4	3
	After 24 hours soaking in 50• C water	2	2	2	2
	After 72 hours soaking in 50• C water	2	-	3	2
Shear	As Received	3	2	3	3
	After 24 hours soaking in 50• C water	2	2	2	2
	After 72 hours soaking in 50• C water	2	-	2	2
Torque	As Received	3	2	3	3
	After 24 hours soaking in 50• C water	2	2	2	2
	After 72 hours soaking in 50• C water	2	-	2	2
Total		21	12	23	21

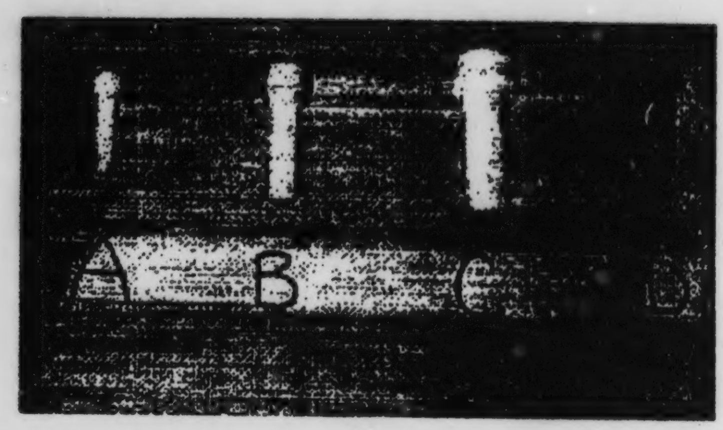

Figure 1: Picture of Failed Composite Fasteners

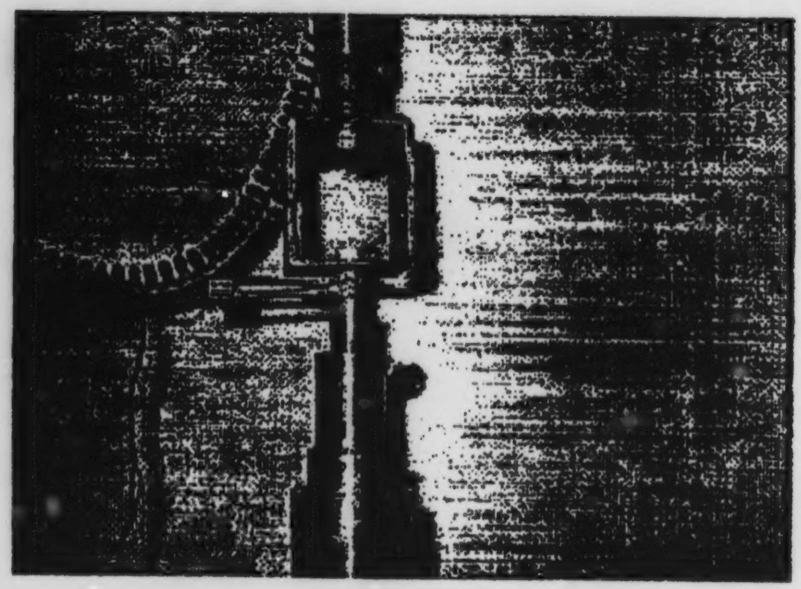

Figure 2 Setup for Tension Tests

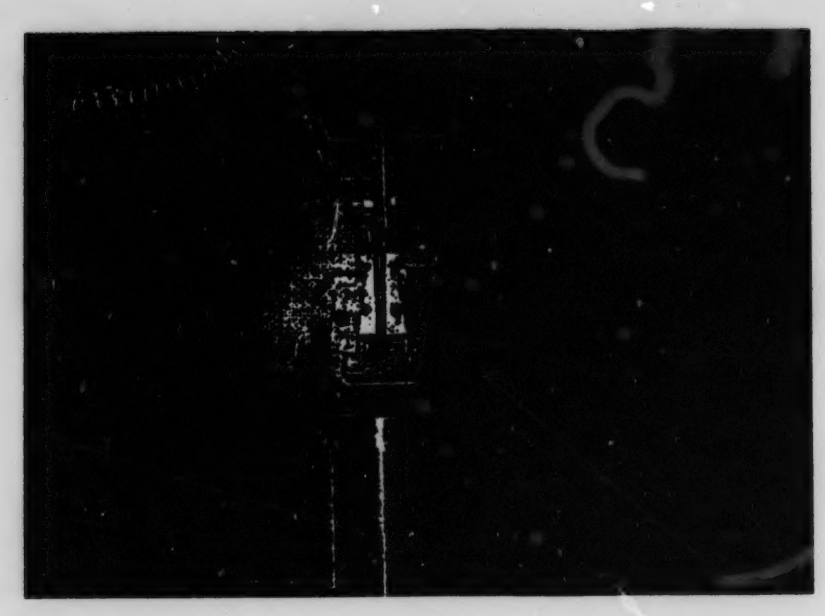

Figure 3 Setup for Shear Tests

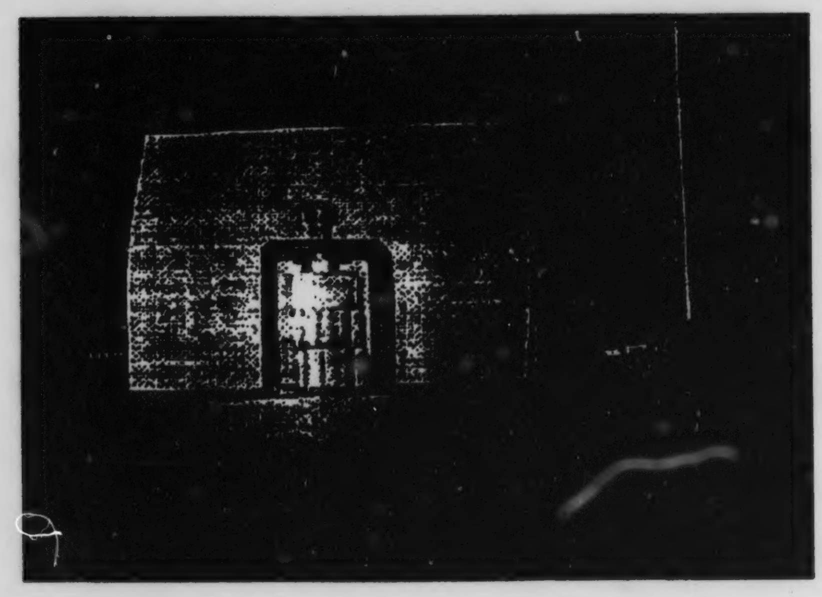

Figure 4 Setup for Torque Tests

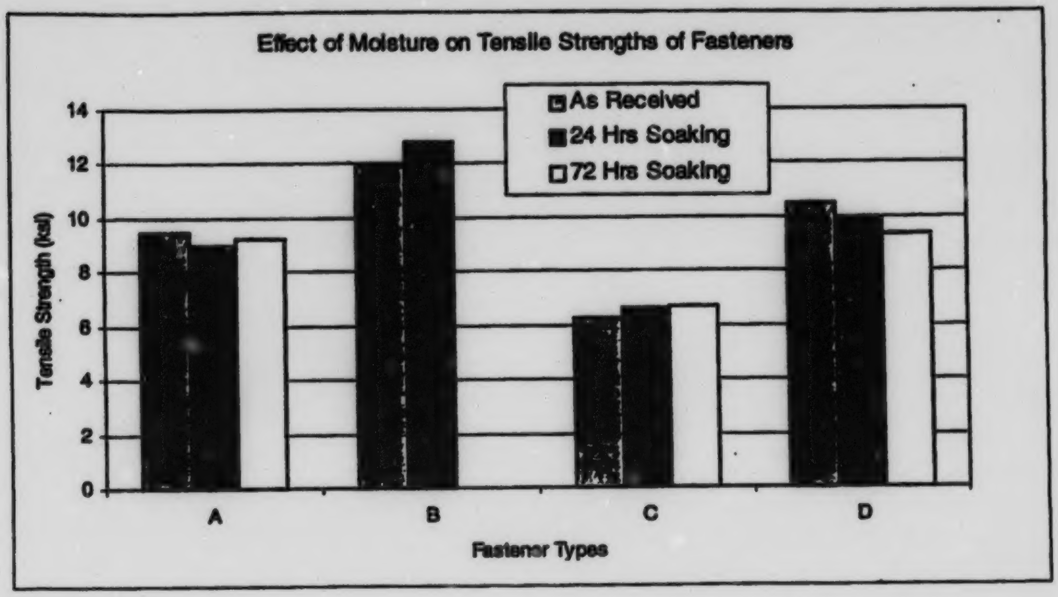

Figure 5: Tensile Test Results

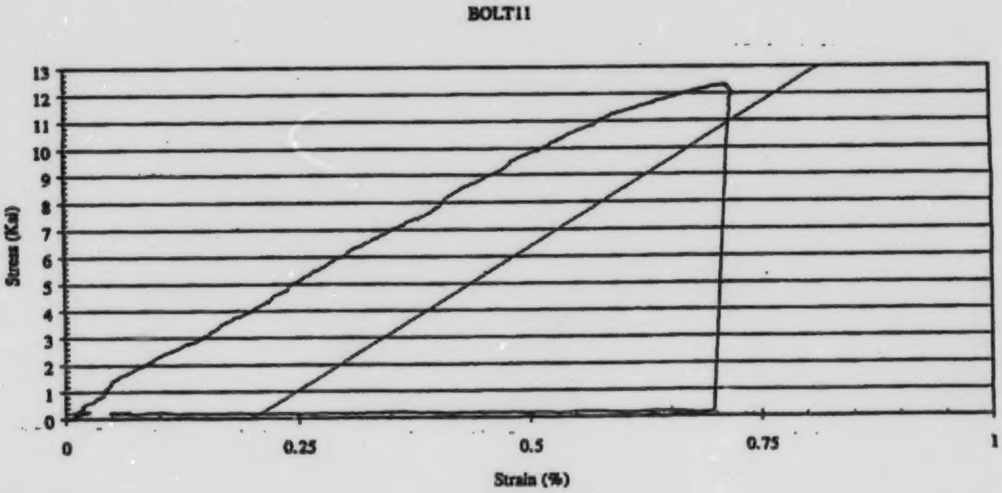

Figure 6: Tensile Load-Displacement Curve of as Received 3/8-16 UNC Fastener

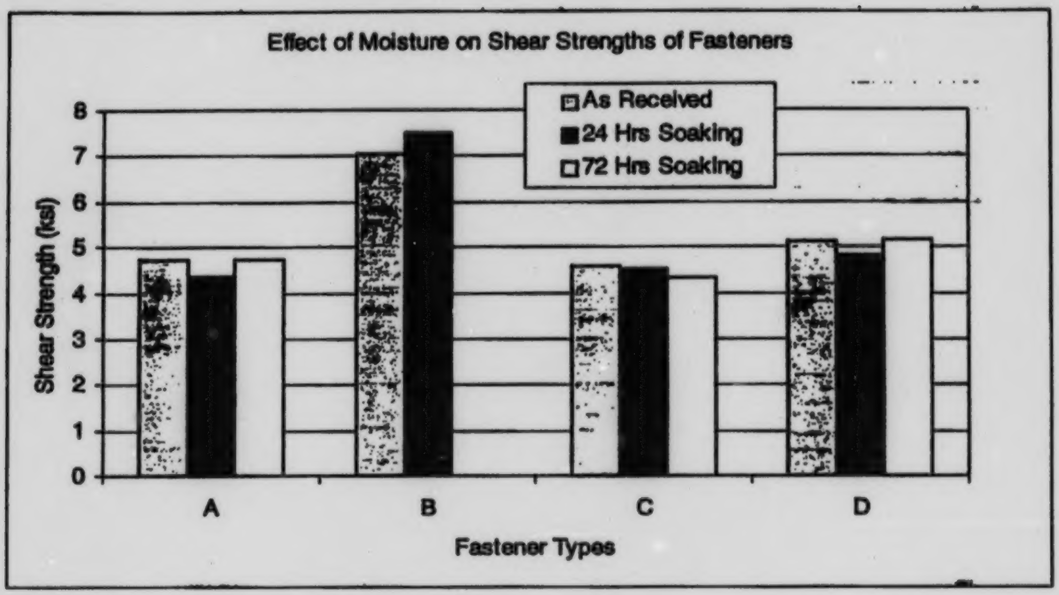

Figure 7: Shear Test Results

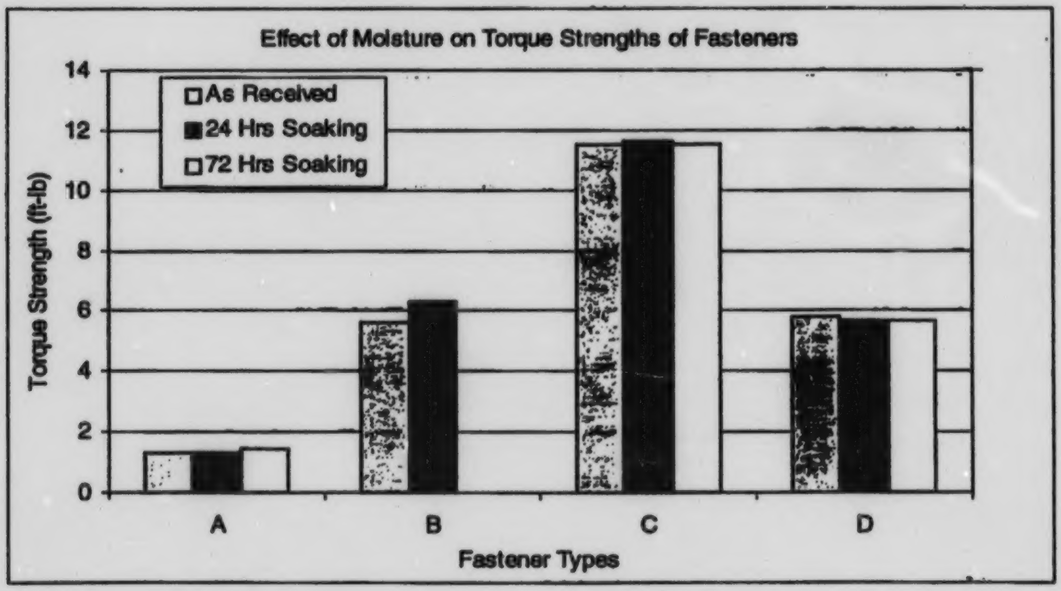

Figure 8: Shear Load-Displacement Curve of as Received 3/8-UNC Fastener

#511907

Inorganic Intumescent Filler for Polymer Composites

by J.O. Bernt

J.O. Bernt and Associates Limited
3375 Laird Drive, Unit 3, Mississauga, Ontario L5L 5R7

ABSTRACT

This discussion is about the use of an inorganic intumescent filler compounded with LDPE (low density polyethylene) and used as the core material for metal composites.

The filler is a further development of the inorganic intumescent coating material developed with DREA and NDHQ support.

The metal composite was developed to meet and exceed the specifications for currently available, non-combustible siding material for commercial/industrial buildings.

Due to the high strength, low weight of this composite we believe it could find use in naval ships for interior partitions, non-structural bulkheads and/or various furnishings, etc. where it would offer significant weight savings.

The paper will further discuss a unique technique for forming glass microballoons in-situ in the composite core material, thus achieving light weight while retaining adequate compressive strength.

INTRODUCTION

This discussion is about the use of an inorganic intumescent filler compounded with LDPE (low density polyethylene) and used as the core material for metal composites.

The filler is a further development of the inorganic intumescent coating material developed with DREA and NDHQ support.

The metal composite was developed to meet and exceed the specifications for currently available, non-combustible siding for commercial/industrial buildings.

Because the composite has high strength, low weight, very low flammability and smoke generation, we believe it could find use in naval ships for interior partitions, non structural bulkheads and/or various furnishings.

We have a few samples of the composites, two made with aluminum and two made with galvanized steel, as well as samples of the core material – both expanded and un-expanded. We will pass the samples around for you to look at.

We have prepared a table (Slide 1) to show you the major characteristics of known commercially available composites.

The first three numbers – flame spread, smoke development and BTU/ft are important from a fire and flammability point of view.

The last number – peel strength, is important for the strength of the composite.

Based on this comparison we have succeeded in developing a material which is about equal in flame spread, but considerably better in respect to smoke development, BTU content and peel strength.

As you saw in the preceding table the composites made by Reynolds and Alucobond both have 5-6000 BTU/ft2 which corresponds to a particulate loading of about 75% by weight.

We knew it was not possible to increase the loading without losing coherence of the compound.

We had observed, that in low level cone-calorimeter test, the samples had expanded, but the LDPE was not completely destroyed. Microscopic examination revealed that the LDPE matrix was full of glass microballoons formed by the expanding silicates.

We then developed a silicate mix which could be compounded at 155 deg.C without expanding, but would have completely expanded at 300 deg.C. The silicate microballoons formed from this mix are nearly insoluble in water.

Slide II

This microphotograph shows the surface of the core material after we have peeled off the metal laminate. If you look closely, you see small bright spots covering the picture.

These spots are light focused by the surfaces of the microballoons, probably by the inside surfaces of broken microballoons.

Because the microballoons are completely surrounded by the LDPE matrix they are very strong in compression. When expanded to twice the original volume the compound has a compressive strength of at least 800 lbs./I2 or about 57 tons/ft.2.

The expansion process, due to the high temperatures involved, must take place in the absence of oxygen to avoid burning the LDPE. Our test shows that LDPE does not degrade due to high temperatures provided oxygen is not present.

We also tested PVC in this process. PVC, however, starts losing chlorine at 200-250 deg.C which destroys the material completely.

Slide III

These curves are TGA and DSC plots from 0-600 deg.C of the intumescent powder. The plots illustrate one of the ways in which we can control the temperature at which intumescence begins. The higher the drying temperature the higher the intumescent temperature.

In conclusion I like to think that we have developed a material which could be useful to the Navy.

We have already received strong expressions of interest from Reynolds Metal Company and from a large Canadian construction materials group.

We will also investigate the use of the core material as acoustic and thermal insulation.

Preliminary testing indicates that it may be possible to expand the core material up to at least 1 ½" thick using high intensity microwaves.

Slide 1

PYROPHOBIC SYSTEMS LTD.
3375 Laird Rd., unit 3, Mississauga, Ontario L5L 5R7
Tel: (905) 569-7392 Fax: (905) 569-7696 Email: jammbco@aol.com

Major Characteristics of Metal Composite Panels

Manufacturer	Flame Spread (E84)	Smoke Develop (E84)	BTU Per FT²	Peel Strength Lbs/Inch
Pyrophobic	**12**	**15**	**2500**	**40**
Reynolds	15	30	5000	20
Alucobond	10	105	6000	26

Slide II

Slide III

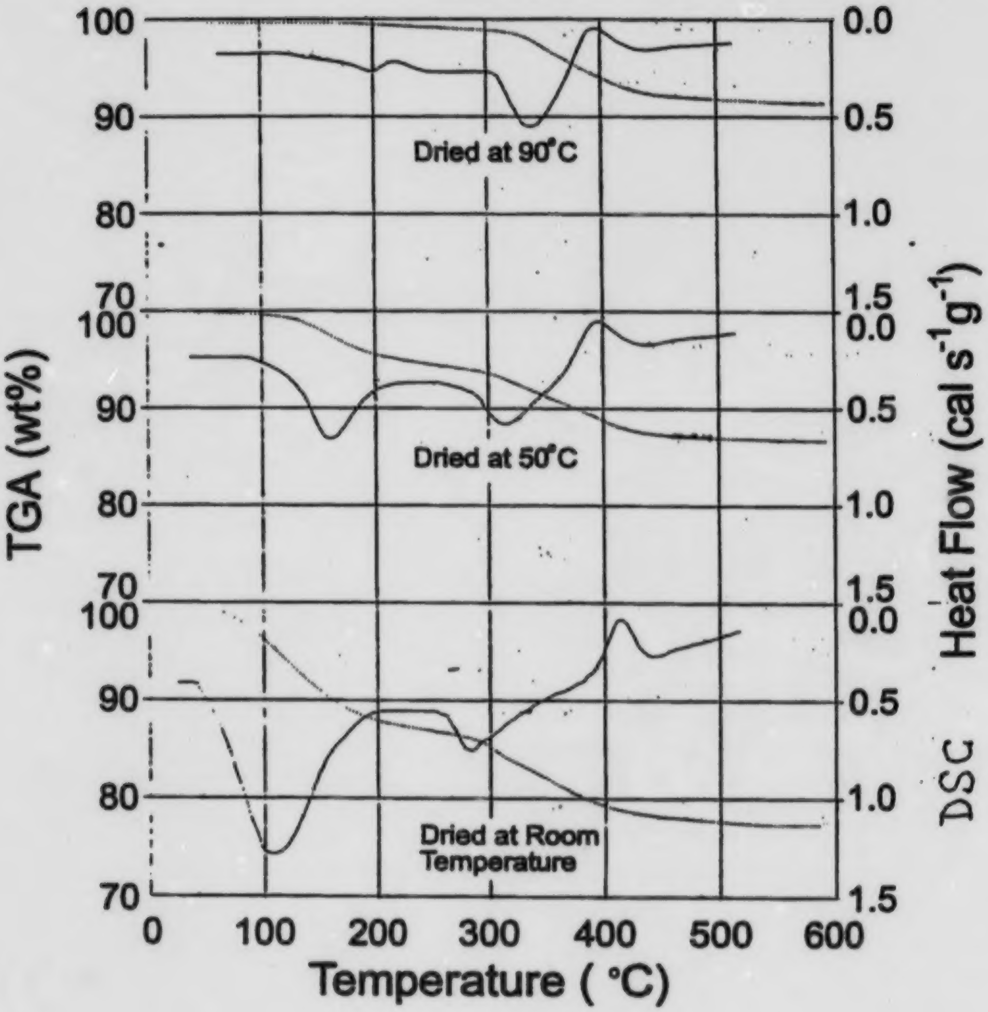
TGA (wt%)
Heat Flow (cal s^{-1}g^{-1})
DSC
Dried at 90°C
Dried at 50°C
Dried at Room Temperature
100
90
80
70
0.0
0.5
1.0
1.5
0
100
200
300
400
500
600
Temperature (°C)

#511908 (334)

Reliability of Smart Composite Materials

by D.O. MacDonald[1], A.L. Kalamkarov[2], A. Georgiades[2], S.B. Fitzgerald[2]

[1] Innovacorp Materials Services Group
P.O. Box 790, Dartmouth, Nova Scotia, B2Y 3Z7

[2] Dalhousie University, Department of Mechanical Engineering
P.O. Box 1000, Halifax, N.S.

ABSTRACT

A smart composite material is a structure which contains a built in sensing device, used to monitor the current state and serviceability of a structure over its entire service life. One such type of sensing device is a fiber optic strain sensor. The small size of these strain sensors and their leads means that they can be embedded within a composite material without degrading its mechanical properties. As well, if the sensor is embedded in the cross section of an FRP composite product such as rebar, then the sensor will be protected from rough handling during fabrication and construction phases. Externally bonded gages are inherently more susceptible to damage or failure. As an added benefit, embedded fiber optic strain gages can be used as a quality assurance tool during the manufacturing process for the FRP composites, in measuring such parameters as degree of cure for the resin matrix system. As compared to conventional types of foil strain gages, fiber optic strain sensors are light weight, resistant to corrosion and electromagnetic interference, and have excellent sensitivity.

The overall goal of the current research is the production of both fiberglass and carbon fiber composite tendons which contain embedded fiber optic strain sensors. These 9mm diameter composite tendons are a good study model for fiber reinforced plastic (FRP) products such as rebar, prestressing tendons, rock bolts, and ground anchorages. The advantages of these FRP products as compared to their steel counterparts include excellent corrosion resistance and a high strength to weight ratio. For example, FRP rebar is resistant to harsh chemical environments including the detrimental chloride attack seen in steel rebar used in marine applications or in areas exposed to deicing salts. The smart composite reinforcements are produced with the pultrusion process, as this is an extremely cost effective manufacturing process for composites, and because pultruded products typically contain a high degree of axial reinforcement, ideal for prestessing tendons and rebar.

Two types of optical fiber strain sensors were used to produce the smart composite reinforcements: Fabry Perot and Bragg Grating sensors. The performance of the smart reinforcements is currently being evaluated through an extensive mechanical testing program which simulate the anticipated in service conditions. These tests are designed to gain information with respect to the long term reliability of the fiber optic sensors, as it is expected that typical applications may have expected life spans of 50-100 years. The strain readings from the embedded optical sensors are compared to that from externally affixed extensometers and foil gages which represent the traditional methods of strain measurement. The performance of the smart composite tendons were evaluated under the following test regimen:

1. Tensile ramp and sinusoidal waveform proof loadings.
2. Proof loadings at temperature extremes ranging from -40 to +60°C.
3. Tension-Tension fatigue testing.
4. Short term creep.
5. Long term creep with harsh environmental exposure.

The results of this testing program will be presented and discussed. Generally, the embedded optical sensors were in good agreement with the extensometer and strain gage devices.

A new phase of the research will begin in the spring of 1999, when the smart composite tendons will be evaluated in field applications. One such project involves the placement of the tendons in concrete seawalls, as part of a restoration project at Halls Harbour, N.S. Other applications for the technology are also being explored.

This work has been supported by the ISIS Canada NCE Project 3.4.

Research Goals:

- *Pultrusion* of GFRP and CFRP composite reinforcements with embedded fiber optic strain sensors.
- *Evaluation* of sensors' performance under tensile loading conditions

Why Composite Materials?

- Corrosion Resistance
- High Strength to Weight Ratio
- Non-Conducting

Civil Engineering/Concrete Applications:

- Prestressing Tendons
- Rebar
- Column Wraps for Rehabilitation

Properties of GFRP vs. Steel Rebar

	GFRP	Steel
Ultimate Tensile Strength	160,000 psi	70,000 psi
Yield Strength	100,000 psi	40,000 psi
Modulus of Elasticity	7 x 10E6 psi	30 x 10^6 psi
Strain at Failure	2-3%	
Weight	0.09 lbs/ft	0.376 lbs/ft
Cost	2x	1

Typical Applications Have Included:

Location	Exposure
Parking Garages	Deicing Salt
Bridge Decks	Deicing Salt
Marine Structures	Saltwater
Reservoirs for Papermills and Chemical Plants	Acidic and Caustic Solutions

Advantages of Fiber Optic Sensors

- Light weight
- Corrosion resistant
- Excellent Sensitivity
- No EMI losses
- No Spark Hazard
- Reduced Cabling
- "Easily Embedded"

Why Smart Composites?

Monitor Structure During:

Fabrication
Installation
In-Service

Examples:

- Degree of Cure
- Damage Detection
- Service or Process Induced Strains

Why Smart Composites? (Cont'd)

Because Composites are "new kid on the block"

The Internal Sensing Component will:

Give designers more confidence in composites

Greater use of composites in traditional industries: Civil, Transportation, Marine

Individual Components of Smart Composite Material

- Reinforcing fiber for strength and stiffness
- Resin matrix to bind and protect fibers from harsh environments
- Optical Sensors to measure strain

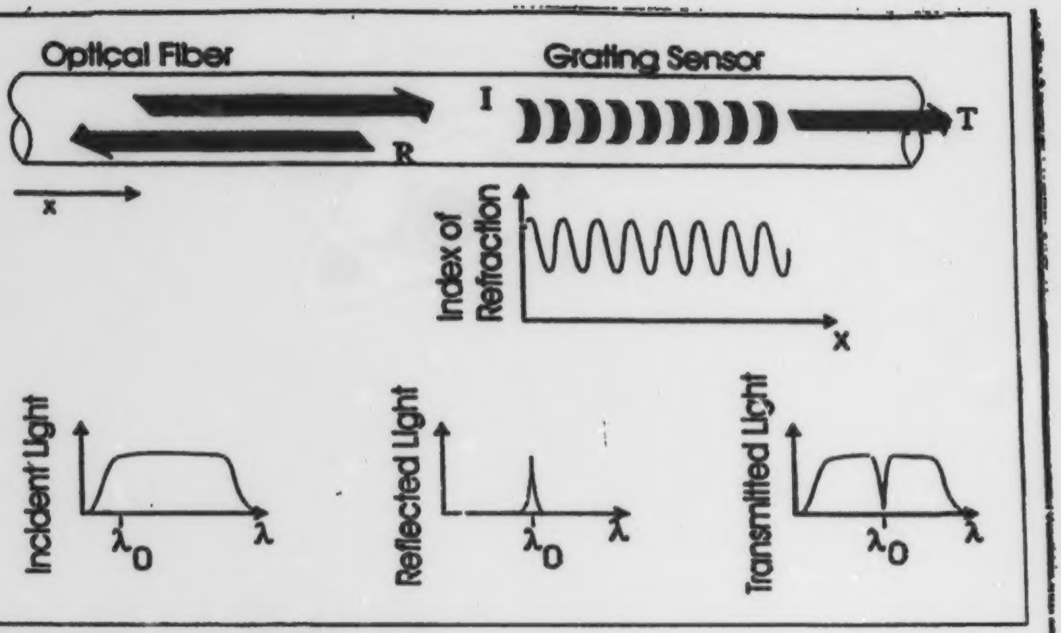
Optical Fiber
Grating Sensor
I
R
T
x
Index of Refraction
x
Incident Light
λ_0
λ
Reflected Light
λ_0
λ
Transmitted Light
λ_0
λ

Figure 2: Bragg Grating Description

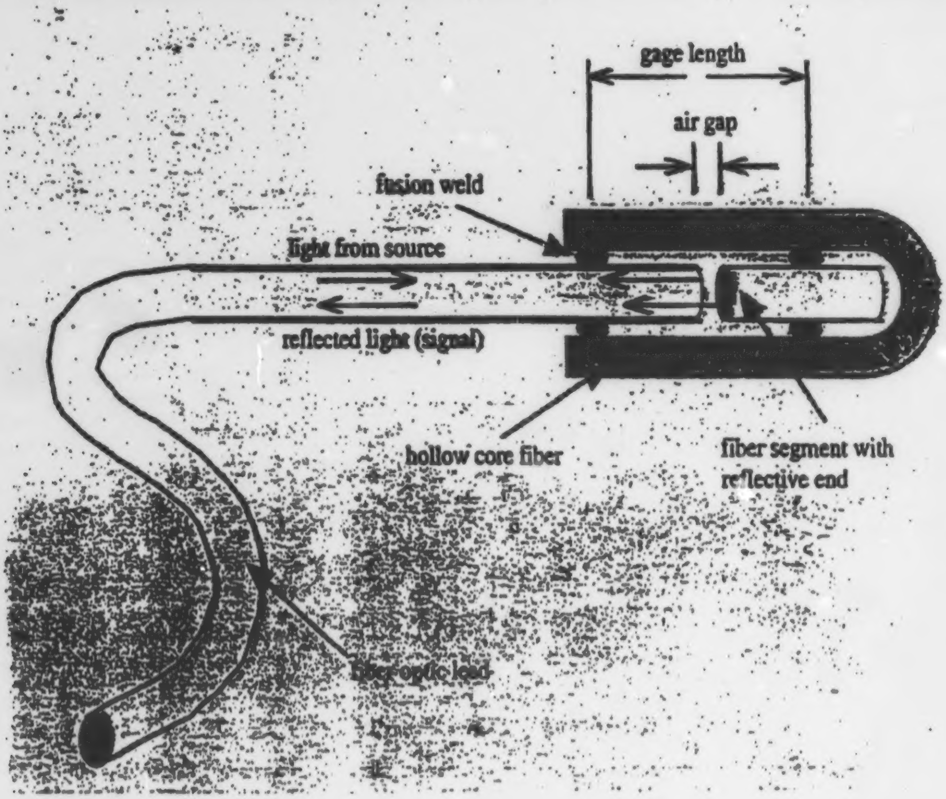
gage length
air gap
fusion weld
light from source
reflected light (signal)
hollow core fiber
fiber segment with reflective end
fiber optic lead

Advantages of Pultrusion

- single machine operator
- continuous 24 hour operation
- low wastage or scrap
- may use inexpensive raw material formats

Limitations of Pultrusion

- Commercially limited to parts with constant cross section

Production Issues for Smart Composites

Optical fiber should not compromise structural integrity of the host composite material.

Composite processing parameters should not compromise the performance of the optical fiber.

Ideally, optical fiber should not affect the producibility of the composite.

Durability and Performance Test Program

- Tensile Ramp & Cyclic Loading Ambient
- Performance at Temperature (-40 to +60)
- Tension-Tension Fatigue Loading
- Short Term Creep (300 Hours)

Durability and Performance

(cont'd)

- Long Term Creep (2000 hrs.)
- Environmental Exposure
- Long Term Creep and Environmental
- Destructive Tests (max. capacity sensor)

Output From Bragg Grating Sensor Embedded in GFRP Rod

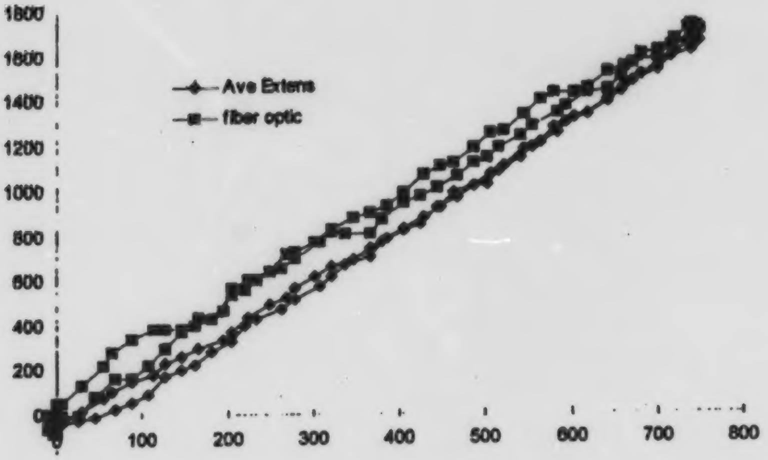

Microstrain versus Load

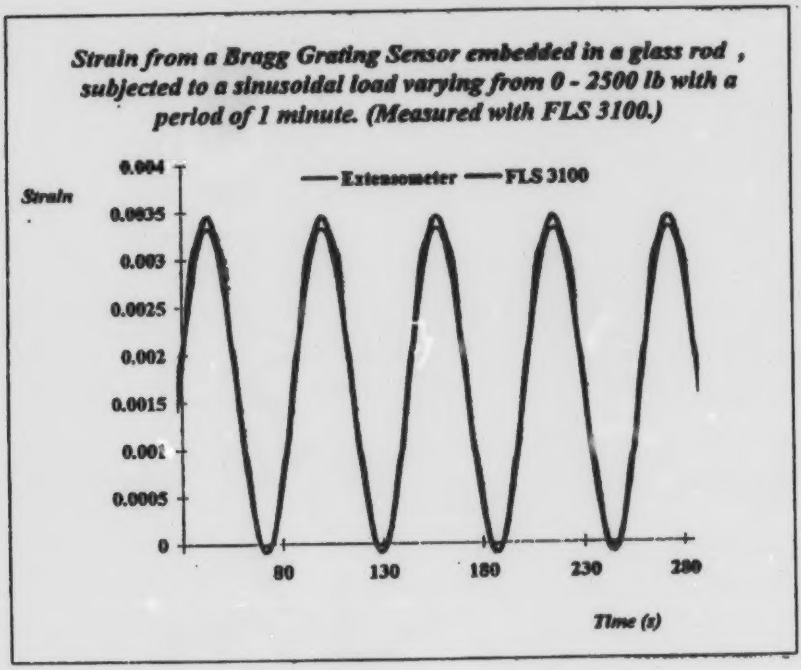
Strain from a Bragg Grating Sensor embedded in a glass rod , subjected to a sinusoidal load varying from 0 - 2500 lb with a period of 1 minute. (Measured with FLS 3100.)

Fiber Optic Strain Sensors Perform Well In The Heat

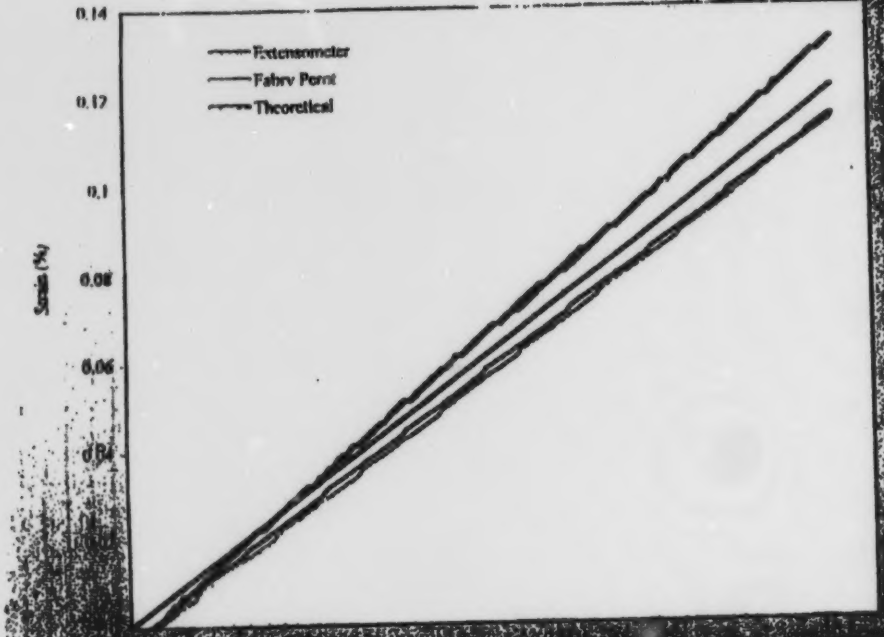

[illegible] Sensors Perform Well In Extreme Cold

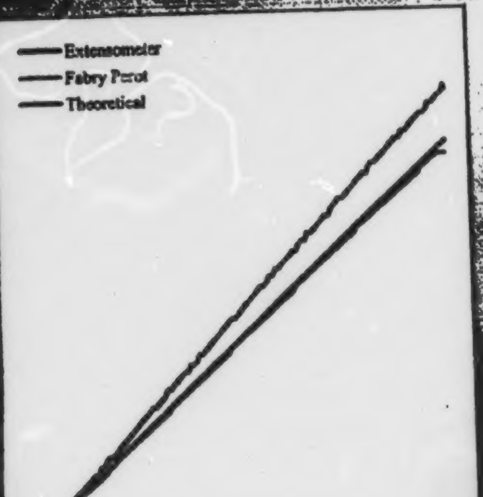

Strain measured with the fiber optic sensor compares well with both the strain measured using an extensometer and with the theoretical strain calculated using micro-mechanics and the known properties of the carbon [illegible]

Carbon rod with Fabry Perot after 70,000 cycles of 1 Hz. fatigue loading

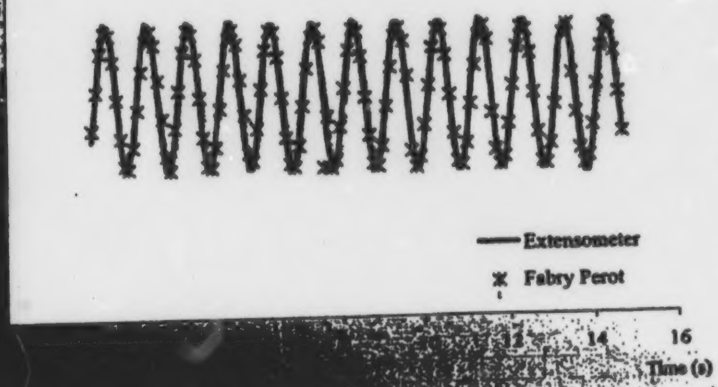

Comparison of the strain in a carbon fiber reinforced rod, measured using an extensometer & a fiber optic sensor after 70,000 cycles of fatigue loading. Load = 2,000 + 500 sin(t x 2 pi) lb.

Bragg Grating Sensor embedded in a carbon rod after 365,000 cycles of 1 Hz Fatigue Testing. (Sampled at 20 Hz with FLS 3100.)

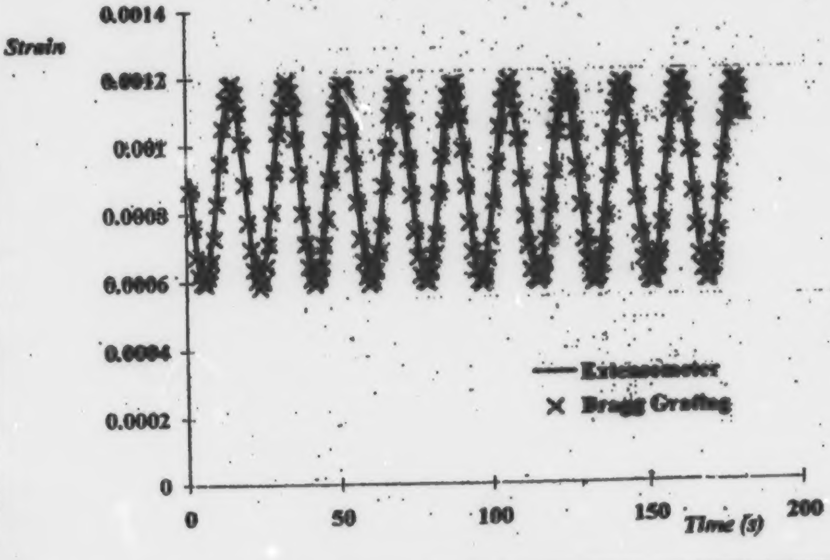

A Glass Fiber Rod with Embedded Fabry Perot Fiber Optic Strain Sensor Gives a Very Stable Reading When Subjected to a 140 Mpa. Continuous Load at Room Temperature.

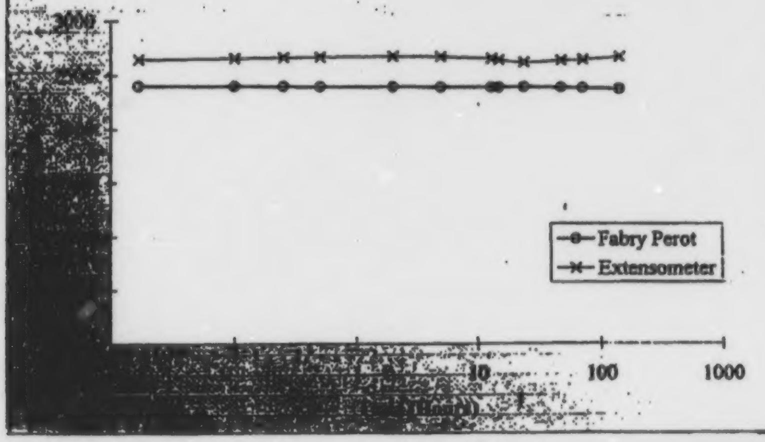

Harsh Environments

Materials:

- Steel, GFRP, CFRP, Rebars
- Polyimide, Acrylate Coatings

Test Solutions:

- Filtered Seawater
- Simulated Concrete Pour Water: pH 13

WATERLOO CREEK BRIDGE

Vancouver Island, British Columbia

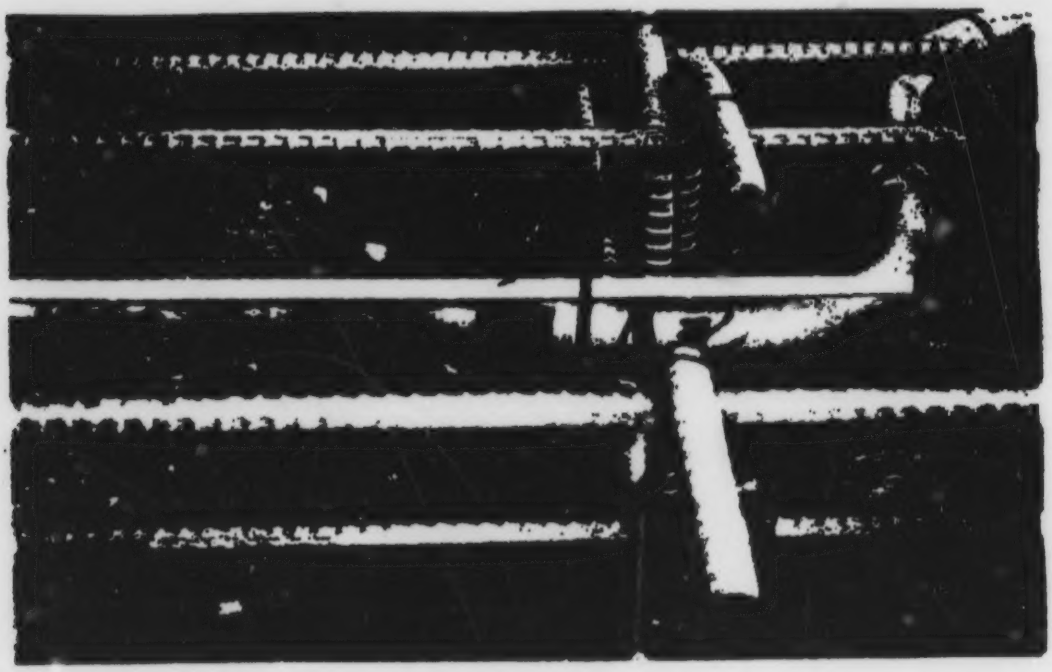

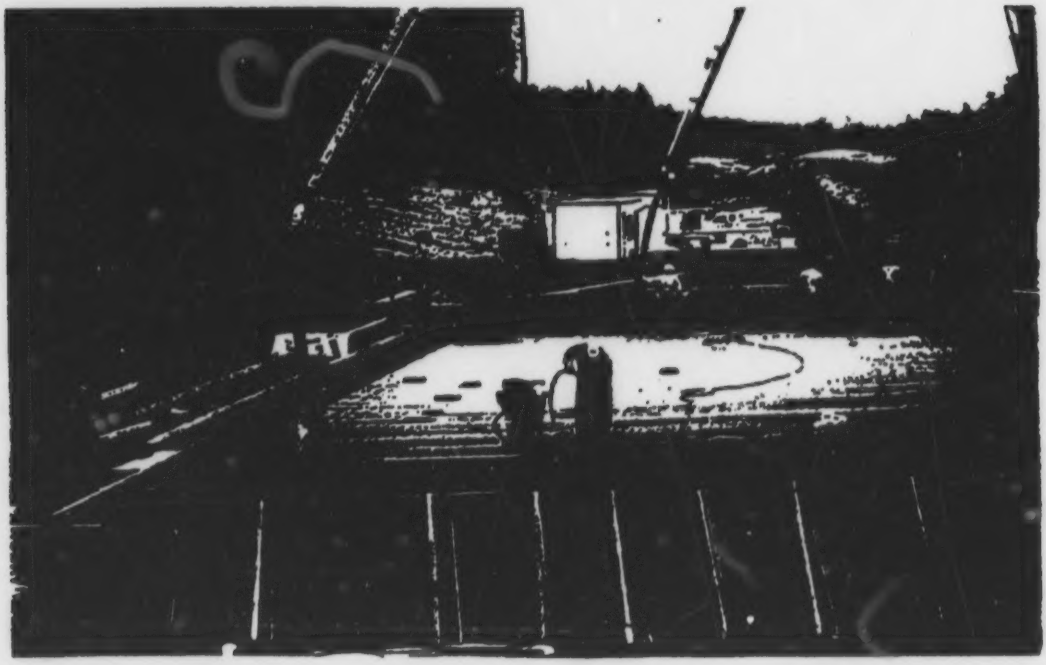

Conclusions to Date

Fabry Perot and Bragg Gratings:

- Survive pultrusion process.
- Provide strain data comparable to externally affixed devices.
- Function over wide range of temps.
- Reliable under sustained loadings.
- Reliable after many load cycles.

#511909 (35)

Designing for Performance in Human-Machine Systems

by Norman G. Vinson, Janice A. Singer and Marceli Wein

Institute for Information Technology
National Research Council, Canada
Ottawa, ON K1A 0R6

ABSTRACT

This paper discusses how user-centered design improves the performance of human-machine systems. The overall performance of such systems is a function of the individual performance of its two major components, the human user and the machine, and the performance of the interface between these two components. Accordingly, errors and inefficiencies can result from the technological limitations of the machine, from the user's human limitations, and from limitations of the interface.

In the vast majority of cases, system development effort is focused on advancing the technology, with little, if any, regard to the human-machine interface or the needs of the human users. Ignoring a major component of the human-machine system, the human, means that potential gains in efficiency and accuracy will not be realized. Worst yet, additional sources of errors and inefficiencies can be introduced by modifying the interface without regard to the user.

In contrast, user-centered design takes into account the needs, characteristics, tasks, and limitations of the users. Based on an understanding of the user and his tasks, the designer can specify the functions the machine must perform so that the tasks are accomplished successfully by the human-machine system. This reduces some of the errors and inefficiencies that can be attributed to the machine component. Knowledge of human limitations can guide interface design to avoid pushing the user beyond his capabilities, thus mitigating the effects of human limitations. Finally, more efficient interfaces are designed through knowledge of how users perform their tasks.

The goals of user-centered design, its cost-justification, and some of its more practical techniques are presented in this paper. Moreover, these design techniques are illustrated by referring to the design of the UNIT (Universal Nondestructive Inspection Tool) system.

Performance of Human–Machine Systems

- **System performance**
  - Errors
  - Speed
- **Sys. performance = *f*(human, machine, interface)**
- **User-centered design**
  - increase system performance
  - increase user acceptance of the system

Increased Performance: Examples of Results

- **Oscilloscope user interface redesign**
  - -> 77% increase in performance speed
- **User-centered design of flight deck for Boeings 575 and 767**
  - -> Aircraft can be operated with 2 rather than 3 pilots
- **User-centered design of interface for software destined for internal use**
  - -> Increased productivity calculated to produce 6.8 million $ US savings in 1st year.

User-Centered Design Saves Time and Money

- **Reduce total development time & cost**
  - Total development = development + post-delivery changes
- **In only 2 % of software projects, software does not require changes after delivery (Davis, 1990)**
- **About 50 % of code for user interface**
- **User centred design IDs real needs before development**
  - Change requirements; not system
  - Don't develop unneeded features & functions

    --> save time & money

User-Centred Design

- **User-centered design is**
  - an approach to design
  - a collection of techniques
- **Design fields practicing user-centered design**
  - Ergonomics
  - Human Factors
  - User-interface (UI) design, cognitive ergonomics, human-computer interaction (HCI)

Increasing Performance

tasks accomplished by human-machine system ->

- Sys. performance = *f*(human, machine, interface)

- **To increase performance**
  - make the interface mesh with user practices
    - user expertise transfers to new system
    - reduces possibility of failure
  - make the interface mesh with user cognition
    - user does not waste cognitive resources transforming data provided by the interface
    - interface can support user analysis and decision-making

Example

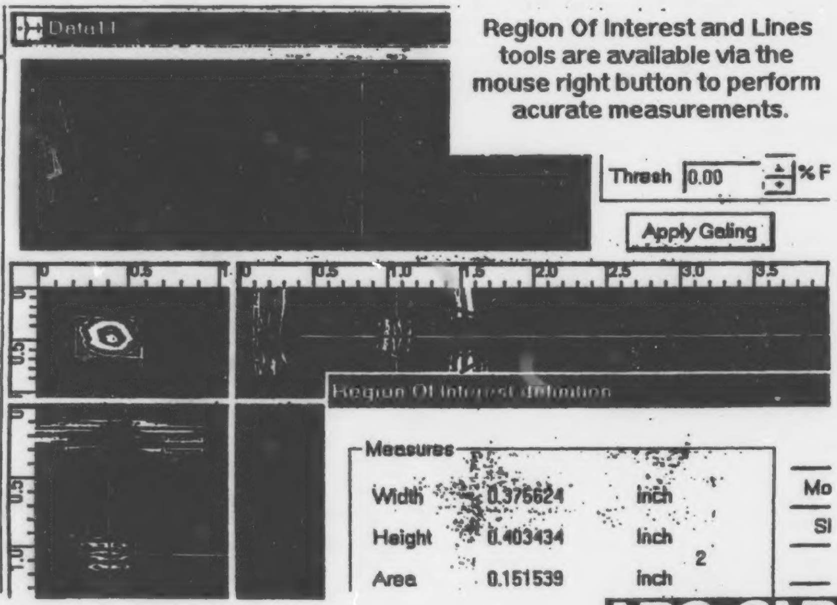

Region Of Interest and Lines tools are available via the mouse right button to perform acurate measurements.

Thresh 0.00 %F

Apply Gating

Region Of Interest definition

Measures

Width 0.376624 inch

Height 0.403434 inch

Area 0.151539 inch 2

Increasing User Acceptance of the System

User participation in design

- **user contributes to system design**
- **shows respect for user's expertise**
- **makes user familiar w/ new system before implementation**
    - (removes "interface shock")

Match between interface & user

- **allows user to apply expertise**
    - user remains valuable
- **increases user familiarity w/ new system**
- **system is usable and useful; not frustrating**

How to Do User–Centred Design

1 Gather user-related requirements
- interviews
- observation
- analysis

2 Design based on 1

3 Test design using
- **mock-ups**
- **heuristics**
- **scenarios**
- **simulations**

iterate

4 Change design based on 3

5 Implement final design in application

Design quality = *f*(requirements gathering, testing)

User–Related Requirements

- **task analysis**
  - required data & heuristics or algorithms
- **organisational profile**
  - e.g. who decides what
- **user requirements & user profile**
  - e.g. user experience
  - e.g. types of users
  - e.g. frequency of use
- **environmental requirements**
  - e.g. lighting (too dark for typing ?)
  - e.g. mobility

Iterative Design and Testing

- **design based on user-related requirements**
- **test**
  - create low fidelity mock-up
    - e.g. paper & pencil
  - real user simulates task performance w/ mock-up
    - testers play role of computer (like puppeteers)
      - difficult for 3D
      - difficult for animation
- **change design, re-test, progressively increase mock-up fidelity**
  - cost of design change = f(mock-up fidelity)

Pros & Cons of User–Centred Design

Pros

- **system performance**
  - perf. = f(interface)
- **high quality interface design**
  - user reqts => quality
  - testing => quality
- **high (quality/dev. cost) ratio**
  - design changes made early => lowers dev. cost
- **lower prob. of failure**
- **user acceptance & satisfaction**

Cons

- **takes time up front**
- **change in user requirements**
  - circumstances change
  - users become more communicative
- **higher user expectations**
  - user wants bells & whistles
  - developer wants to minimise cost

Summary

- **User-centered design**
  - is an approach to design
  - is a collection of techniques
  - can be applied to a variety of projects
  - increases performance of human-machine systems

#511910 (36)

THE CHARACTERISATION OF PIEZOELECTRIC AND ELECTROSTRICTIVE MATERIALS FOR UNDERWATER ACOUSTIC TRANSDUCERS

Binu K. Mukherjee, Stewart Sherrit and Guomao Yang

Department of Physics, Royal Military College of Canada,
Kingston, Ontario, Canada K7K 7B4.
[e-mail: mukherjee@rmc.ca ; tel: 613 541 6000 x 6348]

ABSTRACT

Underwater acoustic transducers are used extensively in Anti-Submarine Warfare and Mines Countermeasures. The majority of these transducers are based on the use of piezoelectric and electrostrictive materials as the active material in the transducer. These materials are also important for the active methods of sound absorption that are being considered for underwater stealth. Since the materials are non-linear and lossy, the design of the various devices requires a good and precise knowledge of the dielectric, elastic and piezoelectric/electrostrictive properties of the materials under the actual conditions of the particular application (e.g. high power, pre-stress, etc..,). The importance of such a precise knowledge of the properties has increased with the development of software, such as PZFlex, which can model piezoelectric materials/transducers and their vibrations very accurately if precise material parameters are provided. The Laboratory for Ferroelectric Materials at the Royal Military College of Canada has, over the last few years, developed a range of experimental methods for determining the full matrix of the dielectric, elastic and piezoelectric/electrostrictive properties of piezoelectric and electrostrictive materials as complex coefficients, to take account of all types of losses in the material, and to determine the coefficients as a function of temperature, frequency and applied fields, stresses and hydrostatic pressures. We review these methods and discuss the kind of detailed information on material parameters that can now be made available to transducer designers.

INTRODUCTION

Piezoelectric and electrostrictive materials are important constituents of electromechanical sensors, actuators and smart structures. Piezoelectric materials produce a strain, S, under the influence of an external electric field, E, or become electrically polarised under the influence of an external stress, T. The property of piezoelectricity is closely related to the phenomenon of ferroelectricity, which describes the spontaneous polarisation in a crystal that can be changed between two or more distinct directions with respect to the crystal axes through the application of an external electric field. This ability of ferroelectric materials to switch polarisation under an external electric field from a random orientation to a preferred direction is used in a variety of polycrystalline ferroelectric materials (ceramics and polymers) to produce a polycrystalline piezoelectric material with a net preferred polarisation direction. This process is described by the term "poling". Prior to poling, individual domains of the ceramic are piezoelectric but the random orientations counteract each other and the net effect is that the macroscopic material shows little or no piezoelectricity. The partial alignment of the domains during poling creates a net spontaneous polarisation in the poling direction and the material shows a C_∞ symmetry around that direction.

Piezoelectricity can be mathematically described by a phenomenological model derived from thermodynamic potentials. The derivations are not unique and the set of equations describing the direct and converse piezoelectric effect depend on the choice of potential and the independent variables used[1,2]. For example, one such set of linear constitutive relations is:

$$\begin{aligned} S_p &= s^E_{pq} T_q + d_{pm} E_m \\ D_m &= \varepsilon^T_{mn} E_n + d_{pm} T_p \end{aligned} \tag{1}$$

where D is the electric displacement, s is the elastic compliance, d is a piezoelectric constant and ε is the dielectric permittivity. The superscripts of the constants designate the independent variable that is held constant when defining the material coefficient and the subscripts define tensor directions which take into account the anisotropic nature of the material. The elements of the tensor form a 9x9 matrix with 1,2,3 designating the orthonormal directions (3 is the poling direction) and 4,5,6 designating the shear directions. For the commonly used polycrystalline piezoelectric ceramic materials with C_∞ symmetry, such as lead zirconate titanate or PZT, there are ten non-zero, independent matrix elements consisting of 5 independent elastic constants, 3 independent piezoelectric constants and 2 independent dielectric constants. For these materials, the reduced matrix form of the above constitutive relationships can now be written as:

$$\begin{bmatrix} S_1 \\ S_2 \\ S_3 \\ S_4 \\ S_5 \\ S_6 \\ D_1 \\ D_2 \\ D_3 \end{bmatrix} = \begin{bmatrix} s^E_{11} & s^E_{12} & s^E_{13} & 0 & 0 & 0 & 0 & 0 & d_{13} \\ s^E_{12} & s^E_{11} & s^E_{13} & 0 & 0 & 0 & 0 & 0 & d_{13} \\ s^E_{13} & s^E_{13} & s^E_{33} & 0 & 0 & 0 & 0 & 0 & d_{33} \\ 0 & 0 & 0 & s^E_{55} & 0 & 0 & 0 & d_{15} & 0 \\ 0 & 0 & 0 & 0 & s^E_{55} & 0 & d_{15} & 0 & 0 \\ 0 & 0 & 0 & 0 & 0 & 2(s^E_{11} - s^E_{12}) & 0 & 0 & 0 \\ 0 & 0 & 0 & 0 & d_{15} & 0 & \varepsilon^T_{11} & 0 & 0 \\ 0 & 0 & 0 & d_{15} & 0 & 0 & 0 & \varepsilon^T_{11} & 0 \\ d_{13} & d_{13} & d_{33} & 0 & 0 & 0 & 0 & 0 & \varepsilon^T_{33} \end{bmatrix} \begin{bmatrix} T_1 \\ T_2 \\ T_3 \\ T_4 \\ T_5 \\ T_6 \\ E_1 \\ E_2 \\ E_3 \end{bmatrix} \tag{2}$$

While the linear constitutive relations can be written in ways other than shown in (1), there are only 10 independent constants and the IEEE Standard on Piezoelectricity[3] contains the appropriate equations that allow one to convert from one set of equations/matrix to another. Ideally, under small fields and stresses and for materials with low losses within a limited frequency range, these 10 constants contain all the information required to predict the behaviour of the material when a stress, strain or electric field is applied to it. However, piezoelectric materials generally exhibit varying degrees of non-linearity. If the above linear equations are used to define the material constants of piezoelectric materials, then the material constants themselves are a function of applied fields and stresses as well as of the temperature of the material. Also, the piezoelectric response is not instantaneous and the response time can be important in some applications.

The most general way to take account of the dielectric, mechanical and piezoelectric losses in a material is to express the 10 material constants as complex coefficients. This paper first reviews the experimental methods for determining these complex material constants for any piezoelectric material and the effects of dispersion on these constants, and it discusses the use of an appropriate equivalent circuit for the material to include all types of losses. The paper then reviews the experimental methods to study the non-linear dependence of the material constants on applied signals as well as the response time of the materials.

RESONANCE METHODS FOR DETERMINING THE COMPLEX MATERIAL CONSTANTS

The most widely used technique for determining the material constants for piezoelectric materials is the resonance technique as outlined in the IEEE Standard on Piezoelectricity[3]. A piezoelectric sample of specific geometry is excited with an AC signal and an impedance analyser is used to determine the complex impedance and admittance as a function of frequency. Typical spectra are shown in Figure 1 and it can be seen that the spectra contain resonances that result from ultrasonic standing waves in the material. Several particular frequencies may be defined from the spectra: the parallel resonance frequency f_p is the frequency at which the resistance R is a maximum; the sideband frequencies $f_{+1/2}$ and $f_{-1/2}$ correspond to the maximum and the minimum in the reactance X; The series resonance frequency f_s is the frequency at which the conductance G is a maximum; and, the sideband frequencies $f_{+1/2s}$ and $f_{-1/2s}$ correspond to maximum and the minimum of the susceptance B.

The five most common modes used for piezoelectric ceramic analysis are shown in Figure 2 along with the recommended geometrical aspect ratios for samples used to determine each mode. The arrow marked on each sample indicates the poling direction for the piezoelectric ceramics. The aspect ratios ensure that the sample is excited in a mode where the one-dimensional approximation is valid and that coupling between the modes is negligible. In some materials (typically low mechanical Q materials) these aspect ratios may be relaxed

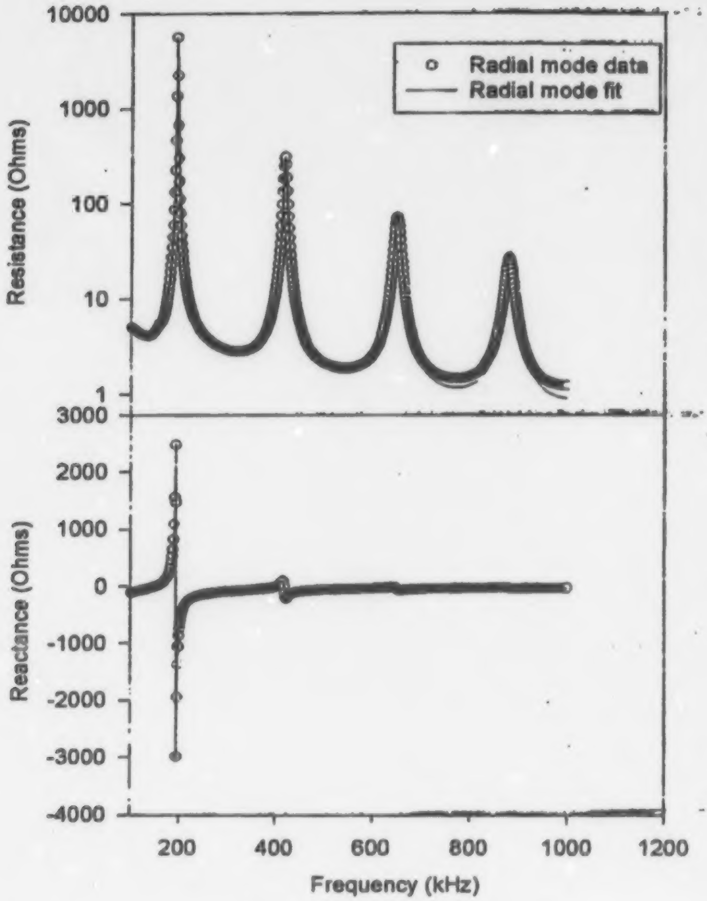

Figure 1. The impedance spectra for the radial mode of a Motorola 3203 HD PZT disk sample.

whereas in other materials (high Q and high electromechanical coupling) they may need to more stringent.

The impedance equations that govern the various resonance spectra have been derived from the phenomenological theory of piezoelectricity[4,5] for the case of real material constants assuming lossless materials. These equations express the impedance as a function of the appropriate material constants and of the particular frequencies defined above. Holland[6] showed that the losses in a piezoelectric material may be taken into account by representing the material constants as complex coefficients. Sherrit[7] has re-derived the expressions for the impedance for the various resonance geometries using complex material constants so as to include the dielectric, mechanical and piezoelectric losses in the material.

The IEEE Standard on Piezoelectricity uses the impedance equations for lossless resonators and the critical frequencies derived from the equations to determine the real parts of the material constants. Numerous techniques have been proposed to measure the material constants as complex coefficients[8,9,10,11,12,13,14]. Basically, the expression for the impedance is compared with the experimental curve around resonance and the material constants are found so as to obtain the best fit.

As an example, Figure 3 shows the impedance plots for the thickness extensional resonance for Motorola PZT 3203 HD ceramic. For this case the linear piezoelectric equations are

$$T_3 = c_{33}^D S_3 - h_{33} D_3 \quad \text{and} \quad E_3 = -h_{33} S_3 + \frac{1}{\varepsilon_{33}^E} D \qquad (3)$$

where h is the piezoelectric constant and c is the elastic stiffness. Considering the material constants to be complex, these equations can be used to derive the expression for the impedance for the thickness extensional resonance:

$$Z = \frac{l}{i\omega A \varepsilon_{33}^S} \left(1 - \frac{k_t^2 \tan\left(\dfrac{\omega}{4f_p} \right)}{\dfrac{\omega}{4f_p}} \right), \qquad (4)$$

where the electromechanical coupling constant k_t and the parallel resonance frequency f_p are given by

$$k_t^2 = \frac{\varepsilon_{33}^S h_{33}^2}{c_{33}^D} \qquad 2f_p = \frac{1}{l} \sqrt{\frac{c_{33}^D}{\rho}}$$

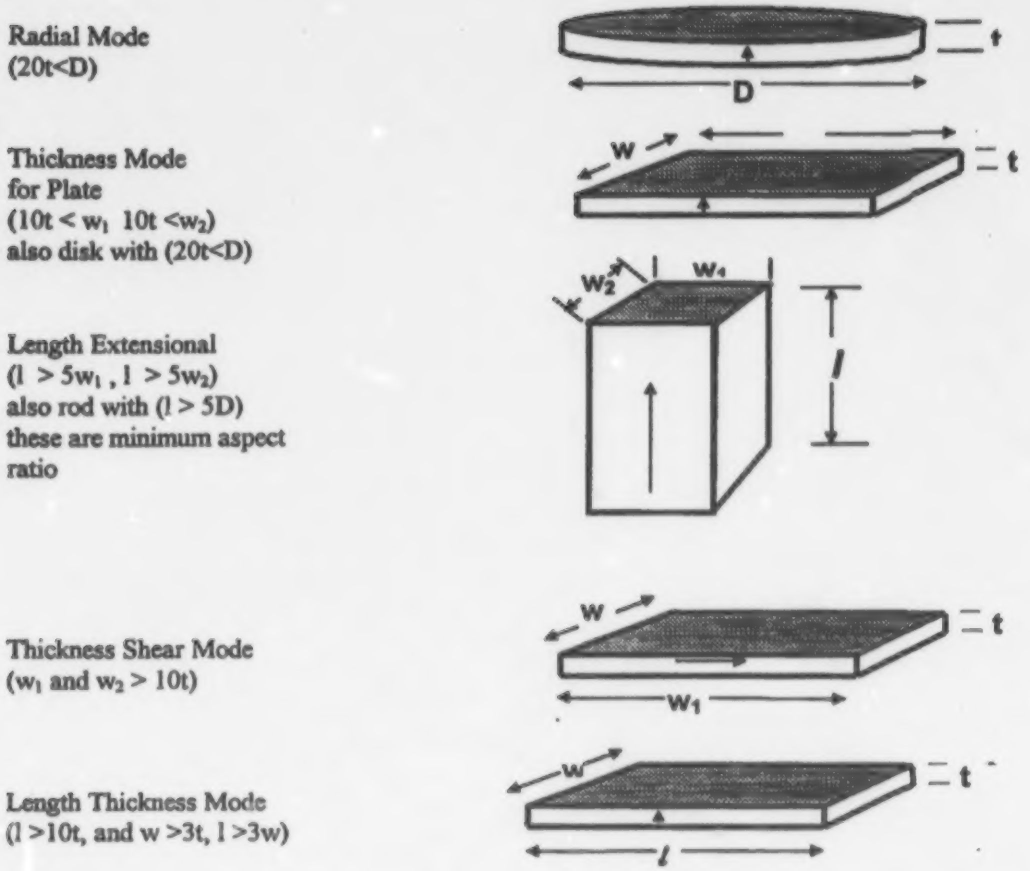
Radial Mode
(20t<D)
t
D
Thickness Mode
for Plate
(10t < w1 10t <w2)
also disk with (20t<D)
w
t
Length Extensional
(l > 5w1 , l > 5w2)
also rod with (l > 5D)
these are minimum aspect
ratio
W2
W1
l
Thickness Shear Mode
(w1 and w2 > 10t)
w
t
W1
Length Thickness Mode
(l >10t, and w >3t, l >3w)
w
t
l

Figure 2. The geometry and poling direction for the five most common modes of piezoelectric resonators for materials characterisation. Note: The radial mode also has a thickness resonance and the length extensional resonator may also be of the form of a long rod.

The material constants around the fundamental resonance can be found by fitting expression (4) to the resonance curves shown in Figure 3. This is done by using Smits' method[11] which uses impedance values at three frequencies of which one is chosen near the frequency at which the resistance is a maximum and the other two are chosen to be above and below the resonance. Two of the points plus an initial guess for the elastic constant, using a relationship between the mechanical Q and the resonance bandwidth described by Land et al[15], are used to calculate electromechanical coupling constant and the permittivity. Using the coupling constant and a third point, a new elastic constant is calculated and the process is repeated until convergence. A disadvantage of Smits' technique is that impedance values can vary by several orders of magnitude around resonance and so care must be taken that the measuring

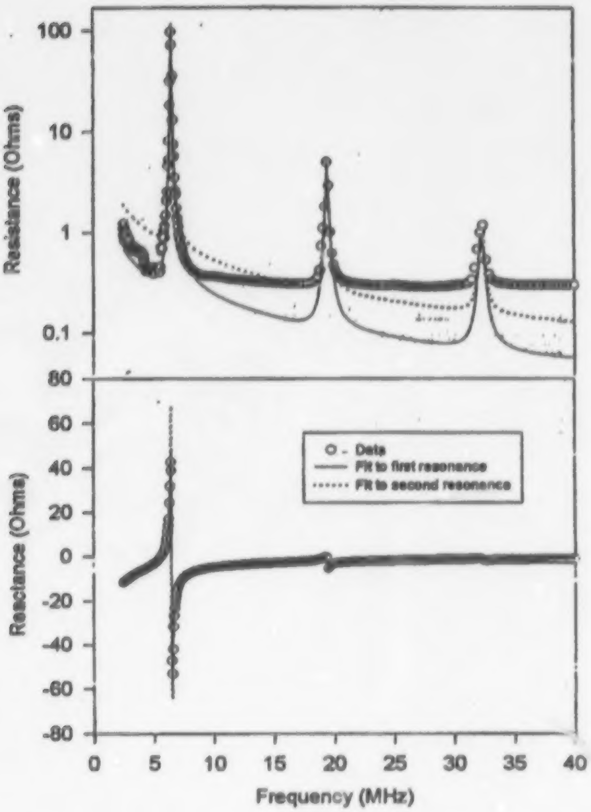

Figure 3. The resistance and reactance data of the thickness extensional resonance and the fit to the first and second resonance peaks for Motorola 3203HD ceramic. The resistance is plotted on a logarithmic scale.

instrument is not overloaded and that the impedance values are carefully determined. The values of the material constants will depend to some extent on the points chosen to analyse the spectrum but this dependence can be corrected by repeating the analysis with a different choice of points followed by an averaging of the results. Alemany et al[14] have looked at procedures to obtain convergence during iterations. A non-iterative technique to determine the material constants has been presented by Sherrit et al[12]. This technique requires frequency data around resonance and impedance data away from resonance. Although the disadvantage associated with Smits' method is removed, this method is less accurate when dispersion in the material constants is significant. Smits' technique can be used to find the material constants that determine the thickness, thickness shear, length and length thickness modes of resonance. The complex material constants for the radial extensional resonance can be found using a method put forward by Sherrit et al[13]. A commercial software is now available for carrying out the analysis of the resonance curves[16]. By analysing all the different modes of resonance the complete set of material constants can be determined around the resonance considered. An example of such a determination for the Motorola 3203 HD PZT ceramic is shown in Table 1[17].

DISPERSION

The effects of dispersion can be studied by determining the material constants at the fundamental frequency of resonance and at higher resonances. Figure 3 shows that the fit obtained by using the material constants around the fundamental frequency does not agree well with the impedance curve around the second resonance and vice versa. This method has been used to study dispersion in the Motorola 3203 HD ceramic by Sherrit et al[17]. Thus, the material constants can be determined for frequencies required by the applications engineer as long as a reasonable resonance curve can be experimentally determined near the required frequencies. In some cases it is possible to express the real and imaginary parts of the material constant as a polynomial in frequency, as shown by Sherrit et al for piezoelectric polyvinylidene difluoride – tetrafluoroethylene (PVDF-TrFE) copolymer[18]; the applications engineer can use the polynomials to find the material constants at a desired frequency.

EQUIVALENT CIRCUIT

In designing devices it is sometimes useful to have an equivalent electrical circuit to represent the material. Currently the most widely used equivalent circuit to represent a piezoelectric vibrator in the thickness mode is the Van Dyke circuit, which is shown in Figure 4(a). This circuit uses four real circuit parameters, C_0, C_1, L_1 and R_1 to represent the impedance of a free-standing piezoelectric resonator around resonance. However the impedance, expressed by equation (4), contains six material constants (the real and imaginary parts of the permittivity,

Table 1: The reduced matrix of Motorola 3203HD PZT including the electromechanical coupling determined at the fundamental resonance of each mode.

Material Constant	Model	Frequency (kHz)	Value		% Standard Deviation	
			Real	Imag	Real	Imag
s_{11}^E (m^2/N) x10^{-11}	LTE	71.5	1.56	-0.030	0.63	5.2
s_{11}^E (m^2/N) x10^{-11}	RAD	150.9	1.55	-0.032	0.45	2.8
s_{11}^E (m^2/N) x10^{-11}	Average		1.56	-0.031		
s_{12}^E (m^2/N) x10^{-11}	RAD	150.9	-0.420	0.012	3.90	4.9
s_{13}^E (m^2/N) x10^{-11}	Calculated	Smits' formula	-0.821	0.034	N/A	N/A
s_{13}^E (m^2/N) x10^{-11}	Calculated	Matrix inversion	-0.825	0.017	N/A	N/A
s_{33}^E (m^2/N) x10^{-11}	LE	199	1.89	-0.034	1.0	0.78
s_{55}^E (m^2/N) x10^{-11}	TS	2730	3.92	-0.13	2.9	4.3
s_{66}^E (m^2/N) x10^{-11}	Calculated	IEEE formula	3.96	-0.086	N/A	N/A
c_{33}^D (N/m^2) x10^{11}	TE	6390	1.77	0.023	2.0	11
d_{13} (C/N) x10^{-12}	LTE	71.5	-297	9.7	0.70	7.1
d_{13} (C/N) x10^{-12}	RAD	150.9	-293	10	0.68	5.8
d_{13} (C/N) x10^{-12}	Average		-295	9.9		
d_{33} (C/N) x10^{-12}	LE	199	564	-15	3.1	17
d_{15} (C/N) x10^{-12}	TS	2730	560	-30	4.6	11
ε_{11}^T (F/m) x10^{-8}	TS	2730	2.14	-0.13	0.44	6.8
ε_{33}^T (F/m) x10^{-8}	RAD	150.9	3.06	-0.11	1.1	6.5
ε_{33}^T (F/m) x10^{-8}	LT	71.5	2.83	-0.061	1.9	9.4
ε_{33}^T (F/m) x10^{-8}	Average		2.95	-0.083		
ε_{33}^S (F/m) x10^{-8}	TE	6390	1.06	-0.053	2.0	4.2
k_{33}	LE	199	0.763	-0.0029	0.52	45
k_{13}	LTE	71.5	0.447	-0.0054	0.90	16
k_{15}	TS	2730	0.611	-0.0034	3.1	37
k_p	RAD	150.9	0.706	-0.0062	0.45	6.1
k_t	TE	6390	0.536	-0.0050	0.46	12

the coupling constant and the elastic stiffness) and therefore six parameters are needed to describe the impedance when losses are significant. We have proposed an alternative circuit model based on the lossless resonator model suggested by Butterworth[19] and Cady[20] and shown in Figure 4(b). The model contains three circuit elements C_0, C_1 and L_1 and we modify the model by assuming that each of these circuit elements be considered to be complex. The circuit now has six parameters and some unique features that make it an ideal model for representing the electrical characteristics of an unloaded piezoelectric resonator. We have shown[21] how the values of the complex circuit elements can be calculated from the complex material constants and vice versa and that spectra obtained by using the complex circuit model give very good agreement with corresponding experimental spectra for high Q as well as low Q materials.

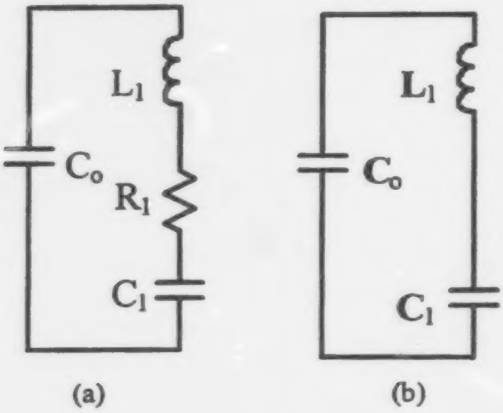

Figure 4. (a) The Van Dyke circuit model; the values of the circuit elements are real. (b) The proposed circuit model; the values of the circuit elements are complex.

QUASISTATIC EXPERIMENTS

The set of equations (1) is used to interpret most quasistatic measurements. Two experimental conditions may be used to simplify the measurement. If the stress is set to zero (i.e. the sample is free to expand unhindered), the equations are no longer coupled and the strain and the electric displacement can be measured as a function of the electric field. Similarly, if the electric field is zero (the short circuit condition), the strain and the dielectric displacement can be measured as a function of the stress. These uncoupled relationships are shown in Table 2.

Table 2. The quasistatic measurements that can be made in the 33 direction (along the poling axis) on a piezoelectric material with one of the independent variables set to zero.

Boundary Condition	Simultaneous Equations	
T = 0 (unclamped) Apply E - measure S and D	$S = dE$	$D = \varepsilon^T E$
E = 0 (short circuit) Apply T - measure S and D	$S = s^E T$	$D = dT$

MEASUREMENT OF THE PIEZOELEECTRIC CONSTANT AND THE PERMITTIVITY AS A FUNCTION OF THE APPLIED ELECTRIC FIELD

The variation of the piezoelectric constant d and the permittivity ε as a function of the applied electric field can be carried out under two different experimental situations: (a) quasistatic experiments, which gives the value of the constants under near DC conditions, and (b) resonance experiments, which yield the material constants at the appropriate resonance frequency. The difference in the significance of these two types of measurement can be understood with reference to Figure 5. The main curve in the figure shows a typical curve that is obtained when a varying electric field, below the coercive field, is applied to a piezoelectric material and the resultant strain is measured. A measurable hysteresis is found and this is due to the reversible and irreversible domain wall motions that are characteristic of ferroelectric materials. Under a large electric field the domain walls move to maintain a minimum in the domain energy and some of the domains engulf other domains or change shape irreversibly, which contributes to the net strain and polarisation. The onset of irreversibility in such materials has been studied by Zhang et al[22] who found that each material has a plateau region where the permittivity and the piezoelectric constant were independent of field and they attributed this field independence to reversible domain motion. In the case of resonance measurements, the AC measurement signal is small, well below the plateau region found by Zhang et al, and so the measurements correspond to reversible domain motions. Such AC resonance measurements have been carried out with an applied DC bias field to determine the variation of the material constants as a function of the DC field. The illustrative diagram in Figure 5 shows clearly that the slopes of the two types of measurement are different and therefore the material constants found from the two types of measurements cannot be the same. This discussion underlines the importance of determining the material constants under conditions appropriate for any particular application.

The quasistatic measurements were carried out with an optical lever experiment[23] that allows the strains in the 1 or 3 directions to be determined directly as a function of an applied dc field in the 3 direction whose maximum value exceeds the reversibility limit. The dielectric displacement was measured at the same time. Results[24] for the case of Motorola PZT 3203HD ceramic are shown in Figure 6 and they exhibit the typical hysteresis behaviour of ferroelectric materials. The shapes of the curves depend on the size and the change in the electric field.

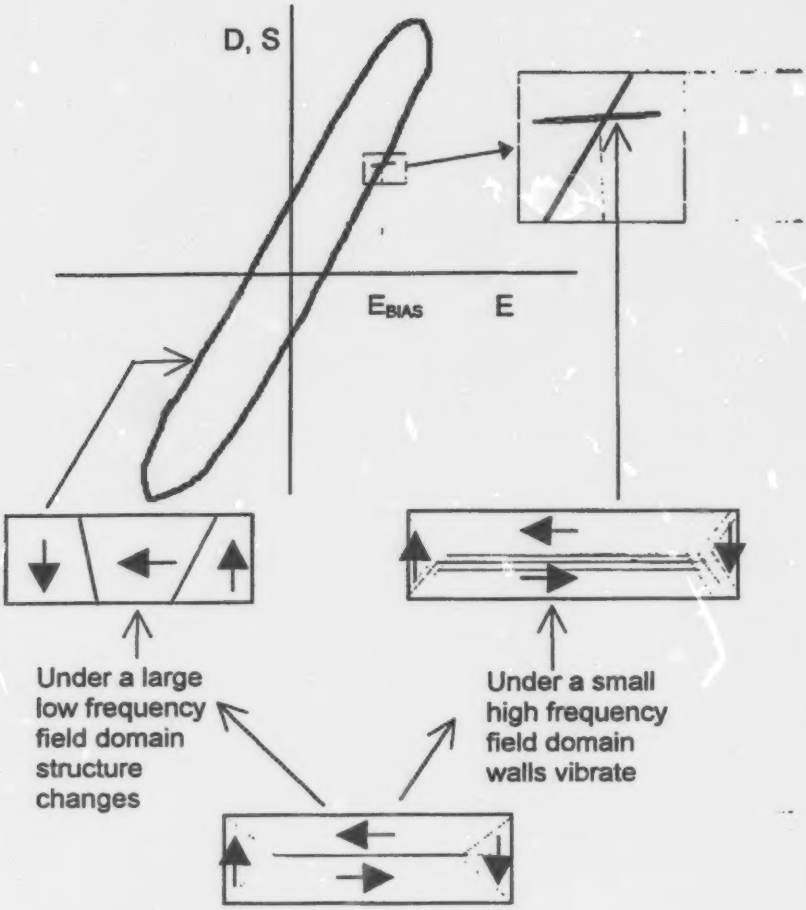
D, S
E_{BIAS}
E
Under a large low frequency field domain structure changes
Under a small high frequency field domain walls vibrate

Figure 5. The relationship between the reversible and irreversible domain motion and the resultant strainor electric displacement as a function of the electric field.

If the maximum applied field is kept below the coercive field (0.5 to 1.0 MV/m for the Motorola ceramic), the non-linearities and the hysteresis are much less significant as can be seen in the curves in Figure 7. The figures show curves (loops) for six different maximum applied fields in each case and it can be seen that the slope and the hysteresis increase as the maximum field of the loop is increased. Since the hysteresis is now less significant, an average slope can be used to determine the material constants. The piezoelectric constants and the permittivity are plotted as a function of the maximum applied field in Figure 8. Although these constants represent average values, they would be useful, for example, to an actuator designer who is mainly interested in the strain level as a function of the applied field. The piezoelectric charge coefficients and the permittivity are found to vary linearly as a function of the applied electric field. These variations can be expressed as follows:

$$S = d_{33}E + q_{33}E^2 \qquad \text{and} \qquad D = \varepsilon_{33}E + (\kappa_{33}/2)E^2, \qquad (5)$$

where q_{33} is the electrostrictive coefficient and κ_{33} is the second order dielectric constant which we call the electrodielectric constant. It should be noted that κ_{33} represents the contribution which is caused by the coupling of the polarisation to the electric field.

The non-linear properties of the piezoelectric materials have also been studied by carrying out AC resonance measurements under DC bias[24] but, as explained above, the material constants obtained by these measurements correspond to reversible domain motions and are different from those obtained from the quasistatic measurements. The difference is illustrated in Table 3 which gives the values of the electrostrictive and electrodielectric coefficients obtained from the two types of measurements.

As pointed out above, the non-linearities are much less significant if the applied fields are below the coercive field so that a greater range of linear behaviour can be found with materials with higher coercive fields. For example, the piezoelectric polymer PVDF-TrFE has properties[25] that are relatively independent of the applied electric field for fields up to ± 0.4 MV/m; however this copolymer exhibits a much greater dispersion than does the ceramic PZT. This shows that the device designer needs to choose his material carefully depending on the performance requirements of the device.

STRESS AND TEMPERATURE DEPENDENCE OF THE DIRECT PIEZOELECTRIC CHARGE COEFFICIENT

The relationship between the dielectric displacement D and the stress T has also been studied[26]; this corresponds to the second experimental condition shown in Table 2 and the results show how the piezoelectric d constant varies as a function of the applied stress and the temperature of the specimen. The experimental arrangement has been described earlier[7,27]; the sample is compressed by a stress T and the resulting piezoelectric current is measured by a low input impedance electrometer operating in the current mode. The sample temperature can be set by a heat lamp and it can be measured by means of a thermocouple.

Table 3: The electrostriction and electrodielectric constants determined from the quasi-static and DC biased resonance spectra.

Non linear Coefficient Real Part	Quasi-static Maximum E_{DC}=0.39MV/m f < mHz	Length thickness Resonator E_{DC}=0.39MV/m f =72 kHz	Length Resonator E_{DC}=0.016MV/m f =572 kHz
κ'_{3} (Fm/V)	$7.3\text{x}10^{-14}$	$1.8\text{x}10^{-14}$	$1.4\text{x}10^{-14}$
q_{3} (m^2/V^2)	$9.5\text{x}10^{-16}$	N/A	$1.4\text{x}10^{-16}$
q_{1} (m^2/V^2)	$3.1\text{x}10^{-16}$	$5.0\text{x}10^{-17}$	N/A

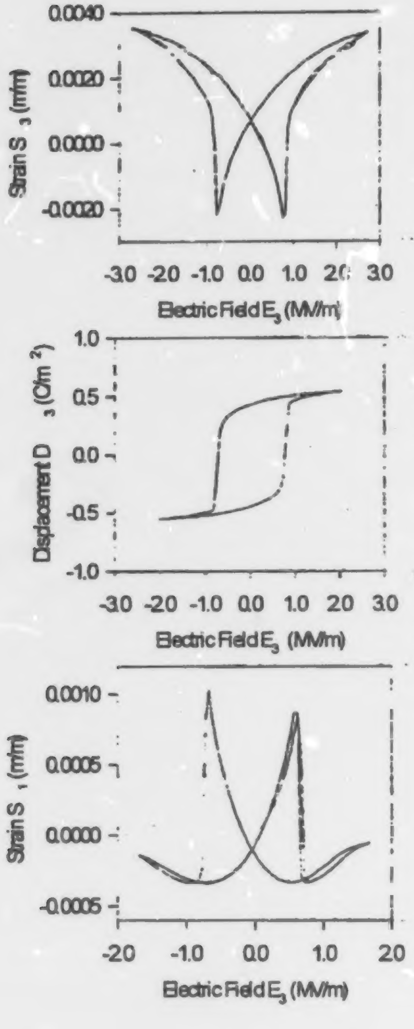

Figure 6. The quasistatic field dependence of the strain S_3, the dielectric displacement D_3 and the strain S_1 as a function of electric field to field levels above the coercive field.

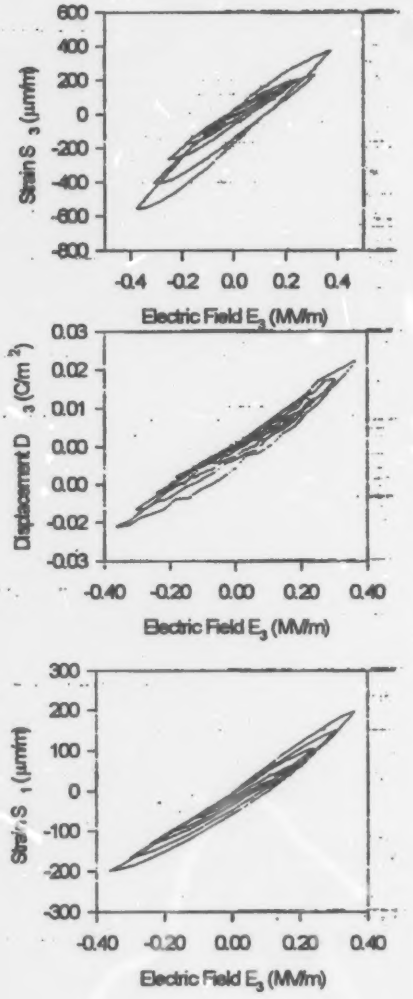

Figure 7. The quasistatic field dependence of the strain S_3, the electric displacement D_3 and the strain S_1 as a function of field to field levels below the coercive field. In each case six loops with different maximum fields are shown.

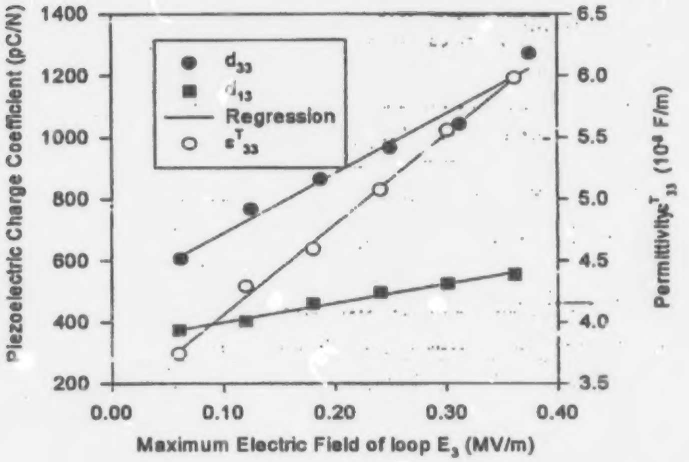

Figure 8. The quasistatic field dependence of the effective piezoelectric constant and permittivity as a function of the field up to field levels below the coercive field. The slopes give the higher order material coefficients.

The application of a steadily increasing stress generates a polarisation that produces a current, I, through the electrometer. If the stress is increased as a function of time, t, the current produced is directly proportional to the piezoelectric charge coefficient and the relationship is given by

$$D_3 = \frac{1}{A}\int I\partial t = d_{33}T_3 \qquad (6)$$

where A is the electroded area of the sample. The technique can determine an integrated average value of the charge coefficient up to the stress level T_3, as defined by

$$d_{33}(T_3) = \frac{\int I\partial t}{AT_3}. \qquad (7)$$

Sherrit et al[7] have used this technique to measure the charge coefficient, d_{33}, for a Channel 5804 PZT ceramic as a function of the applied stress and the temperature and their results are shown in Figure 9. At room temperature, the application of a stress of around 70 MPa increases the value of d_{33} by a factor of about two, once again emphasising the importance of the non-linear effects. The shape of the d_{33} curves as a function of stress appears to flatten and become more linear as the temperature is increased.

THE PIEZOELECTRIC RESPONSE TIME

The curves shown in Figure 9 were measured under increasing stress and hysteresis was observed when the stress was ramped down. This suggested that the results would depend on the ramp rate of the stress and that time dependent effects were involved. In order to study the response time, Sherrit et al[26,27] applied a step stress with a rise time of less than 10 seconds and measured the current as a function of time elapsed after the application of the stress. The step stress resulted in a step increase in the current and, most interestingly, the current then decayed over a period of time, almost exactly following the inverse relationship I = k/t. Any mechanical relaxation in the experimental system or any relaxation in the in the elastic constant would only have resulted in a negative current. Sherrit et al were therefore able to attribute the continued current to the continued generation of charges in the specimen which is likely to result from slow changes to the domain structure in the specimen, particularly the 90° reorientation of domains, which require atomic motion and are therefore expected to be slower than the 180° reorientation of domains that require only a shift in the charge centre of the domain. When a step stress is applied, there is a near instantaneous generation of charge due to 180° domain changes and some 90° domain changes and this is followed by the slow switching of other 90° domains that gives rise to the observed continued generation of charge and slow decay in the current. Both the fast and the slow domain changes contribute to the piezoelectric charge coefficient and, using equation (7), this can now be expressed as

$$d_{33} = d_{33}^{0} + d_{33}^{t}\, ln(t) = d_{33}^{0} + \frac{\int \frac{k}{t} \partial t}{AT_3}, \qquad (8)$$

where $d_{33}^{t} = k/AT_3$ is a constant that describes the time dependence of the current as well as that of d_{33}.

From the point of view of applications, it is important to note that the observed time dependence results in a frequency dependence for the piezoelectric charge coefficient. A high frequency signal will produce a charge that, to a first order, is proportional to d_{33}^{0}, while a low frequency will produce a charge that has contributions from both d_{33}^{0} and d_{33}^{t}.

Figure 10 shows the variation of the charge coefficient, d_{33}, for the Channel PZT 5804 PZT ceramic as a function of the temperature and the time after the imposition of the stress signal. The slope of the curves, which determines d_{33}^{t}, is seen to increase with increasing temperature and Sherrit et al[26,27] were able to obtain a roughly linear Arrhenius plot of $\ln(d_{33}^{t} T)$ as a function of inverse temperature, $1/T$, corresponding to the expression

$$d_{33}^{t} = \frac{d_{33}^{t0}}{T} exp\left(\frac{-E_a}{KT}\right), \qquad (9)$$

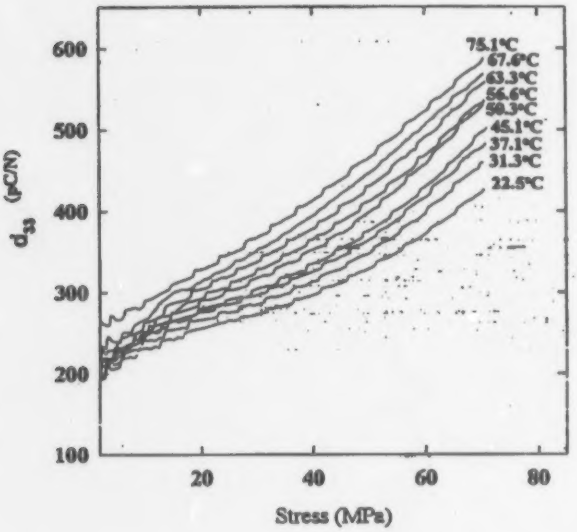

Figure 9. The value of d_{33} as a function of stress and temperature for a Channel 5804 PZT ceramic.

where E_a is an average activation energy for domain motion, d_{33}^{t0} is a pre-exponential factor and K is Boltzmann's constant. They found an average activation energy of 0.39 eV for the Channel 5804 PZT and their measurements on a variety of PZT types yielded activation energies in the range from about 0.2 eV to 0.7 eV. The time dependence coefficient d_{33}^{t} was found to be independent of the stress level while the coefficient k, which describes the time dependence of the current due to the generation of charge, was found to be linearly dependent on the stress T_3 up to 60 MPa..

FUTURE WORK

We are currently setting up to carry out the resonance measurements with the specimen in a thermally controlled temperature. This will enable us to determine the full matrix of material coefficients as a function of temperature.

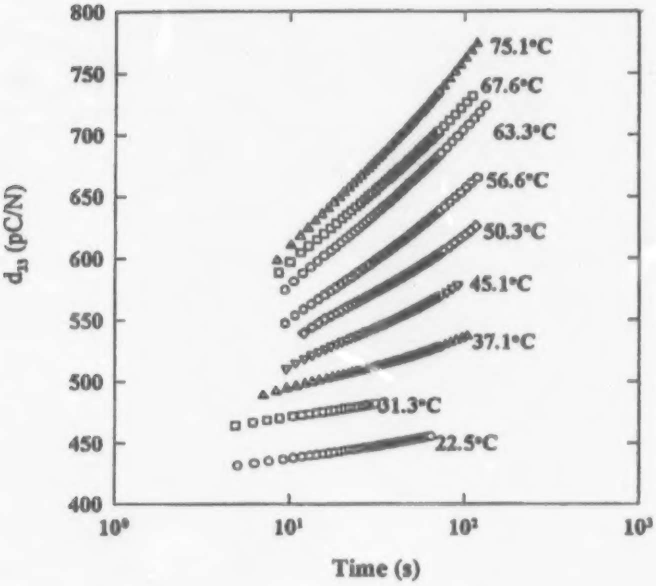

Figure 10. The value of d_{33} as a function of the time after the application of a stress step.

CONCLUSIONS

The experimental results reviewed in this paper clearly show that piezoelectric materials have significant non-linear effects. It follows that the material constants measured under the application of small signals, which are the parameters usually provided by the manufacturers, are not sufficient to predict the behaviour of the materials when large signals are applied, as, for example, in actuators and acoustic projectors. The device designer requires material constants that are measured under the conditions which prevail during the operation of the device, and this paper has reviewed some of the experiments that are available to make such measurements.

ACKNOWLEDGEMENT

We gratefully acknowledge funding support from the Defence Research Establishment Atlantic and the Academic Research Programme of the Department of National Defence, Canada as well as support from the Office of Naval Research, USA given through the Naval Undersea Warfare Centre, Newport, RI, USA.

REFERENCES

[1] A.F. Devonshire, *Phil. Mag. Supp.*, **3**, 85-130 (1952).

[2] W.P. Mason, Physical Acoustics and the Properties of Solids, D. Van Nostrand Co. Inc., (Princeton, New Jersey (19)

[3] IEEE Standard on Piezoelectricity (1987): [ANSI/IEEE Standard 176-1987]

[4] D.A. Berlincourt, D.R. Curran and H. Jaffe, Physical Acoustics I Part A: Chapter 3, pp.169-270, Academic Press, Editor: W.P. Mason.

[5] A.H. Meitzler, H.M. O'Bryan and H.F. Tiersten, *IEEE Trans.on Sonics and Ultrasonics*, **SU-20**, 233-239 (1973).

[6] R. Holland, *IEEE Trans. On Sonics and Ultrasonics*, **SU-14**, pp.18-20 (1967).

[7] S. Sherrit, Losses, Dispersion and Field Dependence of Piezoelectric Materials, Ph.D Thesis at Queen's University, Kingston, Ontario, Canada (January 1997).

[8] R. Holland and E.P.Eernisse, *IEEE Trans. On Sonics and Ultrasonics*, **SU-16** (4), pp.173-181 (1969).

[9] H. Ohigashi, T. Itoh, K. Kimura, T. Nakanishi and M. Suzuki, *Jap. J. Appl. Phys.*, **27**, pp.354-360 (1988).

[10] T. Tsurumi, T. Ichihara, K. Asaga and M. Daimon, *J. Amer. Cer. Soc.*, **73(5)**, pp.1330-1333 (1990).

[11] J.G. Smits, *IEEE Trans. Sonics and Ultrasonics*, **SU-23**, pp.393-402 (1976).

[12] S. Sherrit, H. D. Wiederick and B.K. Mukherjee, *Ferroelectrics*, **134**, pp.111-119 (1992).

[13] S. Sherrit, N. Gauthier, H.D. Wiederick and B.K. Mukherjee, *Ferroelectrics*, **119**, pp.17-32 (1991).

[14] C. Alemany, A.M. Gonsalez, L. Pardo, B. Jimenez, F. Carmona and J. Mendiola, *J. Phys. D: Appl. Phys.*, **28**, pp. 945-956 (1995).

[15] C.E. Land, G.W. Smith and C.R. Westgate, *IEEE Trans. On Sonics and Ultrasonics*, **SU-11**, pp.8-19 (1964).

[16] PRAP (Piezoelectric Resonance Analysis Programme) software available from TASI Technical Software, 174, Montreal Street, Kingston, Ontario K7K 3G4, Canada.

[17] S. Sherrit, H.D. Wiederick and B.K. Mukherjee, Medical Imaging 1997: Ultrasonic Transducer Engineering (SPIE Proceedings Volume 3037), pp.158-169 (1997).

[18] S. Sherrit, J.E. Haysom, H.D. Wiederick, B.K. Mukherjee and M. Sayer, Proc. Of the Tenth Int. Symp. On Applications of Ferroelectrics: ISAF'96, pp.959-962, IEEE, Piscataway, NJ, USA (1996).

[19] S. Butterworth, *Proc. Phys. Soc.*, **27**, pp.410-424 (1915).

[20] W. G. Cady, *Proc. IRE*, **10**, pp.83-114 (1922).

---

[21] S. Sherrit, H.D Wiederick, B.K. Mukherjee and M. Sayer, *J. Phys. D: Appl. Phys.*, **30**, pp.2354-2363 (1997).

[22] Q.M. Zhang, W.Y. Pan, S.J. Jang and L.E. Cross, *J. Appl. Phys.*, **64**, pp.6445-6451 (1988).

[23] H.D. Wiederick, S. Sherrit, R.B. Stimpson and B.K. Mukherjee, *Ferroelectrics*, **186**, pp.25-31 (1996).

[24] S. Sherrit, H.D. Wiederick, B.K. Mukherjee and M. Sayer, Smart Structures and Materials 1997: Smart Materials Technologies (SPIE Proceedings Volume 3040), pp.99-109 (1997), SPIE, Bellingham, Washington, USA.

[25] S. Sherrit, J.E. Haysom, H.D. Wiederick, B.K. Mukherjee and M. Sayer, Proc. Of the 10th Int. Symp.on Applications of Ferroelectrics: ISAF '96, pp.959-962, IEEE, Piscataway, NJ, USA (1996).

[26] S. Sherrit, R.B. Stimpson, H.D. Wiederick and B.K. Mukherjee, Smart Materials, Structures and MEMS (SPIE Proceedings Volume 3321), pp.74-81 (1996), SPIE, Bellingham, Washington, USA.

[27] S. Sherrit, D.B. Van Nice, J.T. Graham, B.K. Mukherjee and H.D. Wiederick, Proc. of the 8th Int. Symp. on Applications of Ferroelectrics: ISAF '92; pp. 167-170, IEEE, Piscataway, NJ, USA (1992).

#511911 (37)

APPLICATION EXAMPLES OF EMAT GENERATED HORIZONTALLY POLARIZED SHEAR WAVES FOR ULTRASONIC INSPECTION

Julie Gauthier, Ahmad Chahbaz and Raymond Bergeron

Tektrend International, Inc.

2113A S-Régis Blvd., Montréal, Québec, Canada

ABSTRACT

Some inspection applications can be greatly improved by the use of shear horizontal waves. In this work, various examples of the uses of ultrasonic horizontally polarized shear (SH) are presented. The ultrasonic waves used in all of the applications examples were generated using Electromagnetic Acoustic Transducers (EMATs) couplantless technology. The inspection were performed using either the traditional bulk inspection or with the non-conventional guided wave inspection methodology. The purpose of the review paper is to demonstrate both the advantages and disadvantage of SH waves inspection performed with the EMAT probes. Individual application examples include a brief description of the problem; the inspection methodology using SH waves and finally some results and comments of SH waves inspection. The examples investigated include methodology for defect detection and integrity assessment.

SH WAVES

SH waves have a propagation displacement, characterized by a null normal displacement on the surface of the material and a particle displacement perpendicular to the propagation direction and always parallel to the surface Auld (1). This feature provides a number of significant advantages over conventional ultrasonic waves. These waves are insensitive to loading; therefore there are no leakage losses in acoustic media such as tar, coatings and water. They do not suffer mode conversion at defect interfaces, a fact, which enhances received signal quality since the reflected signals are not encumbered with the noise of parasitic conversion signals and there is no conversion loss of energy. The displacement of SH waves is illustrated in Fig. 1, and compared to the SV (shear vertical) wave which as an oscillation component having an angle to the surface.

EXCITATION OF SH WAVES

SH waves were generated in the structure using an EMAT (2, 3). Due to the difficulty of excitation and generation of SH waves, an EMAT is an excellent device, providing the capability to match the excitation force with a specific particle motion. When SH-waves are introduced using these transducers, a number of experimental variables that could not be controlled with specially cut piezoelectric transducers can be selected through frequency adjustment. Frequency control permits wave modes to be generated individually in a given structure. Another advantage of using EMATs is that they do not require a liquid couplant, making it simple to scan the inspection structure. SH wave inspection scans cannot be performed with piezoelectric transducers since they require a viscous couplant to generate horizontally polarized shear oscillations in the material. EMATs can also generate SH-waves over layers of rust or dirt of thickness less than 1-2 mm.

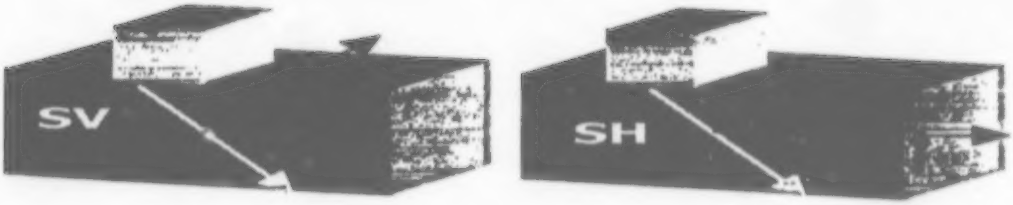

Figure 1 Shear oscillation in material for Shear Vertical (SV) and Shear Horizontal (SH) waves

GUIDED WAVE INSPECTION

SH can propagate as plate waves and be used for guided wave inspection. These waves can propagate in plate-like structures of a few wavelengths thick or even of the order of one wavelength. They are, as Lamb waves, two dimensional stress waves in infinite plate structures whose surfaces are free of stresses. Their propagation characteristics are tailored to the geometry of the structure inspected (the elastic wave-guide). Their elastic motion covers the whole thickness of the structure (wave-guide) due to the guiding effect of the inner and outer surfaces of the pipe. SH–plate waves have small divergence losses and are attenuated less rapidly than bulk waves, resulting in longer propagation ranges than those for bulk waves with the same frequency and higher sensitivity for defect detection. Therefore, SH-plate waves can propagate for distances of several meters in pipes having a thickness of several millimeters. Furthermore, SH-plate waves can follow curvature thus enabling inspection along bends and other irregular geometry.

Unlike longitudinal and shear bulk waves, SH-plate waves offer improved inspection potential due to the availability of a host of different propagating modes, each with its own unique characteristics. Modes can therefore be selected to enhance detection of different types of defects such as cracks, holes, and corrosion. SH-plate waves were used (6-8) in various applications.

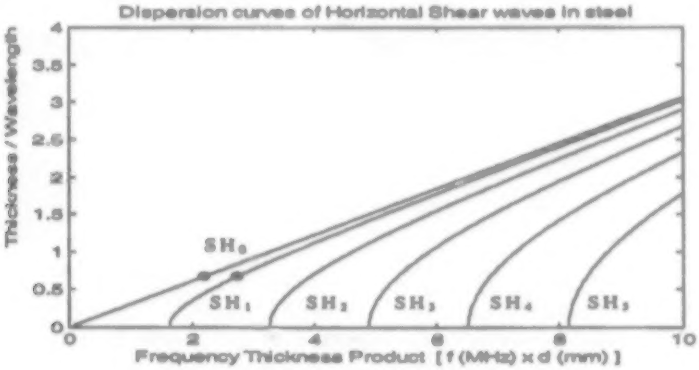

Figure 2 Dispersion curves for SH modes in plates

Prior to investigating detection and interaction of SH wave modes with defects in materials it was necessary to represent their theoretical dispersion curves. This was required to verify the group velocity of the pre-selected modes and to select the frequency on the dispersion curves at which these modes are excited. Dispersion curves depend upon material properties and specimen geometry; in this case the curves are for a steel plate. The curves in Fig. 2 describe the relation between the plate thickness to wavelength ratio versus the frequency-thickness product for the first 6 SH modes.

VERTICAL SPLIT HEAD IN RAILS

The vertical split head defect is a progressive longitudinal fracture in the head of the rail, where separation spreads vertically through the head at or near the middle of the head, Fig. 3.

It is difficult for traditional ultrasonic methods to detect such a defect because of the 0° degree inclination and the orientation in the rail head transversal direction. To improve railroad track inspection reliability a new inspection technique was develops using the oscillation propriety of SH waves. The method consists of generating a bulk Shear Horizontal wave generated with EMAT at 0°, with a shear oscillation polarization direction selected for maximum defect interaction. This polarized oscillation direction is perpendicular to the defect plane as shown in Fig. 4.

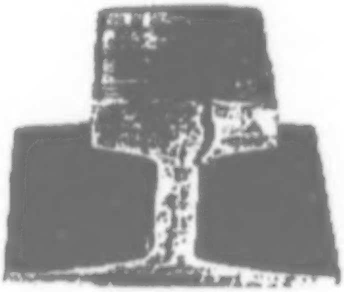

Figure 3 Vertical Split Head in rail

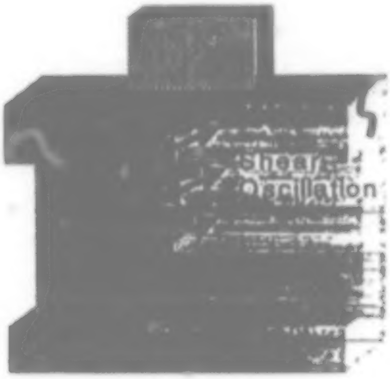

Figure 4 Shear horizontal oscillation in rail

The linearly polarized shear oscillation causes a particle displacement perpendicular to the faces of the vertical split head; therefor a SH wave launched in the railhead will be strongly attenuated if a Vertical Split Head. Fig. 5a shows the multiple back wall reflection of a bulk SH waves generated in a defect free rail, and, Fig. 5b shows the same wave launched in a rail having a vertical split head. In some cases the wave-defect interaction can cause the appearance of an extra reflection from the tip of the vertical split head. The disadvantage of such a method is the lack of a clear reflective indication of the presence of a defect, and loss of back wall could be attributed to other factor such as surface conditions enabling the generation of waves in the material.

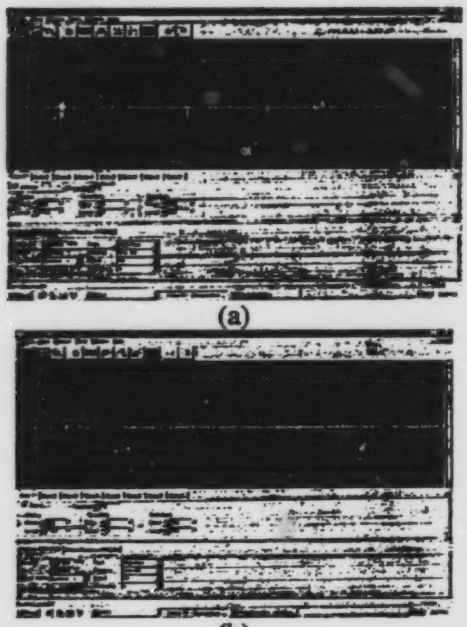
(a)

(b)

Figure 5 Back wall reflections from rail without VSH (a) and with VSH (b)

WELD INSPECTION

Weld inspection is one of the most common applications of UT inspection. Traditional shear vertical waves have demonstrated good and reliable defect detection ability, however the advantages of using SH wave lies in some specific cases of weld inspection. These would be in cases were the use of couplant is impossible because of rust or high temperature conditions or and in cases were mode conversion prevent reliable inspection results because of an excessive amount of spurious echoes.

In this short paper a simple cases is presented to demonstrate the capability of EMAT SH wave inspection. Inspection was performed on 25.4 mm thick steel plate having a weld in which two lack of fusion defects were introduced. This weld was inspected with a 45° shear vertical generated with a piezoelectric and a wedge and a 35° shear horizontal waves generated with an EMAT. The purpose of this inspection was to demonstrate the feasibility of weld inspection using SH waves. The EMAT probe not being optimized for this particular application the signal to noise ratio (SNR) is very low, but the lack of fusion could have been detected at high temperature without any couplant.

Fig. 7 shows the results of these two inspections. The B-Scans images reveal the presence of the two lack of fusion defect.

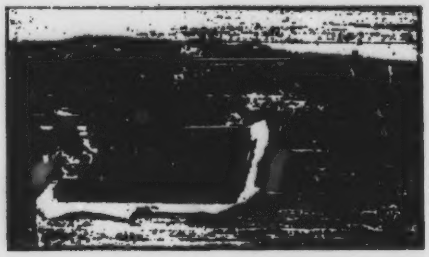

Figure 6 Ultrasonic inspection of weld using a manual scanner

PIPELINE INSPECTION

Defects found in these steel structures range from large discontinuities to small and subtle deterioration process defects such as stress corrosion cracking (SCC). Standard ultrasonic techniques applied for the non-destructive testing (NDT) of pipes include the straight beam method using longitudinal waves and the angle beam method using vertical shear (SV) waves. Although these methods have proven effective they do not have the advantages of SH waves, which could provide a sensitive, fast, and cost effective NDT method to detect, locate and validate discontinuities due to a variety of materials deterioration mechanisms. The application example for this inspection uses of SH guided waves to inspect circumferentially the pipe wall using a single transversal line (4,5).

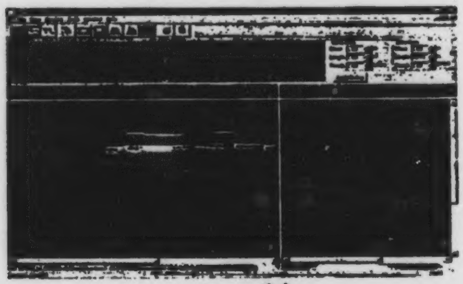

(a)

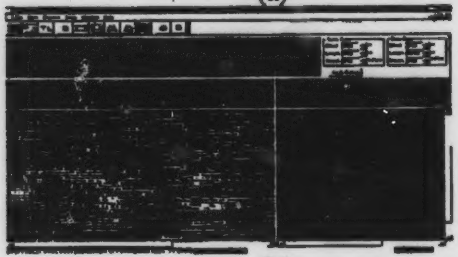

(b)

Figure 7 Detection of two lack of fusion in weld using piezoelectric (a) and using EMAT (b)

Defects were introduced in the cylindrical sample on the inside or outside surface of the pipe wall. After optimization of the power distribution of the modes two inspection modes were selected the SH$_0$ and SH$_1$ mode. These two modes were generated with a single bi-modal EMAT.

The first set of results, shown in Fig 8, are A-Scans of the signal in the pulse echo mode from three defects located in the same circumferential path for the SH$_0$ and the SH$_1$ modes. These defects had different depth ratios: 10% (D$_1$), 30% (D$_2$), and 50% (D$_3$). For the first graph, 6a, the EMAT was placed at 224 mm from the 30% defect (D$_2$) The defect caused a good reflection, however the energy loss was sufficient to reduce considerably the reflection from the second defect (D$_3$ - 50% depth ratio). The SH$_0$ was barely sensitive to the 10% (D$_1$) defect. For the SH$_1$ mode the probe was placed at 140 mm from the 10% defect and the two consecutive defects (30% at 540 mm and 50% at 760 mm) were also detected, although the SNR was reduced appreciably by the presence of D$_2$ This is shown in Fig. 8b. This representation demonstrates that SH guided waves are sensitive to the axial defect and that it is possible to detect a series of defects located in line with each other if the depth of the defect is smaller than the effective sound beam.

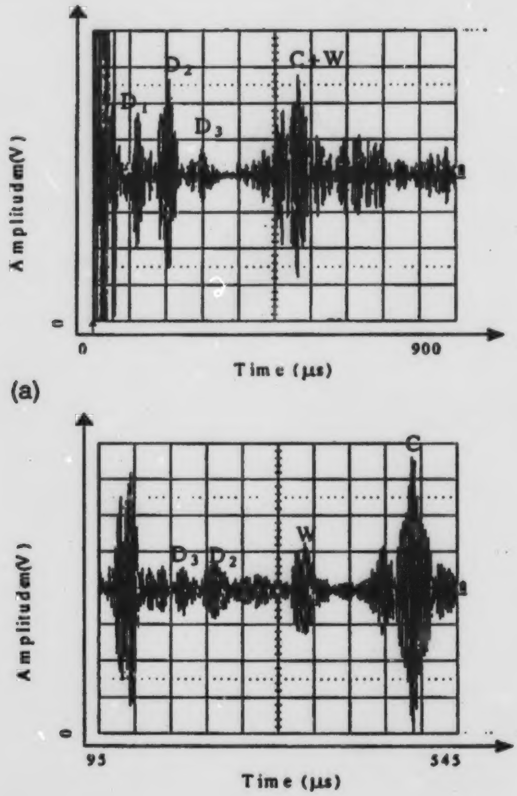

(a)

(b)

Figure 8 A-Scan display of propagation of (a) SH$_0$ mode and (b) SH$_1$ mode around pipe with three defects

The automated scans, as shown in Fig 9 were performed to assess the ability of the SH waves to discriminate between closely aligned defects. Using this setup EMAT probe can easily slide over rust layers, welds or imperfections and the coil surface can be adapted to surface curvature.

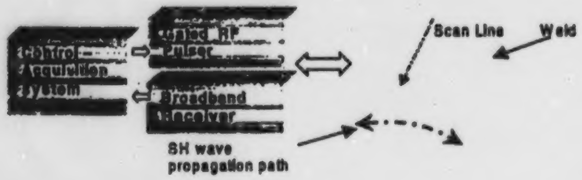

Figure 9 Inspection setup for pipeline scans

The scans were performed with the EMAT located at 300 – 400 mm from the defect region. The B-Scans are shown in a 3-D visualization view for which the amplitude is both color coded in a gray scale format and plotted in the z-axis. The scan is in the x direction, and the time of flight (propagation direction) is in the y direction. The B scan, Figure 10a, shows the image from a single defect scanned with the SH_0 mode. The second image, 10b, shows the image resulting from scanning three defects separated by 10 mm in the axial direction. The last one, 10c, shows the image resulting from three defects separated by 12.7 mm in the circumferential direction. These B-Scan images demonstrate that defects can be isolated in the axial direction but not as easily in the circumferential direction.

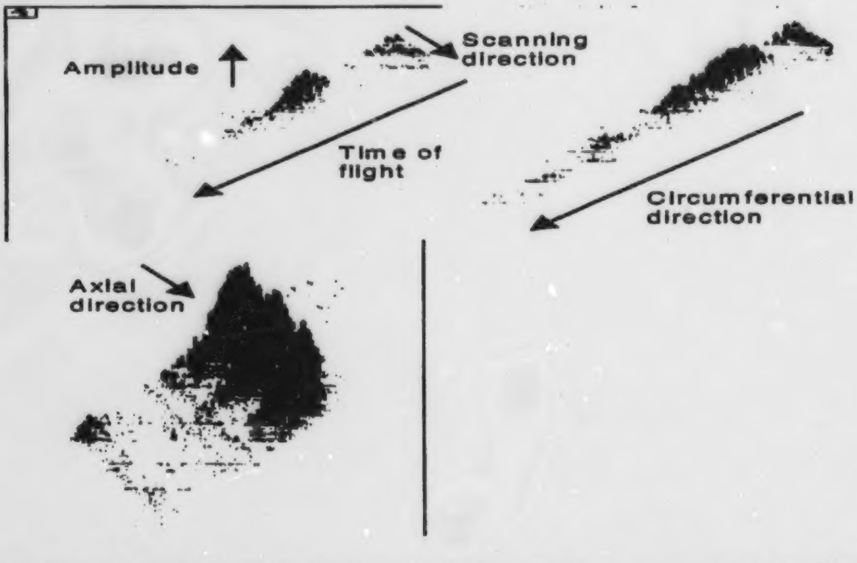

Figure 10 B-Scan image of (a) single defect, (b) four defects separated circumferentialy and (c) three defects separated axially

DISBOND DETECTION WITH GUIDED SHEAR WAVES

Another advantage provided by SH waves is their sensitivity to adhesion defects (6) such as disbond between coating and pipe wall, a site favorable to corrosion problems.
The basic idea in this work relies on inspection with selected horizontal shear wave modes with sufficiently high amounts of ultrasonic energy, which will ensure maximum interaction with the bond-line region to provide information of the adhesive adherent interface. Any material changes such as weak bonding or lack of adhesion between the two inspected layers will affect the propagating (or reflected) mode amplitude, velocity, frequency spectrum and time-of-flight. This measurement information can be then correlated to the bond quality.

For example, inspection of lap joints with guided shear waves in a pitch-catch setup is shown in Figure 11. A good bond will permit the excited wave mode to travel from sender to receiver probe producing relatively high RF signal amplitude. Low RF signals will be received for a disbond since the energy of the transmitted mode will not leak into the second joint. In a pulse-echo setup, the wave will travel from the sender/receiver probe producing relatively high amplitude RF signal when a disbond exists between the two bonded layers. This high amplitude corresponds to reflection from the disbonded region where the transmitted energy does not leak into the other plate but hits the free edge of the plate and reflects back to the transducer in the receive mode. In the case of a good bond, the amplitude is lower because we have leakage of the transmitted energy into the bonded plate.

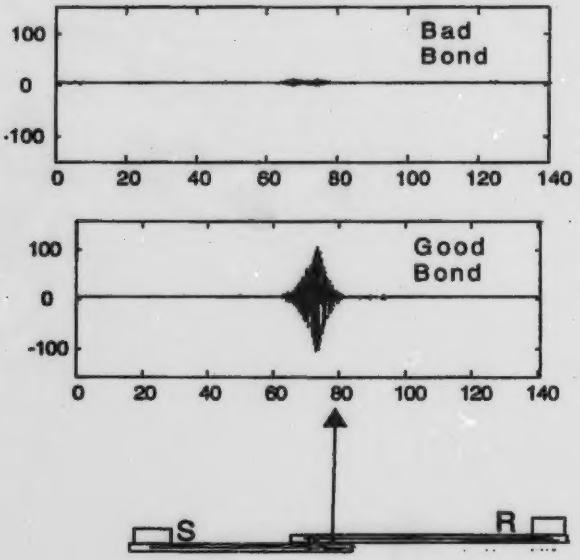

Figure 11 Lap joint transmission results from a) good bond b) bad bond

Disbond assessment in a simulated lap splice joint structure was obtained using pitch-catch setups. EMAT probes with a 3 mm wavelength were used to excite SH_0 and SH_1 at 1.044 and

1.305 MHz. In this test, a single line was scanned by automatically moving the transducer pair along the specimen to compare signals obtained through the well-bonded and disbonded areas. Figures 12a and 12b show the results of pitch-catch inspection. Signals from these two scans were collected and presented in a two-dimensional B-scan format. The well-bonded areas are characterized by high-amplitude signals (most of the energy is transferred to the second part of the joint). Poorly bonded areas resulted in low amplitude of the reflected signals (signals indicated by blue color) since little transfer of energy between the two parts of the joint takes place. To verify the guided wave results, the simulated specimen was also inspected using an automated eddy-current scanner. Disbonds were detected in the middle of the specimen by both techniques as shown in Figure 12a, 12b and 12c. The light gray colors in the eddy current image show good bonded regions while the dark gray represents areas having disbonds.

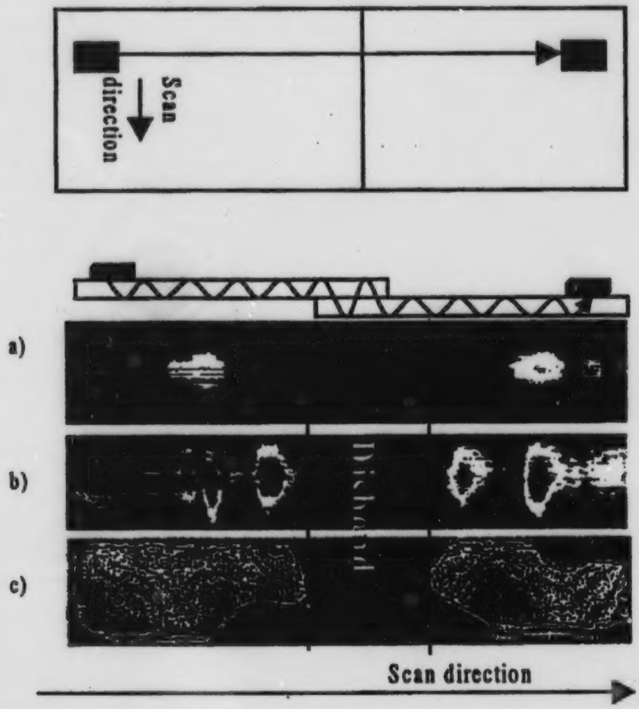

Figure 12 Inspection results of a disbonded sample using (a) SH_0 mode, (b) SH_1 mode and (c) using Eddy Current

CONCLUSION

The results found in this preliminarily work demonstrates the potential of using SH waves for rapid inspection of various structures. SH waves can be used in specific applications were SV waves are not suitable for reliable inspection. SH are best generated with EMAT probe; for guided wave generation the signal to noise ratio is excellent, however for bulk inspection efficient generation of SH waves require a careful design of the EMAT probe. Guided SH modes can be complimentary to one another for detection of defect and integrity assessment. EMAT technology to generate SH waves can be used for automated scans of either aluminum or steel large structures.

REFERENCES

1. B.A. Auld, Acoustic Filed and Waves in Solids" Vol. II, John Whiley & Sons, New York, 1973

2. R.B. Thompson, "Physical Principles of Measurements with EMAT Transducers", Physical Acoustics, Vol. XIX, Academic Presses, 1990, pp. 157-200

3. B.W. Maxfield and C. M. Fortunko, " The Design and Use of Electromagnetic Acoustic Wave Transducers", Material Evaluation, Vol. 41, November 1983, pp. 1399-140

4. H.J. Salzburger, "Long Range UT by Structural Ultrasonic Waves and Electromagnetic Acoustic Transducers (EMAT)", 16th Major International Ultrasonic conference and Exhibition presented by Hawksmere, 5-7 July, 1995, Edinburgh.

5. J.L. Rose, D. Jiao and J. Spanner, "Ultrasonic Guided Waves for Piping Inspection", Review of progress in Quantitative NDE volume 15, 1996, pp. 1285-1290

6. C.H. Yew, "Using Ultrasonic SH Waves to Estimate the quality of Adhesive Bonds: A Preliminary Study", J. Acoust. Soc. Am., 76 (2), August 1984, pp. 525-531

#511912 (38)

Plasticity and Time Dependant Response of Spectra Fabric Composite Laminates

by Alan Russell and Dan Liesch

Dockyard Laboratory Pacific, Victoria, British Columbia

ABSTRACT

This paper will present the results of an investigation into the time dependant non-linear mechanical behaviour of composite laminates re-inforced with high strength polyethlene fibres in the form of woven fabrics. These materials have acoustic transmission properties that make them attractive for sonar window applications but their visco-elastic behaviour and their low compressive yield strength severely limit their structural use. The effect of loading rate on the stress-strain response of test specimens loaded in tension, compression and flexure will be compared and the creep and relaxation response described under the same loading conditions. Where appropriate the test data will be fitted to empirical creep and relaxation models. Hysteresis measurements and hysteretic heating effects under cyclic loading will also be presented and discussed.

DEFENCE R&D DÉFENSE

Plasticity and Time Dependant Response of Spectra Fabric Composite Laminates

Alan Russell and Dan Liesch

Dockyard Laboratory Pacific
Defence Research Establishment Atlantic

National Defence Défense nationale

Canada

Presentation Outline

- Polymer Fibre Composites
- Test Materials
- Stress-Strain Behaviour
- Creep Measurements
- Fatigue Response
- Conclusions

DEFENCE R&D DÉFENSE

Classes of Composite Materials by Matrix Type

	Temperature Capability	Matrix Materials	Fibres
Polymer Matrix	<400°C	Epoxies, Esters, Imides, Thermoplastics	Carbon, Glass, Boron, Aramid, PE, PBT
Metal Matrix	<800°C	Ti, Al, Mg, Cu, Fe/Ni, Be	SiC, Carbon, Boron, Al_2O_3, Tungsten
Ceramic Matrix	<1200°C	SiC, C, Al_2O_3, Si_3N_4, Silicate glasses	SiC, Carbon, Si_3N_4

Polymer Fibre Composites

	"Kevlar"	"Spectra"
Polymer	Extended chain p-aramid	Extended chain Polyethylene
Advantages	Lightweight Strong and stiff in tension E = 130 GPa, σ = 4 GPa	Lightweight Strong and stiff in tension E = 170 GPa, σ = 3 GPa
Disadvantages	Weak fibre/matrix interface Poor compression strength Environmental degradation	Weak fibre/matrix interface Poor compression strength Limited temperature capability
Successful Applications	Lightweight armour Tensile loaded members	Lightweight armour

Classes of Composite Materials
by
Nature of Re-inforcement

Particulate	Isotropic	
Short Fibre	Randomly oriented Textured	
Continuous Fibre	2D	Unidirectional plies Woven fabric plies Non-crimp fabric plies
	3D	Z-pinning Knitted and braided fibre pre-forms

Spectra Materials Evaluated

Laminate ID	Fibre Type	Matrix	Nature of Re-inforcement
4-H EP	Spectra 1000	Epoxy	"988" 4-harness satin weave
8-H EP	Spectra 1000	Epoxy	"985" 8-harness satin weave
4-H CY	Spectra 1000	Cyanate-ester	"988" 4-harness satin weave
8-H CY	Spectra 1000	Cyanate-ester	"985" 8-harness satin weave

All 28 ply [0/90] laminates, 9.5 mm thick

Loading Modes

- Tension
- Compression
- Four Point Bending

Loading Sequences

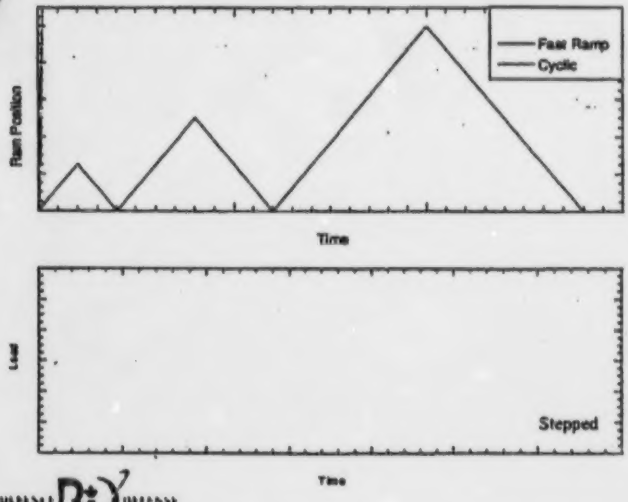

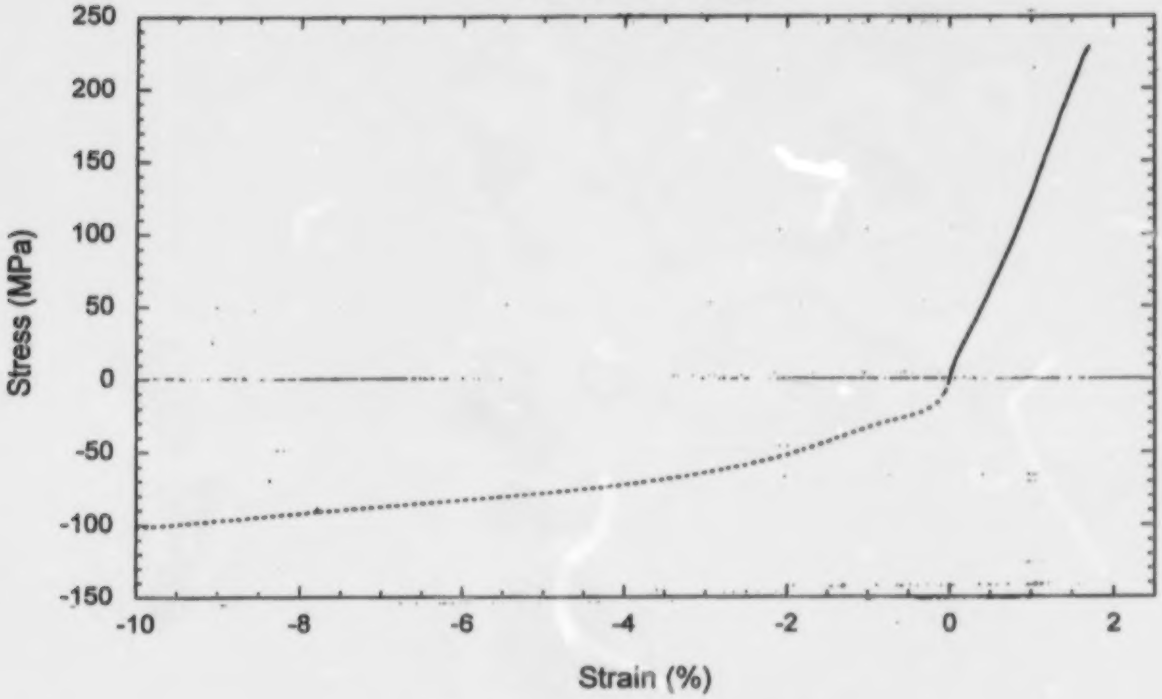

8-H Spectra/Epoxy

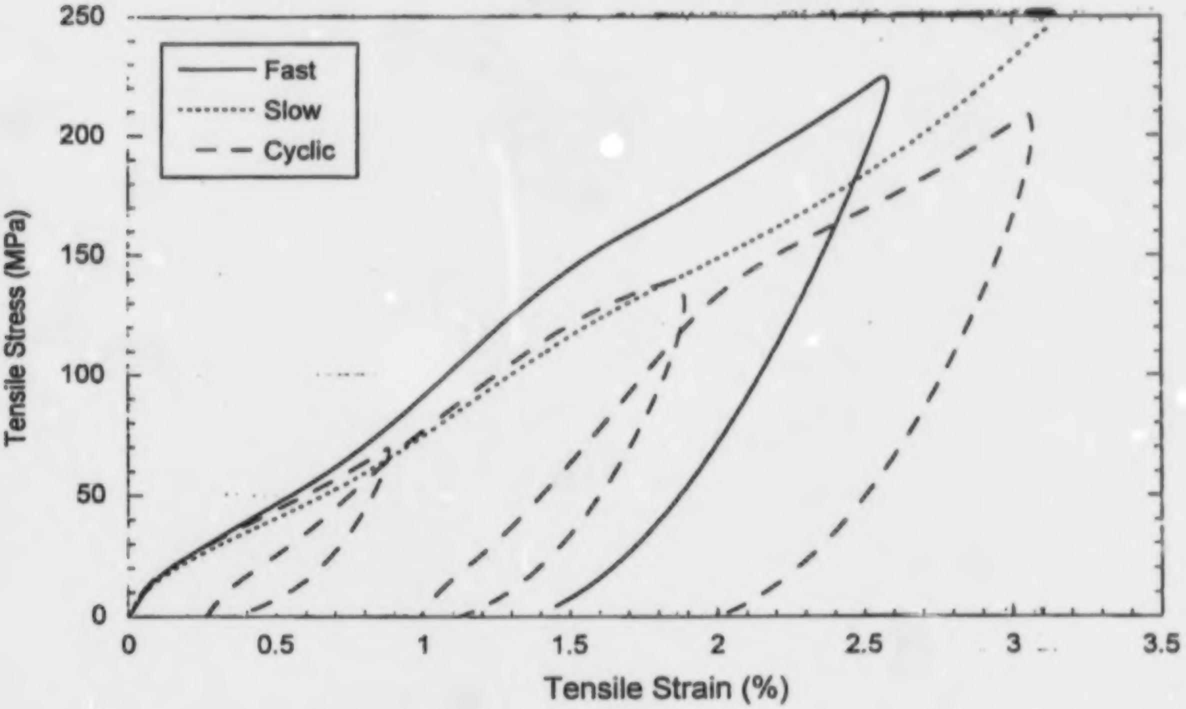

4-H Spectra/Cyanate-Ester

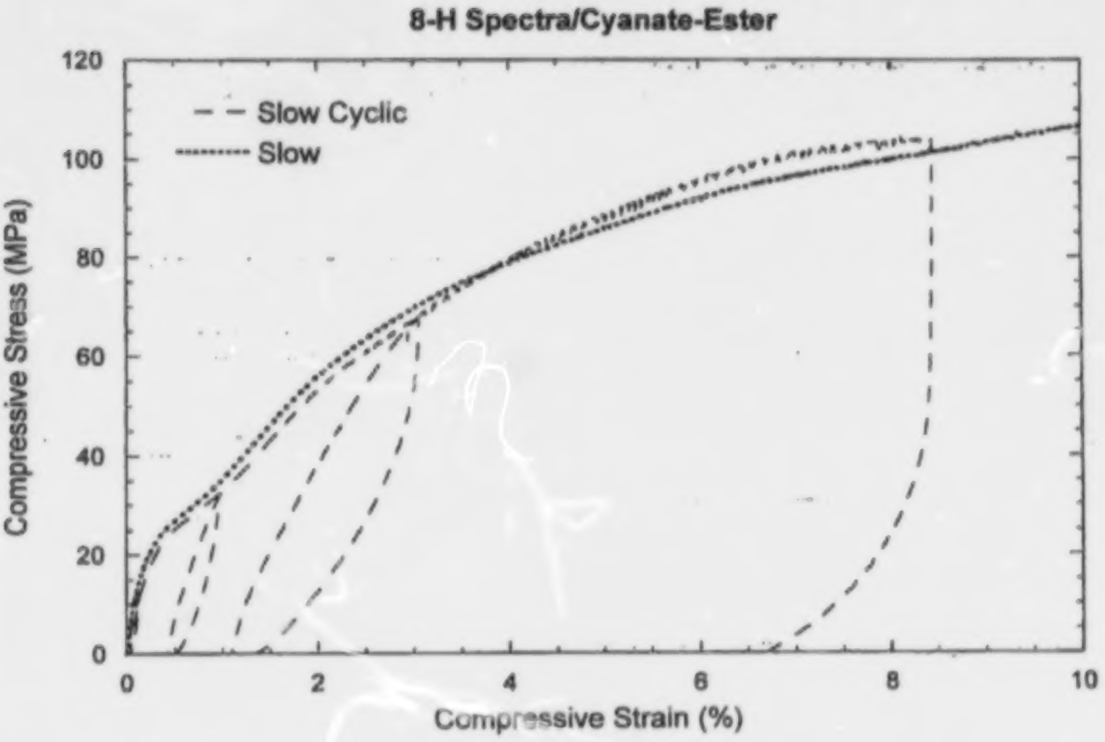
8-H Spectra/Cyanate-Ester
Slow Cyclic
Slow
Compressive Stress (MPa)
Compressive Strain (%)
0
20
40
60
80
100
120
0
2
4
6
8
10

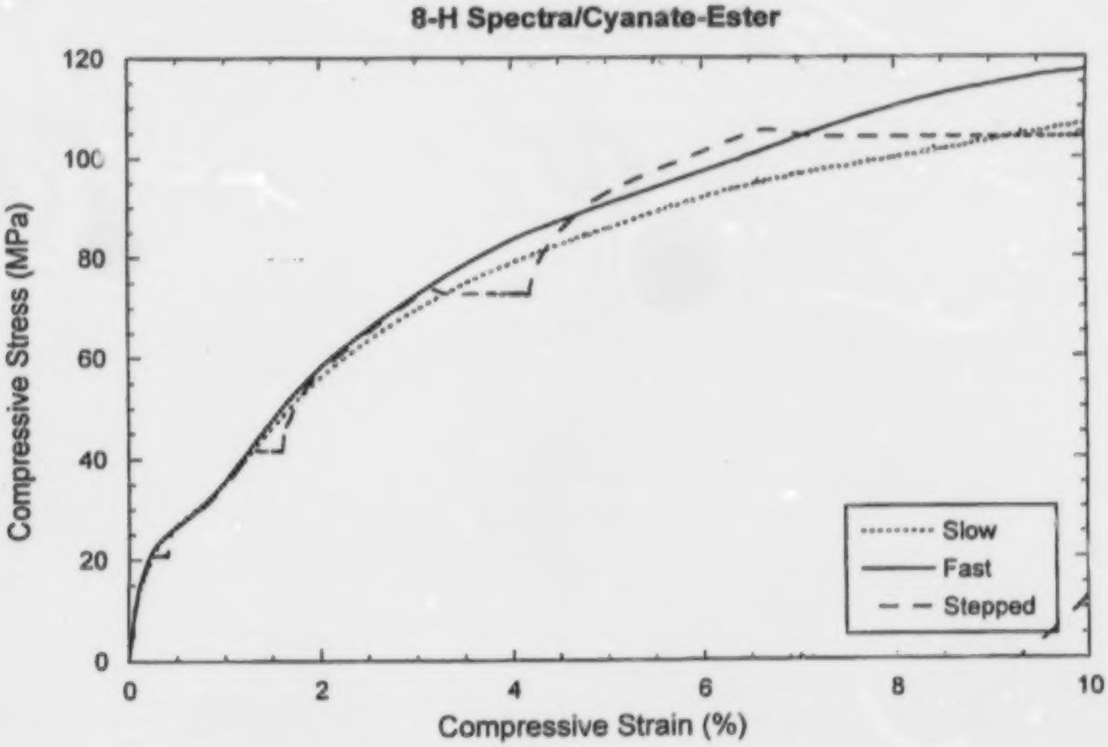
8-H Spectra/Cyanate-Ester
Slow
Fast
Stepped
Compressive Stress (MPa)
Compressive Strain (%)
0
20
40
60
80
100
120
0
2
4
6
8
10

45 Degree Shear failures in Compression Specimens

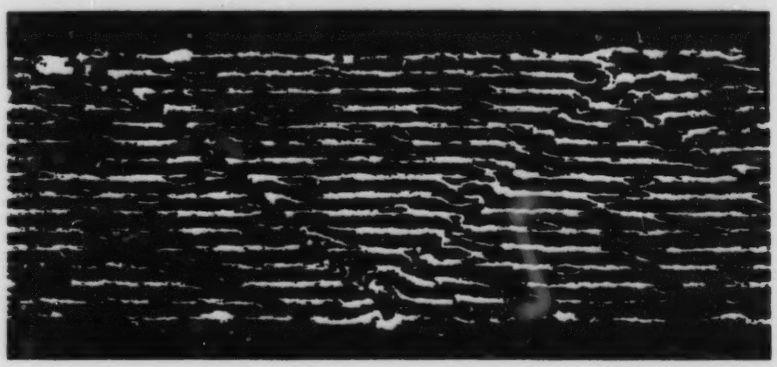

Strain Components

$$\varepsilon_T = \varepsilon_E + \varepsilon_P + \varepsilon_C$$

ε_T = *total strain*
ε_E = *elastic strain*
ε_P = *plastic strain*
ε_C = *creep strain*

$$\varepsilon_C = \varepsilon_C(t, \sigma, T)$$

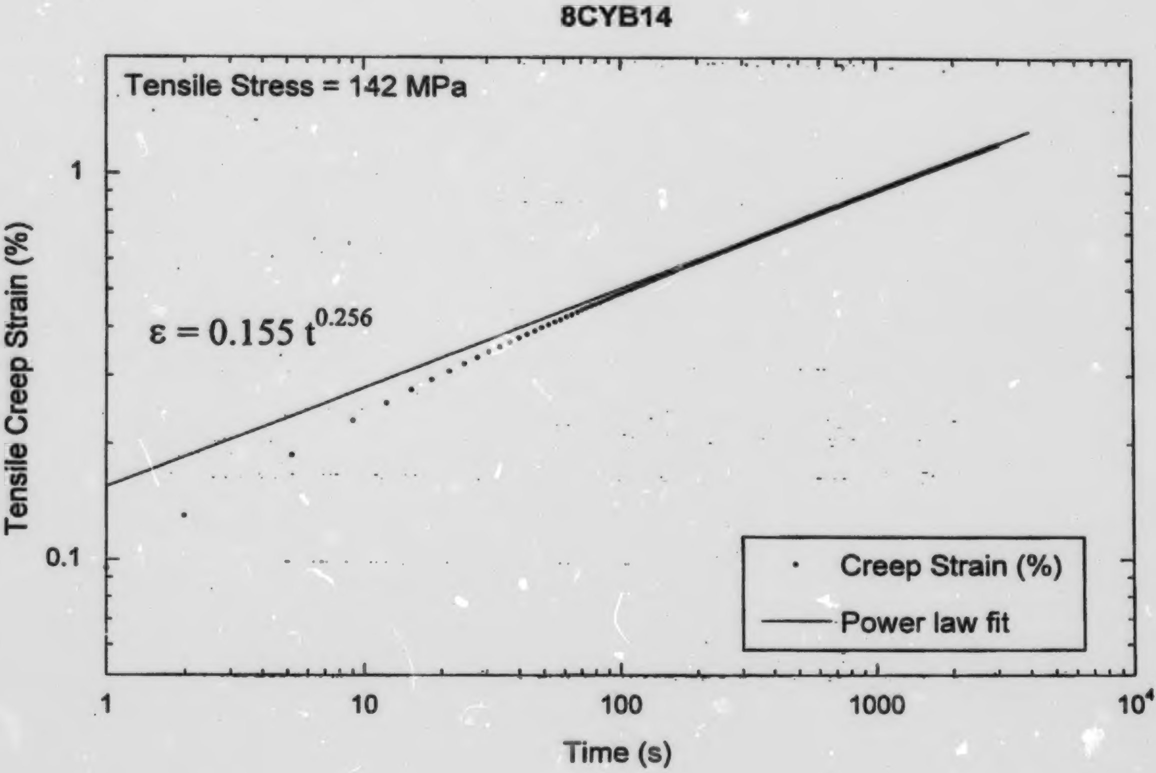
8CYB14

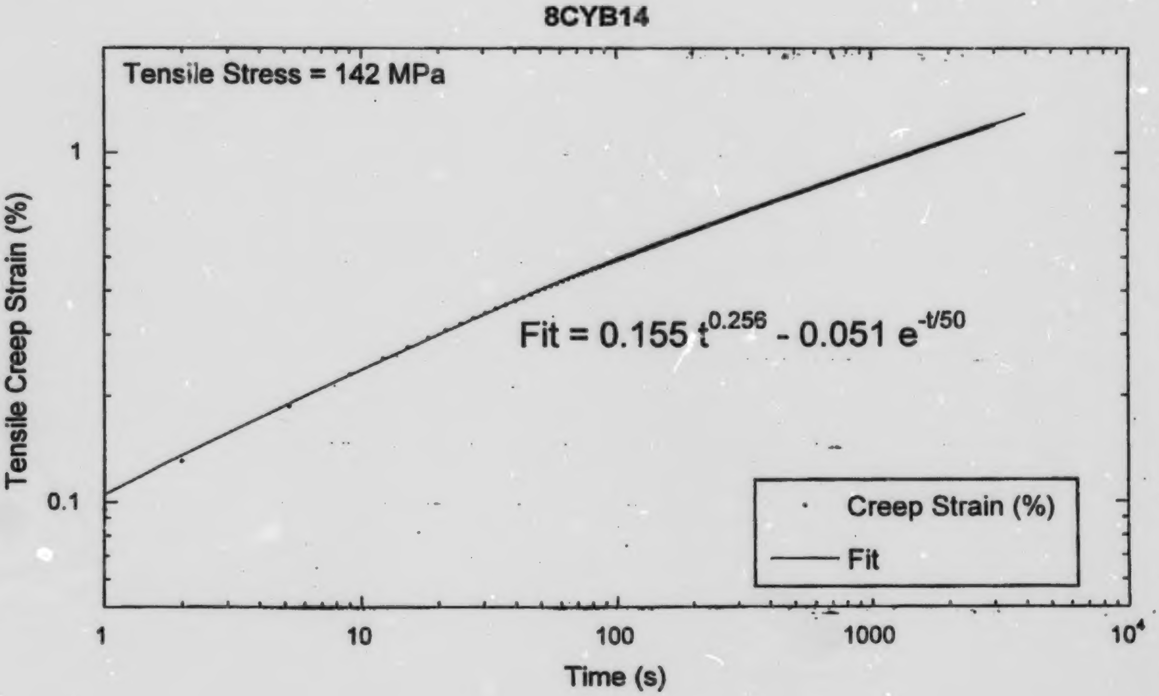
8CYB14

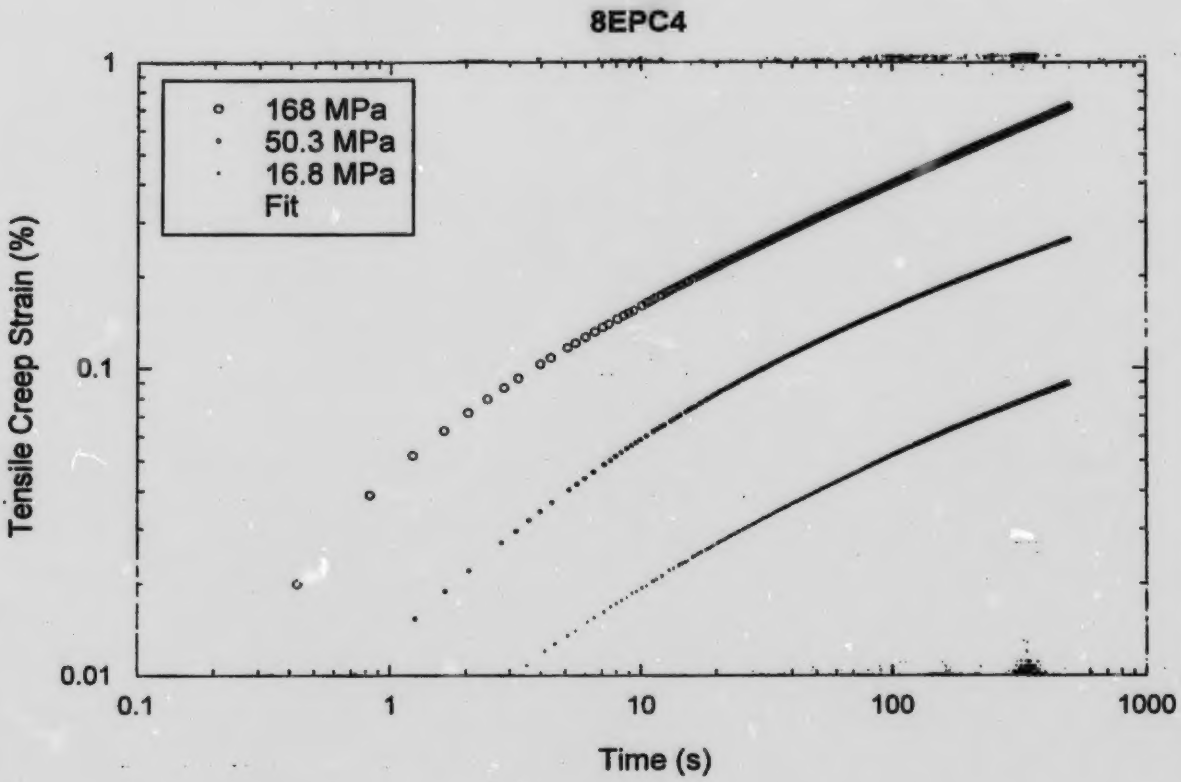
8EPC4
168 MPa
50.3 MPa
16.8 MPa
Fit
Tensile Creep Strain (%)
1
0.1
0.01
0.1
1
10
100
1000
Time (s)

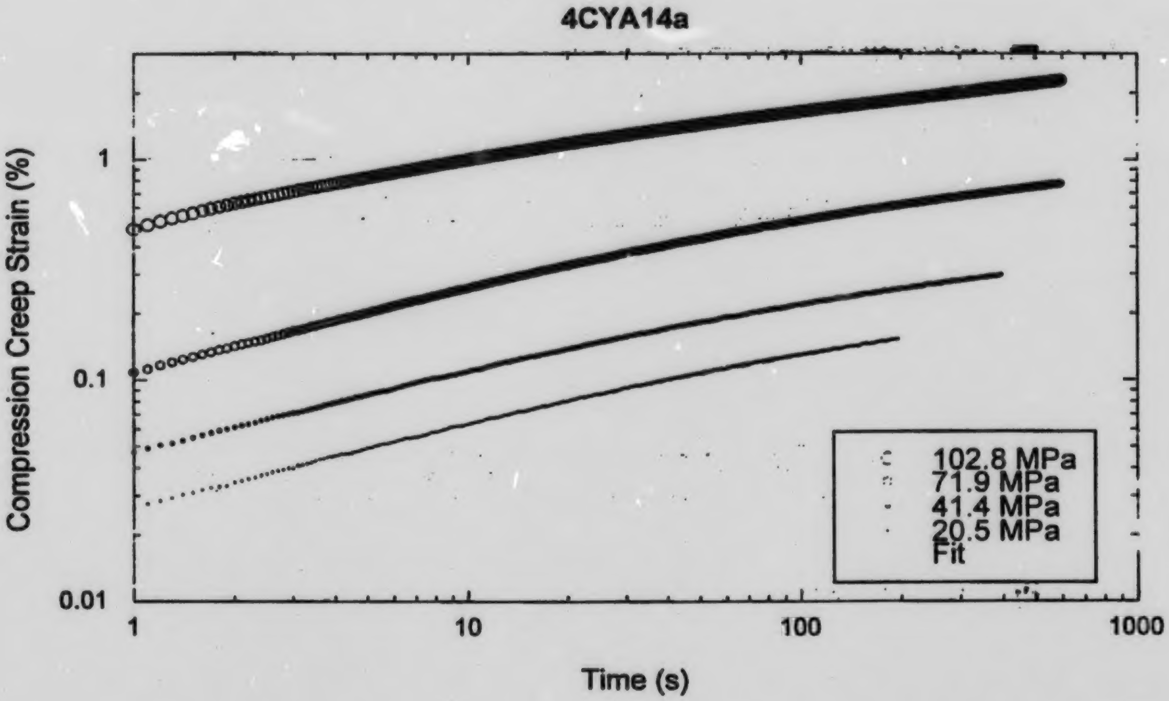
4CYA14a
102.8 MPa
71.9 MPa
41.4 MPa
20.5 MPa
Fit
Compression Creep Strain (%)
1
0.1
0.01
1
10
100
1000
Time (s)

Creep - Time Relationships

$$\dot{\varepsilon}_C = A_o t^{-n} + \frac{B_0}{\tau} e^{-t/\tau}$$

$$\varepsilon_C = \frac{A_o}{(1-n)} t^{1-n} - B_o e^{-t/\tau}$$

Creep - Stress Relationships

Tension	Compression
$A_o = a_o \sigma$	$A_o = a_o e^{m\sigma}$
$B_o = b_o \sigma$	$B_o = b_o e^{m\sigma}$
$n \neq n(\sigma)$	$n \neq n(\sigma)$

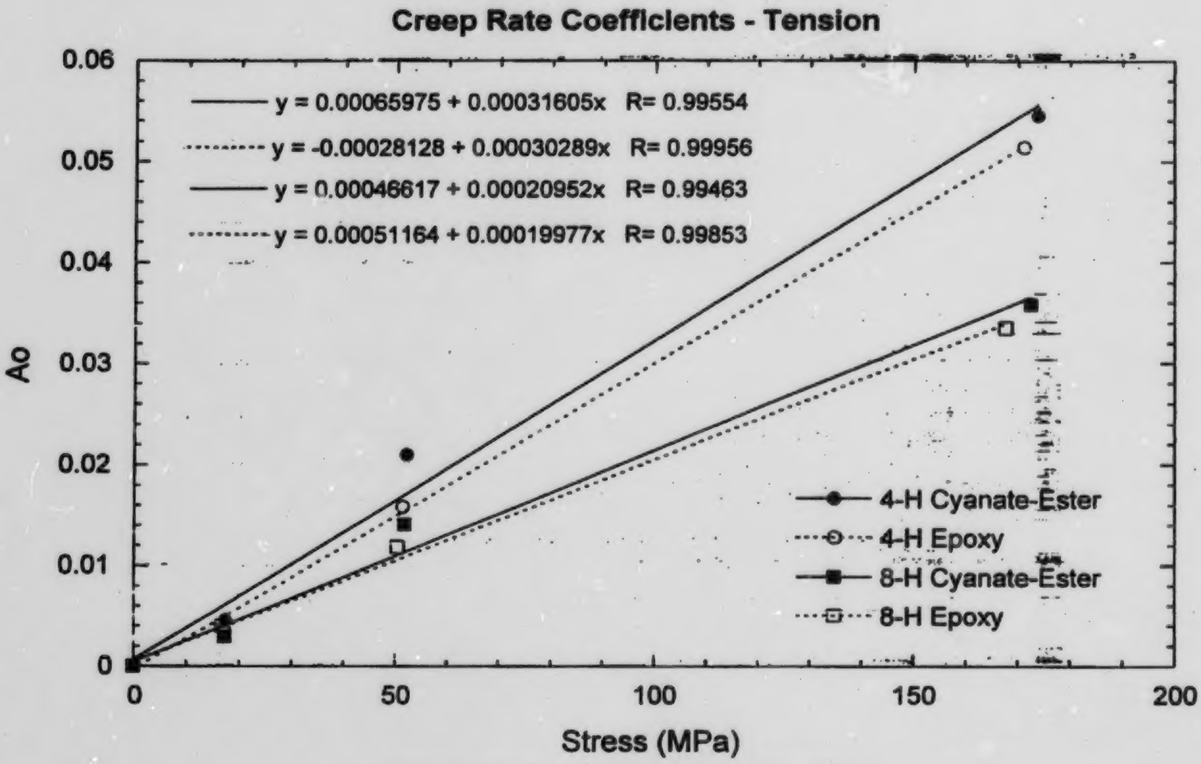
Creep Rate Coefficients - Tension

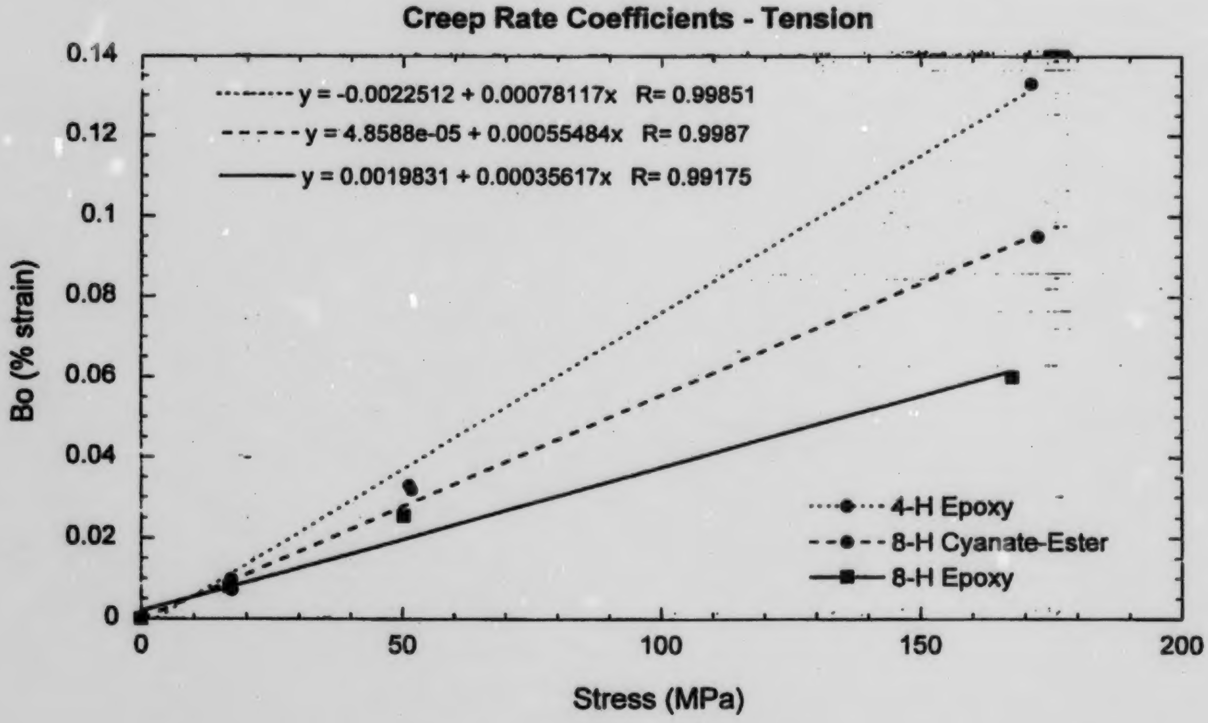
Creep Rate Coefficients - Tension

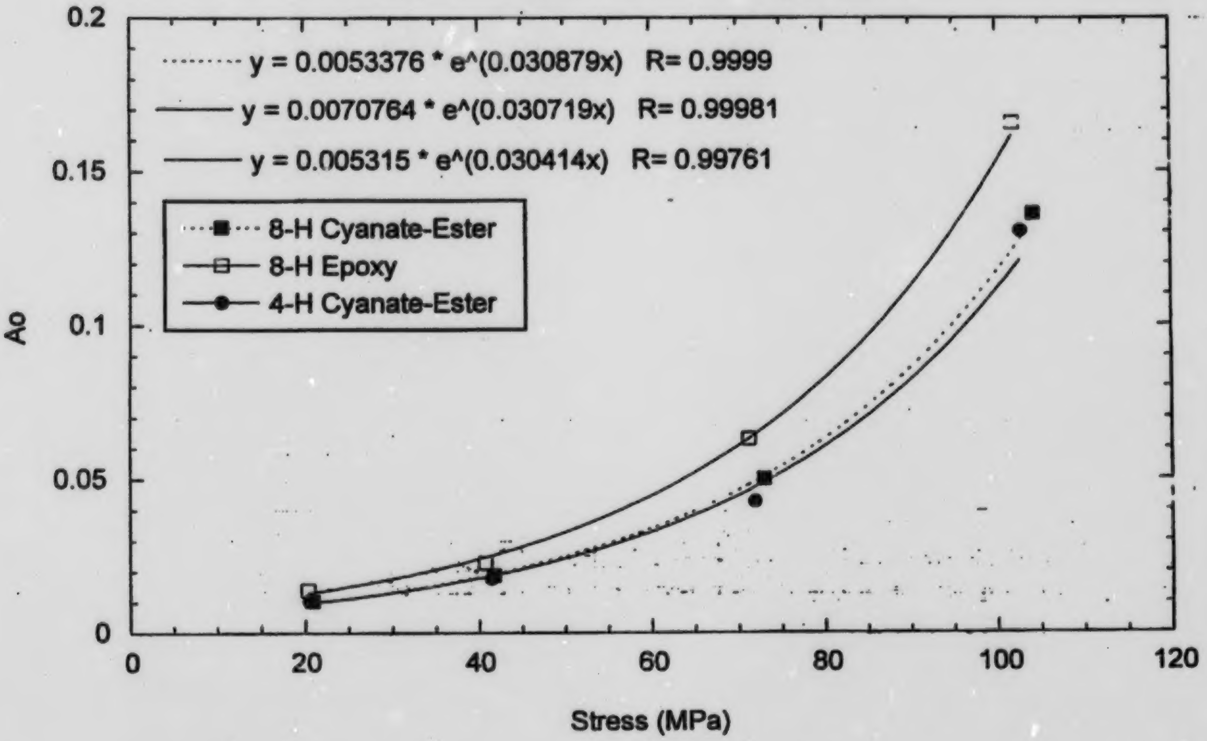
Creep Rate Coefficients - Compression

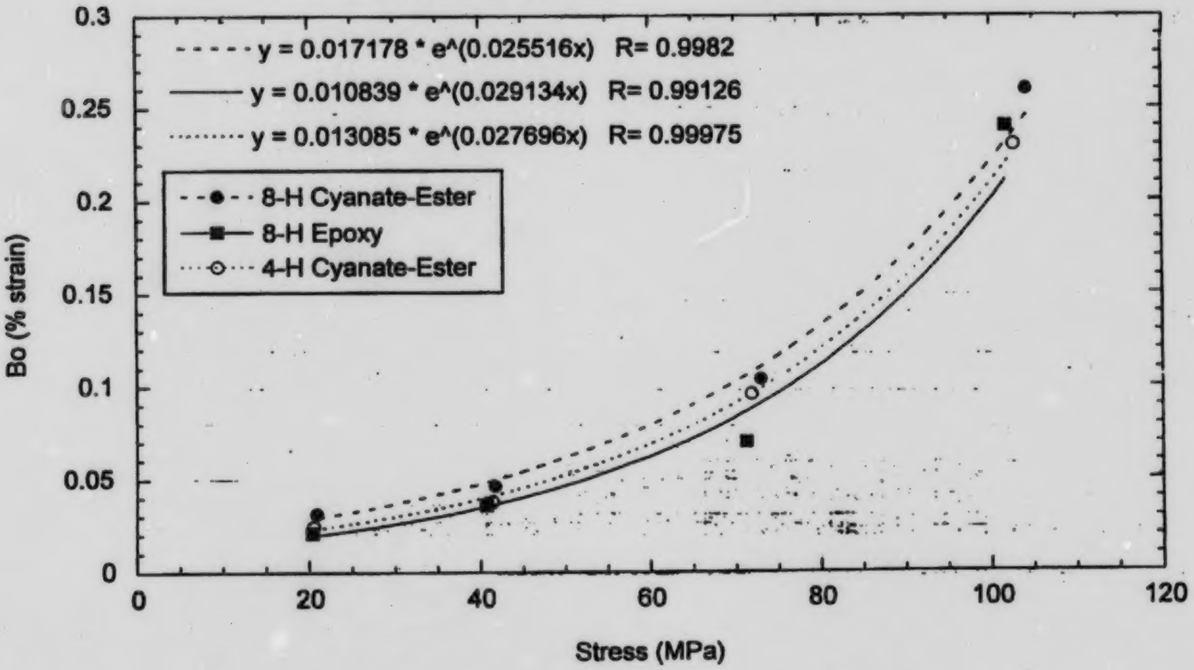
Creep Rate Coefficients - Compression

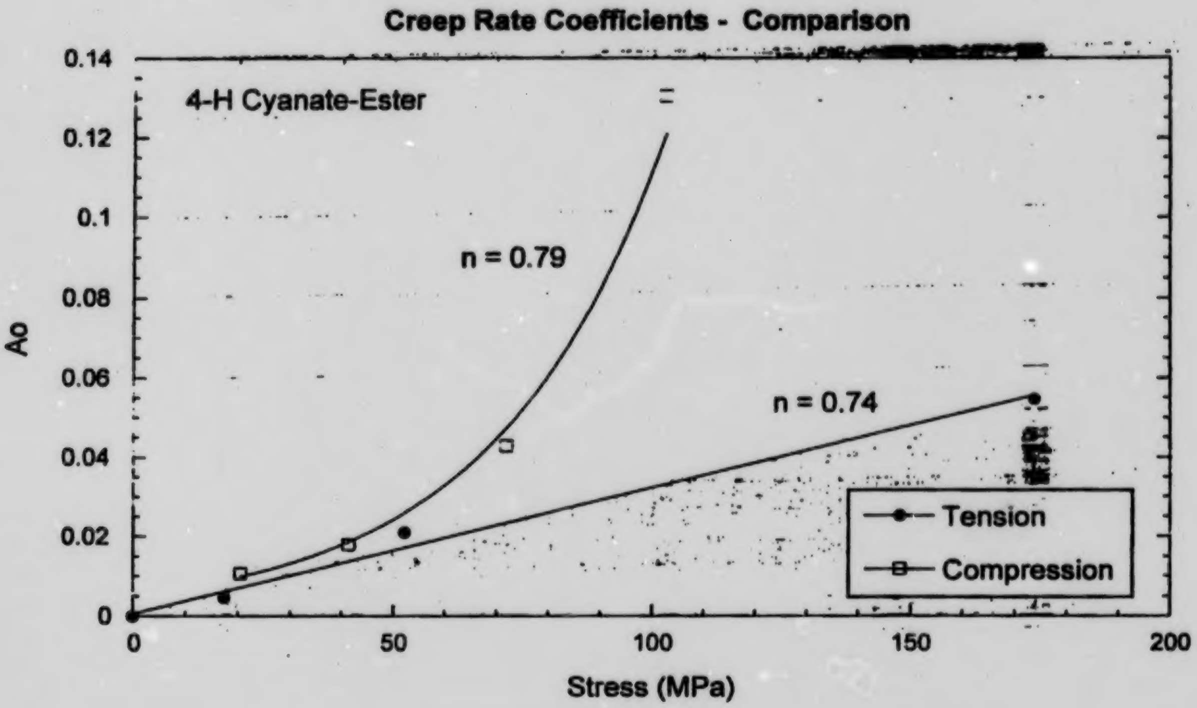
Creep Rate Coefficients - Comparison
4-H Cyanate-Ester
Ao
0.14
0.12
0.1
0.08
0.06
0.04
0.02
0
n = 0.79
n = 0.74
Tension
Compression
0
50
100
150
200
Stress (MPa)

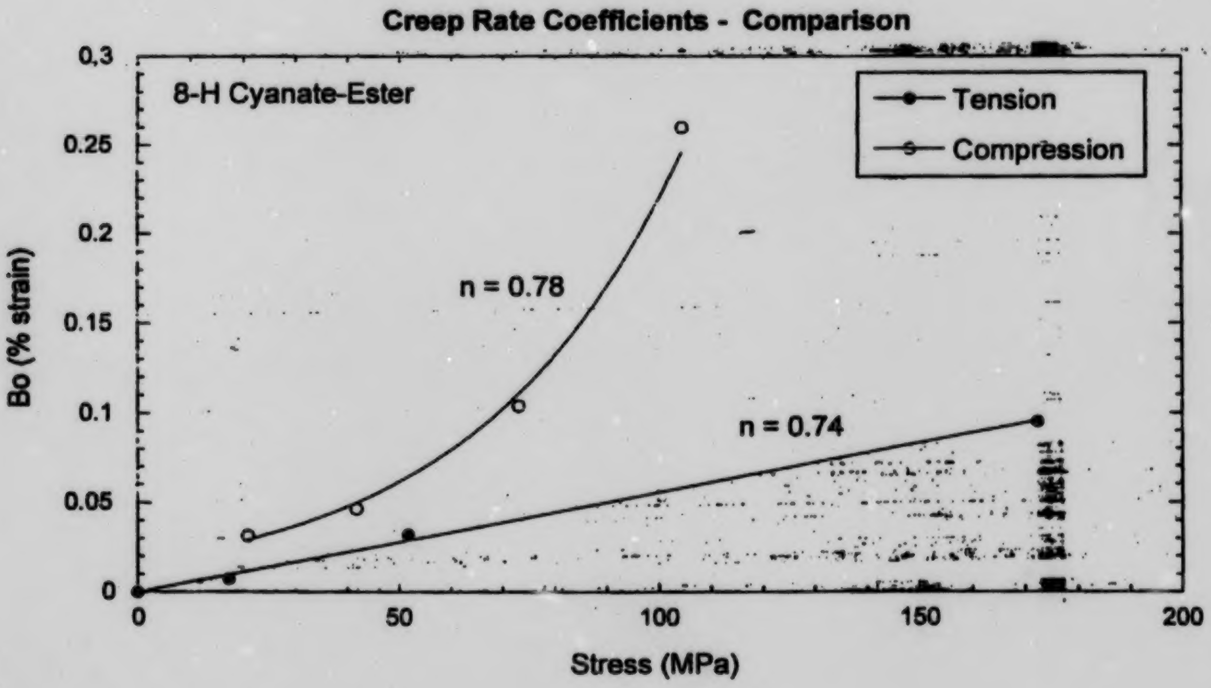
Creep Rate Coefficients - Comparison
8-H Cyanate-Ester
Bo (% strain)
0,3
0.25
0.2
0.15
0.1
0.05
0
n = 0.78
n = 0.74
Tension
Compression
0
50
100
150
200
Stress (MPa)

Spectra Fabric Composites - Creep Equations

Tension $$\dot{\varepsilon}_C = \left[a_o t^{-n} + \frac{b_0}{\tau} e^{-t/\tau} \right] \sigma$$

Material	a_o	b_o	n	τ
8-H Cyanate-Ester	2.1e-4	5.6e-4	0.74	27-100
8-H Epoxy	2.0e-4	3.6e-4	0.74	33-1000
4-H Cyanate-Ester	3.2e-4	-	0.74	25-33
4-H Epoxy	3.0e-4	7.8e-4	0.68	33-500

Spectra Fabric Composites - Creep Equations

Compression $$\dot{\varepsilon}_C = \left[a_o t^{-n} + \frac{b_0}{\tau} e^{-t/\tau} \right] e^{m\sigma}$$

Material	a_o	b_o	n	m	τ
8-H Cyanate-Ester	5.3e-3	0.017	0.78	0.026-0.0309	22-50
8-H Epoxy	7.1e-3	0.011	0.79	0.029-0.0307	12-33
4-H Cyanate-Ester	5.3e-3	0.013	0.79	0.028-0.0303	13-50

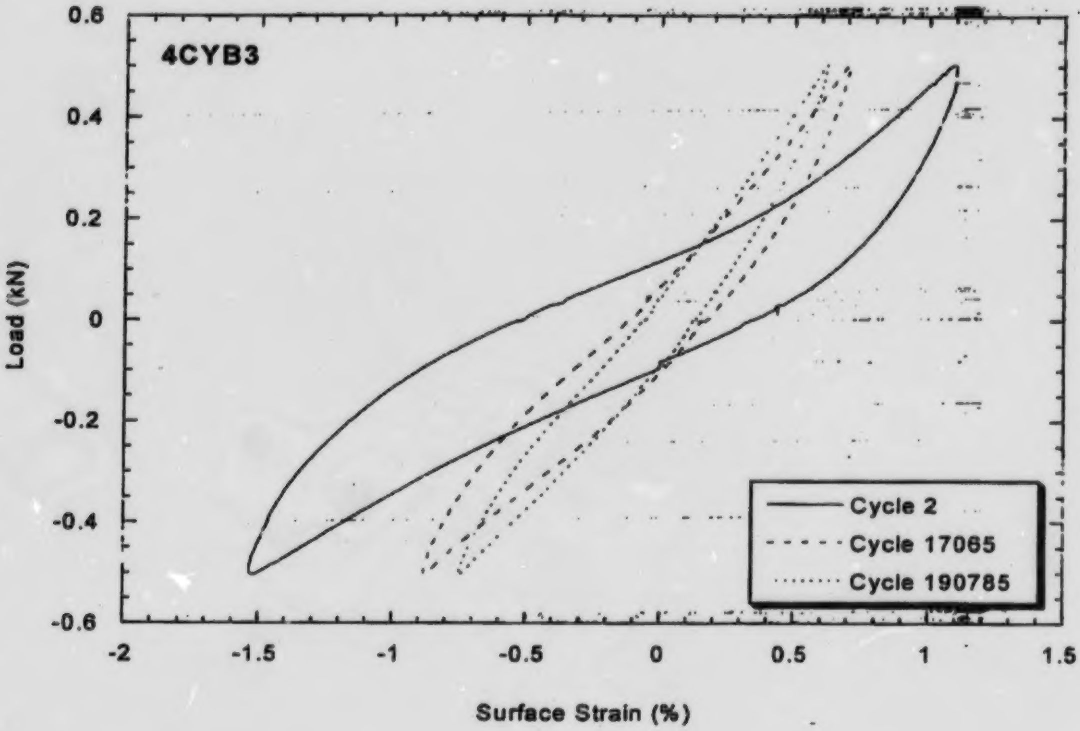
4CYB3
Load (kN)
0.6
0.4
0.2
0
-0.2
-0.4
-0.6
-2
-1.5
-1
-0.5
0
0.5
1
1.5
Surface Strain (%)
Cycle 2
Cycle 17065
Cycle 190785

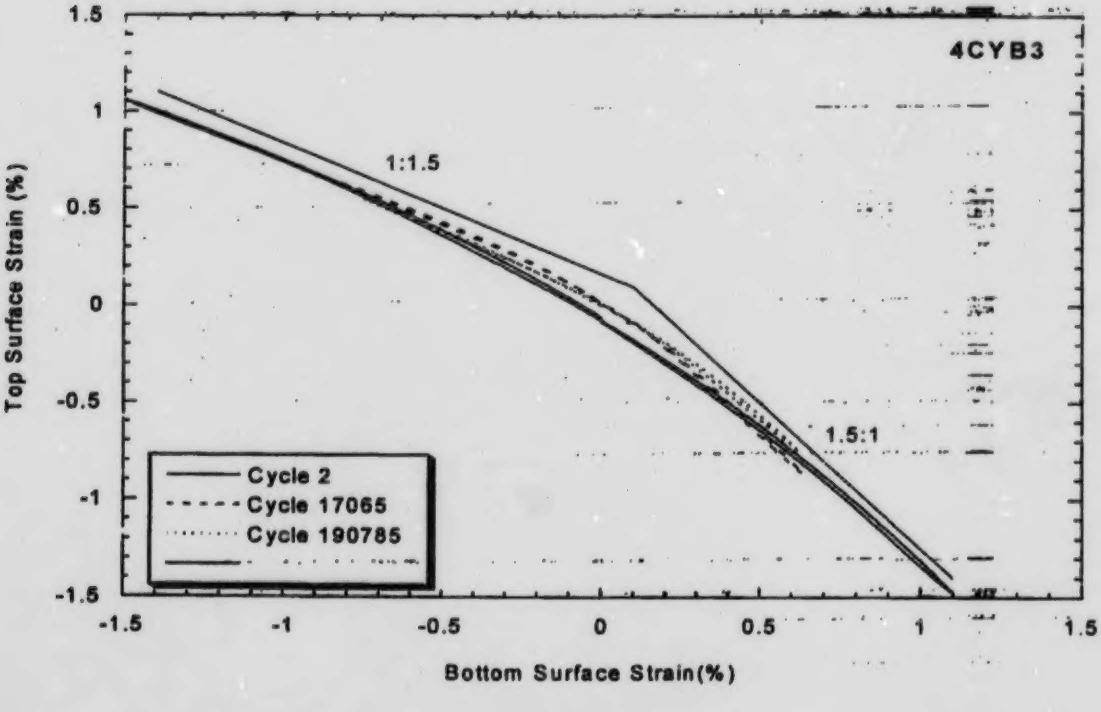
4CYB3
Top Surface Strain (%)
1.5
1
0.5
0
-0.5
-1
-1.5
-1.5
-1
-0.5
0
0.5
1
1.5
Bottom Surface Strain(%)
1:1.5
1.5:1
Cycle 2
Cycle 17065
Cycle 190785

8-H Spectra R = -1 Fatigue

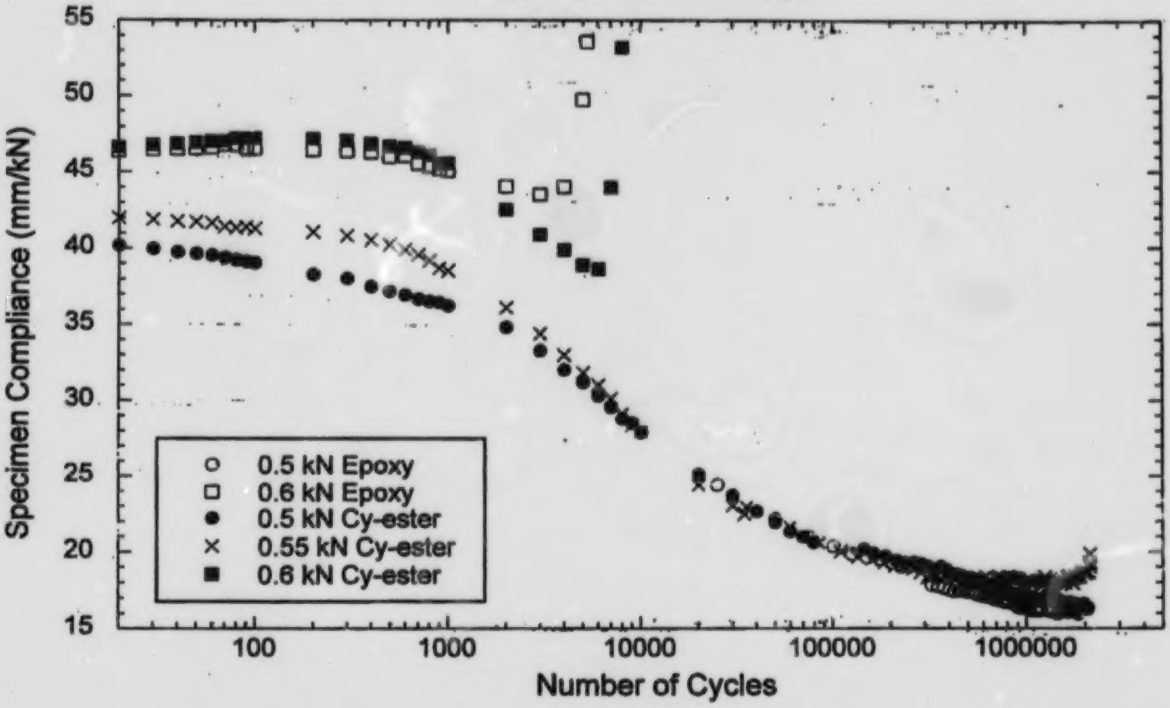

Compression Shear Failure in R = -1 Fatigue Specimen

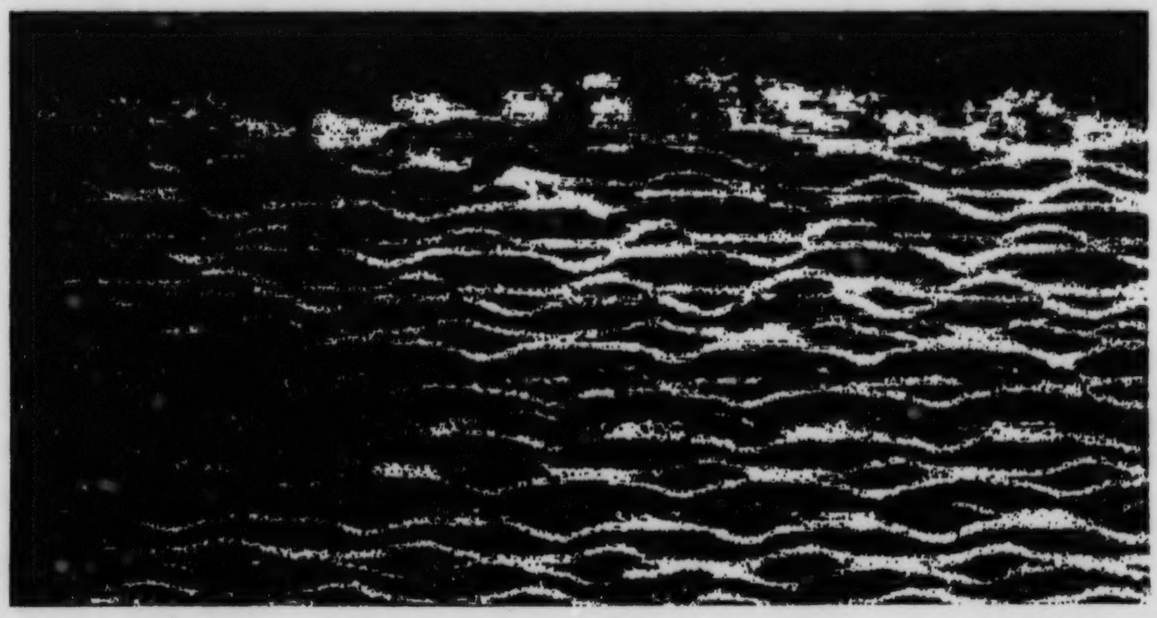

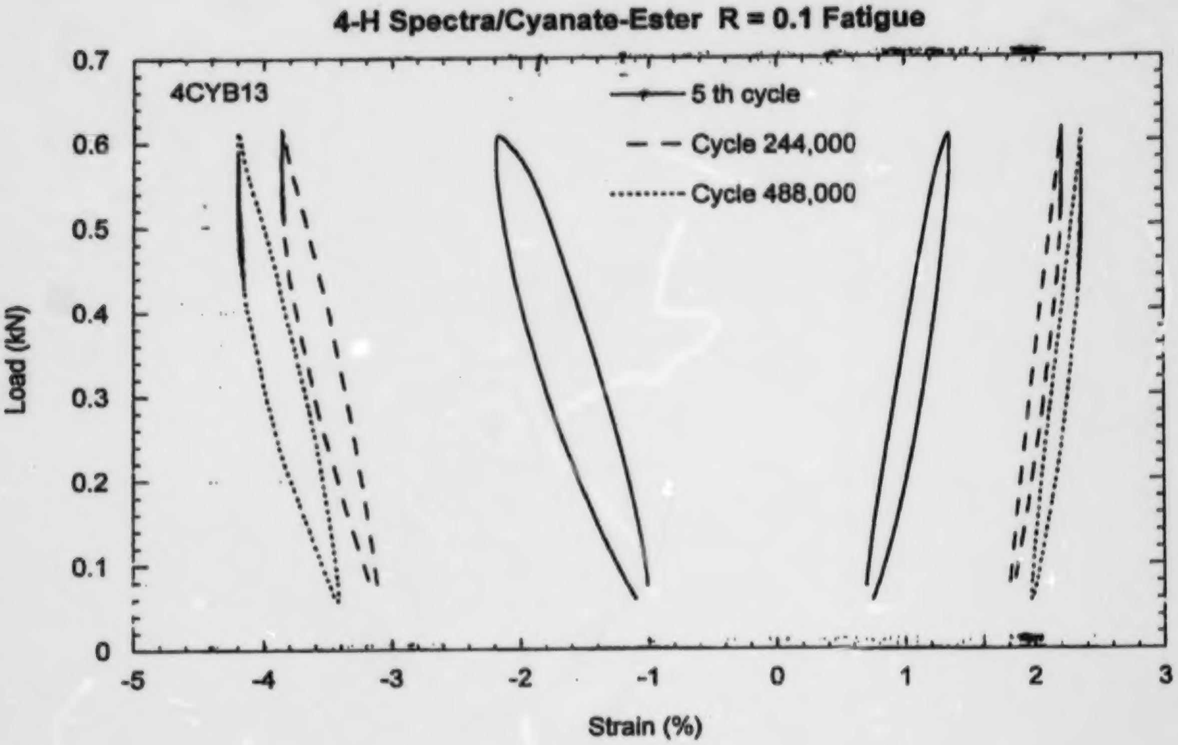
4-H Spectra/Cyanate-Ester R = 0.1 Fatigue
4CYB13
5 th cycle
Cycle 244,000
Cycle 488,000
Load (kN)
0.7
0.6
0.5
0.4
0.3
0.2
0.1
0
Strain (%)
-5
-4
-3
-2
-1
0
1
2
3

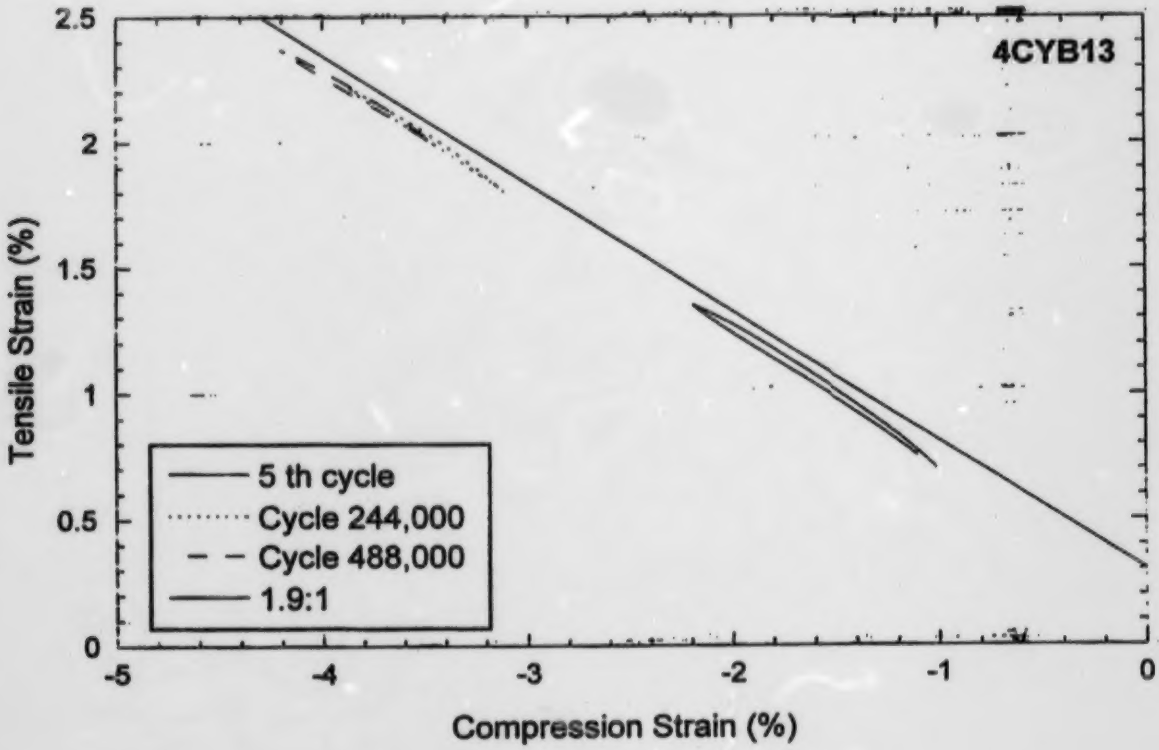
4CYB13
5 th cycle
Cycle 244,000
Cycle 488,000
1.9:1
Tensile Strain (%)
2.5
2
1.5
1
0.5
0
Compression Strain (%)
-5
-4
-3
-2
-1
0

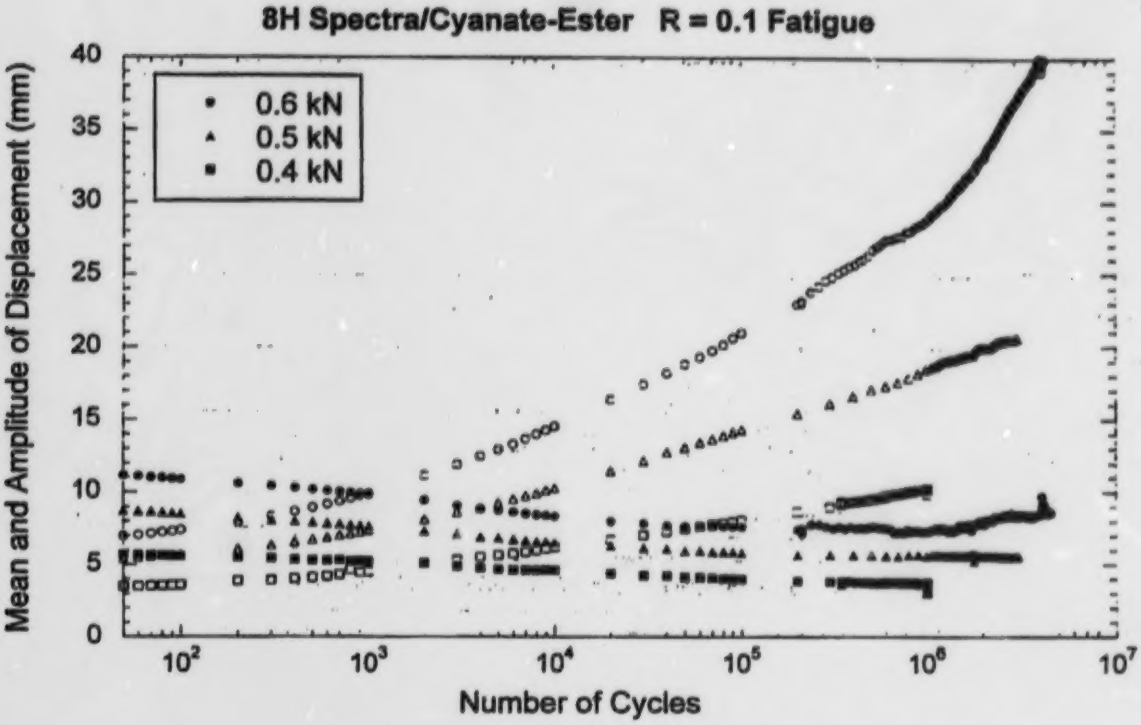
8H Spectra/Cyanate-Ester R = 0.1 Fatigue
0.6 kN
0.5 kN
0.4 kN
Mean and Amplitude of Displacement (mm)
0
5
10
15
20
25
30
35
40
10^2
10^3
10^4
10^5
10^6
10^7
Number of Cycles

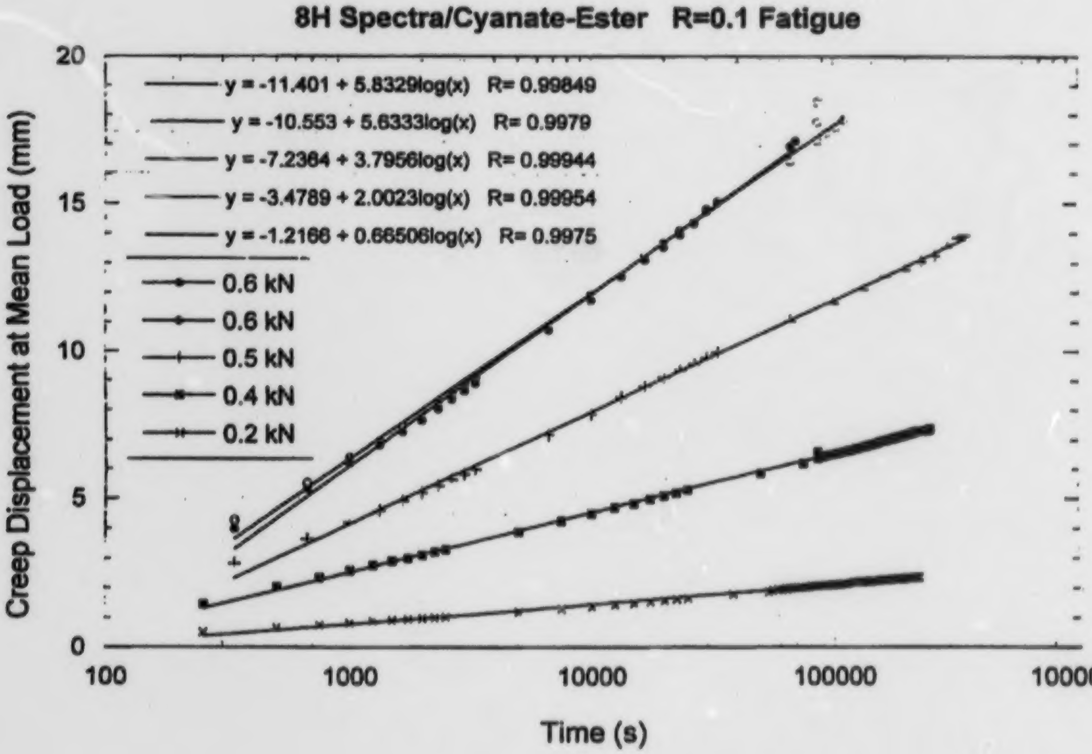
8H Spectra/Cyanate-Ester R=0.1 Fatigue
y = -11.401 + 5.8329log(x) R= 0.99849
y = -10.553 + 5.6333log(x) R= 0.9979
y = -7.2364 + 3.7956log(x) R= 0.99944
y = -3.4789 + 2.0023log(x) R= 0.99954
y = -1.2166 + 0.66506log(x) R= 0.9975
0.6 kN
0.6 kN
0.5 kN
0.4 kN
0.2 kN
Creep Displacement at Mean Load (mm)
0
5
10
15
20
100
1000
10000
100000
1000000
Time (s)

Spectra Fabric Composites - Creep Equations

R = 0.1 Fatigue

$$\dot{\varepsilon}_C = c_o t^{-n} e^{m\sigma}$$

Material	c_0	n	m
8-H Cyanate-Ester	0.0124	1.0	0.059

R = 0.1 Fatigue - Creep Strain Parameters

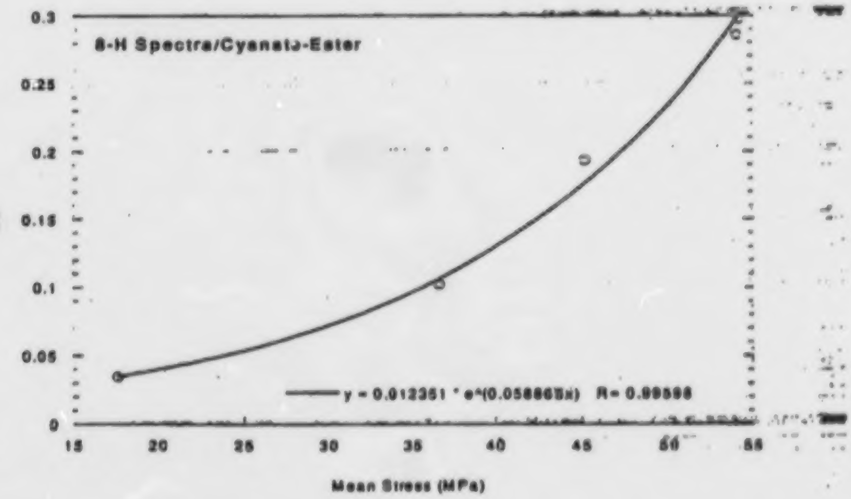

Comparison of Creep Strains in Tension, Compression and at R = 0.1

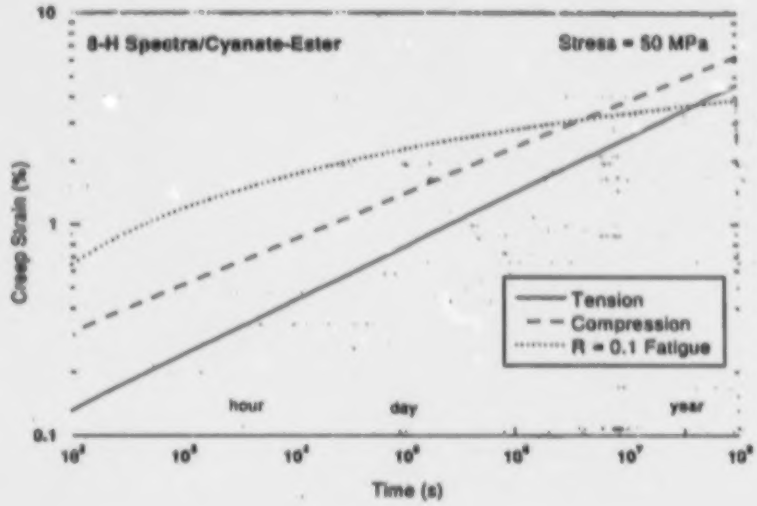

Conclusions

- Spectra fibre composites experience significant amounts of creep at ambient temperatures.
- Both transient and sustained creep are evident.
- The creep rate dependency on stress is different in tension and compression.
- Cyclic loading produces a gradual increase in elastic modulus and decrease in loss modulus.
- A constant ratio of compression strain to tensile strain of between 1.5:1 and 2:1 is maintained during fatigue.

#51913 (39)

An Assessment of an Alternative Submarine Steel

by Dr. J.J.F. Butler[1], J-J. DuFrane[2], K.B. George[1] and J. Bird[3]

[1] **Defence Evaluation and Research Agency, Rosyth, UK**
[2] **Fabrique De Fer, Belgium**
[3] **MOD(PE), Abbey Wood, UK**

ABSTRACT

Steel used in submarine construction has, over the past fifty years, developed from mild steel through Q1N/HY80 in the UK and US navies, HY100/HLES80/BIS812 respectively in the US, French and Australian navies and HLES100 in the French navy. Variants of these which have been considered and evaluated have included HLES65 and HSLA80 at the 550MPa 0.2% proof strength level and HSLA100 at the 690MPa 0.2% proof strength level. The HSLA steels were specifically designed to reduce cost and be more easily weldable, namely with reduced preheat. Unfortunately these steels have not lived up to the earlier promise and the expected full cost savings potential has not been met. Some amongst the naval fraternity have continued an optimistic approach to finding a more construction friendly steel and have been looking at a number of offshore steels, X65, X70, X80 and X100 as possible contenders. This paper looks at one such steel Shoralsim 500, a development of an offshore grade, exhibiting adequate strength, outstanding toughness, increased weldability and with a significant potential for reduced fabrication cost.

Introduction

- Introduction
- Goal/Objective
- Test Programme
- Key Results & Comparisons
- Cost Benefits
- Further Work
- Summary

DERA

Structural Materials Centre

Goal/Objective

- Goal
  - To find a cheaper more readily weldable alternative to Q1(N)-the current UK submarine steel
    - Q1(N)~£1600/tonne
    - requires preheat of 120°C to avoid cold cracking of its hard martensitic heat affected zone (HAZ)
- Objective
  - To evaluate the mechanical properties and weldability of two plates Shoralsim 500 MOD (25mm & 50mm)
  - Comment on its suitability for submarine primary and secondary structure applications

DERA

Structural Materials Centre

Shoralsim 500 MOD Plate Production

- Manufactured by Fabrique De Fer, Charleroi, Belgium
- 250 tonne continuously cast strand (2100mm x 180mm)
- Quenched and Tempered @ 620°C for 2 minutes/mm thickness

DERA

Structural Materials Centre

Test Programme

- Chemical Composition
- Metallography
- Mechanical Properties
  - Through Thickness Hardness
  - Tensiles (Long./Trans.)
  - Charpy & EDM Charpy Impact
  - Drop Weight J tests
  - Hull Toughness Element
  - Corrosion Fatigue
- Weldability
  - Contolled Thermal Severity

DERA

Structural Materials Centre

Chemical Composition (wt%)

Steel	Gauge (mm)	C	Si	Mn	S	P	Cr	Mo	Ni	Al	Cu	V	Nb	B	CEV
Sheralsim 500 MOD	25	0.08	0.28	1.60	0.0005	0.005	0.05	0.25	1.40	0.040	0.03	0.01	<0.01	-	0.55
Sheralsim 500 MOD	50	0.08	0.28	1.60	0.0005	0.005	0.05	0.25	1.40	0.040	0.03	<0.01	<0.01	-	0.55
HSLA80	25	0.06	0.37	0.52	0.007	0.008	0.66	0.20	0.70	0.045	1.10	0.01	-	-	0.50
QT550	25	0.07	0.35	1.38	0.002	0.007	0.10	0.16	0.50	0.050	0.07	0.05	<0.01	0.0025	
X80	9	0.06	0.28	1.55	0.004	0.012	0.05	0.25	0.01	0.027	0.01	<0.01	0.08	-	0.42
Q1(N)	Min.	-	0.15	0.10	-	-	1.00	0.20	2.25	0.015	-	-	-	-	
	Max.	0.18	0.35	0.40	0.015	0.015	1.80	0.60	3.25	-	0.20	0.02	-	-	0.66

DERA

Structural Materials Centre

Microstructure

DERA

Structural Materials Centre

Tensile Properties

Steel	Gauge (mm)	Orientaion	0.2% PS (MPa)	UTS (MPa)	0.2%PS/UTS	Elongation (%)	Reduction in Area (%)
Shoralsim 500 MOD	25	Long.	600	665	0.90	25	83
		Trans.	593	661	0.90	23	79
Shoralsim 500 MOD	50	Long.	603	662	0.91	22	81
		Trans.	604	663	0.91	21	79
HSLA80 (UK)	25	Long.	549	628	0.88	27	78
		Trans.	553	634	0.87	27	78
QT550	25	Long.	544	615	0.89	28	80
		Trans.	524	604	0.87	27	78
X80	9	Long.	600	708	0.85	-	-
		Trans.	568	697	0.81	-	-
Q1(N)	Min.		550	-	-	20	50 Trans
	Max.		655	-	0.88	-	-

DERA

Structural Materials Centre

Charpy Impact Curves for 25mm Shoralsim 500 MOD

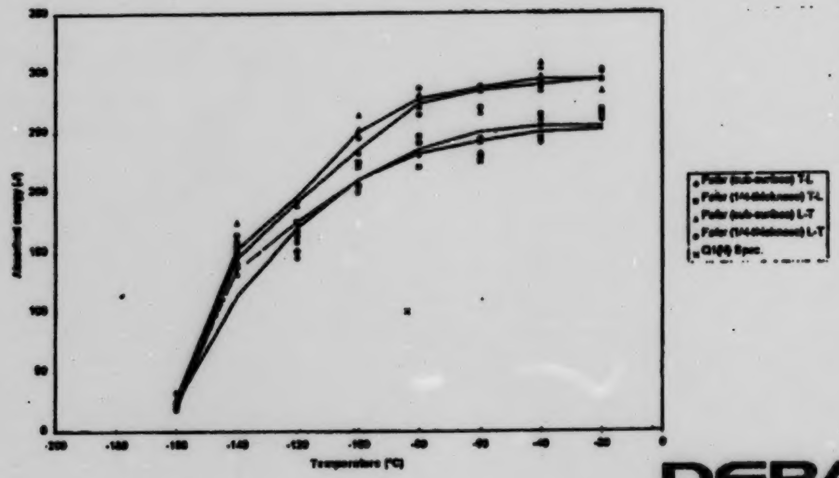

DERA

Structural Materials Centre

Charpy Impact Curves for 50mm Shoralsim 500 MOD

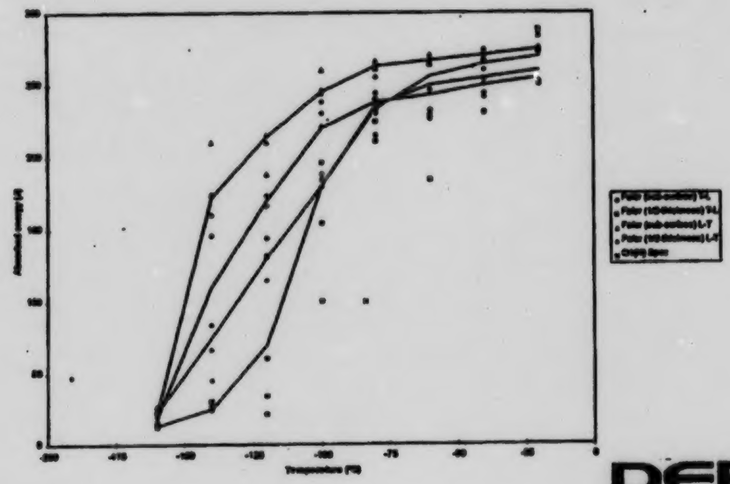

DERA

Structural Materials Centre

Charpy Impact Comparisons

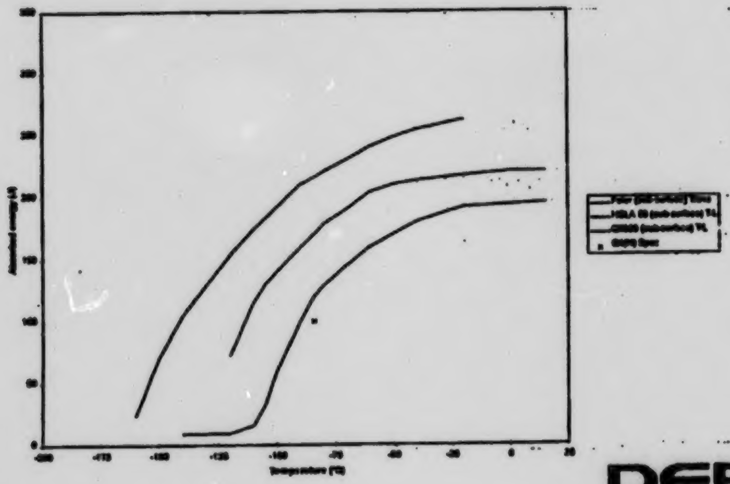

DERA

Structural Materials Centre

EDM Charpy Impact Specimen

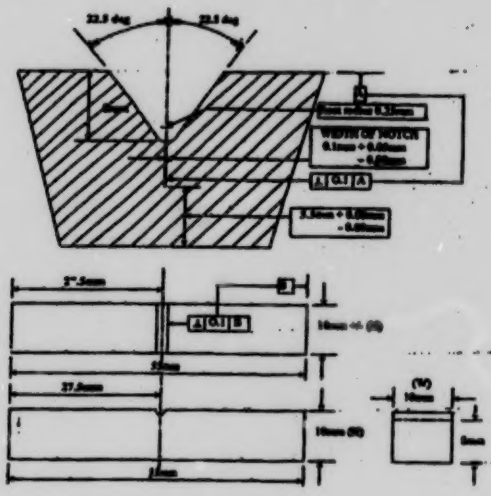
22.5 deg
22.5 deg
WIDTH OF NOTCH
0.1
A
B
27.5mm
55mm
10mm (W)
(W)
10mm
5mm

DERA

Structural Materials Centre

EDM Charpy Impact Curves for 25mm Shoraisim 500 MOD

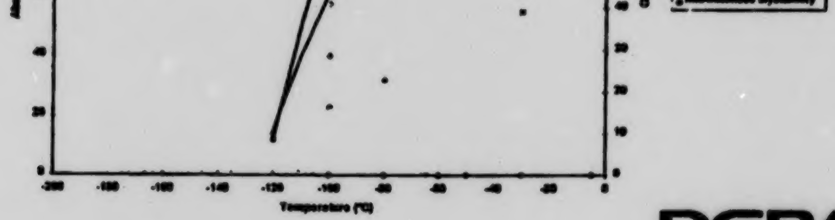

DERA

Structural Materials Centre

EDM Charpy Impact Curves for 50mm Shoraisim 500 MOD

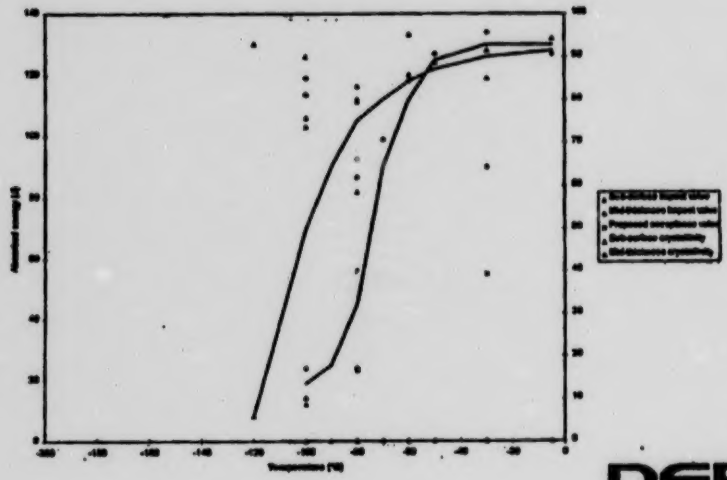

DERA

Structural Materials Centre

EDM Charpy Impact Comparisons

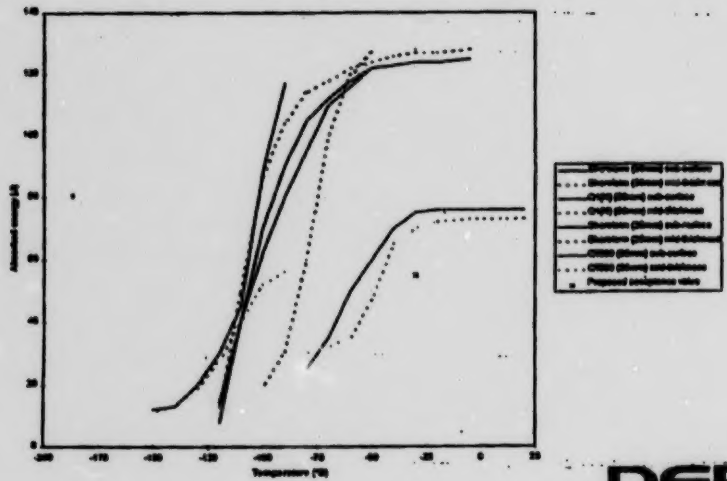

DERA

Structural Materials Centre

Drop Weight J Testing

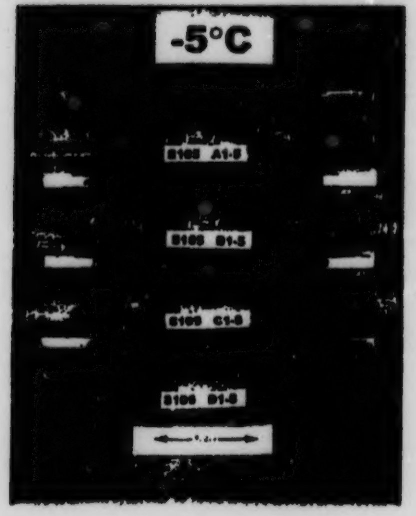
-5°C
S105 A1-5
S105 B1-5
S105 C1-5
S105 D1-5

DERA

Structural Materials Centre

Explosively Loaded Tests (HTE)

DERA

Structural Materials Centre

HTE Fracture Surfaces

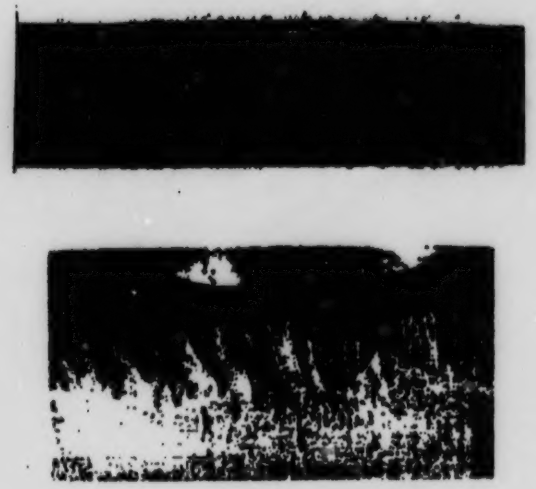

- 25mm Thick Plate (Top)
- 50mm Thick Plate (Bottom)

DERA

Structural Materials Centre

Corrosion Fatigue

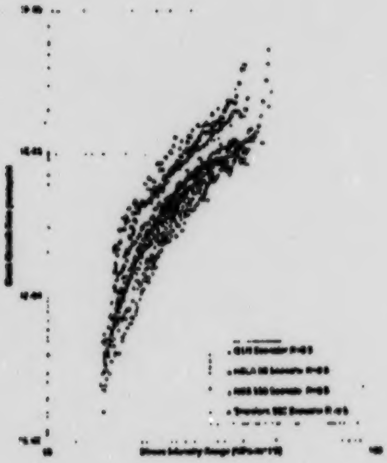

DERA

Structural Materials Centre

Weldability (CTS Specimen)

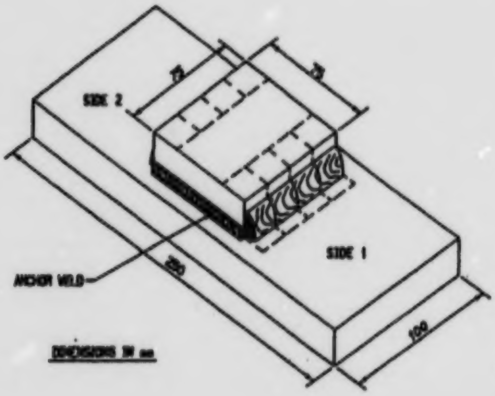

DERA

Structural Materials Centre

CTS Results

Process	Consumable	Heat Input (kJ/mm)	Preheat (°C)	Crack Result
MIG	Fluxofil 41/ATAL 5	1.0	20	Cracked near lack of fusion
MIG	Corofil NQ1	1.3	18	Uncracked
MIG	Fluxofil 41/ATAL 5	1.5	20	Uncracked
MIG	Corofil NQ1	1.6	18	Uncracked
MIG	Corofil NQ1	2.0	18	Uncracked
MIG	Union MoNi/ATAL 5	1.0	20	Uncracked
MIG	Union MoNi/ATAL 5	1.5	20	Uncracked
MMA	Tenacito 65R	1.0	20	Uncracked
MMA	Tenacito 65R	1.5	20	Uncracked
MMA	Fortrex NQ1	2.0	18	Cracked, [H] > 5mls

DERA

Structural Materials Centre

Cost Benefits

- Q1(N) ~ £1600/tonne
- Shoralsim 500 MOD expected to be < £1000/tonne
- Welding without preheat should reduce fabrication costs by ~30%.

DERA

Structural Materials Centre

Further Work

- Short Term
  - Identify the cause of brittle fracture observed in a small number of drop weight J tests.
  - Further weldability studies.
- Longer Term
  - Establish that the properties are reproducible and consistent in all the product forms and exceed the requirements of NES 736.
  - Demonstrate that the material can be welded without preheat in the shipyard environment.

DERA

Structural Materials Centre

Summary

- Shoralsim 500 MOD, Belgian steel, available in gauges up to 50mm.
- Tensile properties exceed the demands of NES 736 Part 1.
- Charpy impact energy >100J @ -84°C.
- EDM Charpy exceeds the proposed test requirements.
- 25mm and 50mm thick plate has passed the explosively loaded test requirement but cleavage fracture has been seen at -5°C in one drop weight J test.
- Corrosion fatigue crack growth rates are higher than Q1(N) but comparable to other high strength low alloy steels.
- Steel is weldable at ambient temperature preheat.

#511914 (40)

Assessment of the Fracture Toughness of Pipeline Girth Welds

by J. A. Gianetto[1], G. Shen[1], W.R. Tyson[1] and A. G. Glover[2]

[1]Materials Technology Laboratory-CANMET
Ottawa, Ontario, Canada

[2]TransCanada PipeLines Ltd
Calgary, Alberta, Canada

ABSTRACT

The crack-tip-opening displacement (CTOD) fracture toughness and Charpy absorbed energy of the base metal, weld metal and heat-affected zone (HAZ) of a pipeline girth weld were measured for several notch orientations, as well as for simulated HAZ regions produced using a Gleeble 2000 thermal-mechanical simulator. The results show that the CTOD toughness variability can be described by a weakest-link model and Weibull statistics. The present work illustrates how the toughness variability associated with girth welds in pipelines may be quantified for use in engineering critical assessment procedures.

Assessment of the Fracture Toughness of Pipeline Girth Welds

J. A. Gianetto, G. Shen, W.R. Tyson

Materials Technology Laboratory-CANMET
Ottawa, Ontario, Canada

and

A. G. Glover

TransCanada PipeLines Ltd.
Calgary, Alberta, Canada

Materials Technology Laboratory-CANMET

Background

- **Fracture toughness assessments of weld metal and HAZ regions are used for:**
- **Pre-qualification testing and defect assessments.**
- **As input parameters for ECA and fracture mechanics analysis.**
- **A major concern is the high degree of variability (scatter) in cleavage fracture toughness, especially in the ductile-to-brittle transition region**
- **Micromechanical and statistical modeling procedures are used to characterize the toughness variability**

Materials Technology Laboratory-CANMET

Objective

To establish the degree of scatter in different regions (base metal, HAZ and weld metal) of a multipass pipeline girth weld.

Materials Technology Laboratory-CANMET

Linepipe Steel - NPS-36 Grade X52

- **914 mm dia. Grade 359 MPa 10.4 mm W.T.**
- **1960's C-Mn hot-rolled steel**
- **Properties**

• Transverse Yield Strength	370-390 MPa
• Transverse Ultimate Strength	550-560 MPa
• Longitudinal Yield Strength	360-380 MPa
• Longitudinal Ultimate Strength	550-570 MPa
• Charpy Impact Energy	16 J at –5°C and 5 J at –45°C
• Drop Weight Energy	270 J at –5°C with 5% shear

Materials Technology Laboratory-CANMET

Girth Welding Procedures

- Two field girth welds were made by NGTL.
  - SMAW E55010-G cellulosic electrodes
  - Vertical down welding technique.
  - Minimum preheat = 100°C
  - Energy input range = 0.56-2.33 kJ/mm

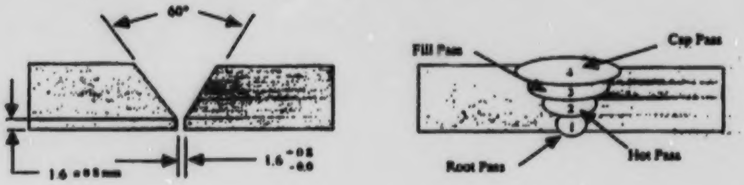
60°
1.6 ± 0.8 mm
$1.6^{+0.8}_{-0.0}$
Fill Pass
Cap Pass
4
3
2
1
Root Pass
Hot Pass

Materials Technology Laboratory-CANMET

Chemical Composition

Material	Element wt %						
	C	Mn	Si	S	P	Cr	Ni
BM	0.19	1.0	0.017	0.037	0.027	0.02	0.04
Weld 1	0.16	0.91	0.08	0.007	0.011	0.12	0.78
Weld 2	0.15	1.1	0.16	0.007	0.011	0.12	0.78

Note: Cu<0.04: Mo<0.03: Ti, Nb and V <0.01; Al<0.006

Materials Technology Laboratory-CANMET

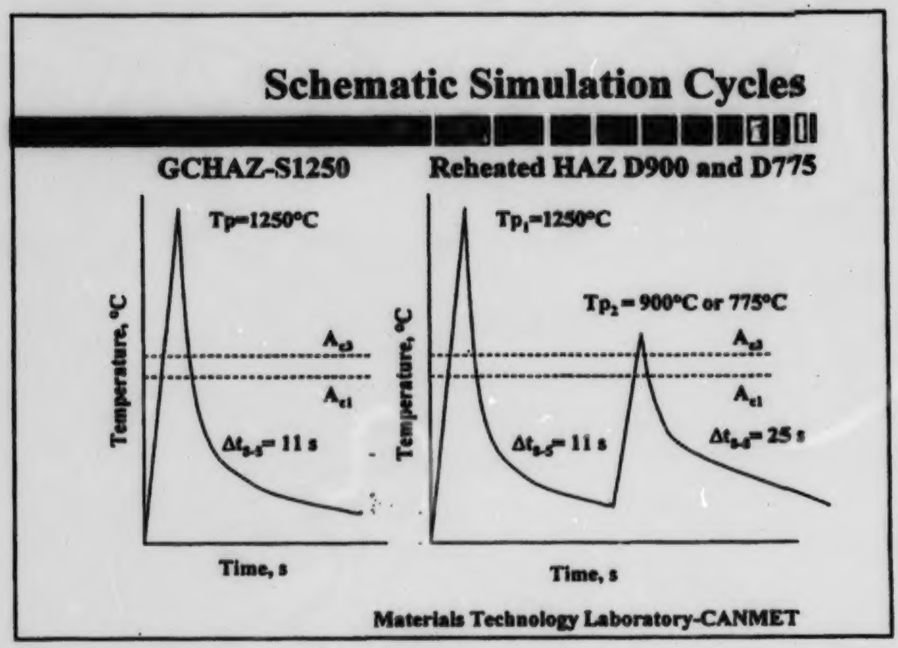

Schematic Simulation Cycles

GCHAZ-S1250

Reheated HAZ D900 and D775

Materials Technology Laboratory-CANMET

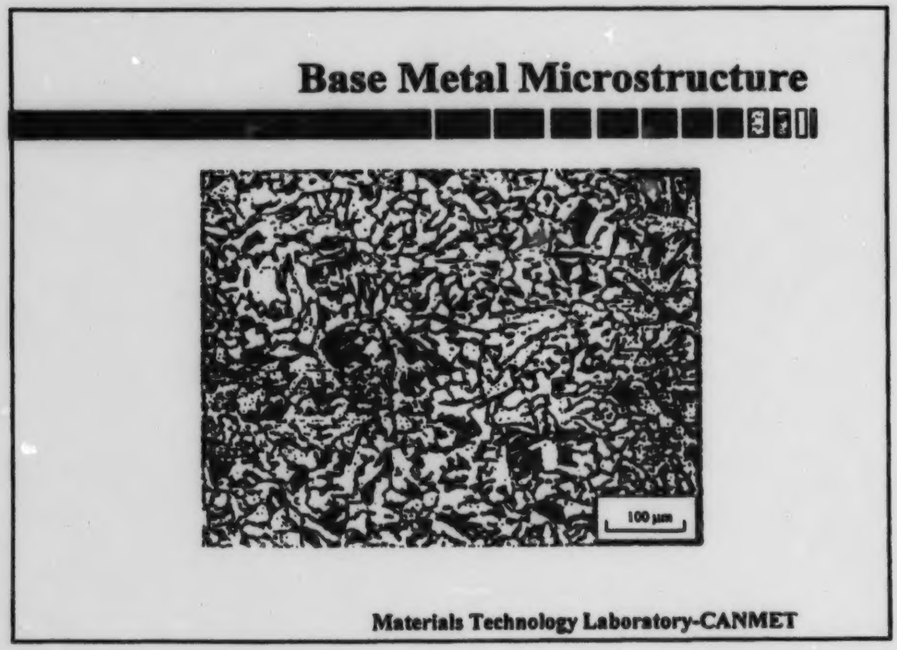

Base Metal Microstructure

Materials Technology Laboratory-CANMET

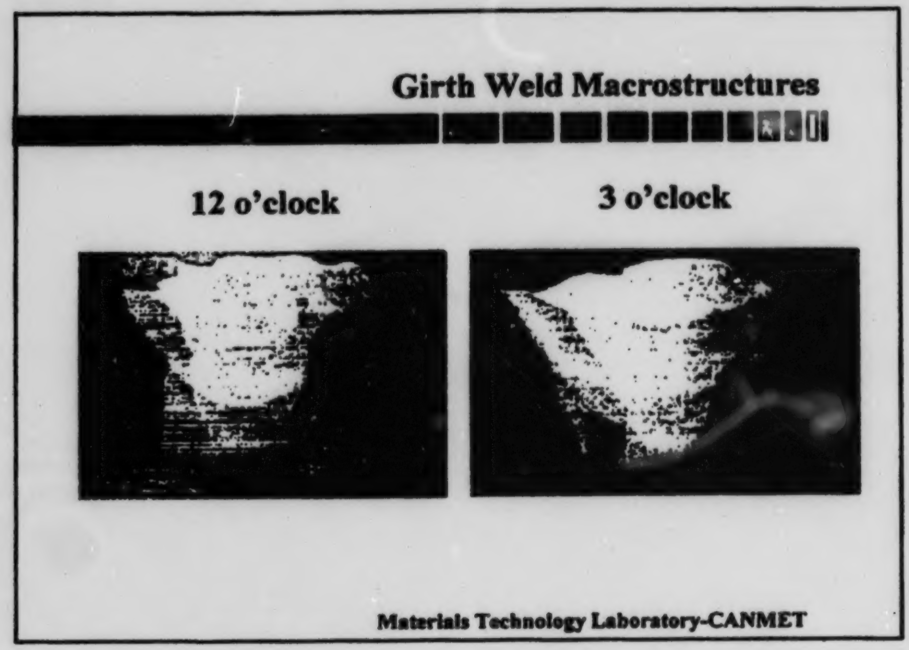

Girth Weld Macrostructures

12 o'clock

3 o'clock

Materials Technology Laboratory-CANMET

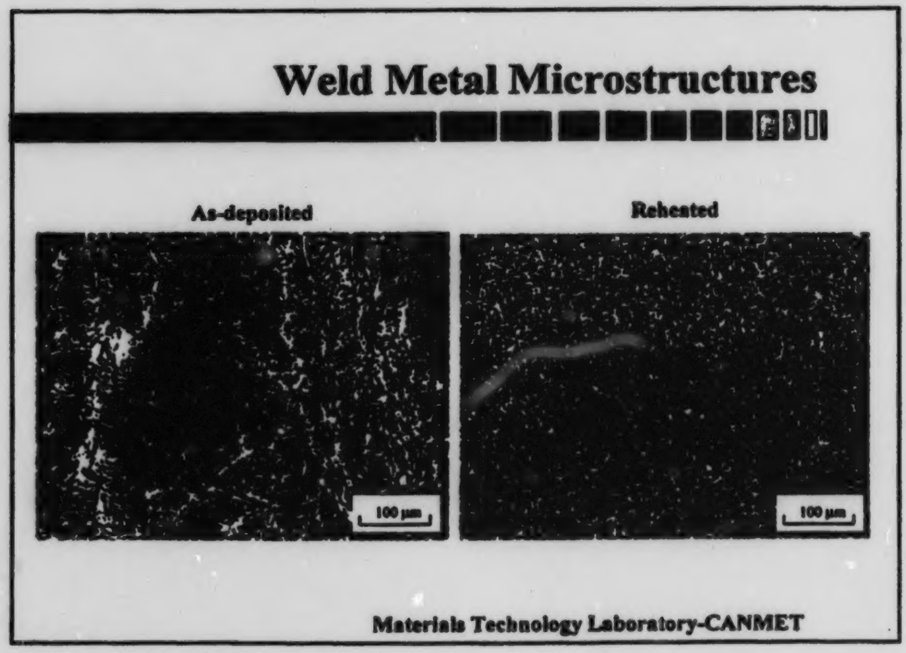

Weld Metal Microstructures

As-deposited

Reheated

Materials Technology Laboratory-CANMET

HAZ Microstructures

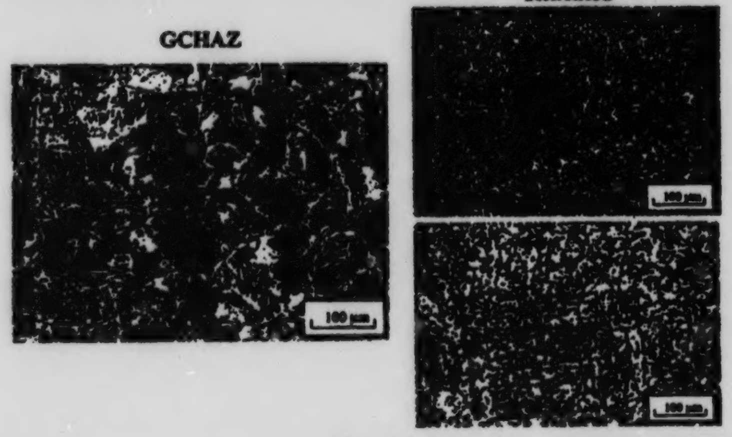
GCHAZ

Reheated

Materials Technology Laboratory-CANMET

Microhardness (VHN)

Location	12 o'clock	3 o'clock
Weld Metal Centerline	171 (157-208)	190 (164-242)
GCHAZ	193 (188-197)	196 (191-200)
Mid-Thickness Reheated HAZ	166 (165-168)	173 (170-177)
Root Region Reheated HAZ	161 (160-161)	165 (157-169)

Note: Base Metal = 170 (159-183)

Materials Technology Laboratory-CANMET

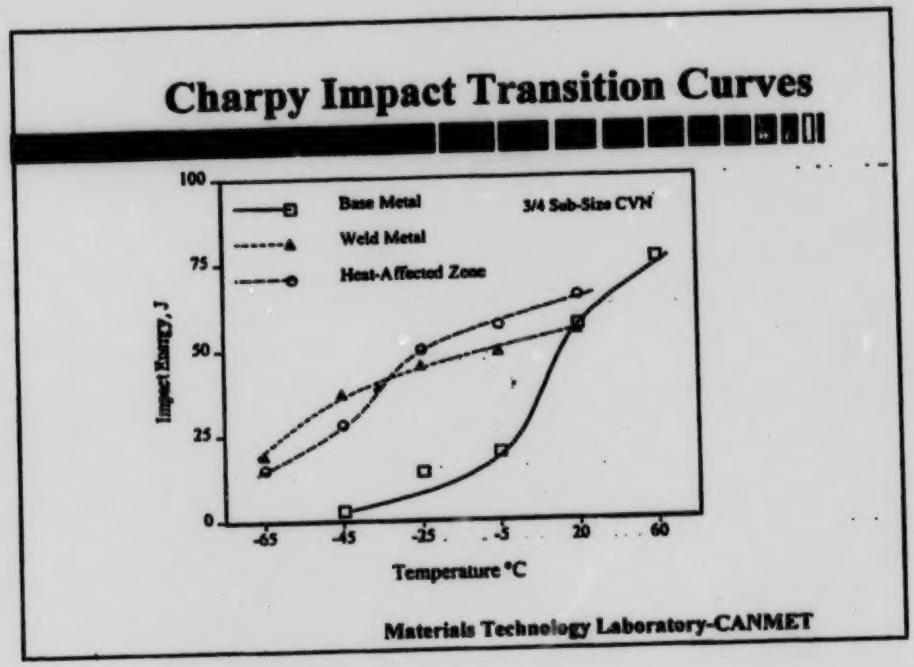

Charpy Impact Transition Curves

Materials Technology Laboratory-CANMET

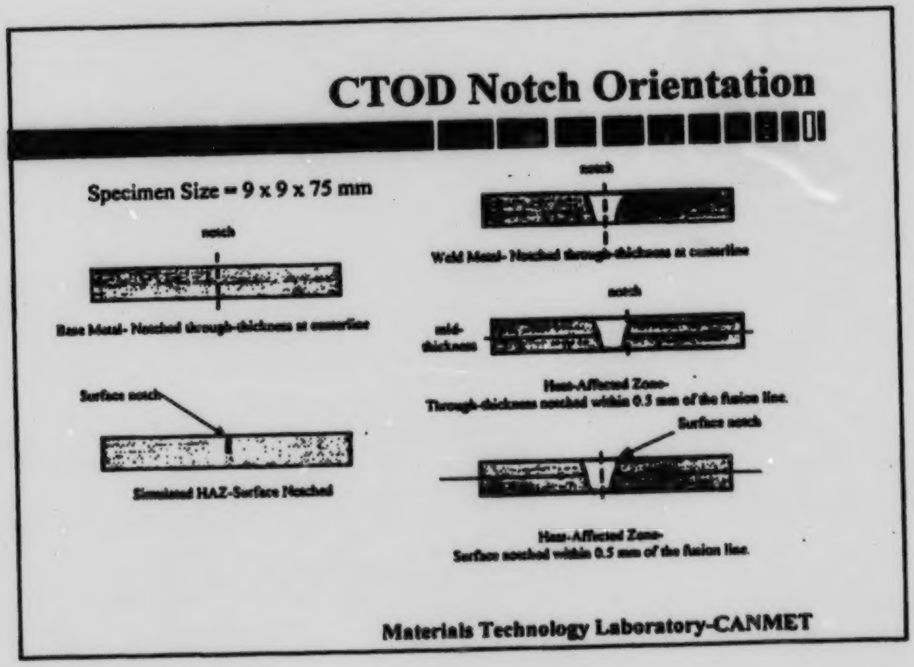

CTOD Notch Orientation

Specimen Size = 9 x 9 x 75 mm

notch
notch
notch
mid-thickness
Surface notch
Surface notch

Base Metal- Notched through-thickness at centerline

Simulated HAZ-Surface Notched

Weld Metal- Notched through-thickness at centerline

Heat-Affected Zone-
Through-thickness notched within 0.5 mm of the fusion line.

Heat-Affected Zone-
Surface notched within 0.5 mm of the fusion line.

Materials Technology Laboratory-CANMET

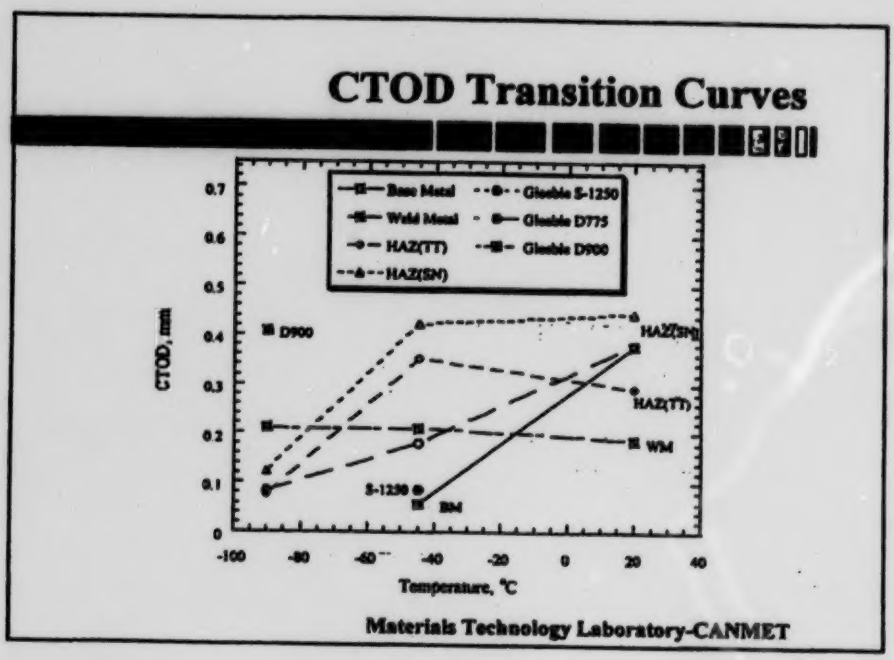

CTOD Transition Curves

Materials Technology Laboratory-CANMET

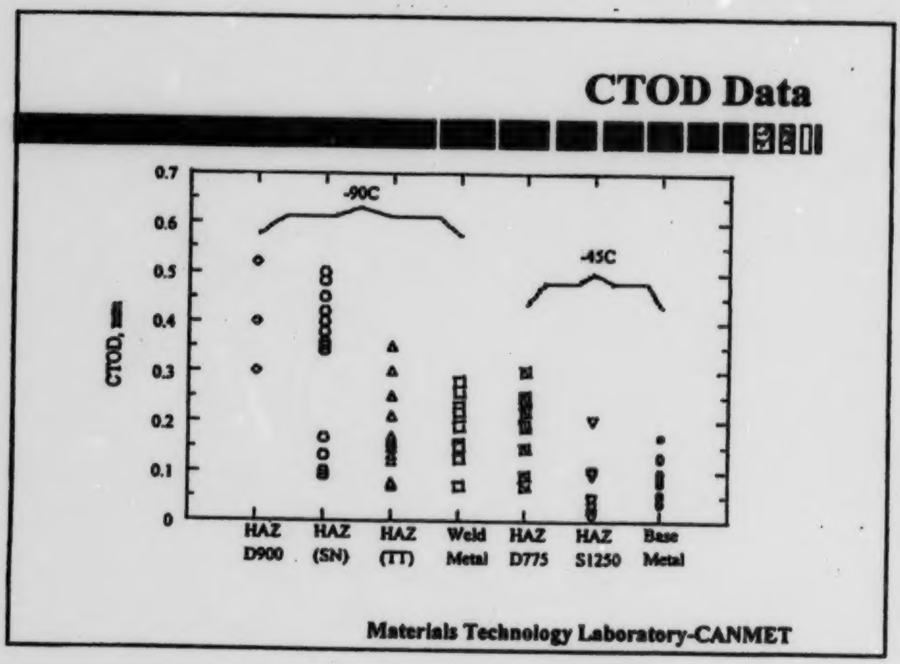

CTOD Data

Materials Technology Laboratory-CANMET

Weibull Plot for CTOD tests at -45°C

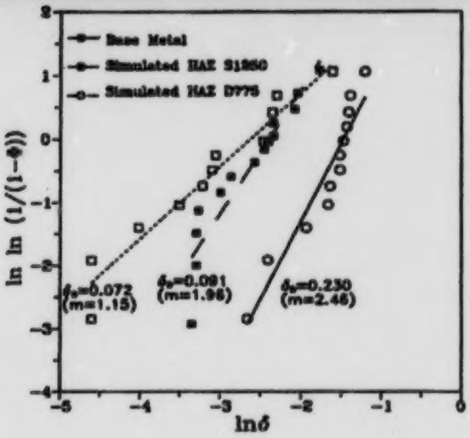

Materials Technology Laboratory-CANMET

Weibull Plot for CTOD tests at -90°C

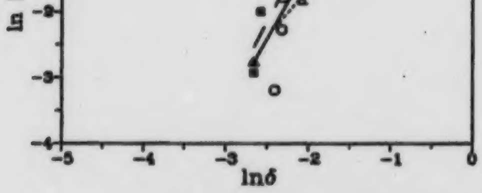

Materials Technology Laboratory-CANMET

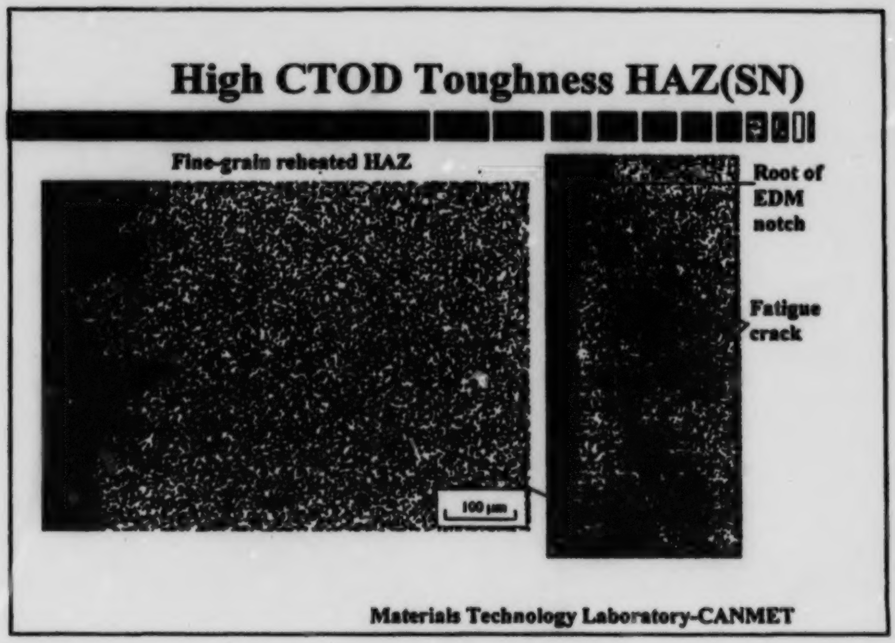

High CTOD Toughness HAZ(SN)

Fine-grain reheated HAZ

Root of EDM notch

Fatigue crack

100 µm

Materials Technology Laboratory-CANMET

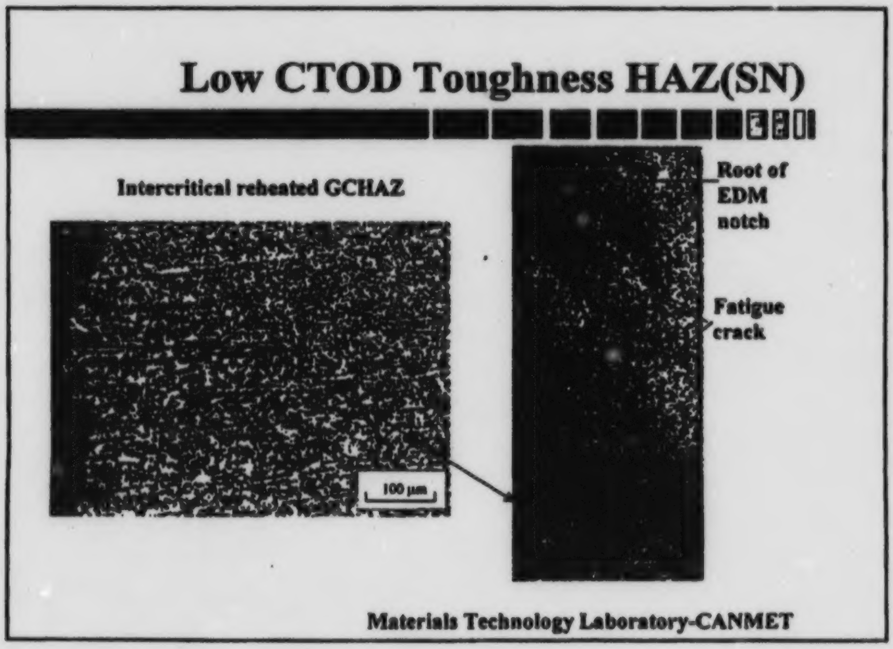

Low CTOD Toughness HAZ(SN)

Intercritical reheated GCHAZ

Root of EDM notch

Fatigue crack

100 µm

Materials Technology Laboratory-CANMET

Secondary Microcracks

Base Metal

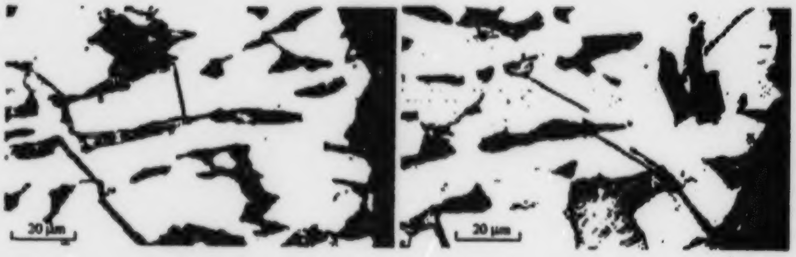

Materials Technology Laboratory-CANMET

Secondary Microcracks

Simulated GCHAZ

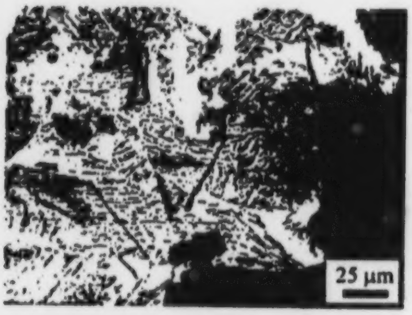

Materials Technology Laboratory-CANMET

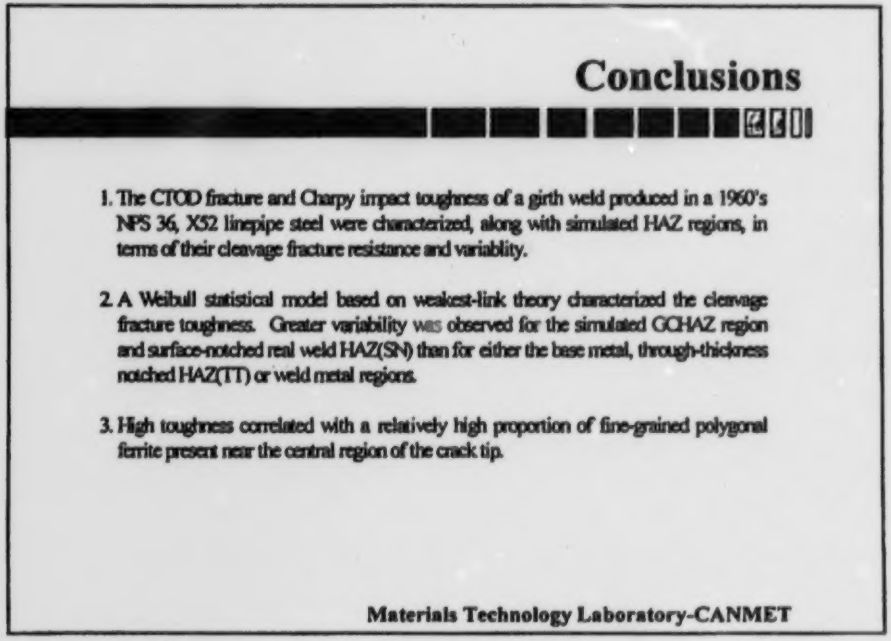

Conclusions

1. The CTOD fracture and Charpy impact toughness of a girth weld produced in a 1960's NPS 36, X52 linepipe steel were characterized, along with simulated HAZ regions, in terms of their cleavage fracture resistance and variablity.

2. A Weibull statistical model based on weakest-link theory characterized the cleavage fracture toughness. Greater variability was observed for the simulated GCHAZ region and surface-notched real weld HAZ(SN) than for either the base metal, through-thickness notched HAZ(TT) or weld metal regions.

3. High toughness correlated with a relatively high proportion of fine-grained polygonal ferrite present near the central region of the crack tip.

Materials Technology Laboratory-CANMET

#511915 (41)

Probabilistic Modeling of Corroded Ship Structural Panels

by I.R. Orisamolu, D.P. Brennan and U.O. Akpan

Research and Emerging Technologies Department
Martec Limited, Suite 400, 1888 Brunswick Street, Halifax, NS, Canada, B3J 3J8

ABSTRACT

Corrosion is one of the most important damage mechanisms for ship structures and a significant portion of the maintenance budget is directed toward corrosion-related problems. A major challenge associated with the assessment of the impact of corrosion on the integrity of engineering structures is the quantification of the amount and severity of the corrosion damage that is present in those structures. Corrosion defects are typically characterized by random spatial distributions and variabilities in sizes, shapes, and morphological characteristics throughout the exposed part of the structure. For ship structures in particular, current corrosion pit survey practices are largely based on a visual assessment of the state of corrosion, making the assessment of the impact of corrosion a highly qualitative process that is also very susceptible to error. The present work has been motivated by the desire to provide a realistic and systematic framework for utilizing data collected during ship structural surveys to assess the probabilistic residual strength of corroded ship structural panels.

In this work some probabilistic models that have been developed to realistically represent corrosion damage on typical engineering structures are presented. These models include extreme value distribution representations of the individual corrosion pits as well as random field models of the distribution of a population of corrosion pits or general corrosion. Random field models offer a powerful strategy for the characterization of the uncertainties that are associated with the spatial distribution, extent, severity, as well as the stochastic interaction between neighboring defects. This study reports the development and implementation of robust computational algorithms for defining appropriate probabilistic models of the corrosion damage on engineering structures from observed data. The application of these algorithms is demonstrated for representative ship structural panels and pipeline structures.

#511916 (42)

Application of Probabilistic Corrosion Model for Reliability Assessment of Ship Structural Panels

by I.R. Orisamolu, U. O. Akpan and D.P. Brennan

Research and Emerging Technologies Department
Martec Limited, Suite 400, 1888 Brunswick Street, Halifax, Nova Scotia, Canada
B3J 3J8

ABSTRACT

Corrosion is one of the most important damage mechanisms for ship structures and a significant portion of the maintenance budget is directed toward corrosion-related problems. There are several forms of corrosion that could be present in ship panels. The two broad categories in this regard are pitting and general corrosion. Although ship engineers have employed this categorization scheme, the natural morphology of real corrosion defects is usually somewhere between the two. In a companion presentation [1] a random filed modelling approach for characterization of the effective thickness of ship structural panels due to corrosion has been developed.

In this work the reliability assessment of the residual strength of ship structural panels based on the random field model of effective thickness is undertaken. Advanced probabilistic reliability techniques namely: the first-order and second-order reliability methods are employed to compute the reliability of corroded ship panels with reference to different failure modes. The merit of the probabilistic approach is demonstrated via the solution of several example problems, and the use of quantitative measures of probabilistic sensitivity to illustrate the most important model parameters and their associated uncertainties is given.

1. I.R. Orisamolu, D.P. Brennan and U.O. Akpan., Probabilistic Modeling of Corroded Ship Structural Panels, to be presented at the 8th CF/CRAD Meeting on Naval Applications of Material Technology, Halifax, NS, May 1999

#311917 (43)

Residual and Applied Stress Characterization of NiAl Bronze using X-Ray Diffraction

by Michael Brauss *, John Porter **, Mohammed Belassel *,
Calvin Hyatt **, and James Pineault*

***Proto Manufacturing Ltd, Oldcastle, Ontario, Canada**
****Dockyard Lab (A), DREA, Halifax, Nova Scotia, Canada**

ABSTRACT

The ability to accurately quantify the residual strains in NiAl bronze components enables a more complete understanding and improved prediction of potential failure mechanisms. The application of x-ray diffraction methods to the measurement of residual strains, while long accepted, has been limited to laboratory based experimentation. In addition, the challenges associated with diffraction measurements in large grained materials have made the application of these technologies to large NiAl bronze castings and components problematic. Developments to create a portable miniature x-ray diffractometer (MXRD) have permitted the field application of diffraction technologies. Specific recent enhancements to optimize the performance of the system, including implementation of automatic Ψ (psi) axis oscillation for large grained materials now permits the characterization of residual strains in these materials, not only in laboratory but also in field experimentation. This presentation outlines the recent MXRD developments, including results obtained from evaluations of NiAl bronze samples loaded in four point bending.

#511918

㊹

Current Developments in Residual Stress Measurement by Invasive But Nondestructive Methods.
Is the Complementarity There?

by G. Roy [1] , J. Porter [2], T. Holden [3], and J., Pineault [4]
[1] CANMET/MTL, [2] DREA, [3] NRC, and [4] Proto

ABSTRACT

Four methods of nondestructive residual stress determination, X-ray Diffraction (XrD), Neutron Diffraction, Magnetic Barkhausen Noise (MBN), and Acousto elasticity using Electromagnetic Acoustic Transducers (EMAT) were used to determine residual stress in a steel plate. The results were compared with analytically calculated and Finite-Element-Method computed stress distributions, based on the plate geometry and boundary conditions, such as forces and displacements.

The plate material was ASTM A517 steel (Grade 117), with an upper yield strength of 810MPa, and its chemical analysis confirmed the low-alloy composition, except for a substantially lower value of Cu, 0.19 instead of 0.40. Its elastic constants, (determined from tensile test specimens) were, Young's modulus, 225GPa, and Poisson's ratio, 0.28. The nominal dimensions of the plate were 610mm (length) x 305mm (width) x 12mm (thickness)

The plate was subjected to a strain-gauge controlled four-point bending beyond the yield strength, and unloaded. After elastic spring back, the plate was in a state of residual stress in a central part of 150mm(length) x 300mm (width).

There was a two-part objective of this study: 1) to assess the accuracy of the methods on a known stress state, and 2) to determine the degree of complementarity of the methods.

The results indicate an adequate correlation between the determined stress states within acceptable engineering error bounds of 5-10%.

#511919 (4

Materials Solutions to the Aging Aircraft Problem

by K.I. McRae

Air Vehicles Research Detachment, National Defence Headquarters, 101 Colonel By Drive, Ottawa, Ontario, K1A OK2

ABSTRACT

The Air Vehicles Research Detachment is responsible for the delivery of all R&D that directly concerns the CF aircraft in the areas of aircraft structures and materials, aeropropulsion, aerodynamics and flight mechanics. The constraints to maintain these fleets of aging aircraft for extended periods of time has required the development of novel approaches and concepts in order to reduce the costs involved in this long term maintenance effort. This paper will outline the severity of the "aging aircraft" problem within the CF and will describe several of these recent developments that are or will be applied from the materials perspective. These will include:

- a novel heat treatment for 7075-T6 aluminum alloys in order to reduce the incidence of stress corrosion cracking and the possible in-situ application on major aircraft structural components;
- the development of methodologies for the repair and re-certification of gas turbine engine components;
- the development of improved techniques for nondestructive evaluation, particularly for the detection of hidden corrosion and cracks under fasteners; and
- the development of new metrics for the quantification of corrosion as well as methods for assessing the interaction of corrosion and fatigue damage.

DEFENCE DEFENSE

Canada

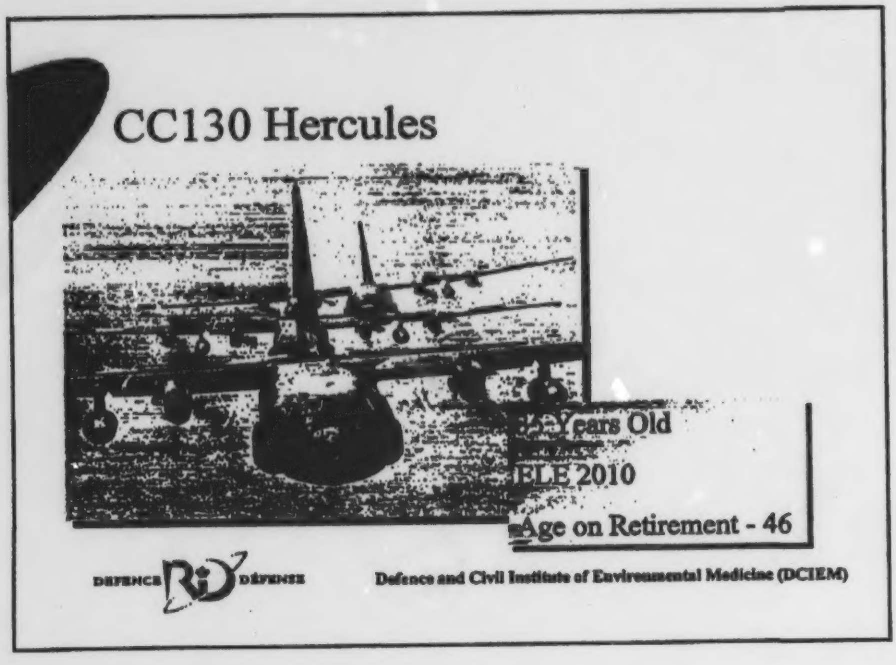

CC130 Hercules

[illegible] Years Old

ELE 2010

Age on Retirement - 46

DEFENCE DÉFENSE

Defence and Civil Institute of Environmental Medicine (DCIEM)

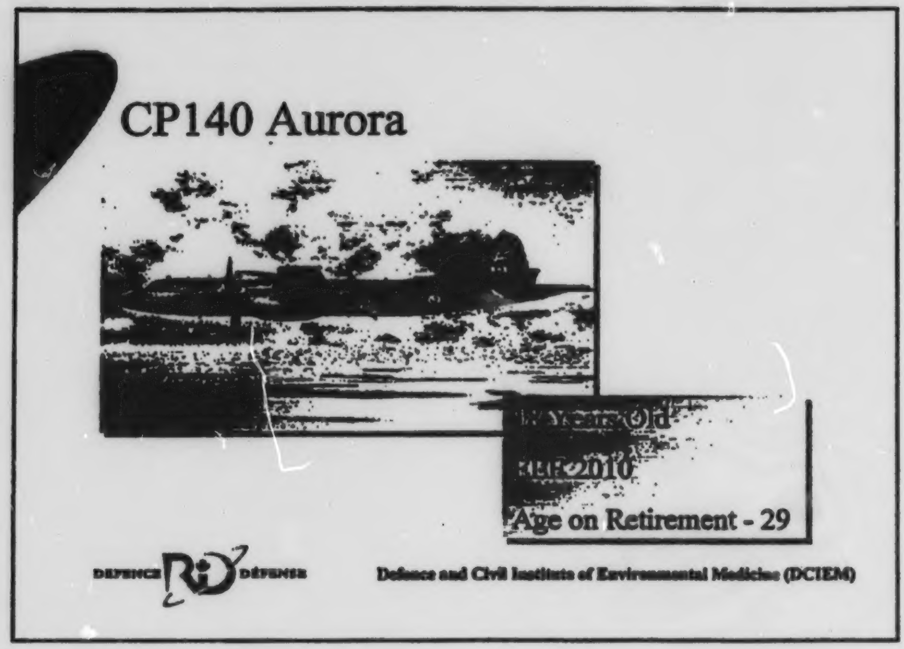

CP140 Aurora

[illegible] Years Old

ELE 2010

Age on Retirement - 29

DEFENCE DÉFENSE

Defence and Civil Institute of Environmental Medicine (DCIEM)

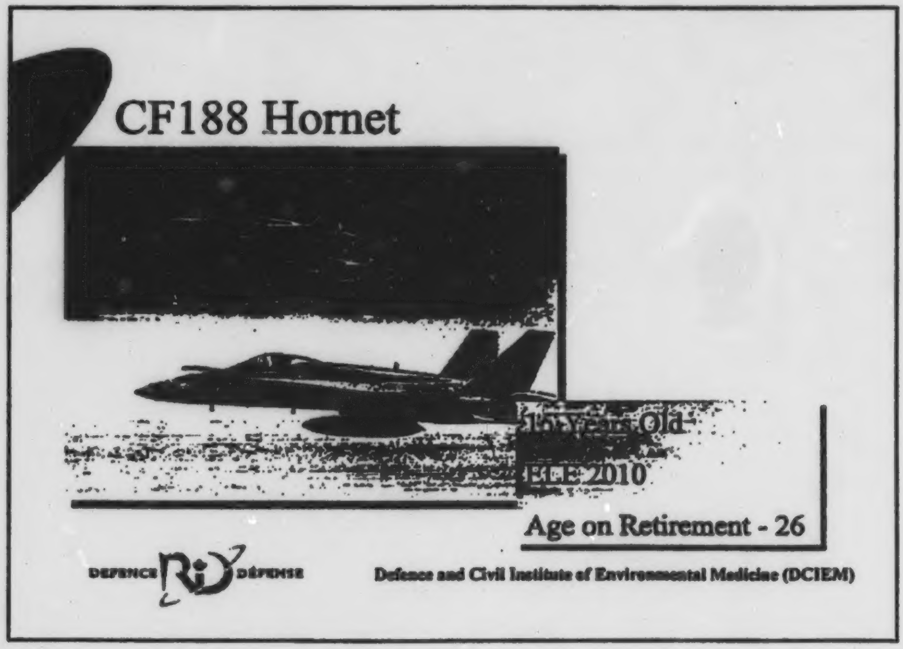

CF188 Hornet

[illegible] Years Old

ELE 2010

Age on Retirement - 26

DEFENCE DÉFENSE

Defence and Civil Institute of Environmental Medicine (DCIEM)

The Aging Aircraft Problem

- All aircraft fleets will see service up to or beyond their original design life.
  - Management of fatigue (airframes and engines) will continue to be an issue.
- The management and abatement of corrosion will become an increasingly important issue.
- Airworthiness of all CF fleets will be maintained, but...
  - How can the cost of maintenance be reduced?
  - When has the economic life of an aircraft been exceeded?

DEFENCE DÉFENSE Defence and Civil Institute of Environmental Medicine (DCIEM)

Presentation Outline

- The Aging Aircraft Problem
- Relationship of DRDB and DGAEPM programs
- Airframe structural repair technologies
- Engine life assessment and extension
- Advanced materials research
- Novel NDT techniques
- Advanced structural integrity concepts
- Conclusion

DEFENCE DÉFENSE Defence and Civil Institute of Environmental Medicine (DCIEM)

Aging Aircraft Program Delivery

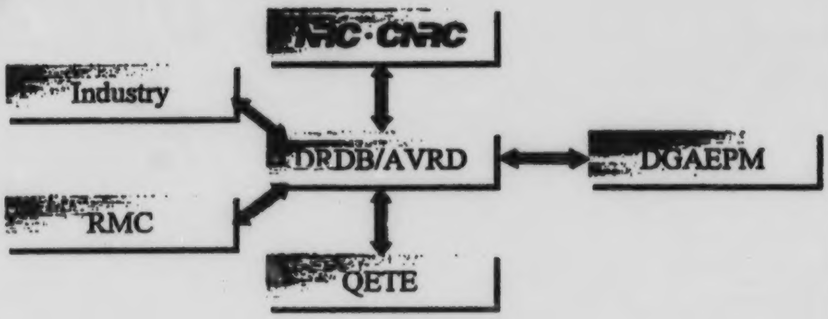

DEFENCE R&D DÉFENSE

Defence and Civil Institute of Environmental Medicine (DCIEM)

Air Vehicles Technologies

DRDB has structured three projects within the Air Vehicles Technologies Thrust to address these problems:

- Aeropropulsion/Gas Turbine Technologies
- Aircraft Structures and Materials
- Gas Turbine Repairs/reworks

DEFENCE R&D DÉFENSE

Defence and Civil Institute of Environmental Medicine (DCIEM)

Airframe Structural Repair

- Composite patch for fatigue life enhancement
  - CF188 Bulkhead Composite Patch
  - Improved patch adhesion and durability

- Novel heat treatments
  - in-situ RRA for CC130 sloping longeron

Defence and Civil Institute of Environmental Medicine (DCIEM)

CF-18 Bulkhead Composite Patch

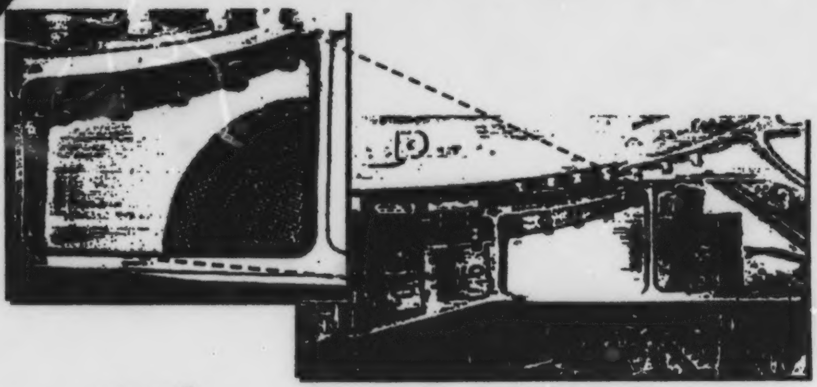

Defence and Civil Institute of Environmental Medicine (DCIEM)

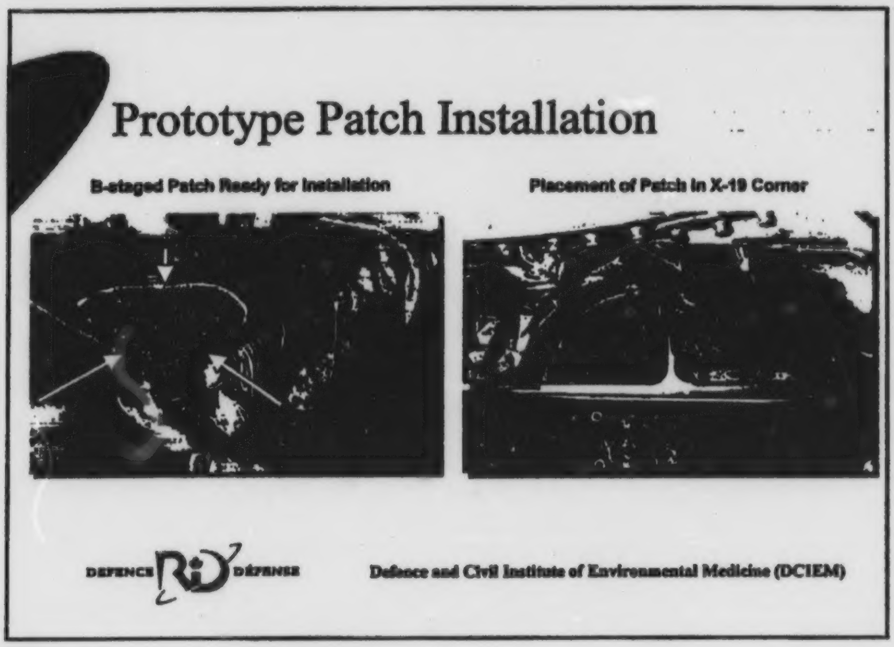

Prototype Patch Installation

B-staged Patch Ready for Installation

Placement of Patch in X-19 Corner

DEFENCE DÉFENSE

Defence and Civil Institute of Environmental Medicine (DCIEM)

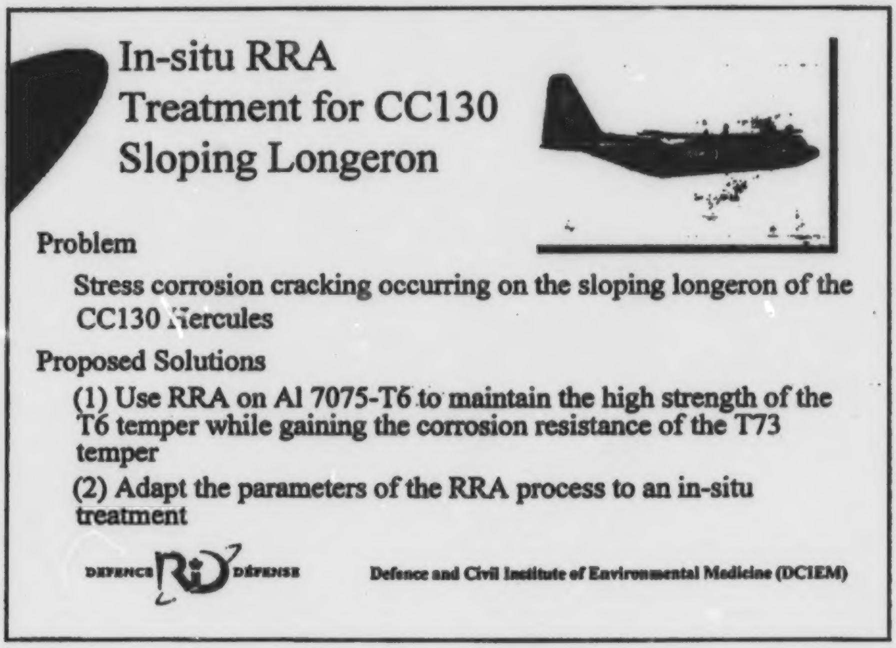

In-situ RRA Treatment for CC130 Sloping Longeron

Problem

Stress corrosion cracking occurring on the sloping longeron of the CC130 Hercules

Proposed Solutions

(1) Use RRA on Al 7075-T6 to maintain the high strength of the T6 temper while gaining the corrosion resistance of the T73 temper

(2) Adapt the parameters of the RRA process to an in-situ treatment

DEFENCE DÉFENSE

Defence and Civil Institute of Environmental Medicine (DCIEM)

RRA - CC130 sloping longeron

Tests were conducted on service-exposed longeron using Zimac hot bonder and heater cells/blankets, heat was applied directly to the longeron in localized regions.

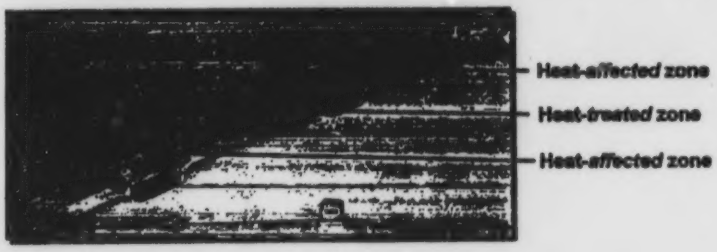
Heat-affected zone
Heat-treated zone
Heat-affected zone

Defence and Civil Institute of Environmental Medicine (DCIEM)

RRA - CC130 sloping longeron

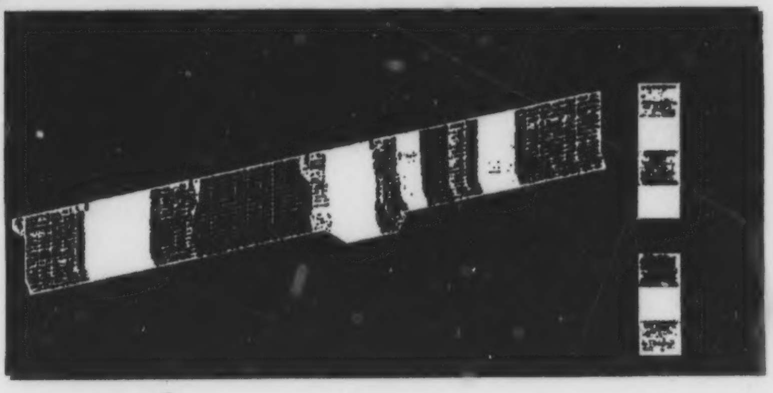

Defence and Civil Institute of Environmental Medicine (DCIEM)

Engine Life Extension

- Damage tolerance and life extension methodologies for:
  - NENE X
  - J-85 CAN 40
- Repair, Re-works and Certification Methodologies for F404

DEFENCE DÉFENSE

Defence and Civil Institute of Environmental Medicine (DCIEM)

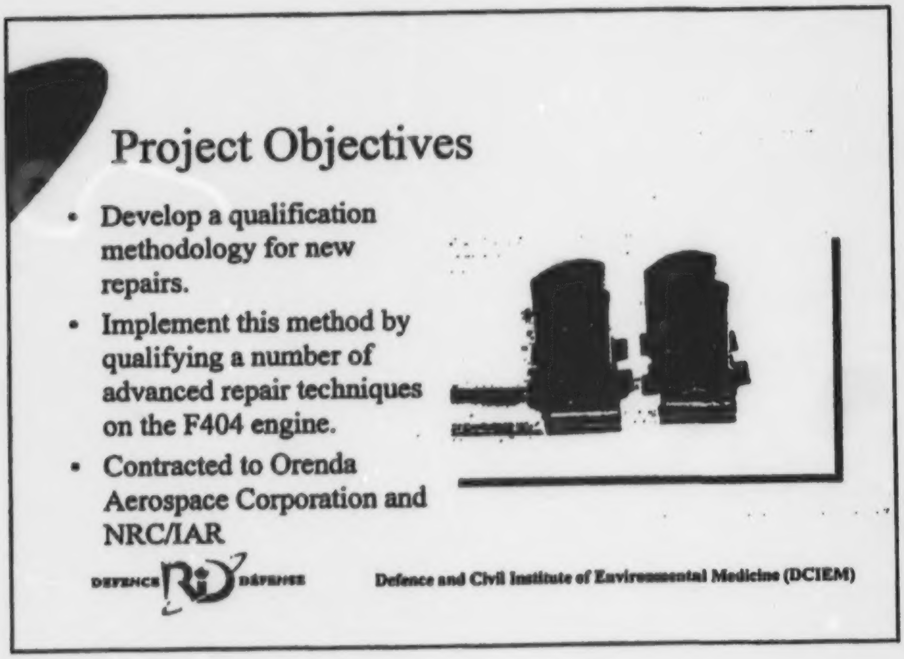

Project Objectives

- Develop a qualification methodology for new repairs.
- Implement this method by qualifying a number of advanced repair techniques on the F404 engine.
- Contracted to Orenda Aerospace Corporation and NRC/IAR

DEFENCE DÉFENSE

Defence and Civil Institute of Environmental Medicine (DCIEM)

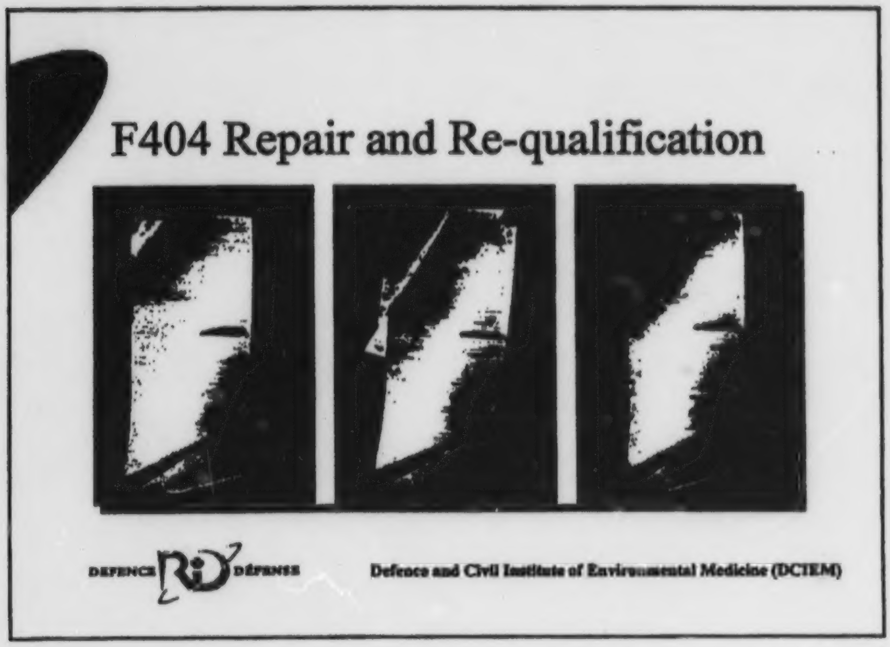

F404 Repair and Re-qualification

Defence and Civil Institute of Environmental Medicine (DCIEM)

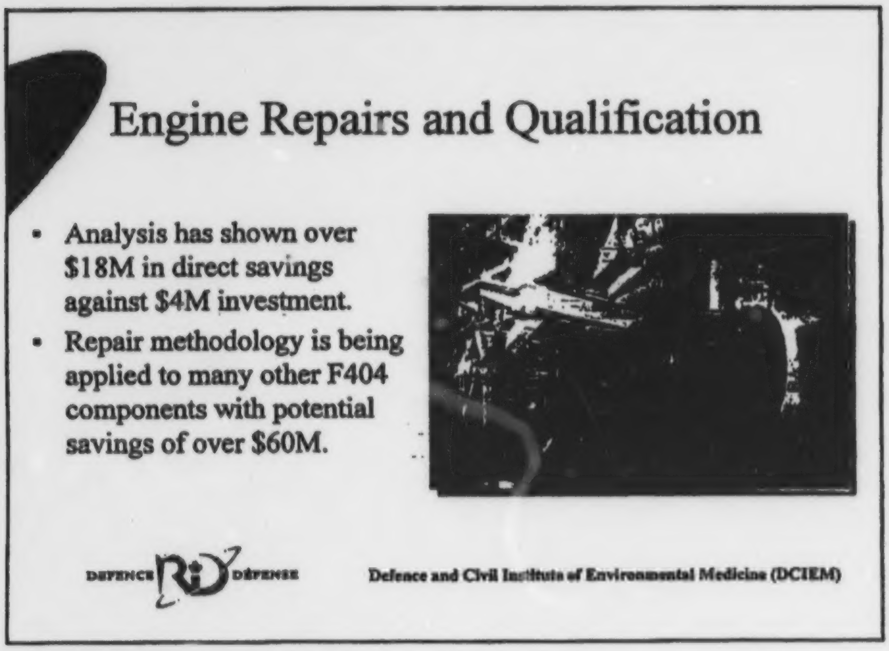

Engine Repairs and Qualification

- Analysis has shown over $18M in direct savings against $4M investment.
- Repair methodology is being applied to many other F404 components with potential savings of over $60M.

Defence and Civil Institute of Environmental Medicine (DCIEM)

Advanced Materials Research

- Improved methods for adhesive bonding and paint adhesion
- High temperature coatings for engine applications
- Thermal spray coatings for corrosion abatement of 7075-T6
- Hard chromium alternative technologies (HCAT)

DEFENCE DÉFENSE

Defence and Civil Institute of Environmental Medicine (DCIEM)

Hard Chromium Alternatives

- US DoD and DND joint program to replace hard chrome on landing gears
- Elimination of Cr^{6+} from the environment
- WC-Co and WC-CoCr coatings applied by HVOF spraying
- Currently limited to landing gear applications but can extend to actuators and engine components

DEFENCE DÉFENSE

Defence and Civil Institute of Environmental Medicine (DCIEM)

Canadian HCAT Project

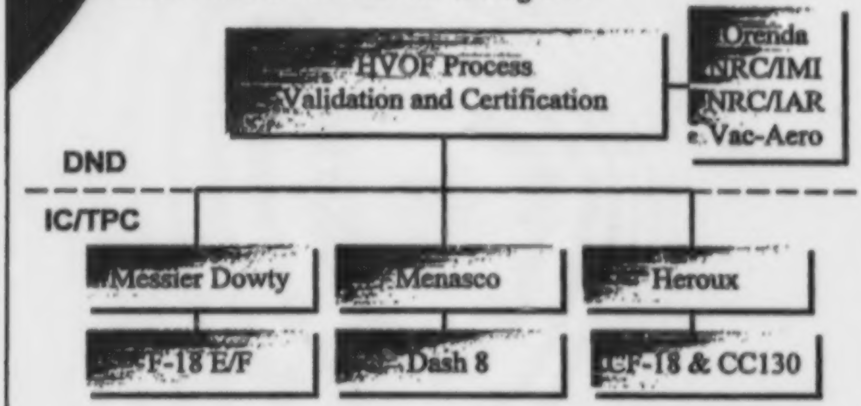
HVOF Process
Validation and Certification
Orenda
NRC/IMI
NRC/IAR
Vac-Aero
DND
IC/TPC
Messier Dowty
Menasco
Heroux
F-18 E/F
Dash 8
CF-18 & CC130

DEFENCE R D DÉFENSE

Defence and Civil Institute of Environmental Medicine (DCIEM)

Canadian Project Benefits

- Compliance with environmental regulations
    - significant cost avoidance - $60M to DoD
- Lower production costs
    - annual savings approx. $1M
- Improved operational capability
    - decreased downtime ⟶ increased availability
- Landing gear manufacturers gain access to US market

DEFENCE R D DÉFENSE

Defence and Civil Institute of Environmental Medicine (DCIEM)

Novel NDT Techniques

- Edge-of-light (NRC/IAR)
- Dual frequency eddy current
- Pulsed eddy current
- Laser ultrasonics
- CF-18 Rudder water ingress
- Cracks under fasteners

DEFENCE R&D DÉFENSE Defence and Civil Institute of Environmental Medicine (DCIEM)

Edge-of-Light for Corrosion Detection

This is a scanner based optical inspection system which finds pillowing caused by corrosion in riveted joints.

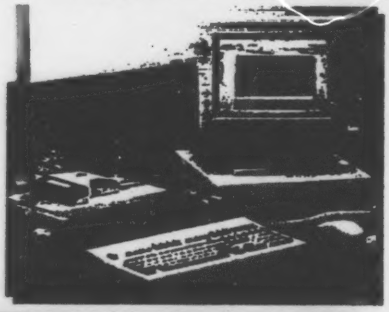

DEFENCE R&D DÉFENSE Defence and Civil Institute of Environmental Medicine (DCIEM)

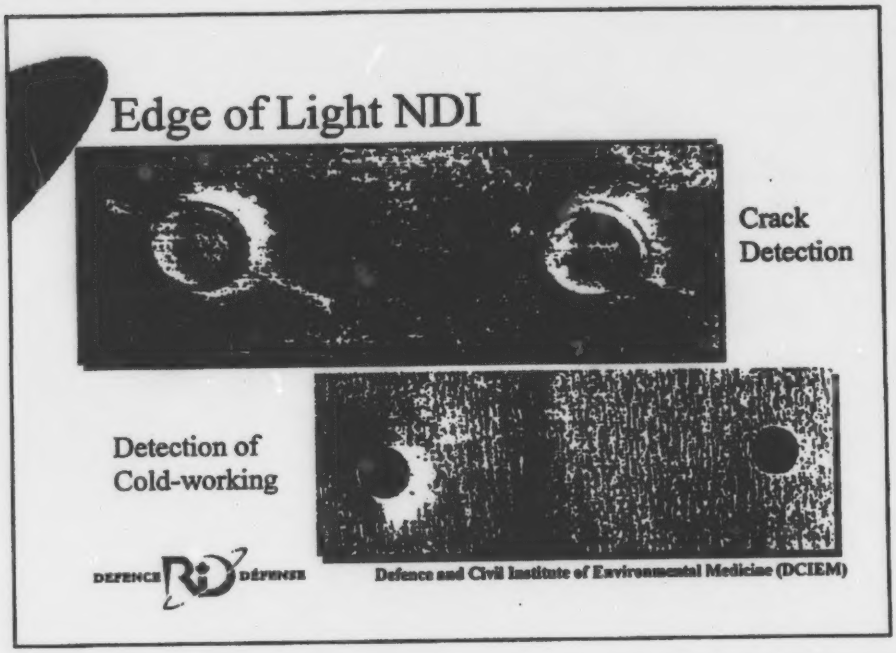

Edge of Light NDI

Crack Detection

Detection of Cold-working

DEFENCE RD DÉFENSE

Defence and Civil Institute of Environmental Medicine (DCIEM)

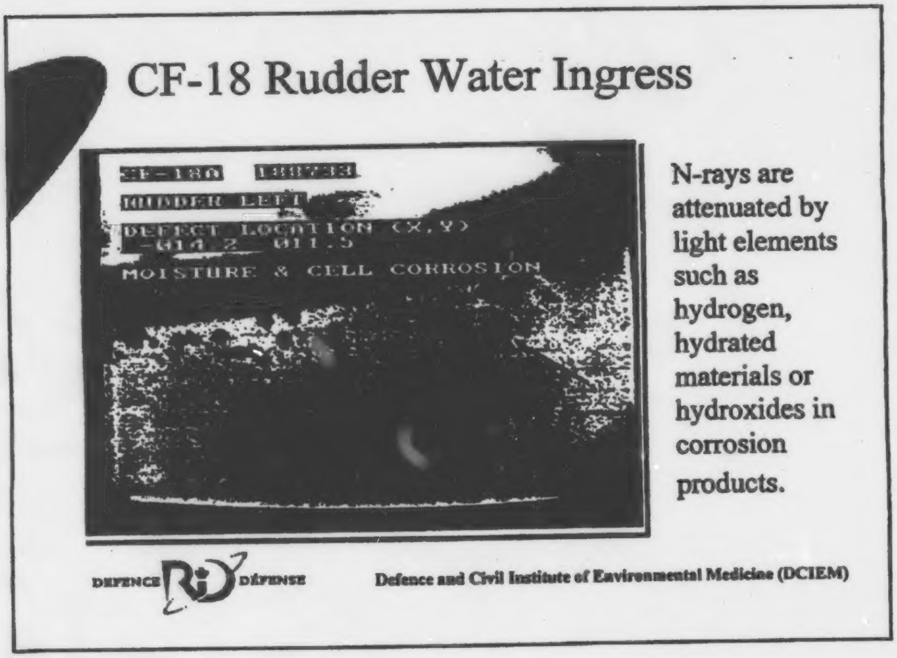

CF-18 Rudder Water Ingress

CF-18A 188733
RUDDER LEFT
DEFECT LOCATION (X,Y)
-014.2 011.5
MOISTURE & CELL CORROSION

N-rays are attenuated by light elements such as hydrogen, hydrated materials or hydroxides in corrosion products.

DEFENCE RD DÉFENSE

Defence and Civil Institute of Environmental Medicine (DCIEM)

NDT Technique Comparison

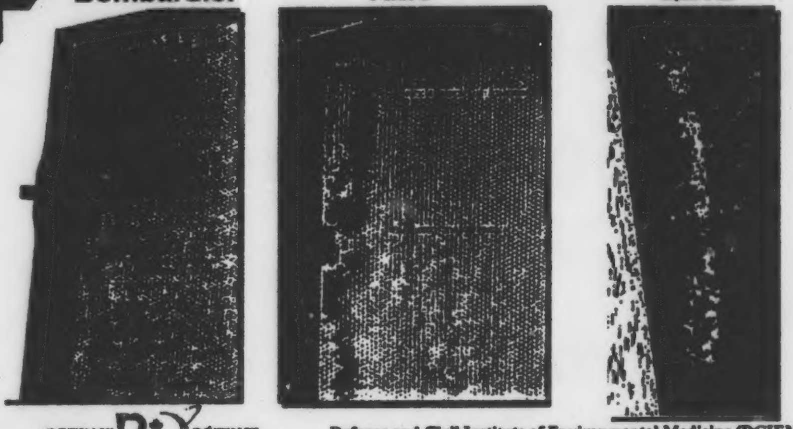

Bombardier **RMC** **QETE**

DEFENCE DÉFENSE Defence and Civil Institute of Environmental Medicine (DCIEM)

Life Cycle Management Issues

- Effect of corrosion pillowing
- Probabilistic reliability assessment
    - fly to a known level of reliability
    - integration with corrosion effects
    - probability of detection (POD) from in-service data

DEFENCE DÉFENSE Defence and Civil Institute of Environmental Medicine (DCIEM)

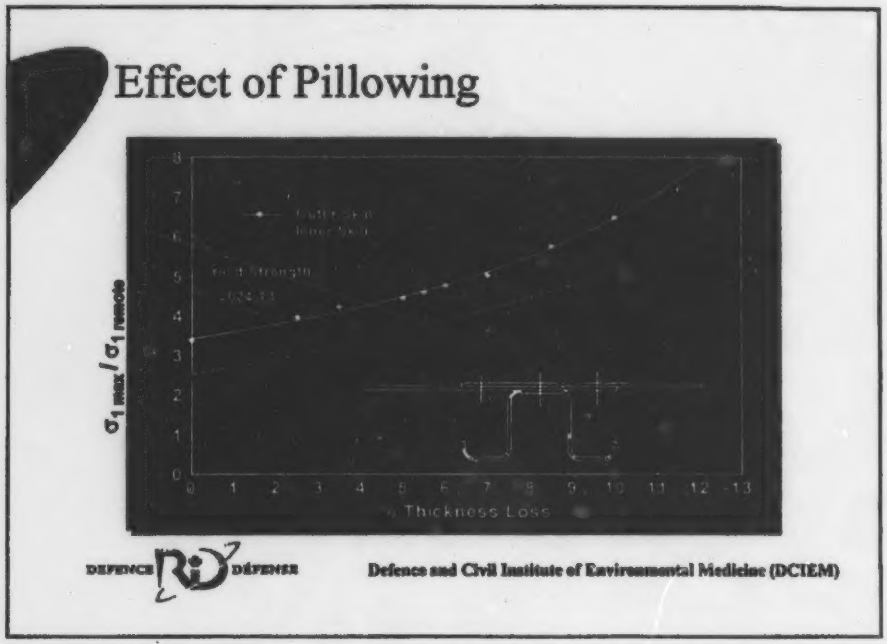

Effect of Pillowing

DEFENCE RD DÉFENSE

Defence and Civil Institute of Environmental Medicine (DCIEM)

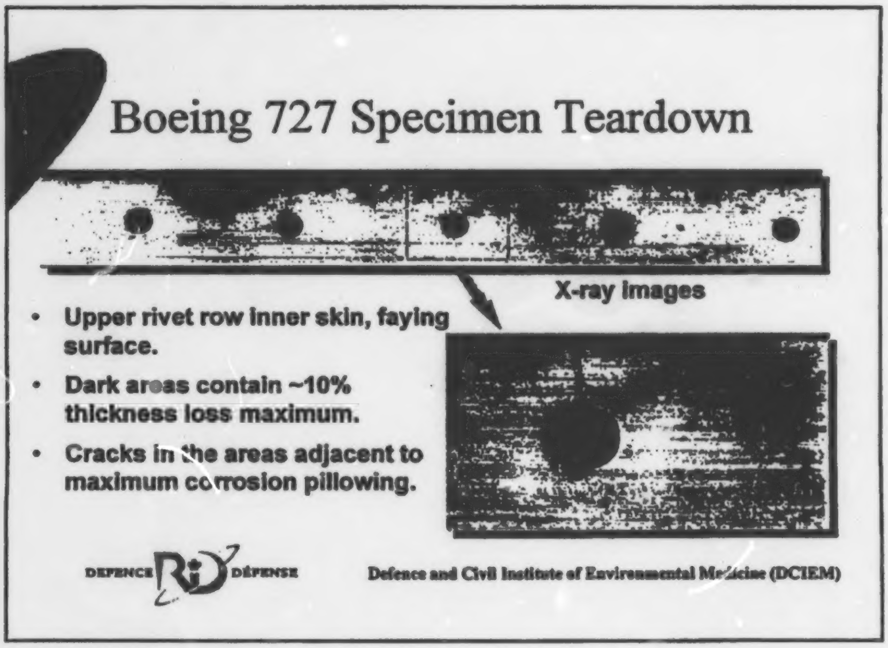

Boeing 727 Specimen Teardown

- **Upper rivet row inner skin, faying surface.**
- **Dark areas contain ~10% thickness loss maximum.**
- **Cracks in the areas adjacent to maximum corrosion pillowing.**

DEFENCE RD DÉFENSE

Defence and Civil Institute of Environmental Medicine (DCIEM)

Reliability Analyses

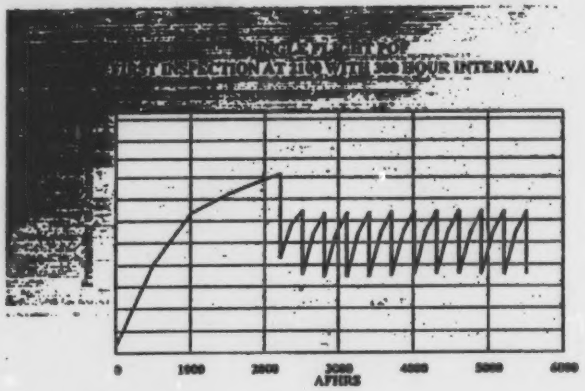

DEFENCE RD DÉFENSE Defence and Civil Institute of Environmental Medicine (DCIEM)

Present DRDB R&D Activities

[illegible] R&D

Composite patching of metallic structure

Novel heat treatment techniques

Improved NDT reliability

Probabilistics

[illegible] Engineering Action

IEOSTP

CP-140 SLAP/SLEP

DEFENCE RD DÉFENSE Defence and Civil Institute of Environmental Medicine (DCIEM)

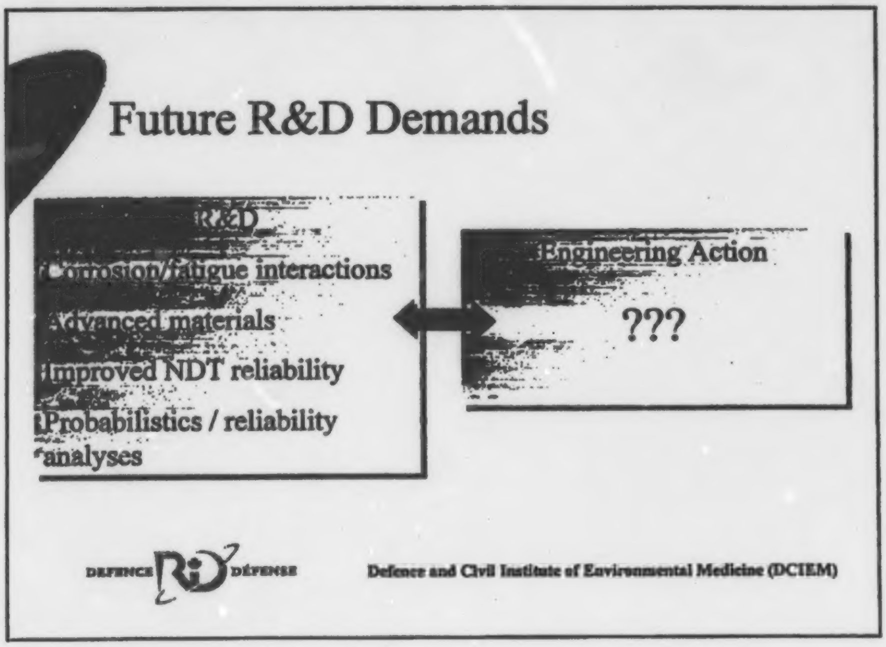

Future R&D Demands

[illegible] R&D

- Corrosion/fatigue interactions
- Advanced materials
- Improved NDT reliability
- Probabilistics / reliability analyses

Engineering Action

???

DEFENCE R&D DÉFENSE

Defence and Civil Institute of Environmental Medicine (DCIEM)

#511920 (46)

Progress and Plans the Improved Ship Structures Maintenance Management (ISSMM) Project

by N.G. Pegg[+], J.F. Porter[+] and A.R. Graham[++]

[+]Defence Research Establishment Atlantic, P.O. Box 1012, Dartmouth, N.S.
[++]Directorate of Maritime Ship Support, NDHQ, Ottawa, Ontario

ABSTRACT

The ISSMM project was initiated by DND in 1996 to provide a validated tool for engineers to use in making rational assessments of the effects of degradation and damage on a ship's structural capability to undertake a given mission. The project encompasses the integration of modern sea load prediction methods, finite element models, fatigue and ultimate strength analysis and an extensive data management system into an engineering software tool. ISSMM is the largest project involving ship structures R&D in Canada, with some components being used by and supported by other nations.

This paper discusses recent progress on ISSMM including the development of structural sea load cases from defined operational profiles, validation of load and response prediction methods via sea trials, an improved method for efficient production of detail finite element models, the object-oriented ship database management system developed for ISSMM, and the integration of load prediction codes and ultimate strength evaluation modules with structural finite element analysis. Example problems of the effects of corrosion on strength and of crack propagation will be discussed.

DEFENCE DEFENSE

Canada

ISSMM
Questions to be Answered

What is ISSMM?

Why is ISSMM important?

How will ISSMM be developed?

Who will use ISSMM?

When will ISSMM be operational?

Defence Research Establishment Atlantic (DREA)

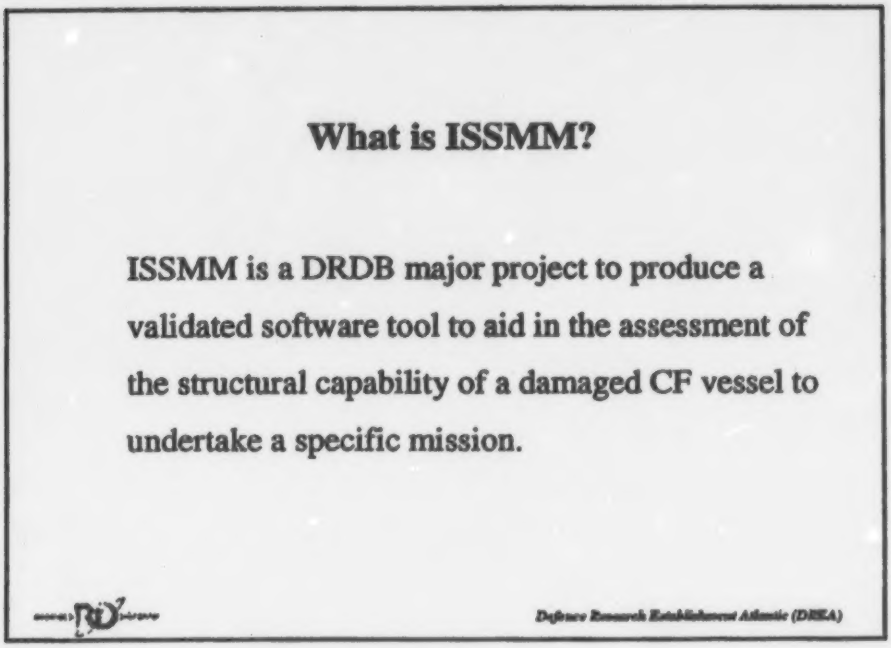

What is ISSMM?

ISSMM is a DRDB major project to produce a validated software tool to aid in the assessment of the structural capability of a damaged CF vessel to undertake a specific mission.

Defence Research Establishment Atlantic (DREA)

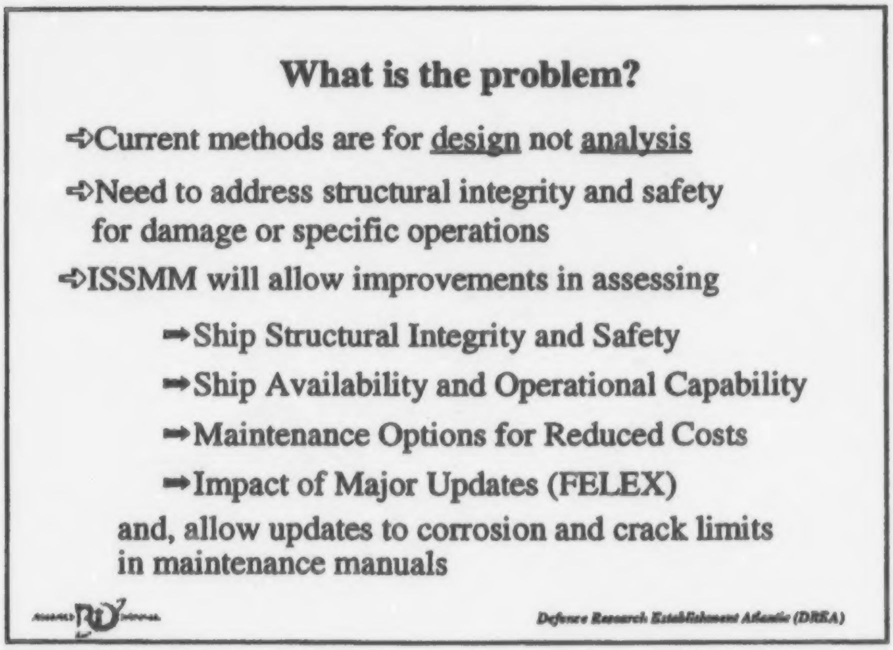

What is the problem?

- ➪Current methods are for design not analysis
- ➪Need to address structural integrity and safety for damage or specific operations
- ➪ISSMM will allow improvements in assessing
    - ➡Ship Structural Integrity and Safety
    - ➡Ship Availability and Operational Capability
    - ➡Maintenance Options for Reduced Costs
    - ➡Impact of Major Updates (FELEX)

and, allow updates to corrosion and crack limits in maintenance manuals

Defence Research Establishment Atlantic (DREA)

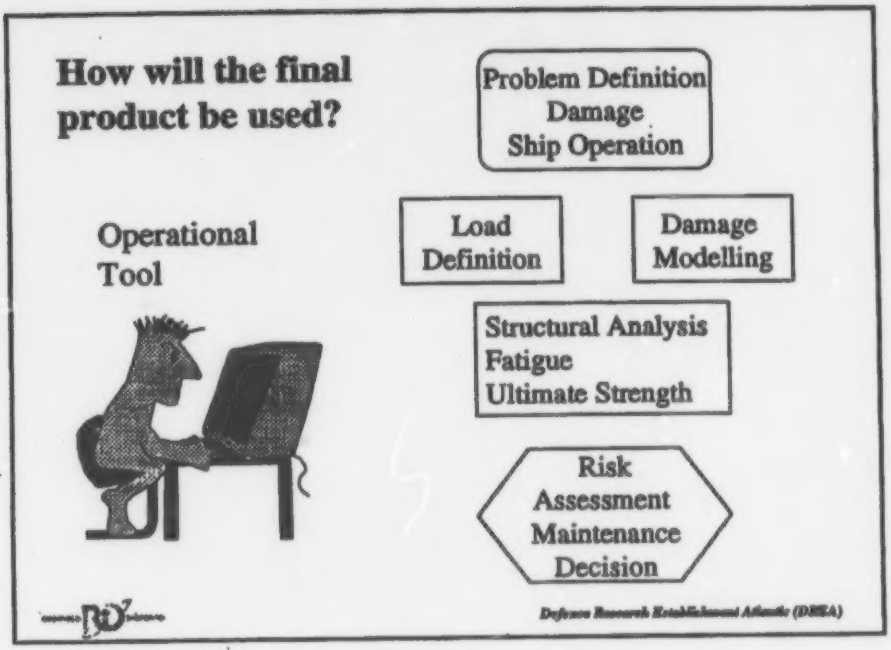

How will the final product be used?

Operational Tool

Problem Definition
Damage
Ship Operation

Load Definition

Damage Modelling

Structural Analysis
Fatigue
Ultimate Strength

Risk
Assessment
Maintenance
Decision

Defence Research Establishment Atlantic (DREA)

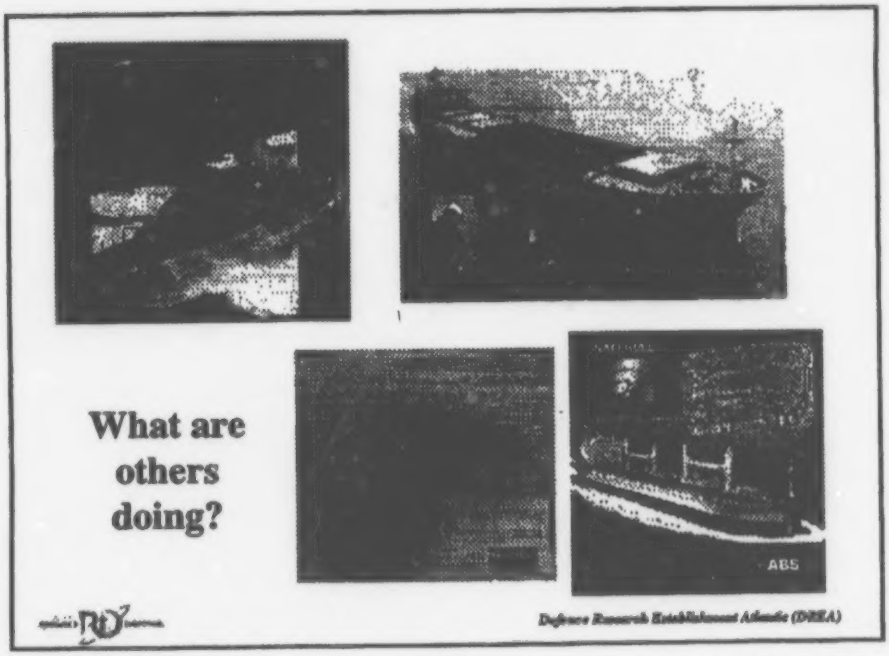

What are others doing?

Defence Research Establishment Atlantic (DREA)

What are we doing?

- ➡ DRDB Major Project to develop tools - ISSMM
- ➡ $4 million over 4 years plus significant in-house DREA effort
- ➡ RFP for Prime Contract at $1.7 million, 1999
- ➡ Collaborative development with Allies
- ➡ Collaboration with industry

Defence Research Establishment Atlantic (DREA)

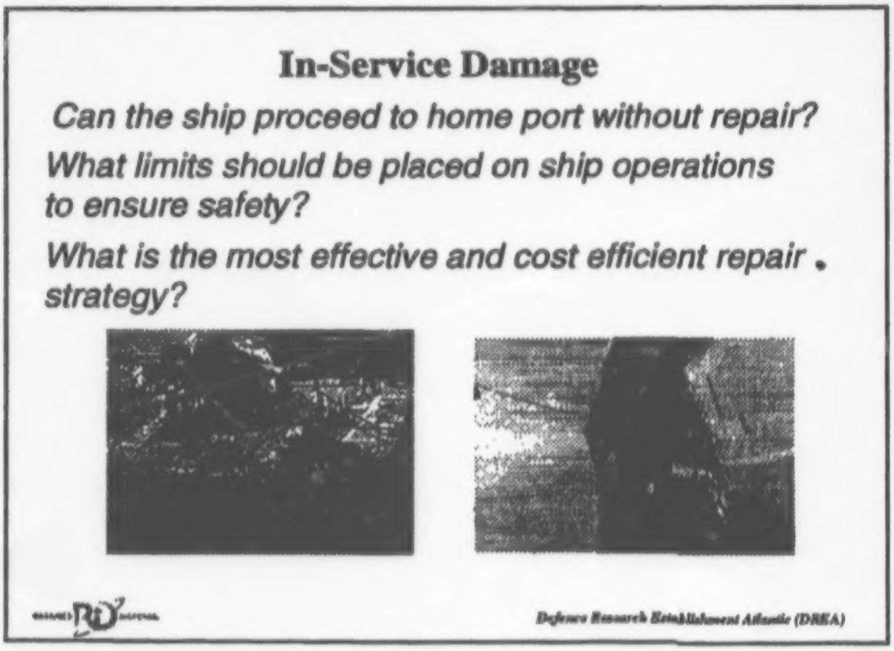

In-Service Damage

Can the ship proceed to home port without repair?

What limits should be placed on ship operations to ensure safety?

What is the most effective and cost efficient repair strategy?

Defence Research Establishment Atlantic (DREA)

Software Tool

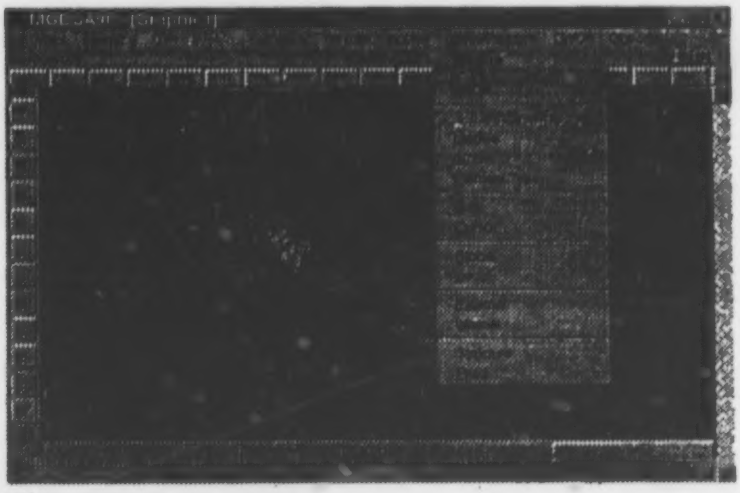

Data Management - *Halifax Class*

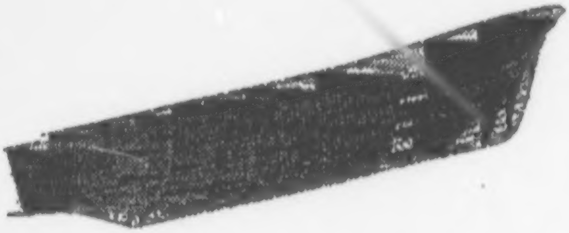

- Structure
- Materials
- Sea Loads
- FE Models
- Analysis Results

Hierarchical Object Oriented Data-manager (HOOD)

{ship..{deck..{grillage..{stiffened panel..{material..{loads..

Structural Analysis

- ➡Top-down finite element analysis of global hull structure and component details
- ➡ Rapid production of structural detail models

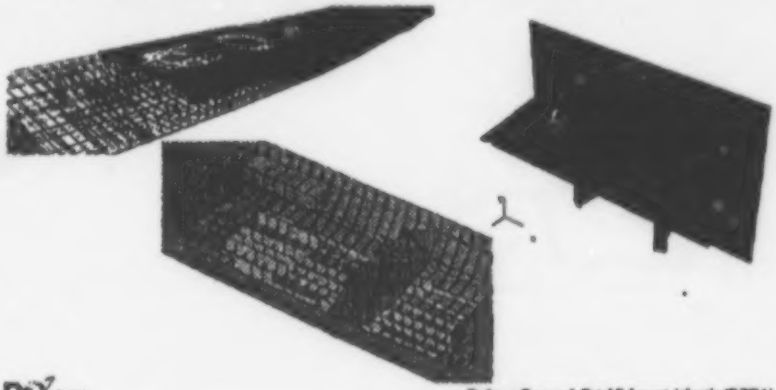

Defence Research Establishment Atlantic (DREA)

Damage Modelling

- ➡Damage from corrosion, cracking and deformation

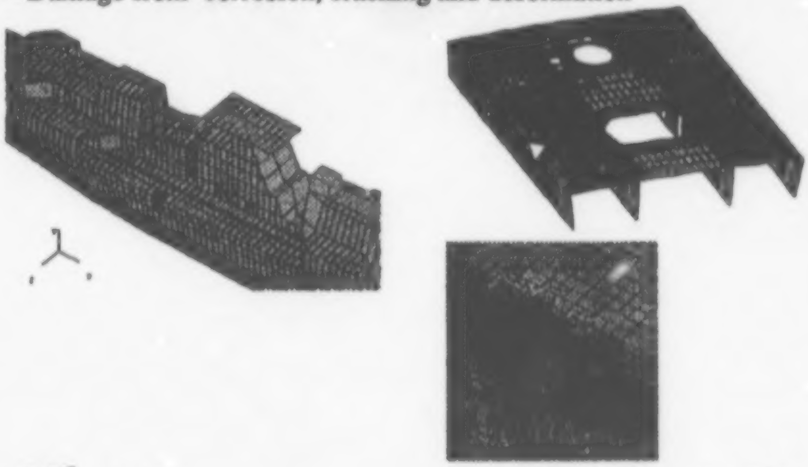

Defence Research Establishment Atlantic (DREA)

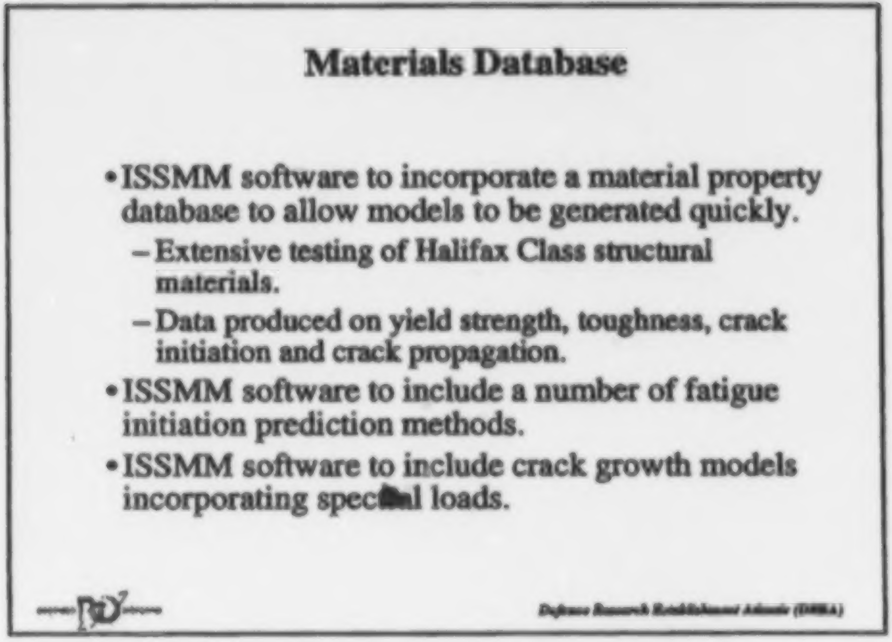

Materials Database

- ISSMM software to incorporate a material property database to allow models to be generated quickly.
  - Extensive testing of Halifax Class structural materials.
  - Data produced on yield strength, toughness, crack initiation and crack propagation.
- ISSMM software to include a number of fatigue initiation prediction methods.
- ISSMM software to include crack growth models incorporating spec[illegible]l loads.

Defence Research Establishment Atlantic (DREA)

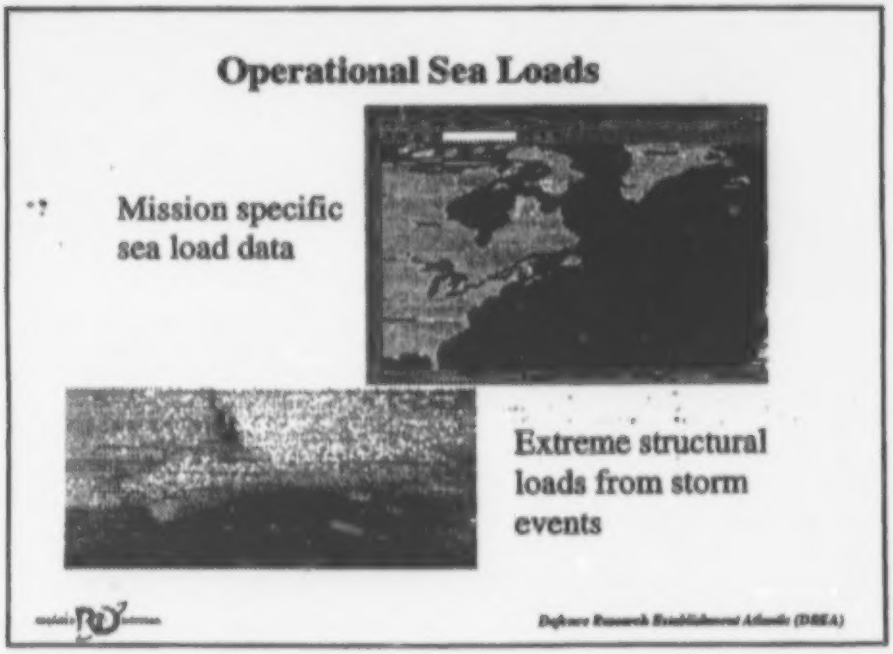

Operational Sea Loads

Mission specific sea load data

Extreme structural loads from storm events

Defence Research Establishment Atlantic (DREA)

Dynamic Sea Load - Structural Response Calculations

Computer model of CPF responding to specific sea conditions

Risk Assessment

For given damage and ship operation:

What is the change in safety level?

What is the probability of structural failure?

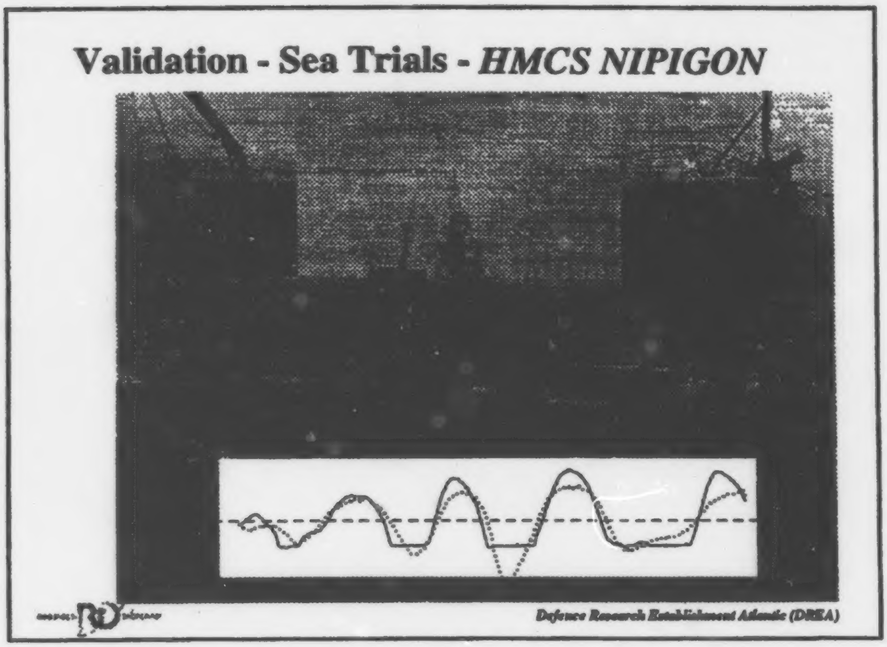

Validation - Sea Trials - *HMCS NIPIGON*

Defence Research Establishment Atlantic (DREA)

ISSMM
Questions Answered

What is ISSMM?

Why is ISSMM important?

How will ISSMM be developed?

Who will use ISSMM?

When will ISSMM be operational?

Defence Research Establishment Atlantic (DREA)

511921 (47)

Fatigue Crack Initiation and Growth in A517 SAW Weldments Under Variable Amplitude Loading

by Christopher Bayley[1] and John Porter[2]

[1]Fleet Technology Ltd, Kanata Ontario

[2]Defence Research Establishment Atlantic, Dockyard Laboratory (Atlantic)
P.O. Box 99000 Stn Forces, Halifax, NS B3K 5X5

ABSTRACT

A comparison between experimental and analytical predicted fatigue lives is made for a A517 SAW Weldment subjected to variable amplitude loading. Three, 10 inch wide butt-welded specimens were tested under a variable amplitude load spectrum consisting of 3 yearly storms. The magnitude of the loads in the storm increased and then decreased in a linear manner with the winter storm representing the most severe loading condition. Fatigue crack monitoring was achieved through the use of 20 localized potential drop probes affixed along the length of the weld. Multiple and independent fatigue crack initiation sites were found along the length of the weld. These eventually coalesced and formed a dominant fatigue crack, which led to the eventual failure of the specimens.

Fatigue life estimates using local notch strain and fracture mechanics approaches were obtained. Fatigue crack initiation life estimates using the strain life approach were found to be un-conservative while the estimates of the fatigue crack propagation life were conservative. Accurate knowledge of the structural and weld geometries was found to be critical in the estimation of the fatigue lives.

Fatigue Crack Initiation and Growth in A517 SAW Weldments

By: Christopher Bayley FTL
John Porter DREA
May 13 1999

FTL FLEET TECHNOLOGY LTD.

Objectives

- Effects of Variable Amplitude Load Spectrum on Fatigue Crack Initiation, Propagation and Coalescence
- Generate Experimental data on Fatigue Initiation and Propagation
- Compare Experimental and Numerical Fatigue Crack Predictions

FTL FLEET TECHNOLOGY LTD.

Experimental Work

- Material Properties
  - Cyclic Stress/Strain Curves
  - Fatigue Crack Initiation
  - Fatigue Crack Growth
- Weld Residual Stresses
- Variable Amplitude Tests on 10" Wide Specimens

FTL FLEET TECHNOLOGY LTD.

Material

- 10 mm A517 SAW Material Received from Dockyard Labs
- Representative of the Deck Material used in the Halifax Class Patrol Frigates
- Samples
  - 6 Round Specimens
  - 3 Center Crack Panels
  - 3 10" Wide Specimens for VA Tests

FTL FLEET TECHNOLOGY LTD.

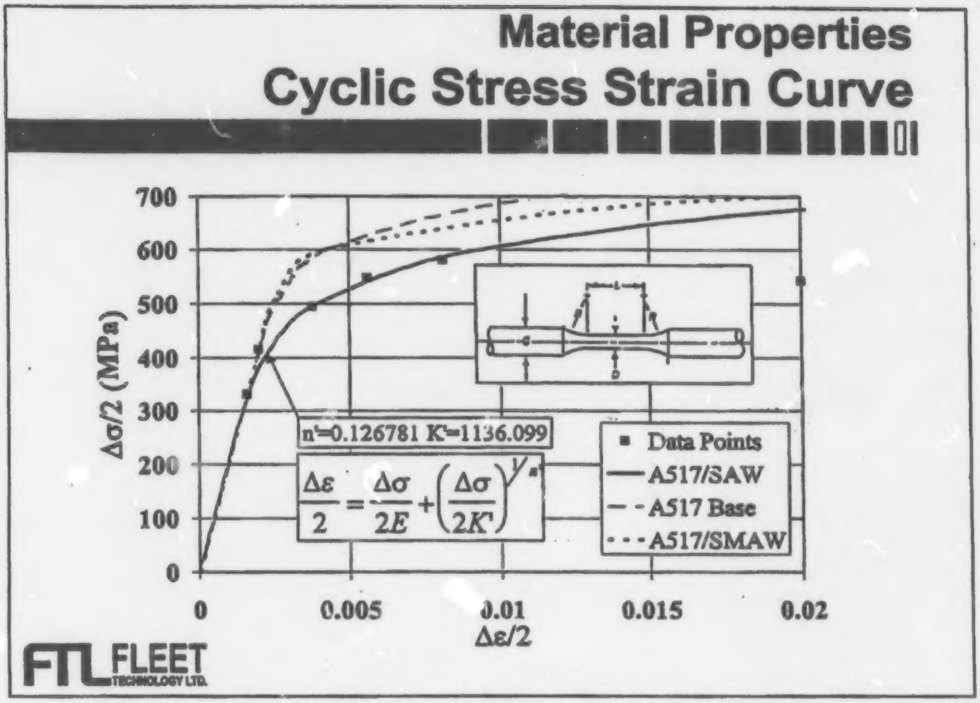

Material Properties
Cyclic Stress Strain Curve

n'=0.126781 K'=1136.099

$$\frac{\Delta\varepsilon}{2}=\frac{\Delta\sigma}{2E}+\left(\frac{\Delta\sigma}{2K'}\right)^{1/n'}$$

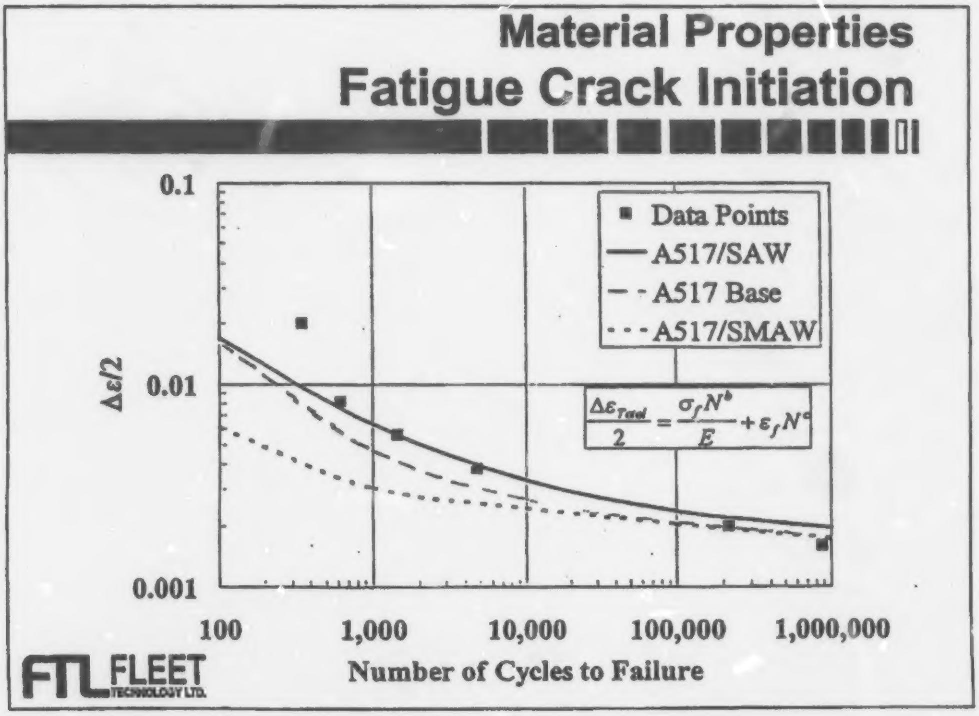

Material Properties
Fatigue Crack Initiation

$$\frac{\Delta\varepsilon_{Total}}{2}=\frac{\sigma_f N^b}{E}+\varepsilon_f N^c$$

Material Properties
Fatigue Crack Growth

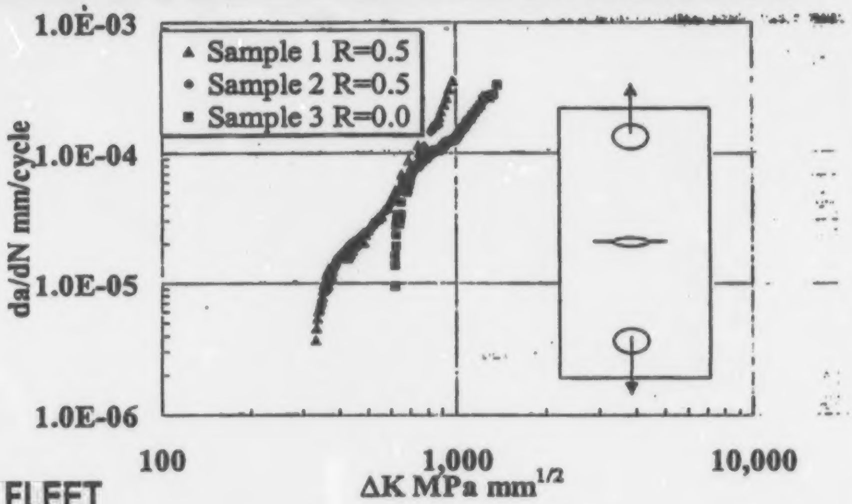

FTL FLEET TECHNOLOGY LTD.

Variable Amplitude Tests
Fatigue Specimens

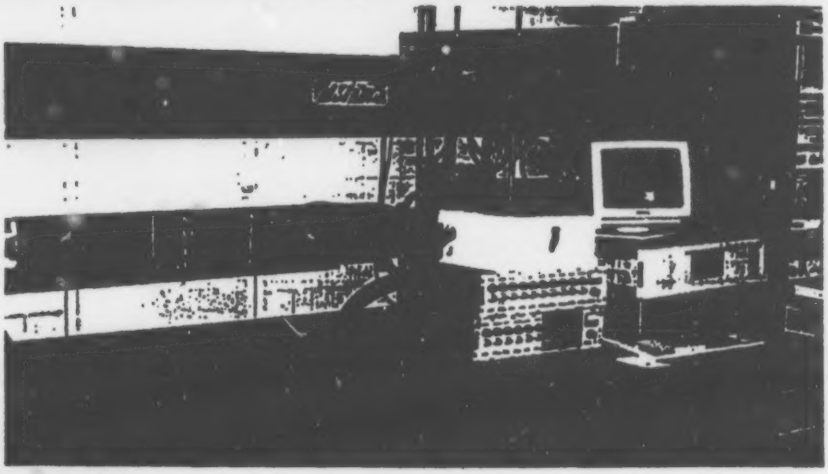

FTL FLEET TECHNOLOGY LTD.

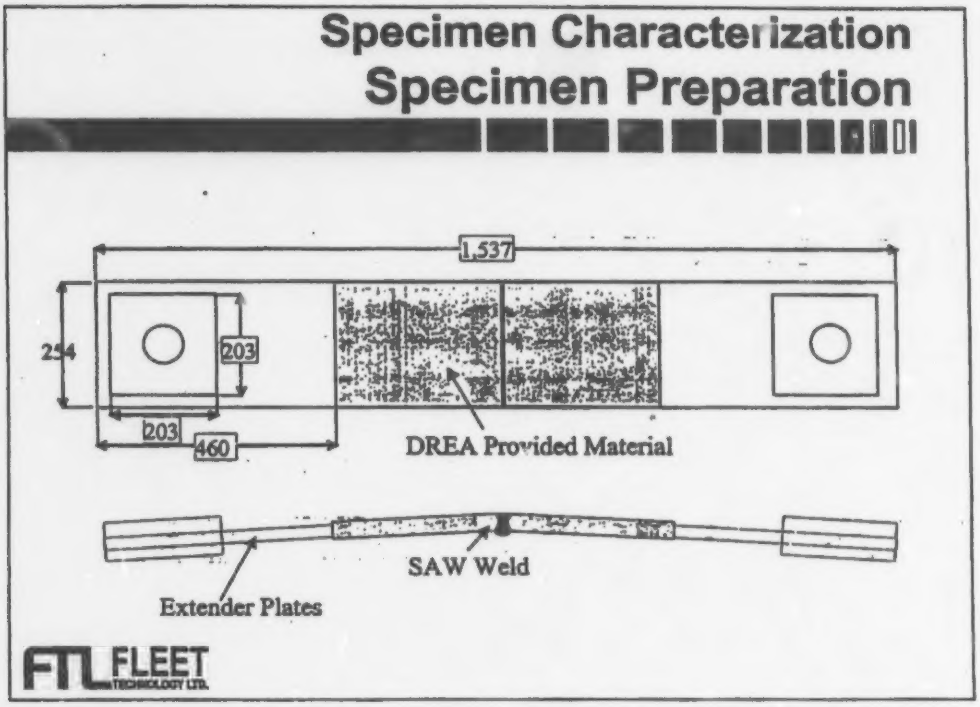

Specimen Characterization
Specimen Preparation

1,537
254
203
203
460
DREA Provided Material
SAW Weld
Extender Plates
FTL FLEET TECHNOLOGY LTD.

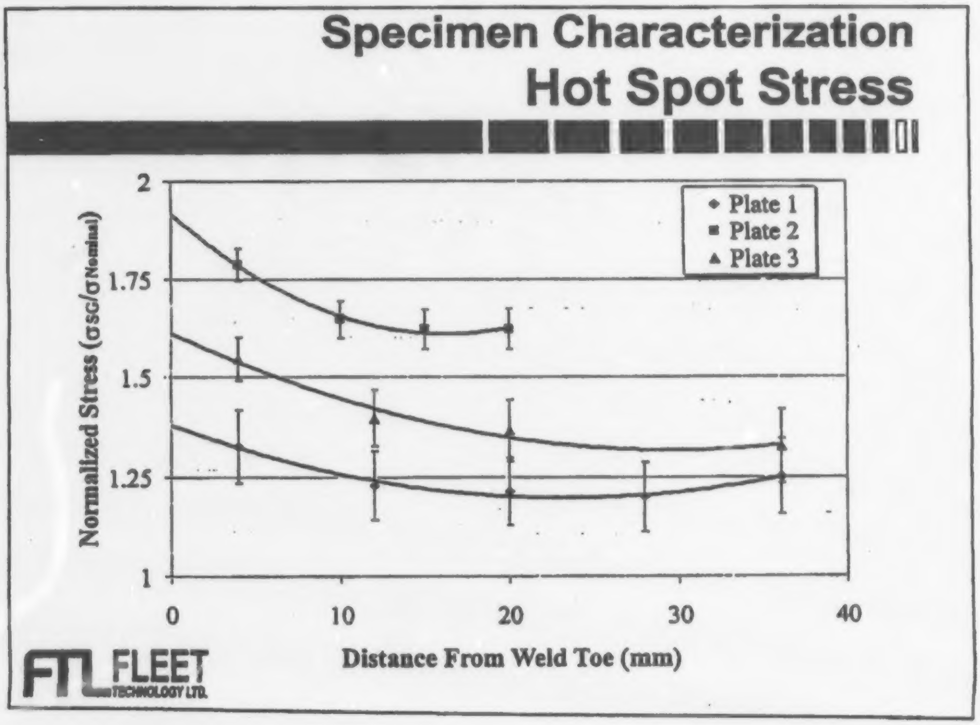

Specimen Characterization
Hot Spot Stress

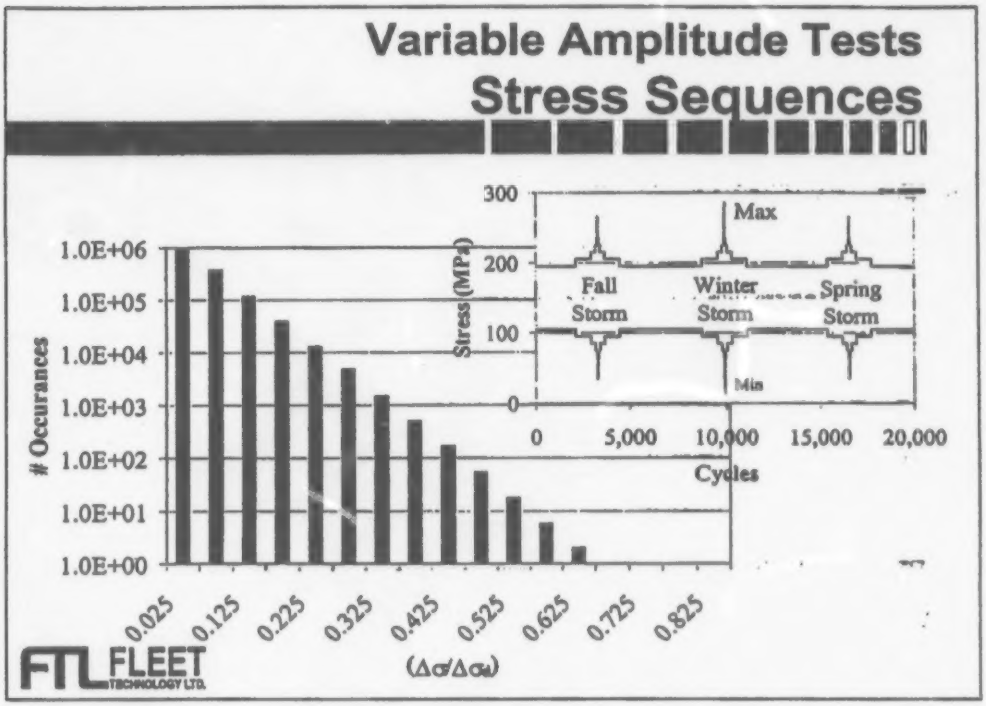

Variable Amplitude Tests
Stress Sequences

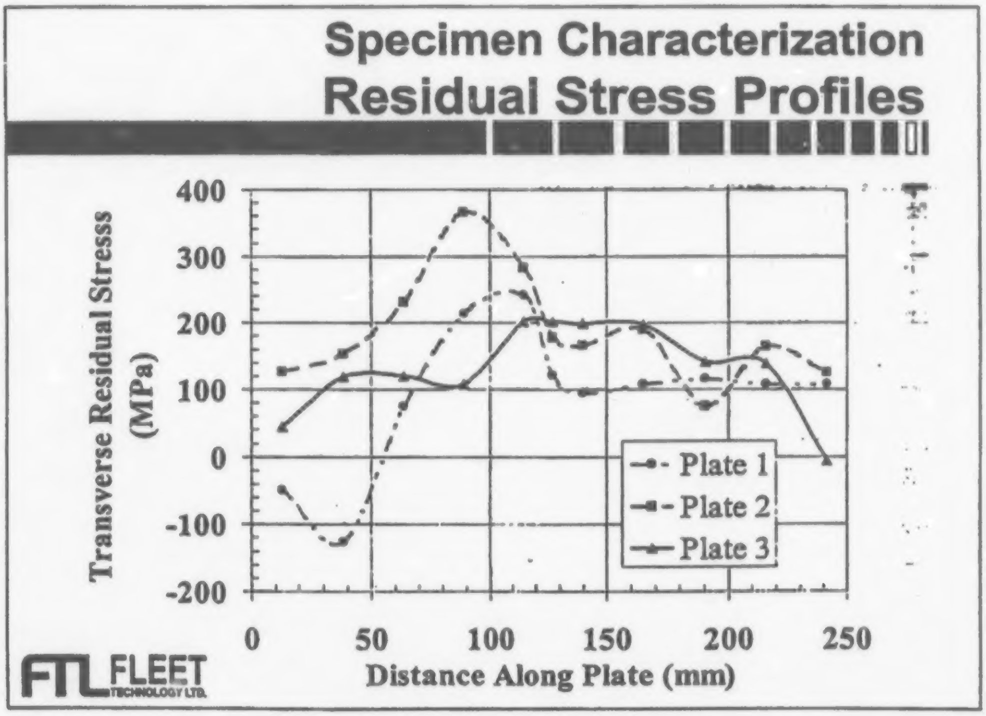

Specimen Characterization
Residual Stress Profiles

Variable Amplitude Tests
Crack Monitoring

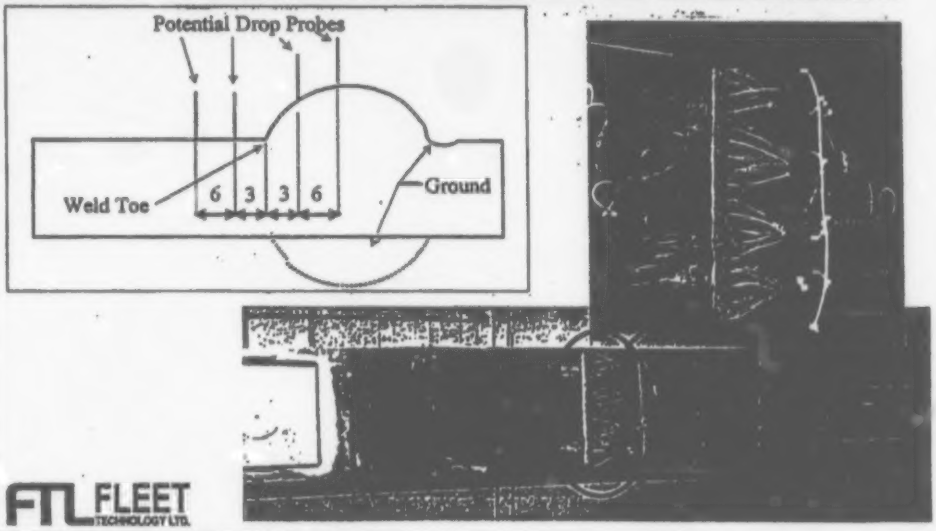
Potential Drop Probes
Weld Toe
6
3
3
6
Ground

Variable Amplitude Tests
PD Time History

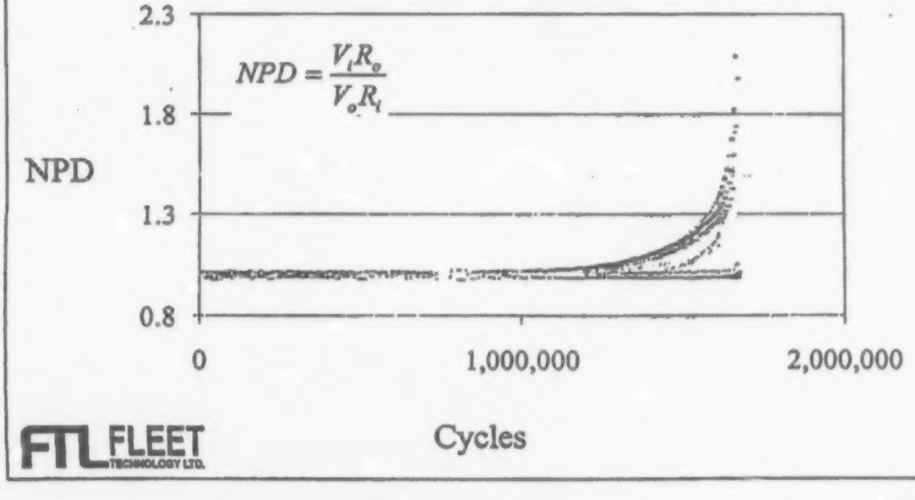

Variable Amplitude Tests
Beachmarks

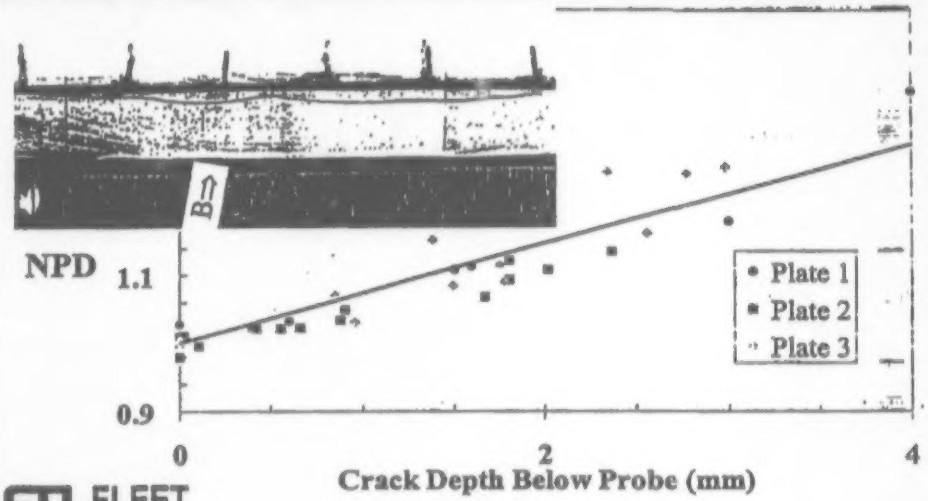

Variable Amplitude Tests
Fatigue Crack Initiation Sites

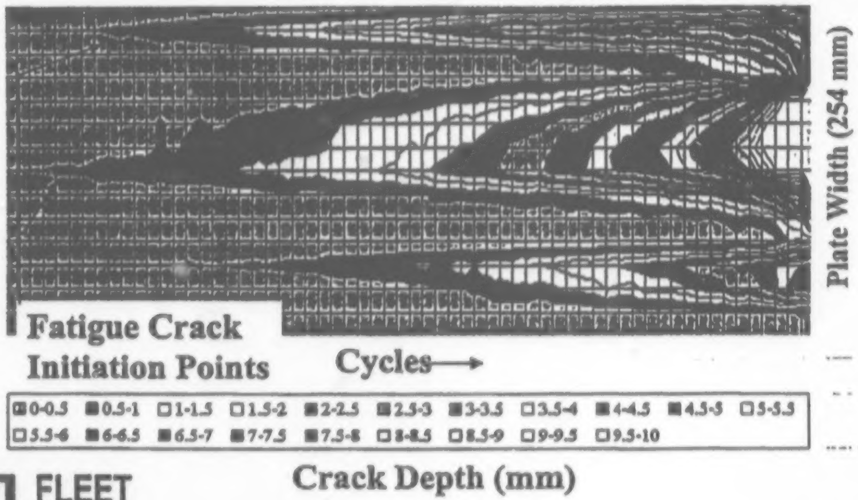

Variable Amplitude Tests Crack Shape Development

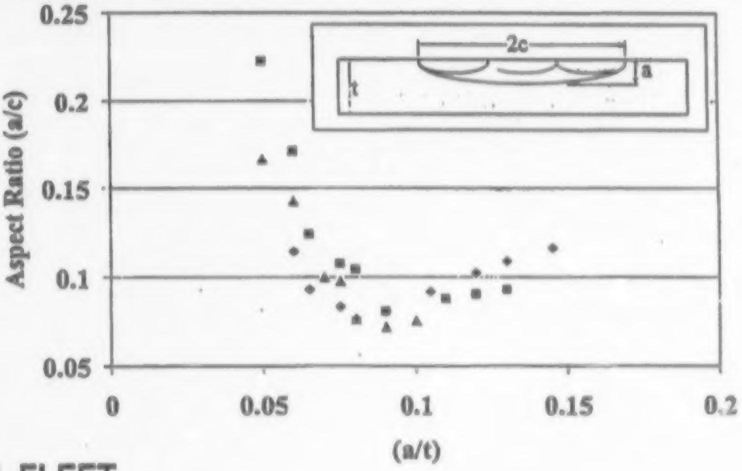

FLEET TECHNOLOGY LTD.

Analytical Approach

- Fatigue Crack Initiation and Propagation Software FALIN and FALPR
- Work Completed by: Dr Gregory Glinka University of Waterloo, Waterloo Ontario
- Stress Life (SN) Approach
- Strain Life (εN) Approach
- Fatigue Crack Growth (da/dN)

FLEET TECHNOLOGY LTD.

Analytical Approach
Stress Life

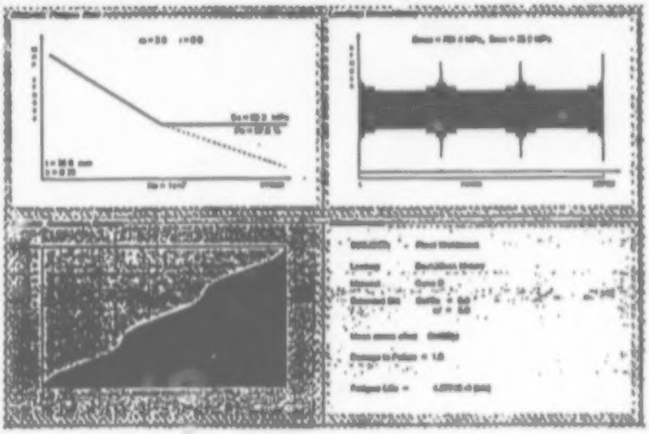

- BS-5400 'D' Detail Weld Transverse to Principle Stress dir.
- Miner's Summation used to sum damage from individual cycles
- Significant Damage Caused by Small Stress Ranges

FTL FLEET TECHNOLOGY LTD.

Analytical Approach
Strain Life

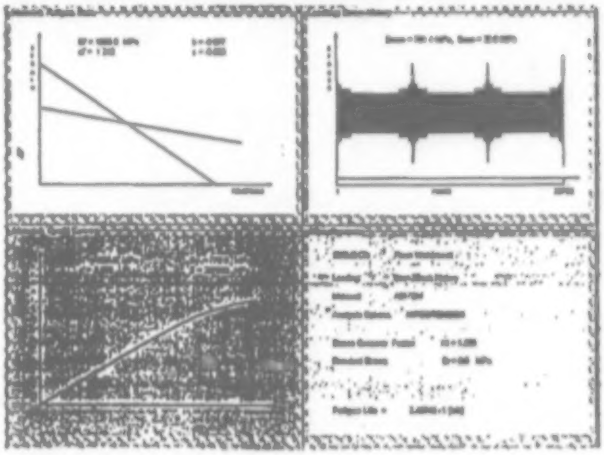

- Local Strain Approach accounts for:
- Geometry of the notch
- Angular Distortion and Straightening of Plates
- Membrane and Bending Components
- Residual Stress State
- Hot Spot Stress

FTL FLEET TECHNOLOGY LTD.

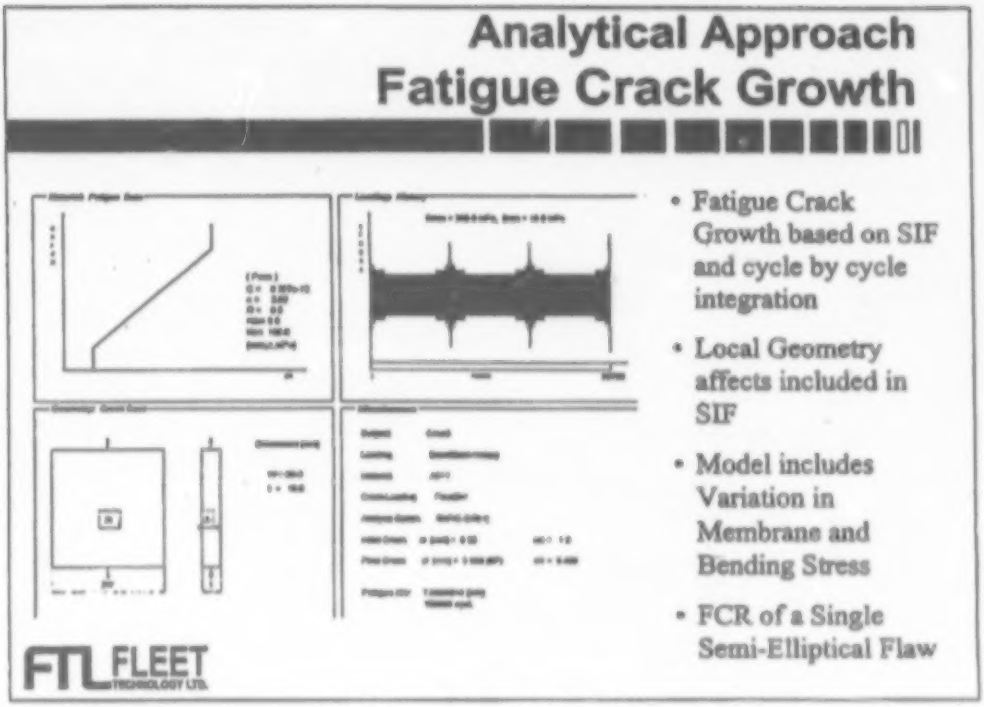

Analytical Approach Fatigue Crack Growth

- Fatigue Crack Growth based on SIF and cycle by cycle integration
- Local Geometry affects included in SIF
- Model includes Variation in Membrane and Bending Stress
- FCR of a Single Semi-Elliptical Flaw

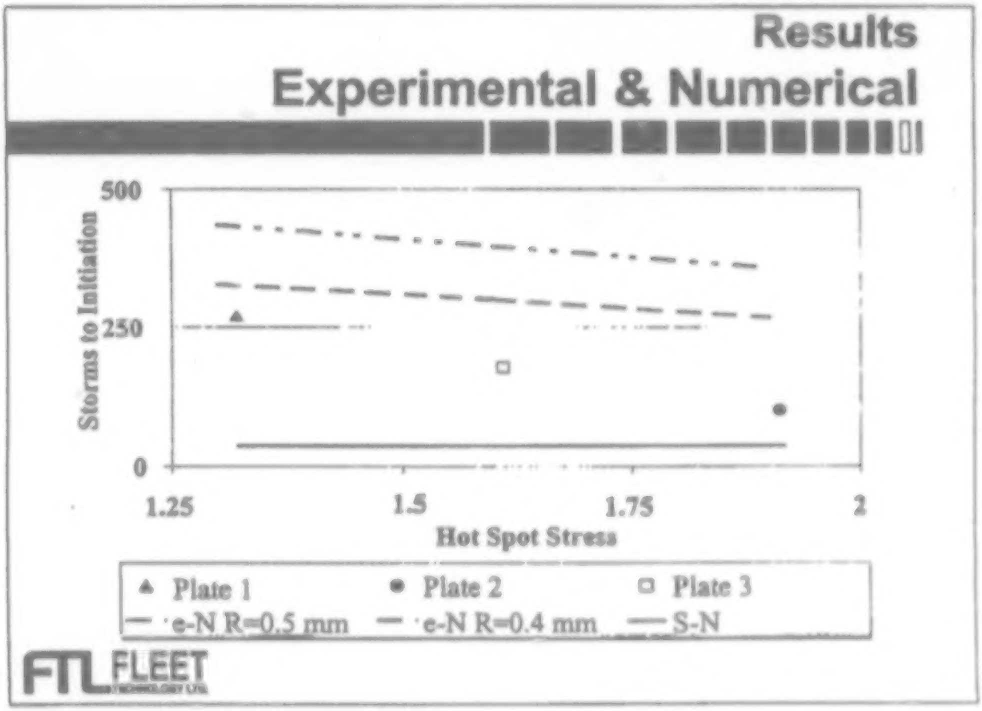

Results Experimental & Numerical

Results
Experimental & Numerical

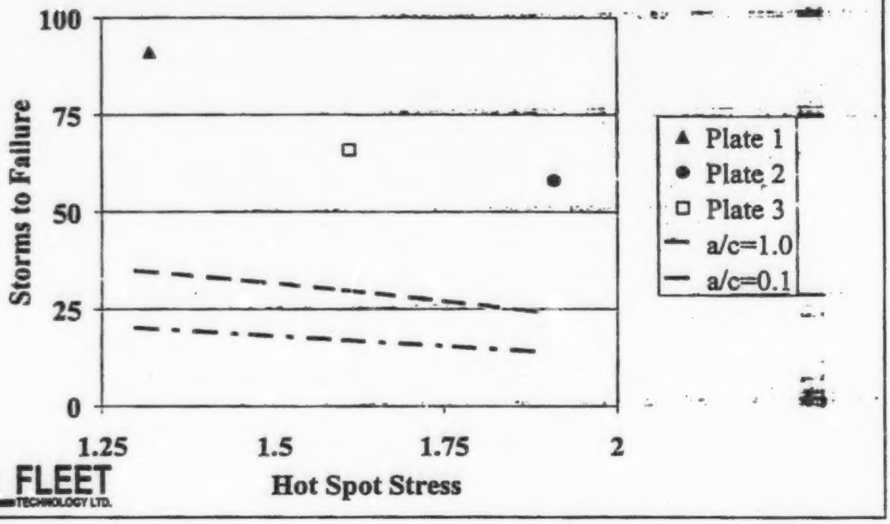

FTL FLEET TECHNOLOGY LTD.

Conclusions
Numerical

- S-N VERY Conservative
- ε-N Over-Predicts Fatigue Initiation
  - Requires detailed information specific to each geometry
- Fatigue Crack Growth
  - Conservative if omit Retardation effects

FTL FLEET TECHNOLOGY LTD.

Conclusions
Experimental

- **Fatigue Crack Initiation accounts for 70% of Total Fatigue Life**
- **Variable Amplitude Loading affects the Number of Initiation Sites**
- **Fatigue Life Affected by:**
  - Hot Spot Stress Concentration
  - Notch Geometry
  - Angular Distortion of Specimens
  - Load Spectrum

FTL FLEET TECHNOLOGY LTD.

Recommendations
Future Research

- **Determine the influence of weld shape and residential strains on the fatigue performance of butt welded joints**
- **Variable and Constant Amplitude Tests**
- **Weld Toe Improvements and Fatigue Life**
- **Examine Agreement between Numerical Predictions and Experimental tests**

FTL FLEET TECHNOLOGY LTD.

#511922 (48)

Developmental Activities Towards a Real-Time Defect Severity Assessment System for Naval Platforms

by John Porter *, Chris Bayley **, LCdr. Chris Hargreaves *, Colin Smith ****, and Luksa Luznik ****

***Dockyard Lab (A), DREA, Halifax, Nova Scotia, Canada**
****Fleet Technology Ltd., Kanata, Ontario, Canada**
*****DMSS, NDHQ, Hull, Quebec, Canada**
******NETE, Lasalle, Quebec, Canada**

ABSTRACT

The Canadian Navy is developing a rational integrated approach to the design, construction, and maintenance of its ships, in order to maximize operational availability and minimize life-cycle maintenance costs. Naval platforms have been and will be required to conduct operations with cracks present in structural components. The requirement exists to provide the operators with a measure of confidence that these defects do not pose a serious risk to structural integrity. To assist in these efforts, Defence Research Establishment Atlantic (DREA), in collaboration with Fleet Technology Ltd (FTL), have undertaken numerous fatigue studies to develop a clearer understanding of the factors that govern fatigue in naval platforms. In addition, DREA and FTL have worked in close collaboration with the Directorate of Maritime Ship Support (DMSS) and the Naval Engineering test Establishment (NETE) on numerous experimental investigations of fatigue prone areas on existing naval platforms. As a consequence of these efforts, it was realized that the development of a shipboard system for the continuous monitoring of detected fatigue cracks and their associated driving forces could provide operators with a continuous measure of the defects severity and the structural integrity. To this end, a developmental activity to create a Defect Severity Assessment System (DSAS) was initiated. This presentation will discuss DSAS developmental activities completed to date, and provide an overview of efforts currently underway.

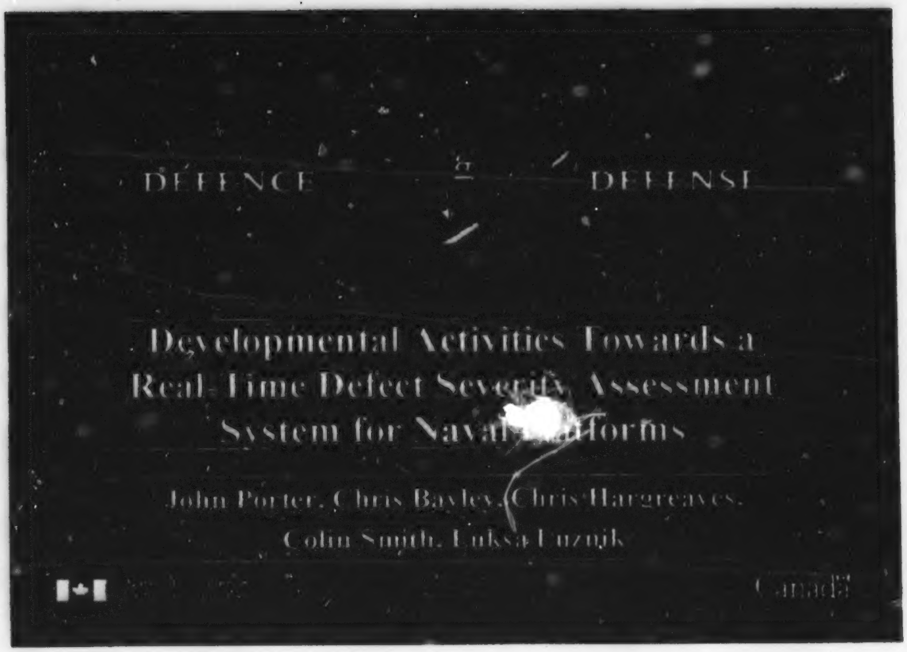

DEFENCE DEFENSE

Developmental Activities Towards a Real-Time Defect Severity Assessment System for Naval Platforms

John Porter, Chris Bayley, Chris Hargreaves, Colin Smith, Luksa Luznik

Canada

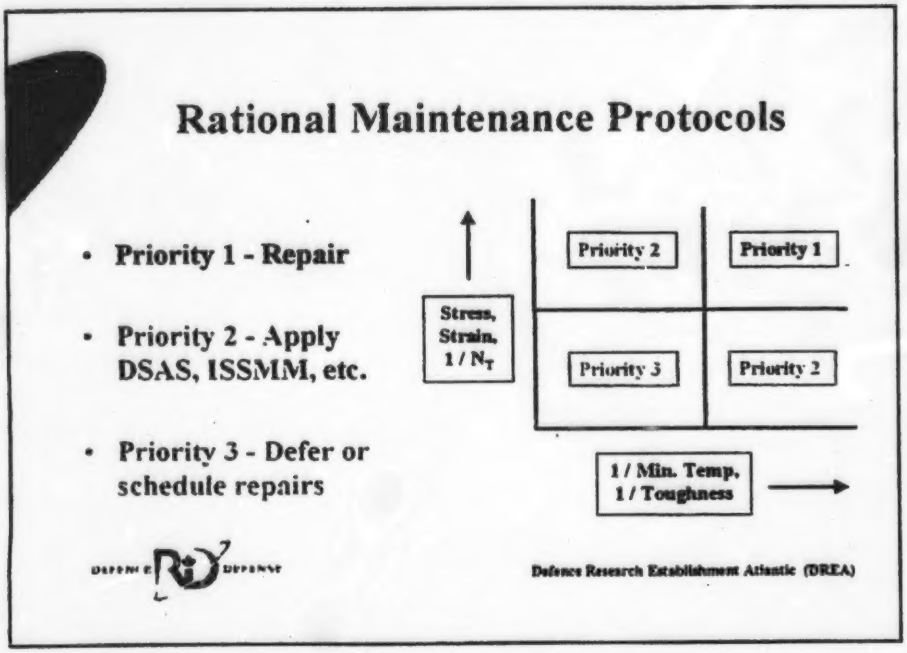

Rational Maintenance Protocols

- Priority 1 - Repair
- Priority 2 - Apply DSAS, ISSMM, etc.
- Priority 3 - Defer or schedule repairs

Stress, Strain, $1 / N_T$ ↑

Priority 2	Priority 1
Priority 3	Priority 2

1 / Min. Temp., 1 / Toughness →

DEFENCE DEFENSE

Defence Research Establishment Atlantic (DREA)

Defect Severity Assessment System "Conception"

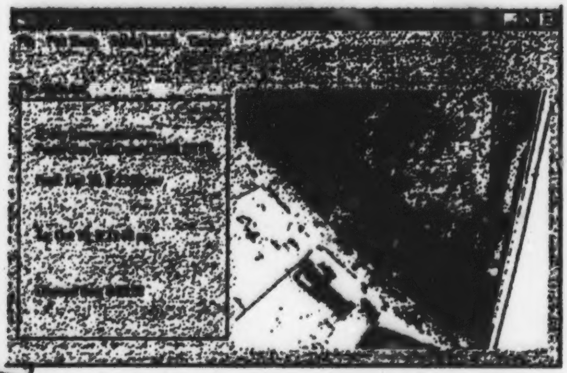

Defence Research Establishment Atlantic (DREA)

DSAS Stress Spectrum

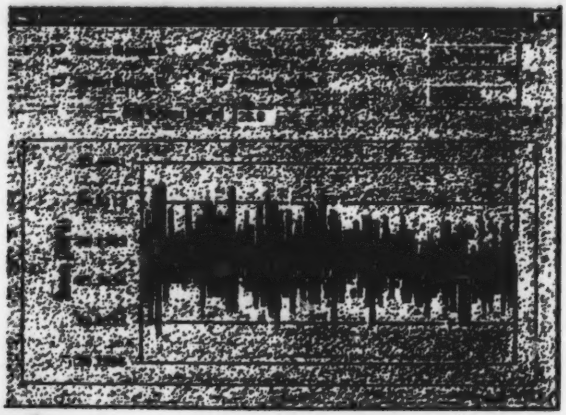

Defence Research Establishment Atlantic (DREA)

DSAS Severity Factor

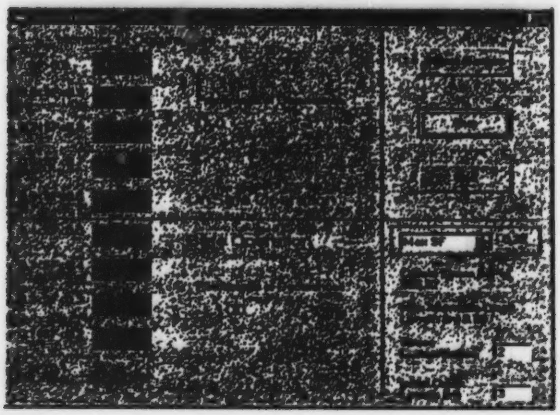

DEFENCE RD DÉFENSE

Defence Research Establishment Atlantic (DREA)

Severity Factor Assessment

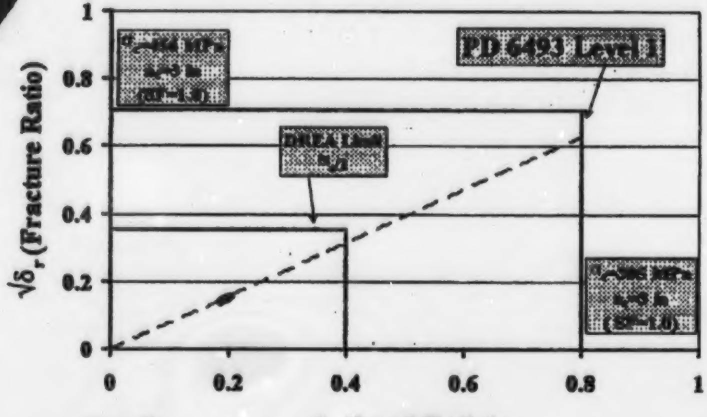

DEFENCE RD DÉFENSE

Defence Research Establishment Atlantic (DREA)

DSAS Severity Factor

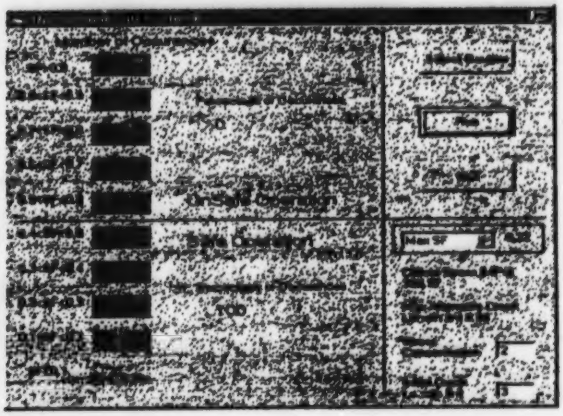

DEFENCE DÉFENSE

Defence Research Establishment Atlantic (DREA)

Defect Severity Assessment System

Development Project Objectives

- Provide operators with real-time assessment of defect severity,
- Facilitate ship-board fatigue experimentation,
- Advance knowledge base of fatigue in complex welded structures.

DEFENCE DÉFENSE

Defence Research Establishment Atlantic (DREA)

Defect Severity Assessment System
Overview

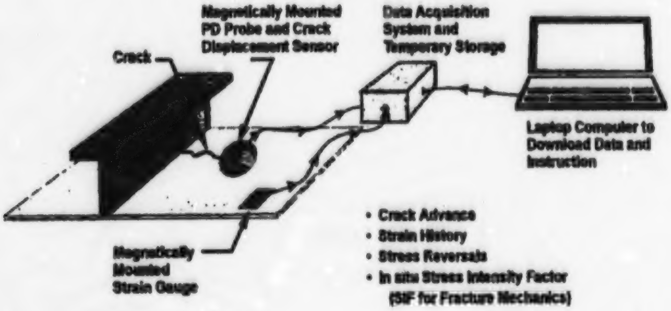
Crack
Magnetically Mounted PD Probe and Crack Displacement Sensor
Data Acquisition System and Temporary Storage
Laptop Computer to Download Data and Instruction
Magnetically Mounted Strain Gauge

- Crack Advance
- Strain History
- Stress Reversals
- In situ Stress Intensity Factor (SIF for Fracture Mechanics)

Defence Research Establishment Atlantic (DREA)

Defect Severity Assessment System
Current Objectives

- Continuous monitoring of crack length
- Quick installation strain monitoring
- Crack opening displacement monitoring
- Advanced severity assessment
- CPF sea trials (Fall / 99)

Defence Research Establishment Atlantic (DREA)

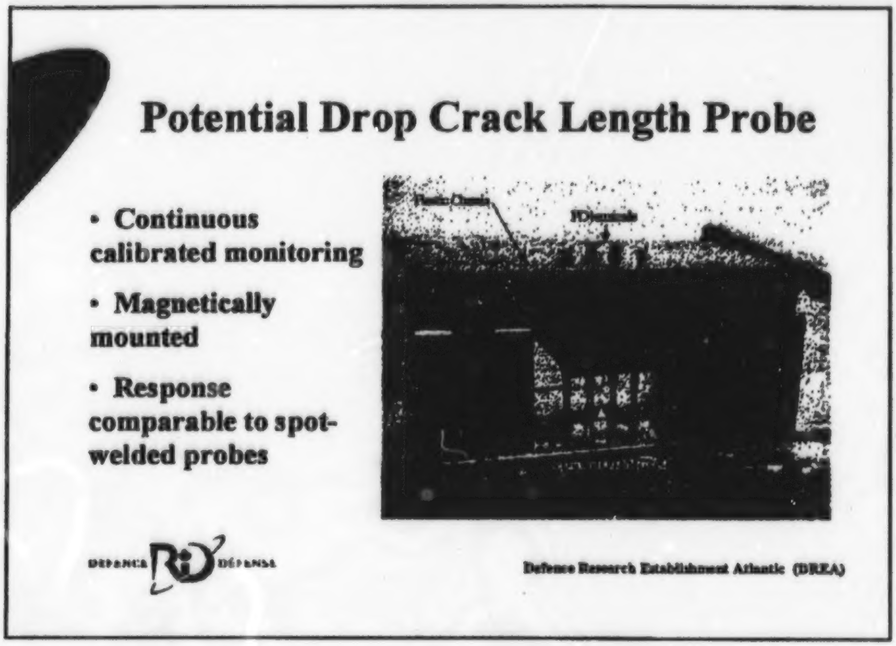

Potential Drop Crack Length Probe

- Continuous calibrated monitoring
- Magnetically mounted
- Response comparable to spot-welded probes

Defence Research Establishment Atlantic (DREA)

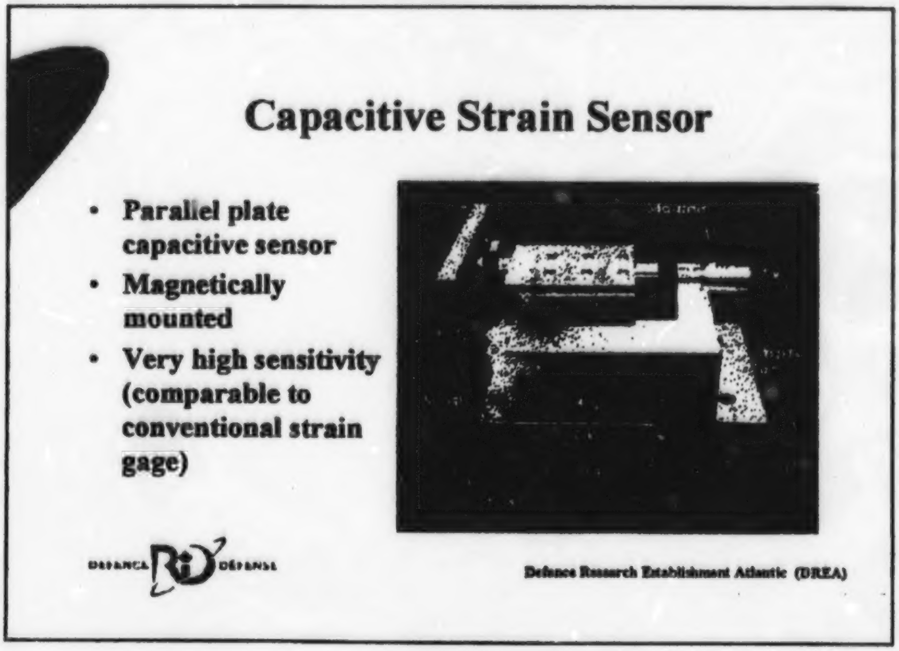

Capacitive Strain Sensor

- Parallel plate capacitive sensor
- Magnetically mounted
- Very high sensitivity (comparable to conventional strain gage)

Defence Research Establishment Atlantic (DREA)

Capacitive Displacement Sensor

- •Varying di-electric sensor
- •Magnetically mounted
- •Linear response
- •Variable sensitivity

DEFENCE DÉFENSE

Defence Research Establishment Atlantic (DREA)

Advanced Severity Assessment

- •Direct incorporation of motion and location data;
  - -Relating environment to severity factors
  - -Learning and forecasting capabilities
- •Additional defect severity definitions;
  - -PD6493 Level 2
  - -Direct crack opening definitions

DEFENCE DÉFENSE

Defence Research Establishment Atlantic (DREA)

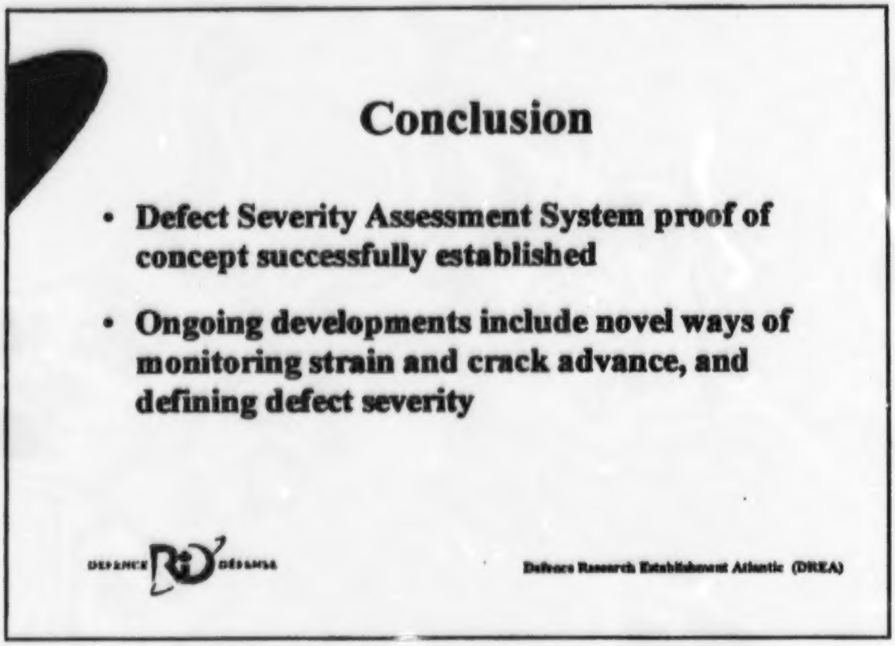

Conclusion

- Defect Severity Assessment System proof of concept successfully established
- Ongoing developments include novel ways of monitoring strain and crack advance, and defining defect severity

DEFENCE R&D DÉFENSE

Defence Research Establishment Atlantic (DREA)

Janette Adeyemi
Dockyard Laboratory (A)
Defence Research Establishment Atlantic
P.O. Box 99000 Stn Forces
Halifax, Nova Scotia B3K 5X5

Mr Alan Aitchison
Welding Engineer
Marconi Marine VSEL
Barrow in Furness
Cumbria
England
LA14 1AF
01229 87 5579
fax 01229 87 4294
alan.aitchison@vsel.gecm.com

Dr Georges Akhras
Professor of Civil Engineering
Royal Military College
PO Box 17000, Stn Forces
Kingston, Ontario, K7K 7B4
613 541 6000 ext 6388
fax 613 545 3481
akhras@rmc.ca

U.O. Akpan
Martec Ltd
1888 Brunswick Street, Suite 400
Halifax, N.S. B3J 3J8
902 425 5101
fax 4211923
uakpan@martec.com

Bob Armstrong
Dockyard Laboratory (A)
Defence Research Establishment Atlantic
P.O. Box 99000 Stn Forces
Halifax, Nova Scotia B3K 5X5

Dr. M.N. Bassim
Dept. of Mechanical Engineering
University of Manitoba
105 Administration Building
Winnipeg, Manitoba R3T 5V6
(204) 474-8524
fax 204 275-7507
bassim@cc.umanitoba.ca

Christopher Bayley
Fleet Technology Ltd.
311 Legget Drive
Kanata, Ontario K2K 1Z8
chris@fleetech.com

Harold Benner
Lanark Coating Services Ltd.
130 Industrial Ave.
Carleton Place
Ontario K7C 3T2
613 257 2792
fax 613 257 7808
harold.benner@sympatico.ca

Craig Bennett
Dept of Physics
Acadia University
Wolfville N.S. B0P 1X0
902 585 1150
fax 902 542 1074
craig.bennett@acadiau ca

Mr. Jorgen Bernt
J.O.Bernt and Associates Limited
3375 Laird Road, Unit 3
Mississauga,Ontario,Canada
L5L 5R7
jammbco@aol.com

Mr. John Bird
Procurement Executive NA114/115
Ministry of Defence
Ash 0, #95
MOD Abbey Wood
BRISTOL
BS34 8JH
United Kingdom
011 44 117 9135050
fax 0117 91 35943
NA115@dawn.pe.mod.uk

John Bird
Consultant Head of Materials
Rolls-Royce
PO Box 31
Fishponds, Bristol, BS16 1XY
0117 974 8500

0117 913 5050
fax 0117 979 2607
fax 0117 913 5943

Mr Orest Bluy DSAM 4
National Defence Headquarters CRAD
Constitution Building
305 Rideau Street, 8th Floor
Ottawa, Ontario K1A 0K2
613 995-8022
fax 996-5177
Orest.Bluy@crad.dnd.ca

Franky Borden
Dockyard Laboratory (A)
P.O. Box 99000 Stn Forces
Halifax, Nova Scotia B3K 5X5

Dr J.E.M. Braid
Materials Technology Lab
568 Booth St.
Ottawa, Ontario K1A 0G1
613 992 6400
fax 613 992 8735
mbraid@nrcan.gc.ca

Mr. Mike Brauss
Proto Manufacturing Ltd.
2175 Solar Cr.
Oldcastle, Ontario N0R 1L0
519 737 6330
fax 519 737 1692
proto@protoxrd.com

D.P. Brennan
Martec Ltd
1888 Brunswick Street, Suite 400
Halifax, N.S. B3J 3J8
902 425 5101
fax 4211923

Michel Brassard
Tektrend International Inc.
2113A St. Regis Boulevard
Dollard des Ormeaux QC H9B 2M9
(514) 421 1417
fax 421 1487
michel.brassard@tektrend-intl.com

Dr J.J.F. Butler
Structural Materials Center
DERA Rosyth
Rosyth Royal Dockyard
Dunfermline
Fife Scotland KY11 2XR
1383 435149
fax 1383 435167

Dr. M.K. Chernuka
Martec Ltd. Suite 400
1888 Brunswick St.
Halifax, Nova Scotia B3F 3F8

Mr Ron Chisholm HF31.3
Engr Dept/NAO/Senior Hull Inspector
Fleet Maintenance Facility Cape Scott
FMO Halifax, N.S. B3K 5X5
902 427 0550 3885

Cdr Peter Crosby
Director of Naval Construction
Royal New Zealand Navy
Naval Staff
HQ NZ Defence Force
Private Bag
Wellington, New Zealand
64 4 4960329
fax 64 4 4960311
weap-eng@hq.navy.mil.nz
pr.crosby@navy.mil.nz

Terry Culliton
AQTS
15 Willett Ave.
P.O.Box 5250
St John, New Brunswick E2L 5C9
506 648 2226
aqts@nb.aibn.com

Ernest J. Czyryca
Naval Surface Warfare Center
Carderock Division
Welding and NDE Branch, Code 610
West Bethesda, MD 20817-5700
(301) 227-4401
fax 301-227-5576
czyryca@oasys.dt.navy.mil

Dr. S. Das Gupta
Electrofuel Manufacturing Company Ltd
21 Hanna Avenue
Toronto, Ont., Canada
M6K 1W8
sdasgupta@gomi.com
www.electrofuel.com
416 535 1114
fax 416 535 2361

Gary Dease
Dockyard Laboratory (A)
P.O. Box 99000 Stn Forces
Halifax, Nova Scotia B3K 5X5

Dr Virginia G. DeGiorgi
Code 6350
Multifunctional Materials Branch
Naval Research Laboratory
4555 Overlook Ave. SW
Washington, D.C.
USA 20375-5000
(202) 767-9027
fax 404-7176
virginia.degiorgi@nrl.navy.mil

Sue Dickout DMSS 2-4
National Defence Headquarters
101 Colonel By Drive
Ottawa, Ontario K1A 0K2
819 994 8649
fax 819 997 7058
sdickout@dmcs.dnd.ca

Gary Fisher
Dockyard Laboratory (A)
P.O. Box 99000 Stn Forces
Halifax, Nova Scotia B3K 5X5
902 427 0550 x3432
fax 902 427 3435
fisher@drea.dnd.ca

Lt(N) Denis Fortin
Canadian Forces Naval Engr School
MSE Division
PO Box 99000 Stn Forces
Halifax NS B3K 5X5
427-0550 Ext 8672

Dr. Terry Foster
Head/Dockyard Lab(P)
Esquimalt Defence Research Detachment
P.O. Box 17000 Stn Forces
Victoria, British Columbia V9A 7N2
250 363 2849
fax 363 2856
Terry.Foster@edrd.dnd.ca

Mr Duane Giffin/Mr Ralph Wallis/
Mr Gary Harding
FMF CAPE SCOTT
P.O. Box 99000 Stn Forces
Halifax, Nova Scotia B3K 5X5

John Galsworthy
Structural Materials Center
Room 2008 Building A7
DERA Farnborough
Hampshire GU14 0LX
United Kingdom
01252 397294
fax 01252 397298

Julie Gauthier
Tektrend International Inc.
2113A St. Regis Boulevard
Dollard des Ormeaux QC H9B 2M9
(514) 421 1417 ext 123
julie.gauthier@tektrend-intl.com

Michael Gharghouri
Assistant Professor
Dept. Of Mining and Metallurgical Engr
Dal Tech, Dalhousie University
P.O.Box 1000
Halifax, Nova Scotia B3J 2X4
(902) 494-3297
Michael.Gharghouri@Dal.Ca

Mr Jim Gianetto
Materials Technology Labs
Natural Resources Canada
555 Booth St.
Ottawa, Ontario K1A 0G1
(613) 992-4425
fax(613) 992-8735
jgianett@nrcan.gc.ca

Layton Gilroy
Defence Research Establishment Atlantic
P.O.Box 1012
Dartmouth, Nova Scotia B2Y 3Z7

LCdr Tony Graham RCNC DMSS 2-2
National Defence Headquarters
101 Colonel By Drive
Ottawa, Ontario K1A 0K2
819 997 2268
fax 819 997 7058
tgraham@dmcs.dnd.ca

Mr. Randy Haggett
Dockyard Laboratory (A)
Defence Research Establishment Atlantic
P.O. Box 99000 Stn Forces
Halifax, Nova Scotia B3K 5X5
(902) 427-0550 Ext 3443
fax (902) 427-3435
haggett@drea.dnd.ca

Dr Robert Hay
TISEC Inc.
2113 St Regis Blvd Suite 250
Dollard, Montreal, QC
H9B 2M9
514 684 9096
fax 514 684 9035
bobhay@TISEC.com

Dr John Hiltz
Dockyard Laboratory (A)
P.O. Box 99000 Stn Forces
Halifax, Nova Scotia B3K 5X5
(902) 427-0550 Ext 3425
fax (902) 427-3435
hiltz@drea.dnd.ca

Mr. Paul Holsberg
Naval Surface Warfare Center
Carderock Division
Welding and NDE Branch, Code 610
West Bethesda, MD 20817-5700
(301) 227-4401
fax 301-227-5576
holsberg@oasys.dt.navy

Capt(N) G.D. Humby
Commanding Officer
FMF CAPE SCOTT
P.O. Box 99000 Stn Forces
Halifax, Nova Scotia B3K 5X5

Mr Don Hussey
Donelad Hydronautics Ltd.
Suite 720 Sun Tower
1550 Bedford Highway
Bedford N.S. B4A 1E6
902 835 5777
fax 902 835 6655
donelad@ns.sympatico.ca

Dr Calvin Hyatt
Dockyard Laboratory (A)
Defence Research Establishment Atlantic
P.O. Box 99000 Stn Forces
Halifax, Nova Scotia B3K 5X5
(902) 427-0550 Ext 3433
fax (902) 427-3435
hyatt@drea.dnd.ca

Terry Jones
Dockyard Laboratory (A)
Defence Research Establishment Atlantic
P.O. Box 99000 Stn Forces
Halifax, Nova Scotia B3K 5X5

Mr Ken KarisAllen
Facts Engineering
P.O.Box 20039
Halifax, Nova Scotia B3R 2K9
902 477 4062
fax 902 477 4062
facts@fox.nstn.ca

Steve Kavanaugh
Dockyard Laboratory (A)
Defence Research Establishment Atlantic
P.O. Box 99000 Stn Forces
Halifax, Nova Scotia B3K 5X5

Irv Keough
Dockyard Laboratory (A)
Defence Research Establishment Atlantic
Halifax, Nova Scotia B3K 5X5

Georges Kipouros
Dalhousie University - Dal Tech
Mining and Metallurgical Engineering
P.O.Box 1000
Halifax, Nova Scotia B3J 2X4
(902) 494 6100
fax (902) 425 1037
georges.kipouros@dal.ca

R.D. Klassen
Department of Chemistry and Chemical Engr
Royal Military College of Canada
PO Box 17000 Stn Forces
Kingston, Ontario K7K 7B4
613 541 6000 ext 6086
fax 542 9489
klassen@rmc.ca

Dr T.S. Koko
Martec Ltd
1888 Brunswick Street, Suite 400
Halifax, N.S. B3J 3J8
902 425 5101
fax 4211923
koko@martec.com

Derek Lenard
Dockyard Lab(E)
Esquimalt Defence Research Detachment
P.O. Box 17000 Stn Forces
Victoria, British Columbia V9A 7N2
250 363 2945
lenard@edrd.dnd.ca

Douglas MacDonald
In NovaCorp
101 Research Dr
PO Box 790
Dartmouth, Nova Scotia B2Y 3Z7
902 424 8670-190
fax 424-4679
dmacdonald@innovacorp.ns.ca

Gord MacDonald D200
FMF Cape Scott
P.O. Box 99000 Stn Forces
Halifax, Nova Scotia B3K 5X5
427 0550 ext 3802

Melanie MacDonald
Dockyard Laboratory (A)
Defence Research Establishment Atlantic
P.O. Box 99000 Stn Forces
Halifax, Nova Scotia B3K 5X5

Mr. Clive MacGregor
SEATECH Ltd.
958 Barrington St.
Halifax NS
B3H 2P7
cmacgreg@seatech.ns.ca

Mr Scott MacIntyre
In NovaCorp
101 Research Dr
PO Box 790
Dartmouth, Nova Scotia B2Y 3Z7
902 424 8670-185
fax 465 7384
SMacintyre@innovacorp.ns.ca

Mr Ken MacKay
Martec Ltd. Suite 400
1888 Brunswick St.
Halifax, Nova Scotia B3F 3F8
Mackay@martec.com

Ken McCormick
AQTS
15 Willett Ave.
P.O.Box 5250
St John, New Brunswick E2L 5C9
506 648 2226
fax 648 3522
aqts@nb.aibn.com

Dr. James R. Matthews
Dockyard Laboratory (A)
Defence Research Establishment Atlantic
P.O. Box 99000 Stn Forces
Halifax, Nova Scotia B3K 5X5
(902) 427-0550 Ext 3444
fax (902) 427-3435
matthews@drea.dnd.ca

Ken McRae A/H/AVRD
National Defence Headquarters
Constitution Building
305 Rideau St
Ottawa Ontario
K1A 0K2
613 991 6908
fax 613 993 4095
ken.mcrae@nrc.ca

Harold Merklinger
DG
Defence Research Establishment Atlantic
P.O.Box 1012
Dartmouth, Nova Scotia B2Y 3Z7

Barry Moore D200
Fleet Maintenance Facility Cape Scott
PO Box 99000 Stn Forces
Halifax, N.S. B3K 5X5
427 0550 ext 3987
fax 4270599

Dr. Richard Morchat
Head/ Dockyard Laboratory (A)
Defence Research Establishment Atlantic
P.O. Box 99000 Stn Forces
Halifax, Nova Scotia B3K 5X5
(902) 427-0550 Ext 3421
fax (902) 427-3435
morchat@drea.dnd.ca

Dan Morehouse
Dockyard Laboratory (A)
Defence Research Establishment Atlantic
P.O. Box 99000 Stn Forces
Halifax, Nova Scotia B3K 5X5

Binu Mukherjee
Professor of Physics
Royal Military College of Canada
PO Box 17000, Station Forces
Kingston Ontario K7K 7B4
Canada
613 541 6000 x 6348
fax 613 541 6040
mukherjee@rmc.ca

Dr. M.K.Murthy
MKM Consultants International
10 Avoca Avenue,Unit 1906
Toronto,Ont.
M4T 2B7

Dr. Sandra Nevill
Esquimalt Defence Research Detachment
Dockyard Lab(Pacific) Bldg 199D
P.O. Box 17000 Stn Forces
Victoria, British Columbia V9A 7N2
250 363 2892
sandra.nevill@edrd.dnd.ca

Mr Corby Nicholson
Materials Technology Centre
311 Legget Drive
Kanata, Ontario K2K 1Z8
Corby@fleetech.com

Mr. Marco Nottegar
University of Ottawa
Department of Chemical Engineering
161, rue Louis-Pasteur. C.P.450, Succ.A
Ottawa, ON
K7N 6N5
613 562 5800 ext 6094
fax 613 562 5172
marco.nottegar@sympatico.ca

Phillipe Ouellet D200
Fleet Maintenance Facility Cape Scott
PO Box 99000 Stn Forces
Halifax, N.S. B3K 5X5

Dr R.H. Packwood
Materials Technology Labs
Natural Resources Canada
555 Booth St.
Ottawa, Ontario K1A 0G1

Susan Pecman DMSS 2-4-2
National Defence Headquarters
101 Colonel By Drive
Ottawa, Ontario K1A 0K2
819 994 8648
fax 819 997 7058
specman@dmcs.dnd.ca

N.G. Pegg
Defence Research Establishment Atlantic
P.O.Box 1012
Dartmouth, Nova Scotia B2Y 3Z7
Pegg@drea.dnd.ca

John Power
Dockyard Laboratory (A)
Defence Research Establishment Atlantic
P.O. Box 99000 Stn Forces
Halifax, Nova Scotia B3K 5X5

Malcom Smith
Defence Research Establishment Atlantic
P.O.Box 1012
Dartmouth, Nova Scotia B2Y 3Z7

Gigi Pelletier
Dockyard Laboratory (A)
Defence Research Establishment Atlantic
P.O. Box 99000 Stn Forces
Halifax, Nova Scotia B3K 5X5

Lt(N) Russ Peters
FMF CAPE BRETON
Engineering Division (NA)
P.O. Box 17000 Stn Forces
Victoria, British Columbia V9A 7N2
250 363 5873
fax 250 363 2941

Mr. John Porter
Dockyard Laboratory (A)
Defence Research Establishment Atlantic
P.O. Box 99000 Stn Forces
Halifax, Nova Scotia B3K 5X5
(902) 427-0550 Ext 3423
fax (902) 427-3435
porter@drea.dnd.ca

Nick Pussegoda
Fleet Technology Ltd.
311 Legget Drive
Kanata, Ontario K2L 2E4
(613) 592-2830 ext 205
fax 613 592 4950
nickp@fleetech.com

David Rice Dept E 20
Research and Development
Newport News Shipbuilding
4101 Washington Ave.,
Newport News, Virginia 23607
757 688 1762
fax 757 688 8032
rice_dp@nns.com

Etienne Robichaud
Dockyard Laboratory (A)
P.O. Box 99000 Stn Forces
Halifax, Nova Scotia B3K 5X5

Dr George Roy
Materials Technology Labs
Natural Resources Canada
568 Booth St.
Ottawa, Ontario K1A 0G1
613 992 0328
fax 613 992 8735
groy@nrcan.gc.ca

Vincent Roy
Dockyard Laboratory (A)
P.O. Box 99000 Stn Forces
Halifax, Nova Scotia B3K 5X5
902 427 0550 x3446
fax 902 427 3435
roy@drea.dnd.ca

Dr. Alan Russell
Dockyard Lab(E)
Esquimalt Defence Research Detachment
P.O. Box 17000 Stn Forces
Victoria, British Columbia V9A 7N2
Russell@edrd.dnd.ca

Kumar Sadayappan
Metals Technology Labs
Natural Resources Canada
568 Booth St.
Ottawa, Ontario K1A 0G1
613 992 0741
fax 613 992 8735
ksadayap@nrcan.gc.ca

Daniel Salvage
Dockyard Laboratory (A)
Defence Research Establishment Atlantic
P.O. Box 99000 Stn Forces
Halifax, Nova Scotia B3K 5X5

Glen Shippam
FMF CAPE BRETON
Engineering Division (NA)
P.O. Box 17000 Stn Forces
Victoria, British Columbia V9A 7N2
250 363 5873
fax 250 363 2941

Shawn Smedmor
Fleetway Inc.
Suite 200
155 Chain Lake Drive
Halifax Nova Scotia B3S 1B3
450 2228
fax 494 5700
Smedmor.Shawn@SJNS.com

Frank Smith
Martec Ltd. Suite 400
1888 Brunswick St.
Halifax, Nova Scotia B3F 3F8
902 425 5101
fax 421 1923
fsmith@martec.com

Dave Stredulinski
Defence Research Establishment Atlantic
P.O.Box 1012
Dartmouth, Nova Scotia B2Y 3Z7

Dr Jeff Szabo
Dockyard Laboratory (A)
Defence Research Establishment Atlantic
P.O. Box 99000 Stn Forces
Halifax, Nova Scotia B3K 5X5
(902) 427-0550 Ext 3427
fax (902) 427-3435
szabo@drea.dnd.ca

Dr. Andre Y. Tremblay
University of Ottawa
Department of Chemical Engineering
161, rue Louis-Pasteur. C.P.450, Succ.A
Ottawa, ON
K7N 6N5
613 562 5800 ext 6094
fax 613 562 5172
ayt@eng.uottawa.ca

Mr. Dwight Veinot
Dockyard Laboratory (A)
Defence Research Establishment Atlantic
P.O. Box 99000 Stn Forces
Halifax, Nova Scotia B3K 5X5
(902) 427-0550 Ext 3428
fax (902) 427-3435
veinot@drea.dnd.ca

Norm Vinson
Institute for Information Technology
National Research Council
Montreal Rd Bldg M50
Ottawa K1A 0R6
613 993 2565
norm.vinson@iit.nrc.ca

Cdr Mark Walker
Defence Research Establishment Atlantic
P.O.Box 1012
Dartmouth, Nova Scotia B2Y 3Z7

J. Xiaozhu Wu
Dockyard Lab(P)
Esquimalt Defence Research Detachment
P.O. Box 17000 Stn Forces
Victoria, British Columbia V9A 7N2
250 363 5715
fax 250 363 2856
wu@edrd.dnd.ca

Lijue Xue
NRC
800 Collip Circle
London ON N6G 4X8
519 430 7059
fax 519 430 7064
lijue.xue@nrc.ca

Information Copies

Director
Defence Research Agency
Dunfermline
Rosyth Dockyard
Rosyth, Dunfermline, Fife, Scotland, U.K.
KY11 5PW

Procurement Executive NA121
Ash 0a
MOD Abbey Wood #95
PO Box 702
BRISTOL
BS12 7DU
United Kingdom

Director
Metals Technology Labs
Energy Mines and Resources Canada
555 Booth St.
Ottawa, Ontario K1A 0G1

Commanding Officer
FMF CAPE BRETON
P.O. Box 17000 Stn Forces
Victoria, British Columbia V9A 7N2

National Defence Headquarters Attn: DMSS
Ottawa Ontario
K1A 0K2

Mr Ray Gordon
National Defence Headquarters Attn: DMSS 2
Ottawa Ontario
K1A 0K2

Mr R. Weaver DMSS 3
National Defence Headquarters
Ottawa Ontario
K1A 0K2

Cdr M. Duncan DMSS 4
National Defence Headquarters
Ottawa Ontario
K1A 0K2

Cdr D. Dubowski Attn: DMSS 5
National Defence Headquarters
Ottawa Ontario
K1A 0K2

Mr. J. Muller Attn: DMSS 6
National Defence Headquarters
Ottawa Ontario
K1A 0K2

Capt. D. Murphy Attn: DMPPD
National Defence Headquarters
Ottawa Ontario
K1A 0K2

DG Ships
Ministry of Defence
Headquarters Building, Main Building
Whitehall SW1, London
UK

Director of Naval Construction
Royal New Zealand Navy
Headquarters New Zealand Defence Force
Private Bag
Wellington
New Zealand

Group Manager Materials
Directorate of Naval Architecture
Naval engineering Services Branch
Department of Defence
Campbell Park
CP-5-06
Canberra ACT 2600
Australia

Mike Sim
DECCNA CP1-5-17
Department of Defence
Canberra ACT 2600 Australia

Dr. Bruce R.W. Hinton
Maritime Platforms Division
Aeronautical & Maritime Research Laboratory
P.O. Box 4331, Melbourne
Victoria 3001, Australia

Gene L. Franke
Naval Surface Warfare Center
Carderock Division Code 615
9500 MacArthur Blvd.
West Bethesda, MD 20817-5700
USA
301-227-5571
fax 301 227 5576
franke@metals.dt.navy.mil

Mr RK Hughes
Department of Defence
Defence Science and Technology Organization
Aeronautical and Maritime Research Laboratory
Maritime Platform Division
PO Box 4331
Melbourne VIC 3001
Australia
Tel 03 9626 8323
fax 03 9626 8999

Dr. R.L. Jones
Structural Materials Center
Defence Evaluation and Research Agency
Farnborough, Hants, GU14 OLX
United Kingdom
011 44 1252 392125

Prof John DG Sumpter
DERA Rosyth
SMC Scotland
South Arm
Rosyth Royal Dockyard
Dunfermline
Fife
KY11 2XR
Scotland
1383 435147
fax 1383 435167

Philip Winter (Majumbar AMRL)
Australian Embasy
Washington
202-797 3380

Mr John Underwood
Army Armament RD&E Center
Building 115
Watervliet
New York
12189-4050
USA
Tel 518 266 4183
fax 518 266 5161

UNCLASSIFIED
SECURITY CLASSIFICATION OF FORM
(highest classification of Title, Abstract, Keywords)

DOCUMENT CONTROL DATA

(Security classification of title, body of abstract and indexing annotation must be entered when the overall document is classified)

1. **ORIGINATOR** (the name and address of the organization preparing the document. Organizations for whom the document was prepared, e.g. Establishment sponsoring a contractor's report, or tasking agency, are entered in section 8.)

Defence Research Establishment Atlantic
PO Box 1012
Dartmouth N.S. B2Y 3Z7

2. **SECURITY CLASSIFICATION** (overall security classification of the document including special warning terms if applicable).

Unclassified

3. **TITLE** (the complete document title as indicated on the title page. Its classification should be indicated by the appropriate abbreviation (S,C,R or U) in parentheses after the title).

Abstracts and Summaries of 8th CF/CRAD Meeting on Naval Applications of Materials Technology

4. **AUTHORS** (Last name, first name, middle initial. If military, show rank, e.g. Doe, Maj. John E.)

Matthews, James R. (editor)

5. **DATE OF PUBLICATION** (month and year of publication of document)

October 1999

6a. **NO OF PAGES** (total containing information Include Annexes, Appendices, etc).

approx 600

6b. **NO. OF REFS** (total cited in document)

more than 200

7. **DESCRIPTIVE NOTES** (the category of the document, e.g. technical report, technical note or memorandum. If appropriate, enter the type of report, e.g. interim, progress, summary, annual or final. Give the inclusive dates when a specific reporting period is covered).

Conference Proceedings (Special Report)

8. **SPONSORING ACTIVITY** (the name of the department project office or laboratory sponsoring the research and development. Include the address).

DREA

9a. **PROJECT OR GRANT NO.** (if appropriate, the applicable research and development project or grant number under which the document was written. Please specify whether project or grant).

1gh

9b. **CONTRACT NO.** (if appropriate, the applicable number under which the document was written).

10a **ORIGINATOR'S DOCUMENT NUMBER** (the official document number by which the document is identified by the originating activity. This number must be unique to this document).

DREA SR 1999-162

10b **OTHER DOCUMENT NOS.** (Any other numbers which may be assigned this document either by the originator or by the sponsor).

11. **DOCUMENT AVAILABILITY** (any limitations on further dissemination of the document, other than those imposed by security classification)

(X) Unlimited distribution
( ) Distribution limited to defence departments and defence contractors; further distribution only as approved
( ) Distribution limited to defence departments and Canadian defence contractors; further distribution only as approved
( ) Distribution limited to government departments and agencies; further distribution only as approved
( ) Distribution limited to defence departments; further distribution only as approved
( ) Other (please specify):

12. **DOCUMENT ANNOUNCEMENT** (any limitation to the bibliographic announcement of this document. This will normally correspond to the Document Availability (11). However, where further distribution (beyond the audience specified in 11) is possible, a wider announcement audience may be selected).

13. ABSTRACT (a brief and factual summary of the document. It may also appear elsewhere in the body of the document itself. It is highly desirable that the abstract of classified documents be unclassified. Each paragraph of the abstract shall begin with an indication of the security classification of the information in the paragraph (unless the document itself is unclassified) represented as (S), (C), (R), or (U). It is not necessary to include here abstracts in both official languages unless the text is bilingual).

This was the eighth naval materials CF/CRAD (Canadian Forces/Chief Research and Development) meeting. These meetings have been held every two years since 1985. The first four meetings were devoted to fabrication and inspection of submarine pressure hulls with sessions on welding, inspection and fracture. The last four have expanded to include all aspects of naval materials.

The purpose of these meetings has been to bring together industrial research contractors, university contractors, defence scientists, and NDHQ (National Defence Headquarters) design authorities from the naval materials technology area and invited scientists and engineers from other countries to share advances in naval materials technology in a conference like setting.

The program includes Welding and Laser Surface Modification, Environmental Research, Corrosion and Coatings, Vibroacoustic Materials, Ship Fracture, Fatigue, Firesafe Materials, Non-Destructive Evaluation, Metallurgy and Failure Analysis, Organic Materials (Polymers), Fuels and Lubricants and Naval Consulting.

14. KEYWORDS, DESCRIPTORS or IDENTIFIERS (technically meaningful terms or short phrases that characterize a document and could be helpful in cataloguing the document. They should be selected so that no security classification is required. Identifiers, such as equipment model designation, trade name, military project code name, geographic location may also be included. If possible keywords should be selected from a published thesaurus. e.g. Thesaurus of Engineering and Scientific Terms (TEST) and that thesaurus-identified. If it not possible to select indexing terms which are Unclassified, the classification of each should be indicated as with the title).

naval materials
corrosion
coatings
welding
fracture
NDE
fatigue
laser surface modification
fire safe materials
organic materials
polymers
vibration materials
damping materials